



JAEA Takasaki Annual Report 2010

(Ed.) Takuji KOJIMA

Takasaki Advanced Radiation Research Institute

January 2012

Japan Atomic Energy Agency

日本原子力研究開発機構

本レポートは独立行政法人日本原子力研究開発機構が不定期に発行する成果報告書です。
本レポートの入手並びに著作権利用に関するお問い合わせは、下記あてにお問い合わせ下さい。
なお、本レポートの全文は日本原子力研究開発機構ホームページ (<http://www.jaea.go.jp>)
より発信されています。

独立行政法人日本原子力研究開発機構 研究技術情報部 研究技術情報課
〒319-1195 茨城県那珂郡東海村白方白根 2 番地 4
電話 029-282-6387, Fax 029-282-5920, E-mail: ird-support@jaea.go.jp

This report is issued irregularly by Japan Atomic Energy Agency
Inquiries about availability and/or copyright of this report should be addressed to
Intellectual Resources Section, Intellectual Resources Department,
Japan Atomic Energy Agency
2-4 Shirakata Shirane, Tokai-mura, Naka-gun, Ibaraki-ken 319-1195 Japan
Tel +81-29-282-6387, Fax +81-29-282-5920, E-mail: ird-support@jaea.go.jp

JAEA Takasaki Annual Report 2010

(Ed.) Takuji KOJIMA

Takasaki Advanced Radiation Research Institute

Japan Atomic Energy Agency

Watanuki-machi, Takasaki-shi, Gunma-ken

(Received November 17, 2011)

JAEA Takasaki annual report 2010 describes research and development activities performed from April 1, 2010 to March 31, 2011 with Takasaki Ion Accelerators for Advanced Radiation Application (TIARA, four ion accelerators), and electron/gamma-ray irradiation facilities (an electron accelerator and three ^{60}Co gamma-ray irradiation facilities) at Takasaki Advanced Radiation Research Institute, Japan Atomic Energy Agency (JAEA Takasaki). These activities are classified into four research fields: 1) Space, Nuclear and Energy Engineering, 2) Environmental Conservation and Resource Exploitation, 3) Medical and Biotechnological Application, and 4) Advanced Materials, Analysis and Novel Technology. This annual report contains 159 reports consisting of 151 research papers and 8 status reports on operation/maintenance of the irradiation facilities described above, and a list of publications, patents, related press-releases, television broadcasting, and the type of research collaborations as Appendices.

Keywords: TIARA, Ion Accelerators, Electron Accelerator, Gamma-ray Facilities, Nuclear and Energy Engineering, Environmental Conservation, Resource Exploitation, Medical Application, Biotechnological Application, Advanced Materials, Analysis, Novel Technology, Materials for Space, Semiconductors, Inorganic Materials, Organic Materials, Functional Materials, Radiation Chemistry, Radiation Biology, Radioisotope Production, Nuclear Chemistry, Material Analyses, Solid State Physics, Microbeam Technology, Accelerator Technology, Accelerator Operation, Safety Control

(Editorial committee) Takuji KOJIMA, Atsushi TANAKA, Masao TAMADA,
Wataru YOKOTA, Kazumasa NARUMI, Shimpei MATSUHASHI,
Kiyoshi MIZUHASHI, Hiroshi YOSHIDA and Yoshiteru NAKAMURA

高崎量子応用研究所研究年報 2010

日本原子力研究開発機構 高崎量子応用研究所
(編) 小嶋 拓治

(2011 年 11 月 17 日受理)

高崎量子応用研究所研究年報 2010 は、同研究所にある TIARA 施設(イオン加速器 4 基)及び電子・ガンマ線照射施設(電子加速器 1 基、 ^{60}Co ガンマ線照射施設 3 棟)を利用して 2010 年 4 月 1 日から 2011 年 3 月 31 日までの間に行われた研究・技術開発成果をまとめたものである。この研究年報には、1) 宇宙・原子力・エネルギー、2) 環境保全・資源利用、3) 医療・バイオ技術応用、4) 先端材料・分析・基盤技術の 4 分野に分類した 151 編の論文及び 8 編の施設の運転・管理状況報告からなる合計 159 編を収録する。また、論文リスト、出願特許、新聞発表、テレビ放映及び研究実施形態・利用施設の一覧表を付録として含む。

高崎量子応用研究所：〒370-1292 群馬県高崎市綿貫町 1233

編集委員：(著者代表) 小嶋 拓治、田中 淳、玉田 正男、横田 渉
鳴海 一雅、松橋 信平、水橋 清、吉田 宏、中村 義輝

PREFACE

This report covers research and development activities in Takasaki Advanced Radiation Research Institute, JAEA, during the period from April 2010 to March 2011 conducted with TIARA (Takasaki Ion Accelerators for Advanced Radiation Application), electron beam and Co-60 gamma-ray irradiation facilities.

This annual report contains 159 papers in the fields of

- 1) Space, Nuclear and Energy Engineering,
- 2) Environmental Conservation and Resource Exploitation,
- 3) Medical and Biotechnological Application,
- 4) Advanced Materials, Analysis and Novel Technology,
- 5) Present Status of Irradiation Facilities.

In the field of Space Engineering, radiation induced damage of semiconductor devices which will be caused by cosmic rays has been evaluated using high energy electrons, protons and heavy ions. The occurring effects in the devices were analyzed by means of transient current and durability for fabrication planning of new radiation-resistant devices. For Nuclear and Energy Engineering, the practically available results were led for radiation stabilities of organic extractants and polymeric insulators for irradiation facilities such as ITER, J-PARC and aging LWRs. The radiation durability of barrier materials for geological disposal, alloys for the next generation reactors and for the reprocessing plant, and lighting for nuclear facilities was inspected in corresponding high radiation environments. Graft polymerization synthesized promising electrolyte membranes for fuel cells as research for future energy.

In the field of Environmental Conservation and Resource Exploitation, naturally occurring polymers such as cellulose fabric and kenaf fiber were used for the trunk polymers for graft polymerization. A graft adsorbent was applied to decolorization of agricultural wastewater from livestock urine. Furthermore, grafting was used for surface modification of vulcanized rubber for car wiper. Hydro-gels produced by crosslinking of hydroxypropyl cellulose have been investigated to improve the characteristics such as transparency and mechanical strength. R&Ds of the decomposition of persistent antibiotics in wastewater using ionizing radiation have been performed to develop new process technologies for environmental conservation. Recovery of platinum was carried out from waste silicon rubber as recovery of rare earth materials.

In the field of Medical and Biotechnological Application, a novel fluorescence-based method was developed to study the quantity as well as the spatial distribution of DNA damage, and the LET dependence of mutational effects of ion beams was investigated to find out the significance of clustering of DNA damage. Radiation-induced bystander cell-killing effects

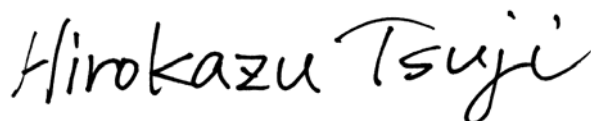
were investigated using heavy-ion microbeams. The survival rate of non-irradiated cells did not change at 6 h but decreased at 24 h following irradiation with the rate of 90% of control cells, suggesting that the radiation-induced bystander effect leads a part of non-irradiated cells to reproductive death and that it is dependent on time following irradiation. The in-air micro particle-induced X-ray/Gamma-ray emission (micro-PIXE/PIGE) system has been utilized for the micron-sized trace-element mapping in bio-medical applications of analysis of asbestos-lung tissues, stress effects on the brain, fluorine uptakes in carious enamel, and so on. The PIXE-CT (computed tomography) technique was also improved in spatial resolution using a new image reconstruction algorithm. Radionuclides, which are produced by the AVF cyclotron, have been used for cancer therapy and diagnosis. Radiopharmaceutical for diagnosis of malignant tumors which is ^{76}Br labeled tyrosine analog (3-[^{76}Br]bromo- α -methyl-L-tyrosine) was successfully prepared as a new positron emission tomography (PET) probe. On the other hand, the plants absorb and utilize carbon and nitrogen from the air, and the other nutrients and pollutants from the soil. Various experimental methods of positron-emitting tracer imaging system (PETIS) have been established which enable quantitative analyses on such plant functions by realizing quantitative image-collection within the field-of-view. The ion beam breeding has been applied for many kinds of plants and microorganisms such as chrysanthemum, petunia, rice, yeast and rhizobium to obtain new useful varieties. By ion-beam irradiation to an endophytic *Pseudomonas* strain, mutants that have enhanced suppressiveness against the tomato bacterial wilt were obtained. Studies on mutational effects of ion beams near range end were progressed using Arabidopsis.

In the field of Advanced Materials and Analysis, various materials were developed by applying ion- or electron-irradiation with analyses of its effect: nano-crystalline SiC nanotubes, SiC nanofibers, SiC membranes with gas permeation, polymer nanowires, polymer optical waveguides, hydrogen-storage alloys, Al-Cu-Mg alloys, Ti nitrides and so on. Radiation damage of the following materials has been investigated: carbon foils for charge-stripping process at J-PARC, SiC/SiC composites, CeO_2 , GaN, high-purity α -quartz, and polyimide polymers. A reflection-high-energy-positron-diffraction (RHEPD) technique, a powerful tool especially for analysis of a surface of a single crystal, has been used to investigate super structures on clean semiconductor surfaces.

As for the Novel Technology, radiation chemistry studies on radiolysis of water or organics were carried out using ^{60}Co gamma-rays, MeV-electron beams, and pulsed heavy ion beams involving the effects of oxide gradients or the development of time-resolved radiolysis techniques. Different kinds of detectors were examined for energy-spectral measurement of low-energy neutrons, position measurement of medical gamma-ray radioisotopes, and absorbed dose measurement of MeV-electron beams or laser-driven He ion beams. The

fundamental studies on the interaction between MeV/atom cluster ions and target materials for C_2 - C_{60} and Au_1 - Au_3 were performed on the basis of the measurement of secondary ions/electrons or luminescence emitted from materials, and energy deposition/loss estimated by the Molecular Dynamics calculation or vacancy-measurement using positron annihilation analysis. The 3D micro-fabrication technique using Proton-Beam-Writing (PBW) was also developed for various nano-structure patterns such as lines, bridge or jigsaw puzzle. Technical developments were in progress for fast single-ion hit, wide uniform-beam formation, quick beam change for microbeams, and emittance/acceptance measurement for higher available intensity at the AVF cyclotron. Developments of new beam generation/irradiation technique for cluster ions as well as real-time detection technique of single-ion hit were also in progress at electrostatic accelerators. The development of new positron sources was also attempted for high spin-polarized beams and microbeams.

About the Present Status of Irradiation Facilities, all the accelerators in TIARA, namely the AVF cyclotron, the 3-MV tandem accelerator, the 3-MV single-ended accelerator and the 400-kV ion implanter were operated steadily and safely as well as MeV-electron and Co-60 gamma-ray irradiation facilities, till the Great East Japan Earthquake on March 11th 2011. Fortunately no severe damages occurred in any facilities by the earthquake, and we operated again electron and gamma-ray irradiation facilities in April, and TIARA in May after the careful inspection. On the other hand, Saturday operation of twelve days for the cyclotron and ten days for three electrostatic accelerators was carried out after October 2010 under the nuclear human resource development program. Total operation times of the tandem accelerator, the single-ended accelerator, and the ion implanter were 34,538, 39,231, and 30,675 hours, respectively. The total number of experiments made by various users using the AVF cyclotron was 8,719 from the first beam extraction in 1991 to March 2011, as a result of continuous efforts such as regular maintenance and trouble shooting.



Hirokazu Tsuji,
Director General
Takasaki Advanced Radiation Research Institute
Japan Atomic Energy Agency

This is a blank page.

Contents

1. Space, Nuclear and Energy Engineering	1
1-01 Effect of Beam Expansion Methods on Radiation Degradation of Solar Cells ...	5
1-02 Effect of Body-tie Structure Fabricated by Partial Trench Isolation for Suppression of Soft Errors in SOI SRAM Investigated by Helium and Oxygen Ion Probes	6
1-03 Improved Radiation Hardness for Angle Irradiation in DICE Latches on a 90 nm Bulk CMOS Process	7
1-04 Heavy-ion Induced Current in SOI p ⁺ n Junction Diode	8
1-05 Estimation of Digital Single Event Transient Pulse-Width in Logic LSIs from Transient Current Waveforms in a MOSFET	9
1-06 TIBIC Mapping of 6H-SiC n-channel MOSFETs	10
1-07 Electric Conductivity of Proton-Irradiated Hydrogenated Amorphous Silicon Semiconductors	11
1-08 Research of Radiation Tolerance for Application of General Electronic Devices to Space Environment	12
1-09 Total Dose Effect on Pentacene-based Organic Thin Films Field Effect Transistors	13
1-10 Yield and Coherence Time of the NV Centers Created by MeV Range Nitrogen Ion Implantation of Diamond	14
1-11 Luminescence Properties and Ion-Beam-Induced Damage in Rare Earth Ion Doped AlGaN	15
1-12 Single Ion Induced Luminescence from ZnS(Ag), CdWO ₄ , YAG:Ce and Diamond	16
1-13 First-Principles Molecular Dynamics Simulation of SiO ₂ /SiC Interface of Silicon Carbide Devices (II).....	17
1-14 Influence of Energy of Helium Ions on Degradation of Diglycolamide in <i>n</i> -Dodecane	18
1-15 Confirming Performance of Expanded Bed for Chromatographic Separation by Gamma Irradiation Experiment	19
1-16 Irradiation Effect of Gamma Rays on Cyanate Ester/Epoxy Resins (2)	20
1-17 Effects of Antioxidants on the Degradation of Flame-Retardant Ethylene Propylene Rubber.....	21
1-18 Alpha-Ray Irradiation Damage on Materials Applied for Glove Box for Plutonium Powder Treatment	22
1-19 Development of an Observation Technique Using a Fiberscope under High Radiation Doses	23
1-20 Electrification of Coaxial Cable Model by Gamma-rays Irradiation	24

1-21	Gamma-Ray Irradiation Test of Centrifugal Contactor with Magnetic Bearing System	25
1-22	Development of Penetration Part Processing Industrial Method in Radiation Controlled Area (Airtight Performance Examination)	26
1-23	Development of Radiation-resistant Lighting	27
1-24	Evaluation of Hydrogen Formation by Gamma-ray Irradiation in Sodium Nitrate Solution with TiO ₂ Colloids	28
1-25	Gas Generation by Gamma-Ray Irradiation to Polyethylene, Polystyrene and Cellulose Resin	29
1-26	Studies on Microstructure and Elemental Distributions of Barrier Materials for Geological Disposal of Radioactive Waste	30
1-27	Effect of Dissolved Hydrogen on Helium Ion beam Radiolysis of Water	31
1-28	Preliminary Models on Radiation Induced Changes of Microstructure and Stress-Strain Relations to Estimate Mechanical Response of Austenitic Steel Components	32
1-29	Microstructural Evolution in Extra High Purity Ni-base Superalloy Ion-irradiated under External Stress	33
1-30	Microstructural Evolution of G-phase Strengthened Ni-base Alloy under Multi-ion Irradiation	34
1-31	Conductometric Analysis of Track Etching in Poly(vinylidene fluoride) Films Irradiated with Different MeV-GeV Ion Beams	35
1-32	Preparation of Anion-Exchange Membranes for Fuel Cell Applications by γ -ray Pre-Irradiation Grafting: Crosslinker Effect	36
1-33	Preparation of Poly(ether ether ketone)-based Polymer Electrolytes for Fuel Cell Membranes Using Radiation-induced Graft Polymerization	37
1-34	Stability of Radiation Grafted Membranes in HIX Solution of Electro-electrodialysis	38
1-35	Radiation Degradation Properties of Grafted Polymer Electrolyte Membranes	39
1-36	Polymerization Kinetics of Ion-Track Grafting with Different Beams	40
2.	Environmental Conservation and Resource Exploitation	41
2-01	A Simple Method for Radiation-Induced Graft Polymerization using a Polyethylene Bottle as a Reactor	43
2-02	Radiation-induced Grafting of Acrylonitrile Monomer onto Cellulose Nonwoven Fabric	44
2-03	The Effect of Partial Delignification on Kenaf Bast Fibers for Radiation Graft Polymerization	45
2-04	Development of Anion Adsorbent for Industry Application Based on Biodegradable Trunk Material	46

2-05	Synthesis of Amine-type Adsorbents with Emulsion Graft Polymerization of 4-hydroxybutyl Acrylate Glycidylether	47
2-06	Decolorization of Secondary Treated Water from Livestock Urine Waste	48
2-07	Effect of Gamma-rays Irradiation of Hydroxypropylmethylcellulose Aqueous Solution	49
2-08	Transparent Hydrogels Prepared by Radiation Crosslinking Hydroxypropyl Cellulose with Functional Monomers	50
2-09	Introduction of Cross-linking into Fluoro-rubber by Gamma-ray Irradiation for the Improvement of Its Compression Set	51
2-10	Surface Modification of Vulcanized Rubber by Radiation Co-grafting	52
2-11	Decomposition of Persistent Antibiotics by Ionizing Radiation	53
2-12	Development of Fibrous Adsorbent for Polyols	54
2-13	Recovery of Platinum from Waste of Silicon Rubber with Amine and Nuclear Acid Adsorbent Synthesized by Graft-Polymerization	55
2-14	Preparation and Characterization of the Low Molecular Weight Funoran	56
3.	Medical and Biotechnological Application	57
3-01	Development of a Method for Estimating Degree of Dispersion of Lesions on DNA	63
3-02	Mutagenic Effects of He Ion Particles in <i>Escherichia coli</i>	64
3-03	Target Irradiation of Individual Cells Using Focusing Heavy-Ion Microbeam of JAEA-Takasaki (II)	65
3-04	Beam Profile Rapid-evaluation of Heavy-ion Microbeam in the Atmosphere Using Semi-automatic Image Analysis	66
3-05	Radiation-induced Bystander Cell-killing Effect Is Dependant on Time Following Irradiation and Independent of LET	67
3-06	Cell Motility of Human Non-Small-Cell Lung Cancer Cells after Carbon-Ion Beam Irradiation	68
3-07	Biological Effects of Combining Temozolomide with Carbon Ions on Glioblastoma Cell Lines	69
3-08	Mechanisms for the Contributions of Bystander Effects to the Responses Induced by Low Dose/Low Dose Rate Radiation	70
3-09	Analysis of Bystander Cell Signaling Pathway Activated by Heavy Ion-Microbeam II	71
3-10	Ion-species Dependent Bystander Lethal Effect in Normal Human Fibroblasts Induced by C-, Ne- and Ar-ion Microbeams	72
3-11	Analysis of Bystander Effect Induced by Cell Membrane Response in Glioma Cells	73
3-12	Expression of Glutathione Peroxidase, p53, Bcl-2, and BAX Genes in Gamma-Irradiated Human Retinal Vascular Endothelial Cells	74

3-13	Bystander Effect of Carbon Ion Beam-Induced Senescent Glioma Cells on Infectivity of Human Immunodeficiency Virus Type 1 (HIV-1).....	75
3-14	Insect Cell Could Restart the Cell Cycle before Sufficient Repair of the DNA Damage by Heavy-ion Irradiation	76
3-15	Comparison of Histological Responses in Medaka Testis after Heavy-Ion Broad- and Micro-Beam Irradiation	77
3-16	Anhydrobiosis-Specific Genes in the Sleeping Chironomid Are also Responsive to Ionizing Radiation	78
3-17	Cytokine Production is Suppressed in Human THP-1 Macrophages by Direct Stimulation with Heavy-ions and Bystander Responses Due to Microbeam Irradiation of a Limited Cell Population	79
3-18	Effects of Carbon-ion Irradiation on Locomotion and Pharyngeal Pumping in <i>Caenorhabditis elegans</i>	80
3-19	Relaxation Behaviors of Electron Spin in Irradiated Fresh Papayas	81
3-20	Initial Decay Process of Radicals Induced in Irradiated Food	82
3-21	Improvement of Spatial Resolution of PIXE-CT Using ML-EM Algorithm in TIARA	83
3-22	The Effects of Essence of Chicken on the Trace Metal Distribution in Stressful Mice Brain Slices by In-Air Micro-PIXE.....	84
3-23	Measurement of Fluorine Distribution in Carious Enamel around 1.5-year Aged Fluoride-containing Materials	85
3-24	The Analysis of Boron Micro-Distribution in 9L Gliosarcoma Cells and HUVEC cells Using PIXE and PIGE.....	86
3-25	Analysis on the Co-localization of Asbestos Bodies and Fas or CD163 expression in Asbestos Lung Tissue by In-Air Micro-PIXE	87
3-26	Analysis of Trace Elements in Erythrocytes Obtained from Dialysis Patients Using In-Air Micro PIXE	88
3-27	Increased Antitumor Effect of Chemotherapy, Using Radiosensitive Microcapsules Containing Anti-RLIP076	89
3-28	Elemental Mapping and Estimation of Elemental Abundances of Lichen by TIARA Micro Beam PIXE	90
3-29	Preparation and Biological Evaluation of 3-[⁷⁶ Br]Bromo- α -methyl-L-tyrosine, a Novel Tyrosine Analog for PET Imaging of Tumors.....	91
3-30	Production of Radioactive Bromine Br-76	92
3-31	Carbon Kinetic Analysis in a Soybean Plant by Using Newly Developed Real-time Whole-plant Imaging Method with Positron-Emitting Tracer Imaging System (PETIS)	93
3-32	Quantitative Study for Nitrogen Fixation in Intact Soybean Plant from PETIS Imaging	94
3-33	Dose Optimization of ¹⁰⁷ Cd for Direct Imaging of Cd Uptake from Culture to Root	95

3-34	Comparison of ^{107}Cd Absorption and Accumulation between Transgenic Tobacco Plants and Control Plants	96
3-35	Effects of Preceding Light Conditions on Translocation of Photoassimilates from a Leaf into a Fruit	97
3-36	Analysis of Source-sink Regulation System Using Cold-girdling and Positron-Emitting Tracer Imaging System (PETIS)	98
3-37	Genetic Interaction between COP9 Signalosome and SMAP1 That Function in the 2,4-D Response in Arabidopsis	99
3-38	Development of Ion Beam Breeding Technology in Plants and Creation of Useful Plant Resources	100
3-39	Ion Beam Irradiation on Rice Seeds for the Mutation Breeding Project of the Forum for Nuclear Cooperation in Asia (FNCA)	101
3-40	Characterization of Ion Beam Irradiated Chrysanthemum Plants	102
3-41	Mutational Effects of Carbon Ions near Range End in Arabidopsis	103
3-42	Analysis of Mutated Region on DNA in Ion Beam-Induced UVB Tolerant or Sensitive Rice Mutant	104
3-43	Stability Evaluation of Mutant Lines Induced by Ion Beam Breeding in Petunia ..	105
3-44	Lethal Effects of Different LET Radiations in Gene Disruptant Strain of <i>Deinococcus radiodurans</i>	106
3-45	Involvement of Universal Conserved Genes, <i>ygiD</i> and <i>yeaZ</i> Orthologs, in DNA Repair of <i>Deinococcus radiodurans</i>	107
3-46	Fundamental Study on Molecular Mechanism Underlying Repair of Heavy-Ion Induced DNA Damage in the <i>Saccharomyces cerevisiae</i>	108
3-47	Characteristics of Mutant Endophytic Bacteria Strains Improved Using Ion beams	109
3-48	Colony Morphology of High Temperature Tolerant Mutants of <i>Bradyrhizobium japonicum</i> USDA110 Obtained by Ion-beam Microbial Mutation-breeding Technology	110
3-49	Repeated FACS-based Screening for Yeast Strain Highly Expressing Cellulase	111
3-50	Fungicide Tolerant Mutation of Entomopathogenic Fungi Induced by Carbon Ion Beams	112
3-51	Ion Beam Breeding of “Sake Yeast” and Test Brewing - the Second Report	113
3-52	The Long-term Storage of Rhizobial Biofertilizer Made from γ -sterilized Carriers	114
4.	Advanced Materials, Analysis and Novel Technology	115
4-01	Oxygen Reduction Activity of Transition Metal and Nitrogen Doped Carbon Films Prepared by Pulsed Laser Deposition	119
4-02	Fabrication of Functionalized Polystyrene Nanowires by the Single Particle Nano-Fabrication Technique	120

4-03	Formation of Poly(vinylphenol) Nanowires Including Au Nanoparticles by Ion Beam Irradiation	121
4-04	Radius Control of SiC Nano Fiber by Two Steps Irradiation Method Using Ion and Electron Beams	122
4-05	Gas permeation Property of Silicon Carbide Membrane Prepared on Porous Alpha Alumina Support Using Radiation Curing of Polymer Precursor Film	123
4-06	Synthesis of Nano-Crystalline SiC Nanotubes by Ion-Irradiation Technique	124
4-07	Study for Damage of Charge Stripper Carbon Foil by Ion Beam Irradiation	125
4-08	Fabrication of Y-Junction Waveguides Using Proton Beam Writing	126
4-09	Hydriding Property of Hydrogen Storage Alloy by Charged Particle Under Different Irradiation Environment	127
4-10	Hardening of Al-Cu-Mg Alloy by Energetic Ion Irradiation	128
4-11	Ion Doping Technique Related to Nano-Machining on Unworkable Oxidation Ceramics	129
4-12	Characterization of N-Behavior in Nitriding Processes of Deposited-Ti Thin Films due to Ion Implantation	130
4-13	The Effects of Displacement Damage and Transmutation Atoms on Dimensional Stability of SiC with Impurities	131
4-14	Detection of Implanted ^{12}C in Ag/Ni/ α - Al_2O_3 (0001) Employing Non-Rutherford Elastic Scattering Process	132
4-15	Radiation Damages in CeO_2 Thin Films Irradiated with Ions Having the Same Nuclear Stopping and Different Electronic Stopping Powers	133
4-16	Irradiation-induced-defect Recovery and Magnetic Property of the Gd^+ Ion Implanted GaN	134
4-17	Gamma-ray Induced Defect Formation in High-Purity α -Quartz	135
4-18	Adsorption Site of Alkali Metals on $\text{Si}(111)-\sqrt{3}\times\sqrt{3}$ -Ag Surface Studied by Reflection High-Energy Positron Diffraction	136
4-19	Structural Phase Transition of Pt/Ge(001) Surface Studied by Reflection High-energy Positron Diffraction	137
4-20	Recovery Behavior of Vacancies in Type 304 Stainless Steels Studied by Positron Annihilation Spectroscopy	138
4-21	Positron Annihilation Lifetime of Irradiated Polyimide	139
4-22	ESR Study of Ion-beam-induced Silyl Radical Generation in Single Crystals	140
4-23	Effect of Alumina Particle on the Enhancement of H_2 Production and the Reduction of H_2O_2 Concentration in the γ -radiolysis of Aqueous Solutions	141
4-24	Incident Energy Dependences of Transient Species in Water under Pulsed H^+ Ion Irradiation	142
4-25	LET Effect on the Radiation Induced Copolymerization of Maleimide with Styrene in 2-Propanol Solution	143
4-26	Measurement of the Ion Beam Pulse Radiolysis Using Scintillator	144
4-27	Three-Dimensional Imaging Test for a Head Module of a Si/CdTe Compton Camera for Medical Application	145

4-28	Improvement of Measurement System for Source Neutron Spectrum to extend the Energy Range down to a few MeV	146
4-29	Measurements of Low Energy Neutron Spectra of Quasi-Monoenergetic Neutron Fields at TIARA	147
4-30	Test Measurement of Neutron Energy Spectra on Thin Targets Bombarded with 13 MeV/nucleon ^{20}Ne	148
4-31	Systematic Measurement of Neutron and Gamma-ray from Thick Targets Bombarded with 12 and 18 MeV Protons	149
4-32	Spectroellipsometric Studies on EB Induced Refractive Index Change of Aliphatic Polyimide	150
4-33	Measurement of Charge States Corresponding to Relative Position of Constituent Ions Resulting from Foil-induced Dissociation of Aligned C_2^+ Ions	151
4-34	Ion Induced Luminescence from Sapphire Irradiated with Swift Cluster Ion Beams - Energy Dependence of Incident Cluster Beams -	152
4-35	Energy Deposition in Carbon by MeV/atom Carbon Cluster Ions	153
4-36	Study on Au Cluster Ion Irradiation Effects for Fz-Si Single Crystal by Using Slow Positron Beam	154
4-37	Energy Dependence of Nonlinear Effects of Sputtering Yields of Si Bombarded with 10-540-keV C_{60} Ions	155
4-38	Secondary Ion Emission from PTFE upon C_{60} Ion Impacts	156
4-39	Status Report on Technical Development of the JAEA AVF Cyclotron Facility •	157
4-40	Development of Beam Generation and Irradiation Technology for Electrostatic Accelerators	158
4-41	Fast Single-Ion Hit System for Heavy-Ion Microbeam at TIARA Cyclotron (IV)	159
4-42	Development of Real-time Single-ion Hit Detection System and IBIL System ••	160
4-43	Research and Development on Heavy-ion Uniform-beam Formation by Nonlinear Focusing	161
4-44	3D Micro-fabrication Utilized Superimposing Technique with Focused MeV Ion Beams	162
4-45	Electroforming of Ni Mold Using High-aspect-ratio PMMA Microstructures Fabricated by Proton Beam Writing	163
4-46	Calibration of Beam Profile Diagnostic Utilizing Back-Scattered Particles for Laser-driven Ions	164
4-47	Development of Fine Devices Using Proton Scanning Microbeam	165
4-48	Spin-Polarize Positron Beam Based on ^{68}Ge - ^{68}Ga Source Produced by Cyclotron	166
4-49	Improvement of a Positron Gun Suitable for Intense Microbeam Production •••	167

5. Present Status of Irradiation Facilities 2010	169
5-01 Feature in FY2010, Utilization Status and Beam Time Proportion at TIARA Facility	171
5-02 Operation of the AVF Cyclotron	172
5-03 Operation of the Electrostatic Accelerators	173
5-04 Operation of the Electron Accelerator and Gamma-ray Irradiation Facilities	174
5-05 Utilization of the Gamma-ray Irradiation Facilities and Electron Accelerator	175
5-06 FACILITY USE PROGRAM in Takasaki Advanced Radiation Research Institute	176
5-07 Radiation Control in TIARA	177
5-08 Radioactive Waste Management in TIARA	178
Appendix	179
Appendix 1 List of Publication	180
Appendix 2 List of Related Patents	200
Appendix 3 List of Related Press-Release and Television Broadcasting	202
Appendix 4 Type of Research Collaboration and Facilities Used for Research	204
Appendix 5 A Typical Example of Abbreviation Name for Organizations in Japan Atomic Energy Agency (JAEA)	206

1. Space, Nuclear and Energy Engineering

1-01	Effect of Beam Expansion Methods on Radiation Degradation of Solar Cells ••	5
	M. Imaizumi, M. Saito, Y. Yuri, S. Sato and T. Ohshima	
1-02	Effect of Body-tie Structure Fabricated by Partial Trench Isolation for Suppression of Soft Errors in SOI SRAM Investigated by Helium and Oxygen Ion Probes •••••	6
	S. Abo, N. Masuda, F. Wakaya, S. Onoda, T. Makino, T. Hirao, T. Ohshima, T. Iwamatsu, H. Oda and M. Takai	
1-03	Improved Radiation Hardness for Angle Irradiation in DICE Latches on a 90 nm Bulk CMOS Process •••••	7
	A. Maru, H. Shindou, S. Kuboyama, H. Abe, T. Hirao and T. Ohshima	
1-04	Heavy-ion Induced Current in SOI p ⁺ n Junction Diode •••••	8
	Y. Takahashi, H. Takeyasu, Y. Okazaki, T. Hirao, S. Onoda and T. Ohshima	
1-05	Estimation of Digital Single Event Transient Pulse-Width in Logic LSIs from Transient Current Waveforms in a MOSFET •••••	9
	T. Makino, S. Onoda, T. Hirao, T. Ohshima, D. Kobayashi, H. Ikeda and K. Hirose	
1-06	TIBIC Mapping of 6H-SiC n-channel MOSFETs •••••	10
	S. Onoda, T. Makino, N. Iwamoto, K. Kojima, S. Nozaki and T. Ohshima	
1-07	Electric Conductivity of Proton-Irradiated Hydrogenated Amorphous Silicon Semiconductors •••••	11
	S. Sato, T. Ohshima and M. Imaizumi	
1-08	Research of Radiation Tolerance for Application of General Electronic Devices to Space Environment •••••	12
	N. Sasaki, Y. Kakimi, K. Adachi, T. Maeda, S. Yamada, T. Ohshima, T. Hirao and S. Onoda	
1-09	Total Dose Effect on Pentacene-based Organic Thin Films Field Effect Transistors •••••	13
	T. Hirao, Li Cai, H. Yano, T. Ohshima and Y. Nishioka	
1-10	Yield and Coherence Time of the NV Centers Created by MeV Range Nitrogen Ion Implantation of Diamond •••••	14
	J. Isoya, T. Umeda, T. Ohshima, S. Onoda, S. Sato and N. Morishita	
1-11	Luminescence Properties and Ion-Beam-Induced Damage in Rare Earth Ion Doped AlGaIn •••••	15
	A. Wakahara, H. Okada, J. -H. Park, S. Sato and T. Ohshima	
1-12	Single Ion Induced Luminescence from ZnS(Ag), CdWO ₄ , YAG:Ce and Diamond •••••	16
	S. Onoda, T. Makino and T. Ohshima	
1-13	First-Principles Molecular Dynamics Simulation of SiO ₂ /SiC Interface of Silicon Carbide Devices (II) •••••	17
	A. Miyashita and M. Yoshikawa	

1-14	Influence of Energy of Helium Ions on Degradation of Diglycolamide in <i>n</i> -Dodecane	18
	Y. Sugo, M. Taguchi, Y. Sasaki and Y. Morita	
1-15	Confirming Performance of Expanded Bed for Chromatographic Separation by Gamma Irradiation Experiment	19
	S. Watanabe, K. Nomura, Y. Sano and Y. Koma	
1-16	Irradiation Effect of Gamma Rays on Cyanate Ester/Epoxy Resins (2)	20
	A. Idesaki, H. Uechi, S. Matsuda and H. Kishi	
1-17	Effects of Antioxidants on the Degradation of Flame-Retardant Ethylene Propylene Rubber	21
	A. Shimada, A. Idesaki, M. Sugimoto, M. Yoshikawa, K. Tamura, T. Seguchi and H. Kudoh	
1-18	Alpha-Ray Irradiation Damage on Materials Applied for Glove Box for Plutonium Powder Treatment	22
	K. Saito, K. Matsuyama and H. Endo	
1-19	Development of an Observation Technique Using a Fiberscope under High Radiation Doses	23
	H. Naito, W. Itagaki, C. Ito, A. Nagai, Y. Okazaki, R. Kitamura, N. Shamoto and Y. Takeshima	
1-20	Electrification of Coaxial Cable Model by Gamma-rays Irradiation	24
	K. Takano, S. Ukon, O. Takeda, N. Morishita and H. Seito	
1-21	Gamma-Ray Irradiation Test of Centrifugal Contactor with Magnetic Bearing System	25
	H. Ogino, A. Sakamoto, K. Fujisaku, S. Koizumi and H. Hirano	
1-22	Development of Penetration Part Processing Industrial Method in Radiation Controlled Area (Airtight Performance Examination)	26
	K. Izumi, M. Iguchi, M. Kawasaki, Y. Ohkawa, K. Oka and R. Yamagata	
1-23	Development of Radiation-resistant Lighting	27
	T. Tsuchida, R. Yamagata, H. Seito, Y. Haruyama, H. Kaneko and S. Kashimura	
1-24	Evaluation of Hydrogen Formation by Gamma-ray Irradiation in Sodium Nitrate Solution with TiO ₂ Colloids	28
	T. Motooka, Y. Ishijima and M. Yamamoto	
1-25	Gas Generation by Gamma-Ray Irradiation to Polyethylene, Polystyrene and Cellulose Resin	29
	K. Saito	
1-26	Studies on Microstructure and Elemental Distributions of Barrier Materials for Geological Disposal of Radioactive Waste	30
	Y. Tsuruta, D. Yamasaki, N. Miyasaka, T. Kozaki, S. Sato, N. Kozai, M. Koka, T. Satoh and T. Kamiya	
1-27	Effect of Dissolved Hydrogen on Helium Ion beam Radiolysis of Water	31
	M. Yamaguchi, M. Taguchi and A. Kimura	

1-28	Preliminary Models on Radiation Induced Changes of Microstructure and Stress-Strain Relations to Estimate Mechanical Response of Austenitic Steel Components	32
	S. Jitsukawa, Y. Abe, M. Ando, N. Ishikawa, N. Okubo, K. Suzuki, H. Oka, D. Liu and S. Ohnuki	
1-29	Microstructural Evolution in Extra High Purity Ni-base Superalloy Ion-irradiated under External Stress	33
	I. Ioka, G. H. Kim, K. Shiba and T. Sawai	
1-30	Microstructural Evolution of G-phase Strengthened Ni-base Alloy under Multi-ion Irradiation	34
	G. H. Kim, K. Shiba, I. Ioka, T. Sawai and S. Yamashita	
1-31	Conductometric Analysis of Track Etching in Poly(vinylidene fluoride) Films Irradiated with Different MeV-GeV Ion Beams	35
	T. Yamaki, H. Koshikawa, S. Sawada, S. Hasegawa, M. Asano, Y. Maekawa, K.-O. Voss, C. Trautmann and R. Neumann	
1-32	Preparation of Anion-Exchange Membranes for Fuel Cell Applications by γ -ray Pre-Irradiation Grafting: Crosslinker Effect	36
	H. Koshikawa, T. Yamaki, M. Asano and Y. Maekawa	
1-33	Preparation of Poly(ether ether ketone)-based Polymer Electrolytes for Fuel Cell Membranes Using Radiation-induced Graft Polymerization	37
	S. Hasegawa, S. Takahashi and Y. Maekawa	
1-34	Stability of Radiation Grafted Membranes in HIX Solution of Electro-electrodialysis	38
	N. Tanaka, T. Yamaki, H. Koshikawa, M. Asano, Y. Maekawa and K. Onuki	
1-35	Radiation Degradation Properties of Grafted Polymer Electrolyte Membranes	39
	S. Sawada, Y. Iwai, T. Yamahishi and Y. Maekawa	
1-36	Polymerization Kinetics of Ion-Track Grafting with Different Beams	40
	T. Sekine, S. Sawada, T. Yamaki, H. Koshikawa, M. Asano, A. Suzuki, T. Terai and Y. Maekawa	

This is a blank page.

1-1 Effect of Beam Expansion Methods on Radiation Degradation of Solar Cells

M. Imaizumi^{a)}, M. Saito^{b)}, Y. Yuri^{c)}, S. Sato^{d)} and T. Ohshima^{d)}

^{a)} Institute of Aerospace Technology, JAXA, ^{b)} Advanced Engineering Services Co. Ltd.,

^{c)} Department of Advanced Radiation Technology, TARRI, JAEA,

^{d)} Environment and Industrial Materials Research Division, QuBS, JAEA

Space solar cells are required to have radiation hardness. Therefore, it is necessary to understand the radiation degradation characteristics of the cells. Currently, solar cell irradiation tests are executed at each facility/organization in the world with their own test procedure and conditions. However, the effects of the test procedure/conditions on degradation of the performance of solar cells have not been understood well.

One of such conditions is a beam expansion method. Two kinds of the methods, the scanning and the defocusing, are generally used. The scanning is relatively popular method because it is easier to achieve a uniform beam area. However, in the case of the scanning, greater degradation is anticipated compared to the defocusing case because an intense spot beam that may cause greater degradation is momentarily irradiated at a local area. In this study, therefore, we compared solar cell degradation with using the two kinds of beam expansion methods.

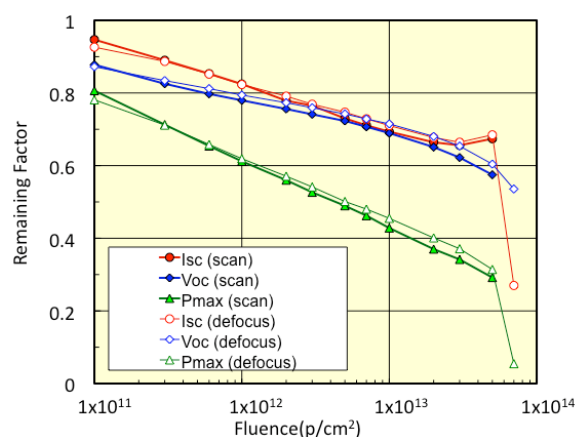
InGaP/GaAs/Ge triple-junction (3J) space solar cells and a high-efficiency silicon (Si) space solar cells were used as samples. Table 1 summarizes the beam conditions in this study. In the case of “scan”, the beam spot size was about 10 mm in diameter, and the spot beam was scanned horizontally (50 Hz) and also vertically (0.5 Hz). In the case of “defocus”, a defocused beam with Gaussian distribution (~80 mm in diameter) was uniformized using multipole magnets. This uniformizing technique was specially developed by one of the authors¹⁻³⁾. In both cases, protons were accelerated to 10 MeV, but the energy was decayed to ~9 MeV due to air in the case of the defocused beam. However, we have confirmed that there is no influence from the difference of energy on the radiation degradation of the two types of the cells.

Figure 1 depicts the results of comparison of the irradiations with the scanning and the defocusing beams on Si and 3J solar cells. The remaining factors (the ratio to the initial values) of the short-circuit current (Isc), the open-circuit voltage (Voc) and the maximum power (Pmax) of the two types of cells are plotted as a function of proton

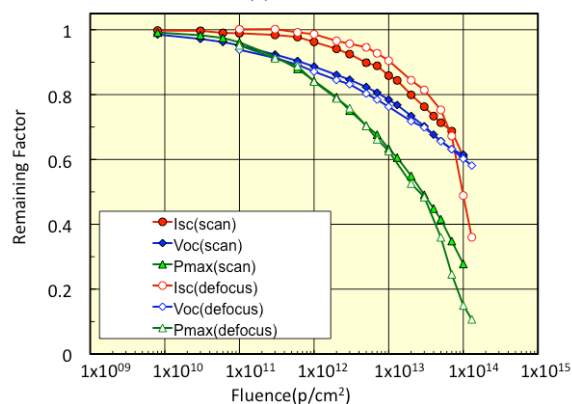
fluence. The cell output deteriorates in both cases of “scan” and “defocus”. However, there is no significant difference in the degradation between the irradiations with scanning beam and the defocus beam. We can conclude that there is no significant influence of the intense spot beam on radiation degradation. This result or knowledge will be reflected to the international standardization activity of solar cell radiation test methods⁴⁾.

References

- 1) Y. Yuri et al., The American Physical Society (2007) 104001(1-11).
- 2) Y. Yuri et al., EPAC08 (2008) 3077-3079.
- 3) Y. Yuri et al., PAC09 (2009) 1-3.
- 4) ISO 23038, ISO.



(a) Si cell



(b) 3J cell

Fig. 1 Comparison of degradation characteristics of (a) Si cell and (b) 3J cell as a function of fluence.

Table 2 Beam conditions for irradiation experiments.

Beam Broadening	scan	defocus
Particle	Proton	
Energy (MeV)	10	9
Fluence (p/cm ²)	1×10 ¹⁴	
Fluence Rate (p/cm ² ·s)	1.0×10 ⁹ ~1.0×10 ¹⁰	1.1×10 ¹¹
Irradiation Area	4cm×7.5cm	6cm×6cm
Sample	Si, 3J	
Cell Size	2cm×2cm	

1-2 Effect of Body-tie Structure Fabricated by Partial Trench Isolation for Suppression of Soft Errors in SOI SRAM Investigated by Helium and Oxygen Ion Probes

S. Abo^{a)}, N. Masuda^{a)}, F. Wakaya^{a)}, S. Onoda^{b)}, T. Makino^{b)}, T. Hirao^{b)}, T. Ohshima^{b)},
T. Iwamatsu^{c)}, H. Oda^{c)} and M. Takai^{a)}

^{a)} Center for Quantum Science and Technology under Extreme Conditions, Osaka University,

^{b)} Environment and Industrial Materials Research Division, QuBS, JAEA,

^{c)} Devices & Analysis Technology Division, Renesas Electronics Corporation

A soft error due to excess carriers generated by high energy particles becomes a serious problem in advanced semiconductor devices. A silicon-on-insulator (SOI) device has an advantage over a conventional bulk device for soft errors. However, the SOI body potential is unstable because the channel region is insulated from the silicon substrate by the buried oxide (BOX) layer. Therefore, a few excess carriers generated in a SOI body by high energy particles increase the SOI body potential, resulting in the abnormal drain current (i.e., floating body effect) and soft errors. A body-tie structure fabricated by partial trench isolation (PTI) is effective for suppression of the floating body effect, in which the generated holes in the neutral region drift out to a body-electrode.

In our previous studies, the soft error rates (SERs) in SOI static random access memories (SRAMs) with the body-tie structure were found to depend on the excess carriers generated in the SOI body induced by various ion probes^{1,2)}. In these studies, SERs were evaluated from the number of the soft errors without considering the metal oxide semiconductor field effect transistor (MOSFET) and metal pad layout on the SRAM chip. In this study, for investigating a difference in suppression of the floating body effect by the MOSFET and metal pad layout, SERs induced by helium and oxygen ion probes were measured as a function of connection length between the body-electrode, put in the side of MOSFET by PTI, and the metal pad for the first metal layer of the chip.

A SOI SRAM chip with a technology node of 90 nm was used in this study. The body-electrode for each of 32

SRAM cells was connected to the metal pad for the first metal layer. The connection length between the body-electrode and the metal pad used in this report was an order of the SRAM cell. The connection lengths of 1 to 16 in Figs. 1 and 2 were the closest to the farthest SRAM cells.

Figures 1 and 2 show normalized SERs induced by helium and oxygen ion probes as a function of connection length between the body-electrode and the metal pad. SERs induced by helium ion probes at 5.0 and 6.0 MeV in closest SRAM cells to the metal pad were 40-50 % lower than those in farthest SRAM cells. This indicates that the body-tie structure has a difference in suppression of the floating body effect. On the contrary, SERs induced by helium ion probe at 2.5 MeV and oxygen ion probes at 13.5, 15.0 and 18.0 MeV did not depend on the connection lengths between the body-electrode and the metal pad. This indicates that the generated charge by helium ion probe at 2.5 MeV and oxygen ion probes at 13.5, 15.0 and 18.0 MeV are enough to induce the soft errors in SOI SRAM. Therefore, the soft errors by helium ion probe at 2.5 MeV and oxygen ion probes at 13.5, 15.0 and 18.0 MeV occurred regardless the connection length between the body-electrode and the metal pad.

The body-tie structure fabricated by PTI has difference in suppression of the floating body effect by the connection length between the body-electrode and the metal pad.

References

- 1) S. Abo, et al., Nucl. Instrum. Meth. B 231 (2005) 482.
- 2) S. Abo, et al., Nucl. Instrum. Meth. B 268 (2010) 2074.

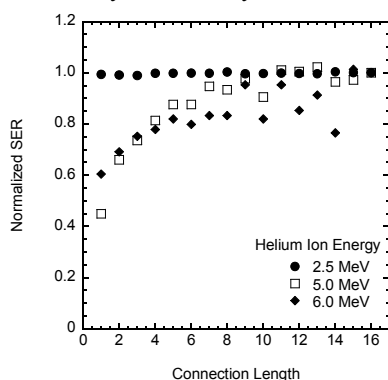


Fig. 1 Normalized SER induced by helium ion probes as a function of connection length between body-electrode and metal pad.

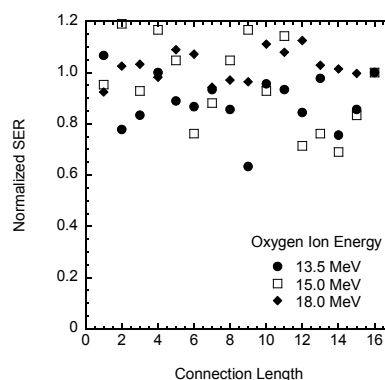


Fig. 2 Normalized SER induced by oxygen ion probes as a function of connection length between body-electrode and metal pad.

1-3 Improved Radiation Hardness for Angle Irradiation in DICE Latches on a 90 nm Bulk CMOS Process

A. Maru^{a)}, H. Shindou^{a)}, S. Kuboyama^{a)}, H. Abe^{b)}, T. Hirao^{b)} and T. Ohshima^{b)}

^{a)} Aerospace Research and Development Directorate, Japan Aerospace Exploration Agency (JAXA),

^{b)} Environment and Industrial Materials Research Division, QuBS, JAEA

Recently, due to the requirements for higher density integration and device scaling, the logical circuits have been fabricated with the process technologies less than 100 nm. Single-Event Upset (SEU) and Single-Event Transient (SET) phenomena are serious problems for those integrated circuits, because their supply voltage and the threshold to the phenomena are also decreasing. It is said that Dual Interlocked Storage Cell (DICE) circuit is the hardened topology against SEU^{1), 2)}. The DICE circuit keeps data using two memory nodes, and if data inversion has occurred by incident particles on the one hand memory node, the correct data is rewritten by the other hand memory node. Therefore, DICE circuit has excellent radiation tolerance. However, in the highly integrated circuits, it is occurred that two neighboring transistors are simultaneously inverted by an incident particle due to the charge sharing mechanism³⁾. Therefore, it is important for the design of those circuits to estimate the extent of the charge sharing.

In this feasibility study, the applicability to space environments of a 90 nm bulk CMOS process was evaluated by heavy ions and the SEU cross section was calculated. For detailed evaluation, we also performed the angled irradiation. The experimental results suggested there are the critical angles in the DICE memory circuit.

In past study⁴⁾, we evaluated the effectiveness of the Radiation Hardness By Design (RHBD) approach for 90 nm CMOS process, by using the heavy ions from AVF cyclotron at JAEA. As a result, the DICE latch circuits indicated the range of sensitive angle. Figure 1 shows SEU cross-section as a function of incident angle when Kr

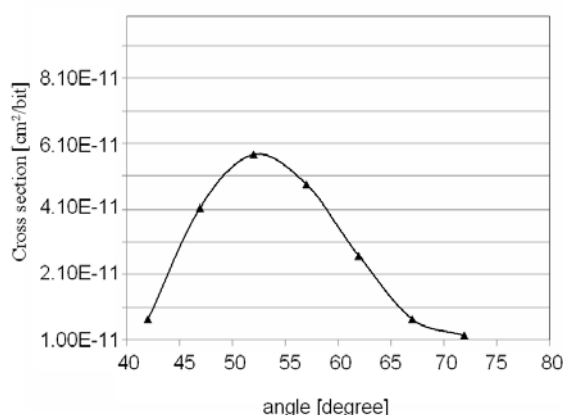


Fig. 1 SEU cross-section as a function of linear energy transfer for the DICE latch circuits.

(LET= 40.3 MeV/mg/cm²) particles were irradiated.

By using Simulation Program with Integrated Circuit Emphasis (SPICE) simulator and DICE cell layout data, it concluded that due to two critical off-transistors in the DICE circuit upset simultaneously, many SEUs were observed with angled irradiation. The SEU rate in the actual space environment was estimated based on the directional SEU sensitivity. The results indicate that the SEUs caused by ions with grazing angle incidence are not negligible for DICE type of data storage cells even in the 90 nm technology. For smaller feature size technologies the effects could be considerable and the development of additional techniques may be required.

Therefore, we designed a new type of DICE memory cell. Figure 2 shows schematic diagram of new type DICE memory cell. Extra p-type transistors were inserted to the conventional DICE memory to prevent to penetrate critical off state transistors in the DICE circuit simultaneously by ion with grazing angle. Although there is an area penalty, this memory cell is expected to have high SEU tolerance even if ions irradiated from all angles. Radiation test samples of this circuit were fabricated and evaluated SEU tolerance continuously.

References

- 1) M. P. Baze et al., IEEE Trans. Nucl. Sci. 55 (2008) 3295.
- 2) K. Wang et al., Canadian Conference on Electrical and Computer Engineering (2009) 1076.
- 3) A. Amusan, et al., IEEE Trans. Nucl. Sci. 53 (2006) 3253.
- 4) A. Maru et al., IEEE Trans. Nucl. Sci. 57 (2010) 3602.

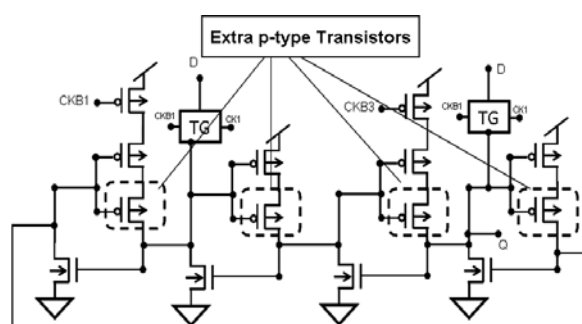


Fig. 2 Schematic diagram of new type DICE memory cell.

1-4 Heavy-ion Induced Current in SOI p⁺n Junction Diode

Y. Takahashi^{a)}, H. Takeyasu^{a)}, Y. Okazaki^{a)}
T. Hirao^{b)}, S. Onoda^{b)} and T. Ohshima^{b)}

^{a)}Nihon University, ^{b)}Environment and Industrial Materials Research Division, QuBS, JAEA

One of the most detrimental effects on semiconductor devices in radiation environments is the single-event effect (SEE). Recently, silicon-on-insulator (SOI) technology has been developed to reduce SEE, because it was believed that the charge collection is suppressed by the existence of a buried oxide (BOX) layer¹⁾. However, anomalous charge collection through the BOX layer was also reported²⁾. In the present work, we concluded that the charge collection through the oxide layer is dominated by a displacement current³⁾. In this work, we discuss about suppression of the displacement current in SOI p⁺n junction diode to improve radiation immunity of SOI devices.

The Al gate p⁺n junction diodes with the junction area of 100 μm in diameter were fabricated on a SOI substrate as shown in Fig. 1. The donor concentration of each silicon layer is about 10^{15} cm^{-3} and the thicknesses of active SOI layer and BOX layer are 1.5 μm and 0.3 μm , respectively. The transient current and the collected charge, the integration value along a time after irradiation, in diodes induced by 15 MeV Oxygen ions were measured. Linear energy transfer (LET) and project range of the ions are 6.5 MeV/(mg/cm²) and 12.3 μm , respectively. Heavy-ion irradiation tests were carried out using the Single Ion Hit (SIH) system in JAEA and the transient current caused by the single ion was measured by Transient Ion Beam Induced Current (TIBIC) measurement system.

Figure 2 shows the collected charge of anode electrode in the device as a function of the heavy-ion hit location, in which the reverse bias of 10 V is applied during irradiation test ($V_p = -10 \text{ V}$). Dotted line shows the results when the back electrode is connected with ground ($V_b = 0$). In this case, the collected charge is about 300 fC when the ion hit to the whole of p⁺ region. However, the charge generated in active SOI layer due to irradiation is 100 fC and the measured charge is about 3 times as much as the generated charge. This phenomenon indicates that the some of charge generated in handle Si substrate due to irradiation is collected by anode electrode through the BOX layer as displacement current. The displacement current is caused by the charge accumulated at the surface of substrate due to an electric field in depletion layer. So it is considered that the current can be suppressed by the reduction of the width of depletion layer. The width can be controlled by the voltage applying to back electrode, V_b . When $V_b = V_p$, the surface of handle substrate is flat-band condition even if the reverse bias is applied to anode electrode. Solid line in Fig. 2 shows the collected charge of anode electrode when $V_b = V_p = -10 \text{ V}$. It was found that the collected charge when the ion hit to the center area of p⁺ region could be

suppressed to almost 0. When the ion hit to the edge of p⁺ region, the amount of collected charge is obtained to be around 100 fC. It is considered that the charge is generated in active SOI layer and collected by lateral electric field at the edge.

From these results, it was confirmed that the collected charge in SOI device could be reduced by reduction of the width of depletion layer at the surface of handle substrate.

References

- 1) O. Musseau, IEEE Trans. Nucl. Sci. NS-43 2 (1996) 603-613.
- 2) T. Hirao et al., Nucl. Instrum. Meth. Phys. Res. B 206 (2003) 457-461.
- 3) Y. Takahashi et al., Nucl. Instrum. Meth. Phys. Res. B 260 (2007) 309-313.

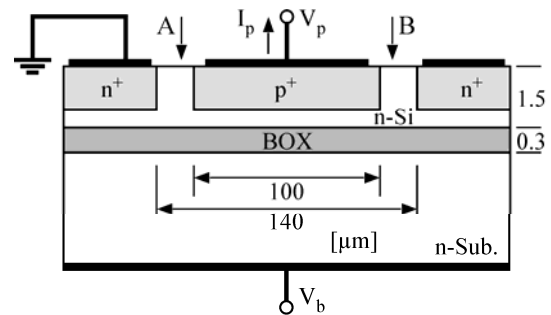


Fig. 1 Device structure of SOI p⁺n junction diode.

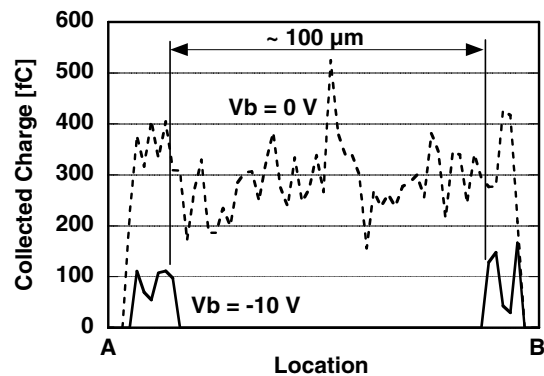


Fig. 2 Collected charge of SOI p⁺n junction diode induced by Oxygen ion irradiation as a function of ion hit location.

1-5 Estimation of Digital Single Event Transient Pulse-Width in Logic LSIs from Transient Current Waveforms in a MOSFET

T. Makino^{a)}, S. Onoda^{a)}, T. Hirao^{a)}, T. Ohshima^{a)}, D. Kobayashi^{b)},
H. Ikeda^{b)} and K. Hirose^{b)}

^{a)} Environment and Industrial Materials Research Division, QuBS, JAEA,

^{b)} Institute of Space and Astronautical Science, JAXA

We first estimated Digital Single Event Transient (DSET) pulse-widths originated in an inverter cell which was fabricated with a 0.2- μm process from heavy-ion-induced transient currents in an n-type Metal-Oxide-Semiconductor Field-Effect Transistor (nMOSFET) by using a theoretical integrated-circuit analysis.

The test sample of nMOSFET was mounted on a chip carrier and connected through short bonding wires to strip-lines carefully designed for high-speed-transient measurement. The heavy-ion irradiation induced transient drain currents in the test sample of nMOSFET were observed under various constant drain biases. The gate of the test sample of nMOSFET was biased in an off-state and the drain bias was swept from 1.8 V to 0.2 V with 0.2 V steps and from 0.2 V to 0.05 V with 0.05 V steps with a power supply. We used a 30 GHz high-bandwidth single-shot digital oscilloscope (LeCroy Model Wavemaster 830Zi) to measure the transient drain currents. Bias-tee, amplifier, and cables limit the bandwidth of the whole measurement system to around 20 GHz. The drain currents were amplified by a charge pre-amplifier with 21.5 dB before input to the oscilloscope.

The heavy-ion irradiation tests were performed using the AVF cyclotron at the Takasaki Ion Accelerators for Advanced Radiation Application (TIARA) in Japan Atomic Energy Agency (JAEA), Takasaki. The test sample of nMOSFET was irradiated in a vacuum chamber with a broad beam of 322-MeV Krypton at an irradiation angle of 0

degrees. To obtain statistically sufficient numbers of transient current waveforms, about 200 current waveforms were observed in each drain bias condition. After each measurement, the ion beam was stopped and the drain bias was changed to a different value.

Figure 1 shows the biggest waveform of transient current for the drain bias of 1.8 V¹⁾. For every drain bias condition, the biggest transient current waveforms were stored in a look-up table to estimate the DSET waveform by using the theoretical integrated-circuit analysis called as a table-based approach. Details of the table-based approach are reported in the reference²⁾.

Figure 2 shows an estimated DSET waveform as an output voltage of an inverter circuit (V_{out}) by using the table-based approach¹⁾. The DSET pulse-width was defined at half voltage of nominal power supply voltage for the tested process and was found to be 420 ps. The value of the DSET pulse-width of 420 ps was consistent with the measured DSET pulse-widths by using a special DSET pulse-width detector³⁾. From this result, we concluded that by using the estimation method it is possible to obtain the heavy-ion-induced DSET pulse-widths, even without any special pulse-width detectors, at least for an inverter circuit fabricated in a 0.2- μm technology.

References

- 1) T. Makino et al., Proc. of 9th RASEDA, (2010) 169.
- 2) D. Kobayashi et al., IEEE Trans. Nucl. Sci. (2007) 2347.
- 3) T. Makino et al., IEEE Trans. Nucl. Sci. (2009) 3180.

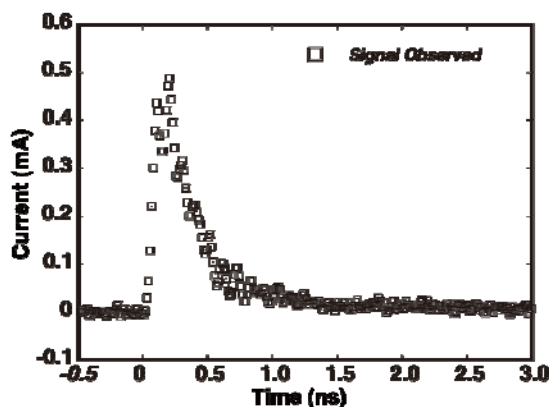


Fig. 1 The biggest waveform of transient currents in the case that the drain biased to 1.8 V¹⁾.

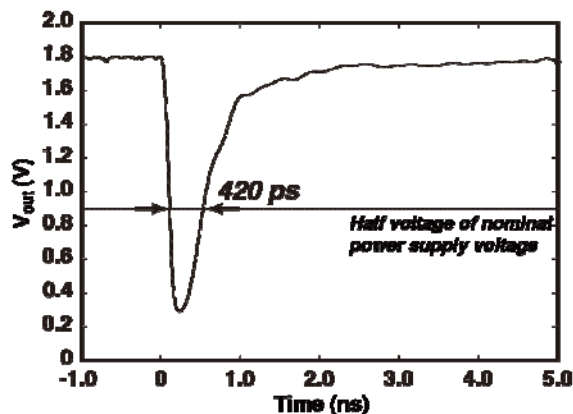


Fig. 2 The estimated DSET pulse waveform. The pulse-width is about 420 ps¹⁾.

1-6 TIBIC Mapping of 6H-SiC n-channel MOSFETs

S. Onoda ^{a)}, T. Makino ^{a)}, N. Iwamoto ^{a,b)}, K. Kojima ^{c)}, S. Nozaki ^{b)} and T. Ohshima ^{a)}

^{a)} Environment and Industrial Materials Research Division, QuBS, JAEA, ^{b)} The University of Electro-Communications, ^{c)} National Institute of Advanced Industrial Science and Technology

Metal Oxide Semiconductor Field Effect Transistor (MOSFET) made of Silicon Carbide (SiC) is regarded as a promising candidate for high-power and high-frequency electronic devices because of its excellent electrical and thermal properties. The benefit to using SiC materials instead of other more established materials such as Silicon (Si) or Gallium Arsenide (GaAs) is that compact, lightweight, and highly energy efficient devices operating at high temperature can be developed. Moreover, it is well known that the SiC crystal has significant radiation tolerance. Therefore, it is expected that the SiC devices will be particularly useful in space applications as well as in terrestrial applications. To use SiC devices in space radiation environments, it is important to understand the effect of various types of irradiation on their electrical characteristics.

Space radiation causes destructive or non-destructive events such as Total Ionizing Dose (TID) effect, Displacement Damage Dose (DDD) effect, and Single Event Effect (SEE). We have studied the TID effects on 6H-SiC MOSFETs over several years¹⁾. In contrast to the TID and DDD effects, few attempts have so far been made to study the transient response when an ion strikes on SiC MOSFETs²⁾. The purpose of this paper is to understand the charge collection phenomena when an ion strikes on SiC MOSFETs.

Fig. 1 (a) shows the cross-sectional structure of the MOSFET. The devices were irradiated at normal incidence with a focused microbeam using 15 MeV O ions at TIARA facility. The bias tees were used for sample biasing. During irradiation, the drain contact was biased with 10 V. The gate, source and substrate (back side of the chip) were grounded. Fast current amplifiers (Picosecond Pulse Lab. 5840A) were connected to all electrodes for amplification. The microbeam was scanned over the

source, gate and drain region. The signal induced by a single ion was recorded together with the struck location by using the 3 GHz digital storage oscilloscope (Tektronix Model TDS694C). The collected charge was estimated from the integration of the transient current signals.

Figure 1 (b) shows two-dimensional (2D) mapping image of the peak value of the drain current induced by the 15 MeV-O ion microbeam scanned on the 6H-SiC n-type MOSFET. When an ion strikes on the drain, the largest signal is observed from drain contact. From the point of view of the SEE tolerance, the largest signal leads to the most serious problems.

The charge is calculated by integrating the transient currents when the drain bias is 20 V and other contacts are grounded. The drain and substrate charges are 281.5 and 250.9 fC. The ratio between drain and substrate charges is about 1.1. This fact suggests that a part of charge is provided from the source or the gate. To understand the charge collection phenomena, we perform the numerical simulations. Fig. 2 shows the calculated contour map of electron current density. As shown in the figure, the current flows between the source and drain through the epitaxial layer. After the ion strikes on the drain region, the potential temporarily spreads through the epitaxial layer and raises the potential of epitaxial layer relative to the source. As a result, the electrons can be transported from the source to the drain, which is called "parasitic bipolar effect". In short, we conclude that the most likely explanation of the enhanced charge collection is the parasitic bipolar effect³⁾.

References

- 1) T. Ohshima et al., J. Appl. Phys. 90 (2001) 3038.
- 2) K. K. Lee et al., Mater. Sci. Forum 645-648 (2010) 1013.
- 3) S. Onoda et al., IEEE Trans. Nucl. Sci. 57 6 (2010) 3373.

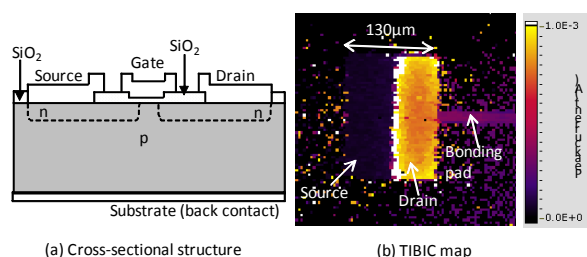


Fig. 1 (a) The cross-sectional structure of n-type MOSFET. (b) Typical TIBIC peak image is observed from drain contact of 6H-SiC MOSFETs induced by 15 MeV-O ions. The drain contact is biased with 10 V and other contacts are grounded.

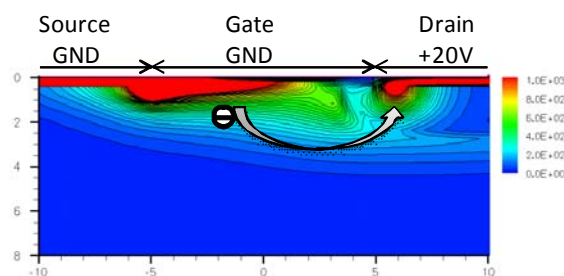


Fig. 2 Electron current density contour map of 6H-SiC MOSFET at 2 ns after ion strike.

1-7 Electric Conductivity of Proton-Irradiated Hydrogenated Amorphous Silicon Semiconductors

S. Sato^{a)}, T. Ohshima^{a)} and M. Imaizumi^{b)}

^{a)} Environment and Industrial Materials Research Division, QuBS, JAEA,

^{b)} Institute of Aerospace Technology, JAXA

I. Introduction

Hydrogenated amorphous silicon (a-Si:H) semiconductor devices are expected to be utilized in radiation environments (e.g. space solar cells and photo-detectors in nuclear reactors or accelerator facilities) since they have a high radiation tolerance¹⁾. In order to make the radiation hardened a-Si:H device design, variations of the electrical properties due to radiation exposure is a primary concern. For this reason, several research groups have investigated about these issues, especially about the high energy electron irradiation effects. However, systematic and comprehensive study about these radiation effects is hardly reported at present despite being very important in order to not only make the radiation hardened device design, but also understand the mechanism of the radiation effects. In this context, we have studied variations of the electrical properties accompanied by radiation exposure^{2,3)}.

II. Experimental

The samples were device-grade, either undoped, phosphorus doped (*n*-type) or boron doped (*p*-type) a-Si:H thin films, fabricated on glass substrates by Plasma Enhanced Chemical Vapor Deposition (PECVD) at National Institute of Advanced Industrial Science and Technology (AIST). The thicknesses of the a-Si:H thin films were 0.27 - 0.45 μm . The carrier concentrations of *n*-type and *p*-type samples were 5.8×10^{17} and $3.0 \times 10^{13} / \text{cm}^3$ according to the Hall measurement results, respectively.

III. Results and Discussion

Figure 1 shows the results of electric conductivity variations of a-Si:H irradiated with 10 MeV protons at room temperature. The conductivity measurements were performed *in-situ* in the irradiation chamber. The conductivity of the undoped a-Si:H sample first increase due to proton irradiation and then decrease dramatically with increasing proton fluence. A gradual conductivity increase at lower fluences and a decrease at higher fluences were also observed in the doped samples. Our measurements also revealed that the conductivity which increased due to proton irradiation decayed with time and thermally relaxed at over 300 K. This cannot be explained in terms of the general interpretation for radiation-induced electrical degradation of conventional semiconductor materials, where the minority carrier lifetime decreases due to the creation of radiation defects. In order to clarify the origin of this effect, we investigated Seebeck coefficient variations due to 3.0 MeV proton irradiation. The Seebeck coefficients were derived

from the thermoelectric power, which was measured *in-situ* by generating a temperature difference between upper and lower parts of the sample just after proton irradiation. The Seebeck effect could not be observed in the undoped sample without proton irradiation, however, the proton-irradiated sample showed a negative Seebeck coefficient only in the low fluence regime. This suggests that donor like centers were temporarily generated. Also, the stability of the Seebeck effect was investigated and as a result, the Seebeck coefficient of the undoped sample irradiated with the 3.0 MeV protons at $2.0 \times 10^{12} / \text{cm}^2$ gradually decreased with time, although the Seebeck effect was observed 40 hours later after the irradiation. Therefore, we conclude that the conductivity increase due to proton irradiation is attributed to temporal donor center generation. Whereas, the conductivity decreased with the accumulation of radiation-induced defects since donor centers are compensated by these defects or disappeared due to additional proton irradiation at fluences of above $10^{14} / \text{cm}^2$.

We would like to thank Hitoshi Sai of AIST for fabricating the a-Si:H samples.

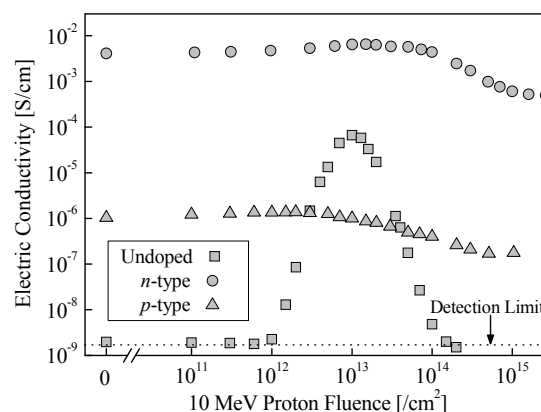


Fig. 1 Electric conductivity variations of undoped, *n*-type and *p*-type a-Si:H thin films irradiated with 10 MeV protons.

References

- 1) P. J. Sellin et. al., Nucl. Instrum. Meth. Phys. Res. A **557** (2006) 479-489.
- 2) S. Sato et al., Proc. 35th IEEE PVSC (2010) 2620-2624.
- 3) S. Sato et al., J. Non-Cryst. Sol., **356** (2010) 2114-2119.

1-8 Research of Radiation Tolerance for Application of General Electronic Devices to Space Environment

N. Sasaki^{a)}, Y. Kakimi^{a)}, K. Adachi^{a)}, T. Maeda^{a)}, S. Yamada^{a)}
T. Ohshima^{b)}, T. Hirao^{b)} and S. Onoda^{b)}

^{a)} Advanced Engineering Services Co., Ltd.,

^{b)} Environment and Industrial Materials Research Division, QuBS, JAEA

We have tested general electronic devices about radiation tolerance since 2008. This purpose is aim to apply these electronic devices to our Small-Satellite design. This time, we tested two MPUs (Micro Processor Unit), which have different architecture each other and a switching power controller by heavy-ion beam irradiation. As a result, both MPUs have strong tolerance for SEE (Single Event Effect). Probability of SEE occurrence which estimated from irradiation results is less than once, on our satellite orbit during Small-Satellite's operation life (1-2 years). Switching power controller showed an irregular event. Test power circuit that was controlled by the switching power controller suddenly stopped generating voltage supply for a second during Kr irradiation. Switching power controller also showed total dose effect at its internal reference voltage generator. Its reference voltage kept reducing during irradiation.

我々は、小型衛星及び搭載機器の開発を行っている。小型衛星を利用することの利点は、他の衛星に比べ短期間、低コストで開発を行えるため、より先進的で挑戦的なミッションを実現できるということである。

一方、小型衛星が搭載機器に提供できるリソースの制限から、機器開発では、質量、大きさ、消費電力の面で大きな制限がかかる。このような理由から、機器開発では、様々なミッションに対応できるように豊富な性能バリエーションと機器の小型化、低消費電力化が重要である。しかしながら、宇宙用部品の多くは、民生部品に比べ大型で消費電力も高く、性能も限られてしまう。そのため小型衛星の機器開発において民生部品を利用することは注目すべきことである。そこで我々は、21年度より民生電子部品に対し重粒子線照射試験を実施し、シングルイベントに関して民生部品の宇宙環境への適合性評価を行ってきた。本稿では22年度に実施した MPU (マイクロプロセッサ)、スイッチング電源コントローラの試験結果について報告する。

照射試験は、AVF サイクロトロン散乱ビーム照射試験装置を用いて、 $^{15}\text{N}^{3+}$ 、 $^{20}\text{Ne}^{4+}$ 、 $^{40}\text{Ar}^{8+}$ 、 $^{84}\text{Kr}^{17+}$ の照射を行った。照射中、試料は動作状態とし、評価項目に応じた動作のモニタリングを行った。

MPU(Micro Processor Unit)の照射試験は、MPU①(RISC 32 bit MPU)と MPU②(MCS-51 互換 8 bit MPU)について行った。評価項目は、SEL(Single Event Latch-up)、SEU(Single Event Upset)、その他動作異常の有無についてである。評価結果を Table 1 に示す。評価は、Weibull 関数を用いて断面積と LET の関係を推定し CREME96 により算出した軌道上での放射線環境より軌道上での各イベントの発生確率を算出した。小型衛星の運用期間は一般的に 1~2 年程度であるが、運用中に予想されるイベントの発生回数は、1 回未満である。

Table 1 Result of MPUs evaluation.

		LET threshold [MeV/mg/cm ²]	Saturated cross section [cm ²]	Probability [event/year]
SEL	MPU①	5.6	4.3×10^{-3}	9×10^{-2}
	MPU②	> 5.9	1.8×10^{-3}	$< 8 \times 10^{-3}$
SEU@Register	MPU①	> 3.0	3.5×10^{-5}	$< 7 \times 10^{-5}$
	MPU②	1.2	1.3×10^{-3}	8×10^{-2}
SEU@ROM	MPU①	> 34.0	$< 2 \times 10^{-5}$	$< 7 \times 10^{-8}$
	MPU②	> 34.0	$< 9 \times 10^{-6}$	$< 4 \times 10^{-8}$
Hung-Up	MPU①	4.5	4.4×10^{-4}	7×10^{-3}
	MPU②	> 3.0	4.0×10^{-3}	$< 2 \times 10^{-3}$

また、仮に SEL や動作異常が発生した場合でも、電源のリセットにより MPU は動作を回復できることが試験で実証されている。従って、MPU①、MPU②については、小型衛星での使用を想定した場合、シングルイベントに関して十分耐性があると判断する。今後は、トータルドーズ効果による処理速度、A/D 変換精度等の劣化や、動作異常の原因について調査を継続する。

スイッチング電源コントローラは、試験回路として試料を用いた DCDC 降圧回路を製作し、照射試験を実施した。評価項目は、SEL とその他動作異常の有無についてである。特に動作異常については、試料の出力電圧コントロール性能等の動作状況をモニタするため DCDC 降圧回路の出力電圧と試料自体に内蔵されるリファレンス電源電圧を 2 Hz の周期でモニタした。試験の結果、SEL は発生しなかったが、Kr の照射にて、DCDC 出力電圧が瞬間的に OFF になる動作異常を確認した。動作異常の継続時間は 0.5 秒~1.5 秒で、その後電圧は自動的に回復した。その他に照射を行った全線種でリファレンス電源電圧の低下を確認した。Figure 1 に Kr 照射時のリファレンス電源電圧の低下の様子を示す。線種による依存性は明らかではないが、低下の割合は 2.7~6.8 mV/Gy(si) であった。また、照射から 1 週間後に再びリファレンス電源電圧の確認を行ったが、電圧の回復は確認されなかった。リファレンス電源電圧低下の原因は、トータルドーズ効果により素子内部に欠損が生じているためと考える。

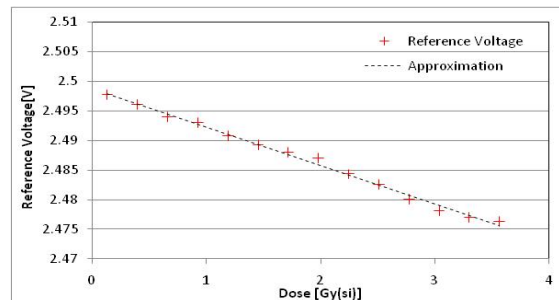


Fig. 1 Total dose effect at device internal reference voltage generator. This figure shows result of Kr irradiation. Dose is calculated with device size, material, and assumption that irradiation particle energy was absorbed by the test device completely.

1-9 Total Dose Effect on Pentacene-based Organic Thin Films Field Effect Transistors

T. Hirao^{a)}, Li Cai^{a,b)}, H. Yano^{b)}, T. Ohshima^{a)} and Y. Nishioka^{b)}

^{a)} Environment and Industrial Materials Research Division, QuBS, JAEA, ^{b)} Nihon University

Organic Thin Film Transistors (OTFT) are attracting much attention to the special applications such as flexible display, smart card, and RF tag, which are difficult to achieve by the conventional Si devices due to the solid property of Si and the cost of fabrication¹⁻⁴⁾. OTFTs are under worldwide investigation mostly focusing on improvement of field effect mobility. In this work, we report on the electrical characteristics of the OTFE irradiated by cobalt-60 source having gamma radiation with 1.33 MeV and 1.17 MeV energy at room temperature.

Figure 1 shows the schematic structure of the OTFTs used in this study. Two kinds of gate insulators, thermally grown SiO₂ films and spin coated polyimide on heavily-doped n-type silicon wafer were prepared. The thickness of both SiO₂ and polyimide were 300 nm. The polyimide was LX-5800-6, Hitachi Chemical DuPont Micro Systems, Ltd. After this gate insulator was formed, pentacene (C₂₂H₁₄) films with a thickness of approximately 50 nm as a semiconductor layer were deposited by thermal vacuum evaporation at an estimated deposition rate of 0.2 nm/s. The vacuum pressure before the pentacene deposition was usually below 10⁻³ Pa. The pentacene was purchased from Wako Pure Chemical Industries, Ltd., and used without further purification. Then, a gold film with the thickness of approximately 50 nm was thermally evaporated through a shadow mask to define the source and drain contacts. The defined channel length L and width W were 50 μm and 2 mm, respectively.

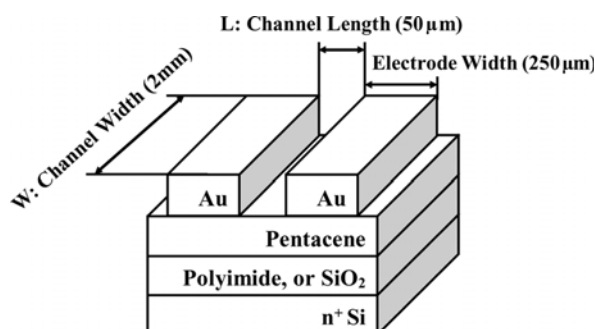


Fig. 1 Schematic of the fabricated pentacene-based organic thin film field effect transistors.

The OTFTs were irradiated with ⁶⁰Co γ -ray up to 1,200 Gy(Si) at a dose rate of 200 Gy/h at room temperature under the dark condition at JAEA Takasaki. No bias voltage was applied to the devices under irradiation. The relationships between the drain current I_D and the drain-source voltage V_{DS} were measured before and after irradiation to evaluate the radiation damage using a Semiconductor Parameter Analyzer (4156B).

Figure 2 shows the variation of the carrier mobility normalized to its pre-irradiation value as a function of total-dose. For OTFT with SiO₂ gate insulator, the mobility continually decreased to nearly 20 percent when the total dose reached 1,200 Gy (Si). For PI gate insulator, when the total dose reached 600 Gy (Si) the mobility decreased to nearly 70 percent.

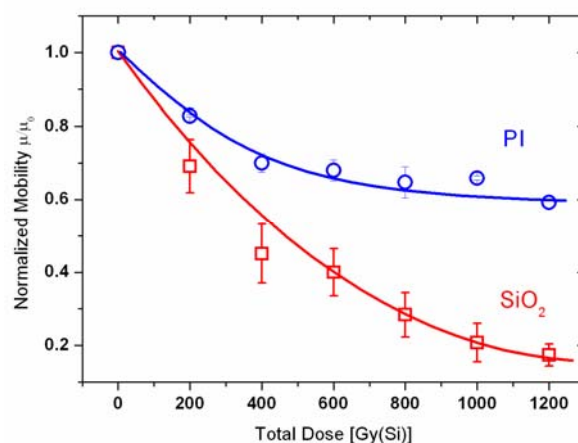


Fig. 2 Variation of the carrier mobility normalized to the pre-irradiation value as function of total dose.

References

- 1) C. D. Dimitrakopoulos et al., Adv. Mater. 14 (2002) 99.
- 2) G. Horowitz, Adv. Mater. 10 (1998) 365.
- 3) J. Zaumseil et al., Appl. Phys. Lett. 82 (2003) 793.
- 4) M. Kitamura and Y. Arakawa, J. Phys.: Condens. Matter. 20 (2008) 184011.

1-10 Yield and Coherence Time of the NV Centers Created by MeV Range Nitrogen Ion Implantation of Diamond

J. Isoya^{a)}, T. Umeda^{a)}, T. Ohshima^{b)}, S. Onoda^{b)}, S. Sato^{b)} and N. Morishita^{b)}

^{a)} Graduate School of Library, Information and Media Studies, University of Tsukuba,

^{b)} Environment and Industrial Materials Research Division, QuBS, JAEA

The nitrogen vacancy (NV) center ($S=1$) in diamond is a potential candidate for solid-state quantum processor operating at room temperature (RT). Using single spins of single centers as qubits, NV can be initialized and readout optically at RT. NV has an extraordinarily long coherence time (T_2) at RT. Native NV which is grown-in defect gives $T_2=1.8$ ms at RT in a ^{13}C ($I=1/2$, natural abundance 1.11%) depleted (0.3%) high-purity CVD single crystal¹⁾.

One of scalable structures is a linear array of NV centers in which 2-qubit CNOT gate using dipole-dipole interaction between each pair of adjacent NV centers is utilized as a universal gate. Desirable distance is ~ 50 nm, which is determined by resolution of optical readout of individual spins and by feasibility of fabrication using ion implantation techniques. The weak dipole-dipole interaction ($g_e\beta_e/r^3 \sim 0.42$ kHz for $r = 50$ nm) requires challenge of diamond growth to lengthen T_2 by higher ^{12}C -enrichment. Additional problem is that T_2 of the NV centers produced by ion-implantation has been shorter by an order of magnitude than the best (0.65 ms) of natural abundance sample which is determined by the local field fluctuation due to ^{13}C nuclear spin flip-flops. Also, the sufficiently high yield is critically important for the position-controlled fabrication.

In the present work, high yield of $\sim 100\%$ and T_2 exceeding ~ 1 ms have been attained for the NV centers produced by 10 MeV ion implantation.

By thermal annealing after N ion implantation, the NV centers are created by diffusion of vacancies to the implanted N atoms occupying the substitutional site. The vacancies created by implantation also form vacancy clusters as residual defects, which have mostly unpaired electrons and shorten the coherence time. Firstly, to obtain the optimum annealing temperature, the high-purity CVD crystals (Element6, electronic grade) were implanted with N ions at energies between 4 and 13 MeV (7-hold implantation with $1 \times 10^{13} \text{ cm}^{-2}$ at each energy) at elevated temperatures (800 to 1,200 °C). The NV^-/NV^0 and the residual defects are characterized by PL and EPR, respectively. In the high temperature implantation (i.e. *in-situ* annealing) experiments, the concentration of the residual defects of vacancy-chain type decreased as the *in-situ* annealing temperature increased. However, the formation of the NVN center is noticed above 1,100 °C.

Secondly, a crystal with ^{12}C enriched to 99.99% was implanted with microbeam (diameter $\sim 1 \mu\text{m}$) N ions (10 MeV) in a two-dimensional array (distance of $4 \mu\text{m}$) of spots at RT. The number of incident N ions per one spot was controlled by single ion hitting technique. After the implantation, the sample was annealed at 1,000 °C. The

yield of the NV center is obtained by counting the NV centers created in each spot against the number of N ions implanted in each spot. The scattering of the locations of NV centers created in each spot, which is determined by the beam profile ($\sim 1 \mu\text{m}$) and the straggling, is not large to be resolved by the confocal microscope imaging (Fig. 1). We employed GSD (ground state depletion) imaging which gives sufficient resolution (~ 30 nm) to measure the number of NV centers created in each spot instead of taking fluorescence photon autocorrelation (Fig. 1). In the case of implantation of five N ions per spot, $\sim 100\%$ yield has been attained.

The coherence time of individual NV was measured by confocal microscope fluorescence detected pulsed EPR using two-pulse sequence. The coherence time measured exceeds ~ 1 ms. Thus, the coherence time of the NV produced by implantation has been greatly improved.

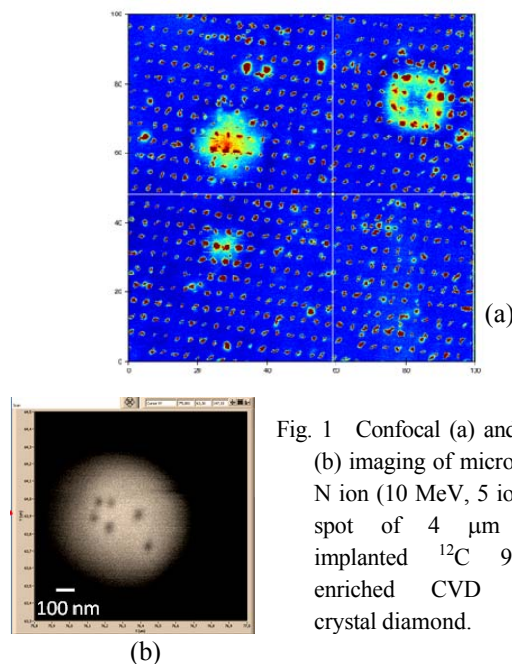


Fig. 1 Confocal (a) and GSD (b) imaging of micro-beam N ion (10 MeV, 5 ions per spot of $4 \mu\text{m}$ step) implanted ^{12}C 99.99% enriched CVD single crystal diamond.

Reference

- 1) G. Balasubramanian et al., Nat. Mater. 8 (2009) 383.

Acknowledgements

The ^{12}C enriched crystal was provided by Dr. Daniel J. Twitchen. This work is carried out by the Strategic Japanese-German Joint Research Project (JST) with collaborators, T. Teraji, T. Taniguchi, K. Watanabe, S. Koizumi, H. Kanda (NIMS), F. Dolde, H. Fedder, J. Honert, F. Jelezko, and J. Wrachtrup (University of Stuttgart).

1-11 Luminescence Properties and Ion-Beam-Induced Damage in Rare Earth Ion Doped AlGaN

A. Wakahara^{a)}, H. Okada^{a)}, J. -H. Park^{a)}, S. Sato^{b)} and T. Ohshima^{b)}

^{a)} Toyohashi University of Technology,

^{b)} Environment and Industrial Materials Research Division, QuBS, JAEA

Luminescence properties and effects of ion-beam-induced damage were studied in rare earth ion (REI) doped AlGaN. In this study, Terbium (Tb) was chosen as REI, and was implanted into AlGaN at JAEA at various doses of 1×10^{12} – 2.8×10^{16} Tb/cm². Rutherford backscattering spectrometry/channeling study showed steep increase of ion-beam-induced damage when the dose exceeds 5×10^{14} Tb/cm². On the other hand, cathodoluminescence (CL) result showed initial increase of intensity related to Tb³⁺ transition, and exhibited saturation above a dose of 1×10^{13} Tb/cm². These results suggest that Tb-related luminescence properties are much susceptible to the defects and non-radiative defects.

広いバンドギャップを有する半導体に添加した希土類元素は、内殻準位の遷移に基づいた鋭い発光スペクトルや、安定した温度特性といった特徴を有する。母材として種々の半導体材料に希土類元素導入が試みられている中で、我々は、Eu や Tb といった希土類元素を III 族窒化物半導体混晶である AlGa_{1-x}N に導入することで良好な発光特性が得られることを報告してきた¹⁾。本研究ではイオン注入法により Tb を AlGa_{1-x}N に添加し、イオン注入時のダメージと発光特性の関連について結晶性および発光特性の評価を行って検討した。

注入に用いた Al_xGa_{1-x}N は有機金属気相成長法によりサファイア基板上に成長したものを用いた。過去の検討から、アルミニウム組成 x が 0.3 より大きい母材で良好な発光特性が得られたため、本研究では x=0.35 の結晶を用いて、TIARA のイオン注入装置により、加速エネルギー 200 keV でドーズ量 1×10^{12} – 1.4×10^{16} Tb/cm² の条件でイオン注入を行った。イオン注入後に結晶性の回復を目的として N₂ と NH₃ の混合雰囲気中で 1,100 °C、120 s の高速熱処理(RTA)を行った。

Figure 1 にドーズ量を変化させた試料のラザフォード後方散乱(RBS)/チャネリング測定のスเปクトルを示す。ドーズ量 5×10^{14} Tb/cm² 以下の低ドーズ量の試料は未注入試料とほぼ変わらないスเปクトルを示し、 1.5×10^{15} Tb/cm² 以上のドーズでは結晶中のダメージ導入を示すピークが現れた。Tb は窒化物半導体中で III 族サイトを占有すると考えられている。この実験結果は、低ドーズ試料では RTA 処理により Tb が III 族サイトに収まるが、ある一定以上のドーズ量では、RTA 処理に

よる結晶性回復が困難なダメージが形成されることを示唆している。

次に、発光特性とドーズ量の関連について評価を行った。Figure 2 にカソードルミネセンス(CL)測定で得られた Tb の $^5D_4 \rightarrow ^7F_6$ 遷移に関連したピークの積分強度のドーズ量依存性を示した。室温および 79 K での測定結果はほぼ同じ特性を示し、Tb が優れた温度安定性を有することを示している。ドーズ量変化に対しては、 1×10^{13} Tb/cm² のドーズ量まではドーズ量の増加とともに発光強度も増加したが、それ以上のドーズでは積分強度が飽和する傾向が得られた。一方、RBS 測定で得られたチャネリングイールド χ_{\min} は一般的に母材の結晶性を反映し、本実験では 5×10^{14} Tb/cm² 以上のドーズに対して急速に増加する傾向を示した。興味深いのは、CL 強度が飽和を示すドーズ量は、RBS で急速な結晶性悪化がみられたドーズ量よりも 1 桁以上低いという点である。この理由は、注入した Tb のうち、結晶欠陥などの影響により限定された Tb のみが発光に寄与しているといったことが考えられる。最近、我々はイオン注入の他に結晶成長で希土類元素を導入する実験を行い、結晶成長条件が希土類元素の発光スペクトルに影響することを見出している。希土類元素の適切な添加条件の選択により、より高効率な発光素子実現が期待できる。

References

- 1) A. Wakahara, Opt. Mater. **28** (2006) 731.
- 2) J.-H. Park et al., Jpn. J. Appl. Phys. **49** (2010) 032401.

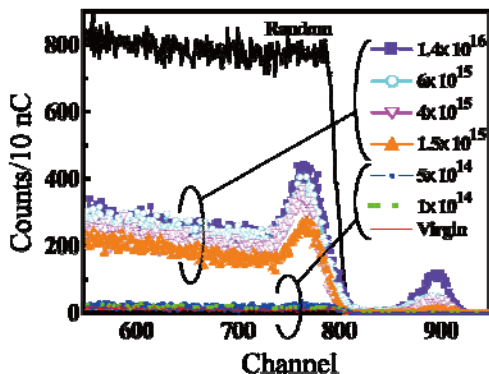


Fig. 1 RBS/channeling spectra for AlGa_{0.35}N:Tb in the range of 1×10^{14} – 1.4×10^{16} Tb/cm².

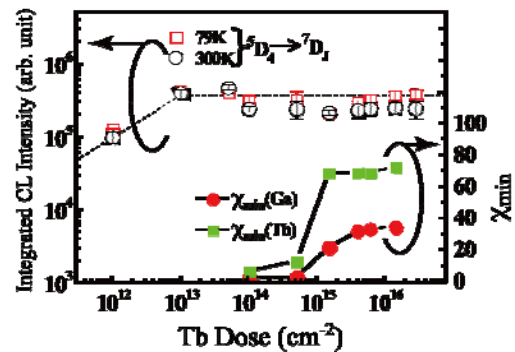


Fig. 2 Integrated CL intensities related to $^5D_4 \rightarrow ^7F_6$ transition of Al_{0.35}Ga_{0.65}N:Tb at 79 K and 300 K as a function of Tb dose after RTA.

1-12 Single Ion Induced Luminescence from ZnS(Ag), CdWO₄, YAG:Ce and Diamond

S. Onoda, T. Makino and T. Ohshima

Environment and Industrial Materials Research Division, QuBS, JAEA

In order to measure the Single Event Effect (SEE) mapping on semiconductor devices, we are developing the Ion Photon Emission Microscopy (IPEM) by using highly-sensitive cooled Charge Coupled Device (CCD) Camera and the Image Intensifier (I.I.). The system contains a beam extraction window (Kapton film) under the mirror, a sample (phosphor on Si diode) on micro XYZ stage, an electronics for charge measurements including amplifier, bias supply and oscilloscope, and a photon detection equipments including the microscope (Olympus, BX51M), I.I. (Hamamatsu, C8600), and cooled CCD camera (Hamamatsu, C4880-50-26A). Ion beams accelerated by the AVF Cyclotron are extracted from vacuum to air via the Kapton film. Extracted ions penetrate the phosphor on diode. The photons from the phosphor are detected by the cooled CCD camera. At the same time the ion induced charge in diode is recorded by the oscilloscope. The position where ion strikes the sample is recorded together with the ion induced charge. In the previous study, ZnS(Ag) has been used as the phosphor. Figure 1 (a) shows the image of cooled CCD when 150 MeV Ar ions penetrate ZnS(Ag). Three spots are detected and each spot can be distinguished. The diameter of spot is about 40 μm . The position where ion hits the sample can be calculated from the center of mass of each spot. Since the spot size determines the resolution of map, it is necessary to find the another luminescence sheet.

Branson et al., reported that YAG:Ce is the most promising materials as a phosphor from the point of view of the luminescence intensity, the decay time, and the radiation hardness^{1,2)}. The maximum resolution of about 5 μm has been achieved by using YAG:Ce. We measure the ion luminescence from CdWO₄, YAG:Ce and Diamond as shown in Fig. 1 (b). For CdWO₄, the intensity of luminescence is very weak and the spot size is larger than that of ZnS(Ag). For both YAG:Ce and diamond, the minimum spot size of about 8 μm is observed. Only for YAG:Ce the spread spots are detected. The intensity of luminescence from Diamond is higher than that from YAG:Ce. According to these results, we suggest that both Diamond as well as YAG:Ce are suitable for IPEM from the point of view of higher spatial resolution.

References

- 1) J. V. Branson et al., Nucl. Instrum. Meth. B in press.
- 2) J. V. Branson et al., Nucl. Instrum. Meth. B, 267, (2009) 2085-2089.

Acknowledgment

The CdWO₄ and YAG:Ce was provided by Mr. A. Yokoyama of the Department of Advanced Radiation Technology, TARRI, JAEA. Diamond was provided by Prof. Isoya of Tsukuba University.

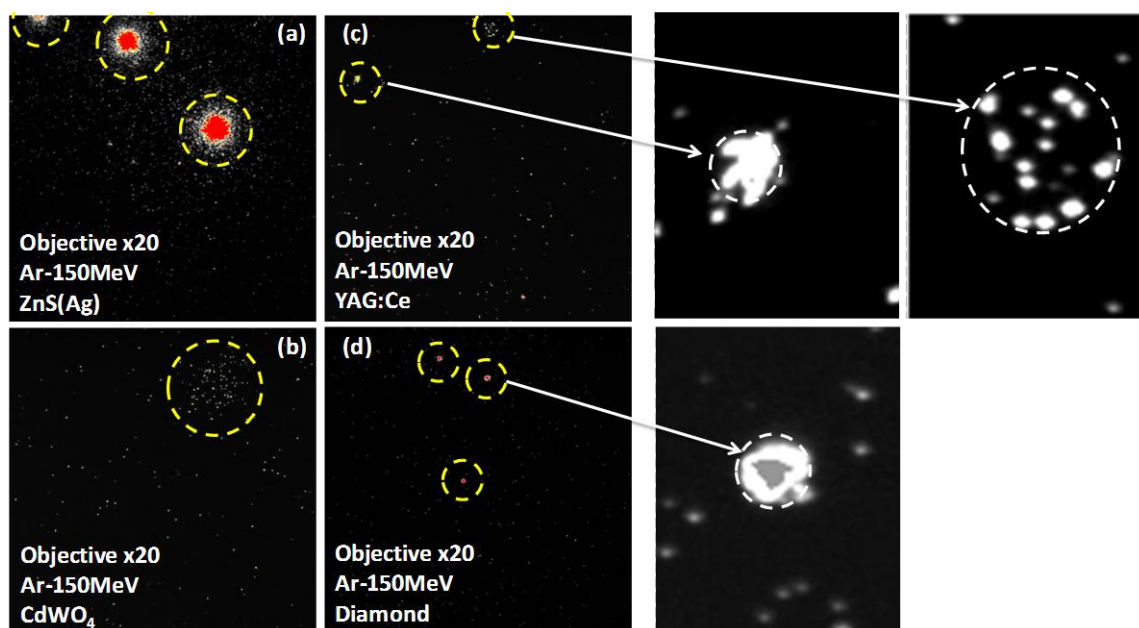


Fig. 1 Luminescence from (a) ZnS(Ag), (b) CdWO₄, (c) YAG:Ce, and (d) Diamond.

1-13 First-Principles Molecular Dynamics Simulation of SiO₂/SiC Interface of Silicon Carbide Devices (II)

A. Miyashita and M. Yoshikawa

Environment and Industrial Materials Research Division, QuBS, JAEA

Silicon carbide (SiC) devices are expected to be applied in severe environments such as outer space and/or nuclear power plants. The performance of SiC metal-oxide-semiconductor (MOS) devices to date has not reached the value theoretically expected. This is considered to be attributed to defects generated at the SiO₂/SiC interface that degrade the electrical characteristics of the MOS devices. Recently, the special attentions have been made for the amorphous SiO₂(*a*-SiO₂)/4H-SiC interface on the C face, since it was reported by several groups that the field-effect mobility at the interface on the C face is higher than that on the Si face¹⁾. However, no report has been found for the improvement mechanisms of the mobility on the C face.

Last few years, we developed large-scale simulation technique of *a*-SiO₂/4H-SiC interface on the Si face in actual MOS devices and successfully obtained the theoretical *a*-SiO₂/4H-SiC interface on the Si face involving various types of defects on a large-scale computer²⁾. In this work, we report the development of simulation technique of the *a*-SiO₂/4H-SiC interface on the C face. The final goal is to clarify the improvement mechanisms of field-effect mobility on the C face by computational science techniques.

A simulation of *a*-SiO₂ on the C face of a 4H-SiC substrate in actual MOS devices was carried out on large-scale computer using the first-principle molecular dynamics calculation, in which Vienna *ab-initio* Simulation Package (VASP)³⁾ was employed as a calculation code. On the basis of an atomic network of beta quartz (β -SiO₂) connected on the C face of 4H-SiC crystal, a slab model was prepared for the simulation. The O atoms on top of β -SiO₂ and C atoms on bottom of 4H-SiC crystal were saturated by H atoms. The number of Si, C, O and H atoms in the slab model is 252, 144, 216 and 36, respectively. The theoretical *a*-SiO₂/4H-SiC interface on the C face was created on computer by applying the heating and quenching method to the slab model for which a periodic boundary condition was adopted. To prevent the electronic cloud on the top and the bottom of the slab model from overlapping due to the periodic boundary condition, the vacuum layer spacing 1 nm was inserted on top of β -SiO₂ in the slab

model. Figure 1 shows the temperature profile of the heating and quenching process. At first, only the atoms of β -SiO₂ were heated theoretically at 4,000 K for 3 ps. The rest of atoms in the slab model were kept frozen in order to maintain SiO₂ at a constant volume. After cooling down to 3,500 K, the H atoms on top of SiO₂ were removed and the 2 layers of 4H-SiC substrate below the interface were defrosted. Then the slab model was annealed at 3,500 K for 1.3 ps to mix the atoms up well near the top of SiO₂ in the slab model. Thereafter all atoms of 4H-SiC substrate except for the H atoms on the bottom were defrosted, the slab model was cool down to room temperature quite rapidly at the quenching rate of -1,000 K/ps.

The obtained slab model was shown in Fig. 2. Although abrupt *a*-SiO₂/4H-SiC interface composed mainly with C-Si bonds is formed by the simulation process mentioned above, C dangling bonds and several different types of bonds such as C-O and C-C are seen at the interface. In order to estimate the effects of interface defects on the electrical characteristics of MOS structure created using C face, the density of state (DOS) at the *a*-SiO₂/4H-SiC interface in Fig. 3 was derived. The energy level of defect which originates in C-C bond at the interface is observed around 0.2 eV above the edge of valence band. It is considered that the energy level generated near the edge of conduction band is related to the degradation of field-effect mobility⁴⁾. It is suggested that the C-C bond at the interface does not have significant influences in the degradation of MOS devices fabricated using C-face. Therefore, further computational experiments are necessary for the interface on the C face of 4H-SiC substrate to reveal the improvement mechanisms of field-effect mobility on the C face.

References

- 1) K. Fukuda et al., Mater. Sci. Forum. **433-436**, (2003) 567.
- 2) A. Miyashita et al., JAEA Takasaki Ann. Rep. 2007 (2008) 13.
- 3) G. Kresse et al., Phys. Rev. **B54**, (1996) 11169.
- 4) M. Bassler et al., Diamond Relat. Mater. **6** (1997) 1472.

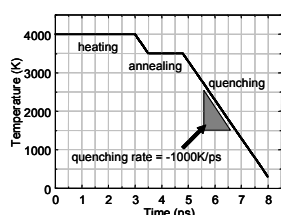


Fig. 1 The temperature profile of heating and quenching process.

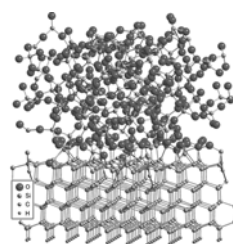


Fig. 2 The calculated slab model.

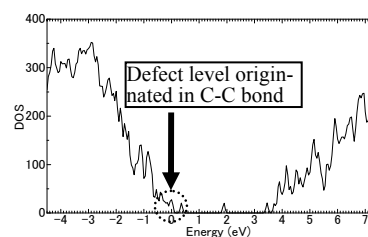


Fig. 3 DOS of the slab model.

1-14 Influence of Energy of Helium Ions on Degradation of Diglycolamide in *n*-Dodecane

Y. Sugo^{a), c)}, M. Taguchi^{b)}, Y. Sasaki^{c)} and Y. Morita^{c)}

^{a)} Life-Science and Biotechnology Division, QuBS, JAEA, ^{b)} Environment and Industrial Materials Research Division, QuBS, JAEA, ^{c)} Division of Fuels and Materials Engineering, NSED, JAEA

1. Introduction

A tridentate extractant, *N,N,N',N'*-tetraoctyl-diglycolamide (TODGA) has high extractability for actinides such as americium and curium from nitric acid into *n*-dodecane. Alpha-Radiolysis study of the organic extractants using an actinide radionuclide has some experimental difficulties. For example, a long-term exposure to actinides is required, and the extractants are contaminated with the radionuclide. In the previous study¹⁾, these issues were solved by irradiation with helium ions provided by an accelerator. It was also found that the radiation chemical yield for the degradation of TODGA in *n*-dodecane by helium ions corresponding to the alpha-particles was less than that by gamma-rays.

In order to prove an effect of linear energy transfer (LET) on the radiolysis of TODGA in *n*-dodecane, the influence of energy of helium ions was investigated in this study.

2. Experimental

The solution of TODGA in *n*-dodecane was irradiated with helium ions according to the schematic diagram of the irradiation system shown in Fig. 1. The thickness of the sample was larger than the penetration range of the ions. Incident energy of the ions on the surface of the sample was attenuated by aluminum foils, and determined by silicon semiconductor detector. Absorbed dose was estimated on the assumption that whole the incident energy was given to the sample, and the sample solution was homogeneous. The sample was also irradiated with ⁶⁰Co gamma-rays for comparison of the degradation efficiency between helium ions and gamma-rays. The concentration of TODGA

before and after irradiation was determined using a capillary gas chromatography equipped with a flame ionization detector.

3. Results and Discussion

The concentration of TODGA in *n*-dodecane after irradiation with helium ions or gamma-rays is logarithmically plotted against dose in Fig. 2. This figure shows the degradation efficiency increases with the incident energy of helium ions, and the decay curve for 99.1 MeV helium ions is close to that for gamma-rays. Furthermore, the number of molecules of TODGA decreased by the single helium ion was obtained at various incident energies, and the differential *G*-value was estimated by differentiating the fitted curve of the number of molecules against energy. It was observed that the differential *G*-values increased with increasing energy or with decreasing LET value.

These results indicate the degradation efficiency decreases with increasing LET value. Because the transient species are densely produced in the track by high LET radiations, and then decreased by recombination in the track at very early time.

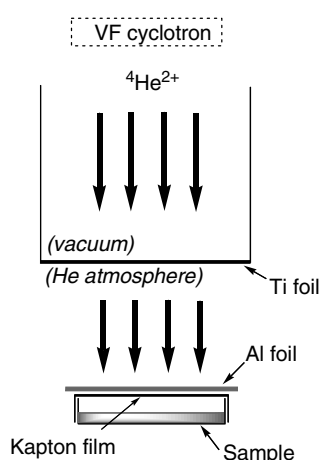


Fig. 1 Schematic diagram of the irradiation system.

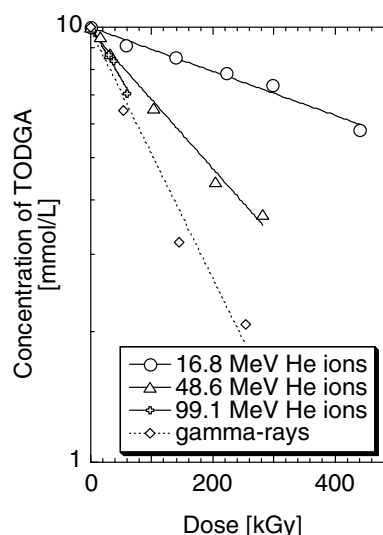


Fig. 2 Degradation of TODGA in *n*-dodecane by irradiation with helium ions at various incident energies and gamma-rays.

Reference

- 1) Y. Sugo et al., Radiat. Phys. Chem. 78(12) (2009) 1140-1144.

1-15 **Confirming Performance of Expanded Bed for Chromatographic Separation by Gamma Irradiation Experiment**

S. Watanabe, K. Nomura, Y. Sano and Y. Koma

Advanced Processing Unit, ANSRD, JAEA

For separation of americium and curium from highly active waste solutions, extraction chromatography technology is useful, although it also brings inherent technical issues of hazardous gas generation by radiolysis and plugging due to foreign solid particles¹⁾. The expanded bed technique is a counter measure by discharging gas and solids more easily than the conventional stationary bed.

An expanded bed is formed by a flow of mobile phase to float adsorbent at its constant density²⁾. The column of 20 mm of ID was used to obtain such an apparent stationary phase of 6 g adsorbent with a 6.2 cm height that is dynamically sustained by a flow of 4 cm/min. As shown in Fig. 1, the bed is sparse and the density of adsorbent is almost a half of a packed column. The adsorbent used was a composite with styrene-divinylbenzene polymer.

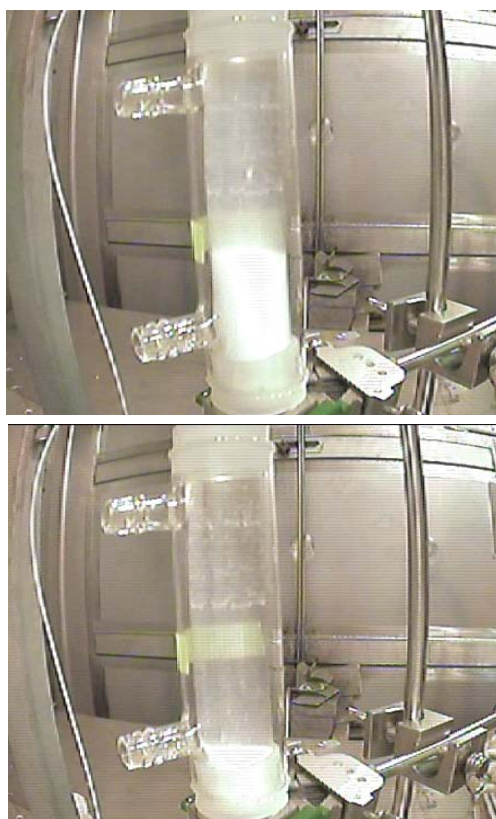


Fig. 1 Appearances of the expanded bed (up) and the packed bed (down). Flow directions of mobile phase were upward and downward for the expanded bed and the packed bed, respectively.

The column system was operated and irradiated with gamma-ray at a dose rate of 3.9 kGy/h for 16 hours. Gas generation from radiolysis was not observed within the column as well as the gas trap, and discharged from the system. This is owing to absorption of hydrogen and oxygen by the mobile phase and their discharge afterwards.

Without pumping water, gas generated was stayed in the stationary phase and at the top of the column. After restarting the flow, the gas was again transported and successfully trapped. This indicates that an accidental halt of the system results in holding gas inside the column, although the resumed mobile phase will safely discharge the hazardous gas.

Water containing the simulated particle and copper as a tracer was fed to the column during irradiation. Elution profile of Cu shows no influence from foreign particles that flows through the expanded bed as shown in Fig. 2.

Acknowledgements

We would like to thank Associate Professor Dr. Tsuyoshi Arai, Tsuyoshi Ogawa and Shota Sakurai of Shibaura Institute of Technology for their advice and assistance on the expanded bed technique, and also Mr. R. Yamagata at Irradiation Service Section in TARRI for his assistance on the experiment.

References

- 1) Y. Koma et al., JAEA Takasaki Ann. Rep. 2009 (2011) 20.
- 2) S. Yamamoto et al., Jpn. J. Food Eng. 1(2) (2000) 51.

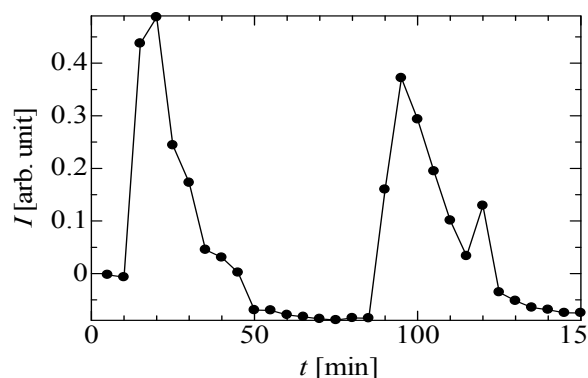


Fig. 2 Elution profile of copper as a tracer.

1-16 Irradiation Effect of Gamma Rays on Cyanate Ester/Epoxy Resins (2)

A. Idesaki^{a)}, H. Uechi^{b)}, S. Matsuda^{b)} and H. Kishi^{b)}

^{a)} Environment and Industrial Materials Research Division, QuBS, JAEA,

^{b)} Graduate School of Engineering, University of Hyogo

Various organic materials are used as electrical insulators for equipment in the atomic energy related facilities. The organic materials are required to possess sufficiently high radiation resistance in order to realize safe and stable operation of the facilities. For example, the electrical insulators of superconducting magnet system in the J-PARC muon beam line are required with radiation resistance of several ten MGy.

Recently, cyanate esters which show excellent properties such as high thermal resistance, low dielectric constant, low absorbency, and so on, have attracted attention as high radiation resistant materials. However, they have drawback of low formability due to high melt viscosity and relatively high curing temperature (~270 °C). In order to lower the melt viscosity and curing temperature and to improve the formability, the co-reaction of cyanate esters with epoxy resins has been adopted. In this reaction, cyanate esters and epoxy resins form crosslinking. We have reported about superior radiation resistance of cyanate ester / epoxy resins¹⁾, and the materials are expected to be applied for the superconducting magnet systems of J-PARC, ITER, and so on. However, the degradation mechanism of cyanate ester / epoxy resins by the radiation has not been clarified. In this work, the degradation mechanism of cyanate ester / epoxy resins was investigated in the view point of gas evolution, change of density, and so on.

Dicyanate of bisphenol A (DCBA) and diglycidyl ether of bisphenol A (DGEBA) were formulated by 50/50 in weight (referred as DCBA/DGEBA). The prepared resins were irradiated by ⁶⁰Co gamma-rays with dose of 100 MGy (10 kGy/h) under vacuum at room temperature.

Figure 1 shows evolved gases from the resins after the gamma-ray irradiation. The main gases evolved from DCBA/DGEBA were hydrogen (H₂), carbon dioxide (CO₂), carbon monoxide (CO), while the CO₂ and CO gases were hardly evolved from pure DCBA. The CO₂ and CO from the DCBA/DGEBA are evolved by the chain scission of structures such as alkylcyanurate, alkylisocyanurate and alkyloxazolidinone which are formed between cyanate ester and epoxy in the co-reaction, because it was found by ¹³C NMR that the number of alicyclic groups and aliphatic chain groups decreased after the irradiation (results are not shown). This indicates that the radiation degradation of DCBA/DGEBA occurs in the crosslinking cite.

Figure 2 shows the change of density of DCBA/DGEBA after the irradiation. Both the density of DCBA/DGEBA and pure DCBA increased slightly after the irradiation. This is probably attributed by the increasing in the packing

density of molecular chains which is caused by the scission of local chemical bonding during the irradiation under vacuum.

In this work, the degradation mechanism of DCBA/DGEBA by gamma ray irradiation was investigated. It was found that the radiation-induced degradation of DCBA/DGEBA occurs in the crosslinking cite where the structures such as alkylcyanurate, alkylisocyanurate and alkyloxazolidinone are formed during the co-reaction.

Acknowledgement

We thank to Mitsubishi Gas Chemical Company, Inc. for providing cyanate ester resins.

Reference

- 1) A. Idesaki et al., JAEA Takasaki Ann. Rep. 2009 (2011) 21.

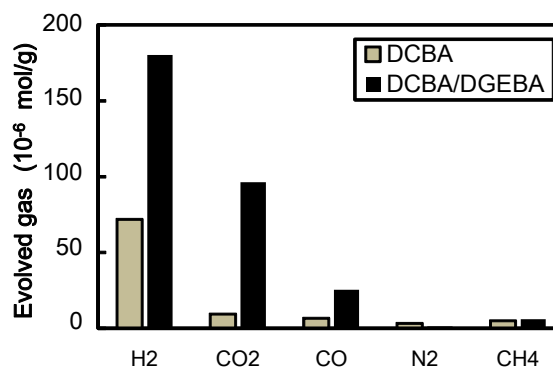


Fig. 1 Evolved gases from DCBA/DGEBA after gamma-ray irradiation.

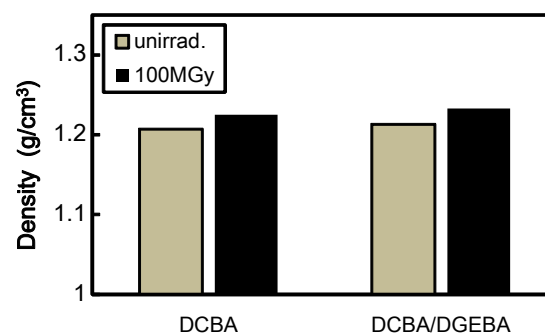


Fig. 2 Change of density of DCBA/DGEBA after gamma-ray irradiation.

1-17 Effects of Antioxidants on the Degradation of Flame-Retardant Ethylene Propylene Rubber

A. Shimada^{a)}, A. Idesaki^{a)}, M. Sugimoto^{a)}, M. Yoshikawa^{a)}, K. Tamura^{b)},
T. Seguchi^{b)} and H. Kudoh^{c)}

^{a)} Environmental and Industrial Materials Research Division, QuBS, JAEA,

^{b)} LWR Long-term Reliability Research Unit, NSRC, JAEA,

^{c)} Graduate School of Engineering, The University of Tokyo

In nuclear power plants (NPPs), many cables are used for electric power supply to instruments, transmission of signals and so on. The insulation of cables is made of polymers such as flame-retardant ethylene propylene rubber (FR-EPR), crosslinked polyethylene, silicone rubber and so on. The insulation of cables is degraded gradually under heat and radiation condition. Various additives are added to the insulation of cables to improve this property. The antioxidant (AX) is added to FR-EPR to decrease the oxidation degradation. In our previous studies, AX was found to be the key agent for the determination of lifetime¹⁾. A small content of AX was very effective to reduce the thermal ageing, but not so much to the radiation ageing. The content of AX in the polymer decrease gradually by evaporation during thermal ageing and by radiation degradation. The rate of decrease is dependent on the molecular characteristics of molecular weight and structure.

In 2010 studies, two types of AX were selected, low molecular weight (Nocrac 200; Mn: 220) and high molecular weight (Nocrac MB; Mn: 300)²⁾. Each AX was formulated in FR-EPR samples (1 mm sheet) with different content (0.0, 0.3, 3.0 phr). The samples were irradiated by Co-60 γ -rays in air at 175 °C, at a dose rate of 1.0 kGy/h, for 25-100 h (25-100 kGy). Irradiation is conducted at Takasaki Advanced Radiation Research Institute. The degree of degradation was measured by tensile tests.

The value of elongation at break of FR-EPR is plotted against the irradiation time in Fig. 1, which are containing 0, 0.3 and 3.0 phr of Nocrac 200. The addition of Nocrac 200 leads to a slight increase in the elongation at break. But, the difference in the concentration of Nocrac 200 leads to subtle difference in elongation at break.

The value of elongation at break of FR-EPR is plotted against the irradiation time in Fig. 2, which are containing 0, 0.3 and 3.0 phr of Nocrac MB. The addition of 0.3 phr of Nocrac MB leads to the increase in the elongation at break. And, the increase in the concentration of Nocrac MB to 3.0 phr leads to more increase in the elongation at break.

One of the reasons why the efficiency of AX is different between Nocrac MB and Nocrac 200 is lower volatility of Nocrac MB. Most amount of Nocrac MB may be remained in FR-EPR at the condition of 175 °C and 1 kGy/h after the passage of 100 h.

References

- 1) T. Seguchi et al., Radiat. Phys. Chem. 80 (2011) 268-273.
- 2) Catalog of rubber material published by Ouchi Shinko Chemical Industrial Co., LTD.

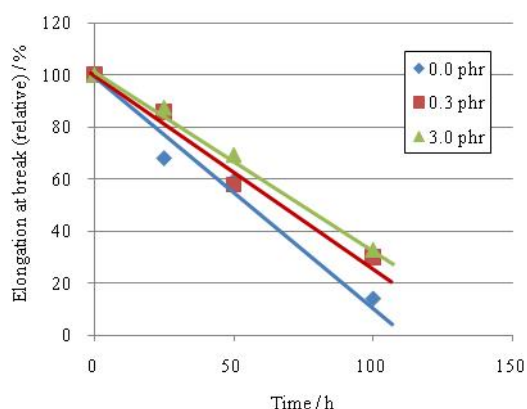


Fig. 1 Elongation at break by the irradiation of FR-EPR containing Nocrac 200 (175 °C, 1.0 kGy/h).

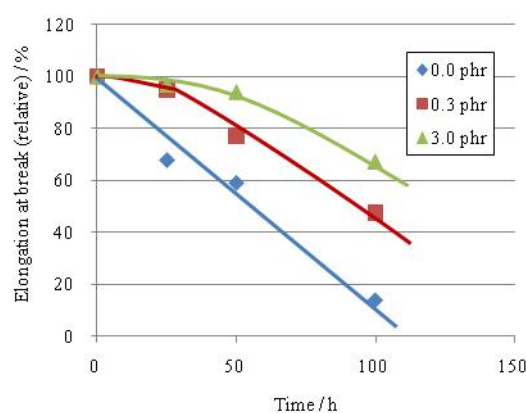


Fig. 2 Elongation at break by the irradiation of FR-EPR containing Nocrac MB (175 °C, 1.0 kGy/h).

1-18 Alpha-Ray Irradiation Damage on Materials Applied for Glove Box for Plutonium Powder Treatment

K. Saito, K. Matsuyama and H. Endo

Plutonium Fuel Development Center, NFCEL, JAEA

Currently, for economical reasons, newly improved long-lasting glove is desired and under development at Plutonium Fuel Development Center (Pu center), Tokai, JAEA. For the basic step of the development, helium ion irradiation experiments have been conducted in order to evaluate α -ray effects against the glove rubber material. In these experiments¹⁻³⁾, effects of dose (fluence) by ion were come to light as the major factor of material deterioration. Then, both another glove and a vinyl bag were investigated additionally. These two types of materials are commonly used on non-severe conditions at glove boxes.

One of sample material is chlorosulfonated polyethylene (CSM) glove which SANKO CHEMICAL INDUSTRY Co. Ltd. manufactures. The other is vinyl chloride sheet whose color and degree of polymerization are yellow and 2000, respectively. JIS K 6251-7 dumbbell-shaped pieces cut from the materials were irradiated in a vacuum with $^4\text{He}^{2+}$ ion beam generated from 3 MV tandem accelerator in TIARA. The kinetic energy of the accelerated ion was 5 MeV close to the average energy of α rays emitted from plutonium isotopes. Main parameter was fluence and this was set at the level of 0.1~3 years by 2.9 MBq/cm^2 of α -contamination, i.e. $0.46 \sim 14 \times 10^{13} \text{ cm}^{-2}$. Since the deterioration-promoting effect under stress by γ -ray irradiation is known, a stress parameter on sample was additionally set as 100%-"elongated" for CSM material. Flux, duration, the corresponding absorbed dose and its rate were $4.9 \sim 10 \times 10^{10} \text{ p/cm}^2/\text{s}$, 1~46 min, 0.7~20 MGy and 41~44 MGy/h, respectively. Four sample pieces were simultaneously irradiated for one condition (fluence and stress) and the irradiated samples are sent to visual inspection and two tensile tests: tensile strength and elongation at break.

There are no differences observed in surface appearance for both CSM and elongated-CSM. Figure 1 shows irradiated elongated-CSM samples and vinyl samples. Elongated-CSM samples showed "curl" because of surface hardening and vinyl samples became amber.

The results of tensile strength and elongation at break are shown in Fig. 2 and 3, respectively. Tensile strength of both CSM and elongated-CSM rapidly decreases with fluence in compare with other glove candidate materials measured so far. Another characteristic feature of CSM is that the both results are not monotonously decrease. Additionally, there is clear difference between CSM and elongated-CSM at maximum fluence experimented.

The results of tensile tests suggest that the CSM is unsuitable for high-radiation-dose ambient in view of not only the radiation exposure of workers but also the

α -radioactive endurance of material. Vinyl material deterioration data can be used for the validity evaluation of the present service life of the material and its protraction.

The obtained data are unexampled and quantitative ones for α -damage of glove and its material.

References

- 1) K. Saito et al., JAEA Takasaki Ann. Rep. 2007 (2008) 20.
- 2) K. Saito et al., JAEA Takasaki Ann. Rep. 2008 (2009) 28.
- 3) K. Saito et al., JAEA Takasaki Ann. Rep. 2009 (2011) 25.



Fig. 1 Photographs of irradiated samples with fluence of $1.4 \times 10^{14} \text{ cm}^{-2}$ (left, elongated CSM) and $4.6 \times 10^{13} \text{ cm}^{-2}$ (vinyl, tensile-tested).

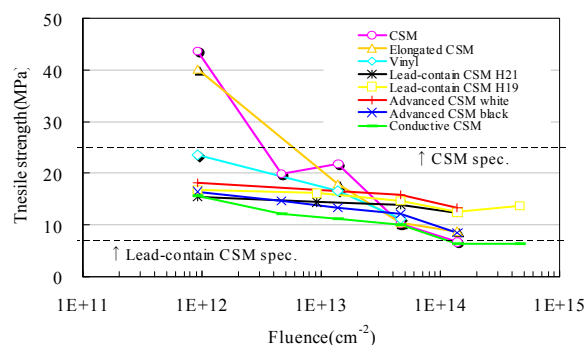


Fig. 2 Results of tensile strength.

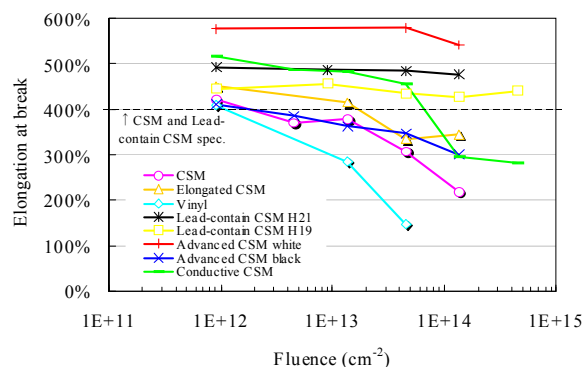


Fig. 3 Results of elongation at break.

1-19 Development of an Observation Technique Using a Fiberscope under High Radiation Doses

H. Naito^{a)}, W. Itagaki^{a)}, C. Ito^{a)}, A. Nagai^{a)}, Y. Okazaki^{a)}, R. Kitamura^{a)},
N. Shamoto^{b)} and Y. Takeshima^{b)}

^{a)} Experimental Fast Reactor Department, ORDC, JAEA,
^{b)} Applied Optics Products Division, Fujikura Ltd.

A high radiation resistant fiberscope has been developed for the sodium cooled fast reactor in-vessel observation which has to be conducted under high temperatures and high radiation doses. The in-vessel repair activities in the experimental fast reactor Joyo take several weeks at 300 Gy/h¹⁾. This environment requires the fiberscope to be durable until 5×10^5 Gy. The current image fiber consists of pure silica core with 200 ppm hydroxyl (OH) and fluorine-doped silica clad. The radiation-induced transmission loss of this fiber is 10 dB/m at 5×10^5 Gy.

The OH associates with a Si which has unpaired electrons. This blocks the formation of a color center. The OH concentration in the core was increased from 200 ppm to 1,000 ppm. The prototype fiber consists of a pure silica core with 1,000 ppm OH and fluorine-doped silica clad. The acrylate is weak against the gamma irradiation and it is used as the clad material of the current light guide fiber. Hence the clad material was changed to fluorine-doped silica.

A gamma-irradiation test was carried out under 5×10^3 Gy/h using a ⁶⁰Co source at 200 °C to confirm the effect of the improvement.

At 5×10^5 Gy, a large absorption at 630 nm was observed and we could not measure the transmitted power at the top of the absorption peak by the non-bridging oxide hole center (NBOHC). We modeled the generation of the NBOHC²⁾ as shown in Fig. 1 to evaluate the radiation-induced transmission loss at 5×10^5 Gy.

The radiation-induced loss is approximated by the summation of the linear part which is attributed to the quantity of the precursors generated by gamma-rays and the exponential part which is attributed to the quantity of the precursors existed before irradiation. The linear part of the equation for an improved fiber is almost 0, and it indicates that OH inhibits the generation of the NBOHC by gamma irradiation. We evaluated the induced loss for visible region (400 - 700 nm) using the spectrum of the light source, the radiation-induced loss at each wavelength, and the quantum efficiency at each wavelength of a CCD. The

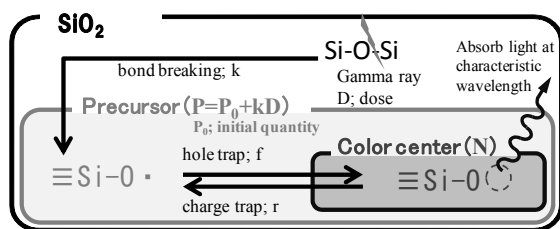


Fig. 1 Model for evaluating radiation-induced loss by gamma-rays.

results are shown in Fig. 2. Under the high dose irradiation, the effect of improvement is appeared and the radiation-induced loss of the modified fiber is saturated and becomes 0.9 dB/m at 5×10^5 Gy. It is possible to use this fiber in the reactor vessel of Joyo because it is considered that the irradiation length is about 3 m.

A mechanical strength of a fiber depends on an amount of small flaws on the surface of the silica glass. In the manufacturing process, an image fiber is coated with some materials to prevent flaws from generating and growing. To confirm the mechanical strength of the coated fiber after irradiation of 5×10^5 Gy at 200 °C, we measured the breaking strength of the samples which were irradiated at various doses by a tensile testing machine after the irradiation. The strength was not varied for each sample (Fig. 3) and we confirmed that there is no weakening the strength of the fiber and no exfoliation of the coating from the glass.

We developed the observation technology using a fiberscope under the 200 °C after 5×10^5 Gy irradiation.

References

- 1) W. Itagaki et al., ANIMMA2009 (2009) 7.
- 2) K. Shibuya et al., Proc. Int. Wire Cable Symp. **31** (1982) 51.

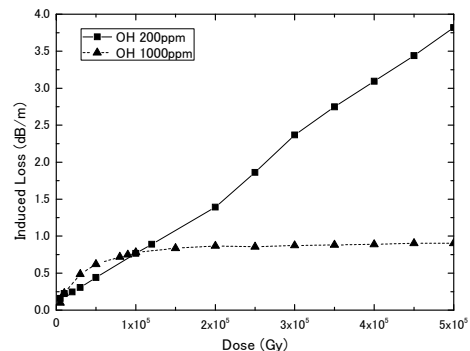


Fig. 2 Induced loss of image fibers for the visible region.

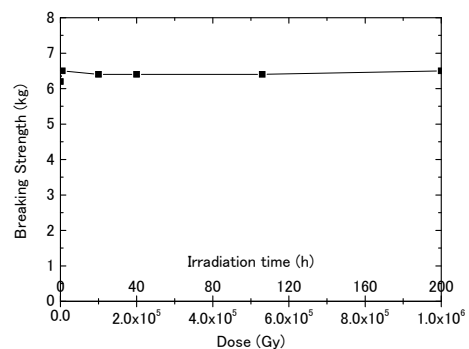


Fig. 3 Breaking strength for irradiated fiber samples.

1-20

Electrification of Coaxial Cable Model by Gamma-rays Irradiation

K. Takano ^{a)}, S. Ukon ^{a)}, O. Takeda ^{b)}, N. Morishita ^{c)} and H. Seito ^{d)}

^{a)} Fujikura Ltd. ^{b)} Accelerator Division, J-PARC, JAEA,

^{c)} Environment and Industrial Materials Research Division, QuBS, JAEA,

^{d)} Department of Advanced Radiation Technology, TARRI, JAEA

When the coaxial cable is put under the radiation environment, the coaxial cable takes charge. Electrification has the possibility of influencing connected equipments and result of measurements. Therefore, it is preferable to suppress the electrification of the coaxial cable as small as possible. In the present study, the structure of the coaxial cable is replaced with a simple model. This model has a structure with the polymer material sheet between copper electrodes. We irradiated the gamma radiation to this model, and measured the induced current. As the results, the induced current became small, when the thickness of sheet thins. In addition, it was confirmed that an inflection point was generated in the curve of the measured current value when the thickness of sheet was 3 mm.

同軸ケーブルを放射線照射環境下で使用すると、帯電することが経験的に知られている。この帯電現象は、ケーブルを構成する高分子材料の内部に荷電担体（自由電子、イオンなど）が発生し、ケーブル内部に蓄積するものと考えられる。同軸ケーブルの帯電は、接続されている機器や測定結果などに影響を与える可能性があり、極力抑圧することが望ましい。そこで本研究では、同軸ケーブルの構造を、単純な銅板電極間に高分子材料シートを挟んだモデルに置き換え、シート材料の種類、厚さ、および照射するγ線の線量率を変えて、銅板電極に流れる誘起電流の測定を行ない、帯電現象を考察したので結果を報告する。

照射するシート材料には、同軸ケーブルの絶縁材料に使用する低密度ポリエチレン(LDPE)および高密度ポリエチレン(HDPE)、シース材料に使用する難燃ポリエチレン、耐放射線難燃ポリエチレンの4種類を選定した。シートの大きさは、200 mm × 200 mmで、厚さを1 mm, 2 mm, 3 mmの3水準とした。またシートを挟む銅板電極の大きさは、シートと同寸法とし、厚さを1 mmとした。シートと銅板電極はFig. 1に示すように、位置を合わせて密着させた状態で固定し、かつ銅板電極を電氣的に絶縁した状態で、アルミ支柱に取り付け移動用ステージに固定した。

試験は、銅板電極に接続した測定リードを照射室外に設置したデジタルマルチメータに接続し、照射を行いながらステージを移動させ、線量率を0.33～3.77 kGy/hの範囲で変化させて各線量率における誘起電流を測定した。測定の構成をFig. 2に示すとともに、測定結果をFig. 3に示す。

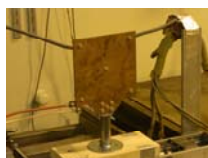


Fig. 1 Appearance of sample.

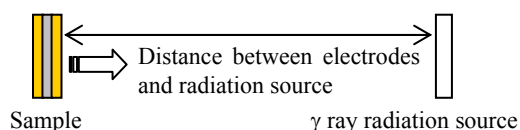


Fig. 2 Test composition.

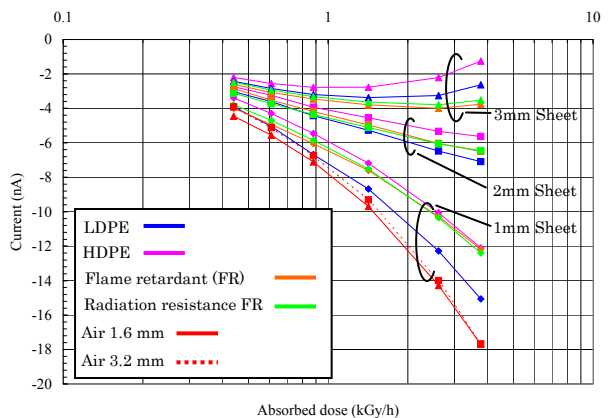


Fig. 3 Induced current of sheet sample.

測定の結果、各シートの厚さにおける誘起電流は、3 mm厚さのときに最も電流値が小さくなり、シートを薄くするに従い、電流値が大きくなることを確認した。また各シートの厚さにおける誘起電流曲線の挙動を比較すると、高線量率域での挙動の違いが著しく、1 mmシート厚さは、線量率が高くなるに従い誘起電流も大きくなる傾向にあるが、3 mmシート厚さでは、1～2 kGy/h付近で変曲点が現れ、線量率が高くなるに従い誘起電流が小さくなる傾向を示す。一方、銅板電極間を1.6 mmおよび3.2 mmの空気層として誘起電流を測定したところ、電流値は、1 mmシート厚さよりも若干大きく、また電流曲線の挙動は1 mmシート厚さと同様であった。これらの結果から、高分子材料内部に発生する荷電担体の挙動についての一考察を以下に示す。

シートの厚さが厚くなると、誘起電流が小さくなることから、高分子材料内部に発生する荷電単体は、銅板電極間を空気層にしたときに流れる電流を妨げる方向に移動すると考えられる。また3 mmシート厚さで変曲点が現れる原因としては、線量率が1～2 kGy/h付近で、高分子材料内部に発生する荷電担体総量が、空気層のときに流れる電流の荷電担体総量を上回り、支配的になるために、変曲点が発生するものと考えられる。

1-21 Gamma-Ray Irradiation Test of Centrifugal Contactor with Magnetic Bearing System

H. Ogino, A. Sakamoto, K. Fujisaku, S. Koizumi and H. Hirano

Nuclear Cycle Engineering Department, NFCEL, JAEA

A centrifugal contactor has an excellent phase separation and a smaller hold-up volume than any other contactor type such as mixer-settler and pulsed column. Therefore, the centrifugal contactor is said to be advantageous for reprocessing a fast breeder fuel of high burn-up and high Pu-enrichment¹⁾. In JAEA, the rolling bearing type centrifugal contactor with anti-corrosion design has been developed. However, the grease becomes deteriorated by radiation, acid mist, temperature and other environmental factors, and that also affects the service life²⁾. To provide a possible resolution to this technical issue, we have developed the centrifugal contactor of non-contact journaled construction using magnetic bearings without grease³⁾.

In order to convince radiation durability, gamma-ray irradiation tests of magnetic bearing type centrifugal contactors had been carried out. The present work is intended to confirm radiation durability of the magnetic bearing improved on basis of previous studies. Figure 1 shows the structure of magnetic bearing and the overview of irradiated magnetic bearing type centrifugal contactors. A magnetic bearing keeps a rotor to a center position by measuring the gap between the rotor and the electromagnetic with the position sensors, and supplying the bias current corresponding to the amount of change of the gap caused in disturbances. Two sets of contactors were irradiated with gamma-rays from ⁶⁰Co source (dose rate; about 120 C/kg/h). The contactors were driven without feeding a solution while irradiated. The irradiation durability test was continued until an abnormality occurred and the contactor stopped.

The No.1 contactor stopped 2,018 hours after the irradiation. Similarly, the No.2 contactor stopped 2,389 hours later. As to accumulation dose, the No. 1 and the No.2 contactor were 2.78×10^5 C/kg (1.08×10^9 R) and 2.88×10^5 C/kg (1.11×10^9 R), respectively. These results are accumulated dose which corresponds to 10 years operation. Figure 2 shows the changes in the position sensor maximum output of the magnetic bearing with the irradiation time. The position sensor outputs show the control results of the magnetic bearing, and its range was set at ± 1 V. The outputs were little change within 0.2 V until 1800 hours. After the irradiation time passed 1800 hours, the position sensor maximum output of the lower radial magnetic bearing increased gradually. As shown in Fig. 3, immediately before the stop, the position sensor output of lower magnetic bearing changed intensely. Therefore it was reasoned that the stop of the No.2 contactor was attributed to the sensor abnormality of the lower magnetic bearing. After the irradiation durability test, the contactors were dismantled for a detailed investigation. As a result, it was seen that the cable covering (polyimide) deteriorated

with both the contactors. And an abnormal insulation resistance and electric strength were measured with the radial position sensor cables of the two contactors. Based on these results, it was presumed that the stop cause of the magnetic bearing was the sensor abnormality due to the insulation failure that originated in the radiation deterioration of the cable covering.

References

- 1) G. J. Bernstein, et al., ANL-7969 (1973).
- 2) T. Washiya, et al., Proc. Global 2005 (2005).
- 3) N. Okamura, et al., Proc. Global 2007(2007).

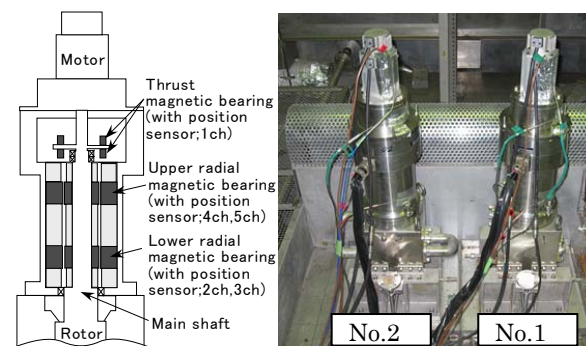


Fig. 1 Irradiated magnetic bearing type centrifugal contactors and structure of magnetic bearing.

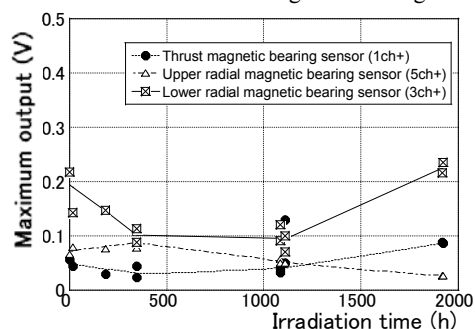


Fig. 2 Changes in the position sensor maximum output of the magnetic bearing with the irradiation time (No.2).

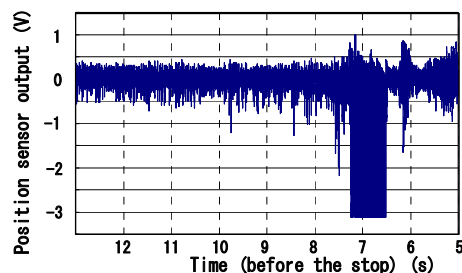


Fig. 3 Position sensor outputs immediately before the stop (No.2 contactor; 3 ch sensor).

1-22 Development of Penetration Part Processing Industrial Method in Radiation Controlled Area (Airtight Performance Examination)

K. Izumi^{a)}, M. Iguchi^{a)}, M. Kawasaki^{a)}, Y. Ohkawa^{a)}, K. Oka^{b)} and R. Yamagata^{c)}

^{a)} Kandenko Co. Ltd., ^{b)} Advanced Photon Research Center, QuBS, JAEA,

^{c)} Department of Advanced Radiation Technology, TARRI, JAEA

In radiation controlled areas, penetration such as walls where cables and cooling water pipes go is required to be airtight in order to maintain negative pressure of air-conditioning. In the original airtight processing method, radiation-proof materials have not been applied to the penetration, which would lead to the deterioration. In this study, the airtight performance examination was carried out with an aim for the development of a new method which enables both airtight and radiation hardness.

1. はじめに

医療施設・加速器施設・核融合施設・原子炉施設・次世代原子炉施設等は、放射線環境となるエリアを有する。放射線エリアでは、空調の負圧管理を行うため、ケーブル・冷却水配管等の貫通部の気密性が要求される。前回、気密処理材料の耐放射線性を確認し 10 MGy の耐放射線性がある事を確認した。本件では、本材料の気密性能の試験を実施した。

2. 試験体の製作

試験体を Fig. 1 に示す。ケーブルを通線して気密材料を流し込み製作した。試験体は、未照射、3, 5, 7, 10 MGy の 5 試験体を製作して試験した。



Fig. 1 Examination body.

3. 気密試験

- 1) 気密試験 1 では、片側の蓋を取外した状態で行いケーブルと気密材料との間の気密性について試験した。
- 2) 気密試験 2 では、片側の蓋を取外すと共に、もう片側の蓋も取り外し、配管と気密材料との間の気密性の確認のため試験した。気密試験 2 の試験は、未照射と 10 MGy 照射試験体の 2 試験体を試験した。
- 3) 気密試験装置の概念図を Fig. 2 示す。A room 側に各試験体を設置し、B room 側より圧力（最大 4,000 Pa）をかけ、A room に漏れてくる通気量を測定した。圧力は、ステップ状に上昇させ、その都度、通気量の測定を行なった。

4. 評価基準

比較評価基準は、JIS A4706（サッシの気密基準）A-4 等級と比較した。

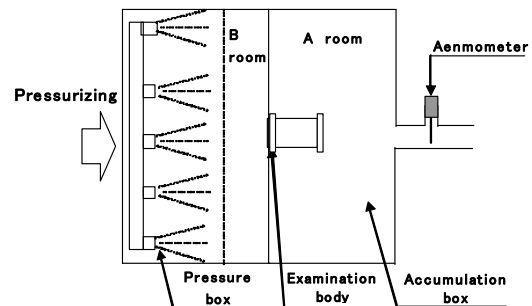


Fig. 2 Airtight examination device concept drawing.

5. 試験結果

通気を確認できた試験体は、7 MGy 片側蓋無し、未照射の両側蓋無し、10 MGy 両側蓋無しの 3 試験体であった。その通気量を Fig. 3 に示す。

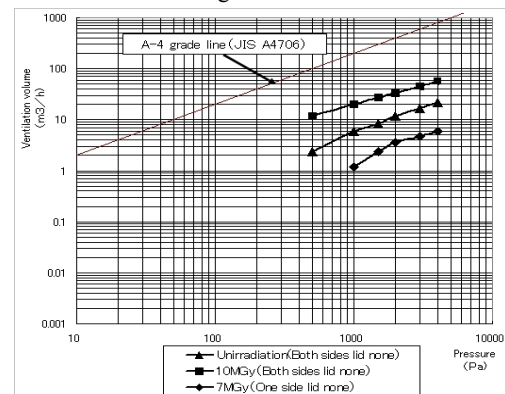


Fig. 3 Ventilation volume.

6. 考察

- 1) 通気量が確認できた試験体は、3 試験体のみであり、JISA4706 サッシの気密基準以下であることから、十分な気密性能があることがわかった。
- 2) 本材料は、約 1% の乾燥収縮があることがわかっているが、気密性能に影響を与えないことがわかった。

7. 今後

本試験により、本材料は、放射線管理区域の気密処理として使用可能な材料であることがわかった。今後は、実際の貫通部処理の工法を検討し、施工性に関する検討を実施する。

Reference

- 1) K. Izumi et al., JAEA Takasaki Ann. Rep. 2009 (2011)

1-23 Development of Radiation-resistant Lighting

T. Tsuchida^{a)}, R. Yamagata^{b)}, H. Seito^{b)}, Y. Haruyama^{b)}, H. Kaneko^{b)} and S. Kashimura^{a)}

^{a)} Kandenko Co., Ltd.,

^{b)} Department of Advanced Radiation Technology, TARRI, JAEA

There are a lot of restrictions of electric installations in a high radiation environment. For example, longevity of electric devices would be shortened remarkably, because of difficulty for lightning equipments in keeping an original function under such condition due to deterioration of insulation resistance of ballasts, luminous flux decrease of lamps and so on. This paper reports on examination of the functionality and safety under three-year gamma-ray irradiation conditions for our developed radiation-resistant lightning.

1. はじめに

加速器施設・材料照射施設・核融合施設・核燃料再処理施設等は、高放射線環境となるエリアを有する。高放射線環境では多くの電気設備は寿命が著しく短くなるなど使用に際しては制約が多い。照明器具も例外ではなく、放射線環境下では安定器の絶縁劣化・光源部の光束低下などにより、本来の機能を保てなくなる。

そこで本課題では、実際に放射線照射施設で、放射線環境下で使用できるように独自の改良を加えた照明器具を運用し、それらの機能性・安全性を検証することを目的とした。

2. 開発した耐放射線照明器具

今回開発した照明器具では、形状を標準の器具と変えずに耐放射線性能を向上させたことが特徴である。以下に主な仕様を示す。

- ・投光器（水銀灯 400 W）及び 安定器
 - 定格電圧 200 V 定格周波数 50 Hz
 - 定格入力電流 3.3 A 定格消費電力 415 W
 - 放射線耐量 30 MGy

3. 試験概要

3.1 照射試験

Co-60 照射施設第2 照射室内に、試験体として開発した投光器 6 台及び安定器 6 台を設置し、室内の作業用の照明器具として運用した。照射試験は、平成 20 年 4 月から平成 22 年 12 月までの 2 年 9 ヶ月間実施した。照射試験終了時の累積吸収線量は、光源部で 2.9～4.4 MGy、安定器部で 4.3～5.2 MGy であった。累積点灯時間は 2258 時間、室内の照度は初期照度（465 lx）の約 55%（255 lx）となった。

3.2 工場試験

照射試験を終えた照明器具 6 セットを工場で性能と安全性の観点から評価を行った。性能に関しては、主に照度低下の原因と割合を特定した。安全性に関しては、主に絶縁抵抗・耐電圧試験によって評価した。

3.2.1 照度低下原因の検討

照度低下の原因を光束測定・反射率測定・配光測定により検討した。また、照度低下の原因について、下記の 2 つの原因と 4 つの要因に分け、それぞれの低下率を求めた。

① 反射鏡の反射率の低下率

- ・放射線照射試験室内に固有の「環境要因」による低下率（LR1）

- ・室内のほこりなどの「汚れ」が反射鏡に溜まることによる反射率の低下率（LR2）

② ランプ本体の光束の低下率

- ・放射線照射試験室内に固有の「環境要因」による低下率（LL1）
- ・「点灯時間」による低下率（LL2）：累積点灯時間から 7% が想定された。

Figure 1 に低下率をまとめた。投光器 No3, No4 の低下率が大きい。これは反射鏡の汚れによる低下率が大きいことから、これらを設置した壁面の天井付近では粉塵が溜まりやすい状況だったことが考えられる。6 台の平均値でみると汚れの影響が最も大きく 17.3%、次いで反射鏡の環境要因が 11.3%、ランプの点灯時間が 7%、ランプの環境要因が 3.1% の順であった。一連の評価から、放射線の直接の影響よりも汚れなどの影響が大きいことが分かった。

3.2.2 安全性の評価

照射試験の実施前後で安定器の電気特性に目立った変化がなく、絶縁抵抗・耐電圧試験も全ての器具で問題がなかった。以上より、今回の安定器は累積吸収線量が 4.3～5.2 MGy であったが、この限りにおいては安全性に問題がないと結論付けられる。

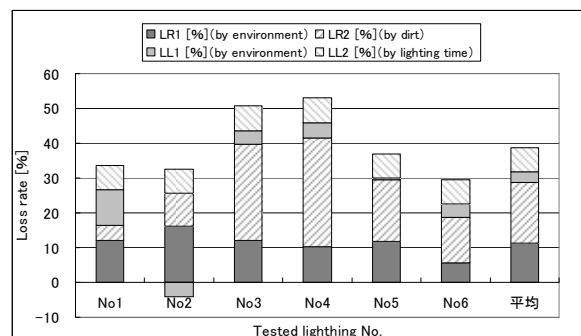


Fig. 1 Summarization of loss rate of tested lightings.

4. おわりに

今回試験した照明器具は、放射線環境下であっても長期にわたり本来の機能と安全性を保つことがわかった。湿度管理された粉塵の影響が少ない利用環境であれば、さらに器具効率の向上が期待できる。機能性・経済性・安全性など総合的な照明器具の最適設計を行うには、利用施設の環境も含めて検討することが重要である。

1-24 Evaluation of Hydrogen Formation by Gamma-ray Irradiation in Sodium Nitrate Solution with TiO_2 Colloids

T. Motooka, Y. Ishijima and M. Yamamoto

Division of Fuels and Materials Engineering, NSED, JAEA

1. Introduction

It is known that titanium and titanium alloy get brittle by hydrogen adsorption. In this paper, the amount of hydrogen gas released from nitrate solution by gamma-ray irradiation was analyzed as an elemental examination for evaluating hydrogen embrittlement of equipments made of titanium alloy like a plutonium concentrator in a reprocessing plant. The relation between the nitrate concentration and the amount of the hydrogen gas was summarized.

2. Test procedures

Test solutions are sodium nitrate solutions made from an analytical grade reagent and distilled water. Some solution was added TiO_2 powder. It formed colloids. A 5 mL of solution was put in the vial container of 22 mL in capacity. We irradiate the solution with gamma-ray at a rate of

~ 7.6 kGy/h. After the irradiation, the amount of the hydrogen gas released from nitrate solution by gamma-ray irradiation was analyzed by gas chromatography.

3. Results and discussion

Figure 1 shows the relation between the concentration of sodium nitrate solution and hydrogen gas released from nitrate solution by gamma-ray irradiation. The concentration of the hydrogen gas was decreased with increase of nitrate sodium concentration. The concentration was about 200 vol. ppm in $5 \text{ mol} \cdot \text{dm}^{-3}$ sodium nitrate solution. A similar result was observed in pure nitric acid solution. It was suggested that nitrate anion inhibits the hydrogen formation. As shown in Fig. 2, the hydrogen gas formation was accelerated by addition of TiO_2 powder. It was thought that the cause of the increase is the catalysis of TiO_2 .

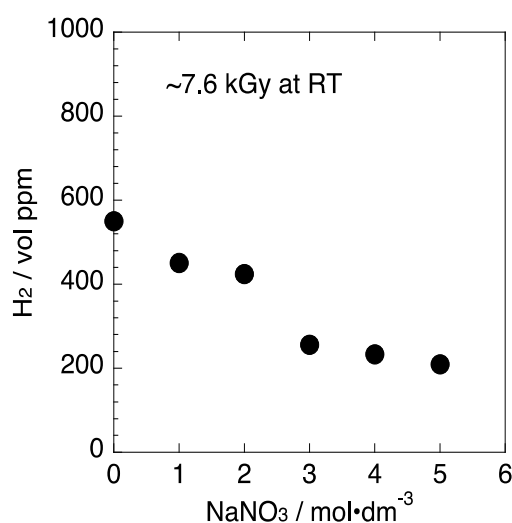


Fig. 1 Concentration of hydrogen gas and NaNO_3 .

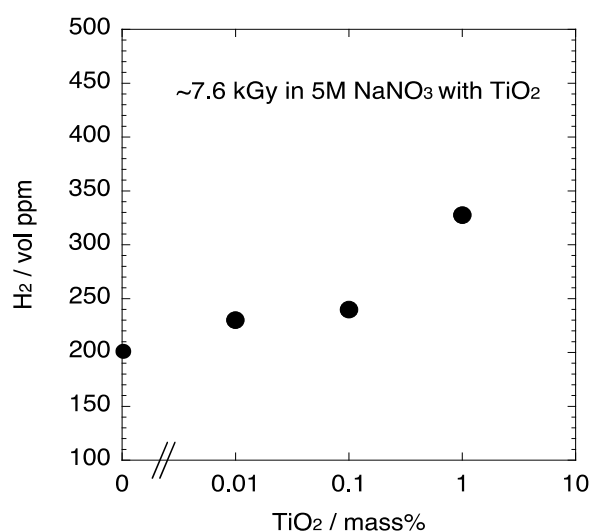


Fig. 2 Effect of TiO_2 addition for H_2 formation.

1-25 Gas Generation by Gamma-Ray Irradiation to Polyethylene, Polystyrene and Cellulose Resin

K. Saito

Plutonium Fuel Development Center, NFCEL, JAEA

At 23rd July 2010, a fire accident broke out in Plutonium Fuel Development Center (Pu Center), Tokai, JAEA. The fire was occurred from the cylindrical container of stainless steel in a glove box which loaded uranium and plutonium compounds. In order to clear up the cause of the fire, Pu Center studied it from all angles. For one of the possible causes, some inflammable gas and/or hydrogen gas were deduced to be generated from irradiated plastic cases and/or cellulose resin which are organic substances in the stainless container. The plastic cases, which were used to reposit nuclear materials, are made of both polyethylene (PE) and polystyrene (PS). The both polymer was known to be decomposed by gamma-ray irradiation and generate hydrogen gas, whose quantitative evaluation as absorbed dose was reported^{1,2)}. As for PE, other gases such as carbon oxides, methane and ethane are also generated. Cellulose resin was used for binder of uranium and mixed nitride powder, but gas generation from cellulose resin by gamma-ray irradiation has not been reported. Then, in order to demonstrate and investigate hydrogen and inflammable-gas generation from polymers and cellulose resins, gamma-ray irradiation to the materials and the analysis of the generated gaseous substances were performed.

Figure 1 shows sample materials of PE (cap) and PS (mixture of cover and body) of plastic case, and cellulose resin. Because expected gas yield is not much, plastic case was fragmented and charged within a syringe as much as possible. Cellulose resin in which volatile solvent is blended was totally dried. The mass of encapsulated PE, PS and cellulose resin per syringe are 3.1, 16 and 0.35 g, respectively. An adopted glass syringe with a stainless-steel gas valve is for gas chromatograph and shown in Fig. 2. The reasons of the adoption of the glass syringe with a little metal are below. First, inorganic and metal materials hardly generate gaseous substances by gamma-ray irradiation and make unnecessary background. Second, though metal stuff possibly works as a shield, such little mass of a valve does not. The syringes are filled with argon gas for inorganic gas (hydrogen) detection, and additional syringes for cellulose resin are filled with helium gas for organic gas detection. The syringes including each sample were irradiated with gamma ray from ⁶⁰Co source up to 30 kGy and the dose rate was 10 kGy/h. Alanine dosimeters were used to evaluate the absorbed doses. In order to evaluate background gas generation from volatile cellulose resin, dummy syringes without irradiation were prepared. After irradiation, the clearance between the cylinder and the piston rod of a syringe were sealed up with

glycerol, and sent to gas-chromatography analysis which was executed by Sumitomo Metal Technology, Inc.

Table 1 shows the result of hydrogen gas generation ratio and other reference values. The values of PS and PE are in good agreement in order with the reference ones. For cellulose resin, the background is under the detection limit and even the foreground is practical detection limit. Therefore, only upper limit was known in regard to the cellulose resin. Other gases were generated just a little.

In conclusion, enough inflammable gas generation as the cause of the fire was denied taking account of the mass of plastic cases and cellulose resins, and its estimated absorbed dose in the stainless container.

References

- 1) 瀬口、ポリエチレンの放射線分解ガスを利用する線量計、放射線利用技術データベース、データ番号: 010258.
<http://www.rada.or.jp/database/home4/normal/ht-docs/member/synopsis/010258.html>.
- 2) Y. Shimizu and H. Mitsui, J. Polym. Sci.: Polym. Chem. Edit. 17 (8) (1979) 2307-16.

Table 1 Results of hydrogen gas generation ratio.

Sample	H ₂ gas generation ratio (mol/g/kGy)	
	Present	ref.
PE	3.50×10^{-7}	4.66×10^{-7} ¹⁾
PS	3.48×10^{-9}	2.66×10^{-9} ²⁾
Cellulose resin (dummy, background)	$< 8 \times 10^{-9}$	-
Cellulose resin (foreground)	8×10^{-9}	-

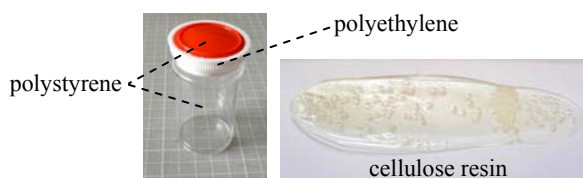


Fig. 1 Photographs of irradiation samples.



Fig. 2 Photograph of a syringe for gas chromatograph.

1-26 Studies on Microstructure and Elemental Distributions of Barrier Materials for Geological Disposal of Radioactive Waste

Y. Tsuruta^{a)}, D. Yamasaki^{a)}, N. Miyasaka^{b)}, T. Kozaki^{c)}, S. Sato^{c)},
N. Kozai^{d)}, M. Koka^{e)}, T. Satoh^{e)} and T. Kamiya^{e)}

^{a)} School of Engineering, Hokkaido University, ^{b)} Graduate School of Engineering, Hokkaido University,
^{c)} Faculty of Engineering, Hokkaido University, ^{d)} Advanced Science Research Center, JAEA,
^{e)} Department of Advanced Radiation Technology, TARRI, JAEA

A compacted Na-bentonite, of which major mineral is Na-montmorillonite having high swelling ability and low hydraulic conductivity, is a candidate buffer material in geological disposal of high-level radioactive waste. However, Na-bentonite would change if its exchangeable cations of Na^+ are replaced with Fe^{2+} which can be released from corrosion of carbon steel waste containers. Therefore, the performance as the buffer should be evaluated in a proper way not only for Na-bentonite but also for Fe(II)-bentonite. In this study, diffusion behavior of Cl^- ions was studied for Fe(III)-montmorillonite, which can be easily handled in the ambient atmosphere as an analogous material for Fe(II)-bentonite. In addition, elemental distributions in Fe(III)-montmorillonite were analyzed by micro PIXE method.

The Fe(II)-montmorillonite sample was prepared from Na-montmorillonite(Kunipia-F, Kunimine Industries Co. Ltd.) by the ion-exchange of Na^+ with Fe(III) in FeCl_3 solution. Excess salt in the sample was removed by washing with dilute solution of hydrochloric acid followed by distilled water. Non-steady diffusion experiments were carried out using the Fe(III)-sample and $^{36}\text{Cl}^-$ tracer. The Fe(III)-sample was compacted and saturated with distilled water at a dry density of 1.6 Mg m^{-3} . After a prescribed time for diffusion at the different temperatures from 288 to 323 K, the Fe(III)-sample was cut into 0.5 mm-thick-slice, and the radioactivity of ^{36}Cl in each slice was determined with a liquid scintillation counter. Apparent diffusion coefficient of Cl^- was obtained from the concentration profile of ^{36}Cl in the sample by assuming the diffusion in an infinite media from a thin source of tracer. Micro PIXE analyses were conducted for the Fe(III)-samples which had been suspended in non-radioactive NaCl solution of 10 mmol/L under the liquid/solid ratio of 150 for 2 d. Detail procedures of the sample preparation for the micro PIXE analyses were described elsewhere¹⁾.

Temperature dependence of apparent diffusion coefficients of Cl^- ions in Fe(III)-sample at the dry density of 1.6 Mg m^{-3} were shown in Fig. 1, together with those in Na-sample reported elsewhere²⁾. It was found that the apparent diffusion coefficients of Cl^- ions in Fe(III)-sample were lower than those in Na-one by a factor of 1/7~1/3. In general, diffusion pathway of anions in compacted bentonite is considered to be restricted due to electrostatic repulsive

force between anions and negatively charged montmorillonite sheets, i.e. “anion exclusion effect”. According to the electrical double layer theory, the anion exclusion effect could be inhibited by the presence of trivalent cations like Fe(III), resulting in higher hydraulic conductivity³⁾ and higher diffusion coefficient for anions. In this study, however, lower diffusion coefficients were obtained for Fe(III)-sample. It can be considered that the diffusion coefficients was reduced by the sorption of Cl^- on ferric oxides (and/or hydroxide) which could formed in Fe(III)-bentonite during the experiment. In the micro PIXE analyses, however, no significant sorption was found; no locally-accumulated Cl was identified in the Fe(III)-bentonite which had been suspended in non-radioactive NaCl solution. Activation energy for Cl^- diffusion in Fe(III)-sample obtained from the temperature dependence was 11.4 kJ mol^{-1} , which is lower than that in free water (17.4 kJ mol^{-1})⁴⁾ and that in Na-sample (22.0 kJ mol^{-1})²⁾. These findings suggest that that the predominant diffusion pathway for Cl^- in Fe(III)-sample is not large pores filled with free water, but spaces markedly affected by the exchangeable cations, Fe(III).

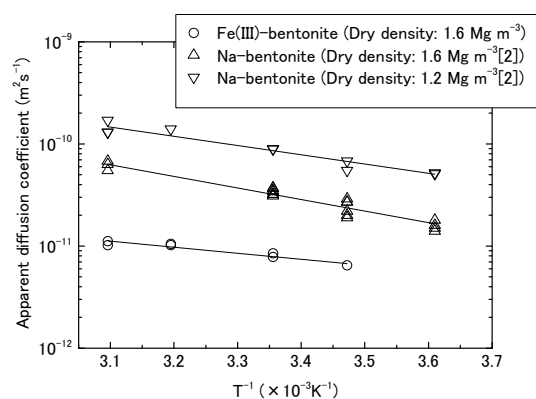


Fig. 1 Temperature dependences of apparent diffusion coefficients of Cl^- in compacted Fe(III)-bentonite, together with those for Na-bentonite¹⁾.

References

- 1) N. Kozai et al., J. Solid State Chem. 180 (2007) 2279.
- 2) T. Kozaki et al., J. Contam. Hydrol. 47(2001) 159.
- 3) H. Ito et al., J. Nucl. Sci. Tech. 44 (2010) 1005.
- 4) R. Parsons, Handbook of Electrochemical Constants, Butterworths Sci. Publ., London, (1959)79.

1-27 Effect of Dissolved Hydrogen on Helium Ion beam Radiolysis of Water

M. Yamaguchi^{a)}, M. Taguchi^{b)} and A. Kimura^{b)}

^{a)} Geological Isolation Research Unit, GIRDD, JAEA,

^{b)} Environment and Industrial Materials Research Division, QuBS, JAEA

High-level radioactive waste (HLW) is planned to be disposed of in a deep underground repository. In the current Japanese design concept of the HLW disposal system, a canister of HLW is encapsulated in a carbon steel overpack. After the overpack finally loses its integrity and the incoming porewater contact with the HLW (it is typically assumed 10^3 years in performance assessment for the disposal system in Japan), alpha-radiolysis would occur and it is anticipated that radiolytic products such as H_2O_2 and O_2 may accelerate migration of radionuclides which are more soluble and less sorptive to barriers in oxidized states.

Actual alpha-radiolytic process of groundwater would be sensitive to some factors in the surrounding conditions during system evolution. In particular, high concentration of dissolved H_2 which may be produced due to anoxic corrosion of carbon steel overpack would suppress radiolytic formation of oxidizing species as expected from its effect well understood for low-LET radiolysis of water. However, Pastina and LaVerne observed no effect of the dissolved H_2 on water radiolysis by 5 MeV He^{2+} irradiation, while homogeneous model calculation predicted total suppression of H_2O_2 formation¹⁾.

Recently Trummer and Jonsson have suggested that the effect of dissolved H_2 on high-LET radiolysis of water would be absent at high dose rates. They have estimated that the dose rate of the actual irradiation volume ($1.2\ \mu\text{L}$: beam spot size of $0.3\ \text{cm}^2$ and penetration depth of $40\ \mu\text{m}$) in the experiment by Pastina and LaVerne is about four

orders of magnitude larger than the value averaged over the whole volume of the sample²⁾. At higher dose rates, H_2O_2 concentration increases linearly as its production rate is too high to be suppressed by dissolved H_2 . In contrast, it is expected that the dissolved H_2 would suppress formation of H_2O_2 in the case of low-LET radiolysis at sufficiently low dose rates. To confirm this prediction we have performed ion beam radiolysis of water at different dose rates by changing beam current.

Sample cells were made of quartz (i.d.: 40 mm, depth: 5 mm, window thickness: 0.15 mm). Gas saturated aqueous solutions were prepared by bubbling either argon or hydrogen and they were transferred to sample cells. Then the sample cells were irradiated with $^4\text{He}^{2+}$ ion beam accelerated to 50 MeV by the AVF cyclotron. Incident energy was decreased to approximately 15 MeV by placing aluminum sheets (0.6 mm thick) on sample cells. Ion beam was scanned over $50 \times 50\ \text{mm}$ to cover the whole area of the sample. Beam current was varied from 20 nA to 0.26 nA. H_2O_2 concentrations were analyzed by either the triiodide method for high concentration or leuco crystal violet with peroxidase for low concentration³⁾.

Figure 1 shows H_2O_2 concentration after irradiation. The concentration increased almost linearly with the accumulated dose. There are little difference between samples bubbled with argon and hydrogen gases, indicating no effect of the dissolved hydrogen even at the lowest beam current. The estimated dose rate at the lowest beam current was $\sim 90\ \text{Gy s}^{-1}$ in the irradiation volume ($23\ \mu\text{L}$: beam radius of 0.5 cm and penetration depth of $290\ \mu\text{m}$). Although this value is two orders smaller than the dose rate in the irradiation volume of the experiment by Pastina and LaVerne, the value may be still higher than the threshold below which the suppression effect of dissolved H_2 would appear. Further experiments with lower beam current density are planned to clarify the dose rate effect.

This study is a part of the project for assessment methodology development of chemical effects on geological disposal system funded by METI, the Ministry of Economy, Trade and Industry, Japan.

References

- 1) B. Pastina and J. LaVerne, J. Phys. Chem. A105 (2001) 9316.
- 2) M. Trummer and M. Jonsson, J. Nucl. Mater. 396 (2010) 163.
- 3) C. A. Cohn et al., Geochem. Trans. 6 (2005) 47.

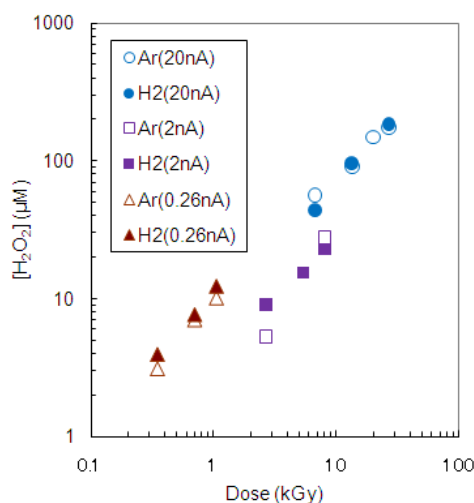


Fig. 1 Hydrogen peroxide concentration after helium ion beam irradiation at different beam current: (open) argon bubbled samples (solid) hydrogen saturated samples.

1-28 Preliminary Models on Radiation Induced Changes of Microstructure and Stress-Strain Relations to Estimate Mechanical Response of Austenitic Steel Components

S. Jitsukawa^{a)}, Y. Abe^{a)}, M. Ando^{b)}, N. Ishikawa^{a)}, N. Okubo^{a)}, K. Suzuki^{a)},
H. Oka^{c)}, D. Liu^{c)} and S. Ohnuki^{c)}

^{a)} Division of Fuels and Materials Engineering, NSED, JAEA, ^{b)} Division of Fusion Reactor Engineering, FRDD, JAEA, ^{c)} Faculty of Engineering, Hokkaido University

Neutron irradiation often introduces severe changes of mechanical properties of structural materials. This affects mechanical response of, for example, reactor core components. A large amount of hot cell work, however, will be required to examine mechanical response of irradiated components experimentally. The methodology to estimate mechanical response of the components based on the knowledge of irradiation induced microstructural changes and post irradiation mechanical properties has been developed. Molecular Dynamics (MD) and Rate Equation calculations to estimate microstructural change during irradiation have been prepared. Also, Swift type constitutive equation based on the semi-theoretical models on work hardening of irradiated steels has been applied^{1,2)}. Then, a preliminary multi-scale method to estimate the mechanical response of irradiated components has been presented.

One of the keys to calculate microstructural change is the estimation of the number density of irradiation produced point defect clusters (IPCs). For the modeling of IPC formation and of the process controlling the number density of IPCs, in situ observation of microstructural change during irradiation of 200 keV Fe-ions has been conducted at TIARA facility. Figure 1 shows damage microstructure obtained during irradiation. Results including those by fission neutron irradiation indicate that the number density of interstitial type of IPCs(SIA-IPCs) is not sensitive to irradiation condition at temperatures below 350 °C; strain field around SIA-IPCs is one of the main controlling factors of the number density, as illustrated in Fig. 2. Using the model described in Fig. 2 and the results of ion irradiation, two critical values of r_c (capture radius of SIA-IPCs for clusters, min. value of r_c ; about 10 nm) and d_{min} (minimum diameter of clusters to accumulate cascade produced clusters; about 1 nm) are determined for model calculation.

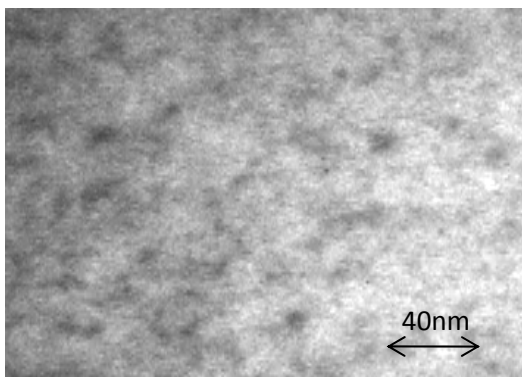


Fig. 1 Radiation produced clusters formed during 200 keV Fe-ion irradiation at 473 K.

Proof stress level after irradiation has been calculated from calculated microstructure using Orowan's equation, as a function of damage level for the 316 stainless steel (see, Fig. 3).

True stress-strain relation has been also obtained from the tensile tests on irradiated austenitic stainless steel specimens. From the results, Swift type constitutive equation has been derived, where ϵ_0 is an equivalent strain for irradiation hardening can be obtained from calculated microstructure and Orowan's equation.

$$\sigma = A(\epsilon_0 + \epsilon_p)^n \quad (1)$$

Results and Eq. (1) indicate that post irradiation plastic properties including ductile fracture behavior are able to be estimated from proof stress level after irradiation. Because proof stress is also able to be estimated from microstructure, therefore behavior of irradiated structural component may be evaluated by the constitutive equation determined from the calculation of microstructural change during irradiation.

References

- 1) K. Suzuki, et al., Nucl. Eng. Design 240 (2010) 1290-1305.
- 2) S. Jitsukawa, et al., Nucl. Fusion 49 (2009) 115006.

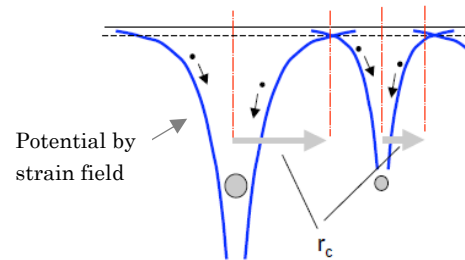


Fig. 2 Schematic illustration of capture radius of dislocation loops for point defect clusters.

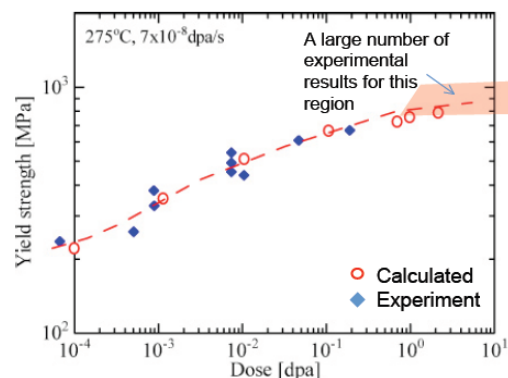


Fig. 3 Calculated proof stress level of irradiated 316 austenitic stainless steel.

1-29 Microstructural Evolution in Extra High Purity Ni-base Superalloy Ion-irradiated under External Stress

I. Ioka ^{a)}, G. H. Kim ^{a)}, K. Shiba ^{b)} and T. Sawai ^{a)}

^{a)} Nuclear Engineering Research Collaboration Center, JAEA,

^{b)} Division of Fuels and Materials Engineering, NSED, JAEA

An extra high purity (EHP) Ni-base superalloy has been developed as MA doped MOX fuel claddings for sodium cooled fast reactors. In EHP alloys, impurities, such as C, O, N, P, S were reduced to less than 100 ppm in total to improve workability, irradiation embrittlement, intergranular corrosion. The cladding materials suffer from stress (external pressure, thermal stress) under the operation. There have been many irradiation experiments done under external stress to investigate stress effects on microstructural evolution of 300 series austenitic stainless steels. It is reported that the total nucleation rate of Frank loops increased with increasing external stress¹⁾. However, there are few studies on the effect of external stress on microstructural evolution of Ni-base superalloy under irradiation. The purpose of this study is to evaluate the effect of external stress on microstructure and void swelling of EHP Ni-base superalloy.

The material used in this study was the ordered γ' -phase strengthened EHP Ni-base alloy, so called EHP(γ') alloy. The EHP(γ') alloy was manufactured by the multiple refined melting process. The ingot was solution-treated at 1313 K for 4 h, and then 60% cold-worked followed by aging at 923 K for 24 h. Then further re-crystallization was carried out at 1023 K for 24 h. The chemical composition of the alloy is given in Table 1. The materials were cut to small coupon type specimens ($6 \times 3 \times 0.4$ mm³). One of the sides was irradiated after polishing with SiC paper #4000 and 0.05 μ m alumina powder. Irradiation was performed under triple ($\text{Ni}^{3+} + \text{He}^+ + \text{H}^+$) ion beams in the Takasaki Ion Accelerators for Advanced Radiation Application (TIARA) facility at 823 K to 90 dpa. Ions of 12 MeV Ni^{3+} , 1.05 MeV He^{2+} and 380 keV H^+ were injected to simulate a FaCT core irradiation environment. The injection rates for He and H are 1 appmHe/dpa and 15 appmH/dpa, respectively.

The cross-sectional cavity microstructure in EHP(γ') specimen irradiated by triple ion-beam is shown in Fig. 1(a). Cavities were mainly located from 0.8 to 1.5 μ m in depth. The TRIM calculated damage distribution and the profiles of He and H were included. The atoms of He and H introduced by ion irradiation distribute mostly in the range of 0.8-1.5 μ m in depth from the irradiated surface, which agrees well with the range of cavities distribution. In the range of 1.5-2.0 μ m in depth cavities were not observed despite being higher dose than that in 0.8-1.5 μ m. It is denoted that the gaseous elements contribute to cavity stabilization. Generally, cavity nucleation in high purity

alloys is very difficult due to the high surface energy of cavities. Figure 1(b) shows cavity structures around 1 μ m in depth in EHP(γ') specimen irradiated. Distribution of cavities shows a two-component distribution consisting of small helium bubbles (diameter < 8 nm) and larger polyhedral cavities which were arbitrarily classified as voids (Fig. 1(b)). The number density and mean size of cavities at 1 μ m in depth were 1.57×10^{22} m⁻³, 3 nm (bubble) and 3.7×10^{20} m⁻³, 21.5 nm (void), respectively. The swelling was about 0.2%. Bond et al.³⁾ reported that the swelling in Nimonic PE16 alloy, which is similar γ' phase strengthened Ni-base alloys; irradiated by dual (Ni^+ and He^+) ion-beams to 80 dpa at 848 K is about 0.25 %. Consequently, present results showed almost the same level of the swelling to the reported value. This suggests that the impurity level in present alloy does not affect much to the void swelling. In future, void swelling and microstructural evolution of irradiated EHP(γ') alloy under external stress will be analyzed to compare with this result.

References

- 1) H. Tanigawa et al., Nucl. Instrum. Meth. Phys. Res. B 102 (1995) 151.
- 2) G. M. Bond, D. J. Mazey, Nucl. Instrum. Meth. 209/210 (1983) 381.

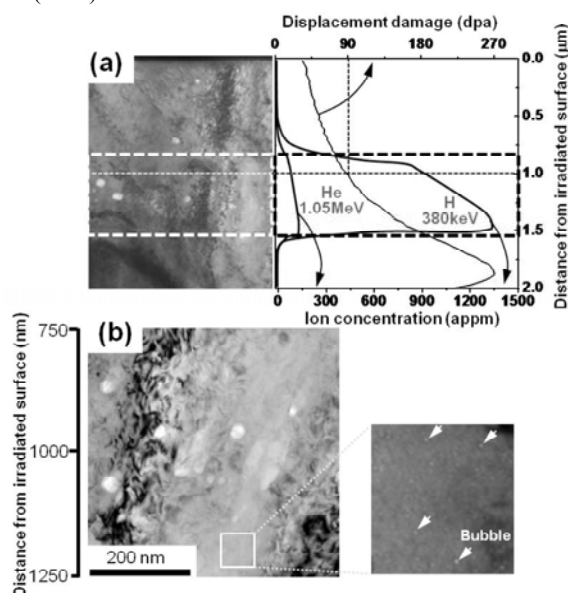


Fig. 1 TEM image and TRIM calculations for EHP(γ') alloy irradiated by triple ion-beams to 90 dpa at 823 K.

Table 1 Chemical composition of EHP(γ') alloy (wt%).

Fe	Ni	Cr	Al	Ti	Si	C	Mn	P	S	O	N	B
bal.	43	20	1.5	1.5	0.3	0.0013	<0.002	0.0007	0.0005	0.002	0.0009	<0.0001

1-30 Microstructural Evolution of G-phase Strengthened Ni-base Alloy under Multi-ion Irradiation

G. H. Kim^{a)}, K. Shiba^{a)}, I. Ioka^{a)}, T. Sawai^{b)} and S. Yamashita^{c)}

^{a)} Nuclear Engineering Research Collaboration Center, JAEA, ^{b)} Advanced Science Research Center, JAEA, ^{c)} Division of Fuels and Materials Engineering, NSED, JAEA

1. Introduction

Ni-base alloys have been studied extensively for fast-breeder reactor core application, because an excellent performance with respect to swelling was shown during high-dose neutron irradiation and ion irradiation test. However, it was found that the Ni-base alloys exhibit the ductility loss due to irradiation. The reason of the ductility loss was believed to be attributable to matrix hardening by radiation-induced point defect clusters and radiation-induced solute segregation.

In the present study, therefore, we approached with two points of view to improve the irradiation resistance of Ni-base alloys. The first is removing the M_6C former elements and other impurities by the extra high purity technology (EHP) to suppress the formation of unexpected precipitates. The second is the phase stability of matrix strengthener at high temperature during irradiation. Generally, in the fast-reactor, the cladding materials used in such high dose irradiations will experience more than 200 dpa of exposure, and have a temperature distribution from 673 to 973 K. In the previous study, we developed Ni-base high Cr-W-Si alloy strengthened by dispersion of W-rich silicides (G phase), which have a good stability at high temperature.

This work is focused on the microstructural evolution and void swelling in EHP G-phase strengthened Ni-base alloy (EHP(WSi) alloy) by the irradiation experiments using single and triple ion-beams. The void swelling resistance of EHP Ni-base alloys was compared with those of the reference austenitic alloy PNC316, which is currently used as the core materials in MONJU.

2. Experimental

EHP(WSi) alloy (Fe-43Ni-25Cr-10W-2.7Si) was used for the ion-beam irradiation experiments. Ion irradiation were performed under single (Fe^{3+} or Ni^{3+}) and triple ($Ni^{3+} + He^+ + H^+$) ion beams in the Takasaki Ion Accelerators for Advanced Radiation Application (TIARA) facility at Japan Atomic Energy Agency at temperature 673 K to dose of 10 dpa and 90 dpa, and at 823 K to 90 dpa. Ions of 10.5 MeV Fe^{3+} and 12 MeV Ni^{3+} were injected to produce radiation damage and ions of 1.05 MeV He^{2+} and 380 keV H^+ were implanted through Al degrader foils to simulate a FaCT core irradiation environment. The injection rates for He and H are 1 appm/dpa and 15 appm/dpa, respectively.

Thin foils for transmission electron microscopy (TEM) were fabricated using a FB-2000A (Hitachi, Japan) focused ion beam (FIB) instrument with micro-sampling system. TEM observation was carried out for the evaluation of

cavity and dislocation structures with a JEM-2100F (JEOL, Japan) operated at 200 kV.

3. Results and discussion

Typical TEM microstructural images for the single (Fe^{3+}/Ni^{3+}) ion-irradiated EHP(WSi) alloys to 10 dpa at 698 K and to 90 dpa at 673 K are shown in Fig. 1. The microstructural feature of the irradiation-induced Ni_3Si was observed, which phases appeared to be oval-shaped, with the major axis of the oval parallel to $\{111\}$ planes. The density and the average size of the Ni_3Si precipitate increased from 1.9×10^{21} N/m³, 15 nm to 1.1×10^{22} N/m³, 22 nm with increasing the dose.

Cavity microstructures of EHP(WSi), EHP(γ') and PNC316 specimens irradiated by triple ion-beam to 90 dpa at 823 K are shown in Fig. 2. Those dominating defect structures are classified as followings, bimodal distribution of small (<8 nm) He bubbles and larger cavities in EHP(γ'), 4 nm or less bubble formation at the matrix/precipitate interface in EHP(WSi) and large (22 nm average) cavities in PNC316. The EHP(WSi) alloy shows the best swelling resistance.

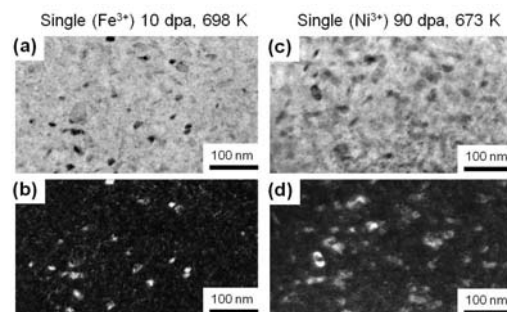


Fig. 1 Typical TEM micrographs for the single (Fe^{3+}/Ni^{3+}) ion-irradiated EHP(WSi) alloy to 10 dpa at 698 K and to 90 dpa at 673 K. (a) and (c) bright field image; (b) and (d) dark field image.

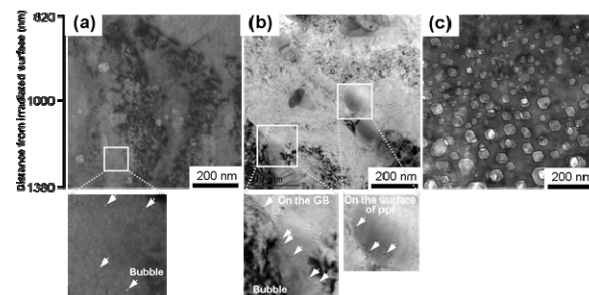


Fig. 2 Cross-sectional TEM images for (a) EHP(γ'), (b) EHP(WSi) and (c) PNC316 specimens irradiated by triple ion-beams to 90 dpa at 823 K.

1-31 Conductometric Analysis of Track Etching in Poly(vinylidene fluoride) Films Irradiated with Different MeV-GeV Ion Beams

T. Yamaki^{a)}, H. Koshikawa^{a)}, S. Sawada^{a)}, S. Hasegawa^{a)}, M. Asano^{a)}, Y. Maekawa^{a)},
K.-O. Voss^{b)}, C. Trautmann^{b)} and R. Neumann^{b)}

^{a)} Environment and Industrial Materials Research Division, QuBS, JAEA,
^{b)} GSI Helmholtzzentrum für Schwerionenforschung GmbH, Germany

We have recently been working on ion-track membranes of poly(vinylidene fluoride) (PVDF) because they have attracted a renewed interest for their applications to fuel cells^{1,2)}. The aim of this study is to investigate the formation of the PVDF track membranes in detail by conductometric analysis. The effect of high-LET ion irradiation was considered here in order to enhance an efficiency of chemical etching³⁾.

A 25 μm -thick PVDF film was irradiated at room temperature with 450 MeV ^{129}Xe from the TIARA cyclotron, and with 2.2 GeV ^{197}Au from a linear accelerator called UNILAC of GSI. The fluence was fixed at 3×10^7 ions/ cm^2 . Track etching was performed by mounting the irradiated film as a dividing wall in the conductometry cell made of Teflon containing a 9 mol/ dm^3 aqueous KOH solution at 80 $^\circ\text{C}$. The electrical conductance of the solution through the film, $g(t)$, was monitored between two platinum electrodes as a function of the etching time under a sine AC voltage using an LCR meter. The amplitude and frequency of the voltage were 0.3 V and 1 kHz, respectively. Assuming cylindrical pores, we calculated the effective pore diameter, d_{eff} , at any given time by

$$d_{\text{eff}} = (4Lg(t)/\pi KNS)^{1/2},$$

where L is the membrane thickness, K is the specific conductivity of the KOH etchant, N is the pore density generally corresponding to the ion fluence (corrected for the contribution of the microscopically-nonhomogeneous irradiation), and S is the area of the measured sample.

Figure 1 plots the converted d_{eff} value as a function of the etching time for the ^{197}Au - and ^{129}Xe -irradiated films. Basically, there were several characteristic regions during the course of the etching. In the beginning, the plateau at a nearly zero diameter represented the process of etchant penetration into tracks and approach of the etched cones from both sides of the film. As soon as these two approaching cones made contact with each other, the d_{eff} suddenly increased. The time associated with this contact is called the breakthrough time, T_B . After the pore breakthrough, the d_{eff} increased, in other words, the pores grew in the transverse direction. Lastly, the rate of the d_{eff} increase became negligibly low, and eventually the curve reached the second plateau. Chemical etching in the unmodified area, that is, bulk etching occurred beyond the width of the latent track.

The d_{eff} vs. time curves provided the T_B value for each sample, and so the track etch rate, V_T ($\mu\text{m h}^{-1}$) is calculated

by dividing the half thickness of the films by T_B . Our interest is to compare the track etching behavior, such as the V_T and pore growth after breakthrough, between the ^{197}Au and ^{129}Xe ions. In this aspect, there were three findings in Fig. 1 as follows. (i) a T_B value for the ^{197}Au -irradiated film was about four times shorter than that for the ^{129}Xe -irradiated one, meaning V_T for the former increased by the same rate as T_B . (ii) The slope of the curve after the T_B also appeared to be greater for ^{197}Au than for ^{129}Xe . This corresponds to the faster pore growth for the former. (iii) The ^{197}Au beam irradiation increased the final plateau d_{eff} by 1.7 times over ^{129}Xe , actually producing the track-etched pores of larger size. In line with the general discussion, the LET effect must be the best theoretically-grounded rationalization for these findings. Bombardment with the higher-LET ions would more densely create macromolecular damage in a wider latent track, resulting in an enhanced etching for ^{197}Au ions in terms of V_T , the pore growth rate, and the final d_{eff} value. We recently observed an analogous effect on the etching behavior for a new ion-track membrane of poly(*p*-phenylene terephthalamide)⁴⁾.

References

- 1) T. Yamaki et al., Proc. Sadoway60 Symp. (2010) 114.
- 2) T. Yamaki et al., GSI Sci. Rep. 2009 (2010) 445.
- 3) N. Nuryanthi et al., Electrochemistry 78 (2010) 146.
- 4) Y Suzuki et al., Nucl. Instrum. Meth. Phys. Res. B 260 (2007) 693.

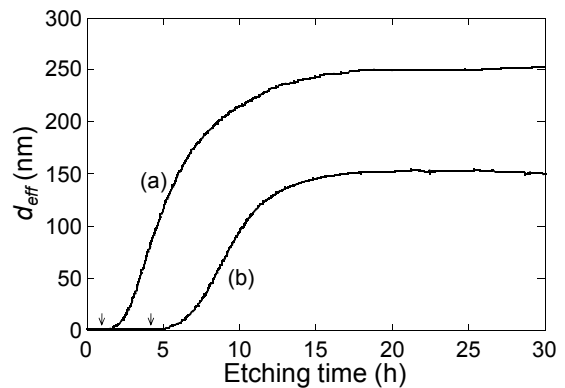


Fig. 1 Plots of the d_{eff} value as a function of the etching time for (a) the ^{197}Au - and (b) ^{129}Xe -irradiated PVDF films. The two arrows denote the T_B values of 1.0 and 4.2 h on curves (a) and (b), respectively.

1-32 Preparation of Anion-Exchange Membranes for Fuel Cell Applications by γ -ray Pre-Irradiation Grafting: Crosslinker Effect

H. Koshikawa, T. Yamaki, M. Asano and Y. Maekawa

Environment and Industrial Materials Research Division, QuBS, JAEA

Widespread commercialization of fuel cells has been hindered by economic problems associated with the extensive use of platinum as well as by many restrictions due to much additional infrastructure and insufficient hydrogen storage capacity. In order to overcome such difficulties, researchers have so far developed anion-exchange membrane fuel cells (AEMFCs), which do not need expensive platinum catalysts in the electrodes. Our recent focus has been the preparation of new membranes for applications to “hydrazine-fueled” AEMFCs¹⁾ by the γ -ray pre-irradiation grafting method^{2,3)}. We investigated here the effect of a chemical crosslinker on the membrane properties such as water uptake.

Our membrane preparation involved the grafting of chloromethylstyrene (CMS) with divinylbenzene (DVB) into poly(ethylene-co-tetrafluoroethylene) (ETFE) films and subsequent quaternization (Fig. 1)²⁾. A 50 μm -thick ETFE film was pre-irradiated at room temperature in an Ar atmosphere with a ^{60}Co γ -ray at doses of 50 kGy. Graft polymerization was performed by immersing the irradiated ETFE film in the CMS/DVB/xylene 49.5/0.5/50 vol% solution in a N_2 atmosphere at 60 $^\circ\text{C}$ for 1-8 h. The ETFE-g-CMS film was then quaternized in a 30%

trimethylamine (TMA) solution at room temperature for 24 h. After the membrane was washed several times in water and in a 1 mol/L HCl solution for 24 h (to remove residual TMA), the chloride (Cl^-) form of the membrane was converted to the alkaline (OH^-) form in a 1 mol/L aqueous KOH solution for 12 h.

Figure 2 shows the water uptake vs. degree of grafting of CMS for the anion-exchange membranes in the Cl^- and OH^- forms. This compares the results between the non-crosslinked and DVB-crosslinked membranes. Overall, the water uptake increased as the degree of CMS grafting became high. The non-crosslinked membranes in the OH^- form exhibited the extremely high water uptake reaching up to 200%, which is known to be one of the critical issues for many AEMFC membrane researchers⁴⁾. In contrast, however, the DVB-crosslinked membranes possessed the lower water uptake at the similar degree of grafting. This result undoubtedly demonstrates that the DVB crosslinker would be effective for decreasing the water uptake of the grafted anion-exchange membranes in both of the Cl^- and OH^- forms.

References

- 1) K. Asazawa et al., J. Electrochem. Soc. 156 (2009) B509.
- 2) H. Koshikawa et al., 59th SPSJ Symp. Macromol. (2010) 3912.
- 3) T. Yamaki, J. Power Sources, 195 (2010) 5848.
- 4) J.R. Varcoe et al., Chem. Mater. 19 (2007) 2686.

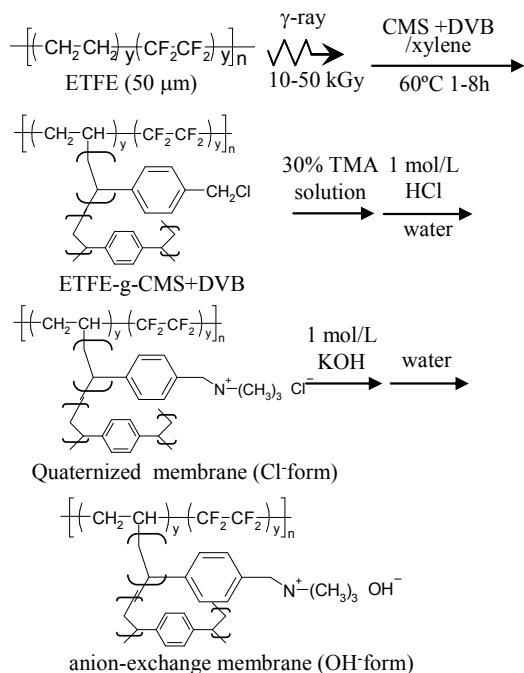


Fig. 1 Scheme for the preparation of DVB-crosslinked anion-exchange membranes.

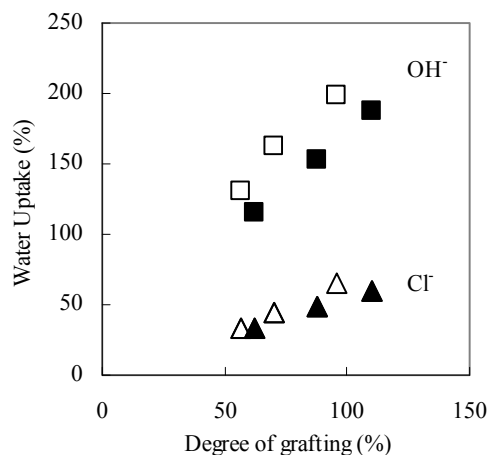


Fig. 2 The water uptake vs. degree of CMS grafting for the anion-exchange membranes in the Cl^- and OH^- forms. This compares the results of the non-crosslinked (open) and DVB-crosslinked (filled) membranes.

1-33 Preparation of Poly(ether ether ketone)-based Polymer Electrolytes for Fuel Cell Membranes Using Radiation-induced Graft Polymerization

S. Hasegawa, S. Takahashi and Y. Maekawa

Environment and Industrial Materials Research Division, QuBS, JAEA

A pre-irradiation grafting method is a fascinating technique for direct introduction of a new functional polymer phase as a grafting chain (grafts) into polymer films serving as a substrate without any damage of those films. The radiation technique has been widely applied to the preparation of a high performance fuel cell polymer electrolyte membrane (PEM) for mobile electricity, vehicles, and a domestic co-generation system. The PEMs of aromatic hydrocarbon polymers, so-called “super engineering plastics” including poly(ether ether ketone) (PEEK) have a useful characteristic such as high mechanical property, gas barrier, and resistance to radiation. However, there have been very few examples of radiation grafting into these super engineering plastic films¹⁾.

In this work, to prevent the damage to PEEK substrate during the sulfonation process, graft polymerization of the sulfo-containing styrene, ethyl 4-styrenesulfonate (E4S) into two PEEK substrates with different crystallinity (degree of crystallinity: 32 and 11%) by the pre-irradiation grafting method was examined (Fig. 1).

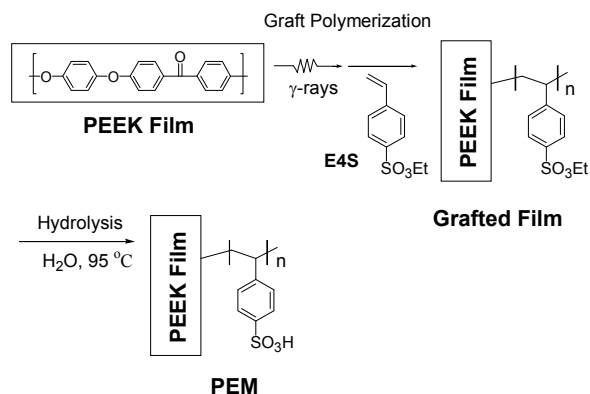


Fig. 1 Radiation induced-graft polymerization of E4S into PEEK films and subsequent hydrolysis of poly(E4S) grafts.

PEEK films 25 μm in thickness were irradiated with doses ranging at 30 kGy (dose rate: 10 kGy/h) using γ -rays from a ^{60}Co source under an argon atmosphere at room temperature. The preirradiated films were immersed in E4S in dioxane (1/1 v/v) at 80°C under an argon atmosphere. The grafting degree (GD) was calculated from the following equation, $GD = 100 \times (W_g - W_0)/W_0$, where W_0 and W_g are the film weights before and after the grafting, respectively.

Graft polymerization of the sulfo-containing styrene, ethyl 4-styrenesulfonate (E4S) into a high crystalline PEEK

substrate (degree of crystallinity: 32%) hardly progressed, whereas graft polymerization into a low crystalline PEEK substrate (degree of crystallinity: 11%) gradually progressed, achieving a grafting degree of more than 50% after 72 hours (Fig. 2).

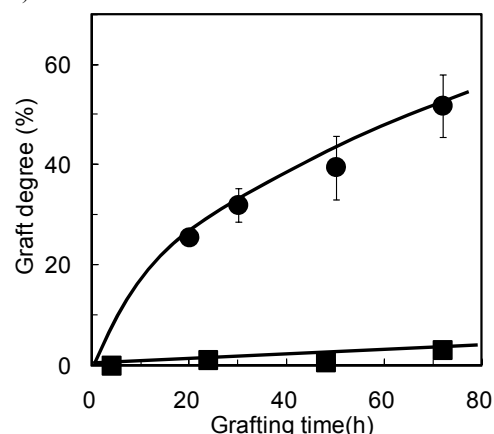


Fig. 2 Plots of grafting degrees of E4S into h-PEEK (degree of crystallinity = 32%) (a) and l-PEEK (degree of crystallinity = 11%) as a function of reaction time.

From ESR spectra analysis, the graft polymerization started from the phenoxy radical, and formed ether linkages at the starting points of grafts, resulting in block type grafts consisting of PSSA, not conventional T-shape grafts such as polystyrene grafts into PE, PP, and PTFE (Fig. 3).

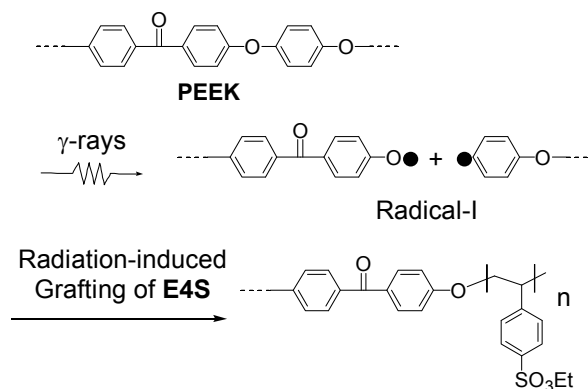


Fig. 3 Radiation-induced graft polymerization of E4S into PEEK substrate.

Reference

- 1) F. Furtado et al., Polym. Bulletin 57 (2006) 415.

1-34 Stability of Radiation Grafted Membranes in HIx Solution of Electro-electrodialysis

N. Tanaka^{a)}, T. Yamaki^{b)}, H. Koshikawa^{b)}, M. Asano^{b)}, Y. Maekawa^{b)} and K. Onuki^{a)}

^{a)} Nuclear Hydrogen and Heat Application Research Center, JAEA,

^{b)} Environment and Industrial Materials Research Division, QuBS, JAEA

JAEA has been conducting R&D on a hydrogen production thermochemical water-splitting Iodine-Sulfur (IS) process as a heat utilization system using HTGR¹⁾. In a hydrogen iodide (HI) decomposition section of the IS process, an electro-electrodialysis (EED) using an ion exchange membrane has been used in order to concentrate a HI in HI-I₂-H₂O mixture (HIx solution) over quasi-azeotropic point. We expected that the polymer electrolyte membranes prepared by the radiation-induced graft polymerization could be applied to the EED operation. In fact, we demonstrated the encouraging results such as low electric resistance and, therefore, high energy efficiency²⁾.

For practical applications to the EED, a membrane also required stability in severe environments of high temperatures (ca. 373 K) and a strongly acidic HIx solution. In the present study, we clarified thermal and electrochemical stabilities of the membranes by a long term stability test.

The membranes were prepared by γ -ray pre-irradiation of cPTFE base film in Ar atmosphere, the graft polymerization of monomer, and sulfonation. Pure styrene (St) and its mixture with 5 vol% divinyl benzene (DVB) as a chemical crosslinker were used as the grafting solution. The ion exchange capacity (IEC) was 1.8 and 1.9 mmol/g, respectively. In the following, the resulting membranes are denoted as cPTFE-g-St and cPTFE-g-DVB/St, respectively. Stability tests were examined using a filter-press type EED cell. The effective membrane area was 5 cm². During the tests, the HIx solution ([HI]=[I₂]=10 mol/kg) was fed into the cell. The solution was heated up to 373 K. And then, the EED operation was performed by supplying direct current to the cell at a current density of 200 mA/cm². After the 6 h operation, the cell and solutions were cooled to room temperature. This cycle was repeated until the total operation time reached 100 or 150 h. The evolution of the cell voltage was monitored during the EED operation.

Figure 1 gives the evolution of the cell voltage during the course of the stability tests when the cPTFE-g-St and cPTFE-g-DVB/St membranes were used. Here, the vertical axis denotes a percentage change from the initial value of the voltage. As seen in the Fig. 1, the cPTFE-g-St membranes exhibited an accelerated increase in the cell voltage with the time, suggesting that the membrane degradation should arise from the EED operation. On the other hand, the cell voltage of the cPTFE-g-DVB/St membrane increased at the initial stage of operation but, interestingly, seemed to level off after about 70 h. This indicated that the degradation could be restrained in the DVB-crosslinked membranes.

In order to confirm the membrane degradation, we compare the IECs before and after the stability test in Table 1. The total operation time was 100 and 150 h for the cPTFE-g-St and cPTFE-g-DVB/St membranes, respectively. A decrease in the IEC appeared in both the membranes, indicating the desorption of sulfonic acid groups from the membrane after the stability tests. Importantly, however, a degradation rate was much lower for the cPTFE-g-DVB/St than for cPTFE-g-St, specifically, the former still held 70% of the initial IEC while, in contrast, the latter lost the ionic content down to a quarter. According to this result, a significant loss probably occurred, thereby enhancing the electric resistivity of the membrane. It is very reasonable to consider that the DVB-based cross-linking in the grafted chains would hinder this degradation process.

The above experimental results clearly demonstrate that the radiation-grafted membranes chemically cross-linked by DVB enabled us to perform the stable EED operation in the HIx solution for a rather long time.

References

- 1) S. Kubo et al., Nucl. Eng. Des. 233 (2004) 355.
- 2) N. Tanaka et al., J. Membr. Sci. 346 (2010) 136.

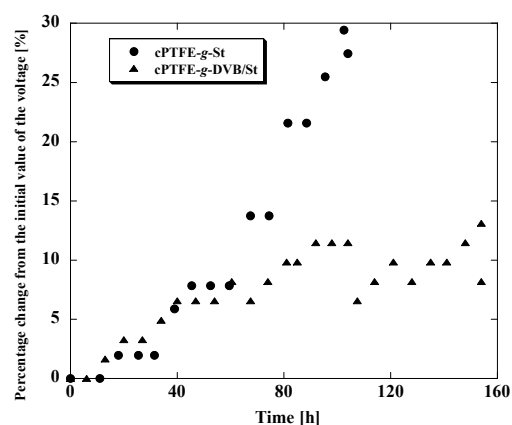


Fig. 1 Evolution of the cell voltage. Initial values were 0.051 V for cPTFE-g-St and 0.061 V for cPTFE-g-DVB/St.

Table 1 IEC compared before and after the stability tests for the cPTFE-g-St and cPTFE-g-DVB/St membranes*.

ID	Before tests [mmol/g]	After tests [mmol/g]
cPTFE-g-St	1.8	0.47
cPTFE-g-DVB/St	1.9	1.3

*The total operation time is described in the text.

1-35

Radiation Degradation Properties of Grafted Polymer Electrolyte Membranes

S. Sawada^{a)}, Y. Iwai^{b)}, T. Yamahishi^{b)} and Y. Maekawa^{a)}

^{a)} Environment and Industrial Materials Research Division, QuBS, JAEA,

^{b)} Division of Fusion Energy Technology, FRDD, JAEA

In the international thermonuclear experimental reactor (ITER) plant, the safe and efficient utilization of tritium is main issue¹⁾. For this purpose, the polymer electrolyte membrane (PEM) electrolysis will be performed for conversion of tritium water (HTO or T₂O) into tritium hydrogen (HT or T₂)¹⁾. What should be considered here is that the used PEM is irradiated by β -ray emitted from tritium water. In the previous studies, the most widely used Nafion PEM was found to be somewhat degraded by irradiation. Thus, much effort has been devoted to search for the Nafion-alternative PEMs with high resistivity against radiation. In this study, we investigated the radiation degradation properties of the graft-type PEMs based on poly(ethylene-co-tetrafluoroethylene) (ETFE) and poly(etheretherketone) (PEEK).

The ETFE-based PEM was prepared by radiation grafting of styrene into an ETFE film and subsequent sulfonation. The PEEK-based PEM, which was originally developed in our group²⁾, was prepared by thermal grafting of divinylbenzene and radiation grafting of ethyl-styrene-sulfonate (ETSS) into a PEEK film and subsequent hydrolysis. The fully-hydrated PEMs were irradiated with 500-kGy γ -rays at dose rate of 10-15 kGy/h at room temperature. Before and after irradiation, the PEMs were characterized in terms of the remaining weight ratio (R_w), water uptake (α), ion exchange capacity (IEC), proton conductivity (σ), and breaking tensile strength (BTS).

First of all, notice that the irradiation conditions in this study are not the same as those in the electrolysis system in ITER. In the actual electrolysis cell, the PEM was irradiated with β -ray at the dose rate of about 0.030 kGy/h. On the other hand, in this study, the irradiation was performed with γ -ray at the dose rate of 10-15 kGy/h. Due to this difference, it is not easy to directly evaluate the radiation resistivity required for the electrolysis system in ITER. Even so, our radiation treatment conditions are the standard ones employed in a previous study on Nafion³⁾. Accordingly, we can clarify the radiation resistivity of the grafted PEMs compared with that of Nafion.

Table 1 shows the properties of the ETFE PEM before and after irradiation. The R_w , IEC, σ and BTS significantly decreased. This should be because some parts of poly(styrene sulfonic acid) (PSSA) graft chains were decomposed and removed out, which hindered proton conduction. Consequently, this PEM cannot be used for practical applications.

Table 2 shows the properties of the PEEK PEM before and after irradiation. In contrast to the ETFE PEM, any

serious deterioration was not observed in all the properties including the BTS. Here, pay attention to the σ value, which strongly influences the electrolysis performance. Even after the irradiation, the PEM exhibited the high σ of 0.10 S/cm, being larger than that of Nafion before irradiation (0.083 S/cm). This result makes us expect the possibility of highly-efficient water electrolysis. Thus, the PEEK PEM may be the good candidate material for electrolyzer in ITER.

Next, let us examine the degradation mechanism of the grafted PEMs. From the degradation in the ETFE-based PEM, one might think that the PSSA main chains tended to be depolymerized by irradiation. However, if this assumption had been true, the PEEK PEM should have also been degraded since they also possessed PSSA graft chains. Actually, the PEEK PEM was stable against irradiation (see Table 2). These discussions imply that the PSSA graft chains possessed enough resistivity to irradiation.

Then, we suspect that the base polymers were degraded. In the ETFE PEM, the backbone ETFE chains should be depolymerized because they are sensitive to irradiation. The PSSA grafts attached to the decomposed ETFE chains were simultaneously removed from the membrane. In the case of the PEEK PEM, the PEEK backbones were very resistant to irradiation. This would be the main reason for excellent stability of this PEM.

References

- 1) K. Kobayashi et al., Nucl. Fusion 47 (2007) 1645.
- 2) J. Chen et al., J. Membr. Sci. 319 (2008) 1.
- 3) Y. Iwai et al., J. Nucl. Sci. 42 (2005) 636.

Table 1 Properties of the ETFE PEM before and after irradiation.

Samples	R_w (%)	IEC (meq/g)	α (%)	σ (S/cm)	BTS (MPa)
Before	100	2.1	58	0.11	39
After	82	1.0	58	0.060	20

Table 2 Properties of the PEEK PEM before and after irradiation.

Samples	R_w (%)	IEC (meq/g)	α (%)	σ (S/cm)	BTS (MPa)
Before	100	2.3	50	0.11	51
After	97	2.0	49	0.10	50

1-36 Polymerization Kineics of Ion-Track Grafting with Different Beams

T. Sekine^{a, b)}, S. Sawada^{a)}, T. Yamaki^{a)}, H. Koshikawa^{a)}, M. Asano^{a)}, A. Suzuki^{b)},
T. Terai^{b)} and Y. Maekawa^{a)}

^{a)} Environment and Industrial Materials Research Division, QuBS, JAEA,

^{b)} Department of Nuclear Engineering and Management, The University of Tokyo

Ion-track grafting involves ion-beam irradiation of a base polymer film followed by graft polymerization directly into the tracks. In recent years, we have developed proton exchange membranes (PEMs) for fuel cells using this technique¹⁾. High graft levels in as small a number of tracks as possible are essential in our strategy because they can keep a balance between proton conductivity (prefers high graft levels) and mechanical properties (prefers lower fluences) of the membranes. In this study, we investigated the polymerization kinetics of the ion-track grafting of styrene into poly(ethylene-co-tetrafluoroethylene) (ETFE) films irradiated with different ion-beams by analyzing the degree of grafting (*DOG*) vs. reaction time curves.

A 25 μm -thick ETFE film was bombarded by 3.7 MeV/n ^{15}N , 3.8 MeV/n ^{20}Ne , 3.8 MeV/n ^{40}Ar , and 3.5 MeV/n ^{129}Xe from the TIARA cyclotron at a fluence of 3.0×10^8 ions/cm². Just after the irradiation, the films were exposed to air to produce peroxide groups, and then immersed in a grafting solution (a volume ratio of styrene to the grafting medium was 20/80) at 60 °C for 1-24 hours. According to our preceding report²⁾, an isopropanol/water mixture at a volume ratio of 25/55% was used as the medium. The *DOG* was calculated by: $\text{DOG}(\%) = (W_g - W_0)/W_0 \times 100$, where W_g and W_0 denote the weights of the styrene-grafted and virgin films, respectively.

In order to analyze the results, the following equation was used³⁾

$$\text{DOG} = \frac{r_{p0}}{\gamma} \ln(1 + \gamma(t - t_0)) \quad (1)$$

where r_{p0} and γ are the rates of polymerization and termination, respectively, t is the reaction time, and t_0 is the delay time. The r_{p0} and γ can be obtained by fitting the *DOG* vs. time curves with eq. (1). The grafting reaction would occur only in latent tracks, and so the *DOG* values were corrected by the volume fraction of the tracks. We defined the track radius considering the following criteria: the distance from the ion trajectory at which the deposited dose reached 1 kGy. Based on the calculations of Magee and Chatterjee⁴⁾, the track radii were estimated to be 29, 41, 63, and 118 nm for the beams of ^{15}N , ^{20}Ne , ^{40}Ar , and ^{129}Xe , respectively. Because almost no overlapping can occur at a fluence of 3.0×10^8 ions/cm², the volume percentages of the tracks were 0.79, 1.5, 3.7, 13%, respectively.

Figure 1 presents the corrected *DOG* vs. time curves for the styrene grafting into the films irradiated with the different ion beams. Overall, the good fit to the data was

seen by eq. (1). Figure 2 shows the values of r_{p0} and γ obtained by this curve fitting. Both the parameters were found to be much higher than those reported for the electron-beam-induced styrene grafting³⁾. This result probably reflects the fact that high-energy ion bombardment produces radicals in extremely high density along each track. Interestingly, there was an increasing trend in these two values as the mass number of the bombarded ions decreased, suggesting a large influence of track structures on the grafting behavior.

References

- 1) T. Yamaki, J. Power Sources 195 (2010) 5848.
- 2) T. Sekine et al., JAEA Takasaki Ann. Rep. 2009 (2011) 36.
- 3) T. Rager, Helv. Chim. Acta 86 (2003) 1966.
- 4) J. L. Magee and A. Chatterjee, J. Phys. Chem. 84 (1980) 3529.

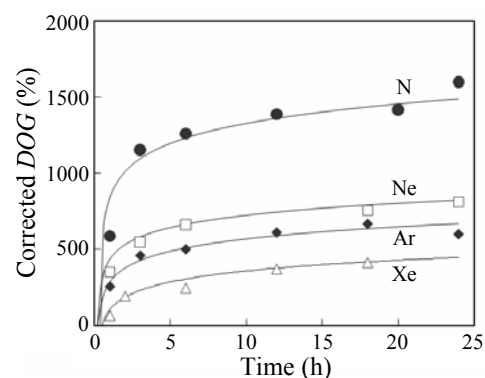


Fig. 1 Corrected *DOG* as a function of reaction time for the styrene grafting into the films irradiated with the different ion beams.

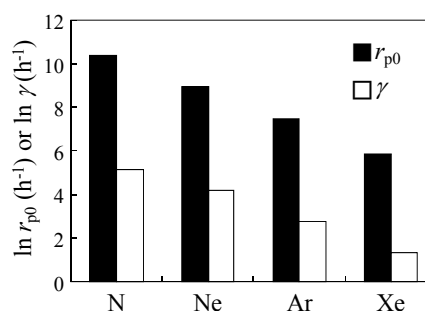


Fig. 2 r_{p0} and γ for the styrene grafting into the films irradiated with the different ion beams.

2. Environmental Conservation and Resource Exploitation

2-01	A Simple Method for Radiation-Induced Graft Polymerization using a Polyethylene Bottle as a Reactor	43
	Y. Ueki, N. C. Dafader, N. Seko and M. Tamada	
2-02	Radiation-induced Grafting of Acrylonitrile Monomer onto Cellulose Nonwoven Fabric	44
	S. Saiki, T. Puspitasari and N. Seko	
2-03	The Effect of Partial Delignification on Kenaf Bast Fibers for Radiation Graft Polymerization	45
	N. H. Mohamed, M. Tamada, Y. Ueki and N. Seko	
2-04	Development of Anion Adsorbent for Industry Application Based on Biodegradable Trunk Material	46
	N. Kasai, H. Hoshina, N. Seko, T. Shibata and M. Takahashi	
2-05	Synthesis of Amine-type Adsorbents with Emulsion Graft Polymerization of 4-hydroxybutyl Acrylate Glycidylether	47
	H. Ma, H. Hoshina and N. Seko	
2-06	Decolorization of Secondary Treated Water from Livestock Urine Waste	48
	M. Takigami, W. Gokan, N. Nagasawa, A. Hiroki, N. Kasai, M. Tamada, S. Takigami, T. Shibata, Y. Aketagawa and M. Ozaki	
2-07	Effect of Gamma-rays Irradiation of Hydroxypropylmethylcellulose Aqueous Solution	49
	T. Haikawa, K. Furusawa, Y. Maki, N. Nagasawa and T. Dobashi	
2-08	Transparent Hydrogels Prepared by Radiation Crosslinking Hydroxypropyl Cellulose with Functional Monomers	50
	A. Hiroki, T. Sato, N. Nagasawa and M. Tamada	
2-09	Introduction of Cross-linking into Fluoro-rubber by Gamma-ray Irradiation for the Improvement of Its Compression Set	51
	T. Hamasuna, A. Iwanade, Y. Fukuta, D. Nogami and K. Watanabe	
2-10	Surface Modification of Vulcanized Rubber by Radiation Co-grafting	52
	N. Mizote, H. Saito, Y. Ueki, N. Seko and M. Tamada	
2-11	Decomposition of Persistent Antibiotics by Ionizing Radiation	53
	A. Kimura and M. Taguchi	
2-12	Development of Fibrous Adsorbent for Polyols	54
	A. Jyo, H. Matsuura, J. Ishizaki, N. Seko and Y. Ueki	
2-13	Recovery of Platinum from Waste of Silicon Rubber with Amine and Nuclear Acid Adsorbent Synthesized by Graft-Polymerization	55
	Y. Kaneko, A. Iwanade, Y. Fukuta, D. Nogami and K. Watanabe	
2-14	Preparation and Characterization of the Low Molecular Weight Funoran	56
	S. Takigami, H. Yamaguchi, R. Takahashi and N. Nagasawa	

This is a blank page.

2-1 A Simple Method for Radiation-Induced Graft Polymerization Using a Polyethylene Bottle as a Reactor

Y. Ueki^{a)}, N. C. Dafader^{b)}, N. Seko^{a)} and M. Tamada^{a)}

^{a)} Environment and Industrial Materials Research Division, QuBS, JAEA,

^{b)} Nuclear and Radiation Chemistry Division, Institute of Nuclear Science and Technology,
Bangladesh Atomic Energy Commission

Radiation-induced graft polymerization, one of the surface modification techniques of polymer materials, has recently been attracting attention as a refined artifice because the adsorption rate of a grafted polymer is 10-100 times higher than that of a commercial granular resin¹⁾. However, this technique is not very popular in Southeast Asian and other developing countries at present, because it is hard or impossible to obtain unique apparatus such as a glass ampoule or vacuum line for grafting, and furthermore the grafting must be carried out under oxygen-free or vacuum conditions to prevent the deactivation of created radicals on the polymer substrate by dissolved oxygen. The objective of this study is to develop new methodology for radiation-induced graft polymerization that can be performed using not unique but general apparatus.

A polyethylene bottle (volume: 305 mL) with a tight-fitting lid was used as a reactor instead of a glass ampoule. A nonwoven polyethylene fabric (diameter: 13 μ m) was irradiated with an electron beam up to 100 kGy under nitrogen atmosphere. The irradiated nonwoven fabric was transferred into a polyethylene bottle. Then, the de-aerated monomer emulsion, composed of 5 wt% glycidyl methacrylate, 0.5 wt% polysorbate 20 and 94.5 wt% water, was directly and immediately poured into the polyethylene bottle under an air atmospheric condition without the use of a vacuum line, since the oxygen in the air was immediately dissolved in the de-aerated monomer emulsion during the operation. After pouring, this bottle was tightly closed with a lid to prevent oxygen in the air from entering the emulsion. An air atmospheric grafting was performed at 40 °C. The degree of grafting (Dg) was evaluated by the increased weight after grafting²⁾.

Figure 1 shows the results of air atmospheric graft polymerization using the polyethylene bottle. For comparison, the results of vacuum grafting are also shown. As seen in Fig. 1, it was found that the reaction of air atmospheric grafting proceeded even when the polyethylene bottle was used as a reactor and the vacuum line was not used for transferring monomer emulsion. In terms of the stop time of grafting, the difference of grafting condition showed a remarkable degree of variation; although vacuum grafting occurred continuously and Dg increased linearly with increases in the grafting time of at least up to 4 hours. The air atmospheric grafting conversely stopped due to the dissolved oxygen in monomer emulsion after a certain

amount of time had elapsed. Under an air atmospheric condition, the stop times of grafting were 3 hours, 2 hours and 1 hour at 100, 50, and 20 kGy irradiation, respectively. The Dg in these cases reached 351% for 3 hours, 209% for 2 hours and 42% for 1 hour, respectively. From the standpoint of the Dg reduction, the grafting at a lower irradiation dose was more susceptible to dissolved oxygen in monomer emulsion than that at a higher irradiation dose. The Dg values under an air atmospheric condition at 100, 50 and 20 kGy were about 80%, 63% and 23% under a vacuum condition at 100, 50 and 20 kGy. In these experiments, the dissolved oxygen concentrations in monomer emulsion were maintained within a range from 0.8 to 1.0 mg/L at any given time, without increasing the dissolved oxygen concentration during grafting. Based on the above results, it was found that air atmospheric grafting could be performed by using general apparatus and a simpler procedure, without using unique apparatus such as a glass ampoule and vacuum line. Additionally, it was also found that the air atmospheric grafting continued for a certain amount of time only in the case of a higher irradiation dose; in other words, air atmospheric grafting could only be achieved when a large amount of radicals was present in the sample, even if some of the generated radicals were consumed by dissolved oxygen in the monomer emulsion. In air atmospheric grafting without using unique apparatus, the graft polymer, which possessed sufficient capacity for use as a metal adsorbent precursor, was prepared at an irradiation dose of 50 kGy or above.

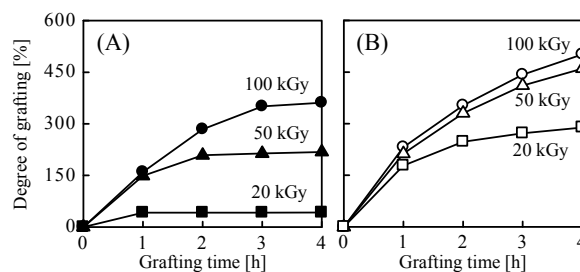


Fig. 1 Time course of (A) air atmospheric and (B) vacuum grafting.

References

- 1) S. Aoki et al., Anal. Sci., **17 Suppl.** (2001) i205-208.
- 2) L. D. C. Nayanajith et al., J. Ion Exchange, **21** (2010) 123-126.

2-2 Radiation-induced Grafting of Acrylonitrile Monomer onto Cellulose Nonwoven Fabric

S. Saiki^{a)}, T. Puspitasari^{b)} and N. Seko^{a)}

^{a)} Environment and Industrial Materials Research Division, QuBS, JAEA,

^{b)} Centre for Application of Isotope and Radiation Technology,
National Nuclear Energy Agency, Malaysia

Cellulose has been studied as trunk polymer for radiation-induced grafting. Recently radiation-induced grafting with an emulsified vinyl monomer solution, which can reduce the dose and the volume of organic solvent for grafting materials¹⁻³⁾. In this topic, to study the effectiveness of radiation-induced emulsion grafting onto nonwoven cellulose fabrics with an acrylonitrile (AN) monomer, which is a typical vinyl monomer, we tried to evaluate the micelle size of AN monomer against for monomer and surfactant concentrations.

Emulsion was prepared by mixing AN (10-30 wt%), Tween80 (Tw-80) (0.3-5 wt%) and Milli-Q water at a certain ratio with homogenizer for 10 minutes. The formation of emulsion was evaluated by visual appearance and micelle size. The visual evaluation was conducted by keeping samples at 60 °C for accelerated test. Micelle size was measured with fiber optics dynamic light scattering spectrophotometer (FDLS-3000, Otsuka Electronics Co. Ltd., Japan). Nonwoven cellulose fabrics were irradiated under nitrogen atmosphere with electron beam (2 MeV, 3 mA) up to 100 kGy. Irradiated fabrics were put into a glass ampule, and AN emulsion bubbled with nitrogen gas, including Tw-80 as a surfactant and Milli-Q water, were sucked into the ampule under vacuum condition. Graft polymerization was carried out at 60 °C for 4 h in water bath. To compare the graft efficiency, organic solvent such as methanol was also examined. After graft polymerization, grafted fabrics were washed by methanol and dried in vacuo. The degree of graft polymerization (Dg) was evaluated as a following equation;

$$D_g [\%] = (W_1 - W_0) / W_1 \times 100,$$

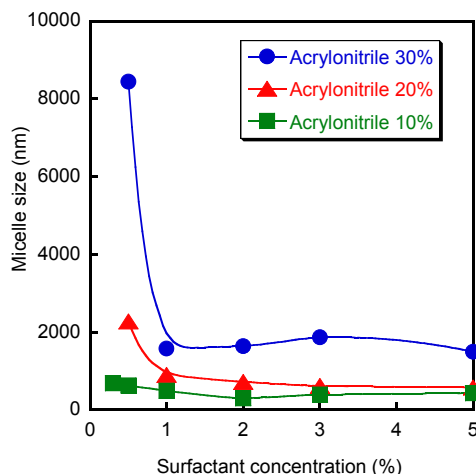


Fig. 1 Micelle size of AN emulsion.

where W_1 and W_0 mean weights of cellulose nonwoven fabric before and after graft polymerization.

The visual evaluation showed that the solution at 5% AN monomer concentration caused phase separation. This is assumed to be because water-solubility of AN is about 7%. At more than 10% AN monomer concentration, these solution could be emulsified to a milky state.

Next, the micelle size of AN emulsion was measured (Fig. 1). On the whole, micelle size increased with increasing AN monomer concentration. At 20% and 30% AN monomer concentrations, micelle size with 0.3% surfactant concentration was over 10,000 nm, and with 0.5% was still large and micelle size distribution had several peaks. At 30% AN monomer concentration with other surfactant concentration, size distribution had a broader peak and sometimes several peaks, and thereby these emulsion condition was seemed to be less stable than 10% and 20%.

The result of Dg is shown in Fig. 2. Compared to the case of methanol, Dg increased obviously by use of AN emulsion. This shows that the AN monomer is consumed for graft polymerization efficiently. And, Dg increased with increment of AN concentration. Moreover, Dg was not affected by surfactant concentration significantly. This tendency is similar to that of micelle size. These facts mean possibly that Dg increased with increasing micelle size.

References

- 1) N. Seko et al., Nucl. Instrum. Meth. Phys. Res. B, 265 (2007) 146.
- 2) N. Seko et al., Radiat. Phys. Chem., 79 (2010) 22.
- 3) A. Sekine et al., Radiat. Phys. Chem., 79 (2010) 16.

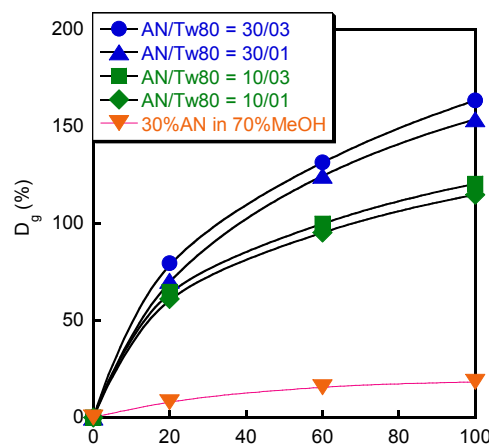


Fig. 2 Dose dependency of Dg.

2-3 The Effect of Partial Delignification on Kenaf Bast Fibers for Radiation Graft Polymerization

N. H. Mohamed^{a)}, M. Tamada^{a, b)}, Y. Ueki^{b)} and N. Seko^{b)}

^{a)} Department of Chemistry and Chemical Biology, Graduate School of Engineering, Gunma University, ^{b)} Environment and Industrial Materials Research Division, QuBS, JAEA

It is well known that during radiation graft polymerization on lignocelluloses fiber, the phenol in the lignin will undergo a structure change to quinone¹⁾ and due to this, the graft polymerization is hindered and instead homo-polymerization occurs. For effective graft polymerization for lignocelluloses fiber, the lignin must decompose through delignification, so that the monomer can reach to the crystal part of cellulose. In this report, the changes in residual lignin of kenaf bast fiber (KBF) using acidic chlorite solution were evaluated.

Acidic chlorite delignification of KBF was performed in a fume hood by using 0.7% aqueous sodium chlorite at pH 4 adjusted with nitric acid at a ratio of KBF/chlorite solution of 1:110 (wt/wt). The mixture was heated from 60 to 90 °C for 6 hour to prepare a series of residual lignin in KBF. After the reaction, the partial delignified KBF was removed from chlorite solution, washed and dried. The residual lignin of the partial delignified KBF was determined by TAPPI method.

For the purpose of radiation grafting copolymerization, dried KBF (400 mg) was purged with N₂ and sealed in PP zipper bag. The KBF was then laid on dried ice and irradiated with electron beam at a dose of 150 kGy. Graft copolymerization of irradiated KBF was carried out by adding 100 mL emulsion containing 3% of 4-Chloromethyl styrene (CMS), 0.3% Tween 20 and 96.7% deionized water in vacuum state for 24 h at 30 °C. The grafted KBF was then recovered from the emulsion and washed repeatedly with methanol to remove the access monomers and homopolymers. The weight of the CMS-grafted KBF was determined after dried overnight in vacuum oven at 30 °C.

The Degree of grafting (Dg) was calculated according to the following formula:

$$Dg (\%) = \left[\frac{W_1 - W_0}{W_0} \right] \times 100 ,$$

where W₀ is the initial weights of KBF and W₁ is the weight of KBF after grafting.

Figure 1 (a, b, c) shows the surfaces of the KBF without

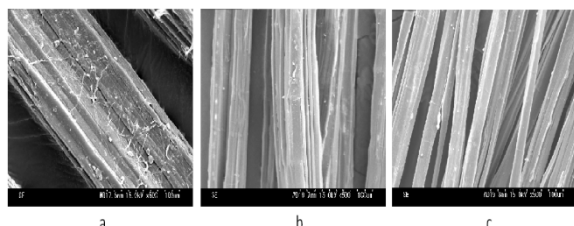


Fig. 1 SEM micrographs of HBF with different residual lignin after delignification (a) untreated, (b) KBF 4.19% residual lignin; (c) KBF 1.12% residual lignin.

delignification, KBF with 4.19% residual lignin and KBF with 1.12% residual lignin respectively. As shown in Fig. 1(a), it is evident that the undelignified KBF indeed coated with thin layer contains dissolved lignin, in which the microfibrils were held together to form bundles. On the contrary to the partial delignified KBF, Fig. 1(b) shows that the surface of the KBF was found to be rather smooth with prominent changes in its arrangement due to the solubilization of cemented layers during the delignification. Accordingly, Figure 1(c) shows that the intense delignification was accompanied by severe fibrillation into different sizes and shapes with the decrease of lignin content down to 1.12%. As delignification proceeds, the KBF became narrow in size and more open with well defined fibrils.

Figure 2 depicts the influence of residual lignin in KBF on the Dg. Clearly, the declining trend in the Dg is ascribed by the increased of lignin content. The absence of Dg was noted when the undelignified KBF was employed. The lignin content at which the partial delignified KBF begins to graft to greater extend was at lignin content below than 4%. On further removal of lignin up 86% (2% residual lignin), the Dg increased up to 143% resulting from the exposure of crystal regions of cellulose at secondary layers, swelling behavior and the porosity of the fibers. Consequently, the emulsion is able to permeate more easily through the fiber.

Reference

- 1) P. Ghosh et al., Eur. Polym. J. 30 (1994) 749.

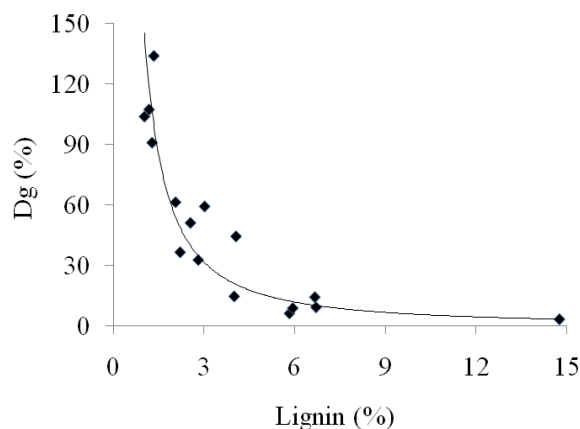


Fig. 2 Experimental results for radiation graft copolymerization of KBF as a function of residual lignin.

2-4 Development of Anion Adsorbent for Industry Application Based on Biodegradable Trunk Material

N. Kasai^{a)}, H. Hoshina^{a)}, N. Seko^{a)}, T. Shibata^{b)} and M. Takahashi^{c)}

^{a)} Environment and Industrial Materials Research Division, QuBS, JAEA,

^{b)} Weegl Co., Ltd., ^{c)} ERH Techno Research Co., Ltd.

1. Introduction

Abandoned mines and industrial waste water includes toxic anionic compounds such as arsenic (As), fluorine (F), boron (B), and so on. The purpose of this study is the practical use of developing anion graft adsorbent using biodegradable material being of plant origin, and which removes As(V) under the effluent standard of water quality. This paper shows that results of characteristic experiment of pilot scale synthesis plant based on the results of synthesis experiment in laboratory scale experiment. The issue was clarified for synthesizing graft adsorbent which has uniform grafting ratio.

2. Methods

(1) Dosimetry

The bonded cellulose material being of plant origin was base material of graft adsorbent in pilot scale. The amount of producing the adsorbent at once synthesis experiment was 0.3×7 m size. The base material was wound with the spacers for being scroll shape, and it loaded in reactor of pilot scale synthesis plant. The capacity of reactor was 35 L ($270 \Phi \times 650$ mm). Dosimetry of gamma-ray for sample in the reactor was carried out to paste up RadixW dosimeter together with base material, shown in Fig. 1, and irradiation time was one hour.

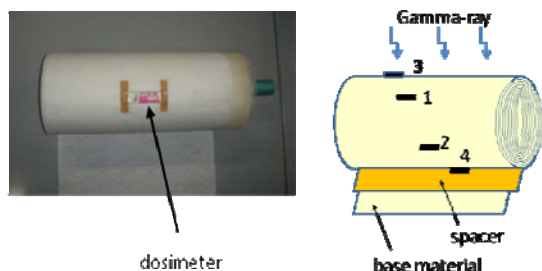


Fig. 1 Method of dosimetry.

(2) Grafting in Pilot Scale

Irradiation of gamma-ray to the base cellulose material wound with the spacers carried out to put in the polyethylene bag and filled with nitrogen gas. Then, it was put into the synthesis vessel which was put dry ice before irradiation.

The zirconium (Zr) has an affinity for anion removal like As(V), so that the component of monomer was phosphoric acid (5%) which is easy loaded with Zr(IV). The process of graft polymerization was as follows. Monomer of phosphoric acid was put into the reactor of the pilot plant after deoxygenization by nitrogen gas. Then, the irradiated

cellulose of scroll shape was put into grafting reactor. Grafting was carried out by keeping 40 °C during 2 h.

3. Results and discussion

Results of dosimetry showed that irradiation doses of positions from 1 to 4 shown in Fig. 1 were 9.0, 9.4, 12.8, and 7.0 kGy. It is clarified that irradiation dose distribution had maximum 1.8 times. Based on this result, sample was irradiated to be turned over after 1 hour of irradiation time that corresponded half of total irradiation time. Results showed that irradiation dose of surface and inside were 19.8 and 18.4 kGy. It is clarified that it was possible to irradiate uniformly so that it was not different irradiation doses of surface and inside.

The particles of the base material of cellulose were fit on scroll shape of it for examination of grafting degree in pilot scale. The results, clarified by weight changes of particles, showed that the degree of grafting is 157%. The result of Dg from 100 to 150% is suitable for anion adsorbent. However, a large amount of homopolymer was occurred.

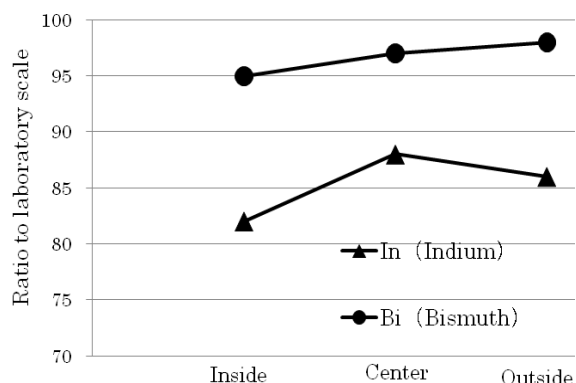


Fig. 2 Irradiation dose of graft adsorbent.

The evaluation of adsorption test using metal standard solutions was done for researching uniformity onto length direction (0.3×7 m) of adsorbent synthesized by pilot scale. The sampling positions were 50 cm from inside as the inside, 350 cm from inside as the center and 50 cm from outside as outside. Figure 2 showed results of the adsorption test. Adsorption ratio was shown to compare with results of laboratory scale with 100% of Dg. Graft adsorbent which has uniformly grafting ratio was synthesized so that ratios of adsorbent distribution in each position are almost same from 80 to 100%.

The authors gratefully acknowledge the support of Japan Science and Technology Agency (JST).

2-5 Synthesis of Amine-type Adsorbents with Emulsion Graft Polymerization of 4-hydroxybutyl Acrylate Glycidylether

H. Ma, H. Hoshina and N. Seko

Environment and Industrial Materials Research Division, QuBS, JAEA

Radiation-induced graft polymerization has driven widespread interest for many years by the benefits of economical efficient and environmental friendly characteristics. Polymeric grafts were covalently connected to the raw material, which can impart the raw material with desirable properties. For the past decades, glycidylmethacrylate (GMA) is considered to be the most widely used monomer for graft polymerization, because the epoxy group can be modified easily into functional groups. However, too much high D_g would lead the brittleness of grafted material. In this work, 4-hydroxybutyl acrylate glycidylether (4-HB) was used as a monomer for graft polymerization to synthesize metal ion adsorbents.

As a suitable graft polymerization condition, 5 wt% of 4-HB was added in water solution with surfactant. The emulsion of 4-HB was prepared with Span 20 at the concentration of 0.5 wt %. The trunk polymer polyethylene-coated polypropylene nonwoven fabric (NF) was irradiated with an electron beam. The irradiated NF pieces were transferred to a glass ampoule and contacted with the aqueous 4-HB emulsion at 40 °C. Degree of grafting (D_g) was evaluated by the increment of weight. 4-HB-grafted NF was aminated in 70% Ethylenediamine (EDA) in isopropyl alcohol at 60 °C to introduce the amino functional group. Adsorption capabilities of GMA and 4-HB type adsorbents were evaluated by column experiment with 10 ppm Cu^{2+} solution at the flow rate of 100 h^{-1} in space velocity (SV).

Figure 1 depicts the D_g of 4-HB onto the NF as a function of irradiation dose after 1 h. The results indicated that the D_g of 4-HB increased linearly with the increase of the absorbed dose below 40 kGy. Grafting saturation with a D_g of 180% was achieved at 50 kGy.

After graft polymerization, the diameter of the fiber was doubled to 20 μm at the D_g of 130%. In our previous study,

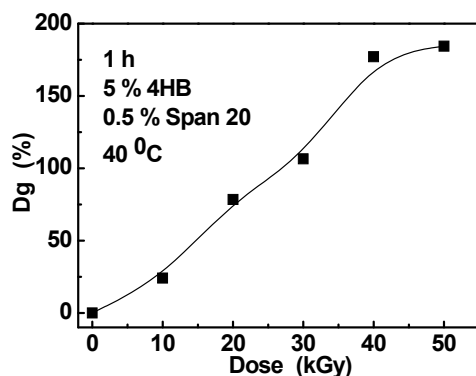


Fig. 1 Effect of pre-irradiation dose on D_g .

the soft trunk NF became hard after grafted with GMA and then turned to brittle at a high D_g of 100%. However, the 4-HB grafted materials kept soft even at a high D_g of 280%. From the tensile strength and breaking elongation of a single NF, it is clearly that 4-HB grafted NF shows better mechanical property under tension, compared with the GMA grafted one (Fig. 2).

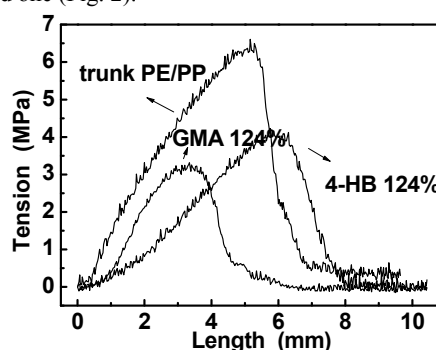


Fig. 2 Tensile curves of NF, 4-HB-grafted NF and GMA-grafted NF.

To compare the adsorption capability of the two adsorbents, certain D_g was designed beforehand in order to obtain similar density of amino groups. The 4-HB grafted NF with a D_g of 135% was treated with EDA at the optimized condition of modification, and the density of amino group was 2.8 mmol/g. Breakthrough curves of Cu^{2+} from the two adsorbents in Fig. 3 show that the capability of 4-HB-type is higher than that of GMA-type. From structure of the two monomers, 4-HB shows 4 methylene groups compared with GMA, which makes the side chain of grafted polymer longer and more flexible. Accordingly, not only the physical properties such as topography and mechanical properties of the grafted material but also their capability were improved.

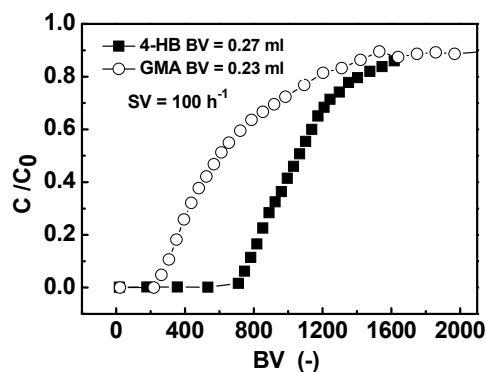


Fig. 3 Breakthrough curves of Cu^{2+} for the 4-HB type (■) and GMA (○) type adsorbents.

2-6 Decolorization of Secondary Treated Water from Livestock Urine Waste

M. Takigami^{a)}, W. Gokan^{a)}, N. Nagasawa^{b)}, A. Hiroki^{b)}, N. Kasai^{b)}, M. Tamada^{b)}
S. Takigami^{c)}, T. Shibata^{d)}, Y. Aketagawa^{d)} and M. Ozaki^{e)}

^{a)} Gunma Industry Support Organization, ^{b)} Environment and Industrial Materials Research Division, QuBS, JAEA, ^{c)} Center for Material Research by Instrumental Analysis, Gunma University, ^{d)} Weeql Corp., ^{e)} Maebashi Institute of Technology

There is no regulation for chromaticity of waste water, however, decolorization of secondary treated water from livestock urine waste is one of the biggest concerns for livestock farmers. The color is attributed to metabolites of microorganisms, to say humic substances including humic acid and fulvic acid. At present both of them are decomposed or aggregated with coagulant.

Since humic substances have carboxyl groups in the structure¹⁾, we have developed an absorbent which has positive charge by radiation-induced grafting reaction at room temperature. Cheesecloth made of polyvinyl alcohol (PVA) fiber (Cremona #300, Kuraray Co.) was used as a trunk polymer and was irradiated up to 60 kGy with electron beams at room temperature. After irradiation, aqueous solution of N-[3-(dimethylamino) propyl] acrylamide (DMPAA, Kohjin Co., Ltd.) up to 20% was led into the irradiated PVA at room temperature. After 2 hours, the PVA cloth was washed with water, dried and used as an absorbent.

To examine the effects of degree of grafting on removal of colored materials, 100 cm² of absorbents with a range of degree of grafting were put in 60 mL of secondary treated water and shaken at room temperature. Chromaticity of the treated water was measured every 24 h by absorbance at 390 nm using a Digital Turbidity-Color Meter (WA-PT-4DG, Kyoritsu Chemical-Check Lab., Corp.). The initial color of the secondary treated water was 2,000. The secondary treated water was exchanged every day and the chromaticity was measured for 30 days. The weight of absorbent was weighed after absorption for 15 and 30 days. The absorbent absorbed humic substances in the secondary treated water as shown in Fig. 1. While PVA cloth did not

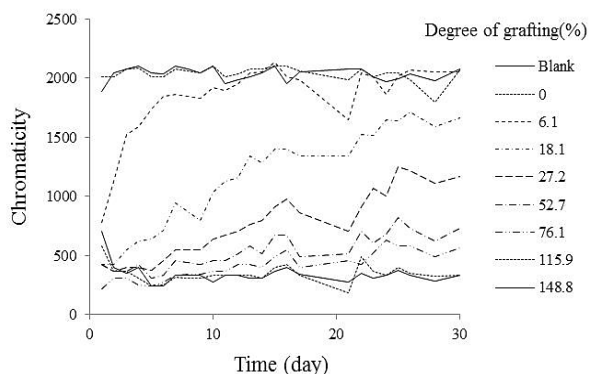


Fig. 1 Change of chromaticity after contacting secondary treated water with absorbent.

absorb humic substances, absorbent with higher degree of grafting absorbed humic substances effectively. Absorbent with low degree of grafting removed colored materials effectively at the first moment, however, it lost the absorption ability day by day.

The absorbed humic substances were easily removed by washing the absorbent with 2 M salt solution. Hydrochloric acid was added to the desorbed solution to precipitate humic acid in the humic substances²⁾. Humic acid is precipitated by acid, however, fulvic acid is not.

Carboxyl groups in humic acid was determined by titration. Carboxyl groups in 100 mg humic acid were 1.18 m mole. The amount of carboxyl groups in humic acid (COOH) per quaternary groups in absorbent (N⁺) was calculated for absorbents which absorbed humic substances for 15 and 30 days and shown in Fig. 2. It depended on degree of grafting and showed maximum value at low degree of grafting. The value exceeded 1, which indicated that not all carboxyl groups had interaction with quaternary group. The value can be a measure of efficiency of absorbents. As described above, absorbents with higher degree of grafting did not lose the absorption ability after 30 days, they have possibility to absorb more amount of humic acid per grafted branch polymer.

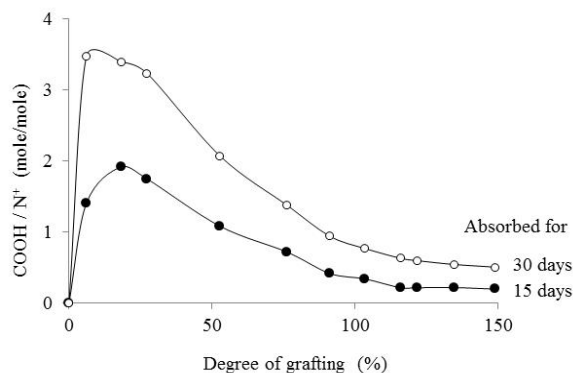


Fig. 2 Relation between degree of grafting and efficiency of absorbent.

References

- 1) J. Stevenson, "Hums Chemistry, Genesis, Composition, Reactions, 2nd edition", John Wiley & Sons. Inc., New York (1994) pp.287.
- 2) D. Asakawa et al., Humic Substances, Res., **3**, (2006) 15-24.

2-7

Effect of Gamma-rays Irradiation of Hydroxypropylmethylcellulose Aqueous Solution

T. Haikawa^{a)}, K. Furusawa^{b)}, Y. Maki^{a)}, N. Nagasawa^{c)} and T. Dobashi^{a)}

^{a)} Department of Chemistry and Chemical Biology, Graduate School of Engineering, Gunma University,

^{b)} Division of Biological Sciences, Graduate School of Science, Hokkaido University,

^{c)} Environment and Industrial Materials Research Division, QuBS, JAEA

Hydroxypropylmethylcellulose (HPMC) is one of water-soluble cellulose-derivatives used for various medical and pharmaceutical materials such as coated tablets and artificial vitreous as well as industrial and food additive use¹⁾. Its aqueous solution has a lower critical solution temperature and sol-gel transition temperature around 50 - 60 °C²⁾. The phase diagram consists of four different phases of turbid gel, transparent gel, turbid sol and transparent sol, which are partitioned by two curves of the cloud point curve and the sol-gel transition curve. The change of viscosity and transparency of HPMC solutions or gels controlled by temperature is sometimes useful for applications. For example, viscosity needs to be low at room temperature and high at physiological temperature for artificial vitreous use. Transparency needs to be low at high temperatures and high at low temperatures for clear/cloud grazing application. Therefore, the cross-sectional point (T_x) of the two curves is one of the key parameters characterizing the system, and the control of T_x by combinations of preparation condition and thermodynamic variables is important. Addition of salt is known to decrease T_x . In this study we report the effect of gamma-rays irradiation on the cloud point curve.

High energy ionizing radiation has been known to modify polymers by cross-linking and scission³⁾. For HPMC solutions, it has been reported that electron beams irradiation results in cross-linking to make a gel⁴⁾. It is interesting to use gamma-rays irradiation with relatively lower energy and to study the effect on the molecular properties of HPMC and the resultant change in the thermal properties from both scientific and application aspects. In this study, we irradiated gamma-rays on HPMC solutions with different concentrations, measured the molecular properties and determined the cloud point curve of the solutions.

HPMC (60SH-50) is a gift from Shin-Etsu Chemical Co. Its nominal weight-averaged molecular weight is 10.4×10^4 and the weight percent of methoxyl and hydroxypropoxyl groups are 28-30% and 7-12%, respectively. In order to prepare the homogeneous solution, HPMC was dispersed in hot water at 90 °C and dissolved thoroughly by gentle stirring, then incubated at 4 °C for more than a day. Finally, 3 mL solution at HPMC weight fractions of $w=0.01 \sim 0.12$ was put in a vial vessels with 12 mm ϕ . The solutions were irradiated at room temperature around 20 °C at the dose rate of 10 kGy/h with gamma-rays generated from ^{60}Co source at Takasaki Advanced Radiation Research Institute of JAEA.

The weight-average molecular weight (M_w) and the radius of gyration ($\langle S^2 \rangle_z^{1/2}$) of HPMC were determined from the Zimm plot for the light scattering data using a laboratory-made apparatus with He-Ne laser at the wavelength of 6.33×10^{-5} cm as the light source⁵⁾. Cloud point curves were determined as the loci of the temperature where the observed transmitted light through the sample disappears by eyes. The critical point was determined by observing the spinodal ring.

The molecular properties such as M_w , $\langle S^2 \rangle_z^{1/2}$ were much different depending on the concentration of the original sample (before irradiation) w being below or above the critical concentration of the original sample $w_{CP} \sim 0.06$. M_w was smaller than the original one for $w < w_{CP}$ and larger for $w > w_{CP}$. On the other hand, $\langle S^2 \rangle_z^{1/2}$ is larger than the original one for $w > w_{CP}$ whereas for $w < w_{CP}$ it decreases at 0.03 and increases again at 0.01 with decreasing w .

As shown in Fig. 1, the cloud point curves were shifted to the higher temperature side by raising the irradiation dose. The increase of the cloud point temperature at $w < w_{CP}$ and $w > w_{CP}$ could be attributed to mainly the lowered M_w and compactness of the molecular structure, respectively.

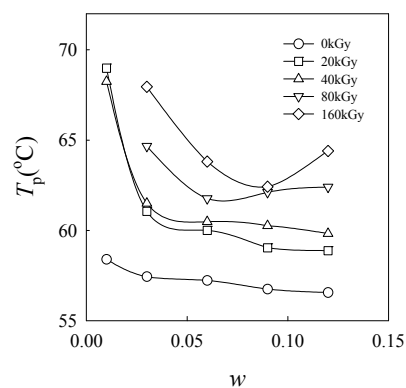


Fig. 1 Cloud point temperatures of irradiated and non-irradiated HPMC solution with different weight fractions.

References

- 1) (for example) E. Fukui et al., Int. J. Pharmaceut., 217 (2001) 33-43; T. J. Liesegang, Surv. Ophthalmol., 34 (1990) 268-293.
- 2) R. Kita et al., Phys. Lett. A 259 (1999) 302-307.
- 3) J. M. Rosiak et al., Radiat. Phys. Chem. 55 (1999) 139-151.
- 4) N. Pekel et al., Carbohydr. Polym. 55 (2004) 139-147.
- 5) Y. Maki et al., J. Chem. Phys. 126 (2007) 134901.

2-8 Transparent Hydrogels Prepared by Radiation Crosslinking Hydroxypropyl Cellulose with Functional Monomers

A. Hiroki^{a)}, T. Sato^{b)}, N. Nagasawa^{a)} and M. Tamada^{a)}

^{a)} Environment and Industrial Materials Research Division, QuBS, JAEA,

^{b)} NIPPON CONTACT LENS INC.

Hydrogels of cellulose derivatives such as carboxymethyl cellulose and hydroxypropyl cellulose (HPC) are prepared by gamma or electron beam irradiation to their highly concentrated aqueous solution¹⁾. The obtained hydrogels are splintery and hard to expand generally. The HPC hydrogels with improved mechanical properties were prepared by the combination of the poly(vinyl alcohol) (PVA) blending and the radiation crosslinking²⁾. However, the transparent HPC hydrogel became slightly cloudy. In this work, the preparation of HPC hydrogels with good mechanical properties as well as transparency was investigated.

HPC and 2-hydroxyethyl methacrylate (HEMA) were purchased from Wako Pure Chemical Industries, Ltd., Japan. Polyethylene glycol 1000 dimethacrylate (23G) was supplied by Shin-Nakamura Chemical Co. Ltd., Japan. The concentrated aqueous solution containing HPC, HEMA, and 23G were prepared, in which the content of HPC, HEMA, and 23G were 20 wt%, 2.0 wt%, and 0.2-1.0 wt%, respectively. The samples shaped by cold pressing were irradiated with electron beams to obtain gel membranes. Gel fraction of the obtained hydrogels was determined gravimetrically by measuring insoluble part after water extraction of sol. The tensile strength and the elongation at break were measured by expanding the hydrogels cut into strip specimen.

The gel fraction of the obtained hydrogels as a function of dose is shown in Fig. 1. The addition of 23G with HPC induced the increase in the gel fraction, especially at less than 20 kGy. It was found that the gel fraction of the HPC/23G/HEMA hydrogel consisting of the three components decreased drastically. This is due to the inhibition of the crosslinking reaction with the formation of

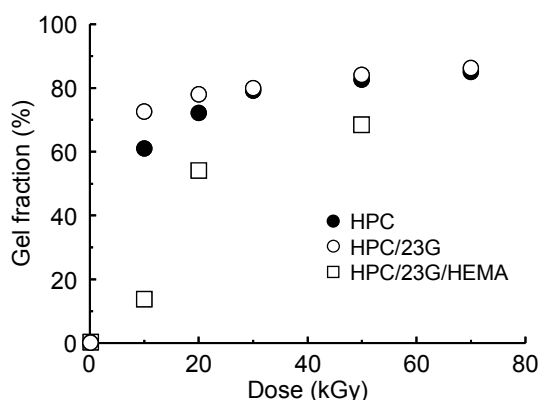


Fig. 1 The gel fraction of HPC, HPC/23G, HPC/23G/HEMA hydrogels as a function of dose.

homopolymer. Degree of swelling of the HPC, HPC/23G, and HPC/23G/HEMA hydrogels at more than 30 kGy was in the range of 10 to 13. Furthermore, it was confirmed that all of the obtained hydrogels were transparent.

Figure 2 shows the tensile strength and the elongation at break of the hydrogels that exhibited the maximum. The mechanical properties were improved by adding only 0.2 wt% of 23G, in comparison with those of the HPC hydrogel. Both values decreased gradually even though the concentration of 23G increased from 0.2 to 1.0 wt%. On the other hand, by adding 2 wt% of HEMA to HPC/23G (20/0.2 wt%), the elongation at break of the HPC/23G/HEMA hydrogel increased to 124%, although the tensile strength decreased to 2.0 kg/cm². These are the almost same as the mechanical properties achieved by PVA blending. Consequently, the hydrogel constructed from HPC, 23G, and HEMA exhibited about 2.0 and 1.8 times larger tensile strength and elongation at break than these of the pure HPC hydrogel, respectively.

From the above results, it was found that the HPC hydrogels with desired properties were obtained by radiation crosslinking HPC with functional monomers such as 23G and HEMA.

References

- 1) R. A. Wach, et al, *Macromol. Mater. Eng.* **287** (2002) 285-295.
- 2) A. Hiroki, et al., *JAEA Takasaki Ann. Rep.* 2009 (2011) 44.

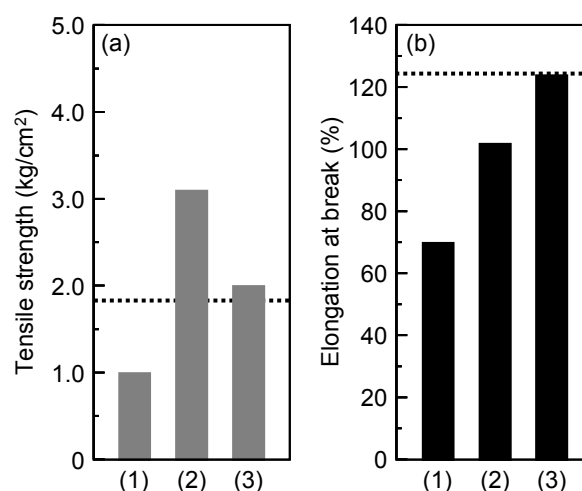


Fig. 2 Tensile strength (a) and elongation at break (b) of hydrogels, 1; HPC, 2; HPC/23G, and 3; HPC/23G/HEMA, obtained at 50, 30, and 50 kGy, respectively. Dotted line; that of HPC/PVA blend hydrogel reported previously.

2-9 Introduction of Cross-linking into Fluoro-rubber by Gamma-ray Irradiation for the Improvement of Its Compression Set

T. Hamasuna^{a)}, A. Iwanade^{b)}, Y. Fukuta^{b)}, D. Nogami^{b)} and K. Watanabe^{b)}

^{a)} MASUOKA Co., Ltd.,

^{b)} Department of Advanced Radiation Technology, TARRI, JAEA

Mechanical properties of fluoro-rubber were evaluated after the irradiation of gamma-ray irradiation. The irradiated fluoro-rubber demonstrated high tensile strength and lower transformation ratio as gamma-ray dose increased. While, the change in its hardness was not detected. The compression set was lower as dose increased because the cross-linking structure prevented from deformation. The fluoro-rubber having resistance to deformation should be developed by irradiation of gamma-ray.

工業製品の切削油を洗い落とす洗浄工程において、以前ではハロゲン系溶媒が使用されていたが、現在では環境負荷を考慮し、グリコールエーテル系溶媒へと転換が進んでいる。これまでに、既存の製品では対応が難しいグリコールエーテル系溶媒に対する耐性に優れた新規フッ素ゴム O-リングを開発した。しかしながら、このフッ素ゴム O-リングは長期間使用下において、無視できない不可逆な変形を引き起こす。そこで、耐変形性をフッ素ゴム O-リングへ付与するために、放射線照射による橋架け構造の導入を提案した。

実験では、加硫条件 170 °C、15 分及び 30 分の板状フッ素ゴム及び円柱状フッ素ゴムをガンマ線照射試料として選択した。コバルト 60 を線源として、室温条件下において、フッ素ゴムへ 10 kGy/h の線量率で線量 10 ~ 100 kGy のガンマ線を照射した。ガンマ線照射後、フッ素ゴムを JIS K 6251、6253 及び 6262 に従って、引張強度、伸び、ゴム硬さ及び圧縮永久ひずみを測定した。

ガンマ線を照射したフッ素ゴムの引張強度と伸びを Fig. 1 及び 2 に示す。今回照射したフッ素ゴムは線量が増加するに従って、引張強度は増加し、伸びは減少する一般的な放射線照射によって橋架けした高分子と同様の挙動を示した。Figure 3 に示すように、ゴム硬さは 0~100 kGy の線量では変化がなかった。従来、フッ素樹脂は放射線照射によって分解する¹⁾。一方、フッ素樹脂への橋架け構造導入には脱酸素条件下においてフッ素樹脂のガラス転移温度付近まで加熱して、照射する必要があった²⁾。使用したフッ素ゴムに加熱することなく橋架け構造を導入できた理由は、加硫によって既に橋架け構造を有しており、放射線照射によって分解が抑制されたため推察する。また、今回使用したフッ素ゴムはフッ素系モノマーとアレン系モノマーの共重合体であるため、アレン系モノマー部位が可溶に関与したと考えられる。以上から、加硫条件にかかわらず、引張強度と変形率は同等の値と挙動を示したことから、ガンマ線照射によって加硫時間の短縮ができることが示された。

耐変形性の指標として、ガンマ線照射したフッ素ゴムの永久圧縮ひずみを評価した。結果を Fig. 4 に示す。線量の増加に伴い、ガンマ線照射により導入される橋架け構造によって、圧縮永久ひずみを低減できること、また、それは加硫時間に依存しないことが示された。

今回の検討により、ガンマ線照射によるフッ素ゴムへの橋架け構造の導入は圧縮永久ひずみの低減に効果

的であることが示された。引張強度及び伸びへの影響と 40 kGy 以上照射したフッ素ゴムの圧縮永久ひずみの変化の幅が小さいことから、フッ素ゴムの橋架け条件は 40 kGy 付近が好ましい。また、ガンマ線照射によるフッ素ゴムへの加硫時間の短縮に加えて、省エネルギー化及び作業環境の向上による環境や作業への貢献も大きいことが分かった。

References

- 1) 幕内恵三、ポリマーの放射線加工、ラバーダイジェスト社、(2000) 178-181.
- 2) A. Oshima et al., Radiat. Phys. Chem. **60** (2001) 467-471.

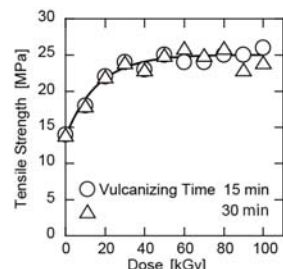


Fig. 1 Tensile strength of irradiated fluoro-rubbers.

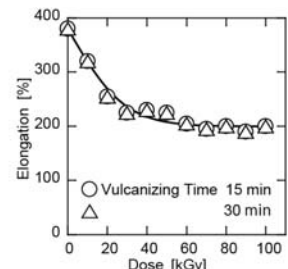


Fig. 2 Elongation of irradiated fluoro-rubbers.

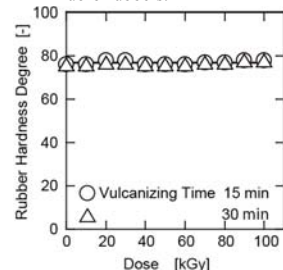


Fig. 3 Hardness of irradiated fluoro-rubbers.

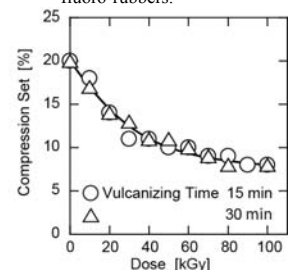


Fig. 4 Compression set of irradiated fluoro-rubbers.

*本研究は先端研究施設共用促進事業「明日を創り暮らしを守る量子ビーム利用支援事業」の支援のもと行いました。

2-10 Surface Modification of Vulcanized Rubber by Radiation Co-grafting

N. Mizote^{a)}, H. Saito^{a)}, Y. Ueki^{b)}, N. Seko^{b)} and M. Tamada^{b)}

^{a)} Mitsuba Co. Ltd.,

^{b)} Environment and Industrial Materials Research Division, QuBS, JAEA

In this study, hydrophilic monomer, 2-hydroxyethyl methacrylate (HEMA), and hydrophobic monomer, 3-(Methacryloyloxy) propyltris (trimethylsiloxy) silane (MPTS), were co-grafted on vulcanized rubber surface by simultaneous electron beam irradiation. Monomer solution was prepared by mixing of HEMA and MPTS. Frictional property and wear resistance of co-grafted rubber were investigated. As a result, abruptly decrease of $\Delta\mu$ and improvement of wear resistance were observed specifically around 90 weight percent MPTS concentration.

ワイパーゴムは摩擦、耐摩耗性の向上を目的として塩素化処理やコーティングなどの表面処理が行われている。しかしながら塩素による環境負荷やコーティング剥離による耐久性の問題を有するため、新しい表面改質が求められている。そこで我々は電子線照射グラフト重合による表面改質の検討を行った。これまでの研究で、MPTS に数%の HEMA を添加した混合モノマーによる共グラフトにおいて、グラフトしたゴムの表面硬さと疎水性が特異的に高まる事を確認している。本研究では、この共グラフトで得られたゴム表面の摩擦摩耗特性を調べた。

ゴム基材として、カーボンブラックを配合した架橋 EPDM ゴムシートを用いた。HEMA と MPTS を所定の割合で混合したモノマー溶液を用い、加速電圧 2 MeV、電流値 1 mA、照射線量 7 kGy の条件で電子線同時照射グラフト重合を行った。グラフトゴムとガラスの水を介した摩擦における枯渇摩擦挙動を、ピンオンディスク試験機を用いて調べた。摩擦により水が枯渇した直後の最大摩擦をセミドライ、乾燥状態で安定した摩擦をドライとし、セミドライとドライの摩擦係数差を $\Delta\mu$ と定義した。耐摩耗性は水で濡らした #400 研磨紙と 1 分間摩擦させた後の摩耗断面積により評価した。

図 1、図 2 にモノマー溶液の MPTS 濃度と摩擦係数および $\Delta\mu$ の関係をそれぞれ示す。MPTS 濃度 80%を超えるとセミドライ摩擦の低下とドライ摩擦の上昇が起き

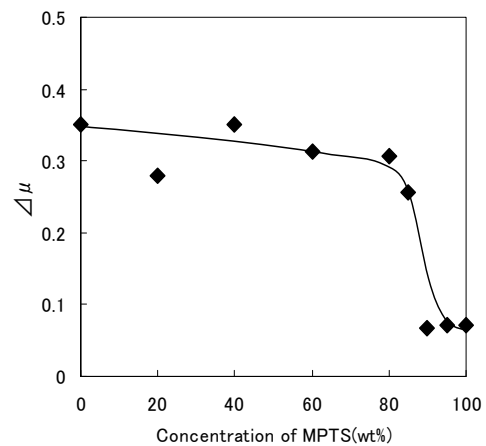


Fig. 2 Relationship between $\Delta\mu$ and MPTS concentration.

た。この結果として MPTS 濃度 80%以上で $\Delta\mu$ が大幅に低下した。図 3 に MPTS 濃度の違いによる摩耗量の変化を示した。 $\Delta\mu$ と同様に、MPTS 濃度が 80%を超えると摩耗量が大幅に低下する。これまでの研究で、疎水性が強くなると $\Delta\mu$ が小さくなる事が分かっており、MPTS80%を超えると疎水性が強くなるため $\Delta\mu$ が小さくなり、また水の膨潤による表面軟化も抑えられるため、耐摩耗性が向上したと考えられる。

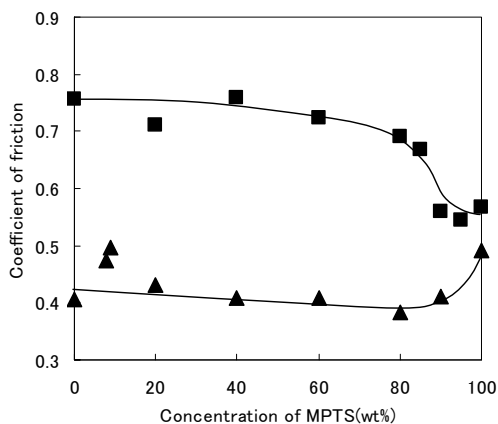


Fig. 1 Relationship between coefficient of friction and MPTS concentration.

▲: Dry state, ■: Semi-dry state.

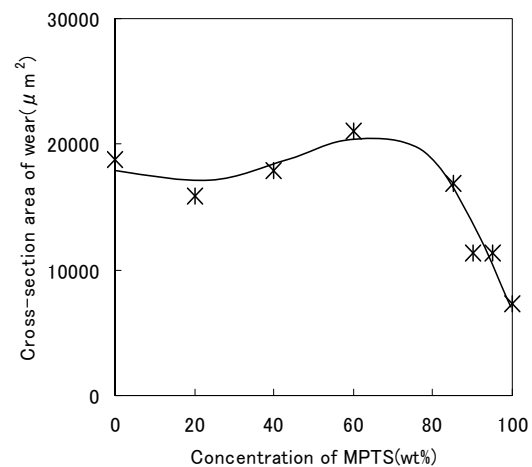


Fig. 3 Variation of wear resistance with MPTS concentration of monomer solution.

2-11 Decomposition of Persistent Antibiotics by Ionizing Radiation

A. Kimura and M. Taguchi

Environment and Industrial Materials Research Division, QuBS, JAEA

The concentrations of antibiotics in the water environment increased gradually because of population growth and the diversification of advanced medical worldwide, and the risk evaluation of them are studied recently ¹⁾. However, it is difficult to manage the environment risk of the antibiotics having great benefits for human life. The antibiotics have been also detected at the downstream of water treatment facilities, indicating that the physical-chemical treatment and the activated sludge system could not be removal of them completely. The development of direct removal methods are considered for them. These persistent organic pollutants in wastewater could be effectively decomposed by ionizing radiation method, which produces oxidative and reductive species homogeneously in water. The purpose of this work is to treat the antibiotics in combination of the activated sludge system, which is used in the existent wastewater treatment facility, and the ionizing radiation method. Decomposition of the pharmaceuticals in wastewater was first carried out by the activated sludge system in order to decompose biodegradable pharmaceuticals and reduce the amount of total organic carbon in wastewater.

Sulfapyridine, sulfamerazine, sulfamethazine, sulfamethoxazole, chloramphenicol, and chlorotetracycline were selected as experimental samples because they were reported to be consumed a lot on the domestic animals and medical treatment site and detected in the water environment ¹⁾. These antibiotics were dissolved at $10 \mu\text{mol dm}^{-3}$ in wastewater at pH value of 7.5 and the amount of total organic carbon at about 0.05 g dm^{-3} , which was collected at an influent of a water treatment facility of Gunma Prefectural Sewerage Management General Office. Activated sludge solution was supplied from the wastewater treatment plant and used for the biodegradation of the antibiotics. The sludge solution was mixed with the equal amount of the antibiotic solution, and stirred at 100 rpm with aeration at 100 mL/min for 8 hours, which is the average aeration time of real wastewater treatment plant with activated sludge system. The γ -ray irradiation of the sludge and antibiotic solution was carried out at 298 K using ^{60}Co γ -ray sources.

The antibiotics in wastewater at $5 \mu\text{mol dm}^{-3}$ were biodegraded by the activated sludge system (Fig. 1). Decomposition yield of chlorotetracycline was 93% for 8 hours though that of oseltamivir was 100% for 2 hours in previous work ²⁾. The chlorotetracycline in spite of aliphatic compounds could not be decomposed completely by the activated sludge since chlorine group of them would cause to be resistance against the biological oxidation.

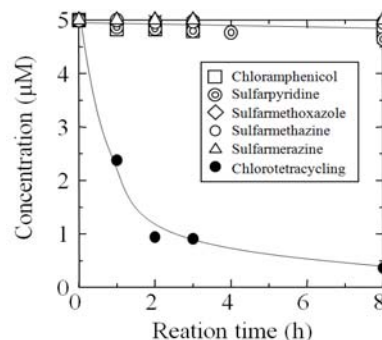


Fig. 1 Biodegradation of antibiotic in wastewater by activated sludge system.

Decomposition yields of other antibiotics were lower than 10%, and these aromatic antibiotics were not decomposed by the activated sludge system completely.

Chlorotetracycline was easily decomposed at a dose of 500 Gy as shown in Fig. 2. Concentration of sulfapyridine, sulfamerazine, sulfamethazine, and sulfamethoxazole were eliminated at 1 kGy, and their decomposition efficiencies were higher than that of chloramphenicol. Chemical structures of 4 sulfonamide antibacterial were similar to each other, and decomposition yield of them were almost the same. Chloramphenicol having phenyl ring substituted chlorine and nitro groups as electron accepters was considered to be lower reactivity with hydroxyl radicals than the other antibiotics. Persistent antibiotics in wastewater could be decomposed efficiently by the ionizing radiation method.

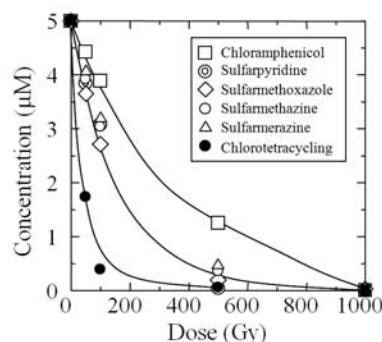


Fig. 2 Decomposition of antibiotic in wastewater by ionizing radiation.

References

- 1) M. Sasaki et al., Miyagi Pref. Inst. Pub. Heal. Environ. Ann. Rep. 26 (2008) 31-34.
- 2) A. Kimura et al., JAEA Takasaki Ann. Rep. 2009 (2011) 49.

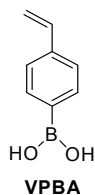
2-12 Development of Fibrous Adsorbent for Polyols

A. Jyo^{a)}, H. Matsuura^{a)}, J. Ishizaki^{a)}, N. Seko^{b)} and Y. Ueki^{b)}

^{a)} Department of Applied Chemistry and Biochemistry, Kumamoto University,

^{b)} Environment and Industrial Materials Research Division, QuBS, JAEA

We reported that poly(vinylphenylboronic acid) beads crosslinked with oligo(ethylene glycol) dimethacrylate take up polyols such as xylose¹⁾. The present study aims at the development of the liquid phase graft polymerization method of vinylphenylboronic acid (VPBA, Scheme 1) onto the electron pre-irradiated polyethylene-coated polypropylene fiber (PPPE) (0.9 denier) to obtain a fibrous adsorbent for polyols, such as xylose.



Scheme 1.

The non-woven cloth (thickness 0.5 mm, density 50 g/m²) of PPPE was used as trunk polymer. Rectangular pieces (2.0 × 4.0 cm, ca. 0.1 g) of the non-woven cloth of PPPE were irradiated with electron (2 MV, 3 mA, 200 kGy) under nitrogen atmosphere. Then, the electron-irradiated cloth pieces were transferred into a glass ampoule and it was fixed to a vacuum line. After degassing the ampoule, a liquid vinyl monomer or an organic solution of VPBA was transferred into the ampoule through the vacuum line. Dimethyl sulfoxide was used as solvent of monomers throughout. After dismounting the ampoule from vacuum line, it was allowed to stand in water bath at 40 °C for a given time. Grafting of monomers was identified by measuring weight increase after grafting and FT-IR spectra of the cloths before and after the grafting.

First, the graft polymerization of VPBA was tested. Table 1 lists experimental conditions and the degree of grafting (*DG*), which is designated by the following equation:

$$DG = 100(W - W_o)/W_o,$$

where W_o and W are weight of cloths before and after the graft polymerization, respectively. The *DG* value of 18.6% was not satisfactory because the concentration of VPBA was as high as 50 wt% and the reaction time was as long as 48 h.

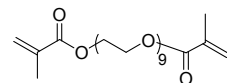
Table 1 Graft polymerization of VPBA.

Entry.	Concentration of VPBA ^{a)} (wt%)	Grafting time (h)	<i>DG</i> (%)
1	38	16	9.2
2	50	48	18.6

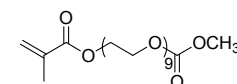
The reactivity of VPBA in grafting onto PPPE is significantly lower than that of styrene. In addition, VPBA grafted PPPE is very hard and scarcely swells with water even at pH 11.

We succeeded in the suspension copolymerization of oligo(ethylene glycol) dimethacrylate with VPBA¹⁾. Then, we tried the co-grafting of VPBA with several esters of oligo(ethylene glycol) with methacrylic acid. Prior to co-grafting, we tested grafting several candidate esters and clarified that nonaethylene glycol dimethacrylate (NEDM)

and methoxynonaethylene glycol methacrylate (MEDM) are effectively grafted onto PPPE as summarized in Table 2. Scheme 2 shows the structure of NEDM and MEDM. In addition, PPPE grafted with NEDM or MEDM is highly swollen with water. Finally, we tested co-grafting of VPBA



Nonaethylene glycol dimethacrylate (NEDM)



Methoxynonaethylene glycol methacrylate (MNEM)

Scheme 2.

with NEDM (or MNEM) onto PPPE non-woven cloth, referring to the results shown in Tables 1 and 2. Because of the lower reactivity of VPBA compared with methacrylate esters, molar ratio of VPBA/NEDM and VPBA/MNEM was fixed at 3/1. Concentration of each monomer mixture in wt% was also fixed at 80 and the grafting time was 16 h. Table 3 summarizes *DG* and uptake of xylose; xylose uptake was evaluated by eluting xylose with 0.5 M sulfuric acid from xylose adsorbed on VPBA-NEDM or VPBA-MNEM co-grafted cloth by equilibrating with xylose sample solutions of pH 11. As listed in Table 3, it turns out that both co-grafted fibers are able to take up xylose.

Table 2 Graft polymerization of NEDM and MNEM.

Entry	Monomer and its concentration ¹ (wt%)	Grafting time (h)	<i>DG</i> (%)
3	NEDM 100	4	240
4	NEDM 80	4	80
5	MNEM 100	4	771
6	MNEM 80	4	281
7	MNEM 45	4	92

Table 3 Uptake of xylose by co-grafted fibers.

Entry	Co-grafted fiber	<i>DG</i> (%)	Xylose uptake (mmol/g)
8	VPBA-NEDM	221	0.37, 0.33
9	VPBA-MNEM	180	0.34, 0.34

Next fiscal year we would like to prepare a series of VPBA and NEDM (or MNEM) co-grafted PPPE cloths by changing systematically compositions of monomers to obtain the optimized cloths with high capacities for xylose.

Reference

- 1) M. Igawa et al., Abst. Book 2009 West Japan Meeting Chem. Soc. Jpn. (2009) 70.

2-13 Recovery of Platinum from Waste of Silicon Rubber with Amine and Nuclear Acid Adsorbent Synthesized by Graft-Polymerization

Y. Kaneko^{a)}, A. Iwanade^{b)}, Y. Fukuta^{b)}, D. Nogami^{b)} and K. Watanabe^{b)}

^{a)} KALEIDO KIKAKU Co., Ltd.,

^{b)} Department of Advanced Radiation Technology, TARRI, JAEA

Fabric adsorbent having amine or adenine function was synthesized by radiation induced graft-polymerization. This adsorbent was applied to the recovery of Pt from silicon rubber waste. The silicon rubber waste was homogenized as a pretreatment. The obtained three layers were used for the Pt adsorption experiment. The adenine adsorbent recovered 6.9% of Pt in the waste solution.

付加反応型シリコンゴムの架橋構造を付加する製造工程において、白金が触媒として用いられている。この白金の一部はシリコンゴムに取り込まれ、シリコンゴムの切削屑等の廃棄物中に1 kgあたり20 mg含まれている。白金は市場価格が高く、この廃棄物からの白金の回収および再利用が望まれる。従来法による白金回収は、多段階のプロセスが必要であり、回収コストが高いという問題がある。そこで、回収コストを低減させるため、白金を含む溶液を調製し、この白金溶液からの吸着材を用いて白金を回収する方法を提案した。このような吸着材の作製に放射線グラフト重合法が利用できる。グラフト（接ぎ木）する高分子鎖に、白金に対するキレート形成能を付与すれば白金吸着材を作製できる。研究の目的は放射線グラフト重合法を利用して、シリコンゴム廃棄物溶液から白金を吸着・回収できる吸着材を作製することである。

本研究で作製した白金吸着材の作製経路を Fig. 1 に示す。グラフト重合の基材として、PE/PP 製不織布を採用した。また、アミノ基を有するモノマーとしてアリルアミンおよびアリルアミンと共重合させるモノマーとして N-ビニルアセトアミドを使用した（それぞれ、以下 AAm および NVA と略記する）¹⁾。まず、PE/PP 不織布に窒素雰囲気下で電子線を 200 kGy 照射した。次に、電子線を照射した PE/PP 不織布を窒素バブリングした AAm-NVA 水溶液（重量比、AAm : NVA : 水 = 1 : 1 : 2）に浸漬させ、50 °C、5 時間反応させた。グラフト重合反応前後の重量変化より、グラフト率を算出した。グラフト率の算出式を式 1 に示す。

$$(\text{グラフト率}) = 100 \left(\frac{\text{付与したグラフト鎖の重量}}{\text{基材不織布の重量}} \right) \quad \text{式 1}$$

得られたアミノ基を有する不織布を AAm-NVA 不織布と呼ぶ。次に、アデニン（以下 Ade と略記）を固定する 2 官能性モノマーとしてビニル基とエポキシ基を有するモノマーであるメタクリル酸グリシジル（以下、GMA と略記）を使用し、AAm-NVA 不織布の作製と同様の手順でグラフト重合をおこなった²⁾。まず、PE/PP 不織布に電子線を 10 kGy 照射した。次に、電子線を照射した PE/PP 不織布を窒素バブリングした GMA エマルジョン液（GMA : 5 wt%, Tween20 : 0.5 wt%）に浸漬させ、40 °C、3 時間反応させた。式 1 よりグラフト率を算出し、本検討ではグラフト率 190% のものを使用した。得られたエポキシ基を有する不織布を GMA 不織布と呼ぶ。得られた GMA 不織布を 0.1 M Ade/水-ジオキサン溶液（pH 13）に 80 °C、48 時間浸漬させ、エポキシから Ade 基へと転化した。転化反応前後の重量変化より、

Ade 基転化率を算出した。Ade 基の算出式を式 2 に示す。
(Ade 基転化率) = 100 (転化した Ade 基のモル数)

$$/ (\text{反応前のエポキシ基のモル数}) \quad \text{式 2}$$

得られた Ade 基を有する不織布を Ade 不織布と呼ぶ。本検討ではアデニン基転化率 32% (1.24 mmol/g) の Ade 不織布を以下の検討で用いた。

作製した白金吸着材の純水中における白金のバッチ吸着実験の結果を Fig. 2 に示す。親水性グラフト鎖を有する AAm-NVA 不織布の方が Ade 不織布よりも白金の吸着が早かった。一方、シリコンゴム溶媒とヘキサン抽出によるシリコン成分の分離を組合せて調整した白金溶液からの白金吸着の結果は、AAm-NVA 不織布は回収率が 0.65% であったのに対し、Ade 不織布は 6.9% であった。これは疎水性のエポキシ基が残存する Ade 不織布の方が、有機溶媒中での白金吸着に優れていることが示された。

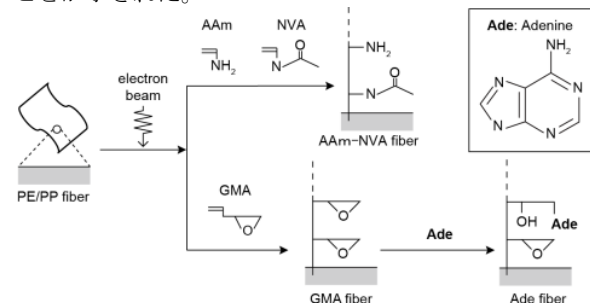


Fig. 1 Preparation scheme of platinum adsorbent.

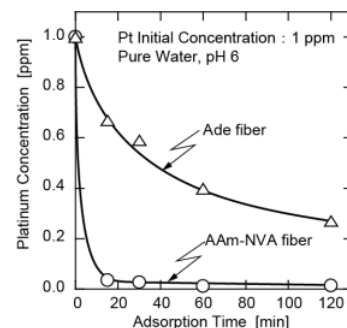


Fig. 2 Result of batch platinum adsorption experiment.

References

- 1) N. Seko et al., J. Ion Exchange. **18** (2007) 232-235.
- 2) T. Yoshikawa et al., J. Membr. Sci. **307** (2008) 82-87.

*本研究は先端研究施設共用促進事業「明日を創り暮らしを守る量子ビーム利用支援事業」の支援のもと行いました。

2-14 Preparation and Characterization of the Low Molecular Weight Funoran

S. Takigami^{a)}, H. Yamaguchi^{b)}, R. Takahashi^{b)} and N. Nagasawa^{c)}

^{a)} Center for Material Research by Instrumental Analysis, Gunma University,

^{b)} Graduate School of Engineering, Gunma University,

^{c)} Environment and Industrial Materials Research Division, QuBS, JAEA

Funoran is a main component of funori, which is a seaweed of the Rhodophyceae and is used as food products and a sizing agent. Funoran is one of sulphated polysaccharides and the main chain is consisted of a common backbone with a repeat of (1→3) - linked β - and (1→4) - linked α -Galactose (or its 3,6-anhydride) residues¹⁾. Recently, hair care agents containing funoran are put on the market. The molecular weight of original funoran measured is 800 kDa. If the molecular weight can reduce, the hair care effect of funoran should be increased.

In this study, γ -irradiation was used to prepare low molecular weight funoran and characterizations of the irradiated funoran were investigated.

Funoran was obtained from commercial funori aqueous solution by sedimentation using methanol. The γ -irradiation was carried out in vacuum. The absorbed dose was varied from 1 to 30 kGy and the dose rate was 1 kGy/h.

Molecular weight of irradiated funoran was determined by a multiangle laser light- scattering (MALS) method. SEC MALS chromatograms of the irradiated funoran are shown in Fig. 1. The chromatogram shifted to lower molecular weight and the width of peak enlarged with absorbed dose. The molecular weight was changed from 800 kDa to 121 kDa by the irradiation.

FT-IR and Raman spectra of irradiated funoran are shown in Fig. 2 and Fig. 3, respectively. As seen in Fig. 2, the irradiated funoran showed absorptions assigned to SO₂ symmetric stretching vibration (~ 1230 cm⁻¹) and anti-symmetry stretching vibration (~ 1065 cm⁻¹) together

with C-O-C anti-symmetry stretching vibration (~ 1160 cm⁻¹) of pyranose ring, regardless of absorbed dose. Similar trends were observed in Raman spectra. The sulfur content of irradiated funoran determined by the elemental analysis was hardly changed even at 30 kGy irradiation, no elimination of sulfate groups occurred by the γ -rays irradiation. Accordingly, it is inferred that the chemical structure of funoran scarcely changed by the γ -rays irradiation. Irradiation method is a useful method to prepare low molecular weight funoran.

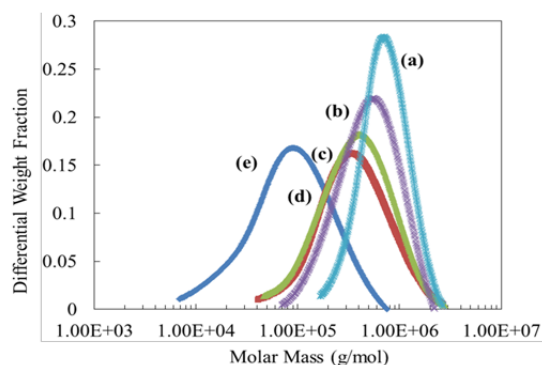


Fig. 1 Molecular weight distribution of irradiated funoran; (a) 0 kGy, (b) 1 kGy, (c) 5 kGy, (d) 10 kGy and (e) 30 kGy.

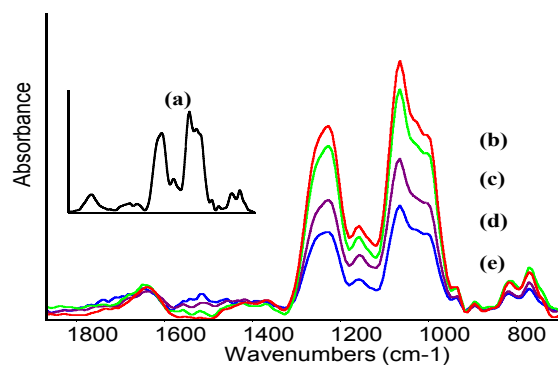


Fig. 2 FT-IR spectra of irradiated funoran; (a) 0 kGy, (b) 1 kGy, (c) 5 kGy, (d) 10 kGy and (e) 30 kGy.

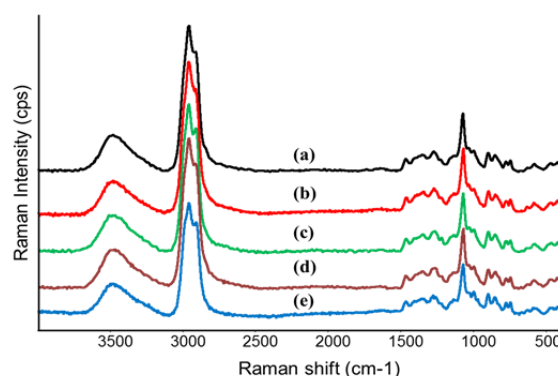


Fig. 3 Raman spectra of irradiated funoran; (a) 0 kGy, (b) 1 kGy, (c) 5 kGy, (d) 10 kGy, and (e) 30 kGy.

Reference

- 1) R. Takano et al., Carbohydr. Polym. **27** (1995) 305-311.

3. Medical and Biotechnological Application

3-01	Development of a Method for Estimating Degree of Dispersion of Lesions on DNA	63
	K. Akamatsu and N. Shikazono	
3-02	Mutagenic Effects of He Ion Particles in <i>Escherichia coli</i>	64
	T. Suzaka, H. Tauchi, N. Shikazono, K. Fujii and A. Yokoya	
3-03	Target Irradiation of Individual Cells Using Focusing Heavy-Ion Microbeam of JAEA-Takasaki (II).....	65
	T. Funayama, Y. Yokota, T. Sakashita and Y. Kobayashi	
3-04	Beam Profile Rapid-evaluation of Heavy-ion Microbeam in the Atmosphere Using Semi-automatic Image Analysis	66
	T. Sakashita, Y. Yokota, H. Kashiwagi, T. Satoh, T. Funayama and Y. Kobayashi	
3-05	Radiation-induced Bystander Cell-killing Effect Is Dependant on Time Following Irradiation and Independent of LET	67
	Y. Yokota, T. Funayama, Y. Mutou-Yoshihara, H. Ikeda and Y. Kobayashi	
3-06	Cell Motility of Human Non-Small-Cell Lung Cancer Cells after Carbon-Ion Beam Irradiation.....	68
	K. Murata, S. Noda, Y. Yoshida, T. Funayama, T. Takahashi, Y. Kobayashi and T. Nakano	
3-07	Biological Effects of Combining Temozolomide with Carbon Ions on Glioblastoma Cell Lines	69
	Y. Yoshida, S. Ishiuchi, T. Funayama, Y. Kobayashi and T. Nakano	
3-08	Mechanisms for the Contributions of Bystander Effects to the Responses Induced by Low Dose/Low Dose Rate Radiation	70
	H. Matsumoto, M. Hatashita, M. Tomita, K. Otsuka, M. Maeda, T. Funayama, T. Sakashita and Y. Kobayashi	
3-09	Analysis of Bystander Cell Signaling Pathway Activated by Heavy Ion-Microbeam II	71
	M. Tomita, H. Matsumoto, K. Otsuka, M. Maeda, T. Funayama, Y. Yokota, Y. Mutou T. Sakashita and Y. Kobayashi	
3-10	Ion-species Dependent Bystander Lethal Effect in Normal Human Fibroblasts Induced by C-, Ne- and Ar-ion Microbeams.....	72
	M. Suzuki, T. Funayama, Y. Yokota, Y. Mutou, H. Ikeda, C. H. Liu, Y. Kaneko, Y. Furusawa and Y. Kobayashi	
3-11	Analysis of Bystander Effect Induced by Cell Membrane Response in Glioma Cells	73
	S. Wada, A. Yoshikubo, A. Baden, T. Kakizaki, T. Funayama, T. Sakashita, Y. Kobayashi and N. Ito	

3-12	Expression of Glutathione Peroxidase, p53, Bcl-2, and BAX Genes in Gamma-Irradiated Human Retinal Vascular Endothelial Cells	74
	K. Akeo, T. Funayama, Y. Kobayashi and Y. Akeo	
3-13	Bystander Effect of Carbon Ion Beam-Induced Senescent Glioma Cells on Infectivity of Human Immunodeficiency Virus Type 1 (HIV-1).....	75
	A. Oue, N. Shimizu, A. Tanaka, T. Mori, A. S. Hoque, S. Islam, T. Funayama, Y. Kobayashi and H. Hoshino	
3-14	Insect Cell Could Restart the Cell Cycle before Sufficient Repair of the DNA Damage by Heavy-ion Irradiation	76
	K. Shirai, K. Fukamoto, S. Kobayashi, K. Kiguchi, T. Funayama, T. Sakashita, Y. Yokota and Y. Kobayashi	
3-15	Comparison of Histological Responses in Medaka Testis after Heavy-Ion Broad- and Micro-Beam Irradiation	77
	S. Oda, T. Yasuda, Y. Urushihara, T. Funayama, Y. Kobayashi and H. Mitani	
3-16	Anhydrobiosis-Specific Genes in the Sleeping Chironomid Are also Responsive to Ionizing Radiation	78
	O. Gusev, T. Kikawada, T. Sakashita, T. Funayama, Y. Kobayashi and T. Okuda	
3-17	Cytokine Production is Suppressed in Human THP-1 Macrophages by Direct Stimulation with Heavy-ions and Bystander Responses Due to Microbeam Irradiation of a Limited Cell Population	79
	Y. Mutou-Yoshihara, T. Funayama, Y. Yokota, H. Ikeda, T. Sakashita, M. Suzuki and Y. Kobayashi	
3-18	Effects of Carbon-ion Irradiation on Locomotion and Pharyngeal Pumping in <i>Caenorhabditis elegans</i>	80
	M. Suzuki, T. Sakashita, Y. Hattori, T. Funayama, Y. Yokota, Y. Mutou-Yoshihara, T. Tsuji and Y. Kobayashi	
3-19	Relaxation Behaviors of Electron Spin in Irradiated Fresh Papayas	81
	M. Kikuchi, T. Sakashita, T. Funayama, M. Ukai, Y. Shimoyama and Y. Kobayashi	
3-20	Initial Decay Process of Radicals Induced in Irradiated Food	82
	Y. Kaimori, Y. Sakamoto, M. Kikuchi, Y. Kobayashi and M. Ukai	
3-21	Improvement of Spatial Resolution of PIXE-CT Using ML-EM Algorithm in TIARA	83
	T. Satoh, M. Koka, W. Kada, A. Yokoyama, T. Ohkubo, A. Yamazaki, Y. Ishii and T. Kamiya	
3-22	The Effects of Essence of Chicken on the Trace Metal Distribution in Stressful Mice Brain Slices by In-Air Micro-PIXE.....	84
	E. Sakurai, K. Yanai, K. Ishii, K. Fujiki, S. Hiraishi, H. Yamazaki, S. Matsuyama, N. Okamura, A. Yokoyama, W. Kada, M. Koka, T. Satoh and T. Kamiya	

3-23	Measurement of Fluorine Distribution in Carious Enamel around 1.5-year Aged Fluoride-containing Materials	85
	H. Komatsu, K. Kojima, Y. Funato, Y. Matsuda, T. Kijimura, K. Okuyama, H. Yamamoto, Y. Iwami, S. Ebisu, M. Nomachi, K. Yasuda, T. Satoh and M. Koka	
3-24	The Analysis of Boron Micro-Distribution in 9L Gliosarmoma Cells and HUVEC cells Using PIXE and PIGE.....	86
	K. Endo, Y. Shibata, T. Yamamoto, K. Nakai, A. Matsumura, T. Satoh, A. Yokoyama, M. Koka, T. Ohkubo, A. Yamazaki, Y. Ishii, T. Kamiya and K. Ishii	
3-25	Analysis on the Co-localization of Asbestos Bodies and Fas or CD163 expression in Asbestos Lung Tissue by In-Air Micro-PIXE	87
	K. Dobashi, Y. Shimizu, S. Matsuzaki, T. Nagamine, T. Satoh, T. Ohkubo, A. Yokoyama, Y. Ishii, T. Kamiya, K. Arakawa, M. Utsugi, T. Ishizuka and M. Mori	
3-26	Analysis of Trace Elements in Erythrocytes Obtained from Dialysis Patients Using In-Air Micro PIXE	88
	H. Kikuchi, T. Nagamine, Y. Tokita, T. Satoh and T. Kamiya	
3-27	Increased Antitumor Effect of Chemotherapy, Using Radiosensitive Microcapsules Containing Anti-RLIP076	89
	S. Harada, S. Ehara K. Ishii, T. Satoh, S. Yamazaki, N. Matsuyama and T. Kamiya	
3-28	Elemental Mapping and Estimation of Elemental Abundances of Lichen by TIARA Micro Beam PIXE	90
	Y. Iwata, K. Ishii, T. Kamiya and T. Satoh	
3-29	Preparation and Biological Evaluation of 3-[⁷⁶ Br]Bromo- α -methyl-L-tyrosine, a Novel Tyrosine Analog for PET Imaging of Tumors.....	91
	Y. Ohshima, H. Hanaoka, Sh. Watanabe, Y. Sugo, Sa. Watanabe, H. Tominaga, N. Oriuchi, K. Endo and N. S. Ishioka	
3-30	Production of Radioactive Bromine Br-76	92
	Sa. Watanabe, Sh. Watanabe, Y. Iida, H. Hanaoka, K. Endo and N. S. Ishioka	
3-31	Carbon Kinetic Analysis in a Soybean Plant by Using Newly Developed Real-time Whole-plant Imaging Method with Positron-Emitting Tracer Imaging System (PETIS)	93
	N. Kawachi, N. Suzui, S. Ishii, H. Yamazaki, A. H. Iwasaki, K. Ogawa and S. Fujimaki	
3-32	Quantitative Study for Nitrogen Fixation in Intact Soybean Plant from PETIS Imaging	94
	S. Ishii, N. Suzui, N. Kawachi, H. Yamazaki, N. Ohtake, T. Ohyama and S. Fujimaki	

3-33	Dose Optimization of ^{107}Cd for Direct Imaging of Cd Uptake from Culture to Root	95
	N. Suzui, N. Kawachi, S. Ishii, H. Yamazaki and S. Fujimaki	
3-34	Comparison of ^{107}Cd Absorption and Accumulation between Transgenic Tobacco Plants and Control Plants	96
	S. Nakamura, N. Suzui, S. Ishii, N. Kawachi, N.S. Ishioka, H. Rai, H. Hattori, M. Chino and S. Fujimaki	
3-35	Effects of Preceding Light Conditions on Translocation of Photoassimilates from a Leaf into a Fruit	97
	K. Kikuchi, S. Ishii, N. Kawachi, N. Suzui, H. Yamazaki and S. Fujimaki	
3-36	Analysis of Source-sink Regulation System Using Cold-girdling and Positron-Emitting Tracer Imaging System (PETIS)	98
	H. Yamazaki, N. Suzui, N. Kawachi, S. Ishii, H. Shimada and S. Fujimaki	
3-37	Genetic Interaction between COP9 Signalosome and SMAP1 That Function in the 2,4-D Response in Arabidopsis	99
	Y. Oono and I. Narumi	
3-38	Development of Ion Beam Breeding Technology in Plants and Creation of Useful Plant Resources	100
	Y. Hase, S. Nozawa, T. Okada, I. Asami, T. Nagatani, Y. Matsuo, A. Kanazawa, K. Honda and I. Narumi	
3-39	Ion Beam Irradiation on Rice Seeds for the Mutation Breeding Project of the Forum for Nuclear Cooperation in Asia (FNCA)	101
	A. Tanaka, S. Nozawa, Y. Hase, I. Narumi, H. Ishikawa and A. Koike	
3-40	Characterization of Ion Beam Irradiated Chrysanthemum Plants	102
	S. Shakinah, A. Zaiton, A. H. Affrida, S. Nozawa, I. Narumi, Y. Hase and Y. Oono	
3-41	Mutational Effects of Carbon Ions near Range End in Arabidopsis	103
	Y. Hase, R. Yoshihara, S. Nozawa and I. Narumi	
3-42	Analysis of Mutated Region on DNA in Ion Beam-Induced UVB Tolerant or Sensitive Rice Mutant	104
	N. Takano, Y. Takahashi, M. Yamamoto, M. Teranishi, Y. Hase, A. N. Sakamoto, A. Tanaka and J. Hidema	
3-43	Stability Evaluation of Mutant Lines Induced by Ion Beam Breeding in Petunia	105
	M. Okamura, Y. Hase, N. Onishi, I. Narumi and A. Tanaka	
3-44	Lethal Effects of Different LET Radiations in Gene Disruptant Strain of <i>Deinococcus radiodurans</i>	106
	K. Satoh, K. Tejima, T. Onodera and I. Narumi	
3-45	Involvement of Universal Conserved Genes, <i>ygiD</i> and <i>yeaZ</i> Orthologs, in DNA Repair of <i>Deinococcus radiodurans</i>	107
	T. Onodera, K. Satoh, I. Narumi and T. Ohta	

3-46	Fundamental Study on Molecular Mechanism Underlying Repair of Heavy-Ion Induced DNA Damage in the <i>Saccharomyces cerevisiae</i>	108
	Y. Matuo, Y. Izumi, Y. Hase, A. Sakamoto, S. Nozawa, I. Narumi and K. Shimizu	
3-47	Characteristics of Mutant Endophytic Bacteria Strains Improved Using Ion beams	109
	M. Aino, K. Matsuura, K. Satoh and I. Narumi	
3-48	Colony Morphology of High Temperature Tolerant Mutants of <i>Bradyrhizobium japonicum</i> USDA110 Obtained by Ion-beam Microbial Mutation-breeding Technology	110
	K. Takeda, K. Tejima, K. Satoh, I. Narumi and T. Yokoyama	
3-49	Repeated FACS-based Screening for Yeast Strain Highly Expressing Cellulase	111
	K. Ninomiya, H. Soda, K. Satoh, I. Narumi and N. Shimizu	
3-50	Fungicide Tolerant Mutation of Entomopathogenic Fungi Induced by Carbon Ion Beams	112
	T. Saito, S. Shinohara, K. Satoh and I. Narumi	
3-51	Ion Beam Breeding of “Sake Yeast” and Test Brewing - the Second Report ...	113
	T. Masubuchi, O. Kamiyama, K. Satoh, Y. Hase and I. Narumi	
3-52	The Long-term Storage of Rhizobial Biofertilizer Made from γ -sterilized Carriers	114
	K. Tejima, T. Yokoyama, K. Satoh and I. Narumi	

This is a blank page.

3-1 Development of a Method for Estimating Degree of Dispersion of Lesions on DNA

K. Akamatsu and N. Shikazono

Life Science and Biotechnology Division, QuBS, JAEA

1. Introduction

It is known that DNA lesions induced by ionizing radiation and chemicals can cause mutation and carcinogenesis. In particular, ‘clustered damage’ site, that is a DNA region with multiple lesions within one or two helical turns, is believed to be hardly repaired. This damage is considered to be induced, e.g., around high-LET ionizing radiation tracks. However, detail of the damage is not known. So, we have developed a method for estimating degree of dispersion of distances between DNA lesions using fluorescence resonance energy transfer (FRET). At first, complementary two 31-mer single-strand DNA with an apurinic(AP)-site at each center nucleotide were synthesized to obtain relationship between FRET efficiency and AP-site-AP-site distance. One DNA strand with an AP-site was labeled with a donor fluorescent probe at the lesion, and the other strand was done with an acceptor one. Fluorescence intensity from acceptor clearly increased with proceeding the annealing. Donor- acceptor distance calculated from FRET efficiency obtained was 4 nm, which was reasonable with the estimated one taking the diameter of B-form DNA duplex (2 nm) and length of each probe (~ 1 nm) into account. Now we have tried to apply the FRET method to plasmid DNA irradiated with $^4\text{He}^{2+}$ and ^{60}Co γ -rays.

2. Experiments

Sample preparation and He beam irradiation

Linear formed pUC19 plasmid DNA digested by Sma I was used. The DNA aqueous solution was mounted on a glass plate and dried thoroughly in vacuum. The plate was irradiated with ~ 72 keV/ μm of $^4\text{He}^{2+}$ beam (3 MV tandem), which was controlled using a depth-tunable cell irradiation equipment¹⁾ at room temperature. The irradiated DNA samples were recovered by water at 0 °C. The aqueous solutions were lyophilized and kept at -20 °C until use.

Preparation of fluorophore-labeled irradiated DNA and the fluorescence spectroscopy for FRET observation

Ten micrograms of the irradiated DNA (10 μL in water) and 10 μL of 100 mM HEPES-NaOH (pH 7) were mixed in a microtube. Two microliters of a mixture containing AP-site-reactive Alexafluor350(AF350) (donor) and AF488 (acceptor) (1:1) was added to the DNA solution and was incubated overnight at 37 °C. The fluorophore-labeled DNA was purified by ethanol precipitation. Twenty microliters of water was added to the residue immediately after removal of the supernatant. Twenty microliters of the purified labeled DNA sample was added to a micro quartz

cell containing 180 μL of 100 mM TrisHCl with 10 mM MgCl_2 (pH 8). The fluorescence spectrum was measured (ex.347 nm). After the measurement DNA digesting enzyme cocktail was added to the solution, and it was incubated for 1 h at 37 °C. The spectrum of the enzyme-treated sample was also measured.

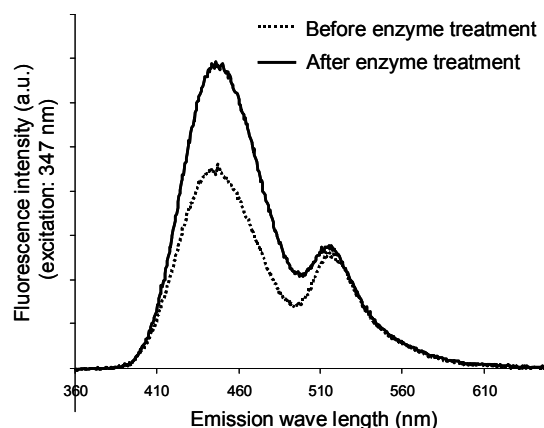


Fig. 1 An example of fluorescence spectral change of AF350/AF488-labeled He-irradiated DNA (126.5 kGy) before /after enzyme treatment.

3. Results and Discussion

Emission at 449 nm from the excited donor was clearly eliminated by enzymatic digestion of the labeled DNA (Fig. 1). The FRET efficiency calculated: E was 0.21. The value means that ~20% of the energy in the excited donor is transferred to the acceptor ones. Thus, relationship between AP-site density (or dose): D and E value would be important for estimating degree of dispersion of AP-sites on DNA. The E value, however, significantly changes as a function of a labeling ratio: $\delta = \text{AF350/AF488}$. Ultimately, these three parameters: D , E , and δ are to be considered for the estimation. We are now constructing a theoretical curve (δ versus E) and doing more experiments considering the three parameters using ^{60}Co - γ ray, X-ray, $^4\text{He}^{2+}$ - ion beam irradiated, and heat treated (pH 5, 70 °C) DNA.

4. Acknowledgments

We would like to gratefully thank Dr. Y. Sugo for operating the TC line, and also thank Drs. M. Kikuchi and Y. Kobayashi for ^{60}Co γ -ray irradiation experiments.

Reference

- 1) A. Tanaka et al., Nucl. Instrum. Meth. Phys. Res. **B129** (1997) 42.

3-2 Mutagenic Effects of He Ion Particles in *Escherichia coli*

T. Suzaka^{a,b)}, H. Tauchi^{a)}, N. Shikazono^{b)}, K. Fujii^{c)} and A. Yokoya^{c)}

^{a)} Department of Environmental Sciences, Faculty of Science, Ibaraki University, ^{b)} Life Science and Biotechnology Division, QuBS, JAEA, ^{c)} Advanced Science Research Center, JAEA

Non-DSB type of clustered damage is induced by ionizing radiation and is proposed to cause deleterious effects to cells¹⁾. Their yields and configurations likely depend on the radiation qualities, such as particle energy or ionization density along the particle track characterized by LET (linear energy transfer)^{1,2)}. To date, the biological consequences of radiation of both low and high LETs have been extensively studied in various organisms, including bacteria, yeasts, higher plants, and mammalian cells. It is, however, still not clear how and to what extent the damage is induced, processed in the cell, and thus related to biological consequences especially to mutation. In this project, we aim to find out the significance of clustering of DNA damage in mutagenesis. Here, we present the results of *lacI* mutation assay of wild type cells after irradiation of soft X-rays and He ion particles with different LETs.

The cells of CSH100 (wild type *E. coli*) were incubated in 0.2 % glucose minimal medium at 37 °C unless otherwise stated. Cells ($2-3 \times 10^8$) were filtered through a nitrocellulose membrane of a diameter of 1.3 cm. To prevent cells from drying, the membrane was placed on a filter paper pre-wetted with 300 μ L of 0.15 M NaCl solution with 20 % glycerol. Subsequently, the membrane was placed on 0.15 M NaCl agar in a Petri dish, and then the dish was covered with a polyimide film (Kapton film, 7.5 μ m thickness). Cells were irradiated with soft X-rays (tungsten target, tube voltage 150 KV, tube current 6 mA) at a dose rate of 0.47 Gy/sec, and He ion particles at dose rates of 1~4 Gy/sec. The LETs of He ions were altered by placing a Ni foil in front of the sample. The LET values were calculated by the ELOSSM code. After irradiation, cells were plated and incubated overnight to determine the fraction of survived cells and the mutation frequency. In this study, the mutation frequency of *lacI* gene was measured. Mutations in the *lacI* gene enable the cells to grow on a medium with phenyl- β -D-galactopyranoside (P-gal) as the only carbon source³⁾. In determining the mutation frequency, irradiated cells were initially propagated in 0.2% glucose minimal medium at 37 °C for 16 hours to fix mutations. Subsequently, cells were plated on a 0.2 % P-gal minimal medium, and were incubated at 37 °C for 40 hours. The mutation frequency was determined by dividing the number of colonies on the P-gal plate by that on the glucose plate.

Lethal and mutagenic effects of radiations with different qualities were assessed from dose response curves. Lethal effects of soft X-rays and He ion particles at LETs of 18 and 89 keV/ μ m did not show significant differences, indicating that the lethality of *E. coli* is largely independent on the LET

(data not shown). The result suggests that the amount of unreparable lethal damage is similar after irradiation of different qualities of radiation in wild type *E. coli* cells. However, dose response curve of mutation induction after He ion-irradiation with an LET of 89 keV/ μ m differed significantly to those after soft X-rays and He ions with an LET of 18 keV/ μ m (Fig. 1). Surprisingly, the radiation with the highest LET gave the lowest mutation frequencies at doses above 200 Gy. Of note, the mutation frequencies increased and then clearly leveled off with increasing dose for radiations such as soft X-rays and He ions (18 keV/ μ m). The amount of dose to show the leveling off seemed to be around 500 Gy for both types of radiation (Fig. 1). We do not have a clear explanation for these dose responses of mutation induction in *E. coli* at present. Studies on mutation induction in glycosylase mutants (*fpg* and *mutY*) are now underway.

References

- 1) N. Shikazono et al., J. Radiat. Res. 50 (2009) 27.
- 2) H. Nikjoo et al., Radiat. Res. 156 (2001) 577.
- 3) J. H. Miller, A Short Course in Bacterial Genetics, Cold Spring Harbor Laboratory Press (1992) 131.

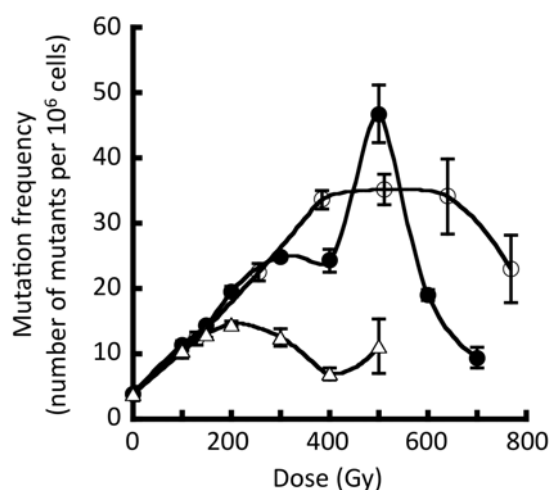


Fig. 1 Mutation frequencies of the *lacI* gene in wild type *E. coli* (CSH100). Cells were exposed to soft X-rays (○), He ions with an LET of 18 keV/ μ m (●), and 89 keV/ μ m (Δ).

3-3 Target Irradiation of Individual Cells Using Focusing Heavy-Ion Microbeam of JAEA-Takasaki (II)

T. Funayama, Y. Yokota, T. Sakashita and Y. Kobayashi

Life Science and Biotechnology Division, QuBS, JAEA

Heavy-ion irradiation has been employed in a wide range of biological applications, including heavy-ion radiotherapy and radiation breeding, because of its high and unique biological effectiveness. However, to advance these useful applications, the elucidation of mechanisms underlying biological response of heavy-ion radiation is necessary. Microbeam irradiation, which target and irradiate individual cells using beam spot smaller than cell size, is a useful means to investigate the mechanism of heavy-ion radiation action. Therefore, we had developed the heavy-ion collimating microbeam system, and utilized for analyzing biological effects of heavy-ion¹⁾. However, there is a difficulty in generating finer beam that is capable for carrying out precise subcellular irradiation by collimating system. Thus we developed a new focusing heavy-ion microbeam system.

To irradiate finer beam of focusing heavy-ion microbeam system to the specific region of individual cells, a cell targeting system was designed and installed under the vacuum window of the beam line. The system consists of a full-automatic inverted microscope and the set of automatic stages. A high-sensitivity CCD camera is installed on a bottom camera port of the microscope to clearly detect weak luminescence of scintillator and fluorescent-stained target cells. A solid state detector is installed on an objective revolver of the microscope to detect ions irradiated on the sample. To avoid vibration for targeting samples precisely, the system was installed on a mounting frame that rigidly fixed to and hanged on the magnetic lens frame.

Using developed system, an irradiation of HeLa cells was carried out. To detect cell position under fluorescent microscopy, cytoplasm of cells were stained with fluorescent vital staining dye, CellTracker Orange, and inoculated on a film of ion track detector. The coordinates of cell position were extracted using image analysis code, which was optimized for detection of CellTracker stained HeLa cells. The cells were, thereafter, targeted and irradiated with focusing neon ion beam. After irradiation, the tracks of traversed ion and foci of γ H2AX were visualized, and the hit positions of ion were confirmed. The ions were well focused and hit on cells precisely and the positions of the γ H2AX focus were well in accord with the position of ion hit (Fig. 1). From the result, we concluded that our system can target and irradiate individual cultured cells by focusing heavy-ion microbeam.

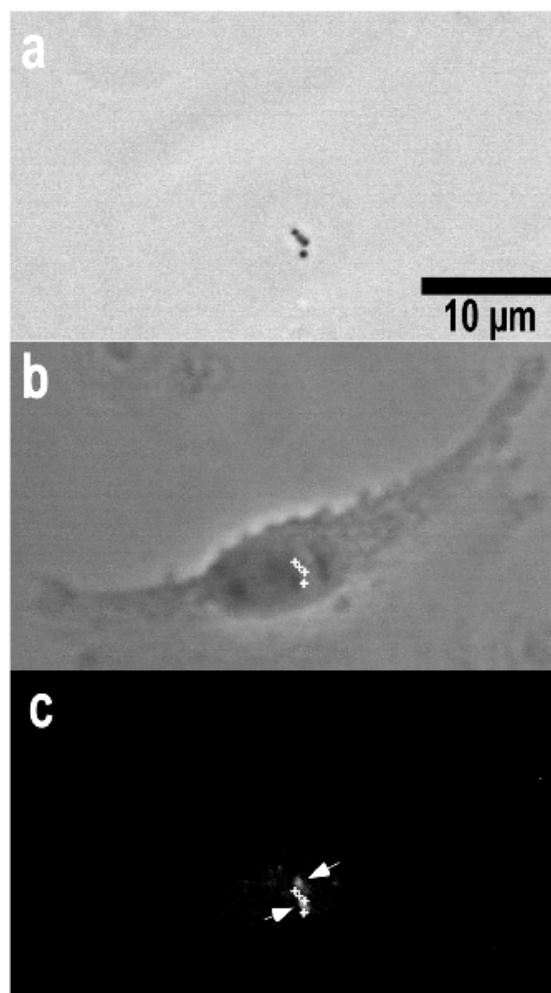


Fig. 1 Irradiation of HeLa cells using focusing heavy-ion microbeam. The cells were irradiated with focusing neon ion microbeam, thereafter the positions of ion hit and foci of γ H2AX were visualized. (a) Ion hit position visualized as etch pits. (b) An image of targeted cell observed by phase contrast microscopy. Cross marks indicates ion hit position. (c) Fluorescent image of immunostained cells using anti- γ H2AX monoclonal antibody. Cross marks indicates ion hit position, and arrow indicates γ H2AX foci.

Reference

- 1) Funayama et al., J. Radiat. Res., 49 (2008) 71-82.

3-4 Beam Profile Rapid-evaluation of Heavy-ion Microbeam in the Atmosphere Using Semi-automatic Image Analysis

T. Sakashita^{a)}, Y. Yokota^{a)}, H. Kashiwagi^{b)}, T. Satoh^{b)},
T. Funayama^{a)} and Y. Kobayashi^{a)}

^{a)}Life Science and Biotechnology Division, QuBS, JAEA,

^{b)}Department of Advanced Radiation Technology, JAEA

Introduction

Focusing heavy-ion microbeam is needed for radiation biology, because the finer beam can target subcellular organera or a specific-part in small organism, e.g. nematode. Thus, we have developed the focusing microbeam. However, beam profile evaluation had been carried out by manually processing microscopic observation and calculation in the excel sheet, and it took about 30 minutes for only 1 photograph analysis with an etch-pit matrix. One etch-pit matrix has 5 by 5 grid points (Fig. 1). In the future application process, at least three matrixes will be involved. Beam experimental time assigned for each user is several hours, and “shortening of a preparation time”, which includes a beam profile evaluation, is strongly needed. Therefore, we developed the rapid evaluation method of heavy-ion microbeam profile in the atmosphere, using a new semi-automatic image analysis system. The reduction of the operation time for evaluating the beam profile was achieved by the present system¹⁾. Also, the beam-profile was simulated by the SRIM software²⁾. These facts made it sure that this present method was worth enough for the rapid-evaluation of heavy-ion microbeam.

Semi-automatic image analysis

We used the Image J³⁾ software for the analysis of the etch-pit matrix. The sequence of the image analysis is as follows; (1) discrimination of etch pits and remove dusts, (2) acquisition of positions of etch pits, and (3) evaluation of the beam profile using FWHM (a full width at half maximum). All processes of this sequence were done by the Java program, and the program was added to Image J as a plug-in program. To calculate the FWHM from the 5 by 5 matrix, we used the Oikawa’s method⁴⁾. Final positions of etch pits is shown in Fig. 2. The present method made the operation time shortening (about 1 minute).

Heavy-ion microbeam profile in the atmosphere

The beam profile of the 13 MeV/n Ne-ion microbeam was evaluated in the atmosphere, which ranges from 1 mm to 4 mm distance from the beam window (Fig. 3). FWHM of heavy ion microbeam changed from 4 μm to 8 μm in the present atmospheric range. Also, we tried to simulate the beam profile using the software for the stopping and range of ions in matter (SRIM)⁴⁾. Observed beam profile was consistent with that of the simulated one (Fig. 3). In conclusion, we have succeeded in the beam profile rapid-evaluation of heavy-ion microbeam in the atmosphere using semi-automatic image analysis.

References

- 1) T. Sakashita et al., RADIOISOTOPES 60 (2011) 47.
- 2) <http://www.srim.org/>.
- 3) <http://imagej.nih.gov/ij/index.html>.
- 4) M. Oikawa et al., Nucl. Instrum. Meth. Phys. Res. B 260 (2007) 85.

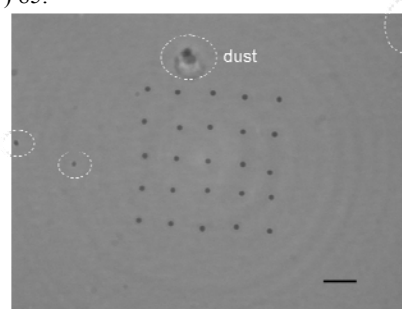


Fig. 1 Matrix (5 by 5) of etch pits at intervals of 20 μm . The scale bar is 20 μm , and a dashed circle indicates a dust of the microscope.

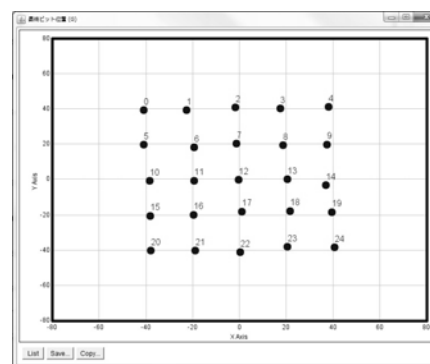


Fig. 2 Distribution of etch pits after semi-automatic image analysis.

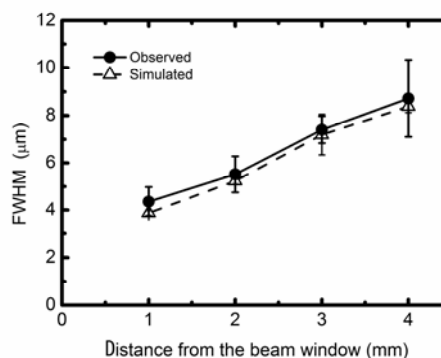


Fig. 3 Observed and simulated beam profiles in the atmosphere. FWHM is a full width at half maximum. Error bars indicate a standard deviation.

3-5 Radiation-induced Bystander Cell-killing Effect Is Dependant on Time Following Irradiation and Independent of LET

Y. Yokota, T. Funayama, Y. Mutou-Yoshihara, H. Ikeda and Y. Kobayashi

Life Science and Biotechnology Division, QuBS, JAEA

A large part of biological effects of low dose/low dose-rate radiation are still unclear. Radiation-induced bystander effect is one of them and manifests various effects in non-irradiated cells which have been near by irradiated cells¹⁾. Therefore, bystander effect may elevate the risk of exposure to low dose/low dose-rate radiation. In the present study, we irradiated normal human cultured cells with ionizing radiation having different LET to investigate bystander cell-killing effect.

WI-38 normal human diploid fibroblasts were used here. For microbeam irradiation, cells were confluent-cultured in the microbeam irradiation vessels²⁾ and 25 sites were irradiated with 10 particles each of carbon (18.3 MeV/u, LET = 103 keV/μm) or neon (13.0 MeV/u, LET = 380 keV/μm) ions. The diameter of microaperture used here was 20 μm. The percentage of irradiated cells in cell population was calculated to be from 0.005% to 0.05%. Irradiated cells and non-irradiated cells were cultured for 6 and 24 h following irradiation (Fig. 1). Both of them were retrieved, counted and then reseeded for a conventional colony formation assay. For γ-ray irradiation, cells were confluent-cultured in cell culture inserts and companion plates (BD Biosciences, NJ, USA) for co-culture. Only cells cultured in the inserts were irradiated with ⁶⁰Co γ-rays (LET=0.2 keV/μm). Non-irradiated cells cultured in the companion plates were co-cultured with irradiated cells for 6

and 24 h following irradiation (Fig. 1). During co-culture, irradiated cells and non-irradiated cells shared medium through the membrane base of the insert. Only non-irradiated cells were retrieved, counted and then reseeded for a conventional colony formation assay.

For carbon- and neon-ion microbeam irradiation, survival rate of irradiated and non-irradiated cells did not change at 6 h but decreased at 24 h following irradiation (Fig. 2). Although the percentage of irradiated cells in cell population was from 0.005% to 0.05%, the survival rate decreased to 90% of control cells. From this result, they are suggested that radiation-induced bystander effect leads a part of non-irradiated cells to reproductive death and that it is dependent on time following irradiation.

For γ-ray irradiation, survival rate of non-irradiated cells did not change at 6 h but decreased at 24 h following irradiation (Fig. 2). This result is similar to the result of heavy-ion microbeam irradiation experiments. Taking together these results, it is suggested that radiation-induced bystander cell-killing effect is independent of LET. This is quite different from direct hit effects of radiation, which are well known to be dependent on LET.

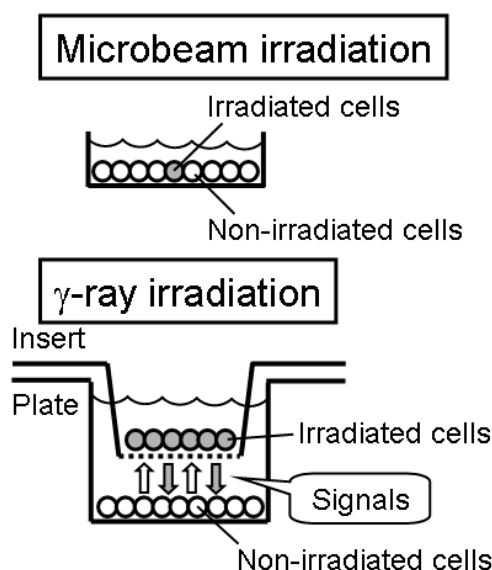


Fig. 1 Experimental design of co-culture between irradiated cells and non-irradiated cells.

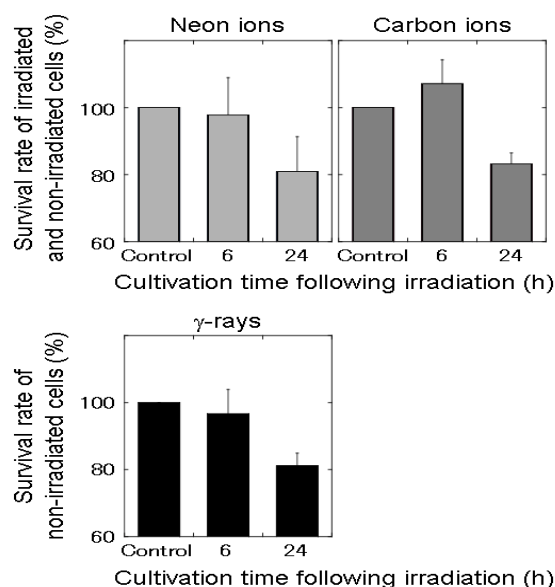


Fig. 2 Radiation-induced bystander cell-killing effect. Control means non-irradiated and non-bystander cells. Data are means ± SEs of 3-5 independent experiments.

Reference

- 1) W. F. Morgan, Radiat. Res. 159 (2003) 567-580.

3-6 Cell Motility of Human Non-Small-Cell Lung Cancer Cells after Carbon-Ion Beam Irradiation

K. Murata^{a)}, S. Noda^{a)}, Y. Yoshida^{b)}, T. Funayama^{c)}, T. Takahashi^{d)},
Y. Kobayashi^{c)} and T. Nakano^{a),b)}

^{a)} Department of Radiation Oncology, Gunma University, ^{b)} Gunma University Heavy Ion Medical Center, ^{c)} Life Science and Biotechnology Division, QuBS, JAEA,
^{d)} Department of Radiation Oncology, Saitama Medical Center

Non-small cell lung cancer (NSCLC) is one of the most lethal types of cancer. Recent reports suggest that increased ability of tumor cells to migrate is associated with an increased rate of local failure after radiotherapy¹⁾. Carbon ion radiation therapy has recently been a focus of interest especially in Japan as an effective modality to treat radioresistant tumors. However, the effects of carbon ion beams on cells migration (cell motility) are not fully investigated. The purpose of this study was to investigate the effect of X-rays and carbon-ion beams on the motility of human NSCLC cells *in vitro*.

The cell motility was measured using a wound-healing assay. A549 (human NCSLC cell) cells were seeded at a high density on 35 mm culture plates. After 24 hours, wounds were formed by scraping through the cell monolayer with a sterile micropipette tip, and the tumor cells were irradiated with carbon-ion beams (0 Gy, 2 Gy, 8 Gy) or X-rays (0 Gy, 2 Gy, 8 Gy) with or without Y-27632 (a specific Rho-associated coiled coil forming protein kinase (ROCK) inhibitor). Images of the microscope were taken to observe cell migration across the wounds at intervals of 12 hours. Then, Western blot analysis was conducted to quantify phosphorylated myosin light chain (MLC) protein, which is phosphorylated by ROCK in the down stream of Rho family protein signal pathway. Survival of A549 was evaluated by the clonogenic assay.

In the wound-healing assay using A549 cells, the migrating distances significantly increased after the irradiation with 2 Gy and 8 Gy of X-ray ($531 \pm 24 \mu\text{m}$, $601 \pm 17 \mu\text{m}$, $637 \pm 38 \mu\text{m}$ after 0 Gy, 2 Gy, 8 Gy of X-ray irradiation, respectively). The migrating distances significantly increased after the irradiation with carbon-ion beams ($534 \pm 47 \mu\text{m}$, $640 \pm 43 \mu\text{m}$, $712 \pm 56 \mu\text{m}$ after 0 Gy, 2 Gy, 8 Gy of carbon-ion irradiation, respectively)(Fig. 1). In Western blot analysis, the quantity of phosphorylated MLC increased in A549 cells after irradiation with X-rays and carbon-ion beams. Y-27632 decreased the migrating distances in the cells irradiated with X-rays ($450 \pm 28 \mu\text{m}$, $431 \pm 52 \mu\text{m}$, $485 \pm 48 \mu\text{m}$, after 0 Gy, 2 Gy, 8 Gy of X-ray irradiation with Y-27632, respectively) or with carbon-ion beams ($504 \pm 37 \mu\text{m}$, $540 \pm 28 \mu\text{m}$, $552 \pm 35 \mu\text{m}$ after 0 Gy, 2 Gy, 8 Gy of carbon-ion irradiation with Y-27632, respectively) (Fig. 2).

Irradiation with X-rays or carbon-ion beams significantly enhanced the cell motility and activated Rho family proteins in A549 cells. Increased amount of phosphorylated MLC and the ability of Y-27632 to reverse the increased motility in the irradiated cells suggest that the activity of ROCK is involved in the increased motility in irradiated cells.

Reference

1) D. B. Hieh et al., Cancer 85 (1999) 47-57.

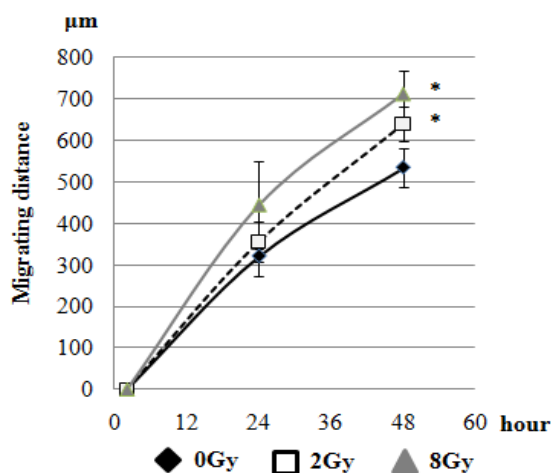


Fig. 1 The migrating distances significantly increased after the 2 Gy and 8 Gy irradiation with carbon-ion beams. The motility of A549 cells increased with irradiation in a dose-dependent manner.

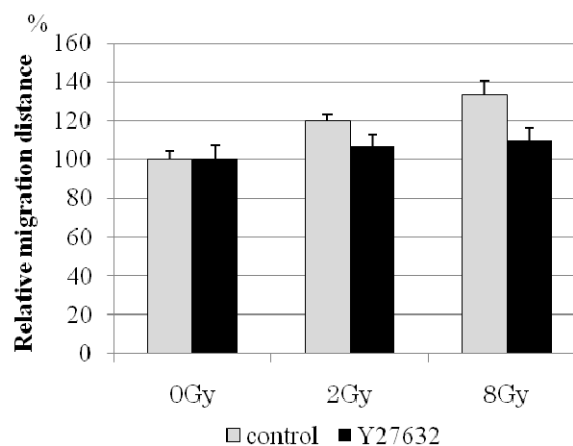


Fig. 2 Effect of Y27632 on cell migration. Y-27632 decreased the migrating distances in the cells irradiated with carbon-ion beams.

3-7 Biological Effects of Combining Temozolomide with Carbon Ions on Glioblastoma Cell Lines

Y. Yoshida^{a)}, S. Ishiuchi^{b)}, T. Funayama^{c)}, Y. Kobayashi^{c)} and T. Nakano^{a)}

^{a)} Gunma University Heavy Ion Medical Center, ^{b)} University of the Ryukyus Faculty of Medicine, ^{c)} Life Science and Biotechnology Division, QuBS, JAEA

Glioblastoma (GBM) is one of the most common and the most malignant tumors occurring in the central nervous system. GBM is notorious for high growth and invasive behavior and makes the surgical intervention ineffective. Recently, though there are many reports about the effectiveness of carbon ion therapy, little is known about effects of carbon ion therapy for GBM. In addition, almost all of GBM patients has not satisfied with treatment of the carbon ion alone for GBM.

Temozolomide (TMZ) is a cytotoxic alkylating agent which has shown an activity in the recurrent anaplastic glioma and GBM. Combining TMZ with radiotherapy has been reported to improve outcome compared with radiation alone, and this treatment is currently considered as the standard treatment for GBM. Hence, in this study, we investigated the effectiveness of combining TMZ with carbon ion therapy for GBM.

【目的】難治性腫瘍の一つである神経膠芽腫は遊走・浸潤性が非常に高いことから正常な脳細胞との境界が不鮮明であり、手術により腫瘍を全摘出することが困難である。また、X線や抗がん剤に対して非常に抵抗性であるため、集学的治療を行っても根治は絶望的である。神経膠芽腫において、新規抗がん剤である temozolomide (TMZ) は細胞毒性を示すアルキル化剤に分類される抗悪性腫瘍剤であり、経口投与で脳脊髄液に良好に移行し、治療効果をもたらすことが報告されている¹⁾。X線との併用療法群において、X線単独療法群に比べ、平均生存期間を延長させることが明らかとなっているが²⁾、重粒子線照射との併用に関しては、基礎研究も含めて報告がほとんどない。本研究では、重粒子線照射と TMZ の併用における生物学的効果についての基礎的なデータを得ることを目的とし、ヒト神経膠芽腫細胞を用いて炭素イオン線もしくは X 線による照射実験を行った。

【方法】細胞は神経膠芽腫細胞株 U87MG と CGNH-PM を用いた。細胞への照射は TIARA にて炭素イオン線 (18.3 MeV/amu, 108 keV/μm, 0~10 Gy)、群馬大学にて X 線 (120 kVp, 4.5 mA, 0~10 Gy) を照射した。TMZ は照射約 1 時間前に単回投与した。評価は主にコロニー形成法により細胞生残率の測定を行った。

【結果】

(1) 放射線生物学的効果比(RBE)の算出

コロニー形成法にて細胞生残率を調べた結果、X 線に対する炭素イオン線の RBE は CGNH-PM 細胞で 1.76、U87MG 細胞で 2.63 であった。

(2) O⁶-methyl-guanine DNA methyltransferase (MGMT) 遺伝子のメチル化解析

Bisulfite 処理により DNA 中のメチル化されていないシトシン残基をウラシルに変換し、PCR 法にてメチル化解析を行った。その結果、CGNH-PM 細胞においては MGMT 遺伝子がメチル化されていた (Fig. 1)。U87MG 細胞においても同様に解析を行った結果、メチル化している細胞は検出されなかった。

(3) 各細胞における TMZ 併用効果

X 線への TMZ の併用は MGMT 遺伝子がメチル化している CGNH-PM 細胞においてのみ相加効果が認められた。炭素イオン線への TMZ の併用は MGMT status にかかわらず、どちらの細胞においても増感効果は認められなかった (Fig. 2)。

【まとめと考察】本実験において、炭素イオン線への TMZ の併用は有意な増感効果を示さなかった。X 線との併用においては MGMT 遺伝子がメチル化している細胞のみコロニー形成法にて増感効果を認めた。神経膠芽腫に対する近年の標準治療は、可及的腫瘍摘出後に、放射線療法と TMZ を併用する集学的治療であるが、平均生存期間は約 14 ヶ月と決して満足のいく成果は得られていない²⁾。本研究で得られた成果からも明らかのように、放射線療法+TMZ 治療に新たな薬剤を追加した治療法を検討する必要があると思われる。

References

- 1) E. S. Newlands et al., Cancer Treat. Rev. 23 (1997) 35-61.
- 2) R. Stupp et al., N. Engl. J. Med. 352 (2005) 987-996.

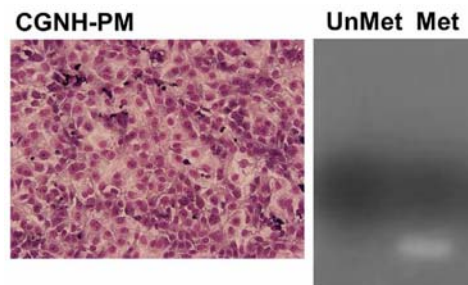


Fig. 1 DNA methylation status of CGNH-PM cell. Representative micrograph of Hematoxylin&Eosin staining (left) and methylation-specific PCR analysis (right). UnMet: unmethylated, Met: methylated.

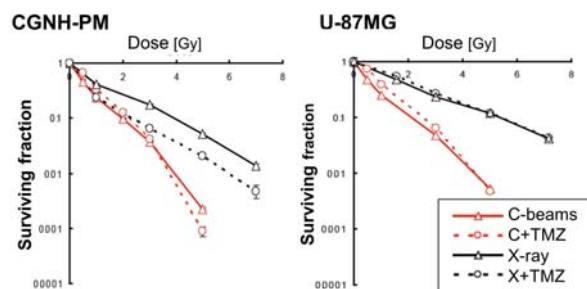


Fig. 2 The effect of TMZ on tumor cell radiosensitivity by clonogenic assay.

3-8 Mechanisms for the Contributions of Bystander Effects to the Responses Induced by Low Dose/Low Dose Rate Radiation

H. Matsumoto^{a)}, M. Hatashita^{a)}, M. Tomita^{b)}, K. Otsuka^{b)}, M. Maeda^{b)}, T. Funayama^{c)}, T. Sakashita^{c)} and Y. Kobayashi^{c)}

^{a)} Biomedical Imaging Research Center, University of Fukui, ^{b)} Central Research Institute of Electric Power Industry, ^{c)} Life Science and Biotechnology Division, QuBS, JAEA

The objective of this project is to elucidate molecular mechanisms for the contributions of bystander response to the responses induced by low dose/low dose rate radiation using heavy ion microbeams in JAEA. We found that the adaptive response was induced by Ar (520 MeV $^{40}\text{Ar}^{14+}$) microbeam-irradiation of a limited number of cells, followed by the broad beam-irradiation and that the adaptive response was almost completely suppressed by the addition of carboxy-PTIO, as an NO scavenger. Our findings strongly suggested that NO-initiated bystander responses contribute to the responses evoked by low dose/low dose rate radiation.

低線量/低線量率放射線に対して生物が示す特異的な応答様式には、放射線適応応答、放射線誘発バイスタンダー応答、放射線超感受性、遺伝的不安定性などがある¹⁾。我々は、日本原子力研究開発機構において開発された重イオンマイクロビーム細胞照射システム（細胞局所照射装置）を用いて、この放射線誘発バイスタンダー応答の低線量/低線量率放射線誘発特異的な応答への寄与、特に放射線適応応答への寄与を明らかにすることを計画した。

1. 実験方法

- (1) 細胞：*p53* 欠損ヒト非小細胞肺癌細胞(H1299細胞)へ正常型 *p53* 遺伝子を導入した H1299/wtp53 細胞を用いた。
- (2) 培養：35 mm ディッシュの内面中央に 2.0×10^6 cells/mL の細胞懸濁液 5 μL を 1 箇所スポットし (1.0×10^4 cells/colony)、15~20 時間培養したものを照射実験に供した。
- (3) 照射：Funayama ら²⁾の方法に従って、中央にスポットしたコロニーの 1~50 個の細胞に 5 粒子の 520 MeV $^{40}\text{Ar}^{14+}$ を HZ1 ポートにおいて照射した。一定時間（3~6 時間）培養後、520 MeV $^{40}\text{Ar}^{14+}$ を HY1 ポートにおいて 1~5 Gy 照射した。
- (4) 細胞の生存率の測定：HY1 ポートでの照射から 6 時間後に、細胞を回収し、T25 フラスコへ 200~1,000 個の細胞を播種してコロニー形成させて生存率を求め、放射線適応応答の誘導を評価した。

2. 結果および考察

- (1) 中央にスポットしたコロニーの 10~50 個の細胞に 5 粒子の 520 MeV $^{40}\text{Ar}^{14+}$ をマイクロビーム照射し、4 時間培養後に同 $^{40}\text{Ar}^{14+}$ をブロードビーム照射（1~5 Gy）した場合、何れにおいても顕著な放射線適応応答が認められた。
- (2) 中央にスポットしたコロニーの 1~10 個の細胞に 5 粒子の 520 MeV $^{40}\text{Ar}^{14+}$ をマイクロビーム照射し、4 時間培養後に同 $^{40}\text{Ar}^{14+}$ をブロードビーム照射（1~5 Gy）した場合、放射線適応応答が認められたのは、10 個の細胞に 5 粒子の同 $^{40}\text{Ar}^{14+}$ を照射した時のみであった(Fig. 1)。
- (3) 一酸化窒素 (NO) 特異的な捕捉剤である carboxy-

PTIO (10 μM) 存在下において、10 個の細胞に 5 粒子の同 $^{40}\text{Ar}^{14+}$ をマイクロビーム照射し、4 時間の培養後、4 時間培養後に同 $^{40}\text{Ar}^{14+}$ をブロードビーム照射（1~5 Gy）した場合、ほぼ完全に放射線適応応答の誘導は抑制された。

以上の結果より、

- (1) 放射線誘発バイスタンダー応答により放射線適応応答が誘導されることが明らかとなった³⁾。
- (2) 放射線誘発バイスタンダー応答による放射線適応応答の誘導に必要な標的細胞数にはしきい値が存在し、細胞の母集団あたり 0.1%以上の標的細胞が必要であった。
- (3) 放射線誘発バイスタンダー応答による放射線適応応答の誘導には、放射線適応応答の誘導因子の一つである NO がバイスタンダー因子として重要な役割を果たしていることが示唆された⁴⁾。

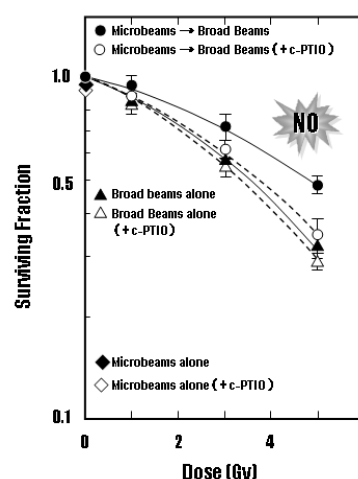


Fig. 1 Induction of radioadaptive response by the irradiation with Ar microbeams.

References

- 1) H. Matsumoto et al., J. Radiat. Res. 48 (2007) 97.
- 2) T. Funayama et al., J. Radiat. Res. 163 (2005) 241.
- 3) H. Matsumoto et al., J. Radiat. Res. 50 (2009) A67.
- 4) H. Matsumoto et al., Curr. Mol. Pharmacol. 4 (2011) 126.

3-9 Analysis of Bystander Cell Signaling Pathway Activated by Heavy Ion-Microbeam II

M. Tomita^{a)}, H. Matsumoto^{b)}, K. Otsuka^{a)}, M. Maeda^{a)}, T. Funayama^{c)},
Y. Yokota^{c)}, Y. Mutou^{c)}, T. Sakashita^{c)} and Y. Kobayashi^{c)}

^{a)}Central Research Institute of Electric Power Industry, ^{b)}University of Fukui,
^{c)}Life Science and Biotechnology Division, QuBS, JAEA

Radiation-induced bystander responses are defined as responses in cells that have not been directly targeted by radiation but are in the neighborhood of cells that have been directly exposed. In our study, we aim to clarify the cell signaling pathway activated by high-LET radiation in the bystander cells. Normal human fibroblast WI-38 cells were cultured on cover glass to form confluent monolayer. Cells were irradiated with 520 MeV ⁴⁰Ar-ion microbeam or broadbeam. When 10 cells within the confluent culture were irradiated with the Ar-ion microbeam, phosphorylation of Akt at Ser473 and accumulation of COX-2 were observed at 6 h after irradiation and were partially suppressed by pretreatment with carboxy-PTIO (c-PTIO), a scavenger of nitric oxide (NO). Accumulation of COX-2 was observed in the bystander cells but not in the irradiated cells. Our results suggest that COX-2 is a marker of bystander cells and NF-κB-dependent signaling pathways involving Akt and COX-2 play an important role in the NO-mediated bystander response.

低線量放射線による生物影響は、高線量放射線の場合とは大きく異なることが明らかになりつつある。近年、低線量放射線のリスクを評価する上で注目されているのが、DNA 初期損傷量に依存しない「非標的効果」である。中でも、放射線誘発バイスタンダー応答は、もっとも特徴的な非標的効果であり、放射線に直接曝露された細胞の近傍に存在する全く放射線に曝露されていない細胞において観察される応答である¹⁾。本研究は、原子力機構の細胞局所照射装置を利用し、バイスタンダー細胞に生じるシグナル伝達経路の変化を、ヒト正常細胞を用いて明らかにすることを目的とする。

昨年度の研究では、ヒト胎児肺由来正常線維芽細胞 WI-38 を用い、1 細胞に 460 MeV ⁴⁰Ar イオンマイクロビームを照射することによって誘導されるバイスタンダー応答を、DNA2 重鎖切断修復タンパク質のフォーカス数を指標として解析した。その結果、コントロールと比較して約 1.5 倍のフォーカスがバイスタンダー細胞に誘導されることを明らかにした。本年度は、細胞の生存シグナル伝達に関与する Akt と炎症反応に関与する COX-2 のバイスタンダー細胞における変化を、ウェスタンブロット法を用いて解析した。

WI-38 細胞を、6 穴プレート内に入れた直径 25 mm のカバーガラス上で 1 週間培養し、コンフルエントにした。照射 2 時間前に 60 mm ディッシュにカバーガラスを移した後、新しい培地もしくは一酸化窒素 (NO) の消去剤である carboxy-PTIO (c-PTIO, 20 μM) を添加した培地を加え培養した。マイクロビームの照射は、HZ1 ポートにおいて行い、5 粒子の 520 MeV ⁴⁰Ar¹⁴⁺ を 10 細胞のみに照射した²⁾。対照実験として、HY1 ポートにおいて 520 MeV ⁴⁰Ar¹⁴⁺ のブロードビーム 5 Gy を全体に照射した。照射 6 時間後にカバーガラス上の全細胞を回収した後、抗 Akt pS473 特異的抗体、抗 Akt 抗体、抗 COX-2 抗体を用いて western blotting を行った。

Akt の Ser473 におけるリン酸化は、Ar イオンを直接照射した細胞とともに、バイスタンダー細胞においても観察された (Fig. 1)。興味深いことに Akt のリン酸化は、c-PTIO によっていずれの場合も抑制された。Akt は NO 合成酵素である cNOS を活性化することが知られ

ている。照射細胞において、c-PTIO により Akt のリン酸化が抑制されるという結果は、cNOS が放出する NO により Akt がリン酸化されるというポジティブフィードバックの存在を示唆する。一方、バイスタンダー細胞では、照射細胞から放出された NO を介して Akt がリン酸化されたと考えられる。

COX-2 の誘導は、Akt のリン酸化とは異なり、照射細胞では検出されず、バイスタンダー細胞においてのみ認められ、c-PTIO によって一部抑制された。この結果は、COX-2 がバイスタンダー細胞の分子指標となることを示唆している。

Akt と COX-2 は、ともに転写因子である NF-κB を介するシグナル伝達機構に関与することが知られている。バイスタンダー細胞において、NO によって活性化された Akt は NF-κB を活性化し、COX-2 を誘導している可能性が高い。今後は、この NF-κB を介したシグナル伝達機構を中心に更なる検討を行い、バイスタンダー細胞に生じるシグナル伝達機構の全貌解明を目指す。

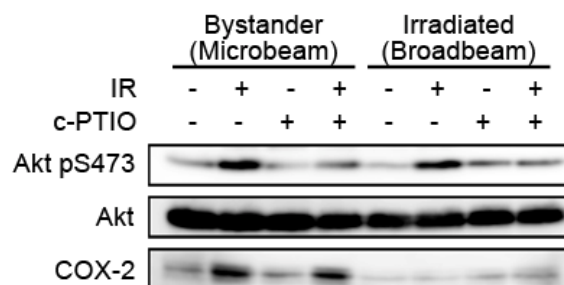


Fig. 1 Phosphorylation of Akt at Ser473 and expression of COX-2 in directly Ar-ion-irradiated and bystander normal human fibroblast WI-38 cell. IR: Ar-ion irradiation; c-PTIO: carboxy-PTIO (20 μM).

References

- 1) H. Matsumoto et al., Curr. Mol. Pharmacol. 4 (2011) 126.
- 2) T. Funayama et al., Radiat. Res. 163 (2005) 241.

3-10 Ion-species Dependent Bystander Lethal Effect in Normal Human Fibroblasts Induced by C-, Ne- and Ar-ion Microbeams

M. Suzuki^{a)}, T. Funayama^{b)}, Y. Yokota^{b)}, Y. Mutou^{b)}, H. Ikeda^{b)}, C. H. Liu^{a)},
Y. Kaneko^{a)}, Y. Furusawa^{a)} and Y. Kobayashi^{b)}

^{a)} Research Center for Charged Particle Therapy, NIRS,

^{b)} Life Science and Biotechnology Division, QuBS, JAEA

Biological effects induced by direct irradiated cells are the basis for the current system for risk estimation from radiation, and the risk of radiation-induced cancer after high and moderate doses is relatively known, based on the data from detailed epidemiological studies of the Japanese atomic bomb survivors in Hiroshima and Nagasaki¹⁾. However, it recently has been challenged by so called non-targeted effects, such as genomic instability, adaptive response and bystander effect, and such radiation-induced non-targeted effects may have important implications for risk evaluation of low doses.

We reported so far that bystander effects in cellular level, such as cell-killing effect and gene mutation induction, were observed in normal human cells irradiated with 220 MeV $^{12}\text{C}^{5+}$ -ion microbeams using the 256 (16×16)-cross-stripe irradiation method²⁾. Furthermore, we identified one of the possible mechanisms that gap-junction mediated cell-cell communications played a critical role in inducing bystander cellular effects. There are many reports concerning bystander effects after exposure to low fluences of alpha particles derived from ^{238}Pu or helium-ion microbeams. However, only a limited number of studies have examined bystander effects after exposure to low fluences of ion species heavier than helium. This year we have begun to examine ion-species dependent bystander cellular effects using C-, Ne- and Ar-ion microbeams.

C-ion ($^{12}\text{C}^{5+}$, 220 MeV), Ne-ion ($^{20}\text{Ne}^{7+}$, 260 MeV) and Ar-ion ($^{40}\text{Ar}^{13+}$, 460 MeV) microbeams were generated with the HZ1 port. Approximately 6×10^5 exponentially growing normal human skin fibroblasts were inoculated into each of microbeam dish, which was made of acrylic resin ring with 36 mm diameter and attached 7.5 μm -thick polyimide film on the bottom of the ring, 2 days before the microbeam irradiation. In order to block up cell-cell communication, half of the sample dishes were treated with a specific inhibitor of gap-junction mediated cell-cell communication (Lindane (L); 40 μM of gamma-isomer of hexachloro- cyclohexane) one day before the irradiation. At the irradiation period, cultures were confluent and around 93% of the cells stayed in G_0/G_1 phase (data not shown). Irradiation was carried out using the 256 (16×16) - cross-stripe irradiation method described in the previous report. The values of linear energy transfer (LET) at the sample position were estimated to be 103 keV/ μm for C ions, 380 keV/ μm for Ne ions and 1260 keV/ μm for Ar ions, respectively. The beam size of each ion microbeam was 20 μm in diameter and the irradiations in each point were carried out to deliver 8 ions for carbon, 2 ions for neon and

1 ion for argon, respectively.

Figure 1 shows cell survivals, which were detected with a colony-forming assay as a reproductive cell death, in microbeam-irradiated (IR) dishes with or without a specific inhibitor of gap-junction mediated cell-cell communication (L). The percent cell survival for C-ion microbeams after 3 h irradiation was around 90% without the specific inhibitor of gap junctions (IR) and 100% with the inhibitor (L+IR), reproducing the our result previously reported²⁾. On the other hand, the cell survivals for Ne- and Ar-ion microbeams were almost 100% whether the inhibitor was applied or not. We can estimate that the percent of direct irradiated cells by microbeams in the 256-cross-stripe irradiation method is around 0.2% of all cells on the dish, when comparing to areas between the cell and the dish. The result suggested that cell-killing effect was induced in almost all of the direct unirradiated cells by bystander effect via gap junction mediated cell-cell communication. There is clear evidence that bystander cell-killing effect is dependent on radiation quality, such as ion species.

References

- 1) D. A. Pierce and D. L. Preston, Radiat. Res., 154 (2000) 178.
- 2) M. Suzuki et al., JAEA Talasaki Ann. Rep. 2006 (2008) 107.

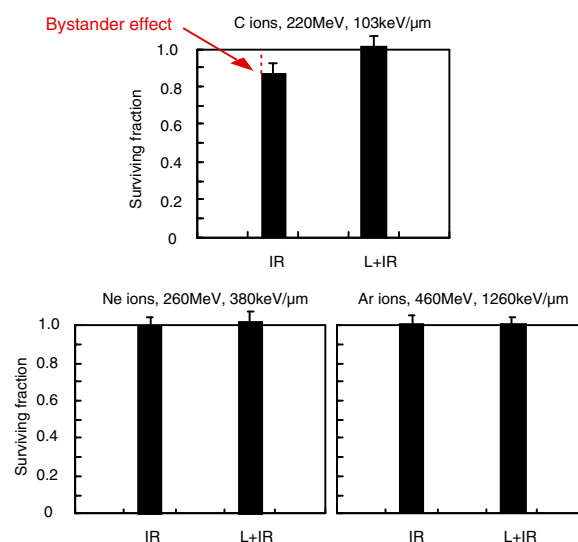


Fig. 1 Cell-killing effect in normal human fibroblasts irradiated with C-, Ne- and Ar-ion microbeams. Microbeam-irradiated cells were treated with (L+IR) / without (IR) a specific inhibitor of gap-junction mediated cell-cell communication. The results were the means and standard deviations from the 2 independent beam times.

3-11

Analysis of Bystander Effect Induced by Cell Membrane Response in Glioma Cells

S. Wada^{a)}, A. Yoshikubo^{a)}, A. Baden^{a)}, T. Kakizaki^{a)}, T. Funayama^{b)}, T. Sakashita^{b)}, Y. Kobayashi^{b)} and N. Ito^{a)}

^{a)} Department of Veterinary Medicine, Kitasato University,

^{b)} Life Science and Biotechnology Division, QuBS, JAEA

So far, we clarified that low dose ion beam irradiation induced cell killing by bystander effect mediated-secreted factor. This phenomenon was related with sphingomyelinase (SMase). In this study we investigated if bystander effect was induced by high dose ion beam irradiation. In medium change experiment, cell killing by bystander effect induced after 2 Gy irradiation. On the other hand, this effect was completely inhibited by SMase inhibitor. This result indicates that bystander effect was induced by high dose ion beam radiation, and high dose irradiation induced-bystander effect is related with SMase and other secreted factors.

1. はじめに

これまでに低線量炭素線照射によって得られる生存率は、高線量域の生存曲線から外挿することによって計算される低線量域での生存率よりも低い値を示し、低線量炭素線照射は高い細胞致死効果を誘導することを明らかにしてきた。また、この低線量炭素線照射による細胞致死効果の増強のメカニズムにはバイスタンダー効果の寄与が大きく、特に、照射された細胞から何らかの液性因子が分泌され、非照射細胞はこの液性因子の作用によって細胞死が誘導されることを明らかにしてきた。さらに、この液性因子による細胞致死効果には細胞膜応答分子であるスフィンゴミエリナーゼが関することも明らかにし、炭素線照射によるバイスタンダー効果誘導には細胞膜応答が引き金となることが示唆され、細胞膜が放射線による細胞応答の重要なターゲットであると考えられた。

一般的に放射線のターゲット分子は DNA であると考えられ、照射線量に応じて DNA 損傷からのシグナル伝達応答も増大する。しかし、放射線による細胞膜応答に関する線量依存性、特に、バイスタンダー効果に関する線量依存性は詳細には明らかにされていない。

そこで、本研究では、高線量域でのバイスタンダー効果による細胞致死効果とこの細胞致死効果誘導メカニズムにおける細胞膜応答の関与を解析した。

2. 実験方法

グリオーマ細胞を用い、AVF サイクロトロンによって加速された 220 MeV C⁵⁺ (LET=108 keV/μm) を照射した。細胞外放出因子による細胞致死効果を解析するため、炭素線 0.1 Gy および 2 Gy 照射した細胞を 1 時間培養後、その培養液のみを回収し、非照射細胞に添加し 1 時間培養後に colony formation assay を用いて、細胞致死効果を算出した (培養液交換実験)。さらに、細胞外放出因子による細胞致死効果のスフィンゴミエリナーゼの関与を解析するため、スフィンゴミエリナーゼ阻害剤による細胞致死効果の解析も行った。また、炭素線照射によるバイスタンダー効果誘導の初期応答を解析するため、細胞膜応答分子であるスフィンゴミエリナーゼの細胞内の局在性を照射細胞および照射細胞の培地を添加した非照射細胞について免疫染色によって観察した。

3. 結果および考察

炭素線 0.1 Gy および 2 Gy 照射における細胞外放出因子による細胞致死効果を観察した (Fig.1)。いずれの放射線においても、培養液交換によって生存率の有意な低下が観察され、2 Gy 照射では 0.1 Gy 照射よりも高い細胞致死効果が観察され、バイスタンダー効果誘導にも線量依存性があると考えられた。さらに、照射細胞をスフィンゴミエリナーゼ阻害剤処理したとき、0.1 Gy 照射ではコントロールレベルまで生存率が回復した。一方、2 Gy 照射ではスフィンゴミエリナーゼ阻害剤処置により生存率が回復する傾向が観察されたが、コントロールレベルまでは到らなかった。

また、照射細胞および照射細胞の培地を添加した非照射細胞の細胞膜応答を観察したとき、いずれの線量においても照射後 5 分~15 分にスフィンゴミエリナーゼの凝集体が観察され、この凝集体は照射線量によって顕著な変化は観察されなかった。

本研究から炭素線照射によって線量依存的に細胞外放出因子によって非照射細胞に細胞死が誘導され、一方、細胞膜応答は線量によって大きな変化は認められなかったことから細胞致死誘導機構にはスフィンゴミエリナーゼが関与すると考えられたが、2 Gy 照射による細胞致死効果にはスフィンゴミエリナーゼ以外の因子も強く関与すると考えられた。

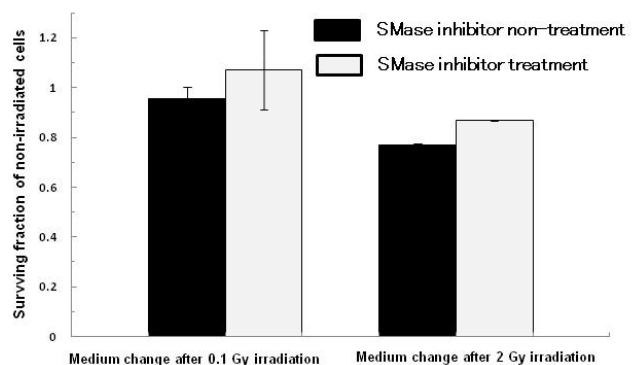


Fig. 1 Killing effect of medium change from irradiated culture cells.

3-12 Expression of Glutathione Peroxidase, p53, Bcl-2, and BAX Genes in Gamma-Irradiated Human Retinal Vascular Endothelial Cells

K. Akeo^{a), b)}, T. Funayama^{c)}, Y. Kobayashi^{c)} and Y. Akeo^{a)}

^{a)} Akeo Eye Clinic, ^{b)} Keio University School of Medicine,

^{c)} Life Science and Biotechnology Division, QuBS, JAEA

Damaged retinal endothelial cells (RE) are characteristic senile macular degeneration and diabetic retinopathy pathogenesis. A retrospective study on macular degeneration treatment using gamma knife radiosurgery (GKR) reported that a majority of the patients maintained stable visual acuity after treatment with a single shot of 12 Gy. However, further studies were required to better define the role of GKR in the treatment of macular degeneration¹⁾. Glutathione peroxidase (GPX) is a selenium-dependent, lipid peroxide-scavenging enzyme that effectively reduces lipid peroxides with concomitant glutathione oxidation, and distributed in the mitochondria²⁾ (Fig.1). Gamma irradiation is known to result in a dose-dependent decline in GPX activity in the skin of mice³⁾. Faucher et al. previously measured the expression of pro-apoptotic BAX and anti-apoptotic Bcl-2 genes in human endothelial-like cell-lines overexpressing GPX⁴⁾. We found that gamma irradiation prevented programmed cell death regulated by the p53 and Bcl-2 genes in organ-cultured ciliary bodies, and was useful in the preservation of organs by protecting against the effects of inflammatory reactions⁵⁾. We applied gamma rays to induce oxidative stress, which influenced GPX expression in the RE cells; further, we measured the expression level of GPX by a quantitative real-time reverse-transcriptase polymerase chain reaction (RT-PCR) using the LightCycler[®] system. We investigated how gamma irradiation influenced GPX and its prevention of phospholipid damage in RE cell membrane, and how the expression of GPX was related to the expression of p53, Bcl-2, and BAX genes regulating programmed cell death.

Human RE cells in vitro were exposed to 20 Gy gamma ray radiation (⁶⁰Co). We collected RE cells after 0, 4, 8, 24 h of irradiation, extracted total cellular RNA, and then synthesized cDNA. The cDNA of GPX, p53, Bcl-2, BAX, and 18S RNA were synthesized by RT-reaction using specifically designed primers. After mixing the cDNA, the primers, and SYBR green[®], the expression level of 18S RNA, p53, Bcl-2, BAX, and GPX was measured using the LightCycler[®] system (Fig.2).

Gamma irradiation significantly increased the expression of GPX and p53 genes in RE cells. The increase in p53 expression was significantly more than that in GPX expression. Furthermore, gamma irradiation increased the expression of BAX genes more significantly than that of Bcl-2 genes.

Gamma irradiation-induced programmed cell death by the expression of p53 genes promoted by pro-apoptotic BAX genes, competing with anti-apoptotic Bcl-2 genes. The increase in GPX indicated a defense mechanism against gamma irradiation induced lipid peroxidation in RE cells.

References

- 1) M. A. Henderson, et al., Stereotact. Funct. Neurosurg. 85 (2007) 11.
- 2) K. Watanabe, Tran. Soc. Pathol. Jpn. 76 (1986) 39.
- 3) J. G. Chandra et al., Clin. Chim. Acta 332 (2003) 111.
- 4) K. Faucher et al., Mol. Cell Biochem. 277 (2005) 81.
- 5) K. Akeo et al., Exp. Animals. 55 (2006) 375.

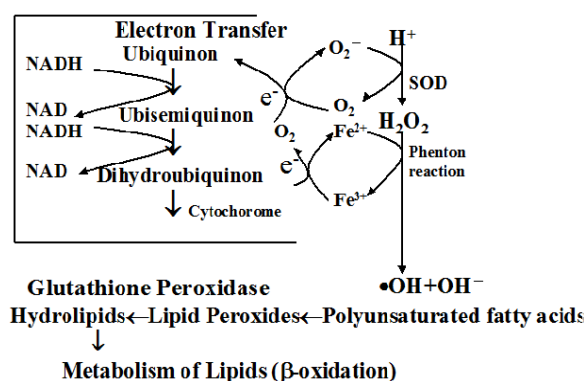


Fig. 1 Role of glutathione peroxidase on lipid peroxide in mitochondria.

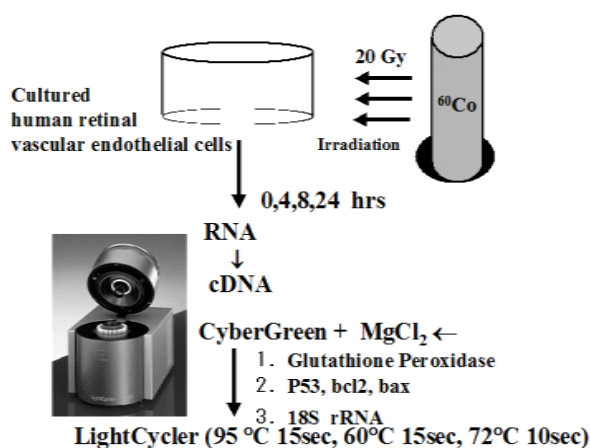


Fig. 2 Scheme of experimental procedure.

3-13 Bystander Effect of Carbon Ion Beam-Induced Senescent Glioma Cells on Infectivity of Human Immunodeficiency Virus Type 1 (HIV-1)

A. Oue^{a)}, N. Shimizu^{a)}, A. Tanaka^{a)}, T. Mori^{a)}, A. S. Hoque^{a)}, S. Islam^{a)},
T. Funayama^{b)}, Y. Kobayashi^{b, c)} and H. Hoshino^{a)}

^{a)} Department of Virology and Preventive Medicine, Gunma University Graduate School of Medicine, ^{b)} Life Science and Biotechnology Division, QuBS, JAEA,

^{c)} Department of Quantum Biology, Division of Bioregulatory Medicine, Gunma University Graduate School of Medicine

Human Immunodeficiency Virus Type 1 (HIV-1) is a causative agent for Acquired Immunodeficiency Syndrome (AIDS). HIV-1 utilizes CD4 as a receptor and also chemokine receptor as a coreceptor, such as CXCR4 or CCR5, to enter susceptible cells. Here we examined the bystander effect of senescent cells on HIV-1 infectivity. To induce cellular senescence, human glioma-derived NP-2 cells were irradiated with carbon ion beams (C-ions). Then, cocultured cells between senescent NP-2 cells (HIV-1-resistant) and HIV-1-susceptible cells (NP-2/CD4/CCR5) were inoculated with HIV-1. Our results indicated that decrease in the production of HIV-1 in NP-2/CD4/CCR5 cells in the presence of senescent NP-2 cells, suggesting the production of anti-HIV-1 cellular factor derived from the C-ion-induced senescent cells. Further study is necessary to clarify the bystander mechanism by which senescent cells negatively regulate the infectivity of HIV-1.

Human Immunodeficiency Virus type 1 (HIV-1) は、後天性免疫不全症候群 (AIDS) の原因ウイルスである。HIV-1 の細胞への感染の主要な receptor は CD4 であり、さらに補助 Receptor (coreceptor) として CXCR4 や CCR5 などの Chemokine receptor も必要とする。最近われわれは、培養ヒトグリオーマ細胞への炭素イオン照射により、細胞老化が誘導されることを見いだした¹⁾。老化細胞からも様々なバイスタンダー効果に関わる生理活性物質が放出されていることが知られており、その中には HIV-1 の感染に影響を及ぼす因子も含まれている可能性がある。そこで、HIV-1 非感受性細胞に炭素イオンを照射し細胞老化を誘導した後、それらと HIV-1 感受性細胞との間で共存培養を行い、老化細胞の存在が HIV-1 感受性にどのような影響を及ぼすかを検討した。

ヒトグリオーマ由来 NP-2 細胞 (HIV-非感受性) を炭素イオン照射の標的細胞として用いた。照射は、日本原子力研究開発機構高崎量子応用研究所にて行った。重粒子線として炭素イオン (18.3 MeV/u, 108 keV/mm) を照射した。細胞老化の誘導については、老化マーカーとして Senescence-associated β -galactosidase (SA- β -gal) 活性の検出で確認した。HIV-1 感受性細胞は、NP-2 細胞に HIV-1 receptor (CD4) と Coreceptor (CCR5) を導入した未照射の NP-2/CD4/CCR5 細胞を用いた。両細胞をシャーレ内で共存培養し、CCR5 を Coreceptor として利用する HIV-1 (SF162 株) を感染させた。数日後、新たに合成された HIV-1 タンパク質をウェスタン・ブロッティング法にて検出した。

NP-2 細胞に炭素イオン (6 Gy) 照射した後約 10 日でシャーレに付着した細胞の巨大化とともに SA- β -gal 陽性の細胞老化が誘導された。NP-2/CD4/CCR5 細胞への HIV-1 感染の程度は、老化 NP-2 細胞を共存させると、そうでない場合と比較して明らかにウイルス産生量の減少が認められた (Fig. 1)。従って、炭素イオン照射によって細胞老化を誘導した NP-2 細胞には、HIV-1 感染を抑制する因子の存在が強く示唆された。この老化細胞に由来する感染抑制因子および感染抑制機序を明らかにすることがウイルス学的にも、また C-ion 照射によって誘導された老化細胞のバイスタンダー効果解明への手がかりとしても今後の重要な検討課題である。

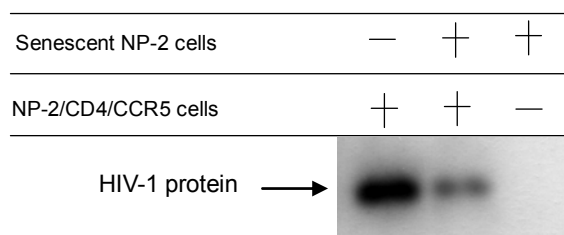


Fig. 1 Reduction of expression of HIV-1 protein in NP-2/CD4/CCR5 cells after coculture with C-ion-induced senescent NP-2 cells.

Reference

- 1) A. Jinno-Oue et al., Int. J. Radiat. Oncol. Biol. Phys. 76 (2010) 229.

3-14 Insect Cell Could Restart the Cell Cycle before Sufficient Repair of the DNA Damage by Heavy-ion Irradiation

K. Shirai^{a)}, K. Fukamoto^{a)}, S. Kobayashi^{a)}, K. Kiguchi^{a)},
T. Funayama^{b)}, T. Sakashita^{b)}, Y. Yokota^{b)} and Y. Kobayashi^{b)}

^{a)} Faculty of Textile Science and Technology, Shinshu University,

^{b)} Life Science and Biotechnology Division, QuBS, JAEA

We have been studying the radiation effects on the insect cells by using heavy ion beams. Previous studies showed the responses to heavy ion irradiation of precursor hemocyte are quite similar to those of other insect cells, such as epidermal cells and Sf9 cells. In this report, we have investigated effects of heavy ion irradiation for the fertilized zygote of the silkworm.

At a dose of 10 Gy of carbon ions, the developmental delays (about 2 hours) were observed on the irradiated eggs. The division of the nucleus was also detected in the almost all eggs irradiated. However, survival of the eggs at larval hatching was only about 6.2 %. These results indicate the fertilized zygote would restart their proliferation after very short time delay, although the radiation-induced damages in the DNA chains are not repaired perfectly.

一般に、昆虫及びその細胞は放射線に耐性であると考えられてきた。しかしながら、研究の多くは照射個体の死または細胞死を指標としており、哺乳類細胞の研究に通常用いられる増殖死を指標とした研究は少なかった。これは昆虫に対する放射線照射の研究が、主にカイコの育種や害虫の不妊虫の作出を目的として進んだ事に一因があると考えられる。著者らは増殖死を指標とした場合の昆虫細胞の放射線耐性を再評価し、昆虫細胞の放射線耐性の要因を明らかにすることを目標に研究を続けている。

これまでの研究から、昆虫細胞は増殖死を指標とした場合も、それまで考えられていた程でないものの、哺乳類と比較し放射線に耐性であることが確認された。その過程でこれまで放射線により耐性と考えられてきた Sf9 細胞 (ヨトウガ由来昆虫培養細胞) と比較的感受性と考えられてきたカイコ幼虫の血球前駆細胞の比較的低線量の照射時における応答がよく似ていることが示された。

すなわちカイコ幼虫の血球前駆細胞に線量 10 Gy の炭素イオンを照射したのち、24 時間毎に細胞数の増加を調査すると、非照射区の細胞の増加割合と有意な差が認められなかった。この 10 Gy は哺乳類の細胞のほとんどで致死線量である。にも関わらず、未分化でかつ分裂盛である血球前駆細胞においても細胞周期の停止と障害を修復する時間が認められないことになる。

この現象を説明する一つの考えは、「昆虫細胞では障害修復能が極めて高く、短期間で修復し増殖を再開するため、24 時間ごとの調査では増殖速度に有意な差は認められなかった」というものである。そこで本研究では約 1 時間に 1 回、同調的に核分裂を行うカイコ受精卵を用い、上記の仮説を検証した。

受精直後の卵に重イオンを全体照射し、その後の発生を調査した。その結果、線量 10 Gy の炭素イオンを照射されたカイコ初期発生卵は約 2 時間程度の発生遅延が認められるものの、ほぼ全ての卵で受精核の分裂が再開と受精核の周辺細胞質への移動が確認された。すなわちこれらの照射卵において、放射線障害の修復

が約 2 時間で終了し、発生を再開したことが明らかになった。しかし、核に形態異常が認められる卵も観察された。またその後、発生途中に致死する受精卵が多数を占めることから、その割合を確認した。胚帯形成前に致死した卵の割合は 552/973 (56.7%) におよび、胚帯形成後催青前で致死したもの 103/973 (10.6%)、催青期に致死したもの 287/973 (29.5%) であった。最終的に孵化した幼虫は 31/973 (6.2%) であった。非照射区の孵化幼虫の割合は 677/728 (93.0%) であった。

孵化幼虫を桑葉で飼育し、後胚発生における影響を引き続き調査した。幼虫はその後発育に伴い致死する個体が多く、成虫になったもの 1 蛾 (雌) のみであった。この成虫雌に正常雄を交配し、次世代への影響を調査使用と試みたが、約 200 粒の卵のうち胚帯形成前に約半数で発育が停止し、その後催青までに全ての個体が致死した。今回は 1 例のみの結果のため、今後の追実験で確認する必要があるが、発生が進んでいることからこれらの卵は未受精卵で無いことは明らかなため、成長した雌蛾の DNA 中に何らかの重大な障害が残されていた可能性が高い。

さらに卵の切片を作製し、発生途中で致死した卵を確認した結果、胚帯形成前の致死卵では組織や細胞が確認されなかった。これは周辺細胞質に到達した分裂核が細胞化する前後でアポトーシスを起こすことを示唆する。胚帯形成以後、孵化までに致死した卵に関しては、現在のところ、致死のステージや要因に傾向は見いだせないことから、致死原因が重イオン照射によるランダムな DNA 障害によると判断される。

本研究ではカイコ受精卵を用いて、重イオン照射を受けた昆虫細胞の (DNA) 障害修復について検討を行った。その結果、重イオン照射 (10 Gy) を受けたカイコ受精卵では受精核の分裂停止は約 2 時間のみで、すぐに核分裂を再開することが明らかになった。また、胚発生の再開後、約 95% の個体が孵化できず致死することから、重イオン照射による障害修復が不完全であることが示唆される。

3-15 Comparison of Histological Responses in Medaka Testis after Heavy-Ion Broad- and Micro-Beam Irradiation

S. Oda^{a)}, T. Yasuda^{a)}, Y. Urushihara^{a)}, T. Funayama^{b)}, Y. Kobayashi^{b)} and H. Mitani^{a)}

^{a)} Graduate School of Frontier Sciences, The University of Tokyo,

^{b)} Life Science and Biotechnology Division, QuBS, JAEA

Histological responses in testis after carbon-ion irradiation (micro-beam and broad-beam) were investigated using Medaka. When a transgenic male with fluorescent testis were irradiated with micro-beam (10 Gy), fluorescence intensity in the irradiated part of the testis decreased transiently. Then, the intensity of fluorescence of the irradiated testis was restored and became normal at 46 days after irradiation. In contrast, carbon-ion irradiation of the same dose with broad-beam induced almost complete disappearance of fluorescence in the testis within 46 days after irradiation. In this study, we developed a protocol for local irradiation of testes in living adult fishes without irradiating any other tissues using micro-beam of carbon-ion. Our results suggest that the responses of the individual tissues, organs could be overwritten by the responses of central and autonomous nervous system and endocrine system, irradiated at the same time with broad-beam.

ブロードビーム照射ではメダカ成魚の全身にわたって重粒子線を照射することから全身的な放射線応答を解析の対象とするのに対して、マイクロビームによる照射ではメダカの特定の組織（内臓器）に限定して重粒子線を照射することが可能である。本研究では、精巣に特異的に GFP を発現するトランスジェニックメダカ系統（olvas-GFP）を用い、重粒子線をブロードおよびマイクロビームで精巣に照射し、精巣が示す放射線応答を比較することによって、精巣が示す応答に全身的な応答、特に脳への重粒子線照射の影響が含まれているのか否かを検証することを目的とした。

Olvas-GFP 系統のオス成魚を麻酔 (MS-222 使用) し、ブロードビーム照射したオス成魚から、照射後 1 日、8 日、36 日に精巣を単離し、パラフィン組織切片を作製しヘマトキシリン-エオジン染色を施して組織像を検討した。照射 1 日後では炭素線 (10 Gy) の照射によって精原細胞におけるアポトーシス像が多数認められた (Fig. 1a)。照射 8 日後では、精子形成の促進が (Fig. 1b)、照射 36 日後では精原細胞の死滅とそれに伴う精巣組織の萎縮、精子形成の停止が認められた (Fig. 1c)。ブロードビーム照射において、メダカ体内の精巣まで炭素線が届いていることが確認された。

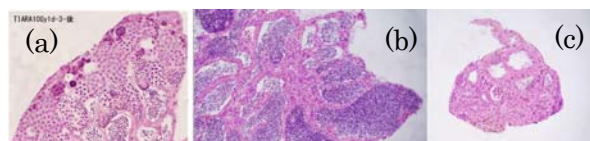


Fig. 1 Histological section of testis irradiated with broad-beam of carbon ion (10 Gy) on 1 day (a), 8 days (b), and 36 days (c) after irradiation.

成魚では体躯の透明度が十分ではなく、蛍光観察によって精巣の位置を特定して照射することはできなかった。そこで、精巣のほぼ中央部と予想される部位を狙ってマイクロビーム（炭素線、10 Gy）照射を行った。照射後、経時的に成魚を麻酔してその腹部を蛍光観察し、精巣におけるマイクロビーム（炭素線、10 Gy）照射の影響を検討した。その結果、照射後 1 日から 16 日後の間、マイクロビーム照射を行った精巣の中央部の蛍光を失ったように見える観察像が得られた (Fig. 2a)。

その後、照射後 25 日、32 日、46 日では、精巣全域で明瞭な蛍光を観察し (Fig. 2b)、マイクロビーム照射では精巣全体としては萎縮せず、しかも照射部位においての精子形成も復活しているように見える結果が得られた。

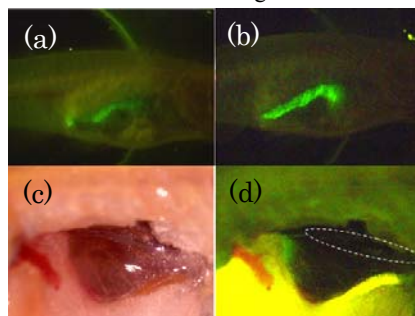


Fig. 2 Fluorescent images of the testis after at 2 days (a) and 46 days (b) after irradiation with micro-beam (10 Gy). Bright field (c) and fluorescent (d) images of the testis at 36 days after irradiation with broad-beam (10 Gy).

これに対してブロードビーム照射による精巣全体への照射では精巣全体が萎縮した (Fig. 2c, d) ことから、全身照射されたメダカの精巣が示す重粒子線照射への応答と考えられてきた反応に、同時に照射された脳の反応が含まれている可能性があるものと考えられる。

上記仮説を検証するために、より確実に生きたメダカ成魚の精巣のみをマイクロビーム照射するための照射法を開発した。腹壁の外観から腹腔内の精巣の位置を正確に予想し、直径を 250 μm 程度に設定したマイクロビームを 10 回程度位置をずらしながら照射するものである (Fig. 3)。

組織学的検証によって、この手法によって精巣全域に重粒子線が照射されていることを確認でき、現在、ブロードビーム照射の際の精巣組織像との詳細な比較検討を進めている。

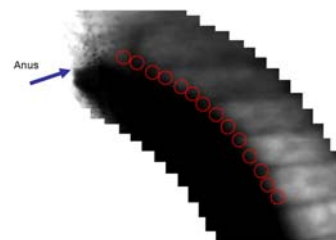


Fig. 3 Whole testis of adult fishes were irradiated with more than 10 shots of carbon-ion micro-beam (10 Gy).

3-16 Anhydrobiosis-Specific Genes in the Sleeping Chironomid Are also Responsive to Ionizing Radiation

O. Gusev^{a)}, T. Kikawada^{a)}, T. Sakashita^{b)}, T. Funayama^{b)}, Y. Kobayashi^{b)} and T. Okuda^{a)}

^{a)} Anhydrobiosis Research Group, National Institute of Agrobiological Sciences,

^{b)} Life Science and Biotechnology Division, QuBS, JAEA

Anhydrobiotic larvae of the sleeping chironomid *Polypedilum vanderplanki* become tolerance to variety of abiotic stresses, including ionizing radiation. It is of significance to know molecular background of the cross-resistance for elucidating radiation tolerance mechanism in high organism.

We have recently found that DNA damage and repair take place upon extreme desiccation and ionizing radiation¹⁾. We then hypothesized that the signaling pathway of response to ionizing radiation-caused events (i.e. generation of ROS) in cells of the chironomid larvae would be similar to that of caused by desiccation. Indeed, expression of antioxidant genes was induced after desiccation and gamma irradiation. Therefore, evolution of desiccation-resistance in this species would be tightly linked to continuous increased of radioresistance.

In the present study, we focused on genes encoding plant-like Late Embryogenesis Abundant (LEA), the most important molecular agents contributing anti-aggregation of proteins and glass-formation during anhydrobiosis, and analyzed the gene expression in response to gamma radiation.

Previously, we found that ⁴He (LET_α=16.2 keV/μm) ion beam (70 Gy) has caused a similar effect on nuclear DNA damage occurred in normal anhydrobiotic chironomid larvae¹⁾. Here we have chosen a gamma-ray at a dose of 70 Gy to see the effect on the gene expression for comparison. Final instar larvae of approximately 1 mg wet body weight were used for all experiments. The larvae were placed on filter paper with 0.44 mL of distilled water in a glass Petri dish (diameter 65 mm, height 20 mm), which was set in a desiccator (20×20×20 cm) with 1 kg of silica gel. For gamma-ray irradiation, approximately 100 hydrated larvae were placed in a plastic vial (Sumilon MS-4503, Sumitomo Bakelite Co., Tokyo, Japan) with 1 mL water. The samples were irradiated with 70 Gy of gamma-ray from a ⁶⁰Co source at 60 Gy/min.

Total RNA from dehydrating and irradiated larvae was extracted using Trizol (Invitrogen) and the RNeasy Mini Kit (Qiagen, Hilden, Germany), and reverse transcribed using Ready-To-GoTM T-Prime First-Strand Kit (GE Healthcare Bio-Sciences, Piscataway, NJ). Real-time PCR was performed using a C-1000 Thermo Cycler apparatus (BioRad, Japan) using RLP-32 and EF1α genes expression as a reference.

Genes coding two members of LEA group 3 family (abbreviated as LEA-8 and LEA-9) were up-regulated after irradiation and desiccation stresses (Fig. 1), although the

expression level in response to radiation was lower than that to desiccation. Microarray analysis suggested that approximately half 40 of LEA-like protein-coding genes found in the sleeping chironomid were both desiccation- and ionizing radiation responsive (our unpublished data).

In this study, it became clear that those two abiotic stresses have common features not only in damaging effect on the cells and tissues of the insect but also in activating a certain set of genes, e.g., chaperons, antioxidants^{2,3)} and LEA proteins. These data may provide a new insight for understanding of cross-resistance mechanism to desiccation and radio-resistance in the sleeping chironomid. Particularly an additional role of LEA proteins as an antioxidant agent upon desiccation should be proposed. The anhydrobiosis ability in this insect species acquired by reducing oxidative damage from desiccation stress could be indeed secondarily contributing to deal with oxidative stress after gamma radiation. Thus, we point out a reason why anhydrobiotic organisms can tolerate radiation stress.

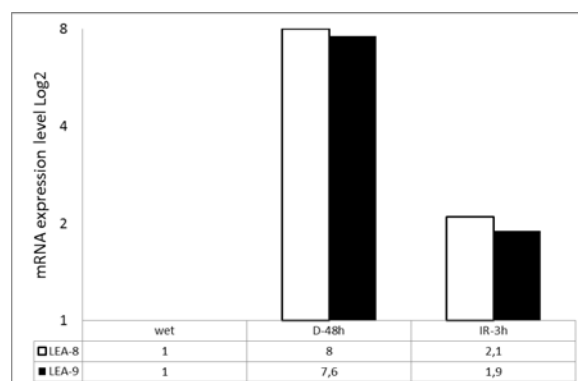


Fig. 1 Relative expression of LEA-8 and LEA-9 mRNA in response to desiccation and gamma radiation in the larvae of the sleeping chironomid, *Polypedilum vanderplanki*. The RNA samples from dehydrating and irradiated larvae were named “D” and “IR”, respectively, and numbers correspond to the hours of treatment and after irradiation.

References

- 1) O. Gusev et al., PLoS ONE. 5 (11) (2010) e140008.
- 2) R. Cornette et al., J. Biol. Chem. 285 (46) (2010) 35889-99.
- 3) O. Gusev et al., Cell Stress & Chaperones. 16 (1) (2011) 81-90.

3-17 Cytokine Production is Suppressed in Human THP-1 Macrophages by Direct Stimulation with Heavy-ions and Bystander Responses Due to Microbeam Irradiation of a Limited Cell Population

Y. Mutou-Yoshihara, T. Funayama, Y. Yokota, H. Ikeda, T. Sakashita, M. Suzuki and Y. Kobayashi

Life Science and Biotechnology Division, QuBS, JAEA

Introduction

The immune system cell is important for cancer patients because it supports them against cancer. Immune cells accumulate in and around cancers and cooperate with each other using specific cytokines to attack the cancer cells¹⁾. The energetic heavy-ion beams for cancer therapy may stimulate immune cells and affect on the immune system²⁾. However, it is still poorly understood how the immune system cells are stimulated by ion-beams. In this study, we irradiated immune cells using heavy-ion beams and analyzed changes in production of tumor necrosis factor (TNF)- α and interleukin (IL)-6 that are important cytokine for the cancer treatment.

Materials and methods

The human acute-monocytic-leukemia cell line, THP-1, was induced to differentiate into macrophages³⁾ and irradiated with carbon-ion broad-beams (18.3 MeV/u, LET = 108 keV/ μ m) generated by the azimuthally varying field cyclotron at the JAEA, Takasaki. After irradiation, cells were cultured for up to 24 or 48 h and the production of TNF- α and IL-6 were analyzed by enzyme-linked immunosorbent assays⁴⁾. To ascertain whether nitric oxide (NO) plays a role in the suppression of cytokine production, THP-1 macrophages were treated with carboxy-PTIO (0.25 mM), an NO inhibitor, prior to radiation exposure. To examine the bystander response after heavy-ion irradiation, a very small fraction of the cell population (approx. 0.45%) was irradiated using heavy-ion microbeams (250 μ m). Within each irradiation spot, 15,000 ion particles (equivalent to 5 Gy) were delivered. In the center of the dish, 256 spots with a matrix distribution of 30 mm \times 30 mm area were targeted and irradiated.

Results

While cells were irradiated with 5 Gy that hardly affect on cell viability, the levels of TNF- α and IL-6 were reduced after both microbeam irradiation and broad-beam irradiation (Fig. 1). TNF- α production of macrophages with the NO inhibitor-treatment increased after carbon-ion broad-beam. NO was involved in the radiation-induced suppression of TNF- α production (Fig. 2).

Conclusions

The production of TNF- α and IL-6 decreased after both

microbeam irradiation and broad-beam irradiation, suggesting that bystander suppression of cytokine production within the human immune system occurs after radiation therapy.

References

- 1) R. van Horssen et al., *Oncologist* 11 (2006) 397.
- 2) S. Conrad et al., *J. R. R.* 50 (2009) 223.
- 3) S. Tsuchiya et al., *Cancer Res.* 42 (1982) 42.
- 4) Y. Mutou et al., *J. H. S.* 56 (2010) 675.

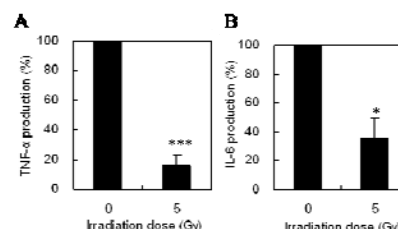


Fig. 1 Effects of heavy-ion microbeam irradiation on TNF- α and IL-6 production.

0.45% of the whole population was irradiated by carbon-ion microbeams and cultured for 24 h (A) or 48 h (B). Cytokine production by irradiated cells is represented as a percentage of that of non-irradiated cells. Each value represents the mean \pm S.D. of four independent experiments with quadruplicate cultures. * p < 0.05; *** p < 0.005; significantly different from the non-irradiated group.

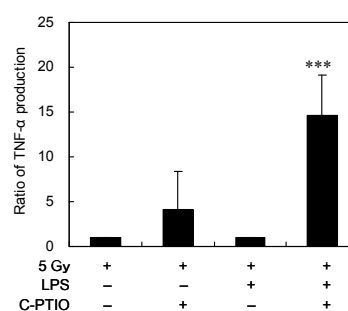


Fig. 2 Effects of heavy-ion broad-beam exposure and a NO inhibitor on cytokine production.

THP-1 macrophages were incubated for 1 h in RPMI culture medium supplemented with the NO inhibitor carboxy-PTIO. After carbon-ion irradiation with 5 Gy, cells were cultured for 24 h. Each value represents the mean \pm S.D. of duplicate cultures. *** p < 0.005; significantly different from the non-irradiated group.

3-18 Effects of Carbon-ion Irradiation on Locomotion and Pharyngeal Pumping in *Caenorhabditis elegans*

M. Suzuki^{a)}, T. Sakashita^{a)}, Y. Hattori^{a, b)}, T. Funayama^{a)}, Y. Yokota^{a)},
Y. Mutou-Yoshihara^{a)}, T. Tsuji^{b)} and Y. Kobayashi^{a)}

^{a)} Life Science and Biotechnology Division, QuBS, JAEA,

^{b)} Department of System Cybernetics, Graduate School of Engineering, Hiroshima University

Introduction

Caenorhabditis elegans is a good *in vivo* model system to examine radiobiological effects. We recently reported that locomotion using body-wall muscles was reduced in a dose-dependent manner after gamma-ray irradiation, and that the locomotion was restored within several hours^{1), 2)}. In addition, we found that pharyngeal pumping motion for chewing and swallowing was reduced in a dose-dependent manner³⁾. However, it is not known whether the same effects are observed in the heavy-ion irradiated animals. Therefore, we examine radiation effects of heavy ion beams on both locomotion and pharyngeal pumping in *C. elegans*.

Materials and methods

Five or more well-fed adult *C. elegans* were placed on an agar dish with a bacterial lawn (food). The animal's whole bodies were irradiated with a graded dose of carbon ion beams ($^{12}\text{C}^{5+}$, 18.3 MeV/u, LET = 113 keV/m). To evaluate radiation effects on locomotion, animals were placed on an agar dish without food and locomotion of five animals was video-recorded. The locomotory rate of each animal was measured using 'body bends', which is defined as the number of bends in the anterior body region at 20-sec intervals. On the other hand, to evaluate radiation effects on pumping motion, animals were placed on an agar dish with food and pumping motion of five animals was recorded using a high-speed camera attached to a microscope. The number of pumping strokes within a 3 s period was counted using 60 continuous recording images of 3 sec duration.

Results

Figures 1 and 2 show the frequency distribution of locomotion and pumping in *C. elegans* immediately after irradiation, respectively. The inverted triangle represents a mean of distribution. Both locomotion and pumping decreased in a dose-dependent manner as well as in the case of gamma-ray irradiation^{2), 3)}. The locomotion of irradiated animals decreased uniformly in a normal distribution in a dose-dependent manner (Fig. 1). In contrast, irradiated animals could be classified into two groups based on the pumping (Fig. 2). One group stopped pumping immediately after irradiation and the other showed normal pumping activity. Our findings indicate that whole body irradiation reduced both locomotion and pumping. However, there was an obvious difference in the aspect of the reduction between the locomotion and pumping. This difference may depend upon the difference in the number and/or type

of neurons controlling the body-wall muscles for locomotion and pharyngeal muscles for pumping.

The results of carbon-ion irradiation were same as those in gamma-ray irradiation^{2), 3)}. Additionally, the dose response, which was evaluated using the averaged body bends or averaged number of pumping strokes in each dose, was comparable with results of gamma-ray irradiation (data not shown). This suggests that radiation effects on locomotion and pumping in *C. elegans* do not depend upon the type of radiation.

References

- 1) T. Sakashita et al., J. Radiat. Res. 49 (2008) 285-291.
- 2) M. Suzuki et al., J. Radiat. Res. 50 (2009) 119-125.
- 3) M. Suzuki et al., 4th East Asia *C. elegans* Meeting Prog. & Abst. (2010) 98.

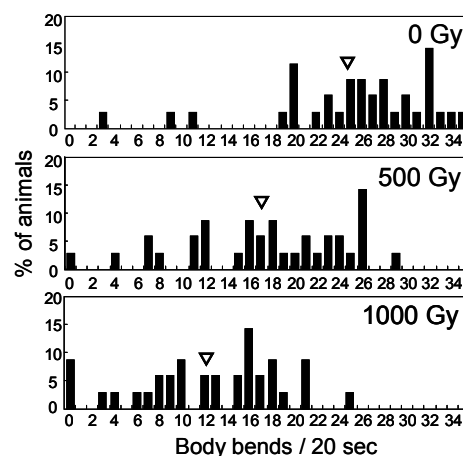


Fig. 1 Effects of carbon ions on locomotion in *C. elegans*.

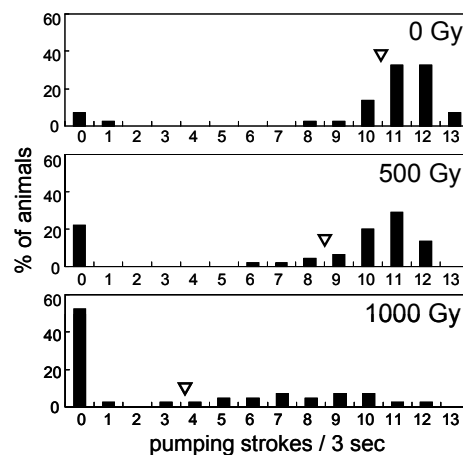


Fig. 2 Effects of carbon ions on pumping in *C. elegans*.

3-19 Relaxation Behaviors of Electron Spin in Irradiated Fresh Papayas

M. Kikuchi^{a)}, T. Sakashita^{a)}, T. Funayama^{a)}, M. Ukai^{b)},
Y. Shimoyama^{a)} and Y. Kobayashi^{a)}

^{a)} Life Science and Biotechnology Division, QuBS, JAEA, ^{b)} Hokkaido University of Education

We had established a procedure for radiation-induced radicals in the irradiated fresh mango¹⁾. We probably detect stable radicals in the fruit from day-1 to day-9 after irradiation by using electron spin resonance (ESR) spectroscopy. Since lifetime of radicals is related to where unpaired electrons exist, interactions of the unpaired electrons were investigated according to Lund's calculation²⁾. The results suggested that two neighbor radicals went far in the distance of inter-electrons by changing molecular conformation after γ -irradiation³⁾. In this report, similar phenomena were observed in irradiated papayas to sustain our hypothesis⁴⁾.

To measure ESR spectra of irradiated fresh papayas, we employed an overnight freeze-dry technique. ESR spectroscopy was performed with an RE-3X (Jeol) at room temperature using the X-band microwave frequency (9.44 GHz). A strong singlet peak at $g = 2.004$ was observed in the specimen (Fig. 1). Therefore, radical behavior would be principally characterized by the main peak of papayas. To estimate the interaction of unpaired electrons on the basis of progressive saturation behavior (PSB) of the singlet ESR signal, the relaxation times of T_1 and T_2 were evaluated using the program code by Lund²⁾.

Figure 2 shows PSB from the main peak measured from freeze-dried specimens of irradiated fresh papaya fleashes by changing microwave powers. The threshold values as the maximum of PSB were around 3 mW, indicating that the singlet peak is attributed to organic free radicals.

The relaxation time T_2 of papaya fleashes was dependent on irradiation doses (Fig. 3). From the previous report for irradiated mango flesh³⁾, the relaxation times of papaya were similar to mango flesh: T_2 was dose-dependent while T_1 was constant (data not shown). In brief, the slope of regression lines was different but y-axis values of the lines were almost equal. It is considered that the dose response might be affected by the surrounding environment of radicals, such as moisture and/or radical scavenger contents in the fruits.

A physical meaning of relaxation time T_2 is related to an energy transfer between unpaired electrons that are located close enough to be capable of their interaction. Hydroxyl radicals and hydrated electrons induced from the radiolysis of water distribute γ -ray damages on biopolymer at random. Therefore, a mechanism corresponding to the neighbor electrons' induction for T_2 might be another pathway from an indirect action of the radiation through hydroxyl radicals.

References

- 1) M. Kikuchi et al., Spectrochim. Acta A 75 (2010) 310-313.
- 2) A. Lund et al., Radiat. Res. 172 (2009) 753-760.
- 3) M. Kikuchi et al., Food Irradiat. Jpn. 44 (2009) 9-13.
- 4) M. Kikuchi et al., Food Irradiat. Jpn. 45 (2010) 34-38.

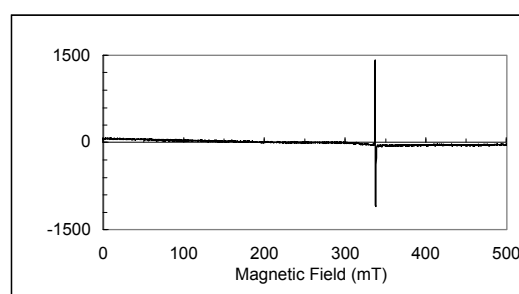


Fig. 1 ESR spectrum of a specimen prepared from the 3 kGy γ -irradiated flesh of a fresh papaya.

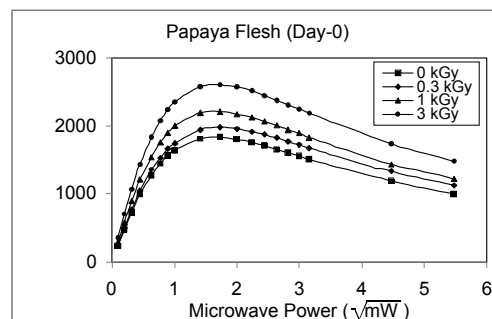


Fig. 2 Progressive saturation behaviors of freeze-dry specimens prepared from irradiated fresh fleashes.

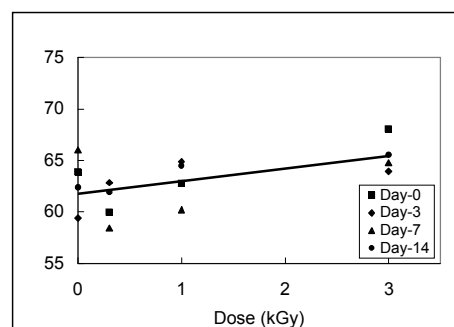


Fig. 3 Dose response of relaxation time T_2 . A regression line was calculated from the average values of three different samples at day-0, 3, 7 and 14.

3-20 Initial Decay Process of Radicals Induced in Irradiated Food

Y. Kaimori^{a)}, Y. Sakamoto^{a)}, M. Kikuchi^{b)},
Y. Kobayashi^{b)} and M. Ukai^{a)}

^{a)} Hokkaido University of Education,

^{b)} Life Science and Biotechnology Division, QuBS, JAEA

In order to determine radical decay behaviors of gamma-ray irradiated food, we analyzed radicals in the food using ESR. We detected the ESR signal of specimens just several minutes after irradiation. The singlet signal intensity at $g=2.0$, originated from organic free radicals was increased as followed by increasing radiation dose. Singlet signal intensity that increased by gamma-ray irradiation was decreased with time. The phenomena of decay of the ESR singlet signal showed two phase that are rapid decay and slow decay. It was suggested that those two phase decay is due to at least the two radical species. Also we concluded that after three hours of radiation treatment long-life radical as ESR signal intensity was detected in irradiated black pepper, coffee raw bean and ginseng, showing the same decay phenomena. But the signal intensity of irradiated black pepper was three times larger than that of irradiated coffee raw bean and irradiated ginseng.

近年、世界各国で放射線による食品や農産物の殺菌、殺虫、芽止め処理が認可され、照射食品の商業規模での流通も盛んになっている。電子スピン共鳴(Electron Spin Resonance; ESR)法は植物性食品に含有されるセルロースや糖から照射により誘導されるラジカルを検出できる。著者らは種々の食品および生薬を ESR 法により計測してきた。輸入から検疫検査までの期間を考慮し、計測には照射から 1 週間以後の試料を用いて、安定したラジカルを測定してきた¹⁾。照射食品検知技術の普及のためには、食品中に生成される放射線誘起ラジカルについて、照射直後のラジカルの確認とその減衰挙動を明らかにして、ラジカルの時間変動を確認しておく必要がある。そこで、ガンマ線照射直後の食品中のラジカルの挙動を、ESR 法を用いて計測した。吸収線量の違いによるラジカルの減衰挙動に変化はあるか、また試料によるラジカル減衰挙動に変化はあるかについて検討した。

実験試料は黒コショウ、コーヒー生豆、朝鮮人参の 3 種である。照射処理は(独)日本原子力研究開発機構にてコバルト 60 を線源とするガンマ線で処理した。吸収線量は 0.1、1、5、10、50 kGy とした。照射処理は室温にて行った。照射処理終了後すぐに試料調製を行った。照射処理終了から ESR 信号観測までの時間は平均して約 10 分であった。

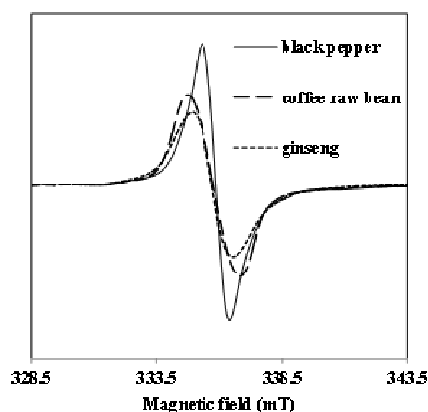


Fig. 1 ESR spectra of irradiated specimens at 10 kGy.

すべての試料において照射直後のラジカル信号の観測に成功した (Fig. 1)。吸収線量の増加につれて g 値が約 2 の一本線信号の強度は増加した。照射後、時間経過とともにラジカルは急激に減衰した。ラジカル減衰挙動が 2 相に分かれることから、少なくとも 2 つの半減期が異なるラジカルの存在が示唆された (Fig. 2)。照射後 3 時間程度で、すべての検体で長寿命のラジカル成分のみが観測されるようになった。照射された黒コショウ、コーヒー生豆、朝鮮人参は類似の減衰挙動を示した。しかし、黒コショウはコーヒー生豆や朝鮮人参より信号強度が強く観測され、信号強度の強弱により減衰挙動も若干の違いが見られた。食品試料によりラジカル減衰挙動に変化があることがわかった。図には示さないが、吸収線量が高くなるにつれて信号強度も増大し、さらに信号強度が強い検体ほど照射直後の減衰は急激であった。

本研究では、照射直後の不安定なラジカルの測定にも、ESR 法を用いて共鳴スペクトルの測定が可能であることを示した。結果として、3 種の植物性乾燥食品の初期ラジカル減衰挙動を明らかにすることができた。

Reference

- 1) Y. Shimoyama and M. Ukai, *Spectrochimica Acta* **63** (2006) 888-890.

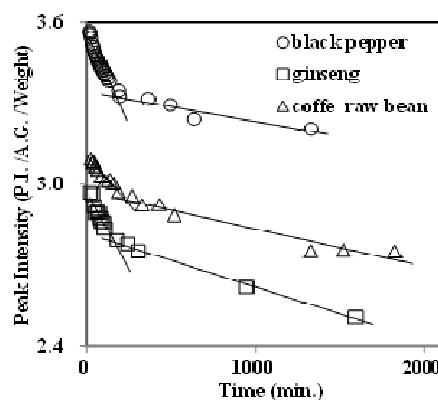


Fig. 2 Decays of ESR peak intensity after irradiation at 5 kGy.

3-21 Improvement of Spatial Resolution of PIXE-CT Using ML-EM Algorithm in TIARA

T. Satoh, M. Koka, W. Kada, A. Yokoyama, T. Ohkubo, A. Yamazaki, Y. Ishii and T. Kamiya

Department of Advanced Radiation Technology, TARRI, JAEA

Introduction

In the previous report ¹⁾, we applied CT (computed tomography) technique, FBP (filtered back projection) algorithm ²⁾ and STIM (scanning transmission ion microscopy) ³⁾ to the micro-PIXE analysis for the 3D measurement. As a result, the spatial resolution of a few 10 μm was achieved but it is not enough for the measurement of a biological cell. In order to get better spatial resolution, ML-EM (maximum likelihood expectation maximization) iterative algorithm ⁴⁾ was used instead of FBP. The ML-EM algorithm had been developed for emission computed tomography such as SPECT (single photon emission computed tomography). It's relatively easy to apply the ML-EM to micro-PIXE because both SPECT and micro-PIXE originated from photon emission phenomena. Moreover, unlike FBP, the ML-EM algorithm has highly resistance against the errors of projection images and is suitable for rare event analyses such as micro-PIXE.

Experiment

Three MeV proton microbeam with a diameter of 1 μm at TIARA was used in this study. The scanning area was 128×128 pixels corresponding to $200 \times 200 \mu\text{m}^2$. For STIM experiment, a planar silicon detector was placed at just behind the sample, while a Faraday cup was placed at the same position in the case of micro-PIXE analysis. The distance and the angle of the lithium-drifted silicone detector for micro-PIXE analysis were 22 mm from the target and 40° to beam axis, respectively. A target was placed on an automatic rotation stage, which made a full turn by rotating 18° at a step in vacuum. As a result, we could obtain twenty projections per a sample. Though the precise alignment of the rotation axis with the center of the scanning area is very important for suppression of artifacts in the image reconstruction, it is very difficult to place a sample on the center of axis precisely. To solve this problem, we used another linear motion stage for lateral alignment and adjusted the position on every angle to scan over the whole of the sample. After the both measurements of STIM and micro-PIXE, the center of gravity in every projection was calculated from the micro-PIXE image on phosphorus, and was defined an imaginary axis of rotation in the 3D reconstruction of STIM and micro-PIXE.

A dried cell of *Paramecium* sp. (*Paramecium bursaria*) was used as a test sample because it is small enough for the range of 3 MeV proton and more durable for the long irradiation than general animal cells. The pre-cultured cells of *Paramecium bursaria* were fixed with a fixative and then washed with purified water repeatedly. Those

pre-fixed cells were introduced to metal solutions containing 0.05 mM lead (Pb) at pH 7 for 24 hours. After the contact, the cells were washed with purified water repeatedly and dried on a carbon foil in air at room temperature. After that preparation, one of dried cells was fixed on the top of a Kapton tube with inner diameter of 500 μm and wall thickness of 25 μm using vinyl acetate emulsion adhesive as in Fig. 1.

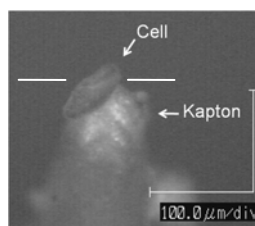


Fig 1 Microphotograph of the sample of a cell, *Paramecium bursaria*. The sample fixed on the cusp of a Kapton tube with glue is made a turn by rotating 18° at a step.

Result

Figure 2 shows the cross sectional images obtained using the ML-EM reconstruction about phosphorus and Pb at the white line in Fig. 1. Phosphorus distributed itself uniformly over the cell because it is the major element of cytoskeleton protein. On the other hand, Pb was detected on the outline of the cell. Pb was absorbed only to the surface of the cell, because the cell had been pre-killed and could not do the biological process such as metabolism and excretion. To estimate the spatial resolution of this method, we get the profile at the white arrows in Fig. 2 and fit a Gaussian curve. The estimated FWHM is $4.4 \pm 0.6 \mu\text{m}$, which is the best performance of PIXE-CT in our study.

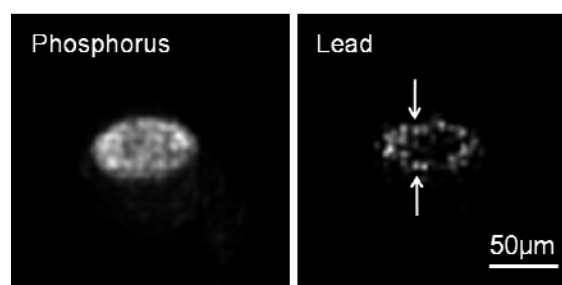


Fig 2 3D distributions of phosphorus and Pb. They were reconstructed from twenty projections of micro-PIXE using the ML-EM algorithm. The white arrows show the position of the profile used for the estimation of the spatial resolution.

References

- 1) T. Satoh et al., Nucl. Instrum. Meth. B 267 (2009) 2125.
- 2) L. A. Shepp et al., IEEE Trans. Nucl. Sci. 21 (1974) 21.
- 3) C. Michelet et al., Nucl. Instrum. Meth. B 158 (1999) 361.
- 4) K. Lange et al., J. Compt. Assist. Tomogr. 8 (1983) 306.

3-22 The Effects of Essence of Chicken on the Trace Metal Distribution in Stressful Mice Brain Slices by In-Air Micro-PIXE

E. Sakurai^{b, c)}, K. Yanai^{b)}, K. Ishii^{a)}, K. Fujiki^{a)}, S. Hiraishi^{a)}, H. Yamazaki^{a)}, S. Matsuyama^{a)}, N. Okamura^{b)}, A. Yokoyama^{d)}, W. Kada^{d)}, M. Koka^{d)}, T. Satoh^{d)} and T. Kamiya^{d)}

^{a)} Department of Quantum Science and Energy Engineering, Tohoku University,

^{b)} Department of Pharmacology, Tohoku University School of Medicine,

^{c)} Faculty of Pharmacy, Iwaki Meisei University,

^{d)} Department of Advanced Radiation Technology, TARRI, JAEA

Stress has many effects on the brain. Histaminergic neuron system has closely associated with acute and chronic stress responses¹⁾. Our previous reports have shown that zinc levels were decreased in the subjected psychological stress histamine H3 receptor knockout mice (H3-KO) brain slices. Histamine H3 receptor exits in pre-synaptic terminals and may alteration histamine release and modulates other neuron-systems¹⁾. We hypothecate that H3-KO mice may have resistance of stress. On the other hand, essence of chicken (BEC) contains a lot of histidine, carnosine (β -alanyl histidine) and anserine (β -alanyl methyl histidine), which have been used for many years as a traditional health food in Southeastern Asia. Histidine is neuronal histamine precursor. In this experiment, we examined the effects of essence of chicken (BEC) on stressful H3-KO mice and distribution changes of trace metal in the brain. Mice were administered orally 1 mL of BEC before subjected stress. And 50 mg/kg /day of 5-bromo-deoxyuridine (BrdU) were injected for 5 consecutive days, 2 h before the behavioral studies. PIXE (Particle Induced X-ray Emission) is a powerful method for the analysis of trace elements. Bromine is a useful marker to detect new born cells in the brain and is used widely for hippocampal neurogenesis experiments. In-air micro-PIXE was developed at the Takasaki Ion Accelerators for Advanced Radiation Application (TIARA), JAEA. Micro-PIXE allows analyzing the spatial distribution of the elements quantitatively.

H3-KO mice were randomly divided into 3 groups. Mice were restrained in a mouse holder for 4 h during 5 consecutive days as a physical group, and the other mice were set next to the restrained cages as a psychological stress group. The control mice were kept in a separate room. After behavioral studies, mice brains were quickly removed and each brain was cryosectioned sagittally at 16 μ m thickness.

Figure 1 shows the beam irradiation image in region of $100 \times 100 \mu\text{m}^2$ in the brain slice of control, subjected psychological stress and physical stress mice. All mice were BEC-treated. The image on the extreme left indicates for the control mice (no-stress). The accumulate image of zinc and bromine were shown under micrograph of the each brain slices.

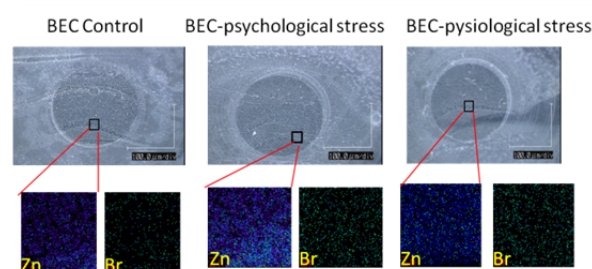


Fig. 1 Beam irradiation, zinc and bromine image ($100 \times 100 \mu\text{m}$) of H3-KO brain slices.

The amount of Zinc in the slices of subjected restraint stress (physical stress) or no-stress control group are almost same when compared with BEC treated group. However, the amount of zinc in the BEC treated slice of subjected psychological stress were significant higher than that of no-treated BEC mice. The amounts of zinc in the slices are shown in Fig. 2.

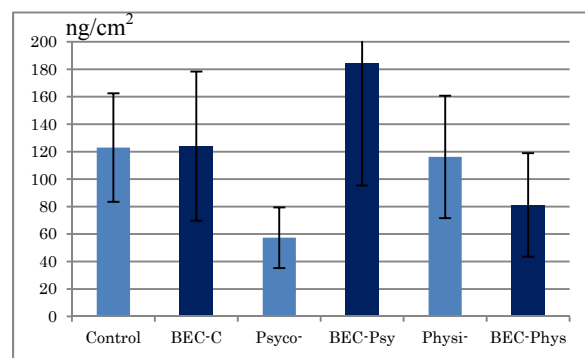


Fig. 2 The effects of BEC on zinc levels in the brain slices.

Bromine level in the brain of BEC treated mice slightly-higher than non-treated mice (Data was not shown). Zinc levels show tended correlation with iron in BEC treated psychological-stress mice brain. BEC might have increased blood flow and the produce anti-stress effect.

References

- 1) T. Watanabe et al., Tohoku J. Exp. Med. 195 (2001) 197-217.
- 2) E. Sakurai et al., JAEA Takasaki Ann. Rep. 2009 (2011) 111.

3-23 Measurement of Fluorine Distribution in Carious Enamel around 1.5-year Aged Fluoride-containing Materials

H. Komatsu^{a)}, K. Kojima^{a)}, Y. Funato^{a)}, Y. Matsuda^{a)}, T. Kijimura^{a)}, K. Okuyama^{a)},
H. Yamamoto^{b)}, Y. Iwami^{b)}, S. Ebisu^{b)}, M. Nomachi^{c)}, K. Yasuda^{d)},
T. Satoh^{e)} and M. Koka^{e)}

^{a)}Graduate School of Dental Medicine, Hokkaido University, ^{b)}Graduate School of Dentistry, Osaka University, ^{c)}Graduate School of Science, Osaka University, ^{d)}The Wakasa wan Energy Research Center, ^{e)}Department of Advanced Radiation Technology, TARRI, JAEA

Introduction

The fluoride contained in some restorative material was demonstrated as a great benefit source for preventing dental caries. However, long-term caries preventive effect of fluoride-containing materials (FCMs) is still a matter of debate, since the amount of fluoride released from FCM decreases with time. The purpose of this study was to measure the fluorine (F) distribution in carious enamel around aged FCMs using an in-air micro-PIGE/PIXE system at TIARA.

Material and Methods

Class V cavities in the buccal surfaces of 6 extracted human teeth were drilled and filled with two glass ionomer cements (fluoride-containing): Fuji IX_{GP} FAST CAPULE (FF) and Fuji IX_{GP} EXTRA (FE), and a fluoride-containing composite resin: Unifil Flow + G-Bond (UF). After storing them in water for 1 day or 1.5 years, 170 µm longitudinal sections including the filling material were obtained from each tooth. All tooth surfaces, except the outer surface of enamel, were coated with a wax. The pH-cycling (pH 6.8-4.5) was carried out for 5 weeks for preparing artificial carious enamel using an automatic pH cycling system¹⁾. After pH-cycling, fluorine and calcium distributions of the outer enamel in each specimen were evaluated using micro-PIGE/PIXE system at TIARA²⁾. The distributions in carious enamel were analyzed at more than 100 µm separation from the cavity wall. The outermost surface of the carious enamel was defined at the position containing 5% of the calcium concentration in intact enamel. For the comparison of F uptake, the average fluorine concentration in each specimen was calculated at area of 150 µm from the defined surface.

Results

Figure 1 shows the fluorine uptake from FCMs into carious enamel after 5-week pH-cycling. There were differences in F uptake among materials and duration of storage in water. Table 1 shows the average fluorine concentration in carious enamel at area of 150 µm from the defined surface. The average fluorine concentration for FF and FE in 1-day storage was significantly higher values comparing to that for UF ($p < 0.05$, Games-Howell test). In 1.5-year storage, there was no difference in the average fluorine concentration among the materials ($p > 0.05$).

Discussion

To estimate caries preventive effect of FCMs, we investigated the F uptake in carious enamel around FCMs during pH-cycling³⁾ as the F uptake resulted from the precipitation of fluorapatite $\text{Ca}_{10}(\text{PO}_4)_6\text{F}_2$ (i.e., remineralization). Therefore, it can be speculated that there was a difference in caries preventive effect among the materials in 1-day storage with the difference in the average fluorine concentration or F uptake. No difference in F uptake among the materials in 1.5-year storage indicated that there was no difference in long-term caries preventive effect among the materials used in the present study. Short-term caries preventive effect of FCM could not predict the existence of long-term effect.

References

- 1) Y. Matsuda et al., Dent. Mater. J. 24 (2006) 280.
- 2) H. Yamamoto et al., Nucl. Instrum. Meth. Phys. Res. B 210 (2003) 388.
- 3) H. Komatsu et al., Nucl. Instrum. Meth. Phys. Res. B 260 (2009) 2136.

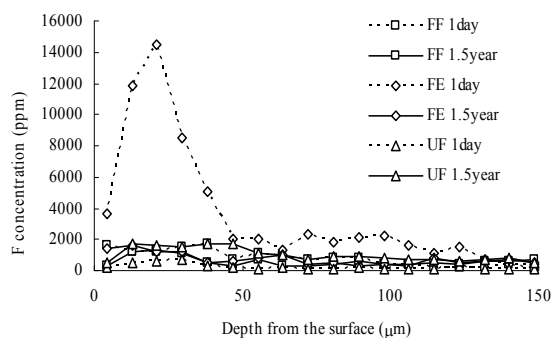


Fig. 1 The fluorine uptake from FCMs into carious enamel after 5-week pH-cycling.

Table 1 The average fluorine concentration (ppm) in carious enamel at area of 150 µm from the surface.

	Duration of storage	
	1-day	1.5-year
FF	795.6 ± 301.1 (5)	595.2 ± 296.2 (4)
FE	3506.1 ± 1876.2 (5)	743.8 ± 255.6 (6)
UF	228.9 ± 125.3 (5)	1021.2 ± 401.9 (6)

Mean ± SD (n)

3-24 The Analysis of Boron Micro-Distribution in 9L Gliosarcoma Cells and HUVEC cells Using PIXE and PIGE

K. Endo^{a)}, Y. Shibata^{a)}, T. Yamamoto^{a)}, K. Nakai^{a)}, A. Matsumura^{a)}, T. Satoh^{b)}, A. Yokoyama^{b)}, M. Koka^{b)}, T. Ohkubo^{b)}, A. Yamazaki^{b)}, Y. Ishii^{b)}, T. Kamiya^{b)} and K. Ishii^{c)}

^{a)} Department of Neurosurgery, Institute of Clinical Medicine, University of Tsukuba, ^{b)} Department of Advanced Radiation Technology, TARRI, JAEA, ^{c)} School of Engineering, Tohoku University

Micro particle-induced X-ray emission (micro-PIXE) was applied to determine the inter- and intracellular distribution of boron-10(¹⁰B) in tumor cells. Because the energy of micro-PIXE from ¹⁰B is too low, particle-induced gamma-ray emission (PIGE) was employed to detect the gamma-rays produced from the nuclear reaction of ¹⁰B (p, γ) ⁷Be.

Cultured 9L gliosarcoma cells and HUVEC cells grown on polycarbonate film were exposed to sodium borocaptate (BSH). To analyze the inter- and intra-cellular distribution of ¹⁰B in 9L gliosarcoma cells, the cells were irradiated with a 1.7 MeV proton beam collimated to a 1 μ m diameter at TIARA and the emitted gamma-rays were detected. The inter- and intracellular distribution of ¹⁰B in cells was directly analyzed using micro-PIXE and PIGE. The results showed that the distribution of ¹⁰B atoms was correctly measured. The distribution of ¹⁰B should have been evenly distributed in 9L gliosarcoma cells. However, there was a significantly high background and the detection of correct ¹⁰B atoms was not easy. The main purpose of this study is to determine the differences of distribution on tumor and normal cells to apply this technique in an *in vitro* experiment.

Cultured 9L gliosarcoma and HUVEC cells were grown for 4 days on a 5 μ m thick polycarbonate film. These cells were treated with 250 ppm of BSH, respectively on the 4th day. These cells were fixed on the polycarbonate film with the acute freezing on the 5th day.

The samples were analyzed to compare the distribution image of the ¹⁰B atoms using the micro-PIXE analysis system at TIARA with a 30 minute measuring time and a measuring range for 100 \times 100 μ m, respectively.

The peak ¹⁰B atom measurement was large on the measurement spectrum in comparison to the circumference background. It was possible to confirm that ¹⁰B atoms were measured.

At the next step, a mask was created from the distribution of sulphur and a suitable threshold value was determined. Thereafter, a PIGE spectrum was created which was specified by the masked portion and the whole spectrum was compared to the masked spectrum.

It was possible to confirm the presence of a correlation in the distribution of sulphur (S) or phosphorus (P) (tumor or normal cells) and the distribution of ¹⁰B atoms because the peak of ¹⁰B atoms appeared more clearly in the masked spectrum.

A more clear correlation was observed between the distribution of tumor and normal cells and the distribution of ¹⁰B atoms when these images were combined. This demonstrated that the ¹⁰B atom was accumulating around and in the cells.

In this *in vitro* experiment, tumor cells and normal cells were compared to show the differences of ¹⁰B distribution. However, we could not see the differences of ¹⁰B distribution clearly (Fig. 1, 2).

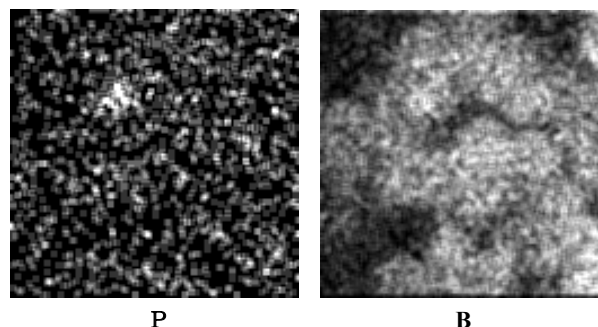


Fig. 1 Distribution of tumor cells(P) and ¹⁰B(B).
Measurement time was 30 minutes.

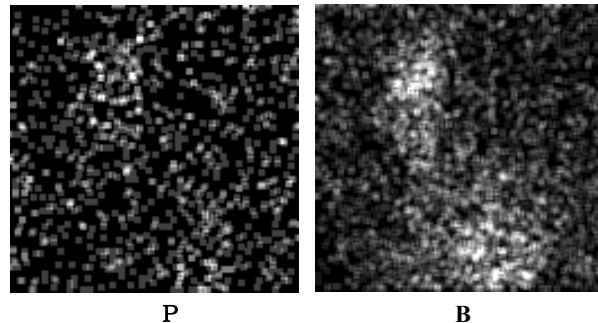


Fig. 2 Distribution of normal cells(P) and ¹⁰B(B).
Measurement time was 30 minutes.

Furthermore the intracellular micro-distribution of boron could not be clearly detected in this analysis. Improvements are therefore necessary in the technical methods of cell fixation, while the micro-PIXE and PIGE analyzing system also needs to be further upgraded.

References

- 1) J. A. Coderre et al., Radiat. Res. 149 (1998) 163-170.
- 2) M. Wegden et al., Nucl. Instrum. Meth. Phys. Res. B 219-220 (2004) 67-71.
- 3) K. Endo et al., Oncol. Res. 16 (2006) 57-65.

3-25 Analysis on the Co-localization of Asbestos Bodies and Fas or CD163 expression in Asbestos Lung Tissue by In-Air Micro-PIXE

K. Dobashi^{a)}, Y. Shimizu^{b)}, S. Matsuzaki^{b)}, T. Nagamine^{a)}, T. Satoh^{c)},
T. Ohkubo^{c)}, A. Yokoyama^{c)}, Y. Ishii^{c)}, T. Kamiya^{c)}, K. Arakawa^{c)},
M. Utsugi^{b)}, T. Ishizuka^{b)} and M. Mori^{b)}

^{a)} Graduate School of Health Sciences, Gunma University,

^{b)} Department of Medicine and Molecular Science, Graduate School of Medicine, Gunma University,

^{c)} Department of Advanced Radiation Technology, TARRI, JAEA

In-air microparticle-induced X-ray emission (in-air micro-PIXE) analysis is based on irradiation of specimens with a proton ion microbeam, and has been modified for biological application. Two-dimensional analysis and quantitative analysis using the system confirmed that asbestos induced apoptosis by upregulating Fas expression and also revealed the accumulation of CD163-expressing macrophages in the lungs of patients with asbestosis. By quantitative comparison of the area of Fas or CD163 expression and the Fas- or CD163-negative area in asbestos lung tissue, the harmful levels which caused the expression of Fas or CD163 could be estimated on Silica, Ferrous iron, and Magnesium deposition. These results indicate that the system could be very useful for investigating the pathogenesis of inhaled asbestos-induced immune reactions and for determining harmful levels of asbestos.

アスベストは、天然の鉱物繊維で長さは約 8 μm 、幅約 0.1 μm 、断熱性、耐火性、防音性、耐腐食性に優れており、建築用製材などに多く用いられてきた。しかし、アスベストの吸入は、肺線維症や肺ガンの原因で、発病までの潜伏期間が数 10 年と長いことから、「静かな時限爆弾」とも言われ、大変な社会問題となっている。早期診断や病態解明には、肺内でのアスベストの種類、量、分布などを、人肺組織内で特定することが不可欠だが、今まで外科的に大きな肺組織を採取しなければならず、簡単に調べられなかった。我々は、独立行政法人日本原子力研究開発機構（以下「原子力機構」と）21 世紀 COE プログラムの一環として共同研究を組織し、原子力機構が開発した大気マイクロ PIXE 分析技術を応用して、数 mg の肺組織の中のケイ素や金属元素の二次元分布を、1 μm の解像度で画像化する分析法を開発した。本法により世界で初めて、吸入したアスベストを肺組織中に存在したままで画像化することに成功し、2008 年 10 月に *International journal of immunopathology and pharmacology* に論文掲載された¹⁾。この新方式は、気管支鏡などで簡単に採取できるわずかな肺組織があれば、肺組織中のアスベストの正確な存在や組成分析を可能にする画期的なものである。これにより、アスベスト吸引の有無を早期に診断し、その後の迅速な対処を可能にした。その他に、環境からの粉じん暴露による肺内の重金属沈着の有無の診断など、種々の応用が期待される。

今年度、病態解明では、我々はアスベストの周囲に一致して、ヘモグロビンを貪食するマクロファージ (CD163 発現細胞) の集積とアポトーシスを引き起こし肺線維化に関与する Fas の発現が増強していることを明らかにした (Fig. 1)。しかも、アスベスト肺患者の肺組織に Fas や CD163 が発現している部分と発現していない部分で、アスベスト成分である Si, Fe, Mg の量を S に対する比率で求めると、Fas, CD163 発現部位でこれらの元素が高値を示し、アスベストの存在が周囲に炎症を惹起し、これらタンパク質の発現を誘導していることが示唆された²⁾。大気マイクロ PIXE による研究は、吸入粒子により引き起こされた免疫反応の病態解明や吸入物質の有害レベルの決定に極めて有用である。

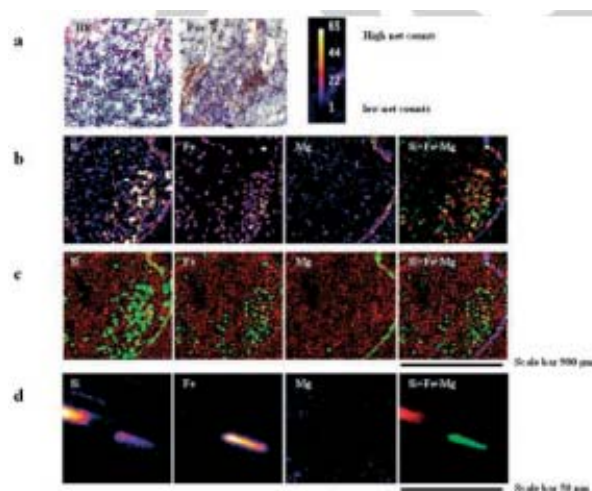


Fig. 1 Immunohistochemical analysis of Fas expression and in-air micro-PIXE analysis of a lung specimen from an asbestosis patient. H-E staining shows lymphocyte accumulation, and immunohistochemistry shows Fas expression by accumulated lymphocytes ($\times 100$) (a). In-air micro-PIXE analysis of the same area of the H-E-stained and immunostained lung section (b-c). In-air micro-PIXE analysis reveals the amounts of Si, Fe and Mg, which are shown by color-coding from white (high) to red (middle) and blue (low) (b). Panels (c) show Si, Fe, and Mg indicated by green and superimposed on the background S (red). Superimposition of Si, Fe, and Mg maps reveals the mixed color pattern of asbestos. In panels (b-c), each element is indicated by a different color: Si (red), Fe (green), and Mg (blue). A small square area in panel (b) is that which was analyzed for confirmation of the elements composing asbestos bodies in the immunostained area. The proton ion microbeam was focused on a small square area of 50 μm . The small area was analyzed for Si, Fe, and Mg (d). Superimposition of Si, Fe, and Mg maps shows a mixed color pattern: Si (red), Fe (green), and Mg (blue). Mg was very low in this area. The findings confirm that asbestos bodies composed of Si, Fe, and Mg exist at the site of Fas expression.

References

- 1) Y. Shimizu et al., *Int. J. Immunopathol. Pharmacol.* 21(3) (2008) 567-76.
- 2) S. Matsuzaki et al., *Int. J. Immunopathol. Pharmacol.* 23(1) (2010) 1-11.

3-26 Analysis of Trace Elements in Erythrocytes Obtained from Dialysis Patients Using In-Air Micro PIXE

H. Kikuchi^{a)}, T. Nagamine^{a)}, Y. Tokita^{a)}, T. Satoh^{b)} and T. Kamiya^{b)}

^{a)} Graduate School of Health Sciences, Gunma University,

^{b)} Department of Advanced Radiation Technology, TARRI, JAEA

1. Introduction

In order to treat hemo-dialysis patients who have advanced anemia, erythropoietin is often prescribed, but the pathogenesis of this kind of anemia is not yet fully understood. Moreover, the trace elements in hemo-dialysis patients, such as aluminum, zinc, iron, lynn, and calcium are suggested to cause the abnormal metabolism associated with the physical conditions in these patients.

Erythrocyte is a specimen which is easy to use for the analysis of the trace elements in internal organs of living subjects and appropriate material to investigate the distributions of those elements. In this research, the trace elements of erythrocyte in hemo-dialysis patients were analyzed by in-air micro-PIXE, and the pathogenesis of the anemia in these patients were elucidated

2. Object and Method

From four healthy controls and five hemo-dialysis patients, bloods were collected in the container containing EDTA-2Na, and the sample for PIXE measurement was prepared by the Ortega strange method¹⁾. Briefly, the physiology salt solution was added into the bloods and were centrifuged at 1,400 rpm for 5 minutes, and removed the supernatants. Residual erythrocytes were dropped on mayler membrane, and this membrane was sunk into isopentane cooled at -150 °C by liquid nitrogen, then lyophilized by vacuum evaporation.

Three point zero MeV proton beams in 1- μ m diameter that was generated by the TIARA single-ended accelerator at JAEA-Takasaki, was used to analyze elemental distribution of erythrocytes.

3. Results and Discussion

Comparison of erythrocytes form in hemo-dialysis patients and healthy controls was shown in Fig. 1. The form of a normal erythrocyte shows a dent at the center of erythrocyte. A large number of erythrocytes in hemo-dialysis patient's bloods did not show a dent at the center of erythrocyte. The change of the erythrocyte form was also observed in patients with hereditary spherocytosis. Iron distribution was similar between the hemo-dialysis patients and healthy controls (Fig. 1). Other elements did not show clear difference of distribution between the hemo-dialysis patients and healthy controls.

The difference of erythrocyte form in hemo-dialysis patients from normal controls was found in this research, however the pathogenesis of the changes was not still clear. The further studies are necessary to clarify the phenomenon.

Reference

- 1) R. Ortega, Cell. Mol. Biol. 42 (1996) 77-88.

Morphological changes of erythrocytes

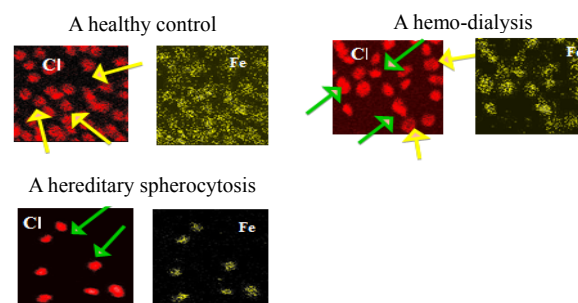


Fig. 1 Erythrocytes are demarcated by the distribution of Cl (red). Erythrocytes showed a dent (yellow arrow) in healthy control, but not dented (green arrow) in patients with hemodialysis and hereditary spherocytosis.

3-27 Increased Antitumor Effect of Chemotherapy, Using Radiosensitive Microcapsules Containing Anti-RLIP076

S. Harada ^{a)}, S. Ehara ^{a)}, K. Ishii ^{b)}, T. Satoh ^{c)}, S. Yamazaki ^{b)},
N. Matsuyama ^{b)} and T. Kamiya ^{c)}

^{a)} Iwate Medical University, ^{b)} Tohoku University,

^{c)} Department of Advanced Radiation Technology, TARRI, JAEA

Introduction

From 2005, we have been developing microcapsules that release their core contents (chemotherapeutic reagents) with response to irradiation ^{1), 2)}. Their antitumor effect in combination with radiation has been tested in inoculated MM48 tumor in VIVO in C3He mice. As a result, the antitumor effect was increased by synergism between released chemotherapeutic reagents and radiation. In addition, encapsulated chemotherapeutic reagents revealed longer antitumor effect ²⁾. The reason for this was considered that the continuous release of chemotherapeutic reagent from outer shell of capsules continuously increased its intratumoral concentration.

RLIP 76 is a peptide (76 kDa) that is activated by radiation, which mediates ATP-dependent primary active efflux of organic anionic compounds (reactive oxygen species, ROS), and cationic chemotherapeutic drugs (doxorubicin, adriacin, carboplatin). Thus, the inhibition of RLIP76 by Anti-RLIP 76 antibody might inhibit the efflux of ROS and chemotherapeutic reagents, and increase intratumoral concentration of chemotherapeutic reagents, which might result in increased antitumor effect. In this study, we encapsulated carboplatin (platinum based anticancer drug) and anti-RLIP 76 IgG, and their antitumor effect was tested in combination with radiation.

Methods and Materials

The MM48 tumor was inoculated in the left hind legs of C3He mice. The microcapsules were prepared following procedures. The mixture of 0.2% (weight/volume) and 0.1% (weight/volume), supplemented with 0.3% H₂O₂ were prepared in agate pestle. To this mixture, 0.2 mmol carboplatin (a platinum (Pt)-containing anticancer drug) and 3 μ mol anti-RLIP-76 IgG was added. A droplet of this mixture was sonicated using an ultrasound disintegrator and atomized to yield a 0.5 mol of each of CaCl₂ and FeCl₂. The polymerization was completed within 5 min to yield microcapsules. 1×10^{10} Micorcapsules were subcutaneously injected around the tumor. Then the 10 Gy of 800 keV soft X-ray generated by Softex 1000 MV was given to the tumor at Iwate Medical University.

Results and Discussion

In micro-PIXE camera imaging, unirradiated microcapsules had smooth surface and distinct liquid core (Fig.-1-A). After radiation, the contour of microcapsules was made irregular and releasing of carboplatin could be observed (Fig.-1 B). 76.2 \pm 4.6% of microcapsules

underwent these morphological changes and releasing of carboplatin and anti-RLIP76 was observed. The released carboplatin was deposited in the tumor tissue (Fig.-1-B) and revealed better antitumor effect in combination with radiation (Fig.-2 (Δ , —)). The encapsulated carboplatin (Fig.-2 (Δ , —)) revealed longer antitumor effect, relative to unencapsulated carboplatin (Fig.-2 (\blacktriangle , \bullet)). Addition of RLIP-76 increased antitumor effect, relative to the radiation and encapsulated carboplatin (Fig.-2 (Δ , —)).

As the reason for these phenomena, it is considered that the continuous release of carboplatin from shell of microcapsules brought about longer increased intratumoral carboplatin's concentration. Then anti-RLIP-76 IgG inhibited the efflux of carboplatin from tumors.

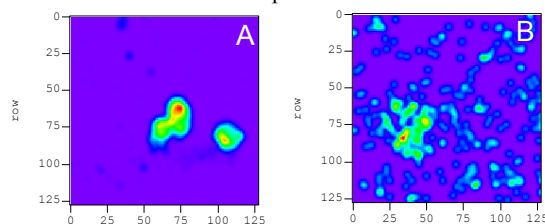


Fig. 1 The distributions of Platinum in microcapsules using micro PIXE camera. A: Before radiation. B: After irradiation.

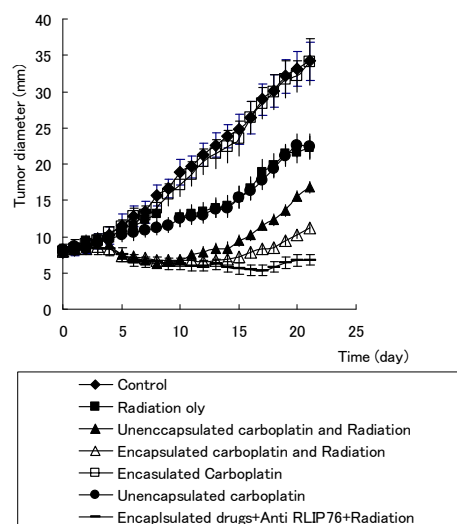


Fig. 2 Antitumor effect. The tumor diameter (mm) was plotted against time (day).

References

- 1) S. Harada et al., Int. J. PIXE 20 (2010) 30-36.
- 2) S. Harada et al., Int. J. Radiat. Oncol., Biol. Phys. 175 (2009) 455-462.

3-28 Elemental Mapping and Estimation of Elemental Abundances of Lichen by TIARA Micro Beam PIXE

Y. Iwata^{a)}, K. Ishii^{b)}, T. Kamiya^{c)} and T. Satoh^{c)}

^{a)} Department of Chemistry, Faculty of Education and Human Studies, Akita University,
Department of Quantum Science and Engineering, ^{b)} Graduate School of Engineering,
Tohoku University, ^{c)} Department of Advanced Radiation Technology, TARRI, JAEA

Distribution and abundance of several elements in a lichen sample were searched by micro beam PIXE. Dried fruticose lichen (*Cladonia amaurocraea* (Florke) Schaer.) was cut to 25 μm slice sample and mounted on the target folder. It was subjected to 3 MeV proton bombardments by the micro beam PIXE system of TIARA. The elemental maps made by the distribution of K and Cl show the shape of the section of the lichen slice. S and P were mainly distributed on the upper cortical layer. Si deposited between inner cortical layer and algal layer, and also deposited on the inner wall of algal layer. Elemental abundances for S, P and Ca were estimated by the intensity of characteristic X-ray and analytical sensitivity of the micro beam PIXE, for instance, S in the upper cortical layer was 2.6 mg cm^{-3} and Ca in the algal layer was 0.2 mg cm^{-3} .

1. PIXE分析における装置の校正や分析値の相互比較のために、イオン交換樹脂中に分析目的元素を正確量含有する標準物質を開発し、TIARAマイクロPIXEにおける、アルミニウム、カルシウム、マンガン、鉄、コバルト、ニッケル、銅、亜鉛、ストロンチウムおよび鉛の分析感度を求めた¹⁾。本研究では、実試料として地衣類をとりあげ、試料調製法と元素分布を調べ、分析感度から元素存在量を見積もったので報告する。

2. 地衣類の照射試料調製 ホグロハナゴケ（樹枝状地衣類、*Cladonia amaurocraea* (Florke) Schaer. 白神山地小岳山頂部 1993年9月15日採取）の乾燥標本を凍結切片作成用包埋剤（Tissue-Tek O.C.T. Compound）を用い、 -21°C で包埋した。これをクライオトームで、樹枝の断面方向に厚さ25 μm で切り出し、薄切片とした。切片は直径0.6 mmの同心円状で、中心部は空洞となった。これを、粘性カーボンテープに接着し、さらにポリカーボネート膜を貼り付けたターゲットホルダーに接着した。

3. マイクロPIXE分析 3 MeV H^{+} ビームをサブミクロンに絞って照射した。スキャンエリアを50×50から200×200 μm とし、大気中100 nCの照射を行った。

4. 地衣類の概形 マイクロPIXE分析による、樹枝状地衣類の断面の塩素の分布図をFig. 1に示す。地衣類は菌類と藻類との共生体で、樹枝状地衣類では、同心円状の組織を持つ。外から菌糸からなる上皮層(A)、藻類細胞からなる藻類層(B)で、中心部は空洞(C)である。塩素およびカリウムの分布図は地衣類の概形をよく表現していた。

リン、硫黄、カルシウムおよびケイ素の分布マイクロPIXE分析による、樹枝状地衣類の断面の硫黄の分布図を示す(Fig. 2)。硫黄は上皮

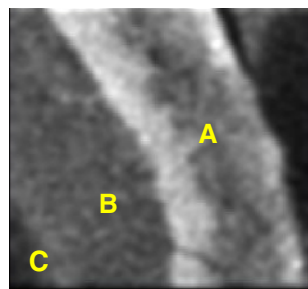


Fig. 1 Elemental mapping of Cl in sectional sample of lichen* by micro beam PIXE.

**Cladonia amaurocraea*, Image Size: 200 × 200 μm .

A: Cortical layer (fungal hyphae),
B: Algal layer (algal cells),
C: (hole).

層の外側(A)に分布していることがわかる。リンも同様であった。一方、ケイ素は、Fig. 1の(B)と(C)の境界、ならびに(C)の内壁に斑点状に沈着していた。またカルシウムは(B)より(A)に多く、それぞれの層では均一に分布していた。このようにマイクロPIXE分析により、地衣類中の元素分布が測定できた。白神山地産の地衣類には比較的多くの鉄、亜鉛等の重金属が含まれているが²⁾、今回はその分布を測定できなかった。

5. 硫黄、リンおよびカルシウムの元素存在度 特性X線の強度とTIARAマイクロPIXEシステムの分析感度¹⁾から、Fig. 2に示すaからcの部分の元素存在度を見積もった。このシステムでは、アルミニウムからカルシウムの感度がほぼ均一であることがわかっており、元素1 pgあたり1 nC照射による特性X線強度は、70カウントとした。なお、試料の厚さは25 μm として単位体積当たりの存在度を計算した。塩素およびカリウムについては、地衣試料のないバックグラウンド部分にも不純物として存在したため、定量できなかった。結果をTable 1に示す。地衣類を一定の厚さで切り出し、マイクロPIXE分析によりその概形を調べることができた。また、標準物質から求めた分析感度から、元素存在度を示すことが出来た。

References

- 1) Y. Iwata et al., JAEA Takasaki Ann. Rep. 2009 (2011) 118.
- 2) 岩田 吉弘他, NMCC 共同利用研究成果報文集, 16 (2009) 212.

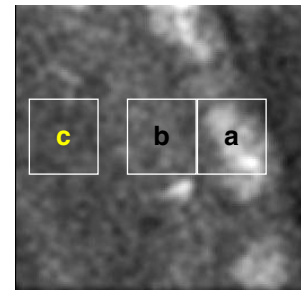


Fig. 2 Elemental mapping for S in a lichen* and analytical areas for elemental abundances.

**Cladonia amaurocraea*, Image Size: 200 × 200 μm .

a: Upper Cortical layer,
b: Inner Cortical layer,
c: Algal layer.

Table 1 Estimation of elemental abundances in lichens by micro beam PIXE (mg cm^{-3}).

	Sampling Section*		
	a	b	c
P	1.3	0.3	ND
S	2.6	0.7	0.2
Ca	0.8	0.7	0.2

*Sections a - c are shown in Fig. 2.

3-29 Preparation and Biological Evaluation of 3-^[76Br]Bromo- α -methyl-L-tyrosine, a Novel Tyrosine Analog for PET Imaging of Tumors

Y. Ohshima^{a)}, H. Hanaoka^{b)}, Sh. Watanabe^{a)}, Y. Sugo^{a)}, Sa. Watanabe^{a)}, H. Tominaga^{c)}, N. Oriuchi^{d)}, K. Endo^{d)} and N. S. Ishioka^{a)}

^{a)} Life Science and Biotechnology Division, QuBS, JAEA, ^{b)} Department of Bioimaging Information Analysis, Gunma University Graduate School of Medicine, ^{c)} Department of Diagnostic Radiology and Nuclear Medicine, Gunma University Graduate School of Medicine,

^{d)} Department of Molecular Imaging, Gunma University Graduate School of Medicine

Introduction: 3-^[18F]Fluoro- α -methyl-L-tyrosine (^[18F]FAMT) is a useful amino acid tracer for PET imaging of malignant tumors¹⁾. However, since the radiolabeling yield of ^[18F]FAMT is low and the half-life of ¹⁸F ($t_{1/2}$ =110 min) is not long, ^[18F]FAMT is not suitable for widespread use. FAMT analogs labeled with ⁷⁶Br, a positron emitter with a long half-life ($t_{1/2}$ =16.1 h), could potentially be widely used as amino acid tracers for tumor imaging. In this study, 3-^[76Br]bromo- α -methyl-L-tyrosine (^[76Br]BAMT) was designed, and its usefulness was evaluated as a novel PET tracer for imaging malignant tumors²⁾.

Methods: In this study, both ^[76Br]BAMT and ^[77Br]BAMT were prepared with radiobromination of α -methyl-L-tyrosine in reaction solution containing *N*-chlorosuccinimide at room temperature (Fig. 1). The *in vitro* and *in vivo* stability of ^[77Br]BAMT was evaluated by HPLC analysis. Cellular uptake and retention of ^[77Br]BAMT and ^[18F]FAMT were evaluated using LS180 colon adenocarcinoma cells. Biodistribution studies were performed in normal mice and in LS180 tumor-bearing mice. PET imaging was performed after administration of ^[76Br]BAMT and ^[18F]FAMT with a small-animal PET scanner.

Results: The radiolabeling yield of ^[76Br]BAMT and ^[77Br]BAMT was approximately 20-30% and radiochemical purity was approximately 99%. The specific activities of ^[76Br]BAMT and ^[77Br]BAMT were over 10 GBq/ μ mol. ^[77Br]BAMT was stable *in vitro*, but was catabolized after administration in mice. Cellular accumulation and retention of ^[77Br]BAMT were significantly higher than those of ^[18F]FAMT. In biodistribution study, the tumor accumulation of ^[77Br]BAMT was higher than that of ^[18F]FAMT (Table 1). However, some level of debromination was seen, which caused more retention of radioactivity in the blood and organs than was seen with ^[18F]FAMT. PET imaging with ^[76Br]BAMT enabled clear visualization of the tumor, and the whole-body image using ^[76Br]BAMT was similar to that using ^[18F]FAMT (Fig. 2).

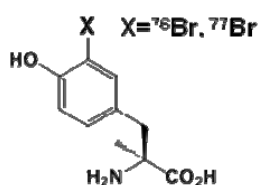


Fig. 1 Chemical structure of BAMT.

Conclusions: ^[77Br]BAMT showed high levels of tumor accumulation, and ^[76Br]BAMT enabled clear visualization of the tumor by PET imaging. Although an improvement in stability is still needed, ⁷⁶Br-labeled FAMT analogs could potentially serve as PET tracers for the imaging of malignant tumors.

References

- 1) T. Inoue et al., J. Nucl. Med. 39(4) (1998) 663-7.
- 2) Y. Ohshima et al., Nucl. Med. Biol. (2011), in press.

Table 1 Biodistribution of ^[77Br]BAMT and ^[18F]FAMT in LS180-bearing mice. Each value represents the mean of % injected dose/g of tissue \pm SD ($n \geq 4$).

	Time after administration		
	30 min	1 h	3 h
^[77Br]BAMT			
Blood	3.17 \pm 0.38	1.47 \pm 0.45	1.03 \pm 0.25
Liver	1.74 \pm 0.36	0.68 \pm 0.25	0.31 \pm 0.09
Kidney	54.00 \pm 7.21	22.74 \pm 3.81	6.15 \pm 2.99
Pancreas	10.65 \pm 3.10	3.57 \pm 1.25	0.94 \pm 0.47
Stomach	0.95 \pm 0.15	0.95 \pm 0.34	1.11 \pm 0.40
Muscle	1.88 \pm 0.53	1.15 \pm 0.24	0.47 \pm 0.12
Tumor	5.62 \pm 0.59	4.47 \pm 1.01	2.38 \pm 0.73
^[18F]FAMT			
Blood	2.56 \pm 0.45	0.91 \pm 0.25	0.19 \pm 0.21
Liver	2.63 \pm 0.34	1.03 \pm 0.30	0.17 \pm 0.09
Kidney	60.48 \pm 9.43	25.45 \pm 5.37	6.07 \pm 2.47
Pancreas	17.12 \pm 3.74	7.12 \pm 2.16	1.28 \pm 1.10
Stomach	0.58 \pm 0.08	0.49 \pm 0.27	0.18 \pm 0.13
Muscle	1.75 \pm 0.52	1.18 \pm 0.25	0.55 \pm 0.11
Tumor	5.91 \pm 0.54	4.19 \pm 0.65	1.35 \pm 0.41

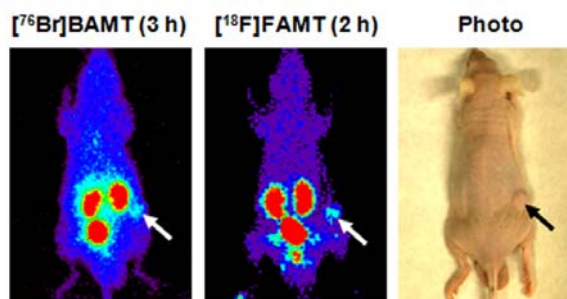


Fig. 2 PET images of LS180-bearing mice with ^[76Br]BAMT (5 MBq) and ^[18F]FAMT (10 MBq). Mice were imaged at the indicated time after intravenous administration of each PET tracer. Arrows indicate the position of the implanted tumor.

3-30 Production of Radioactive Bromine Br-76

Sa. Watanabe^{a)}, Sh. Watanabe^{a)}, Y. Iida^{b)}, H. Hanaoka^{b)}, K. Endo^{b)} and N. S. Ishioka^{a)}

^{a)} Life Science and Biotechnology Division, QuBS, JAEA,

^{b)} Graduate School of Medicine, Gunma University

Positron Emission Tomography (PET) is a powerful noninvasive molecular imaging technique. However, the positron emitting radionuclides used for PET are only ^{11}C ($T_{1/2}=20.4$ min), ^{13}N ($T_{1/2}=9.97$ min), ^{15}O ($T_{1/2}=2.04$ min) and ^{18}F ($T_{1/2}=1.83$ h). Since the half-lives of these radionuclides are very short, the use of these radionuclides must have on-site isotope production facilities. If we can use a novel positron emitting radionuclide with longer half-life than ^{18}F , PET diagnosis can be performed at medical institutions having no on-site isotope production facilities. However, suitable half-life for diagnosis is less than several days owing to the radiation exposure of patients. So we searched the radionuclides with half-life between several hours and several days, and chose ^{76}Br with half-life of 16.2 h as a novel positron emitting radionuclide. The ^{76}Br is suitable for the synthesis of radiopharmaceutical, because ^{76}Br is halogen and can bind directly to biopolymers such as peptide or antibody. And also ^{76}Br labeled radiopharmaceuticals can be simply synthesized by the replacement of ^{123}I , ^{131}I or ^{18}F using these commercially produced radiopharmaceuticals.

For the production of ^{76}Br , Tolmachev et al.¹⁾ reported the separation of ^{76}Br by dry distillation with recovery of 65-75% (Fig. 1), and also mentioned the complete separation between ^{76}Br and Se which were condensed at the different positions on the wall of the PTFE tube. However, there is a possibility that ^{76}Br is contaminated by Se, because the distance between ^{76}Br and Se condensed on the PTFE tube is very close. To avoid the contamination of Se, we decided to recover the ^{76}Br at Br trap (Fig. 1). In the present paper, we develop the method to recover the ^{76}Br at the Br trap with recovery of more than 65-75% of Tolmachev et al.

The ^{76}Br production was carried out by the method of Tolmachev et al.¹⁾. Preparation of ^{76}Se -enriched Cu_2Se is as follows. ^{76}Se metal powder enriched up to 99.67% was mixed with Cu metal powder. The mixture was placed in a high vacuum chamber and evacuated by a rotary pump. The chamber was placed in an oven and heated up to 533 °C for 2-3 weeks. The Cu_2Se powder obtained was pressed to make pellet (10 mm diameter \times 1 mm thick). The prepared pellet was placed into the depression of a tungsten sheet (20 mm \times 20 mm \times 1.5 mm thick with a centered depression of 11 mm diameter \times 1 mm depth) and irradiated with 20 MeV protons at 5 μA . After irradiation, ^{76}Br was separated from the target by dry distillation method (Fig. 1). The target with tungsten sheet was inserted into the quartz tube and placed in the middle of the main furnace. The temperature in the main furnace was raised to 1,050 °C and the auxiliary furnace to 200 °C under a constant stream of

argon gas (30 mL/min). The ^{76}Br leaving the target was transferred to the PTFE tube by carrier gas and condensed on the wall of the PTFE tube. A part of the ^{76}Br was transferred until Br trap. The trace amounts of Se were also transferred to the PTFE tube and condensed on the wall of the PTFE tube. To evaluate the recovery of the ^{76}Br in the Br trap, the radioactivity in it was measured with a calibrated Ge detector.

For the result of the separation, the recovery of the ^{76}Br in the Br trap was 30%. For the remaining ^{76}Br , 20% was on the PTFE tube, 30% was in the Cu_2Se target and 20% was in the quartz tube. The ^{76}Br on the PTFE tube was not separated from Se but condensed at the same position of the PTFE tube near exit of the furnace.

We tried to recover the ^{76}Br of 20% in the PTFE tube. We considered that due to the too much high temperature of the auxiliary furnace, the Se was transferred until the exit of the furnace, and suddenly cooled, and finally condensed on the PTFE tube with ^{76}Br . To turn down the temperature of the auxiliary furnace, the heating of the auxiliary furnace was not carried out. As a result, the ^{76}Br of 20% condensed on the PTFE tube was transferred to the Br trap. The recovery of ^{76}Br in the Br trap increased to 50% from 30%.

We also tried to recover the remaining ^{76}Br of 30% in the Cu_2Se target by higher temperature heating. The maximum temperature of our main furnace was 1,050 °C. Since the melting point of the Cu_2Se is 1,113 °C, the ^{76}Br of 30% was remained in the Cu_2Se target. Therefore we used a new furnace with maximum temperature of 1,200 °C. The ^{76}Br in the Cu_2Se target was completely released by using the new main furnace with 1,120 °C, and the recovery of ^{76}Br in the Br trap increased to approximately 80% from 50%. The remaining 20% of the ^{76}Br is condensed in the quartz tube.

Consequently, we succeeded to recover the ^{76}Br at the Br trap with recovery of approximately 80% by optimizing the temperature of the main and the auxiliary furnace.

Reference

- 1) S. Y. Tolmachev et al., Appl. Radiat. Isot. 49 (1998) 1537.

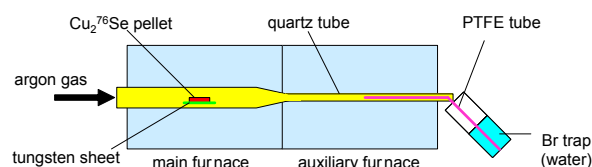


Fig. 1 Schematic diagram of dry distillation system.

3-31 Carbon Kinetic Analysis in a Soybean Plant by Using Newly Developed Real-time Whole-plant Imaging Method with Positron-Emitting Tracer Imaging System (PETIS)

N. Kawachi^{a), d)}, N. Suzui^{a), d)}, S. Ishii^{a), d)}, H. Yamazaki^{a), b), d)}, A. H. Iwasaki^{c), d)},
K. Ogawa^{c), d)} and S. Fujimaki^{a), d)}

^{a)} Life Science and Biotechnology Division, QuBS, JAEA, ^{b)} Faculty of Science and Technology, Tokyo University of Science, ^{c)} Plant Redox Regulation Research Group, Research Institute for Biological Sciences Okayama, ^{d)} JST, CREST

Elucidation of carbon kinetics in a higher plant, in particular photosynthetic carbon dioxide (CO₂) fixation and photoassimilate translocation, is important from viewpoint of environmental reduction in the amounts of atmospheric CO₂ and from an agricultural viewpoint of the growth and development of the plant body. Previously, we have reported that whole-plant imaging for studying the complete carbon kinetics involved in photosynthesis and subsequent photoassimilate translocation and unloading. It was achieved using a positron-emitting tracer imaging system (PETIS) in combination with carbon-11-labeled carbon dioxide (¹¹CO₂) gas tracer^{1,2)}. In this study, real-time carbon kinetics in leaves, roots and other organs of a soybean was analyzed by using the newly developed method.

We performed an experiment with a single plant of the soybean (*Glycine max*) cultivar Jack grown in a square plastic pot filled with vermiculite under a long-day (16-h light / 8-h dark) cycle at a light intensity of 250 μmol photon/m²/s. Three-week-old plant that fit in the PETIS field of view (FOV; 120.8 mm width, 186.8 mm height) was used.

Figure 1 shows time activity curves (TACs) for selected organs. All the TACs were generated from a series of PETIS images that were re-sorted in a sequence covering every 2 min over 60 min for analysis of the selected regions of interests (ROIs). The red dots represent the time course of all activity in the PETIS FOV. The green diamond shaped, blue triangles, orange crosses, and white squares represent the time course of total activity in the leaves, roots, stem, and apex, respectively. We see that approximately 40% of assimilated carbon was translocated to the root area within 1 h. The red dots indicate that the total ¹¹C activity remained stable over the acquisition period, confirming that the PETIS image data indicated the conservative total amount of carbon over the plant body. Newly assimilated ¹¹C was hardly used for respiration, but was translocated and unloaded in the various organs or stored in the leaves in a period of less than 1 h. These kinetics can be analyzed to gain a greater understanding of the plant physiological sink–source relationship. The solid line represents the theoretical translocation rate constant in a leaf predicted by a simplistic exponential kinetic model:

$$L(t) = I_0 \exp\left(-\left(R_{\text{export}} + \lambda\right) \frac{t}{L_s}\right) + L_s,$$

where $L(t)$ is leaf response time–activity curve of the radioactivity concentration at time t after pulse-chase treatment; I_0 , the initial fixation of ¹¹CO₂; R_{export} , ¹¹C-labeled photoassimilate exporting rate; L_s , stored fixed carbon; and λ , the physical decay constant of ¹¹C (0.034 min⁻¹). The translocation rate constant estimated from the fitting process with the simple model was similar to that estimated by compartment analysis. The fitting line of the theoretical prediction was in good agreement with the experimental values for the leaf during the period 10 - 60 min.

We believe this analysis will help it to develop better experimental protocol by understanding of its standard carbon kinetics in plant body. Experiments are now in progress to study the effects of fertilizer application and the environmental conditions.

References

- 1) N. Kawachi et al., JAEA Takasaki Ann. Rep. 2009 (2011)101.
- 2) N. Kawachi et al., Nucl. Instrum. Meth. Phys. Res. A (2011) in press.

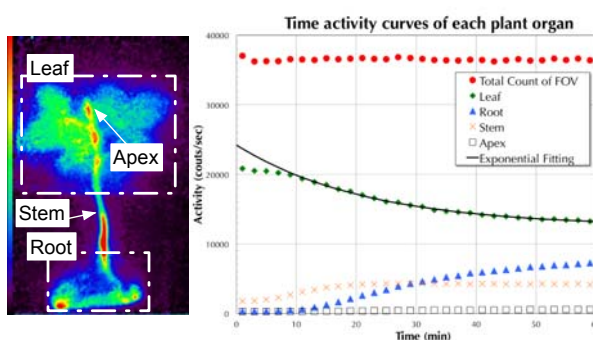


Fig. 1 Time activity curves (TACs) of selected ROIs in the integrated PETIS image data. All TACs were generated from serial PETIS images integrated to one frame every 2 min for 60 min, followed by analysis of the region of interests. The curves were also corrected for radioactive decay of ¹¹C.

3-32 Quantitative Study for Nitrogen Fixation in Intact Soybean Plant from PETIS Imaging

S. Ishii^{a)}, N. Suzui^{a)}, N. Kawachi^{a)}, H. Yamazaki^{a, b)}
N. Ohtake^{c)}, T. Ohyama^{a, c)} and S. Fujimaki^{a)}

^{a)} Life Science and Biotechnology Division, QuBS, JAEA,

^{b)} Faculty of Science and Technology, Tokyo University of Science,

^{c)} Graduate School of Science and Technology, Niigata University

The nodule is a symbiotic organ of leguminous plants with rhizobium. Soybean plants utilize nitrogen (N) fixed by nodules from atmospheric N₂. Until now, ¹⁵N, a stable isotope, has long been used for studies of N₂ fixation. However, because this method is invasive, it has been difficult to analyze an instant response to environmental (ex. temperature, light) changes.

The purpose of our study is to image noninvasively and quantitatively the N₂ fixation in each nodule under various ambient conditions and translocation to the aerial part. Previously, we developed a method of production of ¹³N-labelled nitrogen gas tracer and successfully imaged nitrogen fixation in intact nodules. However, the experimental condition was specially designed for efficient detection and thus unnatural. For example, the composition of the feeding gas to the plant was N₂:O₂:He=10:20:70, in which nonradioactive nitrogen was purposely lowered for high specific radioactivity¹⁾. Moreover, higher radioactivity of the tracer, presumably more than 30 MBq at least, was required for visualization of the translocation of fixed nitrogen to the aerial part. In this study, we set the two objectives. One was to produce ¹³N-labelled nitrogen gas tracer with higher radioactivity. The other was to feed the tracer to test plants with natural composition.

¹³N was produced using the ¹⁶O(p, α)¹³N nuclear reaction. CO₂ was filled in a target chamber and irradiated with proton ions at energy of 18.3 MeV and electric current of 5 μA for 10 min delivered from the cyclotron (TIARA). ¹³N activity at the end of the irradiation was approximately 200 MBq.

We tried various ways to efficiently remove CO₂, which inhibits N₂ fixation in nodules, from the irradiated gas for obtaining a tracer gas with a higher level of ¹³N-labelled nitrogen and a suitable composition. First, we used an alkaline solution. Irradiated gas was blown into vigorously stirred 1 N NaOH solution through spherical filter as small bubbles and the residual insoluble gas was collected.

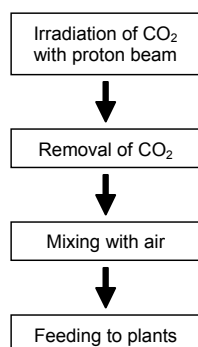


Fig. 1 The scheme of the production of ¹³N-labelled nitrogen.

Unexpectedly, the bubbles of insoluble gas adhered to the side wall of the vessel and/or CO₂ was not removed sufficiently. Radioactivity of the collected gas was only 10 MBq.

Second, we employed freezing of CO₂. The irradiated gas was introduced into a narrow stainless tube chilled with liquid N₂ and methanol, and the outflow gas was collected into another vessel. The temperature was carefully controlled to around the frozen point of CO₂. However, it seemed that too rapid solidification of CO₂ caused trapping of ¹³N-labelled nitrogen gas. The Activity of the collected gas was about 15 MBq.

Lastly, soda lime powder was employed to absorb CO₂ gas. The irradiated gas mixed with a small amount of ambient air was introduced into a vacuum-packed plastic bag including 50 g soda lime. The residual gas was effectively collected by infusing water into bag. In this way, 70 MBq of ¹³N-labelled gas was collected. The collected gas was mixed with ambient air and fed to the underground part of soybean. The serial images by PETIS were collected for 1 h (360 frames × 10 second). As a result, the image as shown in Fig. 2 was obtained. Weak signal was recognized at nodules.

In conclusion, we successfully produced ¹³N-labelled nitrogen tracer with abundant radioactivity and natural composition. However, the signal of nitrogen fixation was too weak to analyze nitrogen fixation and translocation. This was probably because the volume of the feeding vessel was too large and the ¹³N-labelled nitrogen in the feeding gas was diluted too much. Improvement of feeding procedures for higher concentration of ¹³N-labelled nitrogen gas tracer will be the next challenge.

Reference

- 1) S. Ishii et al., Soil Sci. Plant Nutr. 55 (2009) 660-666.

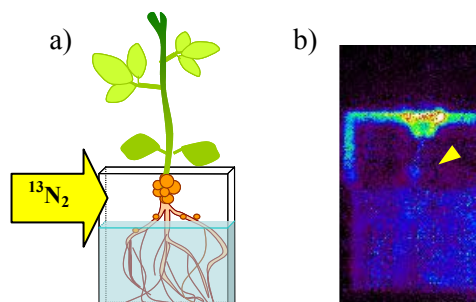


Fig. 2 a) Setting of PETIS experiment, b) Integrated PETIS image. Yellow arrowhead indicates location of nodule.

3-33 Dose Optimization of ^{107}Cd for Direct Imaging of Cd Uptake from Culture to Root

N. Suzui^{a)}, N. Kawachi^{a)}, S. Ishii^{a)}, H. Yamazaki^{a), b)} and S. Fujimaki^{a)}

^{a)} Life Science and Biotechnology Division, QuBS, JAEA,

^{b)} Faculty of Science and Technology, Tokyo University of Science

Introduction

In an effort to understand the mechanism of cadmium (Cd) accumulation in grains, we have conducted noninvasive imaging of Cd in intact rice plants using a positron-emitting tracer imaging system (PETIS) and ^{107}Cd ($t_{1/2} = 6.5 \text{ h}$)¹⁾. In our typical experiment of ^{107}Cd imaging, we feed the hydroponic culture solution including ^{107}Cd to the roots of rice plants and obtain the serial images of ^{107}Cd distribution in the aerial parts, i.e., shoots or grains. Because only 10% of ^{107}Cd fed to the root is translocated to the aerial part in 24 hours, the more dosage of ^{107}Cd enables the more suitable images for subsequent analyses. Specifically, we fed 60 - 120 MBq of ^{107}Cd to the roots of several rice plants, resulting in long-time tracing of Cd dynamics in the aerial parts.

Recently, we attempt to obtain the serial images of ^{107}Cd in underground parts, i.e., roots and culture solutions, in order to estimate the uptake velocity from culture to root. In this case, the dosage of ^{107}Cd should be optimized because the presence of high radioactivity in the field of view (FOV) of PETIS induces the counting loss of annihilation gamma-rays, resulting the underestimation of radioactivity. Although ^{107}Cd is a weak positron emitter (0.2%), other gamma-rays affect the PETIS detector and the counting loss is observed. In this study, we determined the optimal dosage of ^{107}Cd for direct imaging of Cd uptake.

Results and Discussion

^{107}Cd solution was produced and purified at TIARA as described previously²⁾, and was infused into a flat "phantom" container (3 mm thickness, 210 mm width, 330 mm height). This phantom was measured by PETIS for 24 hours while the radioactivity of ^{107}Cd in FOV (120 mm width, 187 mm height) decayed to 1/13 of its initial value. For the comparison with the case of pure positron emitter, the same measurement using ^{18}F ($t_{1/2} = 110 \text{ min}$, positron decay ratio: 96.7%) was also conducted.

Figure 1 shows time-course of PETIS counts of ^{107}Cd and ^{18}F phantom. Although decay correction was applied, counting data sets of ^{107}Cd and ^{18}F phantom were not constant, but showed a plateau curve. This result indicates that the counting loss of annihilation gamma-rays was certainly occurred. In ^{107}Cd phantom, the counting loss was diminished after the radioactivity of ^{107}Cd in FOV decayed to below 8 MBq.

On the other hand, we should allow some degree of counting loss at the initial period of imaging in order to obtain the images for kinetic analyses over the longer time period. When 5% of counting loss was allowed, the optimal dosage of ^{107}Cd for the purpose was determined to be 15 MBq.

References

- 1) S. Fujimaki et al., Plant Physiol. 152 (2010) 1796-1806.
- 2) N. S. Ishioka et al., JAERI TIARA Ann. Rep. 2004 (2006) 277-279.

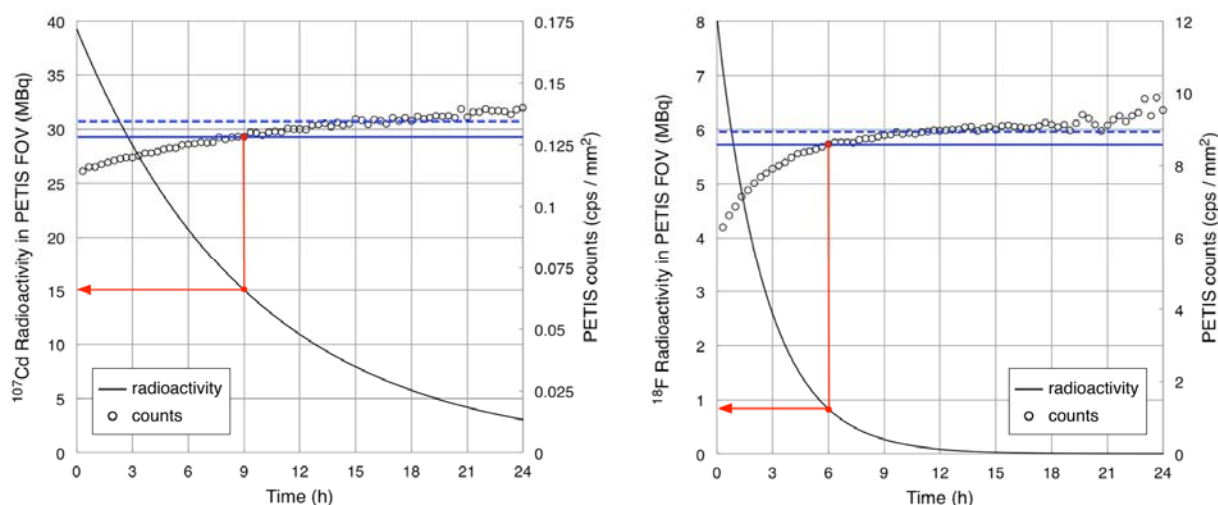


Fig. 1 Time-course of PETIS counts of ^{107}Cd (left) and ^{18}F (right) phantom. All counts were decay-corrected to the start time of imaging. The solid curve indicates radioactivity in FOV of PETIS during the measurement. The blue line represents 100% (dotted) and 95% (solid) of the plateau value of time-count curve. The red arrow indicates the determined optimal dosage.

3-34 Comparison of ^{107}Cd Absorption and Accumulation between Transgenic Tobacco Plants and Control Plants

S. Nakamura^{a)}, N. Suzui^{b)}, S. Ishii^{b)}, N. Kawachi^{b)}, N.S. Ishioka^{b)}, H. Rai^{a)}, H. Hattori^{a)}, M. Chino^{a)} and S. Fujimaki^{b)}

^{a)} Faculty of Bioresource Sciences, Akita Prefectural University,

^{b)} Life Science and Biotechnology Division, QuBS, JAEA

Cadmium (Cd) is well known as one of the toxic heavy metals. In order to reduce Cd accumulation in farm products, it is necessary to remove Cd from Cd contaminated farmland soils. Phytoremediation is one of good technique to recover Cd from these soils. To make this technique more effective, it is necessary to understand the mechanism of Cd dynamics and control them. It is known that Cd movement in the plant body is similar to zinc (Zn) movement¹⁾. However, these mechanisms are not fully understood so far. In this work, we compared Cd absorption and accumulation between control tobacco plants and transgenic tobacco plants, which were transform with zinc transporter genes, in order to examine the effect of zinc transporter on Cd dynamics in the plant body by using positron-emitting tracer imaging system (PETIS). PETIS is a planar imaging system in which we can obtain serial images of distribution of positron emitting molecules in the plant body non-invasively²⁾. We already have succeeded in visualizing Cd absorption, transport and accumulation in rice plants³⁾, oilseed rape plants⁴⁾ and so on by using PETIS.

^{107}Cd (half-life: 6.5 h) was used as positron-emitting radioactive tracer in our PETIS experiments. ^{107}Cd was produced by bombarding silver plate with an energetic proton beam delivered from AVF cyclotron at TIARA (Takasaki Ion Accelerators for Advanced Radiation Application). Produced ^{107}Cd was purified, following the method of Ishioka et al⁵⁾. Purified ^{107}Cd was used for PETIS experiments. In these PETIS experiments, tobacco plants (*Nicotiana tabacum*) (control plants and transgenic plants) were used. Transgenic tobacco plants were generated by following the methods of Hayakawa et al⁶⁾. From the results of Cd absorption experiments, transformants (DT11) were selected. Tobacco plants were grown hydroponically in a growth chamber where the plant growth conditions were controlled completely for two weeks after sowing. After setting these plants in the chamber, PETIS experiments were started by adding purified ^{107}Cd in the nutrient solutions. In these PETIS experiments, 0.1 μM Cd was added to hydroponic solutions as a carrier. Time-series images of the ^{107}Cd distribution were obtained every four minutes for 36 h.

We succeeded to obtain fine serial images of Cd absorption and accumulation in tobacco plants (control plant and transgenic plant) (Fig. 1). Strong ^{107}Cd signals were seen in the basal region of the shoots. In oilseed rape plants, we could see strong ^{107}Cd signals in the basal of the shoot⁴⁾. These results demonstrate that the basal of the

shoot plays an important role in distributing Cd in the shoot of the dicotyledonous plants. Figure 1 also shows that there was no difference in Cd absorption and accumulation between transgenic tobacco plants and control plants. In Cd absorption experiments using non-radioactive Cd, Cd content in transgenic plants was 1.2 times higher than that in control plants (unpublished data). However, such differences were not identified clearly in serial images obtained by PETIS experiments. In this study, PETIS experiments were performed in low Cd condition (0.1 μM). Cd concentration might have a significant impact on these results. Further research to characterize these transgenic plants may provide clues to elucidate the mechanism of Cd absorption and accumulation in tobacco plants.

References

- 1) U. Krämer, Ann. Rev. Plant Biol. 61 (2010), 517-534.
- 2) S. Fujimaki, ITE Let. 8 (2007) 404-413.
- 3) S. Fujimaki et al., Plant Physiol. 152 (2010) 1796-1806.
- 4) S. Nakamura et al., JAEA Takasaki Ann. Rep. 2006 (2008) 123.
- 5) N. S. Ishioka et al., JAERI TIARA Ann. Rep. 2004 (2006) 277-279.
- 6) T. Hayakawa et al., Japan Patent Kokai (2004) 2004-275051.

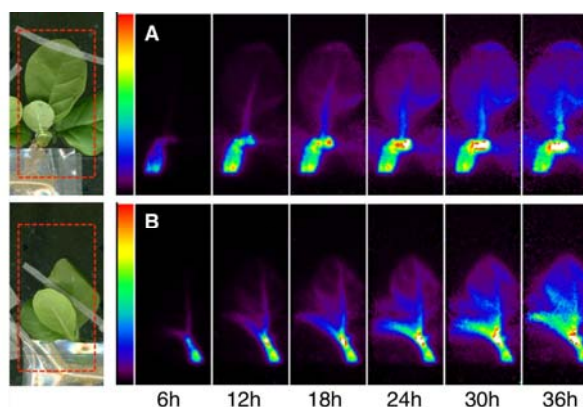


Fig. 1 Accumulation of ^{107}Cd signals in tobacco plants. Each image is integration of 90 original frames, corresponding to six hours. (A) Control tobacco plant (*Nicotiana tabacum* cv. Petite Havana SR-1), (B) Transgenic tobacco plant (DT11) which was transformed with zinc transporter genes from yeast and *Thlaspi caerulescens*.

3-35 Effects of Preceding Light Conditions on Translocation of Photoassimilates from a Leaf into a Fruit

K. Kikuchi^{a)}, S. Ishii^{b)}, N. Kawachi^{b)}, N. Suzui^{b)}, H. Yamazaki^{b), c)} and S. Fujimaki^{b)}

^{a)} Molecular Genetics and Physiology Research Team, National Institute of Vegetable and Tea Science, National Agriculture and Food Research Organization, ^{b)} Life Science and Biotechnology Division, QuBS, JAEA, ^{c)} Faculty of Science and Technology, Tokyo University of Science.

In general, environmental conditions (e.g. light and temperature) strongly affect the accumulation of photoassimilates in the fruits. Therefore, it should one of the most effective approaches for improvement of fruit yield to perform quantitative analyses on dynamics of carbon transport in an individual plant body under various outer conditions. We have previously established a method of non-invasive imaging and quantitative estimation of carbon efflux from an individual eggplant (*Solanum melongena* L.) leaf and influx into a fruit using a positron-emitting tracer imaging system (PETIS) and ^{11}C gas tracer¹⁾. Repetitive experiments on one test plant under various conditions are enabled by the non-invasive measurement with PETIS and quick decay of ^{11}C (half-life: 20 min)²⁾. In this study, we set a focus on quantitative description of the difference of carbon translocation in morning and afternoon time in a plant body. Specifically, effects of dark pretreatment (morning) and light pretreatment (afternoon) on the later carbon transport from an eggplant leaf into a fruit were analyzed.

One of two test plants was subjected to the following sequence of imaging experiments for two days. In the first day, a set of the following experiments was done after 48 h of continuous light pretreatment. Carbon-11-labeled CO_2 gas tracer was fed to the second leaf below the fruit of interest, and carbon dynamics in the leaf (fixation and export) was imaged with PETIS for 120 min. Carbon accumulation into the fruit was also observed for 180 min in the same way after 30 min of interval for sufficient decay of

remaining radioactivity from the first run. In the second day, the same set of experiments was done after 36 h of continuous dark and 30 min of light pretreatment. The inverse order of light and dark pretreatments was given to the other test plant. It should be noted that the environmental conditions including light intensity during the measurement were the same in all the four experimental sets.

As the results, four time-activity curves were obtained from the leaf and fruit from the PETIS data. It was shown that the velocity of outflow of carbon from the leaves was approximately twofold higher in the case after 48 h of light pretreatment than that after 36 h of dark pretreatment (Fig. 1). Accordingly, the influx rate of carbon into the fruits was also twofold (or more) higher with light pretreatment (Fig. 2). These results suggest that the translocation of photoassimilates from the leaves into the fruits is more active in afternoon than morning even if the environmental conditions are the same at the very moment. Detailed analyses according to the actual day length will be performed in the next study for the elucidation of the above hypothesis.

References

- 1) K. Kikuchi et al., Jpn. Soc. Hort. Sci. 77 (2008) 199-205.
- 2) S. Fujimaki, ITE Lett. Batteries New Technol. Med. 8 (2007) 404-413.

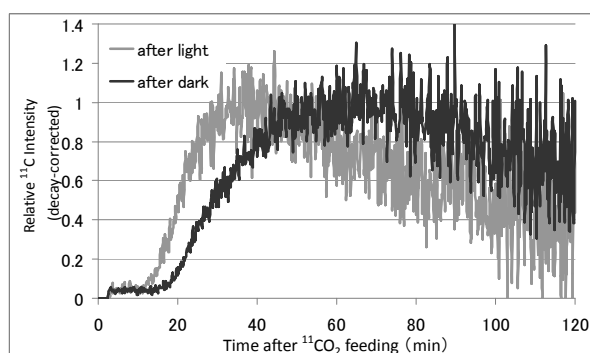


Fig. 1 Time-activity curves in the same region on the petiole of a tested leaf with pretreatment of 48 h of light (gray line) and 36 h of dark (black line). Ratio to counts of peak was indicated as relative intensity.

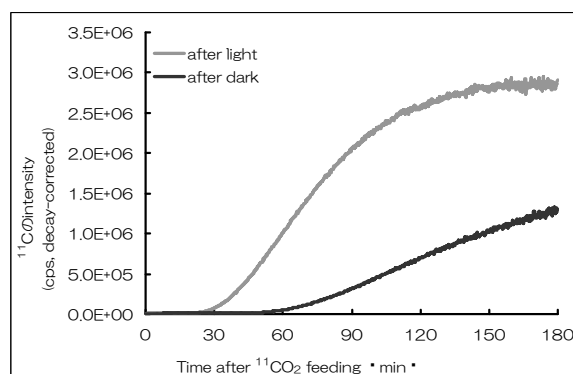


Fig. 2 Time-activity curves in the same fruit with pretreatment of 48 h of light (gray line) and 36 h of dark (black line).

3-36 Analysis of Source-sink Regulation System Using Cold-girdling and Positron-Emitting Tracer Imaging System (PETIS)

H. Yamazaki ^{a, b)}, N. Suzui ^{a)}, N. Kawachi ^{a)}, S. Ishii ^{a)}, H. Shimada ^{b)} and S. Fujimaki ^{a)}

^{a)} Life Science and Biotechnology Division, QuBS, JAEA,

^{b)} Faculty of Science and Technology, Tokyo University of Science

Introduction

Improvement in crop yield is expected by understanding “source-sink regulation system” of higher plants. The system is expressed as supply and demand; source organs (e.g. mature leaves) and sink organs (e.g. roots and fruits) provide and receive photoassimilate, respectively. It is an important issue how photoassimilate from one source is properly distributed to respective sinks. In this study, we analyzed the photoassimilate distribution system to two sink organs, the root and the shoot apex, using cold-girdling technique and positron-emitting tracer imaging system (PETIS). Cold-girdling is known as a method to inhibit photoassimilate translocation by cooling the plant body locally. PETIS visualizes dynamics of photoassimilate translocation non-invasively with ^{11}C (half-life: 20 min.). Quick decay of ^{11}C enables two runs of experiment on one test plant before and during cold-girdling treatment.

Materials and Methods

Carbon-11-labeled carbon dioxide ($^{11}\text{CO}_2$) gas was produced from N_2 gas with nuclear reaction. The N_2 gas was irradiated with protons at energy of 20 MeV, which were delivered from the TIARA AVF cyclotron. The aerial part of soybean (*Glycine max* cv. Jack) was transiently exposed to 40 MBq of $^{11}\text{CO}_2$. Next, ^{11}C -photoassimilate translocation from the source leaf into the sink organs was imaged with PETIS for 120 minutes. $^{11}\text{CO}_2$ exposure and PETIS imaging were conducted two times with the same test plant. Cold-girdling was treated only in the second run by cooling the boundary region on the stem between shoot and root. The interval between two runs was set as more than 30 minutes for sufficient decay of ^{11}C treated in the first run.

Results and Discussion

^{11}C -photoassimilate dynamic images were acquired with PETIS. Time-activity curves were generated from the regions of the root, shoot apex and source leaf in the PETIS data. Then, three indices were analyzed; the influx rates of photoassimilate into the two sink organs, the root and the shoot apex, and the efflux rate from the source leaf. As the results, the influx rate was decreased drastically into the root (Fig. 1). On the other hand, influx into the shoot apex hardly changed (Fig. 2). The efflux rate from the leaf was decreased (Fig. 3). We had expected before the experiment that decrease of the influx rate into the root would lead to increase of influx rate into the shoot apex. However, the

result was different; leaf efflux was decreased. These results suggest that the “source supply” is adjusted so as to keep influx rate of photoassimilate into the untreated sink. Further experiments will be performed to analyze the adjustment mechanism.

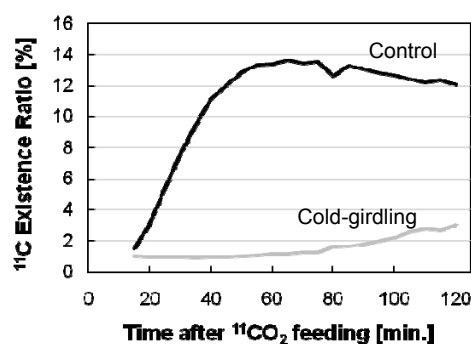


Fig. 1 Time-activity curves in the same region on the root.

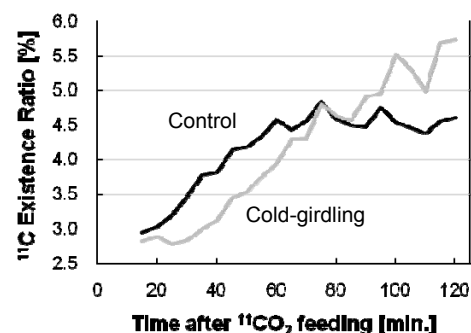


Fig. 2 Time-activity curves in the same region on the shoot apex.

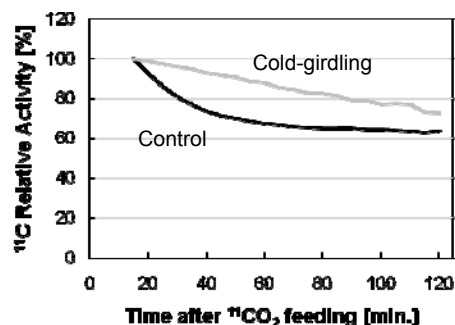


Fig. 3 Time-activity curves in the same region on the source leaf.

3-37 Genetic Interaction between COP9 Signalosome and SMAP1 That Function in the 2,4-D Response in Arabidopsis

Y. Oono and I. Narumi

Life Science and Biotechnology Division, QuBS, JAEA

By using ion beams, we previously isolated an Arabidopsis anti-auxin resistant mutant *aar1-1*, which shows root resistant phenotype to anti-auxin *p*-chlorophenoxy acetic acid and synthetic auxin 2,4-dichlorophenoxyacetic acid (2,4-D). The *aar1-1* mutation has an approximately 44-kbp deletion in chromosome 4; this deleted region presumably generated by ion beams contains at least 10 genes. The *SMALL ACIDIC PROTEIN 1* (*SMAP1*) gene, one of the genes in the deleted region, is responsible for the *aar1-1* mutation, and encodes a 62 amino-acid-protein (6.9 kDa) with a pI of 3.4¹⁾. Physiological and genetic analyses of the *aar1-1* mutants and the *SMAP1* gene suggested that the SMAP1 protein acts upstream of the degradation step of AUX/IAA proteins in auxin signaling¹⁾ and that SMAP1 physically interacts to COP9 signalosome (CSN) in Arabidopsis extract (Nakasone et al., submitted). CSN is also an evolutionally conserved protein complex and known to act on regulation of protein degradation. One of the major activities of CNS is to de-conjugate related-ubiquitin (RUB) protein from RUB-conjugated CULLIN (CUL) protein, one of the subunits of ubiquitin E3 ligase, via the metalloprotease activity of its CSN5 subunit.

To investigate the interaction between *SMAP1* and *CSN* at the genetic level, we crossed the *aar1-1* mutant with the weak *csn* mutant *csn5a-1*, and established a line harboring the *aar1-1* mutation in homozygosis and *csn5a-1* in heterozygosis (*aar1-1 CSN5A/csn5a-1*). From the *aar1-1 CSN5A/csn5a-1* parental line, dwarf seedlings distinguishable from either *aar1-1* or *csn5a-1* mutants segregated (70 dwarf seedlings out of 363 light-grown seedlings; $\chi^2 = 6.33$, $p > 0.01$) (Fig. 1). Genotyping analyses confirmed that these dwarf plants were *aar1-1 csn5a-1* double mutants (data not shown). The root growth of both *aar1-1* and *csn5a-1* was similar to that of the wild-type, but the double mutant showed slower root growth on germination medium than that of the single mutants (Fig. 2). In addition, the double mutant was more auxin-resistant than its parent lines (Fig. 2). These results suggested that there is a synergetic interaction between *aar1-1* and *csn5a-1* mutations.

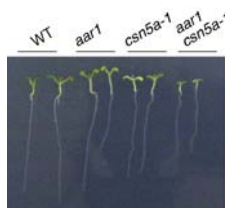


Fig. 1 Morphology of 7-d-old seedlings grown on medium without any growth regulators.

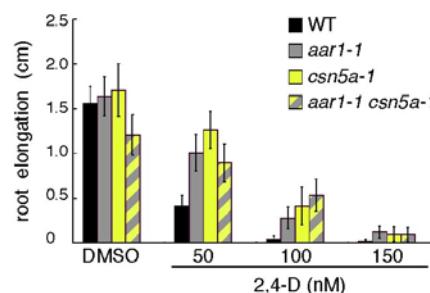


Fig. 2 Root growth sensitivity to 2,4-D. Four-day-old seedlings were transferred onto medium containing 2,4-D at indicated concentrations and further grown for 3 days. The root elongation after transferring was measured and plotted.

We next examined the RUB modification status of the CUL1 protein, which is a core subunit of SCF E3 ligase and one of the most characterized RUB-modified proteins, in the double mutants by western blotting using anti-CUL1 antibody. As previously published, the ratio of RUB-modified and unmodified CUL1 was higher in *csn5a-1* compared with that in the wild-type²⁾. However, there was no significant difference in CUL1 modification status between the wild-type and *aar1-1*, between *csn5a-1* and *csn5a-1 aar1-1* (Fig. 3). This suggested that SMAP1 has no or little effect on the RUB modification, although there were severe morphological effects in the *csn5a-1 aar1-1* double mutant.

Although the precise mode of action of SMAP1 is still unclear, further biochemical research on the function and relationship of SMAP1 with CSN might make clear the precise mode of action of SMAP1 and its biological role on the RUB modification as well as on the mechanism of the downstream ubiquitin-dependent protein degradation system in plant cells.

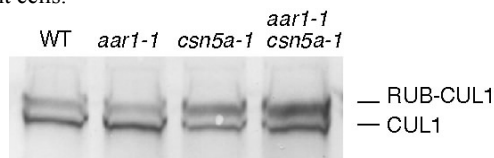


Fig. 3 Twenty μ g of total proteins extracted from 7-d-old seedlings. Proteins were loaded on SDS-PAGE, followed by immunodetection with anti-CUL1 antibody.

References

- 1) A. Rahman et al., Plant J. 47 (2006) 788.
- 2) G. Gusmaroli et al., Plant Cell 19 (2007) 564.

3-38 Development of Ion Beam Breeding Technology in Plants and Creation of Useful Plant Resources

Y. Hase^{a)}, S. Nozawa^{a)}, T. Okada^{b)}, I. Asami^{c)}, T. Nagatani^{d)},
Y. Matsuo^{e)}, A. Kanazawa^{f)}, K. Honda^{g)} and I. Narumi^{a)}

^{a)}Life Science and Biotechnology Division, QuBS, JAEA, ^{b)}Gunma Agricultural Technology Center,
^{c)}Aichi Agricultural Research Center, ^{d)}Kagoshima Biotechnology Institute, ^{e)}Saga Prefectural
Agricultural Fruit Tree Experiment Station, ^{f)}Research Faculty of Agriculture, Hokkaido University,
^{g)}Faculty of Agriculture and Life Science, Hirosaki University

The purpose of this study is to develop ion beam breeding technology and to create useful plant resources. In particular, our current research is focused on the step-wise improvement of traits in flower and ornamental plants. We also focus on improvement of trees and functional ingredients in crops because little knowledge has been accumulated in this area. Here, we describe recent progress made in these studies.

In order to obtain red- and yellow-color variants, leaf cultures of chrysanthemum variety 'Konatsunokaze', which was developed by Gunma Agricultural Technology Center, were irradiated by carbon ions with a dose of 0.1 to 5 Gy. Unfortunately, no characteristic variation has been observed so far in about 500 regenerated plants. We found that the addition of indole acetic acid (IAA) to culture medium with a concentration of 10 mg/L increased the plant regeneration rate by around 30%. This culture condition improves the efficiency of mutant screening in future experiments.

Seedlings of chrysanthemum variety 'Hakusui', which was developed by Aichi prefecture, were exposed to carbon ions to improve agricultural traits. The irradiated seedlings were grown and the cutting was performed 3 times to obtain non-chimeric mutant plants. Fifty mutant plants that have lesser number of adventitious buds were selected from 2,000 plants. In another experiment, 6 mutant plants, which did not show delay in flowering under low temperature condition, were selected from 1,000 plants grown in winter season. In addition, several flower mutants were obtained in a spray variety of chrysanthemum. The trial cultivation of white-color mutant will be done in fiscal year 2011.

We carried out further improvement of chrysanthemum varieties "Araddin" and "Araddin2", which were developed by Kagoshima prefecture and JAEA, by means of two-step improvement with carbon-ion irradiation. In this year, 31 candidate plants, which show early flowering under low temperature condition, were selected from 11,000 plants obtained from leaf cultures re-irradiated with carbon ions. In addition, the second screening was carried out for individual plants selected in fiscal year 2009. Two mutant lines were selected from 49 lines according to the number of adventitious buds, flower size and the growth under low temperature condition.

In order to develop ion beam breeding technology in trees, improvement of Japanese mandarin orange has been carried out. The cut surfaces of hypocotyls were exposed

to carbon ions with the dose of 2 and 4 Gy. The 1,169 plants were obtained from 1,798 of irradiated seedlings. The 165 plants with shorter plant height were selected from them. These plants will be grown by grafting with trifoliate orange to create dwarf variety of mandarin orange.

Soybean is an important crop that provides food, oil, forage and industrial raw materials. Soybean is thought to be derived from a tetraploid ancestral plant. Genome sequence of soybean revealed that ~75% of genes present in multiple copies¹⁾. It is likely that gene duplication lowers the efficiency of mutant production. We carried out a detailed analysis of mutagenic effect of carbon ions in soybean²⁾. Dry seeds were irradiated with carbon ions with a dose of 0.25 to 20 Gy. The number of plants survived until seed-set decreased as the irradiation dose increased. Based on these results, progeny seeds were obtained from plants irradiated with 2.5 and 5.0 Gy in a large scale. Despite the duplicate genome, chlorophyll mutants were obtained with a frequency of 0.47%. These results demonstrate that carbon-ion irradiation with a dose of 2.5 to 5.0 Gy induces genetic changes while allowing the production of a considerable number of seed-setting plants.

In order to create useful plant resources in terms of functional ingredients, dry seeds of traditional pepper variety in Hirosaki, Aomori prefecture were irradiated with carbon ions. Various morphological variations such as shorter internodes, increased branching and fruit characteristics were observed. Among them, a plant with fleshy fruits was thought to be most useful. The HPLC analysis of capsaicinoids in fruits was performed. While preliminary, novel peaks, which can not be usually detected in this variety, were detected in some mutant plants. Genetic analyses of these mutant plants are in progress.

References

- 1) J. Schmutz et al., Nature 463 (2010) 178.
- 2) S. Arase et al., Plant Biotechnol. (2011) in press.

3-39 Ion Beam Irradiation on Rice Seeds for the Mutation Breeding Project of the Forum for Nuclear Cooperation in Asia (FNCA)

A. Tanaka^{a)}, S. Nozawa^{a)}, Y. Hase^{a)}, I. Narumi^{a)}, H. Ishikawa^{b)} and A. Koike^{b)}

^{a)} Life Science and Biotechnology Division, QuBS, JAEA,

^{b)} Nuclear Safety Research Association

1. Introduction

For the spread of radiation application and development of ion beam breeding technique, ion beams have been utilized under the Mutation Breeding Project of the Forum for Nuclear Cooperation in Asia (FNCA) of MEXT (Ministry of Education, Culture, Sports, Science and Technology). This project contributes to increase food production and to improve food quality in Asia, by developing new mutant varieties with resistant to disease, insects, and environment, or higher yields and quality of important crops such as soybean, sorghum, orchid and banana, and so on. As the Sub-Project on Composition or Quality in Rice, utilization of ion beam has been started in 2009. Eight participant countries, i.e., Bangladesh, China, Indonesia, Korea, Malaysia, The Philippines, Thailand and Vietnam joined the ion beam irradiation with rice seeds.

2. Materials and Methods

In general, hulled dry seeds of a rice cultivar (cv.) of participant countries were irradiated with 320 MeV carbon ion beam in TIARA¹⁾. After irradiation, seeds were rightly sent back to the participant countries and grown to obtain the offspring.

At the FNCA workshop on Mutation Breeding held in Philippines in November 2010, we have deeply discussed the appropriate population size for irradiation treatment and suggested that the minimal number of initial cells to be irradiated is at least 5,000 in order to obtain enough mutants. The protocol for selection of seeds after irradiation was also discussed and it was suggested to harvest 5 seeds from 5 panicles from each M₁ plant as shown in Fig. 1.

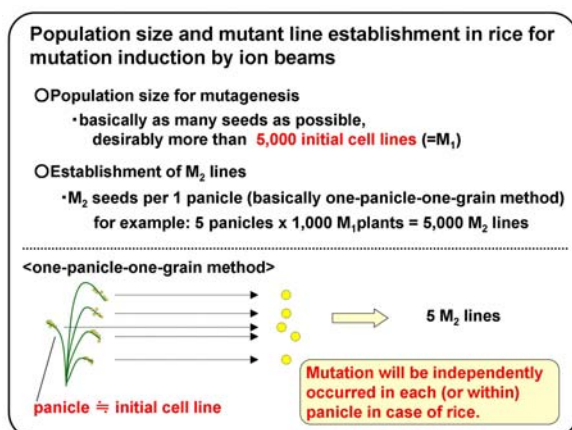


Fig. 1 Protocol for mutation line establishment in rice.

3. Results and Discussion

In 2010, most of participant countries were able to decide the best doses for mutation induction and some countries have also carried out harvesting of M₂-M₃ plants and their screening. For example, in the Philippines, initial result showed that the best dose was found to be 20 Gy and the lethal doses were 160 and 200 Gy. In the M₁ generation, plant height, days to heading, number of productive tillers, number of seeds per panicle, and sterility were affected by the irradiation. However, no differences were obtained on the panicle length and 100 seed-weight. In Vietnam, mutation has been observed in plant height, grain weight, maturity or sterility in the M₂ generation of both Khang dan and Bac thom varieties. In the M₃ generation, some interesting characteristics related to yield were shown and chosen as for grain weight, short grow duration, tolerant to disease, and semi-dwarf plant (Fig. 2). In Bangladesh, the M₃ progenies derived from irradiated seeds of a local salt tolerant cultivar-Ashfal were evaluated. The M₃ progenies derived from either 40 Gy or 200 Gy included photinsensitive mutation. This progenies also included early mature and high yield characters (Fig. 3).



Fig. 2 Khang dan variety (*left*), and its semi-dwarf mutant that is tolerant against lodging (*right*).



Fig. 3 BRRI dhan-29 variety (*right*), and its mutant line with early mature and high yield (*left*).

Reference

- 1) A. Tanaka et al., JAEA Takasaki Ann. Rep. 2009 (2011) 61.

3-40 Characterization of Ion Beam Irradiated Chrysanthemum Plants

S. Shakinah^{a)}, A. Zaiton^{a)}, A. H. Affrida^{a)}, S. Nozawa^{b)}, I. Narumi^{b)},
Y. Hase^{b)} and Y. Oono^{b)}

^{a)} Agrotechnology and Biosciences Division, Malaysian Nuclear Agency,

^{b)} Life Science and Biotechnology Division, QuBS, JAEA

Chrysanthemum has become the leading temperate cut flowers in Malaysia for both local and export market¹⁾. Due to its value, demands are high for new cultivars with good horticultural traits such as unique flower colour and shape, flower uniformity, early flowering under short day condition, firmness of the stalk, growth vigour, leaf quality and suitability of a cultivar for year-round production²⁾. Induced mutation through a combination of ion beam irradiation and *in vitro* floral organ cultures has a great potential to produce new cultivars with wider mutation spectrum³⁾. Thus, the objective of this study was to determine the effects of ion beam radiation on chrysanthemum plants regenerated from ray florets.

Ray floret cultures of *Chrysanthemum morifolium* cv. Reagan Red were irradiated with 320 MeV ¹²C⁶⁺ ion beam from the TIARA AVF Cyclotron as previously reported⁴⁾. Regenerated plantlet from cultures irradiated at 0.5, 1 and 2 Gy were acclimatized and sown in 15-cm² pots containing soil and Perlite with the ratio of 1:2. Screening was carried out at MARDI Cameron Highland. Additional 2-h lighting was applied to provide for the first 28 days of transplanting. Data collection was conducted in a Randomized Complete Block Design (RCBD) with 12 replications. Statistical Analysis System (SAS, version 9.2) software were used to carry out the analysis of variance (ANOVA) and Duncan's New Multiple Range Test (DNMRT) was used for comparison among treatment means, provided the treatment effect was significant at 5% level.

Table 1 shows the detailed characteristics of ion beam-irradiated chrysanthemum plants. Plants from all three irradiation doses have significantly higher plant heights than the control. As shown in Fig. 1, the irradiated plants were taller as compared to the control, which looked sturdy and bushy. No significant difference was observed on the day taken to form first visible buds and flower bud break between the mutants and control, indicating that the irradiation did not affect the plant maturity and flower uniformity. However, irradiation caused reduction in the

number of flower bud and flower size, by more than 50% and 1 cm, respectively. All plants (100%) irradiated at 2 Gy have different flower colour from the control, as compared to slightly above 50% in plants irradiated at 0.5 and 1 Gy. Interestingly, all the irradiated plants exhibited the same mutation in flower shape (spatulate), as in Fig 2.

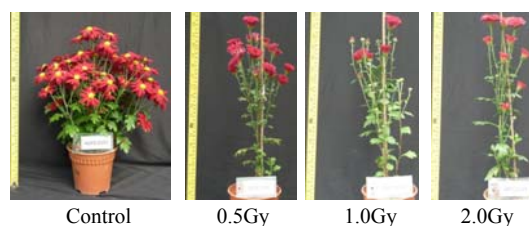


Fig. 1 Plant architecture of the control and irradiated plantlets.

Changes were also observed in leaf colour and shape. The 2-Gy irradiated population showed 100% mutation on both characters, suggesting that ion beam irradiation at 2 Gy is a promising parameter to induce mutations in *C. morifolium* cv. Reagan Red.

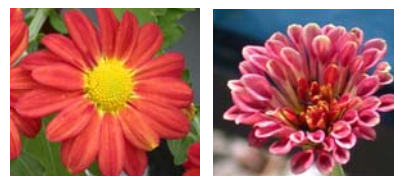


Fig. 2 Petal shape of the control (left) and mutant (right).

References

- 1) H. J. Lim et al., <http://www.fao.org/docrep/005/ac452e/ac452e06.htm> (1998).
- 2) A. M. Van Harten, Mutation Breeding: Theory and Practical Applications, Cambridge University Press. (1998).
- 3) S. Nagatomi et al., Acta Horticulturae 508 (2000) 69.
- 4) A. H. Affrida et al., JAEA Takasaki Ann. Rep. 2009 (2011) 62.

Table 1 Growth and morphological data of chrysanthemum regenerated from ion beam irradiated ray florets.

Dose (Gy)	Total No. of plant screened	Height (cm)	Day to bud (>3 mm) visible	Day to bud break	No. of flower buds	Flower colour mutation (%)	Flower size (cm)	Type of ray florets	Leaf colour mutation (%)
Control	36	17.9 ^b	25.3 ^a	54.3 ^a	39.3 ^a	-	5.4 ^a	Ligulate	-
0.5	36	39.3 ^a	26.7 ^a	55.7 ^a	11.1 ^b	59.1	4.1 ^b	Spatulate	63.6
1	36	37.6 ^a	26.6 ^a	55.6 ^a	15.9 ^b	54.5	4.4 ^b	Spatulate	100
2	36	40.1 ^a	26.3 ^a	55.4 ^a	12.6 ^b	100	4.2 ^b	Spatulate	100

Note: Means followed by the same letter are not significantly different.

3-41 Mutational Effects of Carbon Ions near Range End in Arabidopsis

Y. Hase, R. Yoshihara, S. Nozawa and I. Narumi

Life Science and Biotechnology Division, QuBS, JAEA

The accelerated heavy ions deposit most of their energy close to the end of their range. Little is known about the mutational effects of ion beams near range end, especially in plants. Here, we carried out several experiments to characterize mutational effects of carbon ions near range end in plants.

The carbon ions near range end (Mean LET, 425 keV/μm) showed higher cell killing effect than 220 MeV carbon ions (Mean LET, 113 keV/μm). Doses corresponding to the shoulder of the survival curves were 180 and 80 Gy for 220 MeV carbon ions and carbon ions near range end, respectively. We compared the mutation frequency (MF) using the mutation detection system via plasmid rescue as previously described¹⁾. While MF increased by 2.7 times in the case of 220 MeV carbon ions, MF was unchanged from background level in case of carbon ions near range end (data not shown). This suggests the possibility that large structural alterations, which can not be detected by plasmid rescue, were frequently induced by the carbon ions near range end.

The Arabidopsis mutant plants defective in Ligase IV gene, which plays a major role in non-homologous end joining pathway, showed higher radiation sensitivity than the wild type for both 220 MeV carbon ions and carbon ions near range end (Fig. 1). We found that the difference of radiation sensitivity between the wild type and ligase IV mutant was greatly diminished in the case of carbon ions near range end (Fig. 1(b)). This result suggests that the carbon ions near range end induce much irreparable DNA lesions.

To further characterize the mutational effects of carbon ions near range end, we analyzed the mutations occurred in Arabidopsis *GLI* gene with the emphasis on large deletions. Arabidopsis seeds obtained by crossing wild type Columbia with *gli-1* mutant were used as a material. The DNA markers that can distinguish Columbia and *gli-1* sequence were used to detect deletions. MF on *GLI* locus was not significantly different between 220 MeV carbon ions and carbon ions near range end. However, the carbon ions near range end induced large deletions (> 5 kb) more frequently by 6 times than 220 MeV carbon ions. This suggests that large deletions were frequently induced by ion beams with very high LET.

In order to examine the LET dependency of the type of mutations, we examined the radiation sensitivity of material seeds to four kinds of ion beams and gamma-rays (Fig. 2). The effects on survival reduction clearly depended on the LET. Analyses of mutations that occurred in the *GLI* locus by these radiations are in progress.

Reference

- 1) R. Yoshihara et al., Int. J. Radiat. Biol. 86 (2010) 125.

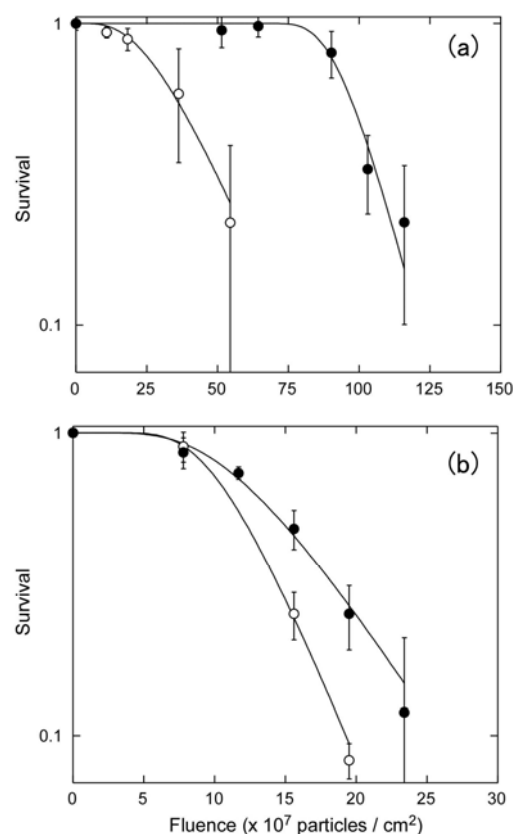


Fig. 1 Dose response curves for survival rate of irradiated seeds. (a) 220 MeV carbon ions, (b) carbon ions near range end. ●, Wild type; ○, ligase IV mutant.

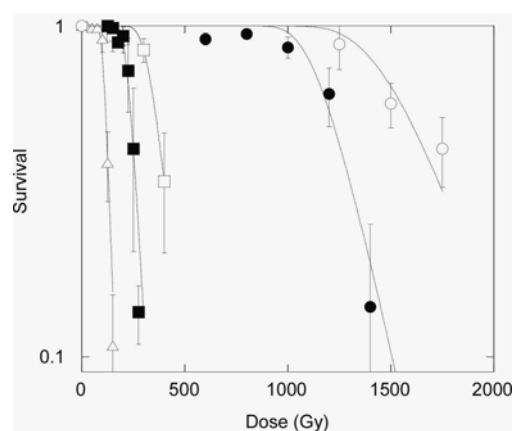


Fig. 2 Dose response curves for survival rate of irradiated seeds. ○, Gamma-rays; ●, 50 MeV helium ions; □, 320 MeV carbon ions; ■, 220 MeV carbon ions; △, 350 MeV neon ions.

3-42 Analysis of Mutated Region on DNA in Ion Beam-Induced UVB Tolerant or Sensitive Rice Mutant

N. Takano^{a)}, Y. Takahashi^{a)}, M. Yamamoto^{a)}, M. Teranishi^{a)},
Y. Hase^{b)}, A. N. Sakamoto^{b)}, A. Tanaka^{b)} and J. Hidema^{a)}

^{a)} Graduate School of Life Sciences, Tohoku University,

^{b)} Life Science and Biotechnology Division, QuBS, JAEA

UVB radiation can affect the plant growth and development. We previously demonstrated that UVB-induced cyclobutane pyrimidine dimers (CPDs), the major UVB-induced DNA lesions, are a principal cause of UVB-induced growth inhibition in the rice plants grown under supplementary UVB radiation¹⁾. Furthermore, increasing the activity of CPD photoreactivation, which is mediated by CPD photolyase that monomerizes the CPDs in DNA by using the energy of near-UV and visible light (300-500 nm), does elevate UVB resistance in rice¹⁾. However, our results also suggest that there is a limit to this beneficial effect. The aim of this study is to identify new factor(s) related to UVB tolerance in plants by bioengineering or breeding programs. In order to accomplish this project, novel mutants with increased or decreased UVB resistance are powerful tools.

To produce UVB tolerant or sensitive mutants, dry seeds of Japanese rice cultivar Sasanishiki (*Oryza sativa* L.), which shows higher UVB resistance among rice cultivars, were exposed to carbon ion beam (320 MeV: $^{12}\text{C}^{6+}$, 80 Gy) and two UVB tolerant mutants and three UVB sensitive mutants were isolated from the offspring of irradiated plants. Within these mutants, we focused on UVB tolerant mutant *utr319* (UV Tolerant Rice 319) and UVB sensitive mutant *usr1* (UV Sensitive Rice 1) because the levels of UV-absorbing compounds and CPD photorepair activities of these mutants were indistinguishable from those of wild type (Sasanishiki). It was thought that these are novel mutants in rice. These results indicate that the mutations of unknown factor(s) could lead to alteration of UVB

sensitivity in rice.

To estimate the mutated regions on DNA of each mutant, we performed array comparative genomic hybridization (Array-CGH) analysis²⁾. As a result, very low signal intensities were detected in 2 genes on chromosome 7 (Os07g0264900, Os07g0265100; function of each gene product has been unknown) in *utr319* (Table 1), and in 2 genes on chromosome 7 (Os07g0462700; encoding a protein with thioesterase domain, Os07g0463100; encoding Rpb6) in *usr1* (Table 2). We, therefore, predicted that the regions on DNA corresponding Os07g0264900 and Os07g0265100 in *utr319* and Os07g0462700 and Os07g0463100 in *usr1* were deleted.

To identify the mutated regions in each mutant, we constructed bacterial artificial chromosome (BAC) libraries of each mutant. We isolated BAC clones which contain genomic DNA fragments surrounding the estimated deletion regions, and analyzed the sequence of them. It was identified that 45,419 bp on chromosome 7 containing Os07g0264900 and Os07g0265100 was deleted in *utr319* (Fig. 1A) and that 52,498 bp on chromosome 7 containing Os07g0462700 and 3' region of Os07g0463100 in *usr1* was deleted (Fig. 1B).

In conclusion, we identified the mutated regions in *utr319* and *usr1*. We are analyzing the relationships between the deleted genes and UVB tolerance.

References

- 1) J. Hidema et al., Plant J. (2007) 70.
- 2) A. Kallioniemi et al., Science (1992) 818.

Table 1 Signal intensities of a part of gene on chromosome 7 in *utr319* detected by Array-CGH analysis.

Gene ID (RAP-ID)	signal intensity	
	Sasanishiki	<i>utr319</i>
Os07g0264800	2215	2261
Os07g0264900	1464	6
Os07g0265100	681	44
Os07g0265600	1903	1800

Table 2 Signal intensities of a part of gene on chromosome 7 in *usr1* detected by Array-CGH analysis.

Gene ID (RAP-ID)	signal intensity	
	Sasanishiki	<i>usr1</i>
Os07g0462200	1125	1083
Os07g0462700	1134	6
Os07g0463100	564	6
Os07g0463400	115	239

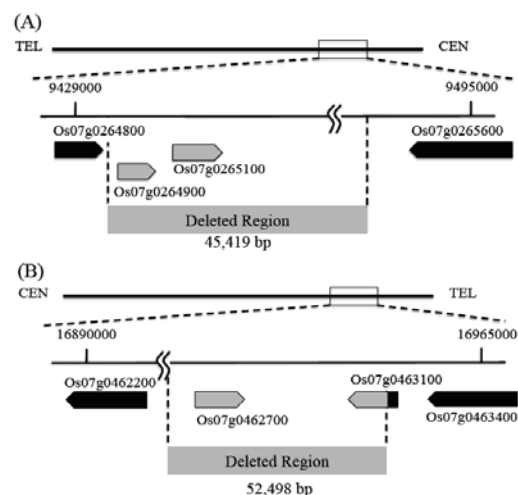


Fig. 1 Overview of mutated regions on chromosome 7 in *utr319* (A) and *usr1* (B).

3-43 Stability Evaluation of Mutant Lines Induced by Ion Beam Breeding in Petunia

M. Okamura^{a)}, Y. Hase^{b)}, N. Onishi^{a)}, I. Narumi^{b)} and A. Tanaka^{b)}

^{a)} Central Laboratories for Frontier Technology, Kirin Holdings Co., Ltd,

^{b)} Life Science and Biotechnology Division, QuBS, JAEA

Ion beams have proved to be an effective tool for mutation generation of plants and have great impact on basic research, plant breeding and plant seed and seedling business. Several series of superior carnation varieties have been developed by ion beam breeding in the joint R&D between Kirin Holdings Co., LTD. and JAEA. These varieties have been commercialized both in Japan and Europe¹⁾, which resulted in producing flower wholesale market of more than 450 million yen per year.

Although several attempts have been made to induce desired mutants intentionally, reports of clear success are yet to be seen. If we could control the direction of mutation, it is very useful to increase the mutation efficiency. We have been trying to develop an advanced application system of ion beams to produce color variation in flowers or to add some improvements in crops. We have shown in our previous report²⁾ that the frequency of flower-color mutation following ion-beam irradiation can be doubled by using such materials as purple-pigmented shoots. The results suggest that the direction of mutation could be controlled.

In this report we describe results of the stability examination of the mutated characteristics listed in the previous report and the trial to develop superior breeding lines for the commercial production of petunia new varieties.

Flower color mutants obtained in M2 generation from the original blue flower petunia BBss11 include magenta, purple, purple vein, light pink, white and burgundy. We collected more than a hundred M3 seeds from each of the M2 plants and examined their segregation. Of the 12 mutant lines tested, six lines clearly showed the stability in flower color, flower shape and plant morphology. Although the other lines showed some segregations in flower color, every one of the individuals tested for flowering showed no flower color segregation within the individual, which indicates changes in flower color derive from gene mutation (Fig. 1).

We have selected three lines of white-colored M2. Several hundred seeds were harvested from each line and the segregation of characteristics was examined. One hundred potted plants were cultivated for each line and grown until flowering. All the lines showed good stability in flower color, flower size and growth habit. They are expected to be superior parents for new varieties of petunia

(Fig. 2).

A part of this study was supported by a grant for the Research and Development Program for New Bio-industry Initiatives from Bio-oriented Technology Research Advancement Institution.



Fig. 1 Stability of flower color in M3 generation of ion beam mutants.

Top: Parent line BBss11, Blue flower color,

Center: M3 flowers of mutant line number 31,

Bottom: M3 flowers of mutant line number 16.



Fig. 2 Superior mutant lines for breeding petunia new varieties.

References

- 1) M. Okamura et al., Floriculture, Ornamental and Plant Biotechnology Vol. I, Global Science Books (2006) 619.
- 2) Y. Hase et al., Plant Biotechnol. 27, (2010) 99.

3-44 Lethal Effects of Different LET Radiations in Gene Disruptant Strain of *Deinococcus radiodurans*

K. Satoh^{a)}, K. Tejima^{a)}, T. Onodera^{a, b)} and I. Narumi^{a)}

^{a)} Life Science and Biotechnology Division, QuBS, JAEA,

^{b)} Graduate School of Life Sciences, Tokyo University of Pharmacy and Life Sciences

Introduction

Ionizing radiation induces DNA double-strand breaks (DSBs), which is a particularly serious form of DNA damage and has an especially deleterious effect in cells. Ion beams have a high linear energy transfer (LET, keV/μm) and give DNA damage containing DSBs locally (clustered damage) than gamma rays do. *Deinococcus radiodurans* exhibits extraordinary resistance to the lethal effects of ionizing radiations. This resistance has been attributed to its highly proficient DNA repair capacity¹⁾. The most noteworthy characteristic of *D. radiodurans* is its capacity for repairing ionizing radiation-induced DSBs. RecA and PprA proteins play important roles in DSB repair through homologous recombination (HR) and non-homologous end joining repair (NHEJ), respectively^{2, 3)}. Previously, we reported that *D. radiodurans* wild-type strain did not show the dependence of LET on the relative biological effectiveness (RBE)⁴⁾. In this study, we investigated lethal effects in *recA* or *pprA* gene disruptant strains and relationship between LET and RBE for different LET radiations.

Experimental procedures

D. radiodurans cells were cultivated at 30 °C in TGY medium with agitation to early stationary phase. Cells were harvested, washed and resuspended in 100 mM Tris-HCl (pH 7.0) containing 2.5% glycerol (TG buffer). Aliquots (1 mL) of the cell suspensions were adhered onto cellulose membrane, frozen at -80 °C for 60 min and dried *in vacuo*. Freeze-dried cells were irradiated with four kinds of ion beams (⁴He²⁺ [50 MeV; 19.4 keV/μm], ¹²C⁶⁺ [320 MeV; 86.2 keV/μm], ¹²C⁵⁺ [220 MeV; 121.8 keV/μm] and ²⁰Ne⁸⁺ [350 MeV; 440.8 keV/μm]) accelerated by an AVF cyclotron, or with ⁶⁰Co gamma rays (0.2 keV/μm) at Food Irradiation Facility, JAEA. The irradiation dose ranged from 0.2 to 10 kGy. Irradiated cells were harvested, diluted appropriately with the TG buffer, spread onto TGY agar, and incubated at 30 °C for 3 or 4 days prior to the enumeration of colonies. RBE was calculated from the equation: $RBE = D_{10} \text{ of gamma rays (Gy)} / D_{10} \text{ of ion beams (Gy)}$, where D_{10} is the dose quantity necessary for decreasing the survival fraction to 10%.

Results and discussion

The *recA* disruptant strain exhibited extreme sensitivities to gamma rays, ⁴He²⁺, ¹²C⁶⁺, ¹²C⁵⁺ and ²⁰Ne⁸⁺ ion beams than the wild-type strain (Fig. 1). The *pprA* disruptant strain also exhibited sensitivities to these radiations than the

wild-type strain (Fig. 1). In both gene disruptant strains, radiosensitivities to four kinds of ion beams were almost equal to that of the gamma rays (Fig. 1). As shown in Fig. 2, both gene disruptant strains did not exhibit the dependence of LET on RBE at range of LET from about 0.2 to 441 keV/μm as shown in the wild-type strain⁴⁾ (Fig. 2). These results indicate that RecA-mediated HR and PprA-mediated NHEJ mechanisms in *D. radiodurans* play important roles in repairing the ion beams-induced clustered damage as well as the gamma rays-induced damage.

References

- 1) I. Narumi, Trends Microbiol. 11 (2003) 422.
- 2) K. Satoh et al., J. Biochem. 131 (2002) 121.
- 3) I. Narumi et al., Mol. Microbiol. 54 (2004) 278.
- 4) K. Satoh et al., JAEA Takasaki Ann. Rep. 2009 (2011) 80.

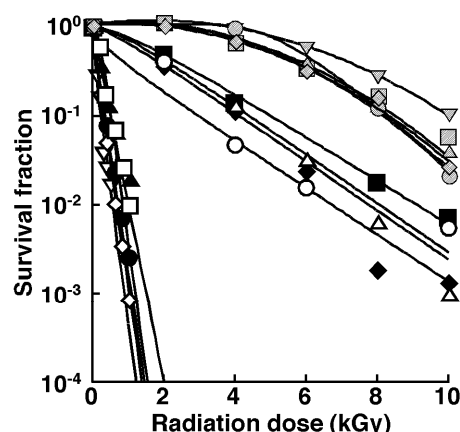


Fig. 1 Survival curves to different LET radiation. Symbols: wild-type strain [gamma rays (○), ⁴He²⁺ (▽), ¹²C⁶⁺ (◇), ¹²C⁵⁺ (□), ²⁰Ne⁸⁺ (△)], *recA* disruptant strain [gamma rays (●), ⁴He²⁺ (▼), ¹²C⁶⁺ (◇), ¹²C⁵⁺ (□), ²⁰Ne⁸⁺ (▲)], *pprA* disruptant strain [gamma rays (○), ¹²C⁶⁺ (◇), ¹²C⁵⁺ (■), ²⁰Ne⁸⁺ (△)].

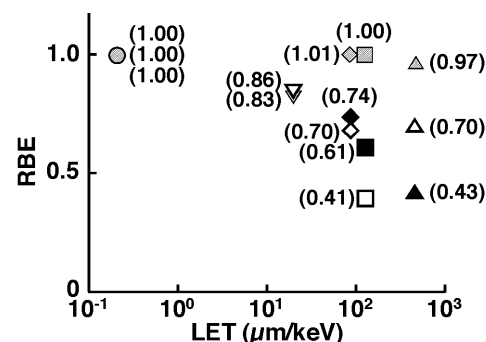


Fig. 2 The relationship between LET and RBE in gene disruptant strains. Symbols same as Fig. 1.

3-45 Involvement of Universal Conserved Genes, *ygjD* and *yeaZ* Orthologs, in DNA Repair of *Deinococcus radiodurans*

T. Onodera^{a, b)}, K. Satoh^{a)}, I. Narumi^{a)} and T. Ohta^{b)}

^{a)} Life Science and Biotechnology Division, QuBS, JAEA,

^{b)} Graduate School of Life Science, Tokyo University of Pharmacy and Life Science

Introduction

The *ygjD* and *yeaZ* gene orthologs are highly conserved in a wide variety of organisms. In prokaryote and eukaryote, YgjD and YeaZ proteins are related to cell division and genome maintenance, such as cell elongation and mitochondrial gene stabilization^{1,2)}. These proteins are essential for *Escherichia coli* and *Saccharomyces cerevisiae* but not in *Synechocystis* sp. PCC6803 and *Thermus thermophilus*. In a hyperthermophilic archaeon, *Pyrococcus abyssi*, it has been reported that *Pa-kaeI*, *ygjD* ortholog, encodes a novel type of AP-endonuclease³⁾.

Deinococcus radiodurans possesses *DrygjD* and *DryeaZ* genes, which are *ygjD* and *yeaZ* orthologs. However, the exact roles of *DrygjD* and *DryeaZ* proteins are poorly understood. In this study, we generated *DrygjD* and *DryeaZ* disruptant strains and investigated the disruption effect to DNA damaging agents in an effort to gain insight into the role of *DrygjD* and *DryeaZ* proteins in *D. radiodurans*.

Experimental procedures

The *DrygjD* and *DryeaZ* gene disruptant strains were generated using directed insertional mutagenesis technique⁴⁾. *D. radiodurans* cells were cultivated at 30 °C in TGY medium (0.5% tryptone-peptone, 0.1% glucose and 0.3% yeast extract) with agitation to early stationary phase. For mitomycin C (MMC) treatment, MMC (20 µg/mL) was directly added to the culture. Cells were incubated at 30 °C and withdrawn at various time points. For gamma irradiation, cells were harvested, washed and resuspended in 10 mM sodium phosphate buffer (pH 7) (PB). Aliquots (0.1 mL) of the cell suspension were irradiated with ⁶⁰Co gamma rays at dose ranges from 2 to 15 kGy at Food Irradiation Facility, JAEA. After the treatments, cells were diluted with PB, spread onto TGY agar, and incubated at 30 °C for 3 days prior to the enumeration of colonies.

Results and discussion

Unlike *E. coli*, we successfully constructed *DrygjD* disruptant, *DryeaZ* disruptant and *DrygjD DryeaZ* double-disruptant strains in *D. radiodurans*. All the disruptant strains did not exhibit the delayed growth compared to the wild-type strain, clearly indicating that neither *DrygjD* nor *DryeaZ* protein is essential for cell viability. These gene disruptant strains exhibited extreme sensitivity to MMC, which causes inter- and intrastrand

DNA crosslinking, compare to the wild-type strain (Fig. 1). On the other hand, these gene disruptant strains exhibited slightly sensitive to gamma rays, which induce DNA double-strand breaks, at high doses (8 to 12 kGy) (Fig. 2). These results suggest that *DrygjD* and *DryeaZ* proteins are involved in the DNA repair mechanism and especially play a critical role in the MMC-induced DNA damage in *D. radiodurans*.

References

- 1) J. Obero et al., Nucleic. Acids. Res. 37 (2009) 5343.
- 2) J. I. Handford et al., J. Bacteriol. 191 (2009) 4732.
- 3) A. Hecker et al., Nucleic. Acids. Res. 35 (2007) 6042.
- 4) T. Funayama et al., Mutat. Res. 435 (1999) 151.

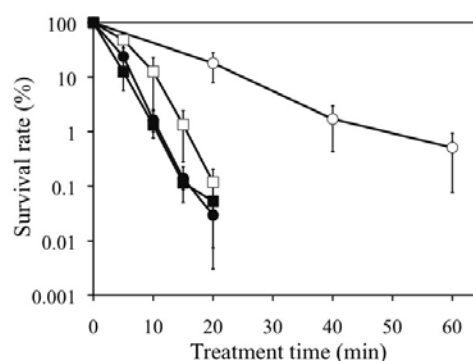


Fig. 1 Sensitivity of gene disruptant strains to MMC. Each point represents the average result obtained from four independent experiments. Symbols: open circles, wild-type; filled circles, *DrygjD* disruptant strain; open squares, *DryeaZ* disruptant strain; closed squares, *DrygjD DryeaZ* double-disruptant strain.

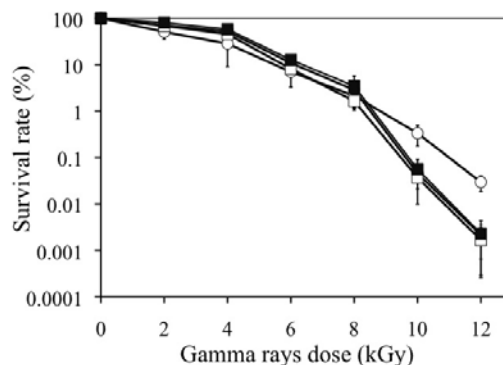


Fig. 2 Sensitivity of gene disruptant strains to gamma rays. Each point represents the average result obtained from five independent experiments. Symbols: See Fig. 1.

3-46 Fundamental Study on Molecular Mechanism Underlying Repair of Heavy-Ion Induced DNA Damage in the *Saccharomyces cerevisiae*

Y. Matuo^{a)}, Y. Izumi^{a)}, Y. Hase^{b)}, A. Sakamoto^{b)}, S. Nozawa^{b)},
I. Narumi^{b)} and K. Shimizu^{c)}

^{a)} Research Institute of Nuclear Engineering, University of Fukui,

^{b)} Life Science and Biotechnology Division, QuBS, JAEA,

^{c)} Radioisotope Research Center, Osaka University

Ion beam irradiation to living body is a research area of intense interest. Several studies have been made on ion beam cancer therapy and ion beam mutagenesis-based breeding technology. Ion beams are high-LET radiation and are known to have dramatic biological effects. However, the detailed molecular mechanism on the biological effects by ion beams has not yet been clarified.

We have been studying ion-beam induced mutations in the budding yeast as a model of eukaryote cell. The *S. cerevisiae* strains used in this study were wild-type S288C, and *rad50*, *rad52*, *msh2* and *ogg1* mutants. RAD50 protein, which makes a protein complex with Mre11 and Xrs2, is required for both non-homologous end joining (NHEJ) and homologous recombination (HR) repair pathways¹⁾. RAD52 protein is a component of HR pathway²⁾. MSH2 and OGG1 proteins are components of the oxidative DNA damage repair. The yeast cells were irradiated with carbon ions ($^{12}\text{C}^{5+}$; 220 MeV; LET 107 keV/ μm) with a dose of 10 to 200 Gy. The carbon ion beams were generated by an AVF cyclotron at JAEA. The survival rates following

irradiation were determined on the basis of colony-forming ability. We also performed the gene expression analysis for *RAD50*, *RAD52*, *MSH2* and *OGG1* following irradiation with carbon ions and gamma-rays. A one-step quantitative RT-PCR method was used to measure the expression level. SYBR Green (Bio-Rad) was used to monitor DNA synthesis. The amplified products lead to an increase in fluorescence intensity and thus allowing DNA concentrations to be quantified. The data was analyzed by a computer software package (Opticon Monitor 3.1, Bio-Rad), and the relative amounts of PCR products were compared.

Figure 1 shows the percentage survival of strains exposed to carbon ions. We used *rad50*, *rad52*, *ogg1* and *msh2* mutant strains. The *rad50* and *rad52* strains showed hyper sensitivity, while the *ogg1* and *msh2* strains showed relatively lower sensitivity to the carbon ion irradiation. Figure 2 shows the gene expression level. While preliminary, the expression of *RAD50* gene was up-regulated in carbon ion beams but was not in gamma-rays. This difference may result from the repair pathway that operates in mutant strains.

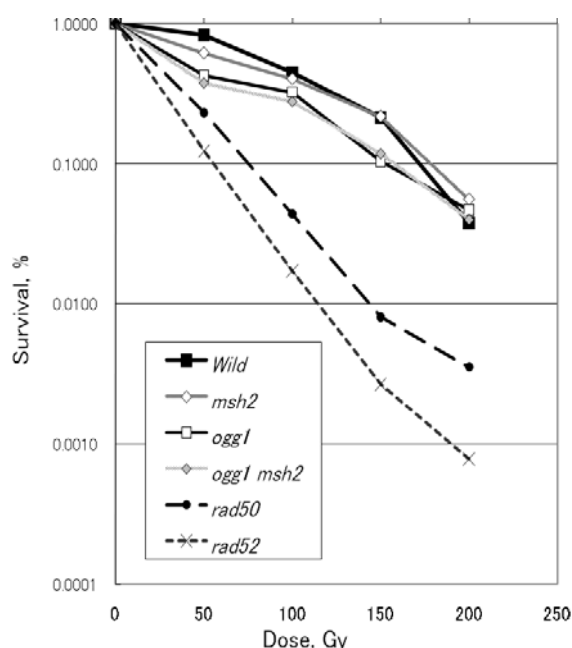


Fig. 1 Survival curves for yeast strains after carbon ion irradiation. Data are from single experiment.

References

- 1) L. H. Thompson and D. Schild, Mutat. Res. 509 (2002) 49.
- 2) L. K. Lewis et al., Genetics 160 (2002) 49.

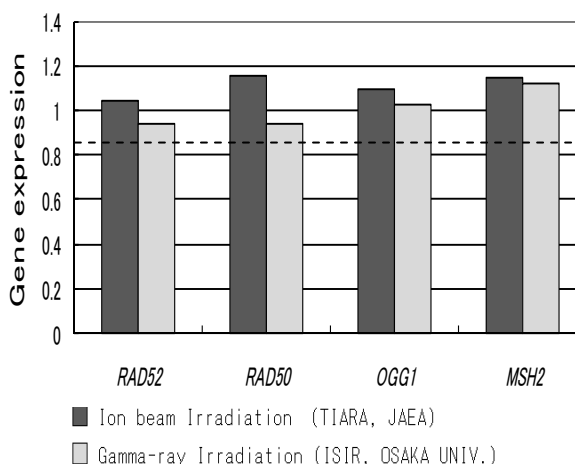


Fig. 2 The expression level of DNA repair genes after irradiation with carbon ions and gamma-rays. Data are from single experiment.

3-47 Characteristics of Mutant Endophytic Bacteria Strains Improved Using Ion Beams

M. Aino^{a)}, K. Matsuura^{a)}, K. Satoh^{b)} and I. Narumi^{b)}

^{a)} Hyogo Prefectural Center for Agriculture, Forestry and Fisheries,

^{b)} Life Science and Biotechnology Division, QuBS, JAEA

The endophytic bacteria produce various kinds of bioactive substances, by which the plants grow well and exhibit resistance to diseases and environmental stress. We could successfully obtain mutants that have enhanced suppressiveness against the tomato bacterial wilt by ion-beam irradiation to *Pseudomonas fluorescens* FPH 9601. In this study, we investigated antagonistic effect, production of antagonistic substance against tomato bacterial wilt and survival inside tomato seedling roots of the mutants. The ability to colonize inside tomato seedling roots of the mutants was not different from that of the parental strain. On the other hands, the ability to produce antagonistic substance from the colonized roots was varied. However, relationship between the production of antagonistic substance and suppression effect of tomato bacterial wilt was not ascertained.

生物農薬に含まれる *Pseudomonas fluorescens* FPH 9601 (以下 FPH) を対象に、イオンビーム突然変異育種の技術を用いて植物への定着や抗菌活性能力の増強が可能かどうかを検討した結果、トマト青枯病に対する発病抑制に対して効果の異なる変異株を得ることができた。そこで、得られた変異株のトマト植物体への内生能と抗菌活性能力の変化を検定し、変異の特定を試みた。

TIARA の AVF サイクロトロンを用い、 $^{12}\text{C}^{5+}$ (220 MeV) で 300 Gy で凍結乾燥菌体を照射した菌株から、シードリングバイオアッセイチャンバー法を用いて、トマト青枯病に対する発病抑制効果が親株と異なる 6 菌株を選抜した。標準培地を流し込んだシャーレ上で 28 °C で 24 時間培養した各菌株を殺菌蒸留水中に懸濁し、以下の試験に供試した。

①FPH 特異プライマーを用いた親株との類別：ITS 領域をから作製した FPH プライマーを用いて 95 °C、5 分間熱処理した各懸濁菌液をテンプレートとし、PCR 反応後その産物を電気泳動した。

②植物病害に対する発病抑制効果検定：各懸濁菌液にトマト種子 (品種：大型福寿) を 30 分間浸漬後、シードリングバイオアッセイチャンバー法を用いて、トマト青枯病 (*Ralstonia solanacearum*) に対する発病抑制効果を検定した。

③トマト植物体への内生能の検討：各懸濁菌液にトマト種子 (品種：大型福寿) を 30 分間浸漬し、トマト育苗倍土 (セルトップ) に播種した。人工気象器内で 25 °C、12 日間育苗し、根部を流水中で洗い、70% エチルアルコールに約 2 秒間漬浸し根表面の消毒を行った。殺菌水中でエチルアルコールを除去し、乳鉢で磨砕後、標準培地を用いて希釈平板法で内生菌数を計測した。

④抗菌活性能力の検定②の試験で表面殺菌したトマト根部をトマト青枯病菌が混入したケルマン培地上に置き、25 °C、2 日間培養した。根部周辺に形成した阻止帯を計測した。

親株の特異プライマーによる PCR 産物を電気泳動した結果、供試した菌株すべてに親株と同じ位置に特異バンドが確認され、親株由来であることが確認された。

供試株のトマト青枯病発病抑制効果は Fig. 1 に示したように、親株よりも高い効果を示した株は No. 8、9、

15、50、54 株で、劣った株は No. 96 株であった。トマト根内部への定着数は、供試菌株が 10^6 CFU/mL とほぼ親株の定着数と比べて変化は認められなかった。供試菌株が生じたトマト根から産生される抗菌活性物質による阻止帯幅は、No. 9 株が 8.7 mm と親株の 7.0 mm を上回ったが、それ以外の菌株では 0.8~4.0 mm と親株よりも劣る傾向があった。しかし、トマト青枯病発病抑制効果と抗菌活性物質産生及び根内部定着量との関係は判然としなかった。

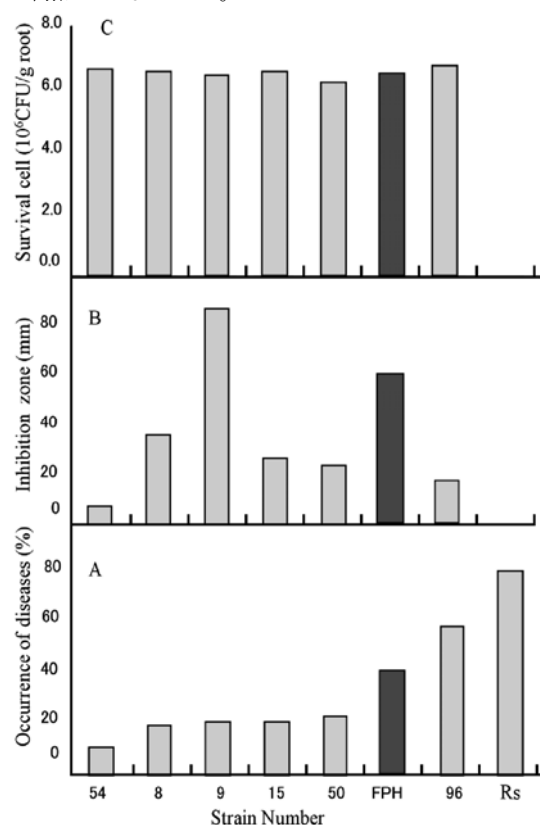


Fig. 1 Characteristics of mutant endophytic bacteria strains improved using ion beams. A: Suppression of tomato bacterial wilt by mutant strains. B: Production of antagonistic substance from roots colonized with mutant strains. C: Colonization of mutant strains inside roots of tomato seedling. Rs: *Ralstonia solanacearum*.

3-48 Colony Morphology of High Temperature Tolerant Mutants of *Bradyrhizobium japonicum* USDA110 Obtained by Ion-beam Microbial Mutation-breeding Technology

K. Takeda^{a)}, K. Tejima^{b)}, K. Satoh^{b)}, I. Narumi^{b)} and T. Yokoyama^{c)}

^{a)} Graduate school of Agriculture, Tokyo University of Agriculture and Technology,

^{b)} Life Science and Biotechnology Division, QuBS, JAEA,

^{c)} Institute of Agriculture, Tokyo University of Agriculture and Technology

Most of the nitrogen fertilizers are chemical nitrogen fertilizers. They are produced using oil and natural gas in terms of the Haber-Bosch process, which exhausts a large amount of CO₂. In order to supply food to increasing population in Asia, agricultural production should be increased and a large amount of nitrogen fertilizer is required. However, the economically minable period of the fossil resources is estimated to be around 40 years. Therefore, a reduction of chemical nitrogen fertilizer input is required in agricultural practices.

In Asian countries, in order to increase crop yield under low input of chemical nitrogen fertilizers, many researchers in agricultural institutes are trying to develop biofertilizers, which contain beneficial soil microorganisms and increase availability of plant nutrients from soils. However, several researchers point out constraints on application of biofertilizers. Major constraint of biofertilizer utilization in agricultural practice is a serious deterioration of qualities in biofertilizers under both storage and transportation conditions. In other words, exposing high temperature and drought stress causes a viability loss of beneficial microorganisms in biofertilizers. This becomes a serious problem on the dissemination of biofertilizer in southeastern Asia. Therefore, in order to prevent deterioration in viability of inoculants in biofertilizers exposed to high temperature, we are trying to improve a phenotypic character concerning high temperature tolerance in *Bradyrhizobium japonicum* USDA110, which is a worldwide superior inoculant to soybean. In this study, ion-beam microbial mutation-breeding technology is used to generate high temperature tolerant mutants.

B. japonicum USDA110 was cultivated in YM liquid medium until they reached to a concentration of 10⁸ cells/mL. Cells were harvested by centrifugation and resuspended in a solution containing 1.0% skim milk and 1.5% sodium glutamate. The suspension was then subjected to vacuum-freeze drying to minimize the effect of water radiolysis during irradiation. Freeze-dried cells of *B. japonicum* USDA110 were irradiated with carbon ion beams (220 MeV ¹²C⁵⁺) at TIARA in JAEA. Irradiation dose ranged from 0 to 800 Gy. Aliquots of irradiated cells were proliferated on YM agar plates in order to fix mutations. In general, *B. japonicum* USDA110 cannot survive at 40 °C. In order to obtain high temperature tolerant mutants, the

irradiated cells were put on YM agar plates and kept for over 1 month at 45 °C in several times. But, we couldn't find any proliferated colony. Therefore, we developed a new method to screen survival cells at 45 °C. In the new method, the irradiated cells were incubated in YM liquid medium at 45 °C for 5 days, and the cultures were put on fresh YM agar. Consequently, we obtained 9 high temperature tolerant mutants of *B. japonicum* USDA110, which can survive at 45 °C for 5 days. These mutants were classified into 3 groups in terms of differences in colony morphology and colony size. As shown in Fig. 1, the colony morphologies of M1 and M2 mutants had white color with flat emarginated shapes and colony sizes were almost same as that of wild type strain. In case of M3, M7, M8, and M9, their colonies had glossy white color with flat emarginated shapes, and colony sizes were almost same as that of wild type strain. Regarding M4, M5, and M6 strains, their colonies had glossy pale pink color with flat emarginated shapes, and colony sizes were clearly smaller than that of wild type at 5 days after plating. We will carry out further characterization of those isolates in terms of temperature tolerant and symbiotic characters.

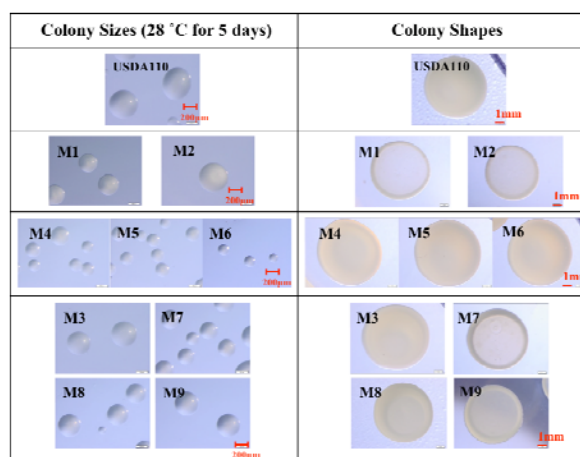


Fig. 1 The colony morphologies of high temperature tolerant mutants.

3-49 Repeated FACS-based Screening for Yeast Strain Highly Expressing Cellulase

K. Ninomiya^{a)}, H. Soda^{a)}, K. Satoh^{b)}, I. Narumi^{b)} and N. Shimizu^{a)}

^{a)} Division of Material Engineering, Graduate School of Natural Science and Technology, Kanazawa University, ^{b)} Life Science and Biotechnology Division, QuBS, JAEA

By using immunocytochemistry and fluorescence-activated cell sorter (FACS), yeast population highly expressing cellulase on the cell surface was enriched from the mutant population prepared by irradiation with carbon ion beams (220 MeV $^{12}\text{C}^{5+}$, 100 Gy). Repeated FACS after irradiation with carbon ion beams was effective for selecting yeast population of interest.

【緒言】近年、非食用バイオマスであるセルロースを原料としたエタノール発酵生産への関心が高まっている。セルロース糖化酵素であるセルラーゼを発現する酵母を用いた“セルロースからの直接エタノール発酵生産”では、酵母のセルラーゼ発現量が生産コストを下げるための律速段階の1つと言われている。我々は、セルラーゼ高発現酵母を育種するために、細胞表面に発現したセルラーゼの酵素量を蛍光免疫染色で蛍光強度に置き換えることにより、fluorescence-activated cell sorter (FACS) を用いて、セルラーゼ高発現株を蛍光強度の高い細胞集団として high-throughput に分取することを試みてきた。今回は FACS による選抜を繰り返した効果について報告する。

【実験方法】使用菌株：3 種のセルラーゼ endoglucanase II (EGII)、cellobiohydraz II (CBHII) ならびに β -glucosidase を細胞表面に発現した酵母 *Saccharomyces cerevisiae* MT8-1/pEG23u31H6/pFCBH2w3/pBG211 株¹⁾ (MT8-1III 株) を用いた。また、MT8-1III 株に炭素イオン (220 MeV $^{12}\text{C}^{5+}$) を 100 Gy 照射し (以下、イオンビーム照射)、変異株集団を調製した。酵母の培養は SD 培地を用いて 30 °C で行った。

蛍光免疫染色及び FACS：酵母表面のセルラーゼ分子の量を蛍光量として評価するため、EGII ならびに CBHII のタグとして融合発現させた RGSHis₆ 及び FLAG に対する一次抗体、それぞれの一次抗体に特異的な Alexa Fluor 488 (FITC) 及び R-phycoerythrin (PE) 標識二次抗体を用いて二重染色を行った。蛍光免疫染色を行った酵母株は、FACS を用いて蛍光強度を測定し、FITC ならびに PE の蛍光強度の高い細胞集団を目的株として cell sorting を行なった (Fig. 1)。

【結果と考察】親株 MT8-1III では、FITC ならびに PE の蛍光強度 (EGII ならびに CBHII の発現量に相当) の相対値が 10^4 以上の領域 (P4 領域) に分布する細胞は全体の 1.6%であった (Fig. 2)。この値は通常の継代培養 (Fig. 1, Selection A) では変化しなかった。

次に、親株 MT8-1III 株に対し「イオンビーム照射による変異導入」は行わず、「FACS による P4 領域の細胞集団の選抜」を繰り返して行なった (Fig. 1, Selection B)。その結果、P4 領域内の細胞の割合は、WT₁ 株で 3.3%、WT₂ 株で 6.3%に増加することが分かった (Fig. 3)。

さらに、親株 MT8-1III 株に対して「イオンビーム照射による変異導入」を一回行い、「FACS による P4 領域の細胞集団の選抜」を繰り返して行なった (Fig. 1, Selection C)。その結果、P4 領域内の細胞の割合は、B₁MT₁ 株で 6.9%に、B₁MT₂ 株で 10.3%に増加することが分かった (Fig. 3)。この結果から、親株 MT8-1III 株に

対して「イオンビーム照射による変異導入」と「FACS による P4 領域の細胞集団の選抜」を繰り返して行なう Fig. 1 の Selection D では、セルラーゼ高発現酵母の選抜が期待できる。

Reference

- 1) Y. Fujita et al., Appl. Environ. Microbiol. 68 (2002) 5136.

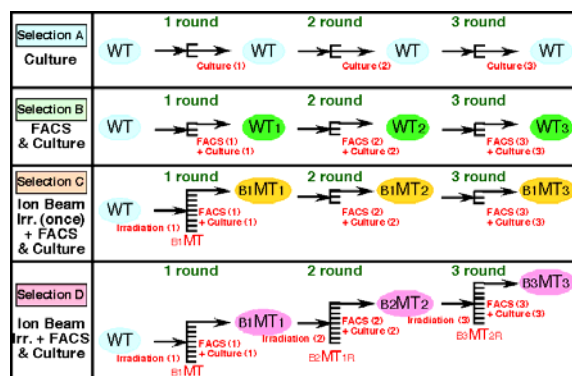


Fig. 1 Procedure of repeated FACS based screening of yeast expressing cellulase from the mutant population prepared by irradiation with carbon ion beams.

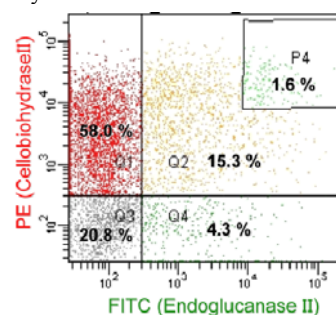


Fig. 2 Scatter plots of FITC and PE fluorescence corresponding to EGII and CBHII expression on parental yeast strain of MT8-1III, respectively.

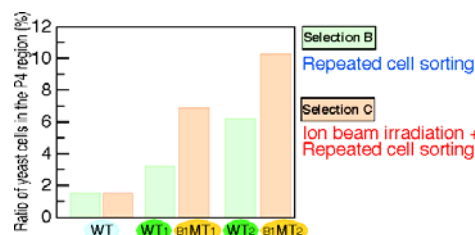


Fig. 3 Ratio of yeast cells in the P4 region of scatter plot of FITC and PE fluorescence.

3-50 Fungicide Tolerant Mutation of Entomopathogenic Fungi Induced by Carbon Ion Beams

T. Saito^{a)}, S. Shinohara^{a)}, K. Satoh^{b)} and I. Narumi^{b)}

^{a)} Faculty of Agriculture, Shizuoka University,

^{b)} Life Science and Biotechnology Division, QuBS, JAEA

Entomopathogenic fungi, *Isaria fumosorosea* and *Beauveria bassiana*, are important agents to control insect pests, but the fungi are highly susceptible to conventional fungicides for plant diseases such as powdery mildew. The purpose of this study is to generate mutants tolerant to fungicides (benomyl and triflumizole) using carbon ion beams (50 to 400 Gy). Fungicide-tolerant mutants were selected on the medium supplemented with fungicides (1,000 ppm for benomyl and 150 ppm for triflumizole). Subsequently, minimum inhibitory concentrations (MICs) of the mutants were determined. In the *I. fumosorosea* mutants, MICs of benomyl and triflumizole increased more than 5 and 4 times, respectively, compared to the original strain. In *B. bassiana* mutants, MICs of benomyl increased more than 5 times. Two-step irradiation with gamma rays (50 and 500 Gy) and carbon ion beams (100 and 200 Gy) was also tested. MICs in mutants obtained by the two-step irradiation were similar to those in mutants obtained by single irradiation with carbon ion beams. These results indicate that carbon ion beam irradiation is greatly useful for making fungicide-tolerant mutants of entomopathogenic fungi. Further studies will be needed to determine pathogenicity of the mutants against host insects.

化学合成農薬は数多くの課題を抱えていることから、IPM (総合的害虫管理技術) の普及が急務とされている。IPM の基幹技術のひとつと目されているのが天敵昆虫や天敵微生物 (昆虫寄生菌) を用いる生物的防除法であるが、昆虫寄生菌は殺菌剤と併用しにくいという課題を抱えている。この抜本的な解決策として、殺菌剤耐性という新機能を有する昆虫病原系状菌を創出することが考えられる。本研究の目的は、炭素イオンビームの照射による突然変異育種技術を用いて、代表的な昆虫病原系状菌 (*Isaria fumosorosea* 及び *Beauveria bassiana*) の殺菌剤耐性変異体を創出することである。

本研究では、炭素イオンビームの単独照射及びガンマ線照射と組み合わせた 2 段階照射によって変異体を選抜した。照射線量は、照射線量と分生子生存率の関係を調べた前年度の結果¹⁾を基に決定した。殺菌剤は、市販のベンレート水和剤 (50%ベノミル) とトリフミン乳剤 (15%トリフミゾール) を供試した。各供試菌は、サブロー寒天 (SDA) 培地で培養 (20 °C、3 週間) し、形成された分生子を 0.1% Tween 80 を含む蒸留水に懸濁し、ろ過装置を用いてメンブレンフィルター (直径 4.5 cm) 上に分生子を集めた。

炭素イオンビームの単独照射：分生子を集めたフィルターをシャーレ (直径 6 cm) に入れ、シャーレ上面をカプトン膜で覆ったのち、イオンビームを照射した (50~400 Gy、50 Gy 間隔)。照射後、フィルターを管ビン (10 mL 容) に移し、サブロー液体 (SD) 培地 2 mL を入れて 20 °C で 1 日間培養した。培養後、ガラス棒を用いてフィルター上の菌体を培地に懸濁させ、その 200 µL を殺菌剤添加 SDA 培地 (ベノミル 1,000 ppm、トリフミゾール 150 ppm) に塗布した。20 °C で 3 週間培養したのち、発育良好なコロニーを殺菌剤耐性変異体として選抜・分離した。

ガンマ線とイオンビームの 2 段階照射：分生子を集めたフィルターをシャーレに入れ、まずガンマ線を照射した (50 及び 500 Gy)。照射後のフィルターを SDA 培地上に置き、シャーレ上面をカプトン膜で覆い、室温で半日~1 日間培養したのち、炭素イオンビームを照

射 (100 及び 200 Gy) した。照射後のフィルターは、イオンビーム単独照射の場合と同様、SD 培地で培養したのち、殺菌剤を添加した SDA 培地に塗布して殺菌剤耐性変異体を選抜・分離した。

上記の殺菌剤選抜変異体の菌糸片 (直径 4 mm) を各濃度段階の殺菌剤添加 SDA 培地に接種し、25 °C で 2 週間培養後の MIC (最少発育阻止濃度) を求めた。その結果、*I. fumosorosea* のベノミル選抜変異体は 5 倍以上の、トリフミゾール選抜変異体は 4 倍以上の MIC を示した (Table 1)。*B. bassiana* のベノミル選抜変異体も 5 倍以上の MIC を示したが (Table 2)、トリフミゾール耐性変異体は得られなかった。2 段階照射によって得られた変異体の MIC は単独照射のそれと同等であった。

以上のことから、炭素イオンビームの照射は昆虫病原系状菌の殺菌剤耐性変異体の作出に利用できると考えられる。今後、得られた殺菌剤耐性変異体の病原力を検討する予定である。

Reference

- 1) T. Saito et al., JAEA Takasaki Ann. Rep. 2009 (2011) 76.

Table 1 MICs (ppm) of fungicides in *I. fumosorosea* mutants.

Mutants	Benomyl	Triflumizole
4-Ben34P1 *	> 5,000	
2-PB1 *	5,000	> 1,200
R1-1B8 **	> 5,000	
R1-2T20 **		> 1,200
R1-2T22 **		> 1,200
Original strain (PF3110)	1,000	300

* Single irradiation, ** Two-step irradiation with gamma rays.

Table 2 MICs (ppm) of fungicides in *B. bassiana* mutants.

Mutants	Benomyl
2-BB22 *	> 5,000
2-BB24 *	> 5,000
5-Ben47B *	> 5,000
R1-2B33-1 **	> 5,000
Original strain (BB1026)	1,000

* and ** See Table 1.

3-51 Ion Beam Breeding of “Sake Yeast” and Test Brewing – the Second Report

T. Masubuchi^{a)}, O. Kamiyama^{a)}, K. Satoh^{b)}, Y. Hase^{b)} and I. Narumi^{b)}

^{a)} Gunma Industrial Technology Center,

^{b)} Life Science and Biotechnology Division, QuBS, JAEA

We are trying to obtain high ethyl caproate producing Sake yeast by carbon-ion irradiation. Freeze-dried yeast was irradiated with 220 MeV carbon ion beams in a range of dose from 50 to 300 Gy by AVF cyclotron at JAEA. We isolated 1135 cerulenin resistant mutants of sake yeast “Kyokai-901” and “No.227 (previously generated ion beam mutant strain)”. A 57 kg-scale test brewing demonstrated that No.227 has enough fermentation ability like KAZE-2, and further suggested that No.227 is suitable for practical use as a new type of yeast for quality sake because of its sweetness and uniqueness in flavor.

群馬県ではオリジナルの吟醸用清酒酵母として「群馬KAZE酵母」を既に実用化しているが、消費者の嗜好の変化に対応した新たな酵母の開発をすべく、平成20年度よりイオンビーム照射による変異処理を行い、優良株の選抜を試みている。平成22年度は、更に優良な変異株を得るべく選抜を継続すると共に、それまでに得られた優良株の試験醸造を行い、実用化を想定した醸造適性の確認を行った。選抜の指標は従来同様に吟醸酒の主要な香気成分であるカプロン酸エチルの生成能とした。

【変異株の選抜】

イオンビーム照射に供する試料の調製、照射後の処理は前報に準じて行った¹⁾。照射は、TIARAのAVFサイクロトロンを用いて加速した¹²C⁵⁺ (220 MeV) を50～300 Gy照射した。本年度はきょうかい901号の他にNo.227酵母を親株として用いた。

カプロン酸エチル高生成株を取得するための選択培地は、市川ら²⁾の方法に準じセルレニン12.5～37.5 μMを含むYPD寒天培地を用いた。これに生育したセルレニン耐性変異株を齋藤ら³⁾の方法を改変した発酵試験に供し、15 °C、7日間の培養後に重量減少量 (CO₂放出量) を測定し発酵力の目安とした。また、得られた上清をヘッドスペースガスクロマトグラフにより、イソamilアルコール、酢酸エチル、酢酸イソamil、カプロン酸エチルの各成分を定量して香気生成能を評価した。

発酵試験は1135株について実施した。良好な香気生成能を示す変異株は主として100～150 Gyの照射区分で得られた。発酵試験で良好な7株について、布宮ら⁴⁾の変即二段仕込みを改変した方法で小仕込み試験 (総米200 g) を行った。

【試験醸造】

平成21年度に得られた変異株のうち、顕著な香気生成能を示したNo.1333酵母を試験に供した。また、平成21年度に有望な結果を示したNo.227酵母について再度試験を行い、実用化に向けた醸造条件の検討を行った。両者とも親株はきょうかい901号である。対照として群馬KAZE酵母 (2号) を用いた。試験醸造は群馬産業技術センター保有の醸造設備を用い、40%精白山田錦を原料とした総米57 kgの吟醸造りを行った。

醪の発酵状態を示す指標であるBMD値の経時曲線

(Fig. 1) と上槽した清酒の成分 (Table 1) をそれぞれ示す。No.1333酵母のカプロン酸エチルは三者の中で最も多いものの、発酵が弱く目標の日本酒度に達しないまま上槽せざるを得なかった。一方、No.227酵母は平成21年度の結果を参考に追水や温度などの管理を適切に行った結果、群馬KAZE酵母とほぼ同様の発酵経過を示し、群馬KAZE酵母よりも多くのカプロン酸エチルを生成した。官能評価においても総合評価は群馬KAZE酵母とほぼ同評価、きめ・あと味の項目では上回る評価を得た。また、平成21年度同様甘さに特徴のある新しい香り傾向が認められた。よってNo.227酵母は新たな吟醸酵母として十分実用化が可能と判断し、平成22酒造年度において実製造規模での醸造試験に着手した。

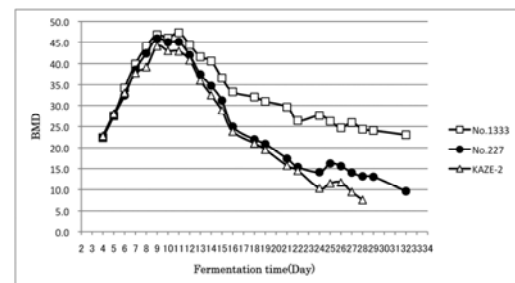


Fig. 1 BMD in sake-moromi by test brewing.

Table 1 Components contained in sake by test brewing.

Strain No.	Alcohol content (%)	Sake meter	Acidity (mL)	Amino acidity (mL)	Sake cake ratio (%)
No.1333	17.9	+0.7	1.7	1.2	43.2
No.227	18.3	+4.0	1.4	1.0	50.4
KAZE-2	18.0	+4.3	1.3	0.8	55.1

Strain No.	Isoamyl alcohol (ppm)	Ethyl acetate (ppm)	Isoamyl acetate (ppm)	Ethyl caproate (ppm)
No.1333	88.8	21.7	0.7	11.0
No.227	120.3	31.8	2.0	7.4
KAZE-2	127.9	23.4	2.5	5.6

References

- 1) T. Masubuchi et al., JAEA Takasaki Ann. Rep. 2008 (2009) 84.
- 2) 市川英治 et al., 1988年度日本農芸化学会大会講演要旨集、(1988) 435.
- 3) 齋藤久一 et al., 醸協 87 (1992) 915.
- 4) 布宮雅昭 et al., 醸協 90 (1995) 217.

3-52 The Long-term Storage of Rhizobial Biofertilizer Made from γ -sterilized Carriers

K. Tejima^{a)}, T. Yokoyama^{b)}, K. Satoh^{a)} and I. Narumi^{a)}

^{a)} Life Science and Biotechnology Division, QuBS, JAEA,

^{b)} Institute of Agriculture, Tokyo University of Agriculture and Technology

Biofertilizer is a substance that holds beneficial microorganisms for plant growth (e.g. Rhizobia) in the carrier such as peat, perlite, charcoal and soil¹⁾. Rhizobia are able to form the root nodule on the leguminous host plants and inhabit as nitrogen-fixing endosymbionts. Numerous studies on the inoculation technique of rhizobia to host plants at agricultural fields have been carried out worldwide. However, except in a case of a low competition with native microbes, the practical technique that shows remarkable effect on the plant growth has not been established. To utilize symbiotic nitrogen fixation for agricultural production more effectively, it is necessary to develop advanced rhizobial biofertilizers that keep the amount of viable inoculants for a definite period of time. The inoculants survival in the biofertilizer could be affected by the physical and chemical properties of carrier materials and by the competition with native microbes in the carrier. Gamma-irradiation is expected to sterilize the carrier materials without changes in physical and chemical properties. In an effort to demonstrate the effectiveness of γ -sterilization, the survivals of inoculants were monitored to assess the shelf life of biofertilizer.

As carrier materials, Japanese peat soil “Keto-tsuchi” and three kinds of Japanese typical soils (forest subsoil of the Kanto Loam Formation, cultivated topsoil of Andosol and Gray Paddy soils) were prepared. To make the soil-based artificial carriers, each Japanese typical soil was mixed with charcoal powder (3:1). In order to optimize γ -ray dose to sterilize soils, the survival rate of native microbes in the prepared soils were determined. As a result, 50 kGy (dose rate: 10 kGy hr⁻¹) was determined to be suitable to sterilize soils (Fig. 1).

Following the sterilization of the carrier materials by 50 kGy of γ -irradiation or autoclaving at 121 °C for 40 min, water suspension of *Bradyrhizobium japonicum*, a member of rhizobia, strain USDA110 was inoculated. *B. japonicum* forms the root nodules on soybeans (*Glycine max*) and supplies fixed nitrogen to host plant. Additionally, biofertilizers that consisted of the inoculants and one of the non-sterilized carriers were prepared as controls. The initial density of inoculants in the biofertilizer was adjusted to 6.6×10^7 cells g⁻¹. The biofertilizer was packed in polyethylene bags and stored for 12 months in 30 °C. After storage, viable inoculants in the biofertilizer were enumerated by the dilution plate method. The number of inoculants in biofertilizers made from non-sterilized carrier was monitored by PCR that amplifies the *nodD-nodY* region of *B. japonicum*.

The inoculants density after 12-month storage was greater than the initial density in biofertilizers made from sterilized carriers, while that was significantly decreased in biofertilizers made from non-sterilized carriers (Fig. 2). Gamma-sterilization was superior to autoclave-sterilization in enhancing the survival of inoculants. Because of the stability of supply, the high sterilization effect with lower radiation doses, and the high performance in maintaining the inoculants density, “Keto-tsuchi” was selected as one of the most suitable for a biofertilizer’s carrier.

Reference

- 1) K. Senoo and I. Narumi, FNCA Biofertilizer Manual (2006) 41.

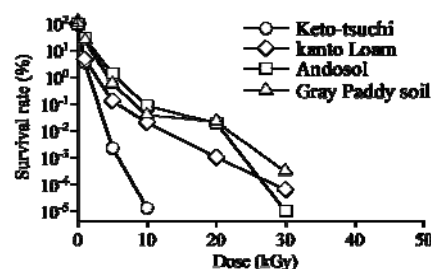


Fig. 1 Survival rates of native microbes in the different kinds of soils after γ -irradiation. Survival microbes were not detected at 50-kGy irradiation.

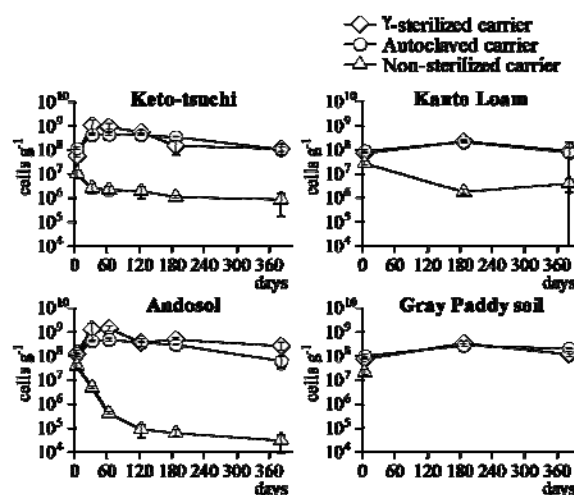


Fig. 2 Survival of rhizobial inoculants in biofertilizer stored at 30 °C. In biofertilizer made from non-sterilized Gray Paddy soil, survival inoculants were not detected at 6 and 12 months. Error bars indicate \pm SD around means.

4. Advanced Materials, Analysis and Novel Technology

4-01	Oxygen Reduction Activity of Transition Metal and Nitrogen Doped Carbon Films Prepared by Pulsed Laser Deposition	119
	S. Yamamoto, T. Hakoda, K. Yoshimura, K. Kawaguchi and M. Yoshikawa	
4-02	Fabrication of Functionalized Polystyrene Nanowires by the Single Particle Nano-Fabrication Technique	120
	S. Seki, A. Asano, Y. Maeyoshi, S. Tsukuda, M. Sugimoto and M. Yoshikawa	
4-03	Formation of Poly(vinylphenol) Nanowires Including Au Nanoparticles by Ion Beam Irradiation	121
	S. Tsukuda, A. Asano, M. Sugimoto, A. Idesaki, M. Yoshikawa, S. Seki and S.-I. Tanaka	
4-04	Radius Control of SiC Nano Fiber by Two Steps Irradiation Method Using Ion and Electron Beams	122
	M. Sugimoto, K. Yoshimura, A. Idesaki, M. Yoshikawa, S. Tsukuda and S. Seki	
4-05	Gas permeation Property of Silicon Carbide Membrane Prepared on Porous Alpha Alumina Support Using Radiation Curing of Polymer Precursor Film	123
	A. Takeyama, M. Sugimoto and M. Yoshikawa	
4-06	Synthesis of Nano-Crystalline SiC Nanotubes by Ion-Irradiation Technique	124
	T. Taguchi, S. Yamamoto, K. Kawaguchi and S. Shamoto	
4-07	Study for Damage of Charge Stripper Carbon Foil by Ion Beam Irradiation	125
	Y. Yamazaki, M. Yoshimoto, O. Takeda, M. Kinsho, T. Taguchi, S. Yamamoto, T. Kurihara and I. Sugai	
4-08	Fabrication of Y-Junction Waveguides Using Proton Beam Writing	126
	K. Miura, T. Satoh, Y. Ishii, M. Koka, M. Uehara, H. Kiryu, K. Takano, T. Ohkubo, A. Yamazaki, W. Kada, A. Yokoyama, T. Kamiya and O. Hanaizumi	
4-09	Hydriding Property of Hydrogen Storage Alloy by Charged Particle Under Different Irradiation Environment	127
	H. Abe, K. Muraki, M. Kishimoto, H. Uchida and T. Ohshima	
4-10	Hardening of Al-Cu-Mg Alloy by Energetic Ion Irradiation	128
	T. Mitsuda, I. Kobayashi, S. Kosugi, N. Fujita, Y. Saitoh, F. Hori, S. Semboshi, Y. Kaneno and A. Iwase	
4-11	Ion Doping Technique Related to Nano-Machining on Unworkable Oxidation Ceramics	129
	S. Ishiyama and M. Satoh	
4-12	Characterization of N-Behavior in Nitriding Processes of Deposited-Ti Thin Films due to Ion Implantation	130
	Y. Kasukabe, Y. Chen, S. Yamamoto and M. Yoshikawa	
4-13	The Effects of Displacement Damage and Transmutation Atoms on Dimensional Stability of SiC with Impurities	131
	T. Nozawa, T. Taguchi and H. Tanigawa	

4-14	Detection of Implanted ^{12}C in Ag/Ni/ $\alpha\text{-Al}_2\text{O}_3(0001)$ Employing Non-Rutherford Elastic Scattering Process	132
	S. Sakai, S. Entani, Y. Matsumoto, M. Ohtomo, P. Avramov, K. Narumi and H. Naramoto	
4-15	Radiation Damages in CeO_2 Thin Films Irradiated with Ions Having the Same Nuclear Stopping and Different Electronic Stopping Powers	133
	N. Ishikawa and K. Takegahara	
4-16	Irradiation-induced-defect Recovery and Magnetic Property of the Gd^+ Ion Implanted GaN	134
	A. Yabuuchi, M. Maekawa, A. Kawasuso, S. Hasegawa, Y. K. Zhou and H. Asahi	
4-17	Gamma-ray Induced Defect Formation in High-Purity α -Quartz	135
	K. Kajihara	
4-18	Adsorption Site of Alkali Metals on $\text{Si}(111)\text{-}\sqrt{3}\times\sqrt{3}\text{-Ag}$ Surface Studied by Reflection High-Energy Positron Diffraction	136
	Y. Fukaya, I. Matsuda, I. Mochizuki and A. Kawasuso	
4-19	Structural Phase Transition of Pt/Ge(001) Surface Studied by Reflection High-energy Positron Diffraction	137
	I. Mochizuki, Y. Fukaya and A. Kawasuso	
4-20	Recovery Behavior of Vacancies in Type 304 Stainless Steels Studied by Positron Annihilation Spectroscopy	138
	A. Yabuuchi, M. Maekawa and A. Kawasuso	
4-21	Positron Annihilation Lifetime of Irradiated Polyimide	139
	T. Hirade, T. Oka, N. Morishita, A. Idesaki and A. Shimada	
4-22	ESR Study of Ion-beam-induced Silyl Radical Generation in Single Crystals ...	140
	K. Yoshimura, M. Sugimoto, A. Idesaki and M. Yoshikawa	
4-23	Effect of Alumina Particle on the Enhancement of H_2 Production and the Reduction of H_2O_2 Concentration in the γ -radiolysis of Aqueous Solutions ...	141
	R. Yamada, Y. Kumagai and R. Nagaishi	
4-24	Incident Energy Dependences of Transient Species in Water under Pulsed H^+ Ion Irradiation	142
	M. Taguchi, K. Iwamatsu, Y. Sugo, S. Kurashima and Y. Katsumura	
4-25	LET Effect on the Radiation Induced Copolymerization of Maleimide with Styrene in 2-Propanol Solution	143
	S. Nakagawa, M. Taguchi and A. Kimura	
4-26	Measurement of the Ion Beam Pulse Radiolysis Using Scintillator	144
	T. Kondoh, J. Yang, K. Kan, Y. Yoshida, H. Shibata, S. Kurashima and M. Taguchi	
4-27	Three-Dimensional Imaging Test for a Head Module of a Si/CdTe Compton Camera for Medical Application	145
	M. Yamaguchi, N. Kawachi, T. Kamiya, T. Satoh, N. Suzui, S. Fujimaki, H. Odaka, S. Ishikawa, M. Kokubun, S. Watanabe, T. Takahashi, H. Shimada, K. Arakawa, Y. Suzuki, K. Torikai, Y. Yoshida and T. Nakano	

4-28	Improvement of Measurement System for Source Neutron Spectrum to extend the Energy Range down to a few MeV	146
	Y. Shikaze, Y. Tanimura, M. Tsutsumi, H. Nemoto, M. Yoshizawa, H. Harano, T. Matsumoto and K. Mizuhashi	
4-29	Measurements of Low Energy Neutron Spectra of Quasi-Monoenergetic Neutron Fields at TIARA	147
	T. Matsumoto, A. Masuda, H. Harano, Y. Unno, M. Hagiwara, T. Sanami, J. Nishiyama, Y. Shikaze, Y. Tanimura, M. Yoshizawa, M. Baba and K. Mizuhashi	
4-30	Test Measurement of Neutron Energy Spectra on Thin Targets Bombarded with 13 MeV/nucleon ^{20}Ne	148
	Y. Iwamoto, M. Hagiwara, N. Matsuda, T. Sanami, Y. Sakamoto, H. Nakashima and K. Mizuhashi	
4-31	Systematic Measurement of Neutron and Gamma-ray from Thick Targets Bombarded with 12 and 18 MeV Protons	149
	M. Hagiwara, T. Sanami, Y. Iwamoto, N. Matsuda, Y. Sakamoto, Y. Nakane, H. Nakashima, K. Masumoto, Y. Uwamino and K. Mizuhashi	
4-32	Spectroellipsometric Studies on EB Induced Refractive Index Change of Aliphatic Polyimide	150
	H. Seito, T. Hakoda, H. Hanaya, Y. Haruyama, H. Kaneko, T. Yamashita and T. Kojima	
4-33	Measurement of Charge States Corresponding to Relative Position of Constituent Ions Resulting from Foil-induced Dissociation of Aligned C_2^+ Ions	151
	A. Chiba, Y. Saitoh, K. Narumi, K. Yamada and T. Kaneko	
4-34	Ion Induced Luminescence from Sapphire Irradiated with Swift Cluster Ion Beams - Energy Dependence of Incident Cluster Beams -	152
	H. Shibata, Y. Saitoh, A. Chiba, K. Yamada, M. Taguchi and K. Narumi	
4-35	Energy Deposition in Carbon by MeV/atom Carbon Cluster Ions	153
	T. Kaneko, Y. Saitoh, A. Chiba and K. Narumi	
4-36	Study on Au Cluster Ion Irradiation Effects for Fz-Si Single Crystal by Using Slow Positron Beam	154
	F. Hori, A. Kawasuso, Y. Saitoh and A. Iwase	
4-37	Energy Dependence of Nonlinear Effects of Sputtering Yields of Si Bombarded with 10-540-keV C_{60} Ions	155
	K. Narumi, H. Naramoto, K. Yamada, Y. Saitoh, A. Chiba, Y. Takahashi and Y. Maeda	
4-38	Secondary Ion Emission from PTFE upon C_{60} Ion Impacts	156
	K. Hirata, Y. Saitoh, A. Chiba, K. Yamada, Y. Takahashi, K. Narumi and T. Kamiya	
4-39	Status Report on Technical Development of the JAEA AVF Cyclotron Facility •	157
	H. Kashiwagi, N. Miyawaki, S. Okumura, S. Kurashima, K. Yoshida, Y. Yuri, T. Yuyama, T. Ishizaka, I. Ishibori, T. Nara and W. Yokota	

4-40	Development of Beam Generation and Irradiation Technology for Electrostatic Accelerators	158
	A. Yokoyama, S. Uno, A. Chiba, K. Yamada, Y. Saitoh, Y. Ishii, T. Satoh, T. Ohkubo and T. Agematsu	
4-41	Fast Single-Ion Hit System for Heavy-Ion Microbeam at TIARA Cyclotron (IV)	159
	W. Yokota, T. Satoh, S. Okumura, S. Kurashima, N. Miyawaki, H. Kashiwagi, K. Yoshida, M. Koka, K. Takano, A. Yokoyama, W. Kada and T. Kamiya	
4-42	Development of Real-time Single-ion Hit Detection System and IBIL System ...	160
	A. Yokoyama, W. Kada, T. Satoh, M. Koka, S. Yamamoto, T. Kamiya and W. Yokota	
4-43	Research and Development on Heavy-ion Uniform-beam Formation by Nonlinear Focusing	161
	Y. Yuri, I. Ishibori, T. Yuyama, T. Ishizaka and S. Okumura	
4-44	3D Micro-fabrication Utilized Superimposing Technique with Focused MeV Ion Beams	162
	K. Takano, T. Satoh, T. Kamiya, Y. Ishii, T. Ohkubo, M. Koka, W. Kada, M. Sugimoto, S. Seki and H. Nishikawa	
4-45	Electroforming of Ni Mold Using High-aspect-ratio PMMA Microstructures Fabricated by Proton Beam Writing	163
	Y. Tanabe, H. Nishikawa, T. Satoh, Y. Ishii and T. Kamiya	
4-46	Calibration of Beam Profile Diagnostic Utilizing Back-Scattered Particles for Laser-driven Ions	164
	H. Sakaki, Y. Fukuda, M. Kanasaki, T. Yamauchi, T. Hori, M. Tampo, K. Kondo, S. Kurashima and T. Kamiya	
4-47	Development of Fine Devices Using Proton Scanning Microbeam	165
	T. Sakai, R. Yasuda, H. Iikura, T. Nojima, M. Matsubayashi, M. Koka, T. Sato, T. Ohkubo and Y. Ishii	
4-48	Spin-Polarize Positron Beam Based on ^{68}Ge - ^{68}Ga Source Produced by Cyclotron	166
	A. Kawasuso, M. Maekawa, Y. Fukaya, A. Yabuuchi and I. Mochizuki	
4-49	Improvement of a Positron Gun Suitable for Intense Microbeam Production	167
	M. Maekawa, A. Yabuuchi and A. Kawasuso	

4-1 Oxygen Reduction Activity of Transition Metal and Nitrogen Doped Carbon Films Prepared by Pulsed Laser Deposition

S. Yamamoto, T. Hakoda, K. Yoshimura, K. Kawaguchi and M. Yoshikawa

Environment and Industrial Materials Research Division, QuBS, JAEA

Polymer electrode membrane fuel cells (PEMFCs) have attracted attention because of their higher energy densities, low operating temperatures and lack of pollutant emissions. However, several issues must be overcome toward their commercially viable technology; the activity and cost of cathode catalysts are crucial. Platinum (Pt) and Pt alloys are the most attractive catalysts for an oxygen reduction reaction (ORR). But they have a drawback of high cost due to their limited supply. Therefore, low Pt loading catalysts and non-Pt catalysts have been developed. One promising catalyst is based on the transition metal (TM)-nitrogen (N)-carbon (C) systems (TM: Co, Ni, etc.). The preparation method generally involved the heat-treatment of a TM precursor, i.e., carbon powder, and a source of nitrogen at 600–1000 °C. The TM-C-N systems were also prepared by a sputtering method. This method enabled one to prepare the TM-C samples at various compositions by sputtering of target materials and subsequent deposition of them to a substrate. Moreover, N species can be doped to the samples by the deposition in the presence of N₂ gas.

In the present study, we prepared TM and N doped carbon films by depositing of TM and isotropic graphite on a heated glassy carbon (GC) substrate in the presence of N₂ gas using a pulsed laser deposition (PLD). The PLD was performed by the second harmonic Q-switched Nd:YAG laser with a wavelength of 532 nm. A typical laser fluence and repetition rate were 300 mJ cm⁻² and 10 Hz, respectively. The ORR activity of the films (thickness: ~3 μm) was electrochemically determined using a rotating disk electrode system. The reference and counter electrodes were Ag/AgCl with a saturated KCl solution and a Pt wire, respectively. The electrolyte was a 0.5 mol dm⁻³ H₂SO₄ aqueous solution at room temperature. The films were characterized using transmission electron microscopy (TEM), X-ray diffraction (XRD), and Rutherford backscattering spectroscopy (RBS). The RBS analysis using a 3 MV single-stage-accelerator at JAEA Takasaki was employed to determine the composition of the films.

Figure 1 shows the ORR activity for Co-N-C, Ni-N-C and N-C films as function of the temperatures of the GC substrates during the PLD. The ORR activity of Co-N-C, Ni-N-C and N-C films increased with elevating temperature (300–600 °C) of the GC substrate during the deposition. The Co-N-C film prepared at 600 °C in the presence of 66.7 Pa N₂ showed the highest ORR activity among the prepared films; its ORR potential (E_{ORR}) was 0.66 V (vs. NHE). However, this ORR potential of the Co-N-C film is

still insufficient compared to the ORR potential of Pt film on GG substrate (E_{ORR} : 0.85 V) measured by our rotating disk electrode system. The results of TEM, XRD and RBS indicated a Co-N-C film deposited at 500 °C has amorphous structure and the following composition, in atomic percent: Co (4.2%), N (21.0%), C (69.8%) and oxygen contamination (5.0%) determined by RBS spectra shown in Fig. 2. Our preliminary results suggest that suitable choice of TM and higher deposition temperature make it possible to improve ORR activity of TM-N-C films.

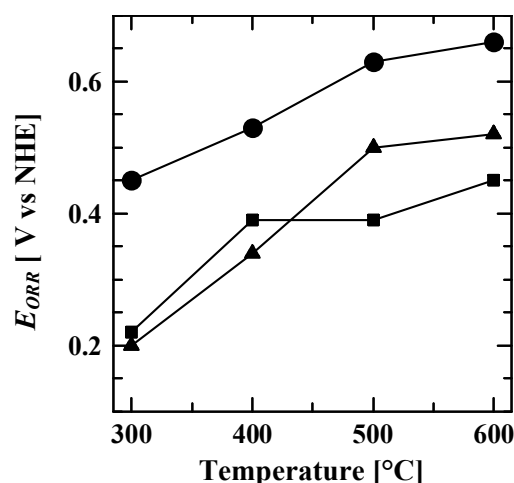


Fig. 1 E_{ORR} for (●): Co-N-C, (▲): Ni-N-C and (■): N-C films as function of the temperatures of the GC substrates during the deposition.

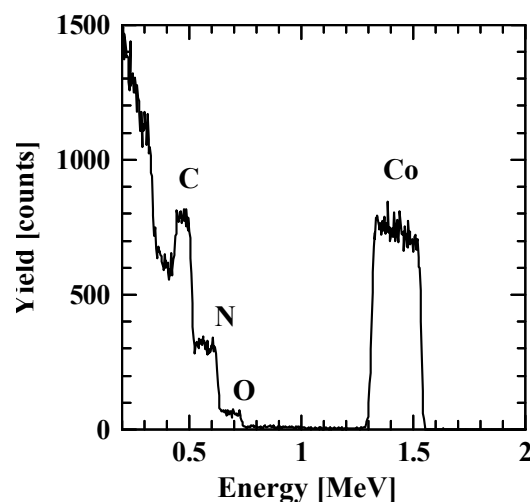


Fig. 2 2.0 MeV ⁴He⁺ RBS spectrum from a Co-N-C film (thickness: ~300 nm) on GC substrate. The film was deposited at 500 °C.

4-2 Fabrication of Functionalized Polystyrene Nanowires by the Single Particle Nano-Fabrication Technique

S. Seki^{a)}, A. Asano^{a)}, Y. Maeyoshi^{a)}, S. Tsukuda^{b)},
M. Sugimoto^{c)} and M. Yoshikawa^{c)}

^{a)}Department of Applied Chemistry, Graduate School of Engineering, Osaka University

^{b)}Institute of Multidisciplinary Research for Advanced Materials, Tohoku University,

^{c)}Environment and Industrial Materials Research Division, QuBS, JAEA

Radiation promotes various chemical effects in materials. In the case of polymeric materials, the main effects of radiation are controlled by chain scission and cross-linking reactions. We have succeeded in direct formation of 1-D nanostructures based on the cross-linking reactions in the thin films of several kinds of polymers by irradiation of high energy charged particles; single particle nano-fabrication technique (SPNT)¹⁻³⁾. Polystyrene gives well-controlled nanostructures in length and number density by SPNT. The Cross-linking G value (number of crosslinks/100 eV of absorbed dose) of polystyrene indicates drastic change by introducing functional groups into the styrene monomers⁴⁾.

In this report, the nanostructures based on the polystyrene derivatives were fabricated by SPNT and observed by atomic force microscope (AFM) measurement. The surface of the nanostructure based on alkyne-functionalized polystyrene was modified by using Cu catalyzed Click reaction.

Pendant acetylene and chloromethyl functionalized copolymers were prepared by living free radical process. Poly(styrene-co-4-ethynylstyrene); PSES and poly(styrene-co-4-chloromethylstyrene); PSC were polymerized from acetylene and chloromethyl functionalized monomers by NMP; nitroxide-mediated radical polymerization, respectively. In order to evaluate the effects of functional groups, polystyrene; PS was also synthesized by the same polymerization method.

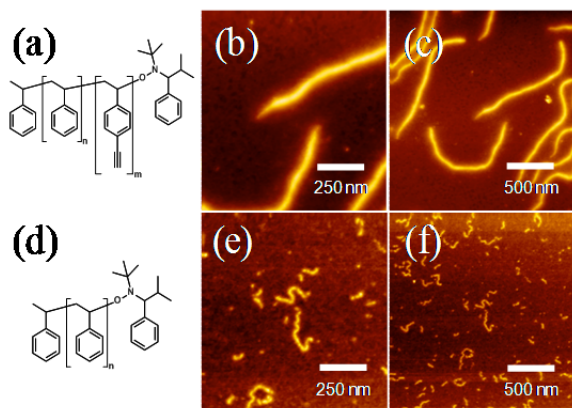


Fig. 1 Chemical structures of polymers; (a) poly(styrene-co-4-ethynylstyrene) and (d) polystyrene. AFM micrographs of nanowires based on (b)-(c) PSES and (e)-(f) PS film prepared by exposing films to a 450 MeV $^{129}\text{Xe}^{23+}$ at 3.0×10^8 ions cm^{-2} .

Nanostructures based on PSES and PSCS were fabricated by SPNT and confirmed by AFM measurement (Fig. 1). The lengths of the nanowires were simply controlled by film thickness, which is likely to the case of polystyrene. When the PSES film was formed by drop-cast method, fabrication of 20 μm nanowires in length was succeeded.

The radii of the PSES, PSCS, and PS nanowires were determined 13.2, 13.0, and 4.6 nm by AFM measurement and calculation on the ellipse model, respectively. The values of $G(x)$ for PSES, PSCS, and PS were calculated 2.7, 2.8, and 0.3 (100 (eV)^{-1}). These results show that acetylene and chloromethyl groups promoted the cross-linking reaction.

It is well known that terminal alkyne groups can react with azide groups under Cu catalyst as Click reaction. The surface of PSES nanowires was modified with Poly(styrene-co-4-azidestyrene) by Click reaction. The height of nanowires was increased after modification (Fig. 2). This result indicates that alkyne groups on the surface of nanowires maintain its function, leading to be points of effective substitution reactions.

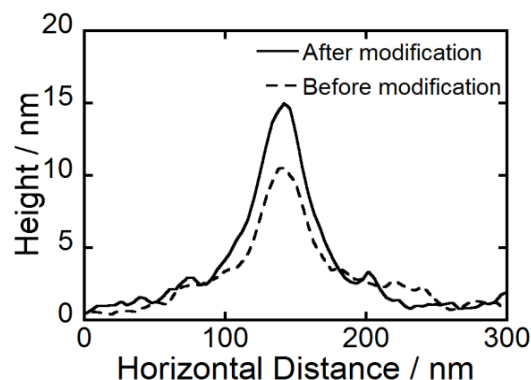


Fig. 2 Cross-sectional profiles of nanowires based on PSES before (dot line) and after (line) modification with poly(styrene-co-4-azidestyrene) by Cu catalyzed Click reaction.

References

- 1) S. Seki et al., Adv. Mater. 13 (2001) 1663.
- 2) S. Seki, et al., Phys. Rev. B 70 (2004) 144203.
- 3) S. Tsukuda et al., J. Phys. Chem. B 109 (2006) 19319.
- 4) S. Watanabe et al., Radiat. Phys. Chem. 78 (2009) 1017.

4-3 Formation of Poly(vinylphenol) Nanowires Including Au Nanoparticles by Ion Beam Irradiation

S. Tsukuda^{a)}, A. Asano^{b)}, M. Sugimoto^{c)}, A. Idesaki^{c)}, M. Yoshikawa^{c)},
S. Seki^{b)} and S.-I. Tanaka^{a)}

^{a)} Institute of Multidisciplinary Research for Advanced Materials, Tohoku University,

^{b)} Division of Applied Chemistry, Graduate School of Engineering, Osaka University,

^{c)} Environment and Industrial Materials Research Division, QuBS, JAEA

Heavy-ion beams are used for high-density energy deposition in polymeric materials. Ion irradiation at low fluence without overlapping between ion tracks produces single ion events in the target materials. Single ion bombardment can release active intermediates at high density within a limited area along the single ion track. In crosslinking-type polymers, the crosslinking reactions along the ion track result in the formation of a cross-linked nanogel (nanowire) in the thin films. The non-crosslinked area can be removed by development procedure, utilizing the change in solubility due to the gelation of polymer¹⁻³⁾. In this paper, we report the direct formation of the poly(vinylphenol) (PHS) and Au nanoparticles hybrid nanowires, produced by single ion irradiation of the PHS films including Au nanoparticles. The direct observation was carried out using AFM, and inner structures of nanowires were observed by TEM. The radial sizes were also discussed in terms of both radiation dose and crosslinking efficiency.

The PHS and $\text{HAuCl}_4 \cdot 4\text{H}_2\text{O}$ were dissolved in MeOH at 5 and 0.1 wt%. This hybrid solution was spin-coated on the Si substrate. These thin films of PHS and PHS/Au hybrids were subsequently placed in a vacuum chamber and exposed to 490 MeV $^{192}\text{Os}^{30+}$ beams at the Takasaki Ion Accelerators for Advanced Radiation Application (TIARA) cyclotron accelerator facility of the Japan Atomic Energy Agency. After irradiation, the samples were developed using isopropylalcohol (IPA) for 1 minute. The direct observation of the surface of the substrates were performed using an atomic force microscope (AFM Seiko Instruments Inc.(SII) SPI-4000). The observation of inner structures of the nanowires was performed using a Transmission Electron Microscope (TEM: JEOL JEM-2010).

The hybrid PHS film including Au nanoparticles was prepared on Si substrate. This film was exposed to 490 MeV Os ion beam at ion fluence of 1.0×10^{10} ions/cm². After development procedure using IPA, the hybrid nanowires based on PHS including Au nanoparticles

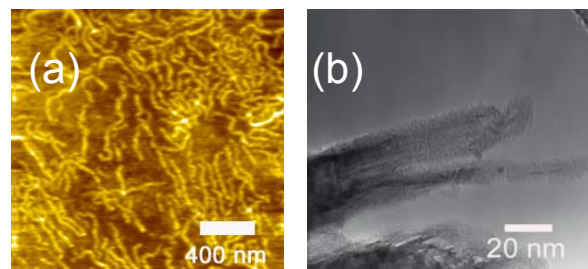


Fig. 1 (a) AFM and (b)TEM micrographs of nanowires formed by 490 MeV Os ion beam irradiation to PHS included Au nanoparticles thin films at the fluence of 1.0×10^{10} ions cm⁻².

(PHS/Au) were successfully formed and isolated on the Si substrate as shown in Fig. 1 (a). The radii of PHS and PHS/Au nanowires were also measured using AFM trace and summarized in Table 1. The radii of nanowires based on PHS/Au were smaller than that of PHS nanowires. These results indicates the including Au-nanoparticles inhibits cross-linking reaction, resulting in reduced cross-linking efficiency of the PHS/Au film compared with that of PHS. The significant decrease on cross-linking efficiency between PHS and PHS/Au influences the radial sizes.

In order to concern the morphology and size of Au nanoparticles in the PHS nanowires, the TEM observation was carried out. The 1~3 isolated nanowires were partially observed as shown in Fig. 1 (b). Here, Au nanoparticles were clearly observed in single PHS nanowires. The included particles sizes were 3.6~5.5 nm, and the number of particles per one wire is 1 to 3. It is expected that the inner-structures of nanowires consisted of three dimensional cross-kinked network structures, and then this inner-network structures of PHS polymer functions to bind the Au nanoparticles within the nanowires.

The hybrids nanowires based on PHS including Au nanoparticles were easily formed by ion beam irradiation to their hybrid film. The size of Au nanoparticles in PHS nanowires was raging from 3.6 to 5.5 nm. The average radial size of PHS/Au nanowires was slightly decreased compared with that of the PHS nanowires.

Table 1 Radii of PHS and PHS/Au nanowires formed by 490 MeV Os ion beam.

Ion beam	Radius (<i>r</i>) [nm]	
	PHS	PHS/Au
490 MeV Os	6.6	6.2

References

- 1) S. Seki et al., Adv. Mater. 13 (2001) 1663-1665.
- 2) S. Tsukuda, et al., Appl. Phys. Lett. 87 (2005) 233119-1-3.
- 3) S. Tsukuda, et al., J. Photopolym. Sci. Tech. 22 (2009) 245-248.

4-4 Radius Control of SiC Nano Fiber by Two Steps Irradiation Method Using Ion and Electron Beams

M. Sugimoto^{a)}, K. Yoshimura^{a)}, A. Idesaki^{a)}, M. Yoshikawa^{a)},
S. Tsukuda^{b)} and S. Seki^{c)}

^{a)} Environment and Industrial Materials Research Division, QuBS, JAEA,

^{b)} Institute of Multidisciplinary Research for Advanced Materials, Tohoku University,

^{c)} Department of Applied Chemistry, Osaka University

Nano fiber with quite large specific surface shows excellent catalyst and absorption activity compared with bulk materials. Recently, we succeeded in obtaining the palladium folded Silicon Carbide (SiC) nano fiber by ion beam irradiation from the polymer-blend thin film with polycarbosilane (PCS) and palladium acetate¹⁻³⁾. However, the nano fiber falls on the substrate during the solvent extraction process, because the strength of the nano fiber decreases by swelling. Therefore, it is necessary to expand the control range of diameter to make the nano fiber with enough strength. In this research, we report the new control method of the radius of the nano fiber by ion beam irradiation and additional electron beam (EB) irradiation.

Polycarbosilane (NIPUSI Type-A), as a precursor polymer of SiC ceramics, was purchased from Nippon Carbon Co. LTD and solved into toluene, then the solution was spin-coated on polished Si substrates to make the polymer thin films. The obtained films were irradiated with 490 MeV ¹⁹²Os³⁰⁺ ion beams in vacuum at ambient temperature. Subsequently, the films were irradiated by EB with total dose up to 2.4 MGy in helium. After this two steps irradiation, the samples were treated by solvent and the cross-linked part insoluble in the solvent was developed as polymer nano fiber. These were fired in argon atmosphere at 1,273 K for 1,800 sec using an electric furnace with a heating ramp rate of 250 K/h, giving the ceramic nano fiber on the substrate. Direct observation of the nano fiber was conducted using Scanning Probe Microscopy (SPM) using dynamic force microscope method. The size of cross-section of a nano fiber is defined as an

average radius of cross-sectional measurements.

Radii of the PCS and SiC nano fiber formed by the additional EB irradiation with various dose are presented in Fig. 1. The value of radius of PCS nano fiber increased with the dose of EB and that of the SiC nano fiber also increased, because the PCS nano fiber shrinks in a constant ratio during firing. Figure 2 shows scheme of radius control mechanism of the nano fiber by the additional EB irradiation. Single ion bombardment can release the energy at high density within a limited area along the ion track and then form the cross-linked cylindrical gelation part with diameter of the critical energy density of gelation for polymers³⁾. On the other hand, the additional EB irradiation produce homogeneous distribution of cross-linking points. Therefore, cross-linking reactions also occur at the outer part of the gelation part formed by ion beam irradiation, resulting in increase of the radial size as shown in Fig. 2.

The two step irradiation will enables to fabricate self-standing nano fiber with supreme large specific surface from much kind of polymers containing catalyst elements; therefore it has been expected as high efficiency catalyst and adsorption materials.

References

- 1) M. Sugimoto et al., Ceram. Trans. 213 (2010) 105-111.
- 2) S. Tsukuda et al., J. Photopolym. Sci. Tech. 22 (2009) 245.
- 3) S. Seki et al., Macromolecules 38 (2005) 10164.

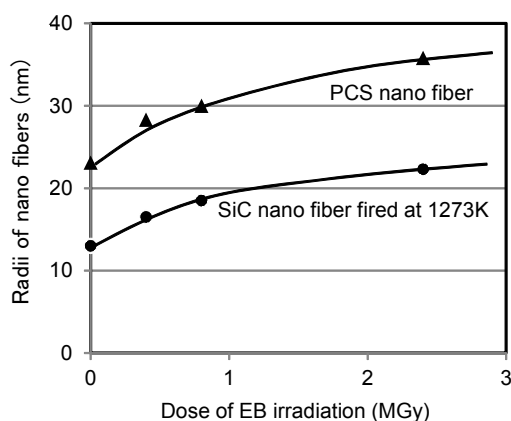


Fig. 1 Radii of nano fiber formed from PCS thin films by EB irradiation with various dose.

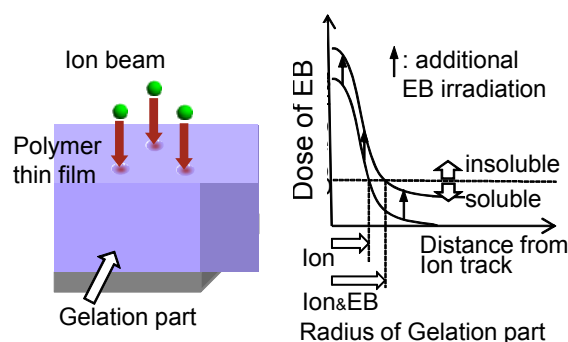


Fig. 2 Scheme of radius control mechanism of the nano fiber by additional EB irradiation after ion beam irradiation.

4-5 Gas permeation Property of Silicon Carbide Membrane Prepared on Porous Alpha Alumina Support Using Radiation Curing of Polymer Precursor Film

A. Takeyama, M. Sugimoto and M. Yoshikawa

Environment and Industrial Materials Research Division, QuBS, JAEA

There is growing interest in separating hydrogen (H_2) from high temperature gaseous streams generated by combustion of fossil fuels. In particular, H_2 production using inorganic membrane in integrated gas combined cycle (IGCC) power plants has received much attention¹⁾. Since the membrane is exposed to highly reactive gases such as carbon monoxide (CO), both membrane and supports are prepared from chemically stable materials. In this study, we prepared silicon carbide (SiC) membrane on porous alpha alumina supports using our reported method reported previously²⁾.

Alpha alumina tube, which is chemically stable but has large sized pore (approximately 100 nm), was used as the support. First, supports were dipped in the 10 mass% polycarbosilane (PCS), polymer precursor solution for 1 s and drawn up by 40 mm/s (the first dipping). After drying, supports coated with PCS film were immersed into another PCS solution whose concentration was 3 mass% for 0.8, 1.5 and 2 s followed by withdrawing by 40 mm/s (the second dipping). Subsequently, they were cured and cross-linked by electron beam irradiation in helium atmosphere and pyrolyzed at 973 K in argon atmosphere. For the comparison purposes, SiC membrane without the second dipping was prepared. Single gas permeance of hydrogen (H_2), argon (Ar) or nitrogen (N_2) of the membrane was measured.

Figure 1 shows the gas permeation property of SiC membrane prepared without the second dipping. Permeance ratio of Ar to N_2 (P_{Ar}/P_{N_2}) was derived to be 0.92 and slightly larger than 0.84 which is expected when N_2 and Ar diffuse through the membrane by Knudsen diffusion mechanism. This indicates some larger sized defects than

kinetic diameter of N_2 of 0.36 nm were leaved in the membrane. The permeance ratio of H_2 to N_2 (P_{H_2}/P_{N_2}) was 11 and larger than 3.7 for Knudsen diffusion of H_2 , indicating a portion of H_2 molecule diffuses by molecular sieving mechanism. Consequently, large defects and sub-nano meter sized pores coexisted in the membrane.

Figure 2 shows gas permeation properties of SiC membrane prepared via immersing. For immersion time of 0.8s, P_{Ar}/P_{N_2} was obtained to be 0.75 and lower than 0.84. Low value means larger sized defects formed in the membrane by the immersion. When the immersion time was increased to 1.5 s, P_{Ar}/P_{N_2} was increased up to 1.7. As shown in Fig. 2, this was caused by decrease of N_2 permeance as a result of discriminately plugging defects larger than 0.36 nm. However, the ratio of P_{H_2}/P_{N_2} of 12 was not large as expected, though higher H_2 permeance than that shown in Fig. 1 was obtained. Accordingly, both sub-nano meter sized pore as large as about 0.36 nm for N_2 diffusion and as large as about 0.29 nm for H_2 diffusion with molecular sieving mechanism, predominantly coexisted in this membrane, whereas large sized defects were plugged. Further increasing the immersion time to 2 s, whole gas permeances were increased. It suggests resistance of the diffusion of molecules was reduced by the decrease of thickness of membrane. Finally, SiC membrane with sub-nano meter sized pore was prepared on alpha alumina support by plugging large sized defects using our preparation method.

References

- 1) M. Abdollahi et al., J. Membr. Sci. 363 (2010) 160.
- 2) A. Takeyama et al., Mater. Trans. to be published.

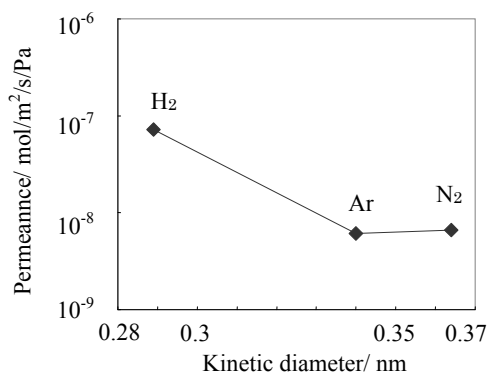


Fig. 1 Gas permeation property of SiC membrane prepared by coating of PCS film using 10 mass% PCS solution. Permeation temperature was 523 K.

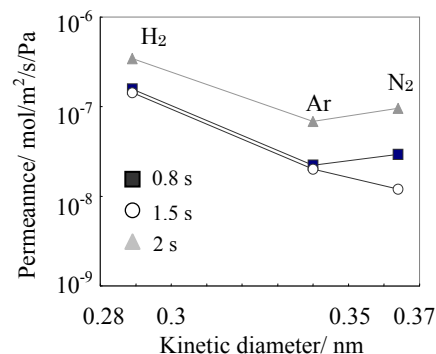


Fig. 2 Gas permeation property of SiC membrane prepared by coating of PCS film using 10 mass% solution followed by immersing of PCS film in 3 mass% solution. Permeation temperature was 523 K.

4-6 Synthesis of Nano-Crystalline SiC Nanotubes by Ion-Irradiation Technique

T. Taguchi^{a)}, S. Yamamoto^{b)}, K. Kawaguchi^{b)} and S. Shamoto^{a)}

^{a)} Neutron Material Research Center, QuBS, JAEA,

^{b)} Environment and Industrial Materials Research Division, QuBS, JAEA

Since the discovery of carbon nanotubes (CNTs) in 1991, significant numbers of researchers have synthesized new one-dimensional nanostructured materials such as nanotubes, nanorods and nanowhiskers for potential applications. Some of them have reported that many nanomaterials such as TiC, NbC, BN, SiO₂ and GaN nanostructures are fabricated from CNTs as the template. SiC is one of the most important wide-band-gap semiconducting materials for high temperature and high power. And SiC is also one of the most important structural materials at high temperature. Therefore, SiC offers exciting opportunities in electronic devices and in structural materials at high temperature. We reported that the polycrystalline C-SiC coaxial nanotubes, which were CNTs sheathed with SiC, and that polycrystalline single-phase SiC nanotubes were formed^{1,2)}. Furthermore, the single-crystalline SiC nanotubes and the amorphous SiC nanotubes were successfully synthesized by the ion irradiation of the polycrystalline SiC nanotubes at 900 °C and 100 °C, respectively³⁾. However, nano-crystalline SiC nanotubes, which have SiC nano-crystals with less than 10 nm diameter in the amorphous SiC matrix, have not been synthesized yet. The purpose of this study is, therefore, to synthesize nano-crystalline SiC nanotubes by ion-irradiation technique.

Carbon nanotubes (GSI Creos Corporation, Tokyo, Japan) were used as the template. The C-SiC coaxial nanotubes were synthesized by heating CNTs with Si powder (The Nilaco Corporation, Tokyo, Japan) at 1,200 °C for 100 h in a vacuum. Single-phase SiC nanotubes were formed by the heat treatment of C-SiC coaxial nanotubes at 600 °C for 2 h in air. Thin films of single-phase SiC

nanotubes were prepared on the alumina plates by depositing the single-phase SiC nanotubes dispersed in ethanol. These thin films of single-phase SiC nanotubes were irradiated with 3-MeV Ni²⁺ ions at 100 °C. The ion fluence was 1.8×10^{19} - 7.4×10^{19} ions/m².

Polycrystalline SiC nanotubes were transformed to amorphous SiC nanotubes by irradiation with 7.4×10^{19} ions/m² at 100 °C. On the other hand, microstructures of polycrystalline SiC nanotubes changed hardly by irradiation with less than 2.0×10^{19} ions/m² at 100 °C.

Figures 1 and 2 showed a low magnification TEM image and the corresponding electron diffraction pattern, and a high resolution TEM image of the SiC nanotubes irradiated with 3.5×10^{19} ions/m² at 100 °C, respectively. According to these TEM images, the nano-crystalline SiC nanotubes were successfully synthesized by irradiation of polycrystalline SiC nanotubes with 3-MeV Ni²⁺ ions. SiC nano-crystals exist in an amorphous SiC matrix. The crystal size of nano-crystalline SiC nanotubes was smaller than 10 nm.

These results indicate that nano-crystalline SiC nanotubes can be synthesized by ion-irradiation technique with controlling the ion fluence.

References

- 1) T. Taguchi et al., J. Am. Ceram. Soc. 88[2] (2005) 459-461.
- 2) T. Taguchi et al., Physica E 28[4] (2005) 431-438.
- 3) T. Taguchi et al., JAEA Takasaki Ann. Rep. 2009 (2011) 127.

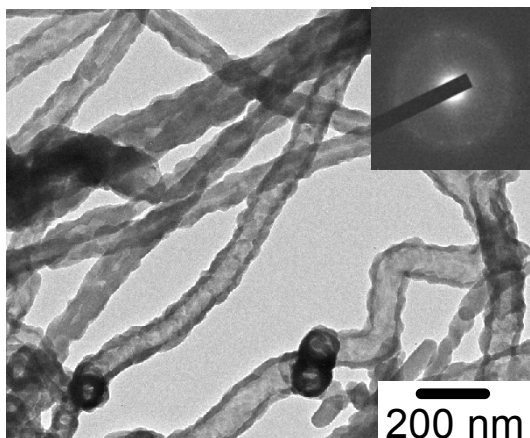


Fig. 1 Low magnification TEM image and the corresponding electron diffraction pattern of SiC nanotubes irradiated with 3.5×10^{19} ions/m².

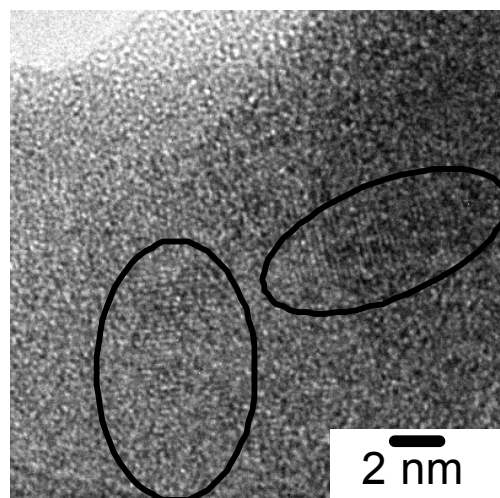


Fig. 2 High resolution TEM image of SiC nanotubes irradiated with 3.5×10^{19} ions/m². Solid circles indicate nano-crystals in an amorphous SiC matrix.

4-7 Study for Damage of Charge Stripper Carbon Foil by Ion Beam Irradiation

Y. Yamazaki^{a)}, M. Yoshimoto^{a)}, O. Takeda^{a)}, M. Kinsho^{a)}, T. Taguchi^{b)},
S. Yamamoto^{c)}, T. Kurihara^{d)} and I. Sugai^{d)}

^{a)} Accelerator Division, J-PARC, JAEA, ^{b)} Neutron Material Research Center, QuBS, JAEA,

^{c)} Environment and Industrial Materials Research Division, QuBS, JAEA,

^{d)} High Energy Accelerator Research Organization, KEK

For multi-turn injection of high power proton synchrotron, a charge stripper foil is one of key technology. Typically carbon-based material is used to strip two electrons off the incident H^- beams. J-PARC also requires carbon stripper foils to strip electrons from the H^- beam supplied by the linac before injection into the Rapid Cycling Synchrotron (RCS). Foil thickness is about $200 \mu\text{g}/\text{cm}^2$ corresponding to conversion efficiency of 99.7% from the primary H^- beams of 181 MeV energy to H^+ . For this purpose, Sugai have successfully developed Hybrid type thick Boron-doped Carbon (HBC) stripper foils and J-PARC RCS applied HBC foil, which showed a drastic improvement not only the lifetime, but also small thickness reduction, and shrinkage at the irradiated area by the ion beam¹⁾. This HBC was made by arc-discharge method, in which the cathode used a boron-doped (25%) carbon rod while the opposite electrode was a pure graphite rod.

We started to study carbon stripper foils microscopically why carbon foils have considerable endurance for the beam impact by boron-doped²⁾. At first step, we made a comparison of ion irradiation effect before and after between normal carbon (NC) and HBC by TEM observation. Although typical foil thickness is $200 \mu\text{g}/\text{cm}^2$ for the practical usage, we used each of NC and HBC foils of $15 \mu\text{g}/\text{cm}^2$ thickness because of ease for TEM analyses. Ar^+ of 300 keV, which we use as irradiated ion from ion implanter in TIARA, can deliver the energy deposition by the ion beam into this thickness foil without ion implantation. The ion beam current was $0.3 \mu\text{A}$ with 5 mm diameter of the beam size. Figure 1 shows variance of the surface appearances for each of foils irradiated by Ar^+ .

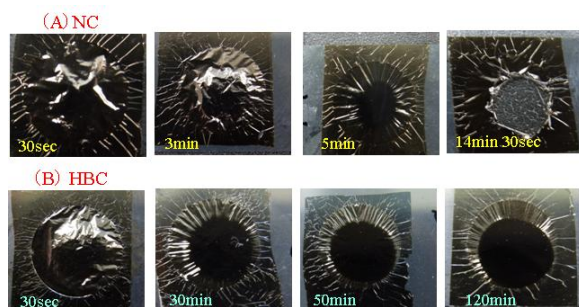


Fig. 1 Time transition of sample surface for (A) NC (normal carbon) and (B) HBC irradiated with 300 keV Ar^+ ions. Aperture of the sample holder is diameter of 8 mm.

It seems that surface of HBC flattened out much slower than NC by the irradiation and that contraction of the volume for foils was occurred by the ion bombardment macroscopically. NC was broken within the short time about 15 minutes by beam irradiation. On the other hand, HBC was not broken more than two hours after smoothed out. In the other verification, we guess that the foil surface temperature was lower than 300°C while irradiating of Ar^+ ion. Although both NC and HBC involved a lot of nano-scale grains of graphite before the irradiation, they had generally amorphous phase. Furthermore we found that both were become disorderly by the ion irradiation because of D-band's growth in the Raman spectrum. But in local area of their foils, crystal growth was occurred for some condition or other. In particular, there were many boron-rich grains in HBC before and after ion irradiation. It seems that grain size of boron-rich area became much larger by irradiation. For example, these boron-rich grains were covered with graphite structure as shown by Fig. 2. This phenomenon of the boron-rich grain growth was also detected by TEM observation simultaneously while a sample is irradiated ion beam.

Now we can't understand explanation in detail for the relation between the volume contraction and crystal growth microscopically by the ion irradiation. But we could get some qualitative behavior of foils for ion bombardment. Further analysis is in progress.

References

- 1) I. Sugai et al., Nucl. Instrum. Meth. A561 (2006) 16.
- 2) Y. Yamazaki et al., IPAC10. Proc. (2010) 3924.

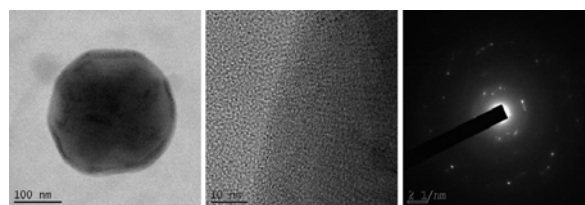


Fig. 2 TEM photographs for one of the boron-rich grain in HBC foil became much larger by Ar^+ ions irradiation. Left is a boron-rich grain of 200 nm in diameter. Center shows graphite structure of 10 nm in width around the grain. Right picture is diffraction pattern of the grain.

4-8 Fabrication of Y-Junction Waveguides Using Proton Beam Writing

K. Miura^{a)}, T. Satoh^{b)}, Y. Ishii^{b)}, M. Koka^{b)}, M. Uehara^{a)}, H. Kiryu^{a)}, K. Takano^{b)}, T. Ohkubo^{b)}, A. Yamazaki^{b)}, W. Kada^{b)}, A. Yokoyama^{b)}, T. Kamiya^{b)} and O. Hanaizumi^{a)}

^{a)} Graduate School of Engineering, Gunma University,

^{b)} Department of Advanced Radiation Technology, TARRI, JAEA

Proton beam writing (PBW) has recently attracted much attention as a next generation micro-fabrication technology. It is a direct-writing technique and does not need any masks to transfer micro-patterns to the surfaces. PBW makes three-dimensional processes easier and provides higher processing throughput than other techniques such as electron beam (EB) lithography¹⁻³⁾. Furthermore, the importance of planar polymer optical waveguides is recently increasing in fields such as optical fiber telecommunication and optical interconnection. Optical waveguides can be directly drawn in poly(methyl methacrylate) (PMMA) using the PBW technique because the refractive index of a PMMA can be increased by proton irradiation⁴⁾. T. C. Sum et al. demonstrated PMMA bulk waveguides drawn by proton beam irradiation⁵⁾. However, their working wavelength (λ) was 633 nm, in the visible range. In this study, we demonstrate Y-junction PMMA film waveguides fabricated using the PBW technique and working at $\lambda=1.55$ μm for long-haul optical fiber telecommunication systems.

An SiO_2 film was deposited as an under-cladding on an Si substrate (20 mm \times 20 mm) by using radio-frequency sputtering. A PMMA (refractive index ~ 1.48) film was spin-coated on the SiO_2 film at 1,350 rpm for 30 sec. The sample was then baked at 120 $^\circ\text{C}$ for 2 min. We repeated these processes twice, and the PMMA film became 10 μm thick. A Y-junction waveguide was drawn on the PMMA film by using the 3 MV single-ended accelerator in TIARA. We set its width to 8 μm in order for it to work as a single-mode waveguide⁶⁾, and we set its branching angle to 2° in order to obtain a low branching loss. The proton irradiation energy was 1.7 MeV, the proton beam current was 10 pA, the dose was 100 nC/mm², and the beam size was about 1 μm ⁶⁾. A 10- μm thick PMMA film was deposited again on the sample as an upper-cladding by spin-coating under the same condition as the first PMMA layer. We cleaved both sides of the sample to observe near field patterns (NFPs) of the waveguides. We used a wavelength-tunable laser (Santec Ltd., ECL-210) for our NFP measurements. The laser wavelength was 1.55 μm , and the light was introduced through a single-mode fiber (SMF) to edges of the waveguides. We observed their NFPs by using a vidicon camera (Hamamatsu Photonics Ltd., C2741-03).

Figure 1 presents a microscopic image of the Y-junction waveguide. We succeeded in drawing an objective Y-junction using the PBW technique. Figure 2 shows an NFP of the Y-junction waveguide at $\lambda=1.55$ μm . Two

spots with an optical power intensity ratio of 1:0.98 were observed. We found that this Y-junction can divide the light of $\lambda=1.55$ μm almost in a 1:1 ratio.

Such single-mode Y-junctions are important components for constructing Mach-Zehnder interferometer (MZI) type thermo-optic switches for optical-fiber telecommunication⁷⁾. As the next step to realize this type of optical switch, we are trying to fabricate MZI type waveguides by symmetrically coupling two Y-junctions using the PBW technique.

References

- 1) A. A. Bettiol et al., Nucl. Instrum. Meth. Phys. Res. B 231 (2005) 364.
- 2) F. Watt et al., Materials Today 10 (2007) 20.
- 3) N. Uchiya et al., Nucl. Instrum. Meth. Phys. Res. B 260 (2007) 405.
- 4) I. Rajta et al., Nucl. Instrum. Meth. Phys. Res. B 260 (2007) 400.
- 5) T. C. Sum et al., J. Lightwave Technol. 24 (2006) 3803.
- 6) K. Miura et al., JAEA Takasaki Ann. Rep. 2009 (2011) 128.
- 7) O. Hanaizumi et al., Key Engineering Materials 459 (2011) 153.

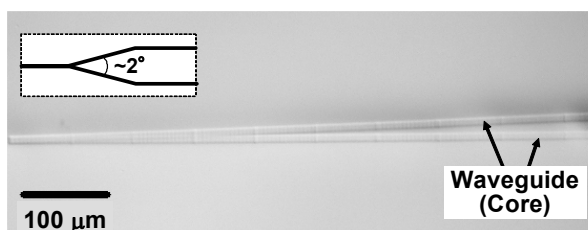


Fig. 1 Microscopic image of the Y-junction waveguide.

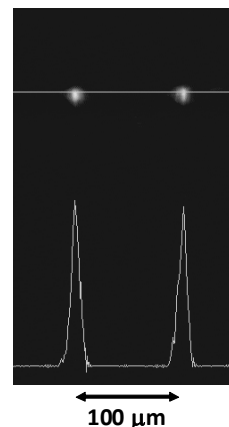


Fig. 2 NFP (upper side) and optical-power profile (lower side) of the Y-junction waveguide.

4-9 Hydriding Property of Hydrogen Storage Alloy by Charged Particle Under Different Irradiation Environment

H. Abe ^{a)}, K. Muraki ^{b)}, M. Kishimoto ^{b)}, H. Uchida ^{c)} and T. Ohshima ^{a)}

^{a)} Environment and Industrial Materials Research Division, QuBS, JAEA,

^{b)} Course of Applied Science, Graduate School of Engineering, Tokai University,

^{c)} Department of Energy Science and Engineering, School of Engineering, Tokai University

Recently, global environmental issues such as warming and air pollution are more serious. Many of environmental problems originate in the energy system using the fossil fuel. The use of hydrogen energy technologies is one of the most prominent solutions to reduce CO₂ emission presumably causing greenhouse effect. Therefore, many research and development of the hydrogen energy technologies becomes important to realize clean energy. The application of hydrogen storage alloys may contribute to energy saving and the reduction of CO₂ emission as is proven by hybrid vehicles which are driven with both an electric motor and a combustion engine. Most of these hybrid vehicles use Ni-MH (Nickel-Metal Hydride) rechargeable battery. Then we are researching the Ni-MH battery that uses hydrogen absorbing alloys that are candidate elements in the hydrogen energy system. For the surface modification of materials, charged particle irradiation is known to be a quite useful method^{1,2)}. Then, charged particle irradiation onto the surface of a metal effectively induces defects such as vacancies, dislocations and micro-cracks in the surface region of the materials. These facts give the possibility that the hydrogen absorptivity in Mm-Ni based alloys is improved by surface modification using electron irradiation. We have investigated the effects of surrounding condition of electron irradiation on the initial rate of hydriding of Mm-Ni based alloys in electrochemical process.

In this study, as a cathode material of Ni-MH battery, a Mm-Ni based hydrogen storage alloy, MmNi_{3.48}Co_{0.73}Mn_{0.45}Al_{0.34} (Mm=La_{0.35}Ce_{0.65}), was prepared by arc melting. The alloy was then flashed to produce powder samples by cyclic hydriding and dehydriding treatments. The produce powder samples had an average grain size of about 38 μm. The powder was then mixed with Cu powder at a rate of alloy/Cu = 1 : 3 in weight, and the pressed under a pressure of 7 t/cm² to prepare a pellet sample with a size of 12 mmφ and 1.2 mm thickness as cathode, Ni(OH)₂ as an anode, for the measurement of hydriding rate in electrochemical process alloys. Surface modification was made by electron irradiation and alkaline treatment. Electron irradiation onto the surface for a sample was made at an acceleration energy of 2 MeV to a dose of 1×10^{17} cm⁻² in the atmospheric air, in a vacuum ($\sim 10^{-1}$ Pa) or in a He gas atmosphere, respectively, using a 2 MV Cockcroft-Walton electron accelerator. For the electrochemical measurements of initial hydrogen absorption reaction rate of the electron irradiated and no-irradiated samples, the rates of hydriding of the samples were measured in a 6 M-KOH using the open cell as a constant voltage -0.93 V and at 298 K, from 0 to 120 min.

Figure 1 shows hydriding curves for samples irradiated under different conditions. A sample irradiated in the air exhibits 4~13 times higher hydriding rate than the other samples irradiated in a He atmosphere or no irradiation. According to surface analyses using ESCA, samples treated under different conditions showed the presence of

complicated oxides of alloy components. Since Mm consists mainly of La and Ce, the contribution of conductive rare earth oxides like CeO_x or LaO_x to the fast kinetics⁴⁻⁸⁾ should be taken into account to explain the different kinetic behaviors measured in this study.

ESCA analyses revealed that the sample irradiated in a He atmosphere was found to have rather reactive surface conditions with thinner surface oxide layers than the sample irradiated in low vacuum. All samples were exposed to air before electrochemical hydriding process. As well known, even at room temperature, surface oxidation proceeds more profound for a metal with a clean surface than for a metal covered with thin oxide layers⁹⁾. Therefore, the sample with reactive surface was heavily oxidized during the air exposure. And this resulted in a subsequent low H₂O dissociation and hydriding rates. The sample treated in low vacuum that was covered by stable oxide layers after the irradiation, and this seems to have inhibited the subsequent H₂O dissociation and hydriding.

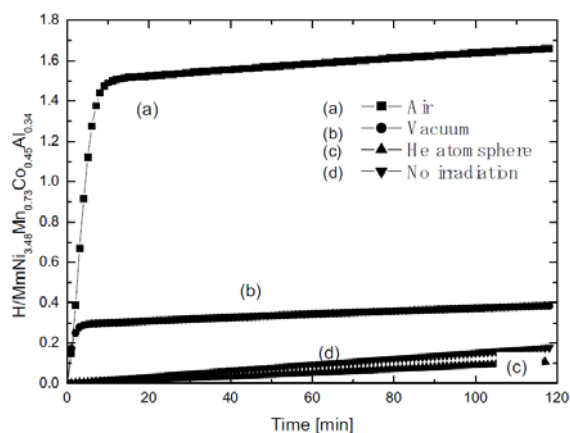


Fig. 1 Hydriding curves for samples (a) with electron irradiation in the atmospheric air, (b) with electron irradiation in low vacuum, (c) with electron irradiation in a He atmosphere, and (d) without irradiation.

References

- 1) H. Abe et al., J. Alloys and Comp. 404-406 (2005) 288.
- 2) H. Abe et al., J. Alloys and Comp. 408-412 (2006) 348.
- 3) H. Abe et al., Nucl. Instrum. Meth. B 206 (2003) 224.
- 4) H. H. Uchida et al., J. Alloys Comp. 231 (1995) 679.
- 5) H. Uchida et al., J. Less Common Met 172-174 (1991) 1018.
- 6) S. Seta et al., J. Alloys Comp. 231 (1995) 448.
- 7) H. Uchida et al., Z. Phys. Chem. 181 (1993) 417.
- 8) H. Uchida et al., Z. Phys. Chem. 181 (1993) 429.
- 9) E. Fromm, Chap. 5 "Low Temperature Oxidation" p.78 in "Kinetics of Metal-Gas Interactions at Low Temperatures", Springer 1998, ISSN 0931-5195.

4-10 Hardening of Al-Cu-Mg Alloy by Energetic Ion Irradiation

T. Mitsuda^{a)}, I. Kobayashi^{a)}, S. Kosugi^{a)}, N. Fujita^{a)}, Y. Saitoh^{b)}, F. Hori^{a)},
S. Semboshi^{a)}, Y. Kaneno^{a)} and A. Iwase^{a)}

^{a)} Department of Materials Science, Osaka Prefecture University,

^{b)} Department of Advanced Radiation Technology, TARRI, JAEA

There have been various investigations of the hardening method of aluminum-based alloys. Above all, a well-known method for hardening is the aging treatment of supersaturated alloys. On the other hand, when supersaturated alloys are irradiated with energetic particles, point defects (interstitials and vacancies) are produced and they enhance the diffusion of supersaturated atoms and their segregation. This phenomenon, which is called the radiation enhanced segregation, is caused by the interaction between point defects and supersaturated atoms. In this study, we applied the irradiation enhanced segregation caused by ion irradiation to control the hardness of a supersaturated Al-Cu-Mg alloy, which is generally known as an age-hardenable “duralumin” alloy.

Supersaturated Al-Cu-Mg alloy was selected for our experiments. Specimens were solution-annealed at 813 K in air and then quenched in water at 273 K. The specimens were irradiated with 10 MeV iodine ions (I^{3+}) using a tandem accelerator at the TIARA. All irradiations were performed at room temperature. To compare the hardness of the ion-irradiated region with that of the unirradiated region in the same specimen, about a half area of each specimen was irradiated and the other half remained unirradiated. After irradiation, the Vickers hardness was measured near the boundary of the irradiated and unirradiated regions.

Figure 1 shows the relationship between the Vickers

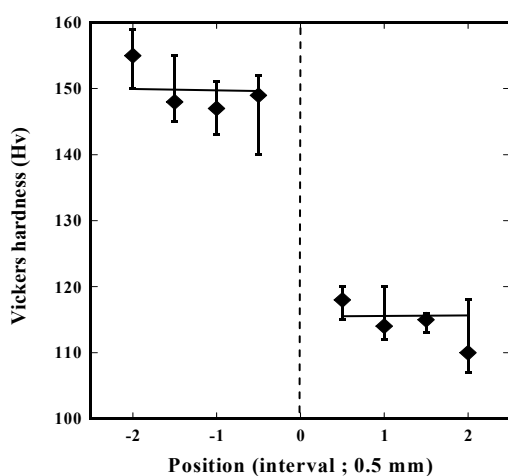


Fig. 1 Relationship between Vickers hardness and measuring positions near the boundary of irradiated and unirradiated regions in specimens irradiated at a fluence of $5 \times 10^{15}/\text{cm}^2$.

hardness with an applied load of 25 gf and the indentation position near the boundary of the irradiated and unirradiated regions for the specimen irradiated at a fluence of $5 \times 10^{15}/\text{cm}^2$. The dashed line at the center of the figure represents the boundary of irradiated (left) and unirradiated (right) regions. It is clear that the Vickers hardness increases by 40 only in the irradiated region.

Figure 2 shows the change in Vickers hardness as a function of processing time for the specimens irradiated with iodine ions and for the specimens aged at 423 K and 453 K. For the specimen aged at 423 K, the hardness reaches a maximum value after 4 days and then decreases. For the specimens aged at 453 K, the time required to reach a maximum hardness is shorter than that for the specimen aged at 423 K. The maximum value of the hardness, however, decreases with an increase in the aging temperature. Meanwhile for the specimens irradiated at room temperature, the surface hardness increases far more rapidly than that for the thermally aged specimens and only 3.5 hours are required to reach a Vickers hardness of 160, which is about the same as the maximum hardness value obtained when aged at 423 K. Further analysis is now in progress.

Reference

- 1) T. Mitsuda et al., J. Nucl. Mater. 408 (2011) 201-204.

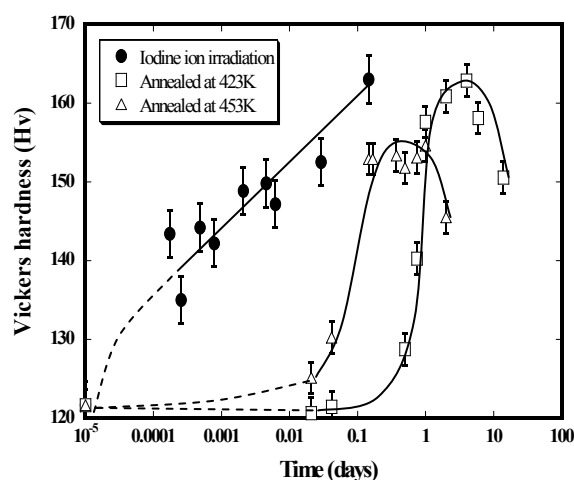


Fig. 2 Comparison of the change in Vickers hardness between irradiated specimens and specimens thermally aged at 423 K and 453 K as a function of processing time.

4-11 Ion Doping Technique Related to Nano-Machining on Unworkable Oxidation Ceramics

S. Ishiyama^{a)} and M. Satoh^{b)}

^{a)} Management Support Section, J-PARC, JAEA, ^{b)} Ube industries, Ltd.

Bombardment effects of 0.3 and 3 MeV H^+ ions on a sapphire surface have been investigated in order to nano-machining on unworkable ceramics in combination with Laser irradiation technique.

In this report, deformation change affected by H^+ ion doping was evaluated by investigating H^+ ion fluence and energy dependence of deformation on sapphire wafer.

Eight pieces of large sapphire wafer ($\phi 50 \times 0.45$ mm t), were irradiated with 0.3 MeV and 3 MeV H^+ ions from ion implanter and single-ended accelerator of TIARA up to the fluence of $0.25 \sim 0.5 \times 10^{16} H^+/cm^2$. Center surface area of sapphire wafer (20×20 mm) were exposed by H^+ bombardment and deformation of sapphire wafers were measured by Laser displacement meter. Figure 1 shows typical deformation profile on opposite sides of the wafer and it can be recognized that front face coming H^+ ion was swelled out and its behind was sagged in the middle.

Figure 2 shows swell-out deformation of irradiated wafers as a function of irradiation energy and fluence. It is found that swell-out deformation was increased as fluence, and accelerated by higher energy irradiation. These wafers were provided to jointing test between un- and irradiation sapphire wafers, assuming sapphire/GaN LED component

fabrication process and very well joint was achieved recently. These jointed wafers will be provided to smart cut process by Laser irradiation.

Reference

1) Patents (Under application of approval).

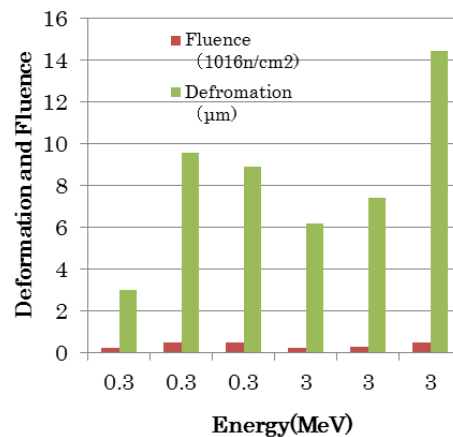


Fig. 2 Fluence and energy dependency of deformation of irradiated sapphire wafers.

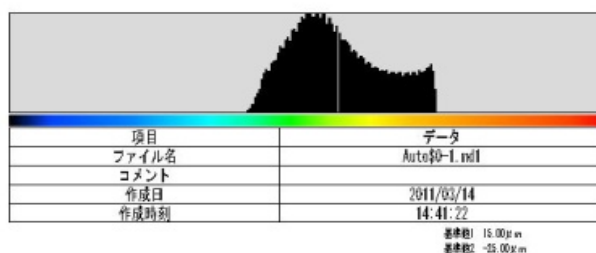
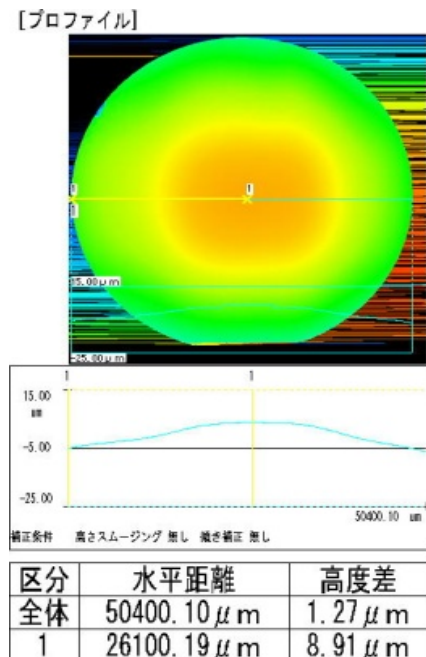


Fig. 1 Typical deformation profile of H^+ irradiated sapphire wafer. Irradiated middle surface of the wafer was swelled out and its behind surface was sagged.

4-12 Characterization of N-Behavior in Nitriding Processes of Deposited-Ti Thin Films due to Ion Implantation

Y. Kasukabe^{a), b)}, Y. Chen^{b)}, S. Yamamoto^{c)} and M. Yoshikawa^{c)}

^{a)} Center for International Exchange, Tohoku University, ^{b)} Department of Metallurgy, Tohoku University, ^{c)} Environment and Industrial Materials Research Division, QuBS, JAEA

It has recently been reported that properties of non-stoichiometric titanium nitrides (TiN_y) such as electrical conduction, diffusion barrier, catalysis, etc. depend not only on chemical composition, but also on orientation relationships between TiN_y films and substrates. Therefore, much interest has been focused on studying atomistic growth processes of TiN_y films¹⁾. In this paper, both hcp-Ti and CaF_2 -type TiH_x ($x \approx 1.5$), and only hcp-Ti, with preferred orientations have been grown in Ti films deposited on NaCl (001) substrates held at room temperature (RT) and 250 °C, respectively. In order to clarify atomistic growth processes of TiN_y films due to the implantation of nitrogen ions (N_2^+) with 62 keV into Ti films, changes of the concentration of N atoms in Ti films by nitriding have been investigated by in-situ transmission electron microscope (TEM) equipped with electron energy loss spectroscopy (EELS), with the aid of molecular orbital calculations. The N-implantation was performed in the analytical TEM combined with ion accelerators at JAEA-Takasaki²⁾.

Figure 1 shows the variation of the area ratio, N/Ti, of energy loss peaks by N 1s (K) and Ti 2p ($L_{2,3}$) electrons in EELS spectra with respect to the atomic concentration ratio of N/Ti estimated by the dose of N. When the ratio of N/Ti estimated by dose of N is 1.0, the corresponding dose of N is 5.66×10^{17} atoms/cm². The solid circle represents the N/Ti ratio of each peak area in EELS spectra for the N-implantation at RT into the Ti films deposited at 250 °C. The open circle represents that for the N-implantation at 350 °C into the Ti films deposited at 250 °C. The solid triangle represents that for the N-implantation at RT into the Ti films deposited at RT. The open triangle represents that for the N-implantation at 350 °C into the Ti films deposited at RT. It can be seen that the N/Ti ratios of each peak area in EELS increase with the ratios of N/Ti estimated by the dose of N until the latter ratios reach near 0.7~0.8. When they are larger than 0.7~0.8, the N/Ti ratios of each peak area in EELS change to nearly constant values near the ratios indicated by dotted and broken saturation lines. These saturation lines only depend on the implantation temperatures, although the temperatures of Ti-deposition and of N-implantation are different from each other. Here, we define the region, where ratios of N/Ti estimated by the dose of N are larger than 0.7~0.8, as the saturation stage during N-implantation, in which some of the implanted N atoms escape from the N-implanted Ti film due to the radiation effect. The variation of the area ratios of N/Ti during N-implantation in Fig. 1 corresponds qualitatively to the result evaluated from RBS: there is no escape of N

before the saturation stage during N-implantation. As a result, it can be considered that with the knowledge of N/Ti ratios of each peak area in EELS, the constitution of Ti films during N implantation before the saturation can be in-situ obtained.

Furthermore, in the saturation stage, the ratios of N/Ti in Fig. 1 are separated into two tendencies characterized by dotted and broken saturation lines depending on different implantation temperatures. The value of broken saturation line of N-implantation at 350 °C is smaller than that at RT indicated by the dotted line. This means that the number of N atoms bonding to Ti atoms decreases with increasing the N-implantation temperature in the saturation stage from RT to 350 °C. Thus, it would be considered that the frequency for the excitation of electrons from bonding states consisting of Ti 3d-4p and N 2p to the anti-bonding states is higher at 350 °C than that at RT during N-implantation in the saturation stage. Besides, the increase in the number of phonons by increasing the temperature would also contributes to make the excitation of electrons from the bonding states to the anti-bonding states easier. As a result, the excited lighter atoms, N atoms, become unstable and escape from the Ti film. Thus, there are lesser N atoms reserved in the film at the higher implantation temperature.

References

- 1) S. Hao et al., Phys. Rev. B74 (2006) 035424-1.
- 2) H. Abe et al., JAERI-Research 96-047 (1996) 1.

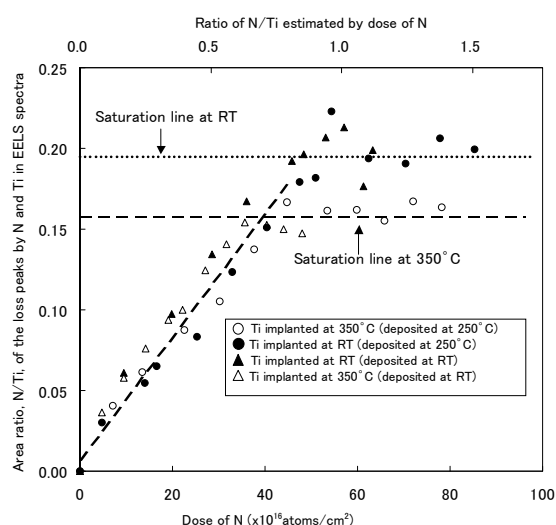


Fig. 1 Variation of N/Ti ratio of each peak area in EELS with respect to ratio of N/Ti estimated by the implanted ion current.

4-13 The Effects of Displacement Damage and Transmutation Atoms on Dimensional Stability of SiC with Impurities

T. Nozawa^{a)}, T. Taguchi^{b)} and H. Tanigawa^{a)}

^{a)} Division of Fusion Energy Technology, FRDD, JAEA,

^{b)} Neutron Material Research Center, QuBS, JAEA

A SiC/SiC composite is a candidate for fusion reactor materials because of the inherently good irradiation resistance of SiC^{1,2)}. Of many composites, a dense and robust nano-infiltration transient-eutectic-phase sintered (NITE) SiC/SiC composite is believed to be viable because of potentially high competitiveness. However, irradiation tolerance of NITE is still uncertain due to the presence of inside impurities as sintering aids¹⁾. By contrast, for the fusion application, understanding the synergistic effects of He and H as representative transmutation products of a fusion reactor on microstructural evolution of SiC under irradiation is important. For instance, by applying the triple ion beam irradiation at the TIARA facility, the significance of H on the He bubble formation was identified for pure SiC³⁾. However, this effect on SiC with impurities is presently uncertain. This study primarily aims to identify the effects of displacement damage and transmutation atoms (He and H) on microstructure of SiC with sintering aids. In 2009, we implied no significant impact of the H implantation ratio (H/dpa) on the dimensional change for limited irradiation conditions. In 2010, this issue was further investigated.

A NITE-SiC ceramic as representative matrix phase of NITE-SiC/SiC composites was tested, coupled with CVD-SiC as reference pure SiC. The sintering aids of NITE-SiC were Al₂O₃ and Y₂O₃. Triple ion beam (Si²⁺, He⁺ and H⁺) irradiation was carried out up to 10 dpa at 1,000 °C. In 2010, a constant He/dpa ratio of 130 appm/dpa and a H/dpa ratio of 400 appm/dpa were applied. The calculated depth profiles of displacement damage and He, H and Si concentration were shown in the annual report in 2009⁴⁾. The radiation-induced dimensional change (swelling) was then evaluated by the step-height (Δh) measurement by the atomic force microscopy⁵⁾.

Figure 1 shows swelling as a function of the H/dpa ratio. For the higher H/dpa ratio, the swelling seems to be suppressed by triple ion beam irradiation. However, this is somehow questionable because the higher H/dpa irradiation enhanced He bubble formation according to the previous results for pure CVD-SiC³⁾. By contrast, it is reasonable that, for ~10 dpa, the amount of implanted H was very little to form He bubbles, which have a impact on the radiation-induced dimensional change. Further evaluation is still required to conclude this.

Figure 2 shows dimensional change of NITE-SiC as a function of displacement damage under the triple ion beam irradiation. As noted previously, under the low H/dpa ratio, formation of He bubbles is hardly enhanced by

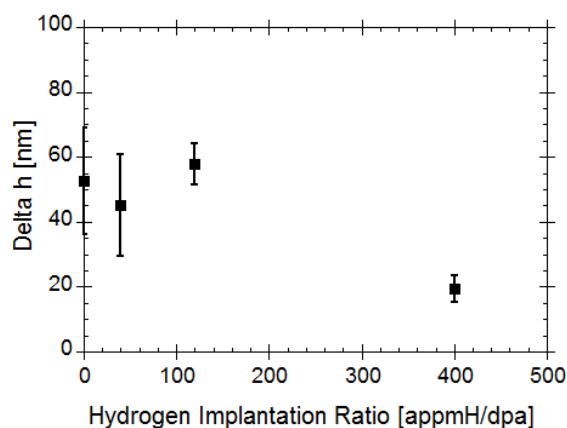


Fig. 1 The effect of H/dpa on swelling of NITE-SiC by triple ion beam irradiation at 1,000 °C.

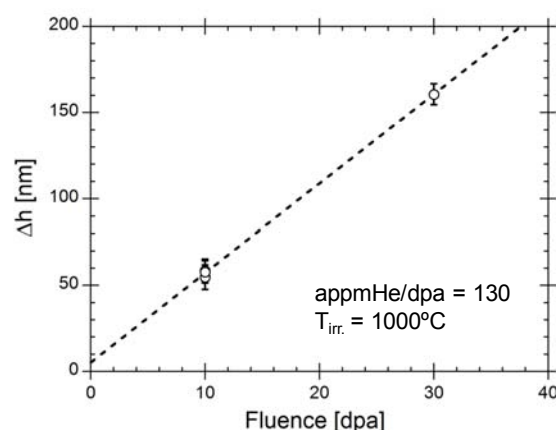


Fig. 2 The effect of displacement damage on swelling of NITE-SiC. Note that the same H implantation ratio of 40 appmH/dpa was applied.

irradiation and, therefore, the major parts of increment of the dimensional change is due to the accumulation of Si²⁺ ions, which is proportional to the fluence.

References

- 1) L.L. Snead et al., J. Nucl. Mater. 371 (2007) 329.
- 2) T. Nozawa et al., J. Nucl. Mater. 386-388 (2009) 622.
- 3) T. Taguchi et al., J. Nucl. Mater. 367-370 (2007) 698.
- 4) T. Nozawa et al., JAEA Takasaki Ann. Rep. 2009 (2011) 138.
- 5) Y. Katoh et al., Mater. Trans. 43 (2002) 612.

4-14 Detection of Implanted ^{12}C in Ag/Ni/ $\alpha\text{-Al}_2\text{O}_3(0001)$ Employing Non-Rutherford Elastic Scattering Process

S. Sakai^{a)}, S. Entani^{a)}, Y. Matsumoto^{a)}, M. Ohtomo^{a)}, P. Avramov^{a)},
K. Narumi^{a, b)} and H. Naramoto^{a)}

^{a)} Advanced Science Research Center, JAEA,

^{b)} Department of Advanced Radiation Technology, TARRI, JAEA

The combination of nano/molecular carbons and magnetic metals is expected to play an important role as the fundamental structure for the efficient transport of spin-polarized electrons¹⁾. The nano/molecular carbons can be formed at the atomic layer level by using sophisticated ways²⁾. As a possible approach for *in-situ* materials processing, the ion beam technique is effective both for carbon incorporation and its sensitive analysis. For the background-free carbon detection, $^{12}\text{C}(\text{d}, \text{p})^{13}\text{C}$ nuclear reactions have been used but those cannot avoid to introduce the undesirable radioactive nuclei. In the present study, two kinds of non-Rutherford elastic scattering processes were examined as alternatives with the reasonable sensitivity for the carbon detection.

Twenty keV $^{12}\text{C}^+$ ion implantation was made up to $1.64 \times 10^{17} / \text{cm}^2$ at ambient temperature to incorporate nano/molecular carbons into Ni layer through the Ag top layer in a bi-layer sample of Ag(10 nm)/Ni(30 nm)/ $\alpha\text{-Al}_2\text{O}_3(0001)$. The element combinations of Ag/Ni and also Ag/C are immiscible, which insures the non-intermixing at the Ag/Ni interface and the biased diffusion of implanted carbons from Ag layer into Ni layer during the implantation and the subsequent annealing at 550 °C for 15 hours under UHV condition. Two MeV $^4\text{He}^+$ Rutherford backscattering (RBS) analysis was made on the layer structure before implantation and after implantation/ annealing. $^{12}\text{C}(\text{p}, \text{p}_0)^{12}\text{C}$ and $^{12}\text{C}(\alpha, \alpha_0)^{12}\text{C}$ non-Rutherford elastic scattering processes³⁾ were examined for the above bi-layer sample using 3 MV single-ended accelerator and 3 MV tandem accelerator, respectively. A whole study of implantation and ion beam analysis was conducted in TIARA facility of JAEA/Takasaki.

Figure 1 illustrates the local spectra for metallic bilayer

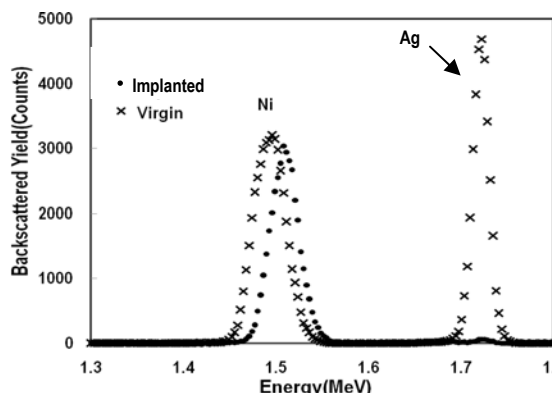


Fig. 1 2 MeV ^4He Rutherford backscattering spectra from Ag(10 nm)/Ni(30 nm)/ $\alpha\text{-Al}_2\text{O}_3(0001)$ implanted with 20 keV ^{12}C ($1.62 \times 10^{17} / \text{cm}^2$), followed by annealing.

of Ag(10 nm)/Ni(30 nm) on $\alpha\text{-Al}_2\text{O}_3(0001)$ taken from 2 MeV $^4\text{He}^+$ RBS spectra. It can be summarized from this figure that the carbon implantation induces the unusual removal of Ag protective layer reflecting the immiscible nature between Ag and C, which favors the possible accumulation of implanted carbon atoms into the surface region of Ni layer.

Figure 2 shows the elastically scattered yield of protons from the same implanted/annealed sample as in Fig. 1, as a function of incident proton energies. The energy region and detection angle were chosen to be around 1.74 MeV and 150° and/or 170° , respectively, through the experimental evaluation of the excitation function for $^{12}\text{C}(\text{p}, \text{p}_0)^{12}\text{C}$ scattering in $\beta\text{-SiC}$. Considering the details of excitation function obtained, the yield changes in Fig. 2 reflects the depth-distribution feature of implanted/annealing carbon atoms located in the near surface region of Ni layer.

Further calibration studies are required to evaluate the precise distribution of incorporated carbon atoms, however, it can be concluded that the present method can be alternative for the sensitive detection of carbon atoms down to around $1 \times 10^{16} / \text{cm}^2$, which can be complemented further by employing a simulation technique down to the carbon amounts of a single layer graphene. The results employing $^{12}\text{C}(\alpha, \alpha_0)^{12}\text{C}$ non-Rutherford elastic scattering was also effective but less sensitive (not shown).

References

- 1) For example: S. Sakai et al., Phys. Rev. B **83** (2011) 174422.
- 2) For example: S. Entani et al., J. Phys. Chem. C **114** (2010) 20042.
- 3) A. F. Gurbich, Nucl. Instrum. Meth. B **268** (2010) 1703.

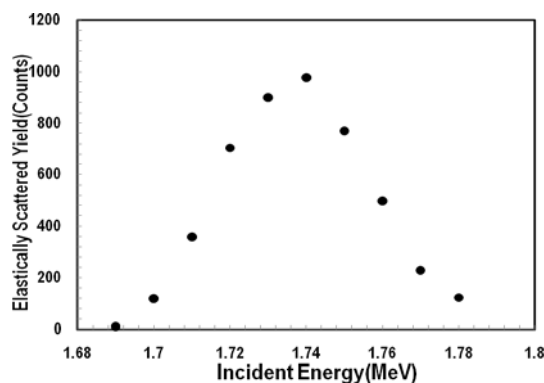


Fig. 2 Backscattered proton yield as a function of incident proton energy reflecting the implanted/ annealed features of incorporated ^{12}C atoms employing $^{12}\text{C}(\text{p}, \text{p}_0)^{12}\text{C}$ non-Rutherford elastic scattering in the same sample as in Fig. 1.

4-15 Radiation Damages in CeO₂ Thin Films Irradiated with Ions Having the Same Nuclear Stopping and Different Electronic Stopping Powers

N. Ishikawa and K. Takegahara

Division of Fuels and Materials Engineering, NSED, JAEA

When MeV ions are irradiated to solid target, energy is transferred from ions to a target via two independent processes; the electronic energy deposition and the energy deposition due to elastic collisions. Since both processes may contribute to defect creation at the same time, it is difficult to extract each effect independently. In order to characterize a possible modification due to high-density electronic excitation, thin films of CeO₂ have been irradiated with 10 MeV Ni and 120 MeV Xe ions, both having the same nuclear stopping powers (0.18 keV/nm), while having different electronic stopping powers (6.1 keV/nm and 23.5 keV/nm, respectively).

Thin films of CeO₂ were prepared on single crystal sapphire substrates by a sputtering method. The films were irradiated at room temperature with 10 MeV Ni ions from the tandem accelerator at JAEA-Takasaki and with 120 MeV Xe ions from the tandem accelerator at JAEA-Tokai. Wide-angle X-ray diffraction (XRD) profiles were measured before and after the irradiations. The film thickness was fixed to be about 0.3 μm which is thin enough to rule out the possibility of unwanted implantation effects.

Since the CeO₂ thin films are highly oriented, only (002) and (004) peaks are the observable peaks in the reflection angle range of $2\theta = 5^\circ\text{--}100^\circ$. As shown in Fig. 1, a monotonic decrease in the peak intensity of the (002) diffraction peak as a function of the fluence is observed for CeO₂ irradiated with 10 MeV Ni ions and with 120 MeV Xe ions. The same tendency of the peak intensity evolution is observed for (004) peak. The intensity decrease can be

attributed to a defect creation by ion-irradiation. In the figure, the fluence axis of 10 MeV Ni ion is intentionally shifted one order of magnitude relative to that of 120 MeV Xe ion in order to facilitate the comparison.

The fluence dependence of the lattice parameter estimated from the shift of the peak angle is shown in Fig. 2. The fluence dependence of lattice parameter does not exhibit a monotonic behavior. It should be noted here that such a complex fluence dependence is not accountable before taking into account the break of peak symmetry appeared after the irradiations. The detailed analysis is not the focus of this paper, and it will be discussed elsewhere. Since the change in peak profiles is due to defect creation, the present results can be interpreted that defects created by 120 MeV Xe ion amount to nearly one order of magnitude larger than those created by 10 MeV Ni ion.

The one order of magnitude difference in the defect density per incident ion is clearly attributable to the difference in the electronic stopping power. Therefore, the present comparative study demonstrates that the difference in the damage creation behavior is due to the difference in the electronic energy deposition, leading to a much higher contribution to damage creation for 120 MeV Xe ion irradiation.

Part of the present study is the result of “Research of highly accurate evaluation of radiation damage in advanced nuclear reactor fuel ceramics” entrusted to “Japan Atomic Energy Agency” by the Ministry of Education, Culture, Sports, Science and Technology of Japan (MEXT).

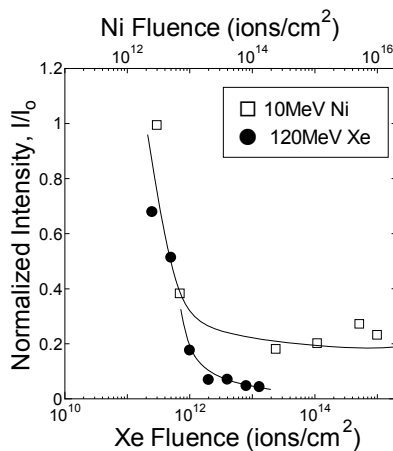


Fig. 1 Intensity of X-ray diffraction peak normalized by that of unirradiated CeO₂ thin films plotted against fluence of 10 MeV Ni and 120 MeV Xe ions. Solid curves are just a guide for the eyes.

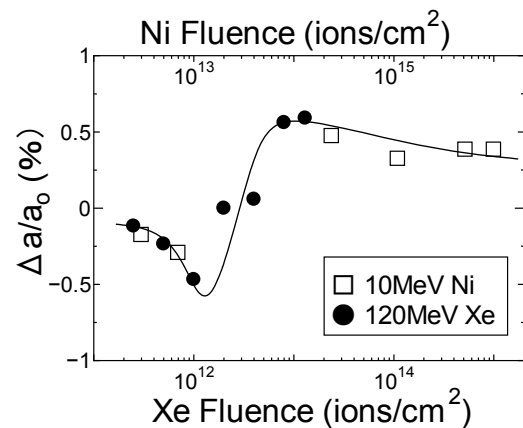


Fig. 2 Fluence dependence of lattice parameter change for 10 MeV Ni ion irradiation and 120 MeV Xe ion irradiation. The change in lattice parameter, Δa , is normalized to the lattice parameter before irradiation, a_0 . The solid curve is just a guide for the eyes.

4-16 Irradiation-induced-defect Recovery and Magnetic Property of the Gd⁺ Ion Implanted GaN

A. Yabuuchi^{a)}, M. Maekawa^{a)}, A. Kawasuso^{a)}, S. Hasegawa^{b)}, Y.K. Zhou^{b)} and H. Asahi^{b)}

^{a)} Advanced Science Research Center, JAEA,

^{b)} The Institute of Scientific and Industrial Research, Osaka University

Ion implantation is a powerful technique for doping impurities into crystals with non-equilibrium concentration. This technique may be used in fabrication of diluted magnetic semiconductors (DMS) that require high concentration magnetic atom doping without a secondary phase formation. Recently, it has been reported that Gd-doped GaN films containing defects tend to show a large magnetization^{1,2)}. Moreover, theoretical calculation also suggests that a presence of vacancies affects magnetic properties in DMS³⁾. In this study, Gd⁺ ions were implanted into MOCVD-GaN film by using ion implantation techniques. Furthermore, we have attempted to clarify the correlation between the magnetic properties and presence of vacancy-type defects.

An MOCVD-grown undoped GaN(0001)/Sapphire single crystal film with a thickness of 2 μm was implanted with 380 keV Gd⁺ ions to a dose of 3×10^{15} ions/cm². After ion implantation, the film was annealed at 500 °C, 1,000 °C and 1,300 °C for 30 seconds in vacuum. The Doppler broadening of annihilation radiation (DBAR) spectra were acquired after each annealing. In addition, magnetizations of the GaN film were measured by using an alternating gradient magnetometer (AGM) technique. All the

measurements were carried out at room temperature.

SRIM-2008 calculation shows the Gd atoms are implanted into GaN to the maximum depth of 150 nm (the projected range $R_p = 66$ nm), and an average Gd concentration is estimated to be 3×10^{20} atoms/cm³. Figure 1 shows the peak intensity of DBAR spectra (S parameters) for the GaN film before implantation, after implantation, and after annealing at 500 °C, 1,000 °C and 1,300 °C as a function of incident positron energy. The irradiation-induced defects decrease greatly after 1,000 °C annealing. However, the irradiation-induced defects do not recover to the unimplanted level after 1,300 °C annealing. This result suggests vacancies are stabilized due to clustering. Figure 2 shows the results of AGM measurement for the GaN film before implantation, after implantation, and after annealing at 1,300 °C. Magnetic hystereses are not observed at all. In further study, high-temperature ion implantation experiments are needed to control defect size.

References

- 1) S. Dhar et al., Appl. Phys. Lett. 89 (2006) 062503.
- 2) Y. K. Zhou et al., Appl. Phys. Lett. 92 (2008) 062505.
- 3) L. Liu et al., Phys. Rev. Lett. 100 (2008) 127203.

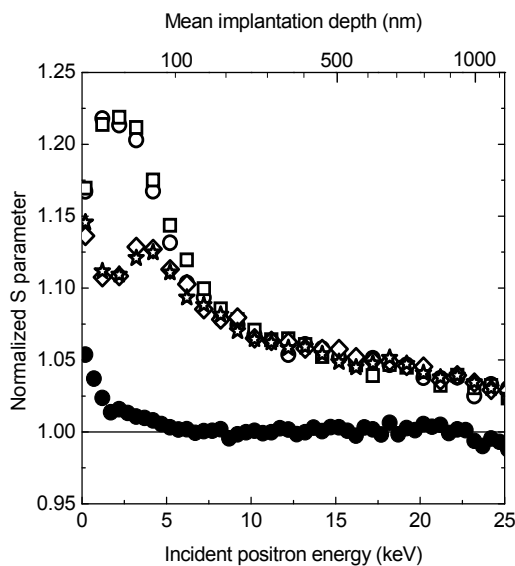


Fig. 1 S parameter for the GaN film before implantation (filled circles), after implantation (open circles), and after annealing at 500 °C (open squares), 1,000 °C (open diamonds), 1,300 °C (open stars) as a function of incident positron energy.

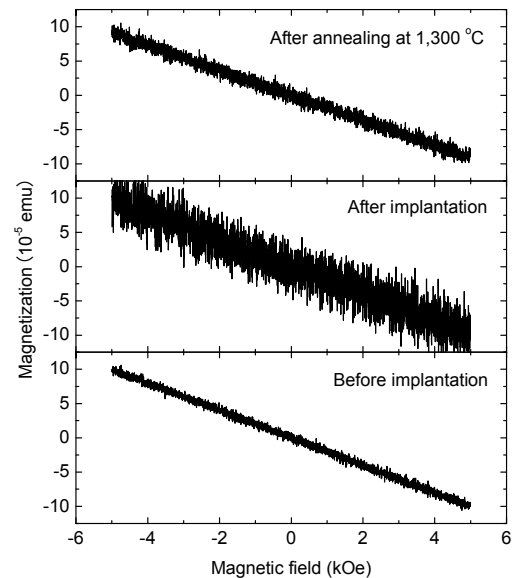


Fig. 2 Room temperature magnetization curves for the GaN film before implantation, after implantation, and after annealing at 1,300 °C.

4-17 Gamma-ray Induced Defect Formation in High-Purity α -Quartz

K. Kajihara

^{a)} Department of Applied Chemistry, Graduate School of Urban Environmental Sciences,
Tokyo Metropolitan University

Gamma-ray induced intrinsic defect formation was examined using high-purity synthetic α -quartz (crystalline SiO_2) of low metallic impurity concentrations. Radiation-induced optical absorption at visible-ultraviolet spectral region which is due to metallic impurities and commonly observed in conventional synthetic α -quartz is greatly suppressed. The main radiation-induced defects are Si-Si bonds exhibiting optical absorption at 7.6 eV, suggesting that the main defect formation mechanism is the Frenkel mechanism, depicted by displacement of bridging oxygen atoms in regular Si-O-Si bonds by dense electronic excitation. However, formation of interstitial oxygen molecules, which are one of the main form of the anion part of the Frenkel pair in amorphous form of SiO_2 (amorphous silica), is not confirmed.

赤外域から深紫外域にわたる広い透明領域を有し、化学的に安定で、かつ大きな結晶が容易に入手できる典型元素の結晶性酸化物である α -石英は、酸化物での照射欠陥形成を調べるうえで重要なモデル物質である。しかし、従来の α -石英は天然石英を原料とするため、Al や Na などの金属不純物を含んでおり、不純物によらない欠陥形成を調べるのが困難であった。今回の実験では、近年開発された、精製したシリカを原料とするため金属不純物をほとんど含まない高純度 α -石英を用い、不純物に妨害されずに真性欠陥過程を調べることを目的とした。

両面光学研磨した高純度 α -石英に3通りの異なる線量で ^{60}Co γ 線照射を行った。照射後、試料の可視・紫外・真空紫外光吸収測定を行った。また、赤外発光測定によってFrenkel過程によって生成する可能性のある格子間酸素分子の有無を調べた。

通常、 α -石英は天然石英を原料として合成され、Al や Na などの金属不純物を含んでいるため、照射によって可視紫外域にブロードな吸収を生じて着色する (Fig. 1, inset)。一方、今回用いた高純度 α -石英は、 ^{60}Co γ 線照射後もほぼ無色であった (Fig. 1)。光吸収測定によって、Si-O-Si結合からOがはずれて形成されるSi-Si結合に帰属される7.6 eV光吸収帯が生じ、その強度が照射時間とともに増大すること、7.6 eV光吸収帯以外の光吸収はほとんど生じていないことが確認された。

この結果より、Si-Si結合の形成が不純物の関与しない真性過程であること、この過程 (Frenkel過程) はSi-O-Si結合にひずみのない α -石英でも進行することが初めて明確となった。また、Si-Si結合濃度の吸収線量依存性 (Fig. 2) より、その形成効率は、 α -石英と同じ組成をもつが歪んだSi-O-Si結合を含むシリカガラスよりも小さいことが明らかとなり、歪んだSi-O-Si結合をもたない α -石英では、Si-Si結合の形成効率が小さくなったことが推察された。一方で、格子間酸素分子(O_2)の生成は確認できなかった。非晶質 SiO_2 である高純度シリカガラスでは、Si-Si結合の生成は格子間 O_2 の形成を伴う¹⁻³⁾。一方で、格子間 O_2 が生成するためには、Si-O-Si結合からははずれたOが二量化する必要があるが、 α -石英ではこの二量化が抑制されていることが示唆される。

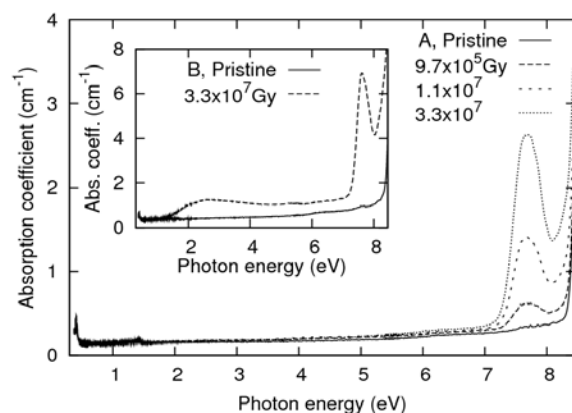


Fig. 1 Optical absorption spectra of high-purity α -quartz (A) irradiated at various γ -ray doses. The inset shows optical absorption spectra of conventional α -quartz (B).

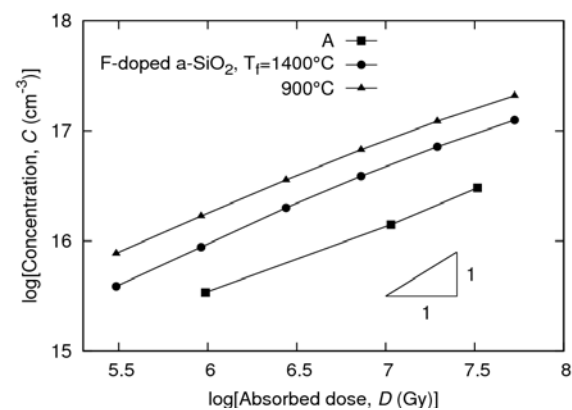


Fig. 2 Variation of concentration of Si-Si bond with γ -ray dose in high-purity α -quartz (A). Data for fluorine-doped synthetic silica glasses annealed at 900 and 1,400 $^{\circ}\text{C}$ ^{2, 3)} are also shown.

References

- 1) K. Kajihara et al., Chem. Lett. 36 (2007) 266.
- 2) K. Kajihara et al., Phys. Rev. B 78 (2008) 094201.
- 3) K. Kajihara et al., Mater. Sci. Eng. B 96 (2009) 161.

4-18 Adsorption Site of Alkali Metals on Si(111)- $\sqrt{3}\times\sqrt{3}$ -Ag Surface Studied by Reflection High-Energy Positron Diffraction

Y. Fukaya^{a)}, I. Matsuda^{b)}, I. Mochizuki^{a)} and A. Kawasuso^{a)}

^{a)} Advanced Science Research Center, JAEA, ^{b)} ISSP, The University of Tokyo

The Si(111)- $\sqrt{3}\times\sqrt{3}$ surface is known as a prototype of two-dimensional metal system¹⁾. The adsorption of noble (Cu, Ag, and Au) and alkali (K and Cs) metals on the Si(111)- $\sqrt{3}\times\sqrt{3}$ -Ag surface leads to the formation of $\sqrt{21}\times\sqrt{21}$ superstructures, accompanied by a drastic increase in the surface electrical conductivity¹⁾. From metallurgical point of view, the $\sqrt{21}\times\sqrt{21}$ superstructures have attracted attention as two-dimensional electron compound alloys^{2,3)}. The noble metal adsorbed Si(111)- $\sqrt{21}\times\sqrt{21}$ superstructures have been extensively studied⁴⁾. However, the atomic configurations of alkali metal adsorbed $\sqrt{21}\times\sqrt{21}$ superstructures still remain unresolved. In this study, we investigated the atomic structure of the Si(111)- $\sqrt{21}\times\sqrt{21}$ -(Ag,Cs) surface by using a reflection high-energy positron diffraction (RHEPD).

The substrates ($10 \times 5 \times 0.5$ mm³) were cut from a mirror-polished *n*-type Si(111) wafer with a resistivity of 1-10 Ω cm. The Si(111) surfaces were heated at 670 K in several hours and flashed at 1,470 K to prepare a well-ordered 7×7 structure. By depositing one monolayer (ML, 1 ML = 7.83×10^{14} cm⁻²) Ag atoms on the Si(111)- 7×7 surface at 740 K, the Si(111)- $\sqrt{3}\times\sqrt{3}$ -Ag surface was formed. To produce the Si(111)- $\sqrt{21}\times\sqrt{21}$ -(Ag,Cs) surface, 0.14 ML Cs atoms were deposited on the Si(111)- $\sqrt{3}\times\sqrt{3}$ -Ag surface at 170 K.

All experiments were carried out in an ultra-high vacuum chamber (base pressure less than 3×10^{-8} Pa) equipped with a positron source (²²Na) and magnetic lens system. The RHEPD patterns were observed using a microchannel plate with a phosphor screen and a charge-coupled device camera. The RHEPD rocking curves were measured by rotating the sample holder from 0.3° to 6° at a step of 0.1°.

Figure 1 shows the RHEPD rocking curves of (0 0), (1/3 1/3), and (2/3 2/3) spots from the Si(111)- $\sqrt{21}\times\sqrt{21}$ -(Ag,Cs) surface along the $[11\bar{2}]$ direction at 170 K. In order to determine the adsorption sites of Cs atoms on the Si(111)- $\sqrt{3}\times\sqrt{3}$ -Ag surface, we calculated the RHEPD rocking curves based on the dynamical diffraction theory. In the calculations, the height of the Cs atoms from the Ag layer was assumed to be 3.04 Å from the previous rocking curve analyses under the one-beam condition. Two different structure models were taken into account, i.e., ontop model where the Cs atoms are located just above the Ag atoms and center model where the Cs atoms are situated at the center of the underlying large Ag triangle. As shown in Fig. 1, the calculated rocking curves using the ontop model is in good agreement with the measured ones. The measured curves cannot be explained by considering the

center model. We found that the atomic configuration of Cs atoms is consistent with the scanning tunneling microscopy observations⁵⁾.

The interaction energy between the adsorbates is given by,

$$\Delta E_{\text{int}}(d) \cong -\varepsilon_F \left(\frac{2 \sin(\delta_F)}{\pi} \right)^2 \frac{\sin(2k_F d + 2\delta_F)}{(k_F d)^2}, \quad (1)$$

where d is the distance between the adsorbates, δ_F the phase shift, ε_F the Fermi energy, and k_F the Fermi wave vector. From Eq. (1), the interaction energy reaches the minimum at around 9 Å, which is close to the value (10.16 Å) determined in this study. Consequently, the Cs atoms are located just above the Ag atoms for the Si(111)- $\sqrt{21}\times\sqrt{21}$ -(Ag,Cs) superstructure. In the case of the Si(111)- $\sqrt{21}\times\sqrt{21}$ -(Ag,Au) surface, the Au atoms are situated at the center of the underlying Ag triangle. The interaction energy between the adsorbates plays an important role in the formation of $\sqrt{21}\times\sqrt{21}$ superstructures.

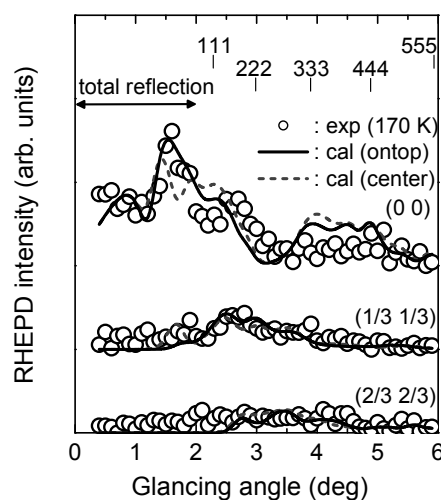


Fig. 1 RHEPD rocking curves from the Si(111)- $\sqrt{21}\times\sqrt{21}$ -(Ag,Cs) superstructure. The open circles denote the experimental curves. The solid and dotted lines indicate the calculated curves using the ontop and center models, respectively.

References

- 1) S. Hasegawa et al., Prog. Surf. Sci. **60** (1999) 89.
- 2) I. Matsuda et al., Phys. Rev. B **82** (2010) 165330.
- 3) Y. Fukaya et al., Phys. Rev. B, submitted.
- 4) Y. Fukaya et al., Surf. Sci. **600** (2006) 3141.
- 5) C. Liu et al., Jpn. J. Appl. Phys. **42** (2003) 1659.

4-19 Structural Phase Transition of Pt/Ge(001) Surface Studied by Reflection High-energy Positron Diffraction

I. Mochizuki, Y. Fukaya and A. Kawasuso

Advanced Science Research Center, JAEA

Defect-free one-dimensional (1D) nanowires with single-atom width are fabricated on the Ge(001) surface by the adsorption of Pt atoms. Recently, it has been reported that the Pt/Ge(001) surface undergoes the Peierls-type structural phase transition (SPT) around 80 K¹⁾. Vanpoucke *et al.* have theoretically proposed several nanowire (NW) models with the different Pt coverage for the Pt/Ge(001) surface²⁾ (Fig. 1). They have also argued that the SPT does not derive from the Peierls transition, but from the change of the Pt coverage. Thus, the atomic arrangement and the displacement of the Pt/Ge(001) surface due to the SPT are still unknown. In this study, we investigated the structure of the Pt/Ge(001) surface above and below the SPT temperature by using reflection high-energy positron diffraction (RHEPD).

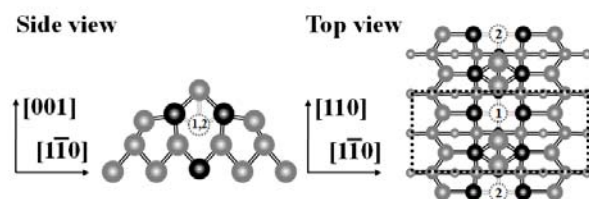


Fig. 1 Ball-and-stick representations of NW model. Black and gray balls show Pt and Ge atoms, respectively. The dotted square indicates the 4×2 unit cell. This model contains 0.75 ML of Pt atoms. The other NW models containing 0.8125 and 0.875 ML of Pt atoms are constructed by adding the Pt atoms at the site 1 and the sites 1 and 2, respectively.

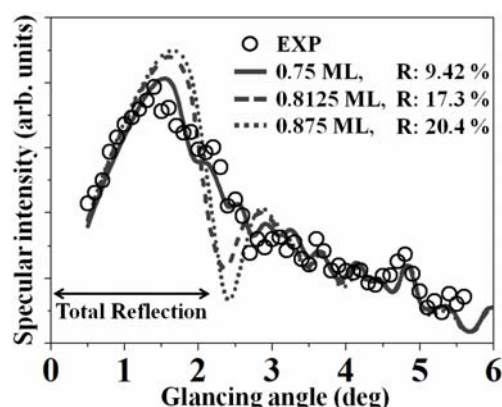


Fig. 2 RHEPD rocking curves along $[1\bar{1}0]$ direction measured from Pt/Ge(001) surface. Open circles show the experimental data at 45 K. The calculated curves using the Pt coverage of 0.75, 0.8125 and 0.875 ML are denoted by the solid, broken and dashed lines, respectively.

Experiments were performed in an ultra-high vacuum chamber equipped with a ^{22}Na positron source, electromagnetic lenses and an electron beam evaporator. The positron beam energy was set at 10 keV. The incident azimuth was set at the $[1\bar{1}0]$ direction or 22.5° away from the $[1\bar{1}0]$ direction (one-beam condition). To produce a Ge(001)- (4×2) -Pt structure, 1.2 monolayers (ML) of Pt atoms were deposited on the clean Ge(001) surface kept at 570 K, where 1 ML corresponds to 6.3×10^{14} atoms/cm².

Figure 2 shows the RHEPD rocking curves from the Pt/Ge(001) surface along the $[1\bar{1}0]$ direction at 45 K. In order to determine the atomic arrangement, we calculated the rocking curves based on the dynamical diffraction theory. As shown by the solid curve, the measured curve is in good agreement with the calculated curve assuming the NW model with the Pt coverage of 0.75 ML. On the contrary, the curve does not agree with the calculated curves using the Pt coverage of 0.8125 or 0.875 ML. Thus, we found that the Pt coverage for the Ge(001)- (4×2) -Pt structure is 0.75 ML. In addition, as shown in Fig. 3, we observed the shift of the peak position at the total reflection region in the rocking curves from the one-beam condition. The result indicates that the SPT is caused by the height difference between the topmost Ge dimer atoms instead of the change in the Pt coverage. Consequently, we found that the SPT for the Pt/Ge(001) surface is consistent with the Peierls transition.

References

- 1) A. van Houselt *et al.*, Surf. Sci. 602 (2008) 1731.
- 2) D. E. P. Vanpoucke *et al.*, Phys. Rev. B 81 (2010) 085410.

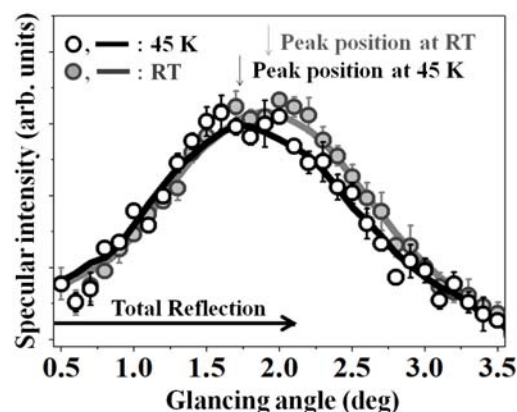


Fig. 3 RHEPD rocking curves under one-beam condition measured from Pt/Ge(001) surface. Open and gray circles show the experimental data obtained at 45 K and RT, respectively. Solid curves show the spline interpolation of the experimental data.

4-20 Recovery Behavior of Vacancies in Type 304 Stainless Steels Studied by Positron Annihilation Spectroscopy

A. Yabuuchi, M. Maekawa and A. Kawasuso

Advanced Science Research Center, JAEA

The stress corrosion cracking (SCC) mechanism of stainless steels is an important research topic concerning the long-term use for light water nuclear reactors. Recently, a hypothesis of the SCC crack propagation mediated by atomic vacancies under the crack tip stress gradient is proposed¹⁻³⁾. In addition, our positron microbeam study has clarified that vacancies were probably generated near the SCC crack tip⁴⁾. The effect of a sensitization caused by welding heat input and the effect of a local plastic strain caused by stress concentration are probable trigger for defects formation around the SCC. However, defect species formed after heating to 450–850 °C by welding or the plastic deformation at crack tips are not clear, moreover, the thermal stabilities of the defects are also unclear. In this study, the sensitization heat treated and the tensile plastic deformed Type 304 stainless steels, which are the factors of SCC, were investigated by means of positron annihilation spectroscopy.

Figure 1 shows the experimental Doppler broadening of the annihilation radiation (DBAR) spectra obtained after the sensitization heat treatment at 650 °C for 24 hours in vacuum and the plastic deformation at $\varepsilon = 14\%$. To see the detailed spectrum shape, the original spectra are divided point-by-point by the spectrum for the reference sample. To compare these spectra with the spectrum obtained from well-defined defective sample, 2 MeV electron irradiation with a total dose of $3 \times 10^{18} \text{ e}^-/\text{cm}^2$ was carried out. The irradiated sample was confirmed by positron annihilation lifetime measurement that includes monovacancies. The

calculated DBAR spectrum for monovacancy is also shown in Fig. 1. As seen in Fig. 1, the DBAR spectra after the sensitization heat treatment and the plastic deformation are in good agreement with that after the electron irradiation. This suggests that monovacancies are responsible for positron trapping in these samples, too.

To reveal thermal stabilities of vacancy defects, the annealing processes were investigated. Figure 2 shows the S parameters after the sensitization heat treatment, the tensile deformation and the electron irradiation as a function of annealing temperature. It is found that these S parameters (S parameter indicates annihilation gamma-rays peak intensity, and increases when vacancies are contained) commonly decrease to defect-free level in the temperature range of 200–400 °C, again increase above 600 °C. The first recovery at 200–400 °C is explained as the disappearance of monovacancies. The increase of S parameters at 600–900 °C may be attributed to re-introduction of vacancy defects due to sensitization. The first recovery of S parameters (200–400 °C) corresponds to the light water reactor operation temperature. That is, monovacancies in stainless steels are mobile at reactor operation temperature. This indicates a possibility that monovacancies accumulate at crack tip grain boundaries and result in the development of tight cracks.

References

- 1) R.W. Staehle, Proc. Int. Conf. Water Chem. Nucl. React. Sys., Jeju Island, Korea (2006).
- 2) K. Arioka et. al., Corrosion 64 (2008) 691.
- 3) K. Arioka et. al., Corrosion 66 (2010) 015008.
- 4) A. Yabuuchi et al., J. Phys. Conf. Ser. 262 (2011) 012067.

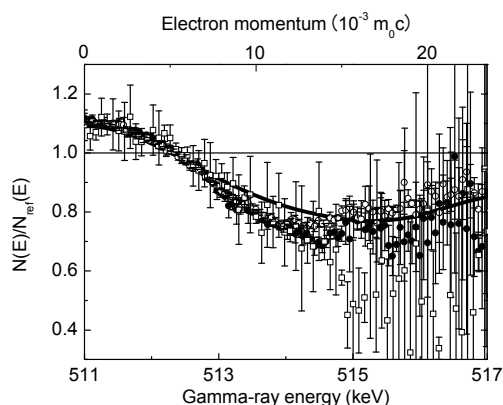


Fig. 1 DBAR spectra obtained after the electron irradiation (filled circles), the sensitization heat treatment (open circles) and the plastic deformation (open squares). The spectrum amplitude of the plastic deformation is multiplied by a factor of 2.5 to compare the spectrum shape. All these spectra are divided by the spectrum for the reference sample. Solid line is the theoretical DBAR spectrum for a monovacancy in a Type 304 stainless steel.

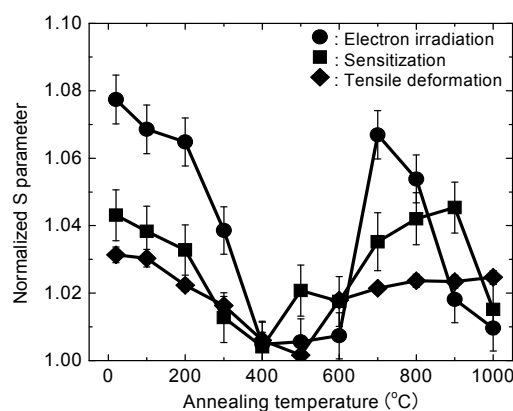


Fig. 2 S parameter for the electron irradiated (filled circles), the sensitization heat treated (filled squares) and the tensile deformed (filled diamonds) samples as a function of annealing temperature.

4-21 Positron Annihilation Lifetime of Irradiated Polyimide

T. Hirade^{a, b)}, T. Oka^{c)}, N. Morishita^{d)}, A. Idesaki^{d)} and A. Shimada^{d)}

^{a)} Division of Fuels and Materials Engineering, NSED, JAEA, ^{b)} Graduate School of Science and Engineering, Ibaraki University, ^{c)} Advanced Science Research Center, JAEA,

^{d)} Environment and Industrial Materials Research Division, QuBS, JAEA

Polyimide like Kapton (DuPont) has no positronium (Ps) formation. It is probably caused by strong electron and positron scavenging according to the spur reaction model¹⁾. On the other hand, positron annihilation lifetime measurement is often used for polymer researches because it can provide information of microscopic free volume. However, it has been studied by the triplet Ps (ortho-Ps) lifetime. No Ps formation in the polyimide polymers means no possibility of studying by use of the positron annihilation lifetime.

No Ps formation means that there will be just one lifetime components that is the free positron annihilation lifetime, about 400 ps, because the other components are singlet Ps (para-Ps) intrinsic annihilation lifetime, about 125 ps, and ortho-Ps pick off annihilation lifetime, about 1-5 ns. The ortho-Ps intrinsic annihilation lifetime is very long, 142 ns, in vacuum and then annihilation by picking off an electron from surrounding molecules is much faster in insulating materials. Hence there is just one lifetime component in Kapton that is often used for the shielding materials for Na-22 source for positron experiments.

Indeed, positrons giving the free positron annihilation lifetime component are not free. These positrons localize somewhere in the materials as the excess electrons do²⁾. The suitable localization site for polymers at room temperatures is on the molecular chains. Therefore a main annihilation probability, λ_m , is caused by the annihilation of the localized positron and the electrons on the molecular chain that the positron localizes on. There is also a minor

annihilation probability, λ_n , that is caused by the localized positron and the electrons on the neighboring molecular chains. The total annihilation probability, λ_{total} , is $\lambda_m + \lambda_n$. Although the main annihilation probability, λ_m , is not affected by the change of measurement conditions, the minor annihilation probability, λ_n , is affected by the changes such as the distance between the molecular chain where the positron localizes and the neighboring molecular chains. This distance is larger when the free volume is larger for polymers, i.e. the minor annihilation probability, λ_n , is affected by the free volume of polymers.

We measured the temperature dependence of the free positron annihilation lifetime for Kapton, showing longer annihilation lifetimes at higher temperatures as shown in Fig. 1. It is indicating that the free positron annihilation lifetime is affected by the free volume of polymers as expected above. We also successfully obtained the free positron annihilation lifetime change caused by the electron beam irradiation as indicated in Fig. 2. This change indicates the free volume change caused by the cross linking. It is possible to conclude that the free positron annihilation lifetime can be a strong tool to study polymers with no Ps formation.

References

- 1) O.E. Mogensen, J. Chem. Phys. 60, (1974) 998.
- 2) T. Hirade et al., physica status solidi (c) 4, 10 (2007) 3714.

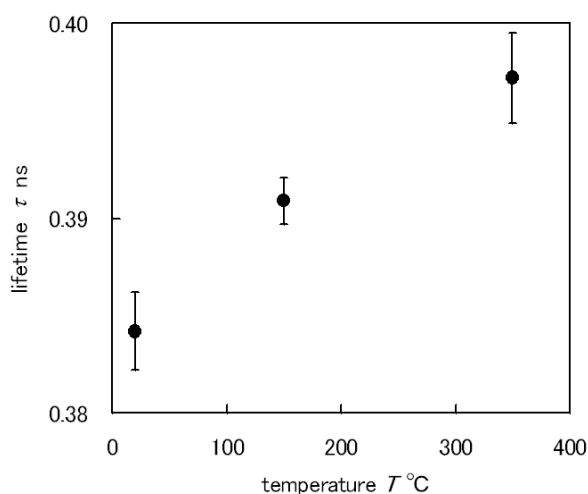


Fig. 1 Temperature dependence of positron annihilation lifetime in Kapton.

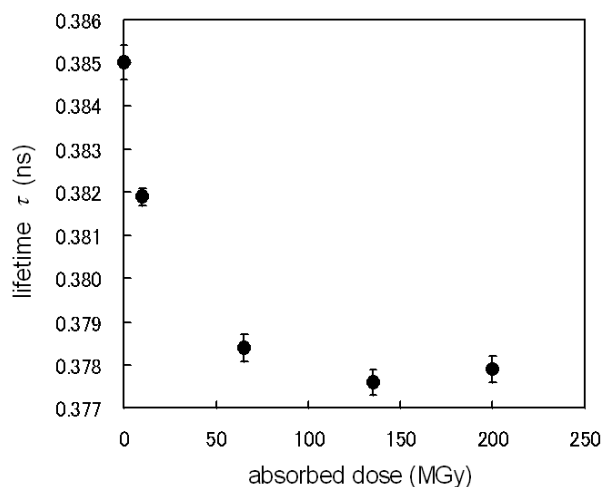


Fig. 2 Absorbed dose dependence of positron annihilation lifetime in Kapton.

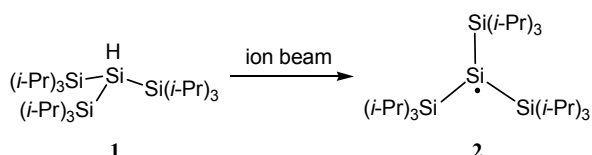
4-22 ESR Study of Ion-beam-induced Silyl Radical Generation in Single Crystals

K. Yoshimura, M. Sugimoto, A. Idesaki and M. Yoshikawa

Environment and Industrial Materials Research Division, QuBS, JAEA

Crystalline-state reaction has been attracting great interest because of its regioselectivity and characteristic products. Photo- and thermally-induced crystalline-state reactions have been studied and unique reactions such as dimerization and racemization were discovered^{1,2)}. In this study, we examined ion-beam-induced crystalline-state reaction by using tris(triisopropylsilyl)silane (**1**), which is the precursor of room temperature stable silyl radical **2**³⁾, to determine the regioselectivity of ion beam irradiation (Scheme 1).

Scheme 1



Granular, colorless single crystals of **1**³⁾ (ca. 0.4 mm × 0.4 mm × 0.4 mm) were pasted on a Si substrate (10 mm × 10 mm) using double-sided adhesive tapes. The pasted crystals were irradiated with 490 MeV $^{192}\text{Os}^{30+}$ ion beam produced from the TIARA AVF cyclotron and the exposure fluence was 5×10^{11} ions cm⁻². After irradiation, the crystals were removed from Si substrate in air. The obtained pale yellow crystals were then transferred into an Ar-filled electron spin resonance (ESR) tube and ESR spectrum was measured.

The ESR spectrum of irradiated crystals was shown in Fig. 1. A single, broaden signal was observed. This indicated that radicals are successfully generated by ion beam irradiation in the single crystals. The irradiated crystals were kept their shape and seemed to have been retaining its crystallinity. Interestingly, irradiated crystals were able to handle in air atmosphere, while other silyl radical crystals were air-sensitive⁴⁾.

The identification of generated radicals was performed by ESR measurement of the cyclohexane solution of



Fig. 1 ESR spectrum of single crystals after ion beam irradiation.

irradiated crystals. Dry, oxygen free cyclohexane was transferred in vacuum into the ESR tube containing irradiated crystals and then ESR tube was refilled with Ar. All of the crystals were dissolved and pale yellow solution was obtained. The ESR spectrum of resultant solution measured at room temperature was shown in Fig. 2. A strong signal was observed and important information was obtained from the splitting pattern. There are three pairs of satellite signals due to coupling of the unpaired electron with the ^{29}Si and ^{13}C nuclei ($I = 1/2$). The two satellite signals with a largest value of the hyperfine coupling constant (hfcc) $a(^{29}\text{Si}) = 5.53$ mT can be ascribed to the coupling with the central α -Si nucleus, whereas two satellites with a middle hfcc value $a(^{29}\text{Si}) = 0.79$ mT can be assigned to the coupling with three neighboring β -Si atoms, and remained two satellites with a smallest hfcc value $a(^{13}\text{C}) = 0.24$ mT can be attributed to γ -positions. This result clearly indicated that the silyl centered radical **2** was generated regioselectively by ion beam irradiation to the single crystal of **1**.

Ion beam irradiation to single crystals which have appropriate structure, crystal packing, and bond strength brings desired products regioselectively, instead of decomposed or polymerized products.

References

- 1) M. D. Cohen et al., J. Chem. Soc. (1964) 1996.
- 2) K. Tanaka et al., Chem. Rev. 100 (2000) 1025.
- 3) S. Kyushin et al., Chem. Lett. (1998) 107.
- 4) A. Sekiguchi et al., J. Am. Chem. Soc. 124 (2002) 9865.

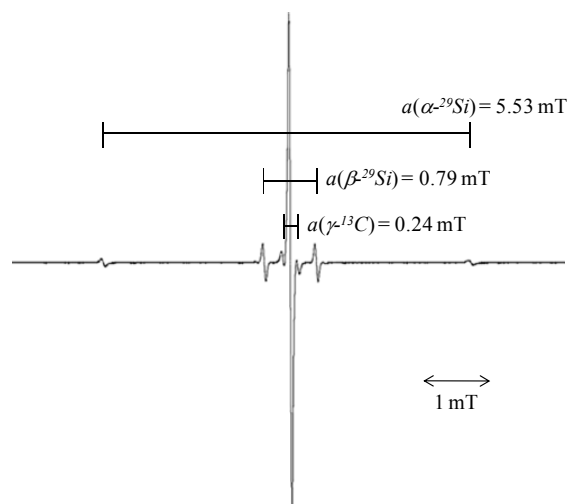


Fig. 2 ESR spectrum of irradiated crystals solved in cyclohexane at room temperature.

4-23 Effect of Alumina Particle on the Enhancement of H₂ Production and the Reduction of H₂O₂ Concentration In the γ -radiolysis of Aqueous Solutions

R. Yamada, Y. Kumagai and R. Nagaishi

Division of Environment and Radiation Sciences, NSED, JAEA

We have previously reported that addition of oxides, such as Al₂O₃, SiO₂, ZrO₂ and TiO₂, to aqueous solution resulted in much increase in yield of H₂ as a final product in γ -radiolysis compared to that in pure water or H₂SO₄ aqueous solutions alone¹⁾. The yield obviously reflects the results after many chemical reactions related to H₂ formation and consumption. In particular, the reactions of OH radical and of H₂O₂ molecule with H atom reduce H₂ production. Regarding the role of oxide in increasing the H₂ yield, the oxide addition possibly affect not only the H₂ formation but also the reduction of OH radicals and/or H₂O₂ molecules in the irradiated solutions. In this study we investigate the relation between the yields of H₂ and H₂O₂ as final products in the radiolysis by ⁶⁰Co γ -rays at JAEA-Takasaki.

The samples were 0.4 M (mol/L) H₂SO₄ aqueous solution or water containing high-purity α -alumina powder (AKP-50) supplied from Sumitomo Chemical. After irradiation, the amounts of produced H₂ gas were analyzed by gas chromatography, and the H₂O₂ concentrations were determined by Ghormely tri-iodide method, where the absorbance peak of I₃⁻ ion at 350 nm corresponds to the concentration of H₂O₂ in the irradiated solution²⁾.

Figure 1 shows the results of the effect of Al₂O₃ powder addition on the H₂O₂ concentrations in the γ -irradiated 0.4 M H₂SO₄ aqueous solutions, where each concentration divided by absorbed dose, namely equivalent to the H₂O₂ yield, was given to each absorbance peak. It is clearly shown that the H₂O₂ yield strongly decreased with

increasing the amount of Al₂O₃ powder in the H₂SO₄ solution. In accordance with the decrease in H₂O₂ yield, the H₂ yield increased with increasing the amount of Al₂O₃ powder as previously reported¹⁾ and shown in Fig. 2.

In the case of water, the decrease in H₂O₂ concentration with increasing the amount of Al₂O₃ powder was also observed. Regarding the relation between H₂ and H₂O₂ yields, similar to the results in the case of 0.4 M H₂SO₄, the more increase in H₂ yield and the more decrease in H₂O₂ yield were observed when the more Al₂O₃ powder was added to water as also shown in Fig. 2. It is noteworthy that the H₂O₂ yield in 0.4 M H₂SO₄ is higher than in pure water, and that the H₂ yield in 0.4 M H₂SO₄ is higher than in pure water¹⁾. When H₂O₂ is considered to be the oxidant counterpart to H₂ in the radiolysis of water, the above results can be reasonable in the absence of Al₂O₃ powder. Such a high H₂O₂ concentration produced in 0.4 M H₂SO₄ alone was effectively reduced by the addition of Al₂O₃ powder. The role of Al₂O₃ surface in the adsorption of OH radical and/or H₂O₂ molecule may be essential to the reduction of H₂O₂ concentration in irradiated solution.

References

- 1) R. Yamada et al., Int. J. Hydrogen Energy 33 (2008) 929.
- 2) A. Allen et al., J. Phys. Chem. 56 (1952) 575.

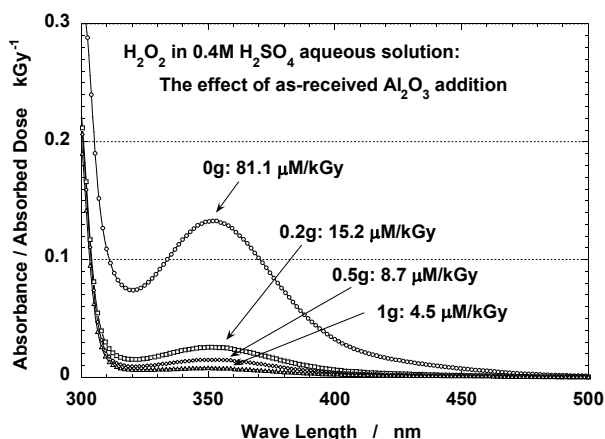


Fig. 1 Absorbance of I₃⁻ ion per ⁶⁰Co γ -absorbed dose for 0.4 M H₂SO₄ with alumina powder. The H₂O₂ concentrations per absorbed dose are given in the figure. Each of 0.2, 0.5 and 1 g of the powder was added to the 2 mL solution.

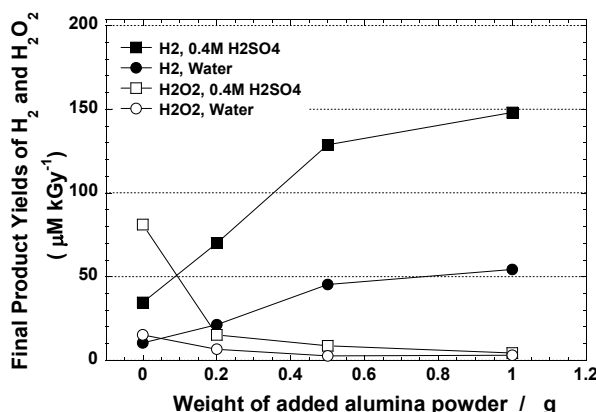


Fig. 2 Final product yields of H₂ and H₂O₂ obtained in ⁶⁰Co γ -radiolysis of 0.4 M H₂SO₄ and water containing alumina powder. Each of 0.2, 0.5 and 1 g of the powder was added to the 2 mL solution.

4-24 Incident Energy Dependences of Transient Species in Water under Pulsed H⁺ Ion Irradiation

M. Taguchi^{a)}, K. Iwamatsu^{b)}, Y. Sugo^{a)}, S. Kurashima^{c)} and Y. Katsumura^{b)}

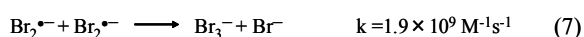
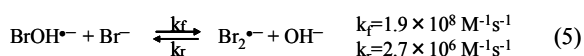
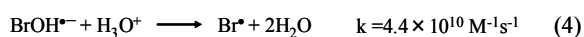
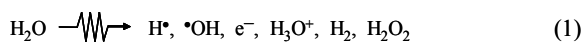
^{a)} Environment and Industrial Materials Research Division, QuBS, JAEA,

^{b)} The University of Tokyo, ^{c)} Department of Advanced Radiation Technology, TARRI, JAEA

Elucidation of the reaction mechanism induced by charged particles is significant for advanced radiation applications in material and biological science. Pulse radiolysis technique can observe reactions of reactive species directly. This technique is widely used not only for pulsed electrons but heavy ions, because it needs high intensity and high quality pulse, and high sensitive detection system. Construction of pulse radiolysis system was succeeded to understand LET effects of MeV-class heavy ions in Takasaki Ion Accelerators for Advanced Radiation Application (TIARA) facility¹⁾.

NaBr was selected as a probe reagent for the OH (hydroxyl) radical and dissolved at 1 to 1000 mmol dm⁻³ in purified water. NaBr aqueous solutions were saturated with oxygen and then put into a stainless irradiation cell. The cell has glass windows at the top and bottom for the irradiation and optical measurements. The ion used in this study was 20 MeV H⁺ ion provided from the AVF cyclotron in TIARA facility. Laser diode, whose wavelength is 375 nm, was used as a light source for observation. Incident energy was varied by setting different thickness of aluminum foils, which absorbs the H⁺ ion energy, on the irradiation cell.

Water molecules are decomposed to H atom, OH radical, electron and so on by H⁺ ion irradiation as shown in equation (1). The H atom and electron react with dissolved oxygen to form low reactive molecules, HO₂[•] and O₂^{•-}. The forward reactions of the reaction (2) to (5) proceed well and Br₂^{•-} is produced from the reaction of the OH radical with Br⁻ because of high concentration of Br⁻. The absorbance of Br₂^{•-} increased just after irradiation, and then decreased gradually in 100 mM NaBr aqueous solution as shown in Fig. 1²⁾. The decay curve is fitted using bi-molecular reaction equation following the reaction (7). The peak absorbance slightly decreased with the decrease in the NaBr concentration.



The formation yield of Br₂^{•-} was estimated as *G*-value (number of molecules per 100 eV absorbed energy) to be 0.92 for 1000 mM NaBr aqueous solution by H⁺ ion irradiation from the peak absorbance. In the case of low LET radiation, the *G*-value was estimated at 2.92 in the same sample. It is considered that Br₂^{•-} is produced by the irradiation and decomposed by the reaction (7) within the pulse width for 50 μs. The *G*-value of Br₂^{•-} decreased with the decrease in the incident energy as shown in Fig. 2. In other words, the yield of Br₂^{•-} decreased with the increasing LET value. It is experimentally and theoretically obtained that the *G*-value of the OH radical decreases when LET value increases. From the reaction (2) to (6), the yield of Br₂^{•-} will decrease by the decrease in the OH radical yields with increasing LET value.

References

- 1) M. Taguchi, et al., Radiat. Phys. Chem. 78 (2009) 1169.
- 2) K. Iwamatsu et al., Trans. Mater. Res. Soc. Jpn., in press.

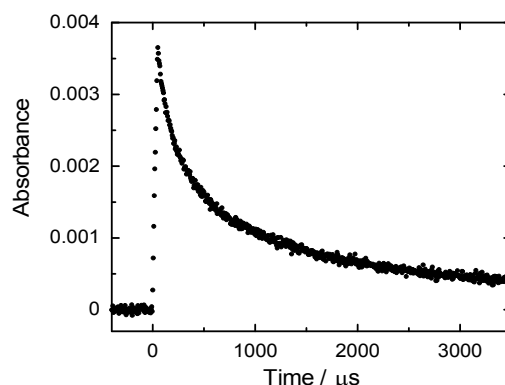


Fig. 1 Time profile of aqueous 100 mM NaBr solution observed at 375 nm under 50 μs pulsed H⁺ ion.

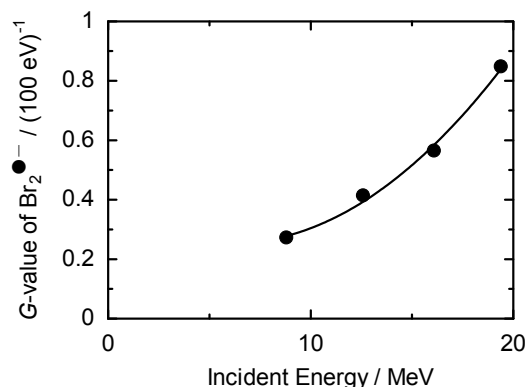


Fig. 2 *G*-value of Br₂^{•-} in NaBr aqueous solution irradiated with H⁺ ion having different incident energies.

4-25 LET Effect on the Radiation Induced Copolymerization of Maleimide with Styrene in 2-Propanol Solution

S. Nakagawa ^{a)}, M. Taguchi ^{b)} and A. Kimura ^{b)}

^{a)} Tokyo Metropolitan Industrial Research Institute,

^{b)} Environmental and Industrial Materials Research Division, QuBS, JAEA

N₂-saturated 2-propanol solutions containing maleimide and styrene were irradiated with 1 MeV electron, 320 MeV C-ion, 107 and 50 MeV He-ion, and 20 MeV proton beams. LET effect on the radiation induced copolymerization of maleimide with styrene was studied. The polymer yield efficiency decreased with increasing LET value. On the other hand, irradiation at a higher LET value and lower dose rate will produce a polymer with a higher molecular weight.

マレイミド (C₂H₂(CO)₂NH) 類とスチレン等オレフィン類を共重合させると耐熱性が向上することが知られており¹⁾、液晶ディスプレイなどへの応用が期待されている。また、マレイミド類をアルコール溶液中 (>0.02 mol/L) でイオン照射したところ、溶媒ラジカルが付加した化合物が生成すること、広い LET 領域で線量率が 1/10 になると効率が 1.5 倍になることなどがわかった²⁾。付加反応の効率は、ラジカル分布により線量率効果も異なると考えられるが、低濃度では影響が小さいと推測される。そこで、高濃度溶液を重イオン照射し、ポリマー生成の効率に及ぼす LET および線量率効果を比較検討する。また、この結果により、活性種密度を制御してポリマー生成効率を制御するための知見が得られると期待される。

マレイミドおよびスチレンを 2-プロパノールに溶かし (各 0.5 mol/L)、窒素置換した試料に、電子線 (1 MeV)、C イオン (320 MeV)、He イオン (50 MeV, 107 MeV)、プロトン (20 MeV) を照射し、生成物の分子量分布を GPC で分析した。分析試料は、真空乾燥した残留物を THF で溶解したものを用いた。

Figure 1 に、20 nA のイオンビーム照射により試料溶液 1 mL 中に生成したポリマー量を吸収線量に対してプロットする。C (320 MeV) < He (50 MeV) < He (107 MeV) < プロトン (20 MeV) の順に、ポリマー生成効率が大きくなっていることがわかる。Fig. 1 の傾きから得られる 1 kGy あたりのポリマー生成量を Table 1 に示す。すべての線種で、線量率の低下によりポリマー生成効率が上昇している。この線量率効果は重イオンほど顕著であった。

Table 2 に、イオンビーム 10 kGy 照射時に生成したポリマーの GPC スペクトルトップの分子量を示す。20 nA では、高 LET 照射ほどポリマーの分子量が減少するが、2 nA では、He イオン照射より C イオン照射で高分子量のポリマーが生成した。重イオン照射では、ポリマー生成の initiator となるラジカルが少ない分、線量率の低下により、溶媒ラジカルとの termination も起こりにくくなり、高分子量のポリマーが生成すると考えられる。

References

- 1) I. Takase et al., Kobunshi Ronbunshu 47 (1990) 569.
- 2) S. Nakagawa et al., Radiat. Phys. Chem. 79 (2010) 890.

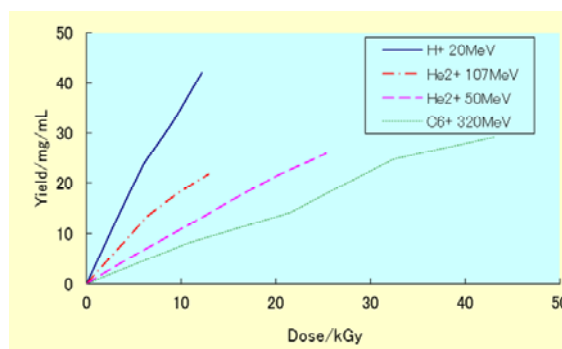


Fig. 1 Dose dependence of the polymer yields per unit volume of the solution obtained by irradiation of ion beams (20 nA).

Table 1 Yield of polymer by 1 kGy irradiation of electron and ion beams.

irradiation source	dose rate	yield(mg/mL/kGy)	ratio ^a
electron	1.0 mA (10 ⁴ kGy/h)	1.3	
electron	0.1 mA (10 ³ kGy/h)	4.8	3.7
H-20MeV	20 nA (60 kGy/h)	3.7	
H-20MeV	2 nA (6.0 kGy/h)	13	3.5
He-107MeV	20 nA (120 kGy/h)	2.2	
He-107MeV	2 nA (12 kGy/h)	9.0	4.1
He-50MeV	20 nA (90 kGy/h)	1.1	
He-50MeV	2 nA (9.0 kGy/h)	4.4	4.0
C-320MeV	20 nA (190 kGy/h)	0.7	
C-320MeV	2 nA (19 kGy/h)	3.7	5.3

a: The ratio of the dose rate effect on each irradiation source.

Table 2 Molecular weight at the peak of chromatogram (Mp) obtained by 10 kGy irradiation of ion beams.

irradiation source	LET value (eV/nm)	dose rate	molecular weight
H-20MeV	2.2-13	20 nA (60 kGy/h)	57100
He-107MeV	7.1-57	20 nA (120 kGy/h)	51500
He-107MeV	7.1-57	2 nA (12 kGy/h)	57000
He-50MeV	13-100	20 nA (90 kGy/h)	45100
He-50MeV	13-100	2 nA (9 kGy/h)	57000
C-320MeV	75-600	20 nA (190 kGy/h)	44500
C-320MeV	75-600	2 nA (19 kGy/h)	61200

4-26 Measurement of the Ion Beam Pulse Radiolysis Using Scintillator

T. Kondoh^{a)}, J. Yang^{a)}, K. Kan^{a)}, Y. Yoshida^{a)}, H. Shibata^{b)},
S. Kurashima^{c)} and M. Taguchi^{d)}

^{a)} ISIR, Osaka University, ^{b)} Faculty of Engineering, Kyoto University,

^{c)} Department of Advanced Radiation Technology, TARRI, JAEA,

^{d)} Environment and Industrial Materials Research Division, QuBS, JAEA

Nano-second time resolved ion-beam pulse radiolysis system using scintillator is developing at TIARA facility to measure the initial process of ion-beam induced reactions in the microscopic ion tracks. Time dependent behavior of optical absorption of pyrene-dichloromethane solution irradiated with 107 MeV He^{2+} ion beam was measured by stabilized ion beam pulse radiolysis system.

イオンビームを用いたがん治療や植物の品種改良、材料改質などの応用技術が近年注目されている。これらの応用技術は、高LET放射線である重イオンビームが、物質に入射した時に生成する高密度イオン化の効果を応用したものであるが、イオンビームの高密度イオン化による活性種反応の初期過程は完全に理解されたわけではない。イオンビームが誘起する高密度イオン化状態での活性種反応にイオンビーム照射の特色があり、高密度に生成した活性種は、高速に反応すると考えられている。高速な活性種反応を光吸収で直接測定することによって、その時間挙動や反応性を解明するために、ナノ秒重イオンビームパルスラジオリシスを開発している。パルスラジオリシスでは、パルスイオンビームが物質中に生成した活性種を光吸収で観測するが、イオンビームの場合、エネルギー付与の空間構造の特異性などから測定システムの構築は非常に困難である。

我々は、ビーム軸上の試料直前にシンチレータを置き、イオンビームによるシンチレータの発光を分析光として、試料中に生成された活性種の光吸収を測定する方法を開発している。この手法では、分析光源と試料中の励起場所がイオンビームの飛跡上なので、トラック内の活性種測定と高時間分解能を同時に実現できる。サイクロトロンで重イオンビームは、通常数10ナノ秒のパルス間隔のため化学反応の観測は困難であるが、PチョッパーとSチョッパーを同時に高度に制御することにより、220 MeV C^{5+} 、107 MeV He^{2+} シングルパルスイオンビームを発生した。HYポートに輸送されたビームは、シンチレータを通過した後、試料に入射して停止する。シンチレータ発光のうち試料を通過した光がフィルターで分光され光電子増倍管で検出される。パルスラジオリシスでの光吸収測定には、分析光強度、ビーム照射時透過光強度、発光等ビームノイズ、バックグラウンドの4つのデータが必要である。

前年度は測定体系の安定化対策を行った。シンチレータ、試料セル、フィルター、光電子増倍管、参照用光電子増倍管など各要素の独立性と位置再現性を確保した。同時にシンチレータ発光の参照光を測定することにより、参照光-信号光相関を測定し、良い相関があることを確認した。

今年度は、安定化した測定システムを用いて、220 MeV C^{5+} 、107 MeV He^{2+} イオンビームを照射しパル

スラジオリシス実験を行った。試料には、シンチレータ発光波長に活性種の光吸収を持つピレン-ジクロロメタン溶液、KSCN水溶液等を用いた。参照光-信号光相関を測定し分析光強度変動を補正した。220 MeV C^{5+} イオンビームをピレン-ジクロロメタン溶液に照射し光吸収を計算した場合、100 nsより速い減衰と減衰しない定常成分が観測されたが、速い減衰は試料中のピレン発光の減衰と全く同じであった。この事は、シンチレータが無い場合に測定したピレンの発光強度と、シンチレータがあるIo測定の場合とで試料へのイオンビーム入射強度が変化し、ピレン発光強度が減少したからと考えられる。減衰しない0.01程度の光吸収信号は、分析光源の3%程度の変動と考えられる。5~20%程度の分析光強度変動は、リファレンス補正により数%程度まで低減されたが、イオンビームパルスが誘起する光吸収を測定するには未だ不十分だった。さらに220 MeV C^{5+} イオンビームは、試料の入射面付近にブラッグピークがあると予想され、分析光およびピレン発光の変動が大きく観測されたと考えられる。

220 MeV C^{5+} イオンビーム照射実験では試料の有意な過渡光吸収が得られなかったため、試料にビームを確実に入射するために、透過性の高い107 MeV He^{2+} イオンビームを照射した実験を行った。その結果をFig. 1に示した。300 nsまで生成挙動が見られる。今後この信号がピレンカチオンラジカルの光吸収であるか再現性を含めて確認する。

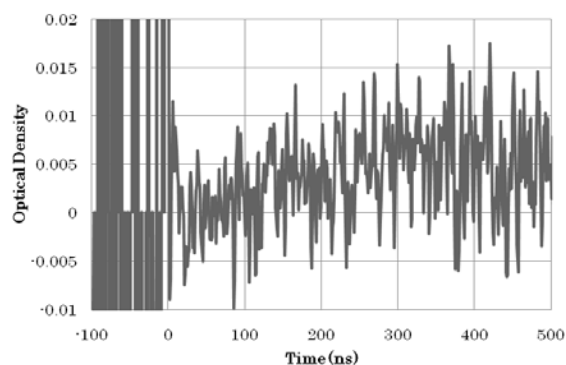


Fig. 1 Transient absorption of 100 mM pyrene dichloromethane solution at 440 nm irradiated by 107 MeV He^{2+} ion beam.

4-27 Three-Dimensional Imaging Test for a Head Module of a Si/CdTe Compton Camera for Medical Application

M. Yamaguchi^{a, c)}, N. Kawachi^{b)}, T. Kamiya^{a)}, T. Satoh^{a)}, N. Suzui^{b)}, S. Fujimaki^{b)},
H. Odaka^{c, d)}, S. Ishikawa^{c, d)}, M. Kokubun^{c, e)}, S. Watanabe^{c, d)}, T. Takahashi^{c, d)},
H. Shimada^{f)}, K. Arakawa^{a, f)}, Y. Suzuki^{g)}, K. Torikai^{f)}, Y. Yoshida^{f)} and T. Nakano^{f, g)}

^{a)} Dep. of Advanced Radiation Tech., TARRI, JAEA, ^{b)} Life Science and Biotechnology Div., QuBS, JAEA, ^{c)} Inst. of Space and Astronautical Science, JAXA, ^{d)} Dep. of Physics, University of Tokyo, ^{e)} Dep. of Space and Astronautical Science, The Graduate University for Advanced Studies, ^{f)} GHMC, Gunma University, ^{g)} Graduate School of Medicine, Gunma University.

We are currently developing a Compton camera apparatus having multiple head-modules at Gunma University for use as a three-dimensional nuclei imaging system for medical applications. It is based on the Compton camera technology of JAXA¹⁾. In this work, a three-dimensional imaging test for a proto-type head module²⁾ was performed using a checking source. The imaging results were compared with a simulation study.

Figure 1 represents the placement of the Ba-133 source and the detectors in the head module. A coordinate system is defined with the central axis as the z-axis, and the x- and y-axes being strip directions of the detectors. The origin of the coordinate is set at the center of the upper Si-detector. The Ba-133 source was placed at the distance of 35 mm from the Si-detector.

The top three diagrams in Fig. 2 represent the projections of the resultant three-dimensional spatial intensity distribution onto the x-y, y-z, and z-x plane from the left, bottom diagrams onto the x-, y-, and z-axes. The number of the Compton event used for the imaging was 1,069. The concentration of intensity appears at the source position within the margin of the installation error for the radiation source. The one-dimensional projections of the bottom diagrams in Fig. 2 are fitted using a Voigt function in order to estimate the FWHM values and center positions. The estimated FWHM values are listed on the top line in Table 1 with fitting errors. The value for the x-axis is consistent with the y-axis value, because of the 4th order rotational symmetry of the geometry of the detectors. In addition, it was observed that the FWHM for the z-axis has some finite value. This suggests that one can also observe the position of the radioactive source for depth direction by using only one head module.

Monte Carlo simulations were performed with the same geometric configuration as the experimental setup. The reconstructed image is shown in Fig. 3. Twenty thousand events were used for the imaging. The FWHM values are listed on the bottom line of Table 1 with the fitting errors. The FWHM values agree with the experimental results.

Presently, three upgraded head-modules are being constructed. We are going to perform medical experiments by using the three dimensional imaging system in this fiscal year.

References

- 1) T. Takahashi et al., SPIE 4851 (2003) 1228-1235.
- 2) M. Yamaguchi et al., NIM A 648 (2011) 52-57.

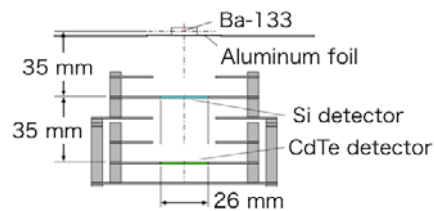


Fig. 1 Placement of detectors and gamma source.

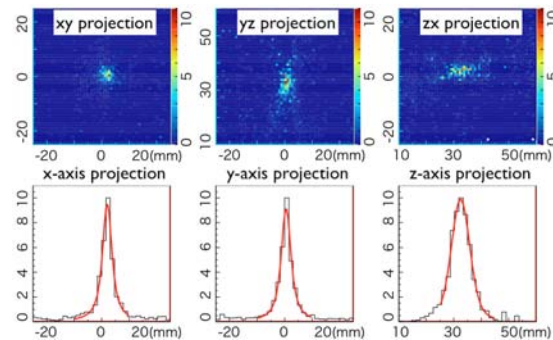


Fig. 2 The projections of the resultant three-dimensional spatial intensity distribution (Experimental).

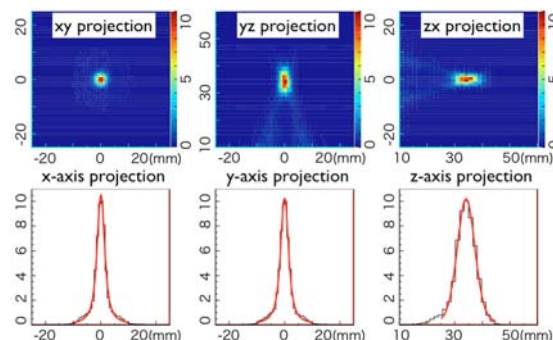


Fig. 3 The projections of the resultant three-dimensional spatial intensity distribution (Simulation).

Table 1 FWHM values of spatial intensity distribution for experimental and simulation result. The unit is millimeter.

	x-axis	y-axis	z-axis
Experimental	4.21 ± 0.98	4.33 ± 0.99	8.06 ± 0.90
Simulation	3.34 ± 0.48	3.50 ± 0.49	7.60 ± 0.68

4-28 Improvement of Measurement System for Source Neutron Spectrum to extend the Energy Range down to a few MeV

Y. Shikaze^{a)}, Y. Tanimura^{a)}, M. Tsutsumi^{a)}, H. Nemoto^{a)}, M. Yoshizawa^{a)}, H. Harano^{b)},
T. Matsumoto^{b)} and K. Mizuhashi^{c)}

^{a)} Department of Radiation Protection, NSRI, JAEA, ^{b)} National Metrology Institute of Japan, National Institute of Advanced Industrial Science and Technology,
^{c)} Department of Advanced Radiation Technology, TARRI, JAEA

For the establishment of the neutron standard fields above 20 MeV in Japan, the calibration fields have been developed by using the quasi-monoenergetic neutron irradiation fields with 45, 60 and 75 MeV peaks at TIARA¹⁻³⁾ of Takasaki Advanced Radiation Research Institute, Japan Atomic Energy Agency. Since energy spectrum of the source neutron has a continuous distribution in the lower energy region below the main peak, the contribution from the neutrons in the lower energy region must be subtracted from the total response of the neutron detectors and monitors for precise response evaluation to the peak energy neutrons. Therefore, measurement of the quasi-monoenergetic source neutron energy spectrum is necessary. The neutron energy spectrum is usually measured by the time-of-flight (TOF) method using the organic liquid scintillation detector. However, it is difficult to measure neutron energy spectrum below 10 MeV since the low energy neutrons with smaller pulse heights than the threshold in some measurement circuit modules were rejected in the data acquisition. Therefore, by the following efforts on the measurement circuits, the lower limit of energy range of the neutron measurement was lowered.

In the TOF measurement, to obtain the timing signal, the constant-fraction-discriminators (CFDs) were used. The anode signal of the photomultiplier tube (PMT) of the detector was used as the stop signal, and the chopper signal of the cyclotron was used as the start signal. Low energy neutrons with pulse heights below the low level threshold of the CFD were rejected to generate the output timing signals. Therefore, the maximum pulse height of the anode signal as the CFD input was adjusted to be slightly lower than the maximum input voltage by using coaxial attenuators in order to measure neutrons of energy as low as possible. The frequency of the cyclotron's beam was reduced to 1/5–1/6 by the beam chopper so as not to prevent from measuring low energy neutrons by the overlapped timing of high energy neutrons in the next beam bunch.

The neutrons can be separated from gamma rays by using the difference of the rise time of the signals. The dynode signal of the PMT was amplified and divided for use of the pulse height and the rise time data to obtain the 2-dimensional distribution of both data. In this case of the 2 parameter data taking, low energy neutrons with smaller

pulse heights than the lower level threshold of the pulse-shape-analyzer for rise time data could not be measured. To measure such low energy neutrons, the pulse height must be enlarged by higher amplification gain. However, in such a gain setting, the pulse height to the main peak energy became higher than the maximum input voltage of the analogue-to-digital converters. Therefore, another set of the simultaneous measurements of the pulse height and the rise time was incorporated. Divided dynode signals were led to the inputs of the normal gain amplifier for high energy neutrons and the 10 times higher gain amplifier for low energy neutrons.

Figure 1 shows the 2-dimensional distributions on pulse height versus rise time for two amplification gains of the pulse height. As shown in lower half in Fig. 1, by the measurement with two amplification gains of the pulse height, the threshold to the pulse height could be lowered, and the improved separation from gamma rays of neutrons was achieved in the low energy range.

In conclusion, the improvement of the measurement system enabled to extend the energy range down to a few MeV for precise separation from gamma rays of neutrons.

References

- 1) M. Baba et al., Nucl. Instrum. Meth. Phys. Res. A 428 (1999) 454.
- 2) Y. Shikaze et al., Radiat. Prot. Dosim. 126 (2007) 163.
- 3) Y. Shikaze et al., J. Nucl. Sci. Tech. Suppl. 5 (2008) 209.

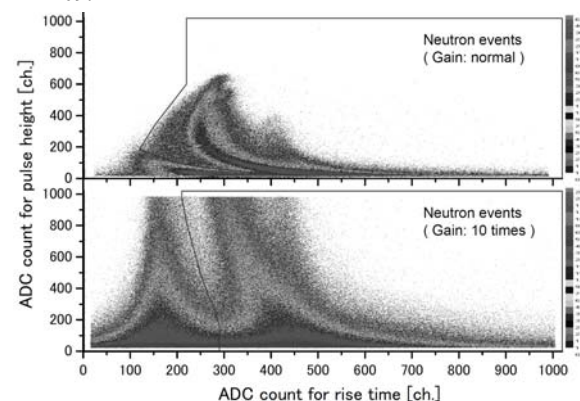


Fig. 1 The 2-dimensional distributions on pulse height v.s. rise time are displayed with each region of neutron events for normal (upper) and higher (lower) gain.

4-29 Measurements of Low Energy Neutron Spectra of Quasi-Monoenergetic Neutron Fields at TIARA

T. Matsumoto^{a)}, A. Masuda^{a)}, H. Harano^{a)}, Y. Unno^{a)}, M. Hagiwara^{b)}, T. Sanami^{b)}, J. Nishiyama^{a)}, Y. Shikaze^{c)}, Y. Tanimura^{c)}, M. Yoshizawa^{c)}, M. Baba^{d)} and K. Mizuhashi^{e)}

^{a)} National Metrology Institute of Japan, National Institute of Advanced Industrial Science and Technology, ^{b)} High Energy Accelerator Research Organization, ^{c)} Department of Radiation Protection, NSRI, JAEA, ^{d)} CYRIC, Tohoku University, ^{e)} Department of Advanced Radiation Technology, TARRI, JAEA

Precise measurements for high energy neutrons are important in studies on the neutron dose estimation around large accelerator facilities such as J-PARC, nuclear data, exposure in aircrafts and neutron induced soft error rate in semiconductor devices. High energy quasi-monoenergetic neutron fields at energies of 45 MeV, 60 MeV and 75 MeV at cyclotron facility TIARA are promising candidate for reference fields in order to calibrate measurement devices¹⁾. The peak neutron fluence was measured with a proton recoil telescope and a liquid scintillator¹⁻³⁾. However, it is also necessary to precisely evaluate neutron spectra of the low energy region in the field, because most of neutron dosimeters have large sensitivity for low energy neutrons. In TIARA, quasi-monoenergetic neutrons were produced by the ⁷Li(p,n) reaction. The neutron spectrum of low energy region in the field was measured with a ³He loaded multi-moderator spectrometer (BSS)⁴⁾. The moderators are composed of polyethylene and lead. The response function of the BSS was determined by calculation with the MCNPX simulation code and experimental results obtained at monoenergetic neutron fields with energy range from 100 keV to 15 MeV in AIST⁵⁾. The BSS was placed 15 m away from the target. The neutron spectrum was extracted by an unfolding method with the MAXED code⁶⁾ from the experimental data. Figure 1 shows the continuous part of neutron spectral fluence measured with the BSS at the 60 MeV quasi-monoenergetic neutron field. The peaks in the thermal region and around 1 MeV are shown in the experimental results. The neutron fluence in the thermal region was also experimentally evaluated by the Au foil activation method. In the Au foil activation method, the thermal neutron fluence was determined by the Cadmium difference method, using the Au foil with 20-mm diameter and 1-mm thickness. The gold foils were placed 6.4 m away from the target. The activities of ¹⁹⁸Au was measured with a high purity Ge detector. The thermal neutron fluence rate was 0.14 cm⁻²s⁻¹. The thermal neutrons are able to become backgrounds in calibration for neutron dosimeters. The experimental data obtained from the BSS and the Au foil activation method indicate the thermal neutron fluence rate are very low. A thermal neutron detector was also developed to measure the thermal neutron fluence. The thermal neutron detector consists of a ⁶LiF foil and an Si semiconductor detector. The foil and the Si detector are set in a vacuum chamber. A position of

the Si detector is out of the beam cone to prevent radiation damage. In the thermal neutron detector, the thermal neutron fluence was obtained by measuring charged particles produced by the ⁶Li(n,α) reaction. The efficiency of the thermal neutron detector was obtained from calibration in a thermal neutron field produced by a graphite pile at AIST. It is necessary to more precisely evaluate the low energy neutron spectra to improve the reliability of the experimental results.

A part of this study is the result of “Development of a progressive calibration method for neutron dosimeters using white neutrons” carried out under the Strategic Promotion Program for Basic Nuclear Research by the Ministry of Education, Culture, Sports, Science and Technology of Japan.

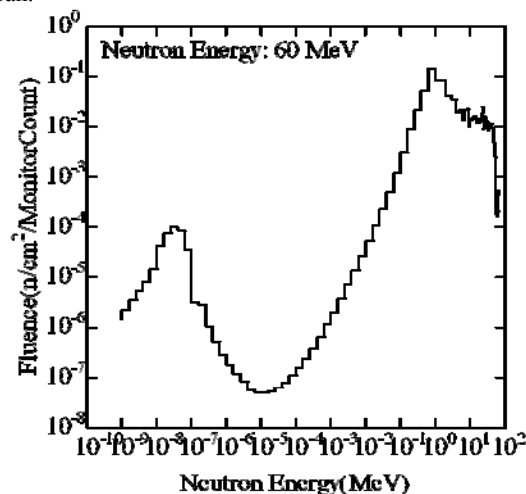


Fig. 1 The continuous part of neutron spectral fluence measured with the BSS at the 60 MeV quasi-monoenergetic neutron field.

References

- 1) H. Harano et al., Radiat. Meas. 45 (2010) 1076.
- 2) M. Baba et al., Nucl. Instrum. Meth. Phys. Res. A 428 (1999) 454.
- 3) Y. Shikaze et al., Nucl. Instrum. Meth. Phys. Res. A 615 (2010) 211.
- 4) B. Wiegel and A. V. Alevra, Nucl. Instrum. Meth. Phys. Res. A 476 (2002) 36.
- 5) A. Masuda et al. IEEE Trans. Nucl. Sci (to be published).
- 6) M. Reginatto, et al, Nucl. Instrum. Meth. A476 (2002) 242.

4-30 Test Measurement of Neutron Energy Spectra on Thin Targets Bombarded with 13 MeV/nucleon ^{20}Ne

Y. Iwamoto ^{a)}, M. Hagiwara ^{b)}, N. Matsuda ^{a)}, T. Sanami ^{b)}, Y. Sakamoto ^{a)},
H. Nakashima ^{c)} and K. Mizuhashi ^{d)}

^{a)} Division of Environment and Radiation Sciences, NSED, JAEA,

^{b)} Radiation Science Center, KEK, ^{c)} Safety Division, J-PARC, JAEA,

^{d)} Department of Advanced Radiation Technology, TARRI, JAEA

There is currently a renewed interest in low-energy heavy ion reactions with the availability of newly developing techniques such as the acceleration of intense (~ 1 particle μA) low-energy (~ 15 MeV/nucleon) rare isotope beams from ISOL targets. New facilities are under development at ReA3 and the Facility for Rare Isotope Beams (FRIB) facility at Michigan State University (MSU). It will be sometimes desirable to allow personnel to work around experimental endstations, where heavy ions interact with targets or beam transport components producing possibly significant levels of neutrons. It is useful to be able to easily and reliably predict neutron radiation levels around such new facilities.

The Monte Carlo-based heavy ion transport codes system PHITS ¹⁾ has been typically used to predict radiation levels around high-energy (above 100 MeV/nucleon) heavy-ion accelerator facilities. However, predictions by PHITS around low-energy (around 10 MeV/nucleon) heavy-ion facilities have not yet been investigated. In this report, we describe the test measurement of neutron energy spectra from 15- μm -thick ^9Be and 1- μm -thick $^{\text{nat}}\text{Fe}$ targets bombarded with 13 MeV/nucleon ^{20}Ne and comparisons between the experimental data and calculation results.

The experiments were carried out at the HB-1 beam line at the AVF cyclotron of TIARA. The targets are installed in a vacuum chamber. The NE213 organic liquid

scintillators (5.08 cm in diameter and 5.08 cm in length) were placed in directions of 15° at a distance of 2.0 m from the target to measure the light outputs by neutrons and the time-of-flight (TOF). A 2-mm-thick plastic scintillator NE102A placed in front of the neutron detector tagged events induced by a charged particle. The events of neutrons and γ -rays were separated by using a pulse shape discrimination technique and neutron energy spectra were analyzed by the TOF method. Figures 1 and 2 show the neutron energy spectra with comparison between measured and calculated results using the JQMD model and the evaporation models, GEM and DRES. The calculated results generally overestimated the measured data due to the emission of many neutrons following the decay of excited fragments with high energies. The agreement between experimental and calculated results for iron target was better than that for beryllium target.

We will measure neutrons at other angles with beryllium, iron and tungsten targets to check the accuracy of calculation codes over wide angles and mass ranges.

Reference

- 1) K. Niita et al., PHITS: Particle and Heavy Ion Transport code System, Version 2.23, JAEA-Data/Code 2010-022 (2010).

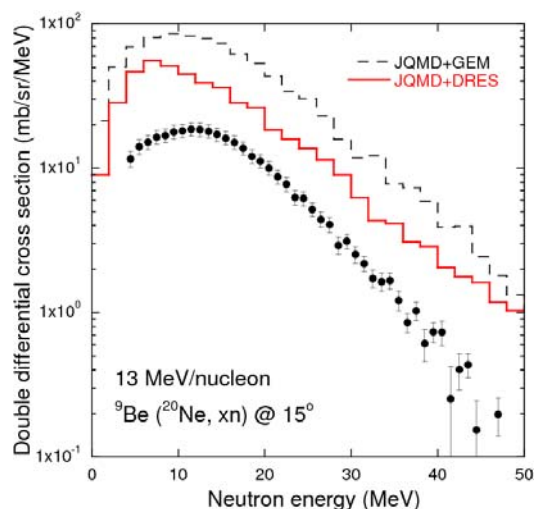


Fig. 1 Energy spectra of neutrons from a 15 μm -thick beryllium induced by 13 MeV/nucleon ^{20}Ne bombardment.

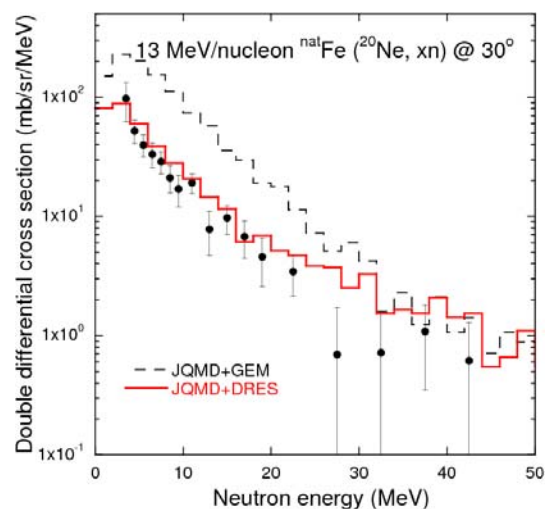


Fig. 2 Energy spectra of neutrons from a 1 μm -thick iron induced by 13 MeV/nucleon ^{20}Ne bombardment.

4-31 Systematic Measurement of Neutron and Gamma-ray from Thick Targets Bombarded with 12 and 18 MeV Protons

M. Hagiwara^{a)}, T. Sanami^{a)}, Y. Iwamoto^{b)}, N. Matsuda^{b)}, Y. Sakamoto^{b)}, Y. Nakane^{c)},
H. Nakashima^{c)}, K. Masumoto^{a)}, Y. Uwamino^{d)} and K. Mizuhashi^{e)}

^{a)} Radiation Science Center, KEK, ^{b)} Division of Environment and Radiation Sciences, NSED, JAEA,
^{c)} Safety Division, J-PARC, JAEA, ^{d)} RIBF Research Division, Nishina Center, RIKEN,
^{e)} Department of Advanced Radiation Technology, TARRI, JAEA

Nuclear data on proton-induced neutron and γ -ray production in an energy range from 10 to 20 MeV is important to execute the shield design and to estimate activation of low-energy accelerator facilities for medical use such as production of radiopharmaceuticals in positron emission tomography (PET) and a neutron source of an accelerator-based boron neutron capture therapy (BNCT). A number of cyclotrons are installed in medical facilities to produce positron emission radioisotopes such as ^{18}F through the $^{18}\text{O}(p,n)^{18}\text{F}$ reaction for label tracers used in PET. The $^9\text{Be}(p,n)$ reaction is one of possible neutron sources used in an accelerator-based BNCT. These nuclear reactions simultaneously produce neutrons and γ -rays, and neutrons severely activate the accelerator components and the cyclotron room. The energy and angular distribution of neutrons should be estimated for radiation safety as well as clearance of the facility decommission.

Currently, shielding of the neutrons and γ -rays as well as activation of accelerator components and the room wall are calculated by using calculation codes such as PHITS¹⁾ and MCNPX²⁾. The accuracy of the codes for such a low energy region should be checked by experimental data, because most of physical models implemented in the codes were developed to describe reactions of high-energy particles. However, the experimental data on the energy and angular distribution for neutron and γ -ray production are very scarce especially for proton energies from 10 to 20 MeV. In this report, we describe the measurement of neutron and γ -ray energy spectra from various thick targets (2.8 mm-thick ^9Be , 2.8 mm-thick $^{\text{nat}}\text{Cu}$, 3 mm-thick ^{27}Al ,

2.8 mm-thick $^{\text{nat}}\text{Cu}$, 0.7 mm-thick ^{181}Ta , 6 mm-thick pure water; H_2^{16}O , 6 mm-thick ^{18}O -enriched water; H_2^{18}O) induced by protons, and comparisons between the experimental data and calculation results.

The experiments were carried out with 12 and 18 MeV proton beams delivered to the HB-1 beam line at the AVF cyclotron of TIARA. The targets are installed in a vacuum chamber. The NE213 organic liquid scintillators (5.08 cm in diameter and 5.08 cm in length) were placed in directions of 0, 15, 30, 45, 60, 75, 90, 120 and 150° at a distance of 2.0 - 5.0 m from the target to measure the light outputs by neutrons and γ -rays, and the time-of-flight (TOF). The events of neutrons and γ -rays were separated by using a pulse shape discrimination technique and these energy spectra were analyzed by the TOF method for neutrons and the unfolding method with FERDOU code²⁾ for γ -rays, respectively. Figures 1 and 2 show the typical γ -ray energy spectra with comparison between measured and calculated results using MCNPX with LA150 data library for aluminum and copper, respectively. The calculated results generally well reproduce the measured energy spectra.

We will expand systematic measurements of neutron and γ -ray spectra from accelerator components induced by lower energy deuteron bombardment to check the accuracy of evaluated data libraries and calculation codes.

References

- 1) H. Iwase et al., J. Nucl. Sci. Tech. 39 (2002) 1142.
- 2) M. B. Chadwick et al., Nucl. Sci. Eng. 131 (1999) 293.
- 3) K. Shin et al., Nucl. Tech. 53 (1981) 78.

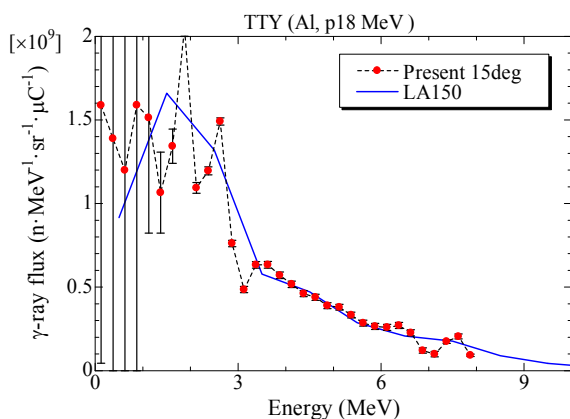


Fig. 1 Energy spectra of γ -rays from a thick aluminum target induced by 18 MeV proton bombardment.

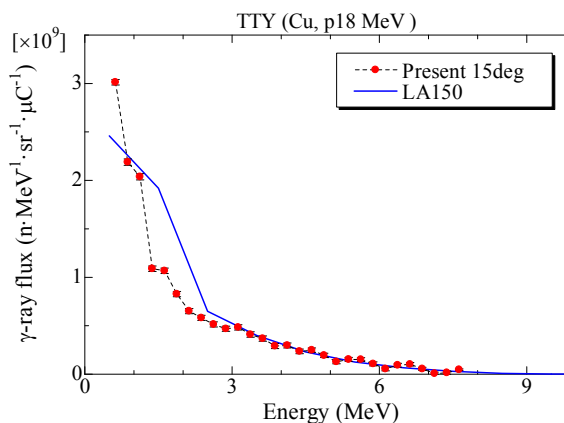


Fig. 2 Energy spectra of γ -rays from a thick copper target induced by 18 MeV proton bombardment.

4-32 Spectroellipsometric Studies on EB Induced Refractive Index Change of Aliphatic Polyimide

H. Seito^{a)}, T. Hakoda^{b)}, H. Hanaya^{a)}, Y. Haruyama^{a)}, H. Kaneko^{a)},
T. Yamashita^{c)} and T. Kojima^{a)}

^{a)} Department of Advanced Radiation Technology, TARRI, JAEA,

^{b)} Environment and Industrial Materials Research Division, QuBS, JAEA,

^{c)} Department of Pure and Applied Chemistry, Tokyo University of Science.

An electron beam (EB) generator of a few tens of keV is frequently used for surface modification such as the addition of the hydrophilicity for various polymeric materials¹⁾. Thin radiochromic film dosimeters such as FWT-60, GAF and B3 are mainly used in low energy EB industrial processing. But these film dosimeters have a few ten μm thickness, which has limitation for dose evaluation at extremely thin layer of polymeric material surface. Therefore dose measurement technique with higher resolution than the film dosimeter is required to control the surface modification by such low energy EB.

Then the ellipsometric properties of EB induced refractive index change of aliphatic polyimide (PI) were examined. Ellipsometry is an optical measurement of the polarization change occurring when light interacts with materials²⁾. It is able to measure refractive index with high resolution of 1 nm order in depth. This work aims to reveal relationship between dose and dose response (refractive index) of aliphatic polyimide by ellipsometry. The dose measurement with high resolution based on ellipsometry is useful for development of functional materials in a few tens of keV EB processing.

Films of PI (PMDA/DCHM) used in this study were supplied from Teraoka Seisakusyo Co., Ltd. The PI film was prepared from mixing equimolar amount of pyromellitic dianhydride (PMDA) and diamino-dicyclohexyl methane (DCHM) in dimethylacetamide, added with trifluoroacetamide under nitrogen atmosphere at 0 °C for 1 hour, followed by heating at room temperature for 6 hours³⁾. The PI film is colorless and transparent in the visible wavelength region due to the restriction of the charge transfer. Irradiation by 2 MeV-EB was performed by a Cockcroft accelerator. The refractive index change by EB was measured, using ellipsometer (model M-2000, J.A. Woollam Co., Inc).

The characteristics of dose response were examined at readout wavelength of 400 - 1600 nm. The dose response read-out at shorter wavelength is higher than that at longer wavelength (Fig. 1). The refractive index change is larger at absorbed dose value for every wavelength of 400 - 1600 nm. This result shows that charge transfer must have occurred by EB irradiation. The dose response at wavelength of 400 nm is appropriate to the evaluation of relative absorbed dose (Fig. 2). This suggests that PI film would be applicable to dose evaluation for wide range of 0.5 - 10 MGy. Ellipsometry results of the irradiated

PMDA/DCHM film need to be discussed further.

As the next step, 50 keV EB irradiation of PMDA/DCHM film is to be conducted.

Acknowledgments

We would like to gratefully thank several engineers in J. A. Woollam Japan Corporation, Mr. Y. Kuge, M. Matsuda and M. Suzuki for the measurement of refractive index using spectroellipsometer.

References

- 1) A. Oshima et al., Radiat. Phys. Chem. 80 (2011) 196.
- 2) J. N. Hilfiker et al., J. Vac. Sci. Tech. A 21 (2003) 1103.
- 3) T. Yamashita et al., J. Photopolym. Sci. Tech. 20 (2007) 739.

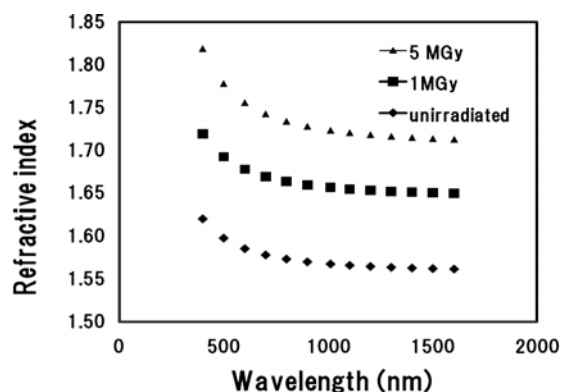


Fig. 1 Spectral dependence of refractive index before and after EB irradiation.

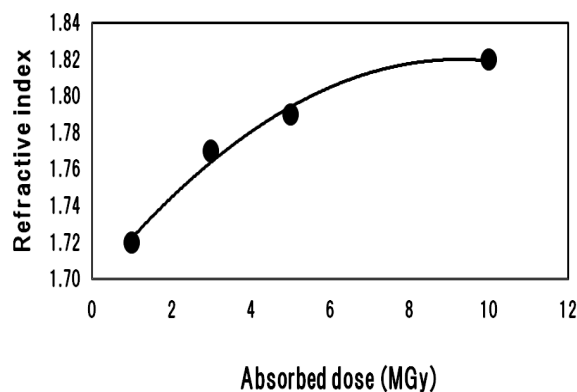


Fig. 2 Dose response curve of refractive index of aliphatic polyimide at wavelength of 400 nm.

4-33 Measurement of Charge States Corresponding to Relative Position of Constituent Ions Resulting from Foil-induced Dissociation of Aligned C_2^+ Ions

A. Chiba^{a)}, Y. Saitoh^{a)}, K. Narumi^{a)}, K. Yamada^{a)} and T. Kaneko^{b)}

^{a)} Department of Advanced Radiation Technology, TARRI, JAEA,

^{b)} Department of Applied Physics, Okayama University of Science

When the swift cluster ions, with velocities exceeding the Bohr velocity, interact with a matter, the characteristic phenomena which never appear in a case of the single ion irradiation are caused. It has been known that energy losses per atom of the swift cluster ions passing through a thin foil are larger than that of the single ions at the same speed. Such a behavior of cluster ions can be typically interpreted as resulting mainly from factors of both a symmetric screened Coulomb interaction among the cluster constituent ions and an interference of asymmetric excitations of the target electrons induced by the correlated motions of constituent ions. That is called a “vicinage effect”. It is considered, in particular, that the later factor gives rise to the dependence of the orientation angle of the internuclear axis of cluster ion on the vicinage effect. In fact, the energy losses of cluster ions aligned parallel to the beam direction were shown to be lower than that of the single ions in contrast with the cases for the random orientation angle¹⁾.

The vicinage effect influences the charge states of cluster constituent ions. In the experimental measurements using the carbon clusters (C_n ; $n=3-10$), Brunelle *et al.*²⁾ found that the average charges of cluster constituents emerging from the foils are reduced as compared to that of the single ions. It was shown by the theoretical calculation that the reductions of charges are mainly due to a perturbation of the Coulomb potential by the neighbor constituents³⁾, but the contribution to the charges from the interferences of electron excitations cannot be disregarded. Such contribution to the charges, however, has not been verified experimentally so far. Therefore we performed the preliminary experiments to investigate the relationship between each charge and the relative position (i.e., leading and trailing ion) of the constituent ions of cluster aligned to the beam direction.

Experiments were conducted using 3-MeV/atom C_2^+ ions accelerated by 3-MV tandem accelerator at the JAEA Takasaki. A schematic drawing of the experimental setup is shown in Fig. 1. The C_2^+ ion beam was shaped to achieve the high directional pulsed beam (1 kHz, 5 μ s in pulse width) by scanner and collimator (0.1 mm ϕ) before incidence to the scattering chamber. The beam intensity was reduced to a rate of approximately 20 clusters per second by beam attenuators and slits. The vertical

component of the velocity of constituent ions dissociated in a carbon foil of 80 Å in thickness is enhanced depending on the orientation angle by the mutual Coulomb repulsion. Hence, only if the orientation angle of incident cluster ion was almost parallel to the beam direction, its constituent ions can pass through a pinhole (0.6 mm in diameter) adjusted upon the beam axis located downstream of the foil. The orientation angle of such clusters depends on the product of charges $q_i \times q_j$ of their constituents, and could be calculated by a Monte Carlo simulation⁴⁾, e.g., the product of charges $q_i \times q_j = 3 \times 4$ was estimated to be $< 9.1^\circ$. Two ions after passing through the pinhole were deflected vertically to a certain angle corresponding to their charge by the electric field applied to the deflector, and were preferentially detected as a timing signal by each Micro-channel plate (MCP) according to their charge. Two timing signals were individually fed into a high-speed digitizer, and the arrival time difference between two ions was obtained by an analysis program on a PC.

Distributions of the arrival time differences for the product of charges 2×3 , 2×4 , and 3×4 are shown in Fig. 2. The horizontal axis in Fig. 2 is defined as subtracting the arrival time of a lower-charged ion from that of a higher-charged ion, i.e., the right-hand distributions indicate the cases in which the lower-charged ions were leading. The time differences were consistent with the calculated values by the simulation⁴⁾. Moreover, it could be confirmed that the time differences slightly increase with increasing the product of charges by the enhanced mutual Coulomb repulsion. The significant dependence of the relative position between two constituent ions on their charges could not be verified due to the insufficient amounts of data. However, this measurement is considered to be useful for getting a new insight that would be necessary to elucidate the origin of the vicinage effect.

References

- 1) M. F. Steuer *et al.*, Nucl. Instrum. Meth. 194 (1982) 137.
- 2) A. Brunelle *et al.*, Phys. Rev. A 59 (1999) 4456.
- 3) T. Kaneko, Phys. Rev. A 66 (2002) 052901.
- 4) A. Chiba *et al.*, Nucl. Instrum. Meth. B 269 (2011) 824.

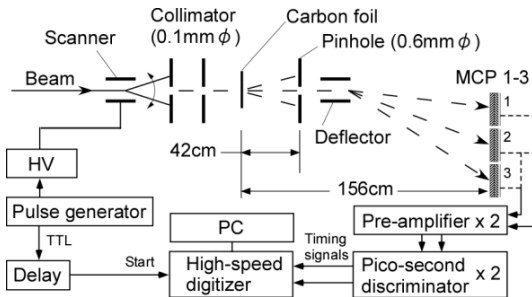


Fig. 1 Schematic drawing of the experimental setup.

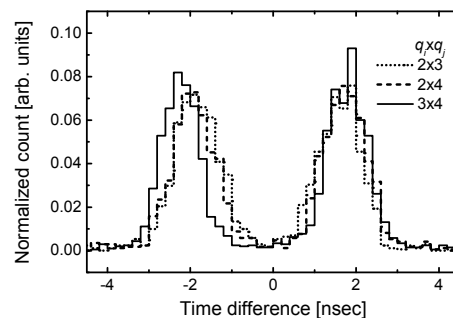


Fig. 2 Distributions of the arrival time differences for the product of charges $q_i \times q_j$ of the constituent ions of 6-MeV C_2^+ , emerging from a carbon foil.

4-34 Ion Induced Luminescence from Sapphire Irradiated with Swift Cluster Ion Beams - Energy Dependence of Incident Cluster Beams -

H. Shibata^{a)}, Y. Saitoh^{b)}, A. Chiba^{b)}, K. Yamada^{b)}, M. Taguchi^{c)} and K. Narumi^{b)}

^{a)} Graduate School of Engineering, Kyoto University,

^{b)} Department of Advanced Radiation Technology, TARRI, JAEA,

^{c)} Environment and Industrial Materials Research Division, QuBS, JAEA

The interaction of swift cluster ions with matter has attracted an attention in these years, because cluster ions bombard a very small area of a solid surface with many energetic atoms simultaneously and release large energy in the time range around picosecond. These situations cause non-linear effects or synergetic effects, which are not normally caused by a single atom collision with solid targets.

Our purpose of this study is to elucidate the characteristics of the interaction between energetic cluster ions and solids by means of measuring luminescence from solid surfaces irradiated with cluster ions. In this report we will present results of luminescence measurement from sapphire target irradiated with $C_1^+ \sim C_8^+$ cluster ions.

Luminescent spectra from sapphire ($\alpha\text{-Al}_2\text{O}_3$) induced by 0.5~1.5 MeV/atom (42~126 keV/u) $C_1^+ \sim C_8^+$ ion irradiation were measured in the wavelength range of 250~800 nm as a function of ion fluence at room temperature. Cluster ion beams accelerated by the TIARA 3 MV tandem accelerator were used for this study. Beam intensities were typically 2.5 nA for C_1^+ and 40 pA for C_8^+ ions. The luminescence measurement has been carried out by using an optical multichannel analyzer (Hamamatsu Photonics PMA11). Energy dependence of incident cluster ion beams on luminescence yield has been measured. Ion induced luminescent spectra peaked at 326 and 411 nm were observed. Luminescence of 326 nm was identified as F^+ center, whose intensity grew up and decayed gradually with irradiation. Luminescence of 411 nm was F center, whose intensity grew up rapidly and decayed faster than F^+ center luminescence with irradiation¹⁾. Intensities of luminescence reached peaks with less fluence as the cluster size increased.

The incident cluster ion size dependence on the yield of the F^+ center luminescence from sapphire target is shown in Fig. 1. The incident energy dependence is also shown in this figure. In this study the maximum intensity of luminescence was set as the luminescence yield and each yield was compare to the yield for C_1^+ ion irradiation, since the intensity of luminescence was dependent on the ion fluence. The ratios R_n of luminescence yields from sapphire target irradiated with 0.5, 1.0 and 1.5 MeV/atom $C_2^+ \sim C_8^+$ incident cluster ions to that for C_1^+ ion are described as $R_n = I(n) / nI(1)$, where n is number of cluster ion, $I(n)$ is the yield for C_n^+ cluster ion and $I(1)$ is the yield

for C_1^+ ion. The luminescence yields increase as the cluster sizes increase for every incident energy range, but the ratios R_n become less than unity in the energy range of 0.5 and 1.0 MeV/atom. The ratio is unity if the yield increases linearly as cluster size increases. In case of 1.5 MeV/atom incident energy, the ratio seems to be over unity though this is preliminary result. This tendency also appears in the theoretical calculation of the stopping power ($S = -dE/dx$) for the united atom limit of cluster ions²⁾. The ratio R_n of stopping power of cluster ion to that of single atom ion describes as $R_n = S(n) / nS(1)$. This value is independent to kinds of targets and depends on incident velocity only. The experimental results show the same tendency as the calculation of stopping power theory and exist between unity and the value for the united atom of the cluster ion. This suggests that luminescence caused by irradiation defects directly relates the stopping power of incident cluster ion.

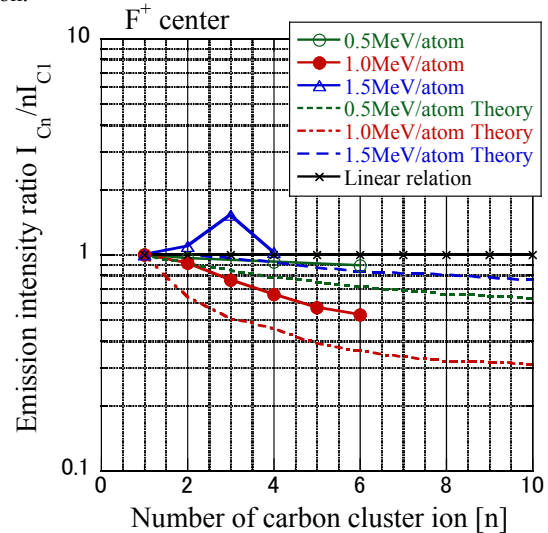


Fig. 1 The ratios of yields of luminescence from F^+ center of sapphire target irradiated with 0.5 ~ 1.5 MeV/atom $C_2^+ \sim C_8^+$ projectiles to that for C_1^+ ions in each energy indicate with continuous lines. Dashed and dotted lines show the theoretical stopping power calculation for the united atom of projectile.

References

- 1) Y. Aoki et al., Nucl. Instrum. Meth. Phys. Res. B 114 (1996) 276.
- 2) P. Sigmund et al., Meth. Phys. Res. B 112 (1996) 1.

4-35 Energy Deposition in Carbon by MeV/atom Carbon Cluster Ions

T. Kaneko^{a)}, Y. Saitoh^{b)}, A. Chiba^{b)} and K. Narumi^{b)}

^{a)} Department of Applied Physics, Okayama University of Science,

^{b)} Department of Advanced Radiation Technology, TARRI, JAEA

Cluster-ion-solid interaction has been attracted attention in that the irradiation effects are different from that expected in single-ion irradiation. The resultant effect will be characterized by the term of cluster effect, which has been found in the average charge, energy-loss, and secondary electron emission under MeV carbon cluster impacts. The cluster effect is classified in two aspects: negative (or sub-linear) region, and positive (or over-linear) region¹⁾. So far, the positive cluster effect in energy-loss was reported experimentally. Recently, a clear evidence of negative cluster effect in the energy loss per ion was reported for 0.5 MeV/atom carbon cluster ions penetrating thin carbon foil²⁾. In this report, we represent the positive cluster effect in a refined treatment.

The theoretical basis in the present study is to describe the incident cluster as an ensemble of partially stripped ions, where their charges are determined by the self-consistent cluster average-charge theory, and their spatial charge distribution is described in a statistical manner. The forces acting on each ion in a solid is composed of the screened coulomb repulsive force and the dissipative polarization force due to the induced electrons in a matter. The excitation of target electrons is treated in an electron gas model. In a case of carbon target, four electrons per atom participate in electron gas and the rest two electrons are in the 1s state.

The energy loss of each constituent ion in a cluster is evaluated using Molecular Dynamics Method by solving the Newtonian equation of motion. Here we assume the cluster structure is a linear-chain so that the incident condition is characterized only by the polar angle between the cluster axis and the direction of incidence. Figure 1 shows the average energy-loss of constituent ions for C_2^+ incidence at 675 keV/atom (solid line) and at 3.675 MeV/atom (dashed line) on carbon foil of 480 Å thickness as a function of the incident orientation angle θ . At the higher energy, the average energy loss per ion becomes maximum at about $\theta = 45^\circ$. This is a large contrast to the case of the lower energy, where the maximum reaches at $\theta = 90^\circ$. The average charge per ion at the incident energy of 3.675 MeV/atom are shown in Fig. 2 as a function of θ . Here, we found that the average charge per ion is maximum at $\theta = 0^\circ$, while at 675 keV/atom it does at $\theta = 90^\circ$.

By averaging over the orientation angle with the appropriate weight function, we can obtain the orientation-averaged energy loss per ion, $\Delta E(n)/n$, and the orientation-averaged average charge per ion, $Q(2)/2$, for C_2^+ incidence on carbon foil. At 675 keV/atom, we obtained $\Delta E(2)/2 - \Delta E(1) = -1.845$ keV, which means the negative cluster effect. On the other hand, at 3.675

MeV/atom, we obtained $\Delta E(2)/2 - \Delta E(1) = 3.90$ keV. This means the positive cluster effect. Here $\Delta E(1)$ and $Q(1)$ denote, respectively, the average energy loss and the average charge of a single carbon ion at the corresponding incident energies. Regarding the average charge per ion, $Q(2)/(2 \times Q(1))$ amounts to be 0.947 at 675 keV/atom and 0.942 at 3.675 MeV/atom. It is well known that the cluster average charge per ion is always less than that of a single ion with corresponding incident energies¹⁾. The calculated energy-loss values are in agreement with the trend of existing experimental data. This report displays that the present theoretical treatment can also derive both the negative and the positive cluster effect in the energy-loss process. In this respect, the present treatment will be able to predict the energy-loss and the average charge more widely. Applications to other clusters are now in progress.

Finally we acknowledge a partial support from a Grant-in-aid of Scientific Research (C) from JSPS.

References

- 1) T. Kaneko, Phys. Rev. A66 (2002) 052901.
- 2) S. Tomita, et al., Phys. Rev. A82 (2010) 044901.

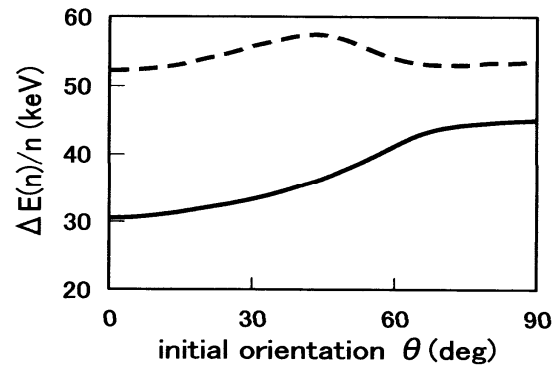


Fig. 1 Average energy loss per ion as a function of incident orientation angle for a 3.675 MeV/atom C_2^+ (dashed line) and a 675 keV/atom C_2^+ (solid line).

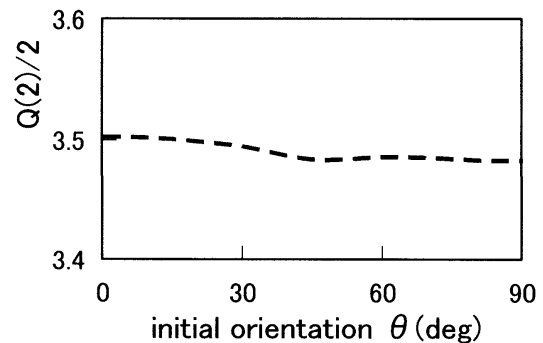


Fig. 2 Average charge per ion as a function of incident orientation angle for a 3.675 MeV/atom C_2^+ (dashed line).

4-36 Study on Au Cluster Ion Irradiation Effects for Fz-Si Single Crystal by Using Slow Positron Beam

F. Hori^{a)}, A. Kawasuso^{b)}, Y. Saitoh^{c)} and A. Iwase^{a)}

^{a)} Department of Materials Science, Osaka Prefecture University,

^{b)} Advanced Science Research Center, JAEA,

^{c)} Department of Advanced Radiation Technology, TARRI, JAEA

Doppler broadening S-parameter measurements have been performed to study Au cluster ion irradiation effects on Fz-Si single crystals by using slow positron beam apparatus. The depth profile of Doppler broadening S-parameter clearly shows that vacancy type defects are introduced in both irradiation case, but different types of defects, such as gold-vacancy and vacancy-impurity complexes, are produced in Fz-Si by Au and Au cluster ion irradiation.

高エネルギークラスターイオンは、通常の単原子イオン照射と比べて、固体内でのエネルギー散逸の空間密度が著しく大きい。そのため、それが固体に与える効果も、単原子イオン照射の場合と大きく異なることが予想される。我々は、Au クラスターイオンを Si 単結晶に照射し、電子顕微鏡観察を行った結果、Au 単原子イオン照射の場合と比べてサイズの大きい 2 次欠陥が多数観測されることを見出した。結晶中の微細欠陥の検出には陽電子消滅法が最適である。そこで、今回は、イオン 1 個当たりのエネルギーを同じにし、照射される Au イオンの総数が同じになるような条件で Au 単原子イオンおよび Au-3 クラスターイオンを照射した Fz-Si において低速陽電子ビーム実験をおこなったので、その結果を報告する。

帯熔融法精製法により作成された直径 8 cm の Fz-Si 単結晶を厚さ 1 mm の厚さにスライスしたものを、およそ 1 cm × 1 cm に切り出したものを試料として用いた。この単結晶 Fz-Si を TIARA タンデム加速器にて単原子 Au、および 3 原子クラスター Au のイオンをそれぞれ 1.67 MeV および 5 MeV のエネルギーで室温照射を行った。照射量は $1 \times 10^{13}/\text{cm}^2$ である。照射試料は 0~30 keV のエネルギー可変低速陽電子により深さに対する欠陥の評価を行った。各深さでの陽電子消滅 γ 線のエネルギー分布から、特に空隙のサイズおよび数密度を反映する 511 keV 付近の電子運動量を積分規格化した S パ

ラメータで評価を行った。

Figure 1 は単原子およびクラスター Au イオン照射した Fz-Si の陽電子消滅ドップラー広がり測定から得られるドップラー S パラメータの深さに対する分布を示す。この図において ref-Si は未照射試料の状態を示す。いずれの照射によっても明らかに照射によって試料に損傷による欠陥が導入されていることがわかる。どちらの照射でも S パラメータは未照射に比べ高い値を示していることから、空孔型欠陥であることがわかる。これらの欠陥は単原子照射でおよそ 3 μm 、3 原子クラスター照射でおよそ 2.3 μm 付近でほぼ未照射と同程度になっている。すなわち、単原子とクラスターでは同じエネルギーでの照射でも欠陥生成に違いが現れ、単原子照射のほうがより深くまで損傷を与える事がわかる。今回の照射では照射 Au イオン 1 個当たりのエネルギーはクラスターでも単原子イオンでも同じ 1.67 MeV であるため、損傷の深さの違いはクラスター効果によるものであると考えられる。また、欠陥の堆積分布にも違いが観察された。特に単原子イオン照射において深さおよそ 0.5 μm および 2 μm 付近に二つのピークが観察された。セルフイオンや軽イオンなどによるシリコンへの照射効果の陽電子消滅による実験^{1,2)}では、このような特徴的な欠陥分布の多重効果は報告されておらず、重イオンである Au に特有の効果であることが考えられる。そのため、照射によるイオンの堆積効果も考えられ、可能性として Au-空孔あるいは、空孔を含む Au 原子と不純物（例えば、炭素や酸素原子）等との複合体の形成が考えられる。今回の結果から、この特徴的な欠陥分布はクラスターイオンにすることでその照射効果は現れなくなることがわかった。そのため、今後は各深さに生成した照射欠陥のネイチャーを特定するために低速陽電子消滅 γ 線エネルギーの分布から欠陥周囲の元素の特定を試みる。また照射条件に関して、クラスター数および照射量を系統的に変化させて、クラスター照射効果についてより詳細な検討を進める。

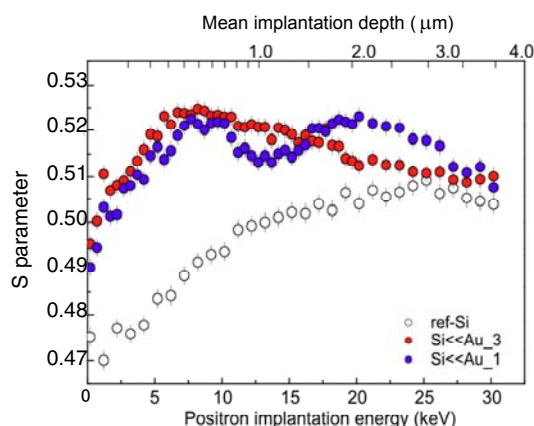


Fig. 1 Doppler broadening S-parameters as a function of positron implantation energy for before and after Au-1 and Au-3 ion irradiated Fz-Si.

References

- 1) J. Xu et al., Appl. Surf. Sci. 149 (1999) 193-197.
- 2) T. Akahane et al., Appl. Surf. Sci. 194 (2002) 116-121.

4-37 Energy Dependence of Nonlinear Effects of Sputtering Yields of Si Bombarded with 10-540-keV C₆₀ Ions

K. Narumi^{a)}, H. Naramoto^{b)}, K. Yamada^{a)}, Y. Saitoh^{a)}, A. Chiba^{a)},
Y. Takahashi^{b)} and Y. Maeda^{b, c)}

^{a)} Department of Advanced Radiation Technology, TARRI, JAEA, ^{b)} Advanced Science Research Center, JAEA, ^{c)} Department of Energy Science and Technology, Kyoto University

The sputtering yield of a polycrystalline or amorphous single-element solid bombarded with monatomic ions is well described by the linear-collision-cascade theory by Sigmund¹⁾. When the atomic numbers of the projectile and the target become large, however, the deviation of experimental sputtering yields from the theoretical predictions, which is called nonlinear effect, is found; especially, it is more significant in the case of molecular/cluster-ion bombardment²⁾. In the case of Au self-sputtering by Au_n-ion ($n \leq 13$) bombardment, it has been reported that the sputtering yield is proportional to n^2 in the energy range where the nuclear stopping is dominant³⁾. This nonlinear effect can be attributed to an elastic-collision thermal-spike model⁴⁾. In the present report, we have determined Si sputtering yield as a function of energy of C₆₀ ions in the energy range from 10 to 540 keV in order to investigate nonlinear effects on the sputtering yield.

Experimental details are described elsewhere⁵⁾; thus they are omitted here. Figure 1 shows the obtained sputtering yield of Si bombarded with C₆₀ ions as a function of the energy per atom as well as of the energy of a C₆₀ ion. The observed sputtering yield has the maximum around 100 keV, which is approximately 600 Si/C₆₀ or 10 Si/C. In order to evaluate the observed sputtering yields, they were compared with those bombarded with a carbon monatomic ion calculated both based on the linear-collision-cascade theory

by Sigmund¹⁾ and using the SRIM2008 code⁶⁾. Calculated results are shown in Fig. 1 as the solid line and the open diamonds, respectively. Comparing with the calculated sputtering yield for an equi-velocity monatomic ion, nonlinear effect on the sputtering yield has been found. Here, we introduce the sputtering-yield ratio $Y_{60}/(60 \times Y_1)$, which gives the magnitude of the nonlinear effect of the Si sputtering by C₆₀-ion bombardment; it is shown in Fig. 2. The sputtering-yield ratio depends on the energy of C₆₀ ions: It is very large around the energies where the sputtering yield has the maximum and hardly observed at 10 keV. No n^2 dependence is observed. The present results support that the observed nonlinear effect is not attributed to “the thermal spike” but to “the dense collision cascades”.

References

- 1) P. Sigmund, Phys. Rev. 184 (1969) 383.
- 2) H. H. Andersen and H. L. Bay, Radiat. Effects 19 (1973) 139.
- 3) S. Bouneau et al., Phys. Rev. B 65 (2002) 144106.
- 4) P. Sigmund and C. Claussen, J. Appl. Phys. 52 (1981) 990.
- 5) K. Narumi et al., JAEA Takasaki Ann. Rep. 2008 (2009) 163.
- 6) J. F. Ziegler, SRIM version 2008, <<http://www.srim.org>> (2008).

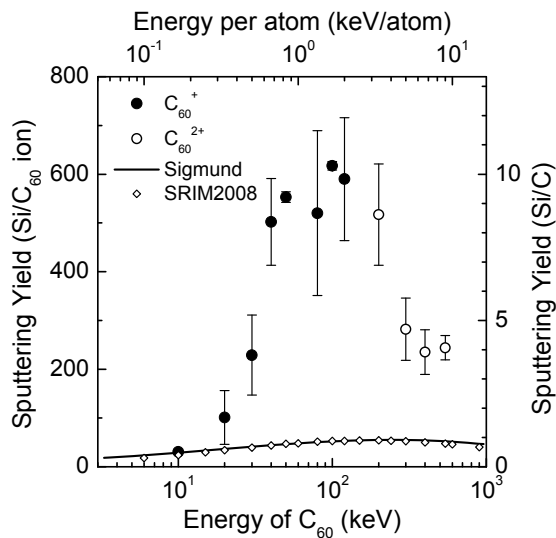


Fig. 1 Energy dependence of the Si sputtering yield for C₆₀-ion bombardment. The solid line shows the sputtering yield for monatomic-ion bombardment calculated based on the theory of Sigmund. The result simulated with SRIM2008 is also shown.

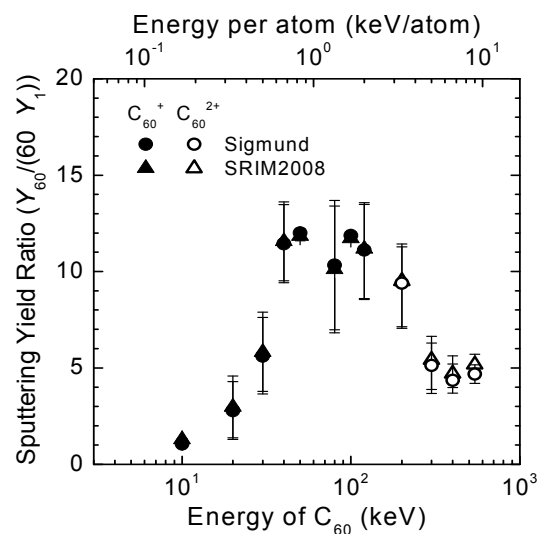


Fig. 2 Energy dependence of the sputtering-yield ratio $Y_{60}/(60 \times Y_1)$, where Y_{60} is the present experimental sputtering yield for a C₆₀ ion and Y_1 is the sputtering yield for a C monatomic ion calculated based on Sigmund's theory or using the SRIM2008 code.

4-38 Secondary Ion Emission from PTFE upon C_{60} Ion Impacts

K. Hirata^{a)}, Y. Saitoh^{b)}, A. Chiba^{b)}, K. Yamada^{b)}, Y. Takahashi^{b)},
K. Narumi^{b)} and T. Kamiya^{b)}

^{a)} National Institute of Advanced Industrial Science and Technology (AIST),
^{b)} Department of Advanced Radiation Technology, TARRI, JAEA

Secondary ion (SI) mass spectrometry is based on the phenomenon that secondary ions (SIs), produced by a primary ion impact on a target, provide information on the elements, chemical structure, and surface composition. Enhancement of SI emission yields has been required for further surface-sensitive chemical analysis and high contrast imaging of SIs. Cluster ion impact on a target produces different SI yields compared with those for monoatomic ions because of the unique irradiation phenomenon that the constituent atoms of an incident cluster simultaneously impact on a very small region of the target surface. Generally, the larger the primary cluster ion is, the larger the enhancement effect is on SI yields. C_{60} is one of the most useful primary cluster ions for SI mass spectroscopy due to its large cluster number and stability. We had developed time-of-flight (TOF) SI mass spectroscopy using primary C_{60} ions in the medium energy range (from several tens to several hundreds of keV), where few attempts have been made to study C_{60} impacts¹⁾. In this paper, we report comparison of SI yields from a Poly(tetrafluoroethylene) (PTFE) target for incident ion impacts of C_{60} ion impacts with an energy range from 30 keV to 270 keV by TOF SI mass analysis combined with SI electric current measurements.

The medium energy C_{60} TOF SI mass spectroscopy was developed using a 400 kV ion implanter of the Japan Atomic Energy Agency (JAEA)/Takasaki, as described elsewhere¹⁾. Briefly, pulsed C_{60} ion beam was produced by chopping direct current C_{60} ion beam with electrostatic deflection plates triggered by a pulse generator and a series of collimators before injecting into the target. The pulsed ion beam was incident on the target at an angle of 45° to the target surface. SIs produced by C_{60} impacts were accelerated between the target and a TOF drift tube before hitting a microchannel plate (MCP). The start and stop signals for TOF measurements were provided by the pulse generator used for pulsing the incident ion beam and a constant fraction discriminator (CFD) connected with the MCP output via a pre-amplifier, respectively. A SI counting system of the spectrometer was improved using a fast digital storage oscilloscope in order to obtain more accurate TOF SI mass spectra²⁾. For comparison of SI yields per C_{60} impact, peak intensities of the TOF SI spectra was scaled based on qI_p/I_o (q : incident ion charge number, I_o : incident beam electric current, I_p : positive secondary ion current for each irradiation condition), where I_o and I_p are directly measured using highly sensitive electrometers respectively connected to a Faraday cup and a movable metal plate with a grid, as described elsewhere³⁾.

Figure 1 shows the positive SI mass TOF spectra from m/z (mass to charge ratio) = 0 to 140 of PTFE for (a) 30 keV

C_{60}^+ , (b) 60 keV C_{60}^+ , (c) 120 keV C_{60}^+ and (d) 270 keV C_{60}^{2+} , respectively. The relative SI intensity on the vertical axis is proportional to the SI yield per C_{60} impact, as the total counts of the spectra are scaled based on qI_p/I_o as described above. The major peaks in the figures were assigned to fluorinated carbon compounds $C_xF_y^+$. We note that the characteristic peak intensities of PTFE increase with increasing incident energy. This result demonstrates that impacts of C_{60} with increased incident energies (60 keV C_{60}^+ , 120 keV C_{60}^+ and 270 keV C_{60}^{2+}) are advantageous for sensitive detection of the characteristic SIs of PTFE over the lower energy 30 keV C_{60}^+ impact.

In conclusion, the use of impacts of C_{60} ion with the increased incident energies (60 keV C_{60}^+ , 120 keV C_{60}^+ and 270 keV C_{60}^{2+}) provided higher yields of the characteristic positive SIs for PTFE than those of lower energy C_{60} ions (30-keV C_{60}^+) and advantageous for highly sensitive chemical analysis of PTFE.

References

- 1) K. Hirata et al., Nucl. Instrum. Meth. B **266** (2008) 2450.
- 2) K. Hirata et al., Rev. Sci. Instrum. **82** (2011) 033101.
- 3) K. Hirata et al., Appl. Phys. Lett. **86** (2005) 044105.

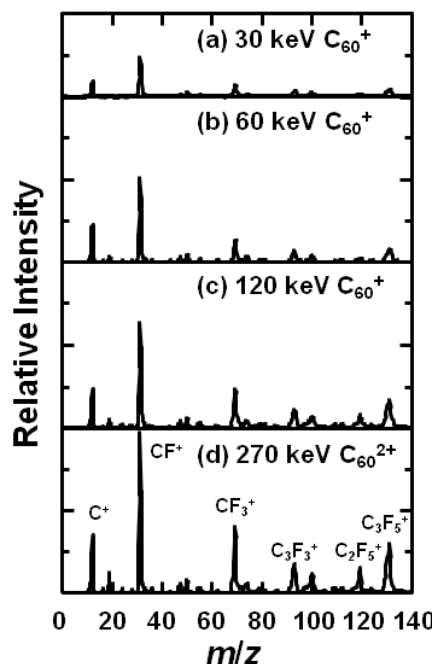


Fig. 1 Positive secondary ion TOF spectra of PTFE for (a) 30-keV C_{60}^+ , (b) 60-keV C_{60}^+ , (c) 120-keV C_{60}^+ , and (d) 270-keV C_{60}^{2+} .

4-39 Status Report on Technical Development of the JAEA AVF Cyclotron Facility

H. Kashiwagi, N. Miyawaki, S. Okumura, S. Kurashima, K. Yoshida, Y. Yuri, T. Yuyama, T. Ishizaka, I. Ishibori, T. Nara and W. Yokota

Department of Advanced Radiation Technology, TARRI, JAEA

Correction system of the cyclotron magnetic field for reduction of beam changing time

It takes a few hours to change ion species or energy of cyclotron beams, the main cause of which is a long-time process to form the cyclotron magnetic field for acceleration. Then the reduction of the forming time is strongly required to increase the available beam time. While the forming time with the previous process is about 40 minutes, we developed a new substitute process¹⁾, which can reduce to about 10 minutes in a restricted start-up condition. A correction system of the cyclotron magnetic field consisting of a bipolar power supply and a 5-turn coil was developed. We confirmed that this system can reduce the forming time to about 10 minutes in most start-up conditions.

Emittance reduction effect of the extracted beam by the beam buncher

The emittance of the beam extracted from the cyclotron probably increases with a wider beam phase width in the cyclotron because the accelerating beam extends spatially by the expansion of the energy spread caused by the difference of the acceleration voltage according to the RF phase in a sinusoidal waveform. Smaller emittance of the extracted beam is expected by the beam buncher, which compresses the direct current beam in the low energy beam transport line within a narrow RF phase width. In order to verify this speculation, the emittance of the extracted beam was measured by the emittance monitor at CS0, the first diagnosis chamber after extraction from the cyclotron. The measured horizontal 80% emittance of the 260 MeV $^{20}\text{Ne}^{7+}$ beam was 1.29π and 1.67π mm·mrad with and without the buncher, respectively. The result shows clear reduction of emittance by the buncher. Moreover we confirmed that the extraction efficiency increased by reduction of the emittance with the buncher.

Measurement of injection beam emittance and acceptance of the cyclotron system

We are developing an emittance and acceptance measurement system to evaluate transverse phase-space matching of an injection beam to the acceptance of the cyclotron system. The system is planned to use to improve the transverse matching for higher beam transmission from ion sources to the irradiation chambers. Emittance and acceptance measurements were tested.

The system is composed of the phase-space collimator²⁾ (PSC) and beam intensity monitors. The PSC, which is installed in the low energy beam transport line, consists of

two pairs of slits. One pair of slits pass the beam within an arbitrary area in the x-x' phase plane and the other in the y-y' phase plane. In emittance evaluation, beam intensity distributions in transverse phase planes are measured using the PSC and a metal plate just behind the PSC as a beam intensity monitor in the low energy beam transport line. In acceptance evaluation, beam transmission distributions in transverse phase planes are measured using the PSC and a Faraday cup or a scintillation counter³⁾ installed in the high energy beam transport line after the cyclotron.

Preliminary tests of this system were carried out under the 160 MeV $^{16}\text{O}^{6+}$ accelerating condition. The emittance of the injection beam, which is the 50.2 keV $^{16}\text{O}^{6+}$ beam from the 14.5 GHz ECR ion source (Hypernanogan), and the acceptance from the PSC to the Faraday cup at HA2 chamber in the high energy beam transport line were measured. Figure 1 shows results of both measurements in the x-x' phase plane. We confirmed that the whole beam emittance and a part of the acceptance were successfully measured. Concerning the acceptance, however, only the area overlapped with the emittance was able to be measured because the injection beam did not cover the area of whole acceptance. To extend the measurable area, the injection beam needs to be enlarged or to be scanned in the phase planes to simulate the large emittance. Equipment for scanning the beam in each phase plane will be added to this system to measure whole acceptance.

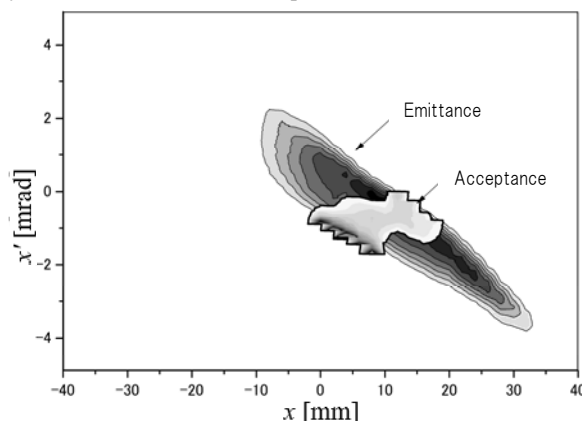


Fig. 1 The measured emittance and part of acceptance.

References

- 1) N. Miyawaki et al., Proc. 7th Ann. Meeting Part. Accel. Soc. Jpn. (2010) 975-978.
- 2) H. Kashiwagi et al., Proc. IPAC'10 (2010) 945-947.
- 3) H. Kashiwagi et al., Proc. 7th Ann. Meeting Part. Accel. Soc. Jpn. (2010) 628-630.

4-40 Development of Beam Generation and Irradiation Technology for Electrostatic Accelerators

A. Yokoyama, S. Uno, A. Chiba, K. Yamada, Y. Saitoh,
Y. Ishii, T. Satoh, T. Ohkubo and T. Agematsu

Department of Advanced Radiation Technology, TARRI, JAEA

Cluster ion acceleration

One of the key points in accelerating cluster ions using a tandem accelerator is the transmission, which is defined as the ratio of incident negative cluster ion beam current upon the tandem to accelerated intact positive cluster ion beam current. Most negative cluster ions injected into the tandem get destroyed in collisions with the target gas in the charge exchange section from negative to positive in the high voltage terminal, thus making the transmission of cluster ions is much lower than that of mono-atomic ions. Therefore, we investigate the charge exchange and destruction mechanism on the MeV energy cluster ions colliding with gas targets to select the suitable charge exchange gas which has not only a small destruction cross section but also a large charge exchange cross section without destruction¹⁾ (production cross section). In this fiscal year, the destruction and production cross sections for 2.5 MeV carbon cluster ions C_n ($n=2, 4, 8, 10$) in collisions with a neon gas target were evaluated from a beam transmission through the tandem accelerator²⁾. As a result, it was revealed that the destruction cross sections for C_n were on the order of 10^{-16} cm^2 and were proportional to the number of atoms in the cluster. We have tried to calculate the destruction cross sections by assuming that C_n clusters are liner chains and their colliding directions with a neon gas are random. As a result, the calculated line (dashed line) in Fig. 1 almost consists with experimental values. It indicates that the destruction cross sections strongly depend on the geometry of the cluster ions. We will investigate the dependence on geometrical size of target gases.

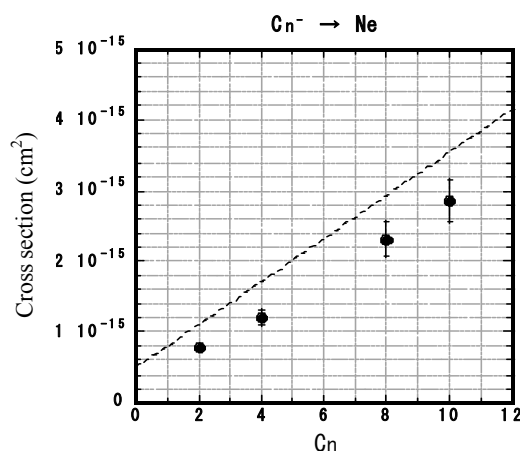


Fig. 1 Destruction cross section of C_n ($n=2, 4, 8, 10$). The dashed line represents the calculated cross sections, cf. text.

Development of beam profile monitor using multi Faraday cups

We developed an ion beam profile monitor using multi Faraday cups (MFC). Suitable depths and bottom shapes of each FC unit for the measurement of a fullerene ion beam profile were studied in last fiscal year²⁾. In this fiscal year, the MFC's performance was tested. Twenty-five Faraday cups with 3 mm in diameter, 15 mm in depth and oblique bottom were arrayed at intervals of 5 mm in a square lattice arrangement. The lower limit of beam current measurement was about 20 pA due to background and switching noises which were measured using the digital multi-meter (DMM); National Instruments PXI-4071. The readout time from twenty-five FCs was usually 85 msec, and 7.5 sec when the DMM was used at 20 pA sensitive range. The beam profile of 30 keV C_{60}^+ generated with the 400 kV ion implanter was successfully measured, as shown in Fig. 2.

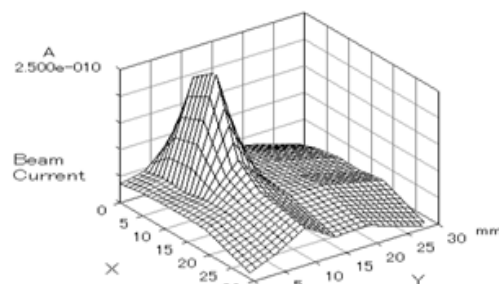


Fig. 2 Beam profile of C_{60}^+ beam at 30 keV. It was measured using the developed multi Faraday cups.

Emittance measurement using scintillator luminescence induced by MeV proton beams

Emittances of proton beams accelerated by the 3 MeV single-ended accelerator are measured using an emittance monitor with a scintillator developed in TIARA. In this fiscal year, the improvement of the proton beam emittance was observed using the emittance monitor, finely adjusting the extraction voltage of the ion source in the accelerator. Since the obtained emittance and brightness were relative, they will be measured using a scanning fine metal wire to obtain the beam current in the next fiscal year as compared with those of the scintillator.

References

- 1) Y. Saitoh et al., Rev. Sci. Instrum. 80 (2009) 106104.
- 2) A. Yokoyama, et al., JAEA Takasaki Ann. Rep. 2009 (2011) 175.

4-41 Fast Single-Ion Hit System for Heavy-Ion Microbeam at TIARA Cyclotron (IV)

W. Yokota, T. Satoh, S. Okumura, S. Kurashima, N. Miyawaki, H. Kashiwagi, K. Yoshida, M. Koka, K. Takano, A. Yokoyama, W. Kada and T. Kamiya

Department of Advanced Radiation Technology, TARRI, JAEA

The development of the fast single-ion hit system is continuously proceeded in order to improve the quality of microbeam and single-ion hit at the HX course of the TIARA cyclotron. The major subjects are reduction of miss hit in the single-ion-hit irradiation and development of a real-time detection system of single-ion hit. New microbeam development was also carried out.

The miss hit, no hit on the targeted point by any ions, appears on occasion at more than ten percents of the total hit number depending on tuning of beam focusing or transport¹⁾. The experiment of irradiation on living cells requires its reduction down to less than 1%. The process where the miss hit takes place is currently considered as follows: Some ions passing through the micro slits collide the slit edge and their charges change into plural states by the collision as shown in Fig. 1. Ions with changed charges consequently feel different force of magnetic field of the focusing lens and electric field of the scanner. Then such ions go along paths not leading to targeted points.

This speculation was clearly demonstrated in the case of 260 MeV-²⁰Ne⁷⁺. The ion beam focused on a film detector of CR-39, 100 μm thick, was deflected by a constant voltage of the scanner downstream of the micro slit. Four groups of etch pits created by ions, each of which contained hundreds of pits, were observed on the CR-39 hit by ten thousand ions. The ratio of distances between the group without voltage and those with voltage was roughly 7:8:9:10. This strongly indicates that the ion charges spread from 7+ to 10+ by collision at the slit.

The energy spectrum of the ions measured with a silicon surface barrier detector was of a single peak and its width appeared normal within the resolution of the detector. In the case of 320 MeV-¹²C⁶⁺, only one group of etch pit was observed because 6+ is the highest charge of a carbon ion.

The above result indicates that ions with changed charges

did not lose their energy significantly, therefore the charge state change took place by a small-angle collision in a short path in the micro slit (Fig. 1). Under this speculation, three different curvature of the slit edge (R in Fig. 1), 4 mm, 8 mm and 10 mm, were examined to compare ratios of charge change. The result shows a tendency that the ratios reduce with larger curvature. However, the ratios also depend on the tuning of beam transport. It is difficult to quantitatively evaluate the effect of the curvature at present. The relative intensity of each charge should be inspected further in detail taking account of a reason why the charge does not change to lower states. This knowledge will lead to understanding of the mechanism of the charge change and to establishment of a method for complete removal of miss hit.

A technique of real-time detection of single-ion hit position is dearly desired by the microbeam users because it allows them to improve efficiency of a single-ion hit experiment. The single-ion hit position is currently detected with an off-line method using CR-39. The irradiated CR-39 is chemically etched to make pits at positions hit by single ions that penetrated the target and the pits are observed with an optical microscope. This detection procedure takes about an hour.

The real-time detection system has been constructed by assembling a scintillator, a high sensitivity cooled CCD camera and an image intensifier. The detection performance was examined using ZnS:Ag irradiated with 3 MeV-Ni ions accelerated by the TIARA tandem accelerator. A microbeam at the tandem accelerator can be formed much swiftly than that at the cyclotron. The linear energy transfer of the 3 MeV-Ni is almost the same as that of 260 MeV-Ne after passing through a living-cell target. The scintillation could be detected by the system at a hit rate of about 10 ions per second.

The development of new microbeam was carried out with two different ion species. The microbeam of 400 MeV-Fe is required from semiconductor radiation-tolerance study and its diameter reached a size of around 4 μm . It was used at very low intensity as single-ion hit in a preliminary experiment. The 320 MeV-C microbeam is under development for use of radiation biology study. Acceleration of C beam by cyclotron with single-turn extraction and transport to the HX course completed to date.

Reference

- 1) W. Yokota et al., JAEA Takasaki Ann. Rep. 2009 (2011) 173.

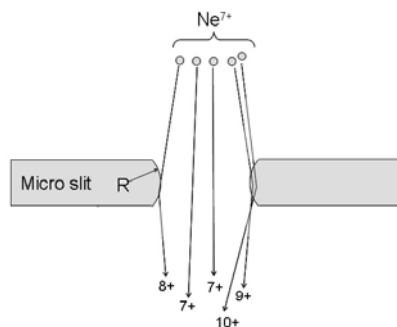


Fig. 1 Schematic image of charge change of Ne⁷⁺ by collision at the micro slit.

4-42

Development of Real-time Single-ion Hit Detection System and IBIL System

A. Yokoyama^{a)}, W. Kada^{a)}, T. Satoh^{a)}, M. Koka^{a)}, S. Yamamoto^{b)},
T. Kamiya^{a)} and W. Yokota^{a)}

^{a)} Department of Advanced Radiation Technology, TARRI, JAEA,

^{b)} Environment and Industrial Materials Research Division, QuBS, JAEA

The single-ion hits for the microscopic irradiation experiments are performed using a microbeam of hundreds MeV heavy ions at the TIARA cyclotron. The studies of irradiation effects on biological cells and on semiconductor devices are conducted with this system. Single-ion hit position detection is essential in these experiments.

A film of CR-39 is currently used as a position detector of single-ion hit. It is placed under the target during irradiation. The ion tracks in the film are observed off-line after chemical etching. This procedure takes more than an hour. It limits efficiency of experiment in the case of irradiation to living biological cells. Therefore real-time single-ion hit detection is required. Various scintillators have been tried for this purpose, however, they haven't worked perfectly. So, photostimulated luminescence (PSL) of $\text{Al}_2\text{O}_3\text{:C}$ at 420 nm, which is sensitive enough to be used as dosimeter, have been taken notice of. It is a recombination process of trapped electron at color center and holes at luminescent center. The wavelength of PSL is usually shorter than that of excitation light. Photostimulable samples, which are not for use of dosimeter but of real-time single-ion hit detector, are possible to be prepared by optimizing parameters such as the density of implantation and the depth of ion layers.

The development of real-time single-ion hit detection system was carried out as follows. First, phosphors were prepared by implanting C^+ or Eu^+ ions into $\alpha\text{-Al}_2\text{O}_3$. Second, the system was assembled and its detection sensitivity was tested. In order to search optimal density of C^+ in Al_2O_3 , Ion Beam Induced Luminescence (IBIL) system was installed in the beam line and prepared phosphors were analyzed.

Real-time single-ion hit detection system

1. Preparation of phosphor

It is necessary for preparation to investigate how the luminescent intensity depends on the implantation density and the depth of ion layers. Ions of C^+ or Eu^+ were implanted in $\alpha\text{-Al}_2\text{O}_3$ with the density from 1.0×10^{13} to $1.0 \times 10^{17} \text{ cm}^{-2}$. In order to enlarge the depth distribution of ions, the ions was implanted at 350 keV and 300 keV for multi-layer. After implantation, the samples were annealed at 800 °C to diffuse implanted ions for an hour.

2. Assemble and performance test

The detection system was assembled with the prepared phosphors, band pass filter, LED with 530 nm as excitation

light, air-cooled CCD camera (Hamamatsu, C488050-26A) and Image Intensifier (Hamamatsu, C8600). The phosphor was set in the vacuum chamber at the microbeam line of the TIARA tandem accelerator. The LED was used to excite trapped electrons to conduction band for emission of PSL at 420 nm. A band pass filter was placed in front of the CCD camera to cut off unnecessary light from LED.

Test of detection sensitivity was carried out using scintillators of ZnS:Ag and $\text{Al}_2\text{O}_3\text{:C}$. Ion of 3 MeV- Ni^+ was selected because its linear energy transfer is equal to that of 260 MeV- Ne^{7+} when it get into the phosphor after penetrating biological cell and CR-39. The system detected scintillation at a hit rate of higher than 10 ions per second from ZnS:Ag and thousands ions per second from the multi-layer $\text{Al}_2\text{O}_3\text{:C}$.

IBIL system

The IBIL system was installed in the beam line of the TIARA single-ended accelerator. The system consists of an aspheric optical micro-lens, a glass optical fiber of 1,000 μm in diameter, a spectrometer (Hamamatsu, PMA-11) and a photo-multiplier tube for photon-counting.

Luminescent response of the system was calibrated by scintillators of ZnS:Ag , YAG:Ce and $\text{CaF}_2\text{:Eu}$. The IBIL spectra of $\text{Al}_2\text{O}_3\text{:C}$ for three cases of C^+ density were obtained. They had peaks of 326 nm and 415 nm corresponding to F^+ and F center, respectively (Fig. 1). Each Spectrum had acquired using 3 MeV- H^+ microbeam in 5 minutes.

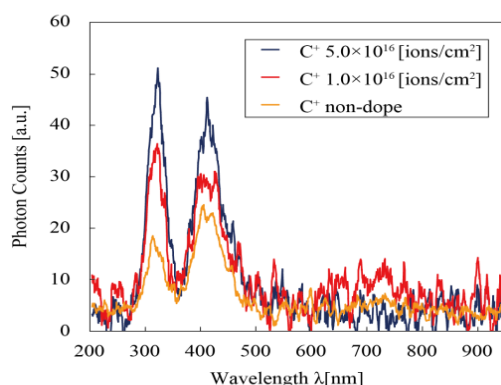


Fig. 1 $\text{Al}_2\text{O}_3\text{:C}$ spectrum obtained by IBIL system.

Reference

- 1) W. Kada et al., Int. J. PIXE. 21(2011) 1-11.

4-43 Research and Development on Heavy-ion Uniform-beam Formation by Nonlinear Focusing

Y. Yuri, I. Ishibori, T. Yuyama, T. Ishizaka and S. Okumura

Department of Advanced Radiation Technology, TARRI, JAEA

In the past few years, the formation of a beam with a uniform transverse intensity distribution by means of nonlinear focusing of multipole magnets was explored using proton beams at the TIARA cyclotron¹⁻⁴⁾. The successful experimental results have motivated us for further research and development (R&D) on the uniform-beam formation with heavy ions toward applications to material and biological research at TIARA.

In order to conduct the R&D systematically with heavy-ion beams, a versatile experimental chamber was designed, fabricated and installed at the end of the LB course. The chamber consists of two parts as shown in Fig. 1: One is a main target chamber on the beam axis, equipped with several flanges designed for different types of beam diagnostics and sample irradiation. The other is a small side chamber mounting a 22-sheet sample changer, which enables us to load/unload samples (radiochromic films, thin membranes, etc.) readily without affecting vacuum in the main chamber. The whole of the chamber is settled on a linear motion guide and movable in the beam direction so that the target position can be readily changed for in-air irradiation and installation of diagnostic devices downstream of the chamber. In the side chamber, the degree of vacuum on the order of 10^{-4} Pa, which is required for irradiation, can be obtained with a 450-L/s turbo-molecular pump in one or two hours (if samples are sufficiently pre-degassed). The sample can be exchanged on the target position within one minute by the motor-driven changer controlled through a LabVIEW program.

In parallel with various activities to make the chamber available, an experimental beam study was also conducted using a few kinds of heavy ions. Beam conditioning, i.e., obtaining a smoothed Gaussian-like beam using multiple Coulomb scattering by a thin foil, is the first necessary step toward realization of a large-area uniform beam since the

beam profile from the cyclotron is usually very complicated and this is an obstacle to forming a uniform beam with multipole magnets. Therefore, the kinetic energy loss and charge state transformation due to multiple scattering of the heavy-ion beams were investigated. Three different kinds of thin foils (Al, Ti and Cu of 2~3 μm thicknesses) were tested for a 520 MeV $^{40}\text{Ar}^{14+}$ beam. For each foil, the loss ratio of the beam energy is estimated at 1~2% (5~10 MeV), which is much larger than that of a 10 MeV H^+ beam. The charge state q of the beam is also changed. It was found, by analyzing with a dipole magnet, that the charge state of a large part of the Ar ions changed to $q=17$ and 18. For a 450 MeV $^{129}\text{Xe}^{23+}$ ion, by a 1.5- μm -thick Al foil, the beam energy was reduced down to about 400 MeV and the charge state was widely distributed around $q=35$. Only one charge state of the beam can be transported down to the target through bending magnets. Thus, large reductions of kinetic energy and intensity are unavoidable in multiple scattering of heavy-ion beams. In order to make the energy reduction as small as possible with a given scattering effect, a thinner foil of a larger atomic number appears to be desirable. Further experiments are needed to optimize foil specifications and conditioning effects, considering easiness on handling a thin foil and its durability.

For effective beam conditioning, the scattering foil should be inserted in the location of the beam line where the beam envelope does not have a waist and thus is large. In addition, we have found that the degree of the conditioning depends on the beam-optical condition. To suppress these optical dependences and thus generate a highly Gaussian-like beam, a double scattering method has been proposed, where the beam is scattered at two different locations along the beam line⁵⁾. Employing this technique, it is expected that the uniformity of the beam focused by multipole magnets can be improved.

Note that these multiple-scattering techniques are not limited to obtaining a uniform beam, but useful in obtaining a clear round beam spot on the target.

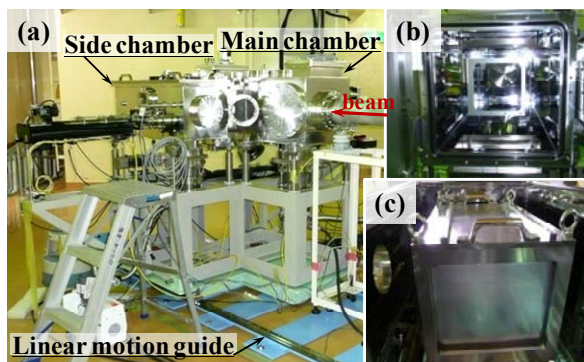


Fig. 1 Experimental chamber installed in the TIARA LB course. (a) Outside, (b) Inside of the main chamber, (c) 22-sheet sample changer in the side chamber.

References

- 1) Y. Yuri et al., Proc. 23rd Part. Accel. Conf. PAC'09 (2009) 3895.
- 2) Y. Yuri et al., Proc. 1st Int. Part. Accel. Conf. IPAC'10 (2010) 4149.
- 3) T. Yuyama et al., Proc. 19th Int. Conf. Cyclo. Their Appl. CYCLOTRONS'10 (2010) 90.
- 4) Y. Yuri et al., Proc. 9th Int. Workshop Radiat. Effects Semicond. Dev. Space Appl. RASEDA-9 (2010) 121.
- 5) Y. Yuri, J. Phys. Soc. Jpn. **79** (2010) 125002.

4-44 3D Micro-fabrication Utilized Superimposing Technique with Focused MeV Ion Beams

K. Takano^{a)}, T. Satoh^{b)}, T. Kamiya^{b)}, Y. Ishii^{b)}, T. Ohkubo^{b)}, M. Koka^{b)},
W. Kada^{b)}, M. Sugimoto^{c)}, S. Seki^{a)} and H. Nishikawa^{d)}

^{a)} Graduate School of Engineering, Osaka University,

^{b)} Department of Advanced Radiation Technology, TARRI, JAEA,

^{c)} Environment and Industrial Materials Research Division, QuBS, JAEA,

^{d)} Department of Electrical Engineering, Shibaura Institute of Technology

A unique micro-processing technique for epoxy resin films has been developed at the TIARA, utilizing the ion beam writing with multiple energies of light and heavy ion beams¹⁾. In previous report, to avoid the problems of lying down, distorting and flowing away on fabrication of wire structures, stringing a wire array between a frame structure and the substrate was demonstrated by the spot pattern writing with 1,000 hits/spots of 260 MeV $^{20}\text{Ne}^{7+}$, aiming the bridge structures fabricated by the writing with 0.5 and 3 MeV H^+ beam. However, there was a problem as that the wires were sticking to neighbor wires and bending, due to drive a surface-tensions effect caused by the solvent at the developing and drying. In this study, a superimposing with the H^+ beams and 520 MeV $^{40}\text{Ar}^{14+}$, of which transfer energy to induce the curing reaction for epoxy resin is estimated to be three times larger than that of 260 MeV $^{20}\text{Ne}^{7+}$, was tried to fabricate a detached wire array strung under the bridge girder.

The target samples were fabricated by coating SU-8 epoxy gel with 20 μm thickness on an epoxy resin sheet cured by irradiating electron beam 0.5 MeV or ^{60}Co gamma ray in advance to promote the bond of fabricated structures. The ion beam writing was performed with a procedure shown in Fig. 1. At first, a bridge piers and girders were writing with focused proton beam with the energy of 0.5 and 3 MeV, respectively. The next, spot pattern writing with 5 μm pitch was performed in the air by the single ion hit of 520 MeV $^{40}\text{Ar}^{14+}$ aiming the girder. The one point of the left is 500 ions/spots, the other points are 100 ions/spots. After a baking at 95 $^{\circ}\text{C}$ for 1 minute, developing and drying with low surface tension was performed with supercritical CO_2 at 12 MPa, 40 $^{\circ}\text{C}$, using a supercritical rinser & dryer, SCR66, Rexam Co., Ltd. The fabricated structures were observed using a SEM with multiple detectors, ERA-9000, ELIONIX Co., Ltd. As the result, optical traces of 520 MeV $^{40}\text{Ar}^{14+}$ hitting can be observed at the aimed points, as shown in Fig. 2(a). Under the middle part of the bridge, structures like a wire and a fin were formed between the pier and the substrates shown Fig. 2(b). The fin formed by Ar^{14+} hitting with 500 ions/spots was peeled from the substrate. A wire formed by the hitting with 100 ions/spots was attached at the bottom of the fin. At just middle of girder, neighbor wires were gathered to be strung between the girder and the substrate. The cause of the bending and the gathering are considered to be a softening of the

structure by the infiltration of the solvent, and some driving forces at the developing and the drying. In the next time, more rigid girder will be fabricated and the developing and drying method will be improved.

Reference

- 1) K. Takano et al., JAEA Takasaki Ann. Rep. 2009 (2011) 170.

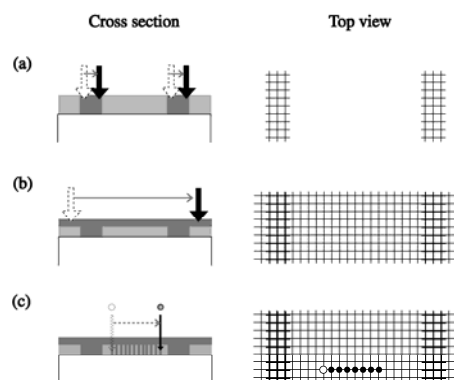


Fig. 1 Scheme of the ion beam writing for wire array supported by bridge structure. (a) writing of the pier patterns with 3 MeV H^+ beam. (b) writing of the girder with 0.5 MeV H^+ beam. (c) spot pattern writing with 520 MeV $^{40}\text{Ar}^{14+}$. Open and filled circles in the left of (c) denote the hitting number of 500 and 100 ions/spots, respectively.

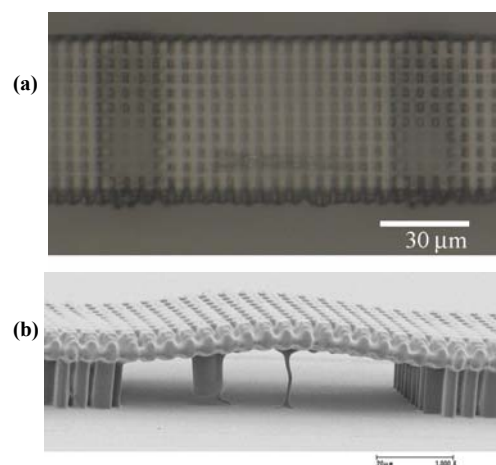


Fig. 2 Images of the bridge structure strung the wires. (a) is top view taken with a microscope, and (b) is cross section taken with SEM.

4-45 Electroforming of Ni Mold Using High-aspect-ratio PMMA Microstructures Fabricated by Proton Beam Writing

Y. Tanabe^{a)}, H. Nishikawa^{a)}, T. Satoh^{b)}, Y. Ishii^{b)} and T. Kamiya^{b)}

^{a)} Department of Electrical Engineering, Shibaura Institute of Technology,

^{b)} Department of Advanced Radiation Technology, TARRI, JAEA

Proton Beam Writing (PBW) is a direct-write technique using focused beam of MeV protons. The PBW has several advantages in comparison with other techniques¹⁾. We can expose and develop typical resists such as PMMA (polymethylmethacrylate) and SU-8 to fabricate high aspect-ratio structures^{1,2)}. We report on Ni electroforming using high-aspect-ratio PMMA microstructures by PBW³⁾, so that the Ni microstructures can be used as a mold for imprint lithography.

The PMMA mother was fabricated by PBW with beam energy of 1.0 to 3.0 MeV on 15- μm or 30- μm thick PMMA on Cu substrates, either using a microbeam line of the Takasaki Ion Accelerators for Advanced Radiation Application (TIARA), or using a dedicated PB (proton beam) writer at the Center for Flexible Micromachining, Shibaura Institute of Technology (SIT). After the exposure to PB, the PMMA samples were developed with IPA (isopropyl alcohol)-water (7 : 3) for 20 min and rinsed in deionized water^{2,3)}.

There are several issues to be addressed in the fabrication process of the high-aspect-ratio Ni mold. First, with increasing thickness of the mother PMMA, we found a problem in the development caused by residue on the PMMA mother. Figure 1 shows SEM images of PMMA mother after exposure and development by PBW at 3.0 MeV with different fluences of (a) 150 nC/mm² and (b) 500 nC/mm². The residual PMMA can be seen in the exposed lines from Fig 1 (a), while the development is successful in Fig 1 (b). This can be explained by effect of the increased PB fluence to promote the chain scission of the PMMA molecules and further dissociation by developer. Second, we found defects in the form of voids inside Ni molds for larger thickness of PMMA mothers on Si substrate with a seed layer after development formed by Au sputtering^{2,3)}. Such phenomenon was avoided by using a seed layer placed only at the bottom by replacing Si substrate with a 600- μm thick Cu substrate. This type of seed layer only permits the bottom-up growth of Ni. Figure 2 shows the result of Ni electroforming with 30- μm PMMA mother on the Cu substrate. Despite with the structure with an aspect ratio of 30, no voids can be seen in the cross section revealed by a FIB (focused ion beam) milling.

We performed a trial to use the electroformed Ni as an imprint mold. Figure 3 (a) shows a Ni mold with a grid and circle pattern fabricated using a 15- μm thick PMMA on a Cu substrate. The front surface of the Ni mold is rough, since the mechanical polishing step of the surface was

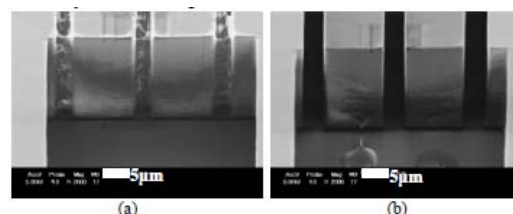


Fig. 1 SEM images of (a) 30- μm thick PMMA by PBW at 3.0 MeV with a fluence of 150 nC/mm², and (b) 30- μm thick PMMA by PBW at 3.0 MeV with a fluence of 500 nC/mm².

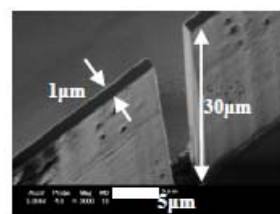


Fig. 2 SEM image of 30- μm thick Ni line structure by electroforming with a high-aspect-ratio PMMA mother on a Cu substrate fabricated by PBW at 3.0 MeV. The cross section was revealed by FIB milling.

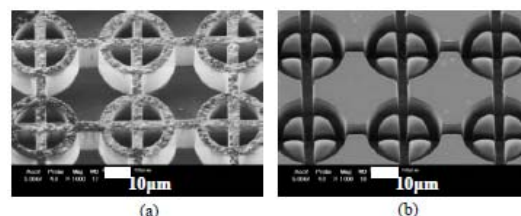


Fig. 3 SEM images of (a) 15- μm thick Ni mold structure using a PMMA micromachined by PBW at 1.0 MeV and (b) 180- μm thick PMMA film after thermal imprint by LTNIP-5000 at 140 °C with a pressure of 2,000 N.

skipped. The Ni sidewall roughness is smooth as expected from the straight trajectory of MeV protons. Figure 3 (b) shows the result of imprint with the Ni mold on a PMMA film. We succeeded in thermal imprint without damages on the Ni mold even after many times of trials. Further trials using a Ni mold with a higher aspect ratio are in progress.

References

- 1) F. Watt et al., Mater. Today, 10, 6 (2007) 20-29.
- 2) N. Uchiya et al., Microsystem Tech. 14 (2008) 1537-1540.
- 3) Y. Seki et al., Microsystem Tech. 86, (2009) 945-948.

4-46 Calibration of Beam Profile Diagnostic Utilizing Back-Scattered Particles for Laser-driven Ions

H. Sakaki ^{a)}, Y. Fukuda ^{a)}, M. Kanasaki ^{b)}, T. Yamauchi ^{b)}, T. Hori ^{a)}, M. Tampo ^{a)},
K. Kondo ^{a)}, S. Kurashima ^{c)} and T. Kamiya ^{c)}

^{a)} Kansai Photon Science Institute, JAEA, ^{b)} Faculty of Maritime Science, Kobe University,
^{c)} Department of Advanced Radiation Technology, TARRI, JAEA

In recent years, laser-driven acceleration systems have generated beams with energies up to tens-MeV ions¹⁾ from laser-plasma interaction. These ions are combined with X-ray and high energy electrons. The diagnostic most using for these ion beams is the CR-39 detector that has a characteristic of an effective way for ions detection under these conditions. It is useful diagnostic of these ions in which a profile of ions are accelerated.

However, the directly-detectable limit (un-etchable track) of the CR-39 detector is ${}^4\text{He}^{2+}$ ions with energy of 10 MeV/n. In the diagnostic of energies up to tens-MeV ions, it is necessary to develop the new diagnostic method with the CR-39 detector.

According to PHITS code²⁾, the back-scatterer is put behind the 0.1 mm thickness of CR-39 detector, when up to 20 MeV/n ions are generated, the secondary particles are detected by it on the rear surface of the CR-39 detector. To measure the energies up to tens-MeV ions with the CR-39 detector, we proposed utilizing these back-scattered particles which are generated by the ion beam injection towards the detector. It is important to be calibrated between the number of injection ions and backscatter particles for the measuring of these ions profile. The irradiation for the calibration of the CR-39 detector conducted at TIARA.

CR-39 detectors used in this study were BARYOTRAK (nominal thickness is 0.1 mm). And an acrylic sheet is selected as a scatterer to generate the back-scattered particles. The CR-39 detector is put on the acrylic sheet of 3 mm thickness that is piled up on the teflon sheet of 2 mm thickness. To reduce the influence of the background particles, the 6 μm aluminum filter is set up on forward of the CR-39 detector. The ${}^4\text{He}^{2+}$ beam from AVF cyclotron transported to the 3rd heavy-ion irradiation room in TIARA and the detector was irradiated with this beam. The beam energy (6.25 MeV/n, 18.75 MeV/n, and 25 MeV/n) and irradiation ions number (10^5 , 10^6 , 10^7 , and 10^8) are changed as the calibration parameters.

Figure 1(a) is the beam profile measured by the imaging plate. This profile was obtained by the ${}^4\text{He}^{2+}$ beam irradiation directly. Figure 1(b) shows the beam profile by the spatial distribution of the etch pit with the back-scattering particle on the rear surface of the CR-39

detector. The distribution of the etch pit on the rear side is corresponding to the intensity distribution of the beam measured by the imaging plate.

The the CR-39 detector with back-scatterers will enable to diagnose in the high-energy ions profiles. It turns out that most of etch pits on the rear surface are made by the back-scattered particles by investigating the growth pattern of each etch pit with multi-step etching technique. This method allows simple diagnosis of the ion beam profile and intensity distribution in mixed radiation field such as laser-driven ion acceleration experiments. The calibration parameter for this technique is being constructed with the detailed analysis now.

References

- 1) Y. Fukuda et al., Phys. Rev. Lett. 103 (2009) 165002.
- 2) K. Niita et al., Radiat. Meas. 41, (2006) 1080.

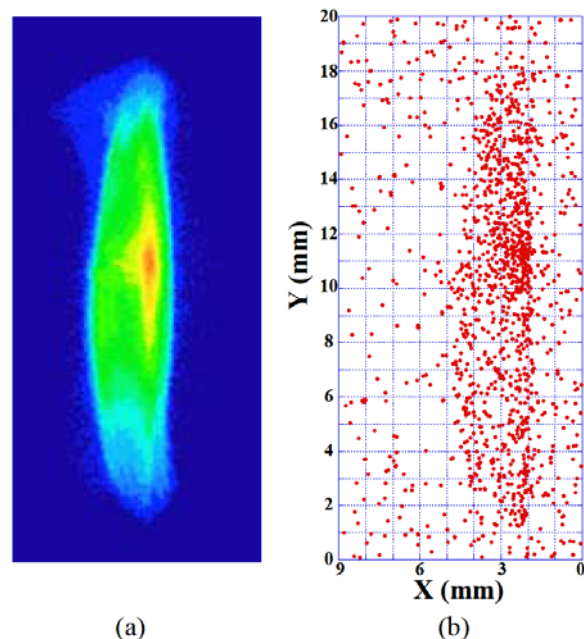


Fig. 1 Radial intensity distribution of ${}^4\text{He}^{2+}$ ion beam recorded on the imaging plate (a), and comparable spatial distribution of etch pits on the rear surface of the CR-39 detector (b) from the view of beam axis.

4-47 Development of Fine Devices Using Proton Scanning Microbeam

T. Sakai^{a)}, R. Yasuda^{a)}, H. Iikura^{a)}, T. Nojima^{a)}, M. Matsubayashi^{a)}, M. Koka^{b)},
T. Sato^{b)}, T. Ohkubo^{b)} and Y. Ishii^{b)}

^{a)} Materials Science Research Division, QuBS, JAEA,

^{b)} Department of Advanced Radiation Technology, TARRI, JAEA

We have developed micro machining technique to manufacture microscopic devices using proton scanning microbeam. A line&space test-chart for spatial resolution measurement on neutron radiography and a fine jigsaw puzzle are successfully created.

中性子ビームは水素により大きく散乱されるため、水や水素の挙動を調べるために広く利用されている。特に、中性子ビームの透過強度分布をイメージ（像）として撮影する中性子ラジオグラフィ（NRG）法は、学術研究や産業利用をはじめ、水や水素を可視化する非破壊分析法として良く用いられている手法の一つである¹⁾。一方、プロトンマイクロビームによる微細加工技術においては、レジスト材である炭化水素系材料に対して、アスペクト比の高い加工が可能であり、中性子光学用の素子を作製するのに有効な手法と考えられる。

昨年度において、任意の画像データを座標データに変換するためのソフトウェアを開発し、この座標位置に対して、正確にビーム照射できることを確認した²⁾。今年度においては、実際の中性子光学素子を作製するため、よりアスペクト比の高い加工技術の確立を目指し、エッチング条件等の最適化を行った。

今回作製を行った素子は、NRGの空間分解能を評価するためのテストチャートである。形状は、線幅として、50 μm から 3 μm までのラインペア（Line&Space）5パターンからなる。作製手順は、3 MeV のプロトンビームにより、75 μm 厚のアクリルシート上に描画照射を行った後、70%のイソプロピルアルコール溶液でエッチングを行った。また、エッチング中の試料に対して、光学顕微鏡によるその場観察を行い、条件の最適化を行った。Figure 1 に作製したテストチャートの顕微鏡写真を示す。上段のラインペアの線幅は 25 μm 、下段左は 6 μm 、下段右は 3 μm である。線の中央部が端部に比べて若干拡がっているが、アスペクト比で 20 程度の貫通孔が作製出来ることを確認した。

また、この技術を基に極小のジグソーパズルの作製を試みた。ピース数 104 で、1 ピースの大きさは、およそ 50 μm 四方である。作製したジグソーパズルの写真を Fig. 2 に示す。エッチングの際に、幾つかのピースは失われてしまったが、ピース毎に分離できることを確認できた。

今後、空間分解能評価用のテストチャートに関しては、実素子として活用する予定である。また、本技術を利用して、新たな微細素子の開発に着手することを計画している。

本研究は、科研費（22604010）の助成を受けたものである。

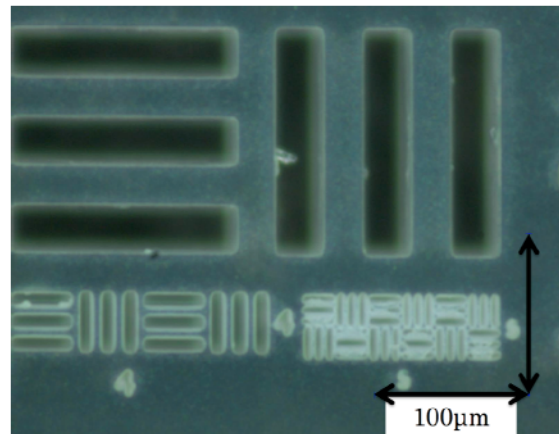


Fig. 1 Microscopic photograph of a fabricated test-chart. The line patterns pass through the sheet.

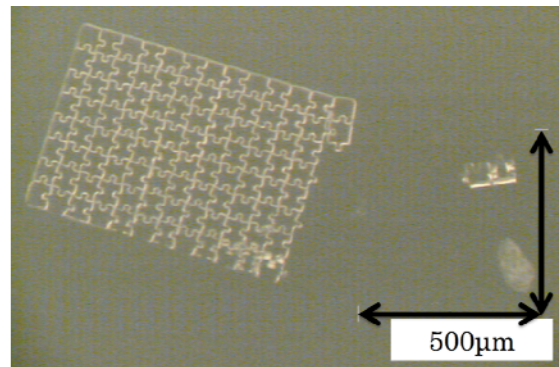


Fig. 2 Microscopic photograph of a fabricated fine jigsaw puzzle. The piece size is about 50 μm \times 50 μm .

References

- 1) (社) 日本アイソトープ協会 理工学部会 中性子ラジオグラフィ専門委員会編、「中性子イメージング技術の基礎と応用」(2009).
- 2) T. Sakai et al., JAEA Takasaki Ann. Rep. 2009 (2011) 172.

4-48 Spin-Polarize Positron Beam Based on ^{68}Ge - ^{68}Ga Source Produced by Cyclotron

A. Kawasuso, M. Maekawa, Y. Fukaya, A. Yabuuchi and I. Mochizuki

Advanced Science Research Center, JAEA

For realizing a highly polarized positron beam for the study of spin-electronics materials, we are currently producing a positron source (^{68}Ge - ^{68}Ga) using the $^{69}\text{Ga}(p, 2n)^{68}\text{Ge}$ nuclear reaction. Owing to the relatively long half-life, the source strength can be increased by repeating proton irradiation annually (once in one to two months). So far, the total proton irradiation amount is 361 $\mu\text{A h}$ and the last source strength is 140 MBq. Using this positron source, we succeeded to generate an electrostatic positron beam.

放射性同位元素から放出される陽電子のスピンは、弱い相互作用に伴うパリティ非保存のため、進行方向に偏極している。スピン偏極陽電子ビームは、物質中のスピン偏極電子を直接検出するプローブとして期待される。各種の放射性同位元素の中でも、 ^{68}Ge - ^{68}Ga から放出される陽電子のスピン偏極率は 94%と高く、半減期も比較的長い (288 日)。そこで我々は、そのスピントロニクス材料研究における潜在能力を実証することを目的に、核反応により ^{68}Ge - ^{68}Ga 線源を製造し、これを用いたスピン偏極陽電子ビームを開発している。

昨年度の年報において、金属 Ga 標的または GaN 単結晶基板に 20 MeV プロトンを照射することで、 ^{68}Ge - ^{68}Ga 線源が製造できることを報告した。今年度はその後の累積照射による線源強度の到達値、スピン偏極率測定の結果、及び、スピン偏極陽電子ビームの発生実験について報告する。

Figure 1 は、GaN 単結晶に対して 20 MeV プロトン照射を行った際の ^{68}Ge - ^{68}Ga 線源の強度と照射回数関係を示している。ここで 1 回毎の照射量は、照射実験毎に異なっているが、照射回数とともに累積照射量が増加し、線源強度も増加することが分かる。実線は、1 回あたりの照射量と照射後の経過時間を考慮した計算予測である。実測された ^{68}Ge - ^{68}Ga 線源の生成量は概ね計算予測と合う。実測以後の線は、今後計画されている照射実験が行われたことを想定したものである。これによれば、今後、上の条件で到達し得る線源強度は、概ね 170 MBq と予想される。

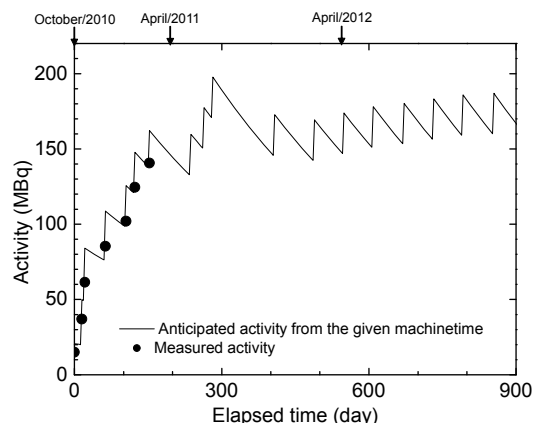


Fig. 1 Measured activity of the ^{68}Ge - ^{68}Ga source (filled circle) and anticipated activity from the given machine time (straight line).

上で生成した陽電子線源を用いて、静電レンズ方式による陽電子ビーム発生を試みた。Figure 2 はビーム発生部の概略図である。陽電子線源から放出された陽電子は、タングステン製の減速材に投入され、再放出された熱化陽電子を静電場により加速・収束する仕組みとなっている。Figure 3 は、このようにして形成した陽電子ビームをマイクロチャンネルプレートにより観察した像である。この陽電子ビームフラックスは 1.5×10^3 陽電子/秒であった。また昨年度と同様の方法でスピン偏極率を測定したところ、40~50%であることが分かった。これは現在市販されている ^{22}Na を用いて発生した陽電子ビームのスピン偏極率を上回るものである。

今後、さらにプロトン照射を繰り返すことで陽電子ビームを増強し、これを磁性薄膜や表面スピン効果などの研究に応用して行く予定である。

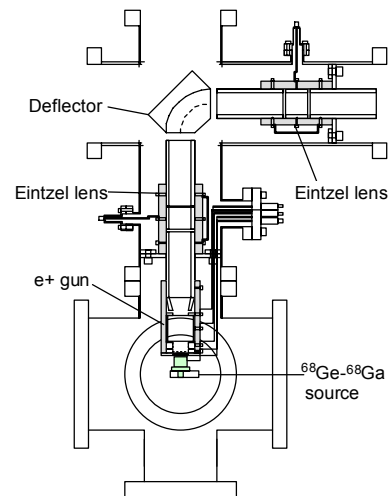


Fig. 2 Schematics of the positron beam generation part.



Fig. 3 Positron beam image obtained with the ^{68}Ge - ^{68}Ga source and the above system.

4-49

Improvement of a Positron Gun Suitable for Intense Microbeam Production

M. Maekawa, A. Yabuuchi and A. Kawasuso

Advanced Science Research Center, JAEA

Employing a positron microbeam, spatial distribution of positron annihilation near subsurface region can be obtained. We have already developed a positron microbeam by fabricating a small source which is suitable for the positron microbeam production^{1,2)}. The positron source of 55 MBq $^{22}\text{NaCl}$ was deposited into a 2 mm-diameter hole on a tungsten-copper block and sealed by a Ti window. Because of its limited source activity, the beam intensity was 1×10^4 e⁺/sec. An enhancement of source activity is needed for further experiment using the positron microbeam. We have thus fabricated a new positron source having much higher activity than that of the previous one.

Figures 1(a) and 1(b) show the schematics of the previous and new source capsules, respectively. Figure 1(c) shows the picture of the new capsule. The $^{22}\text{NaCl}$ source of 330 MBq could be put into the source deposition area using an automatic deposition system shown in Fig. 2. In this system, the $^{22}\text{NaCl}$ solution injected into a micro-syringe was sequentially dropped into the well. The

syringe pump and the positions of syringe and capsule were remote-controlled by the computer.

Fast positrons emitted from the source ^{22}Na were moderated by the solid neon film³⁾ grown on the source window and surrounding cone shown in Fig. 1(b). The cone shape and depth were determined from a beam simulation.

Consequently, the beam intensity is enhanced to be 1×10^5 e⁺/sec, which is 10 times greater than before. Normal beam diameter was 10 μm . For the scan area of 100×100 μm by 10 μm step, total measurement time is estimated to approximately 3 hours.

References

- 1) M. Maekawa and A. Kawasuso, Appl. Surf. Sci. **255** (2008) 39-41.
- 2) M. Maekawa et al., Mater. Sci. **607** (2009) 266-268.
- 3) A. P. Mills, Jr. and E. M. Gullikson, Appl. Phys. Lett. **49** (1986) 1121.

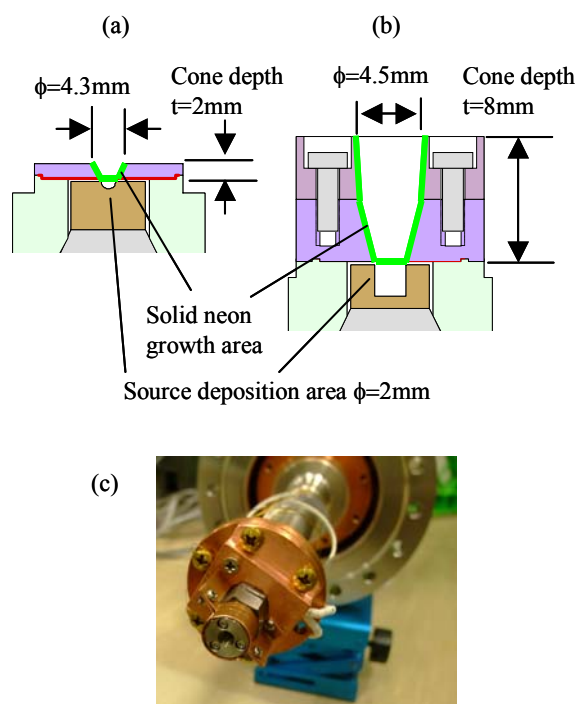


Fig. 1. (a)(b) Schematic of the old-type and new-type source capsule and (c) picture of the new positron gun.

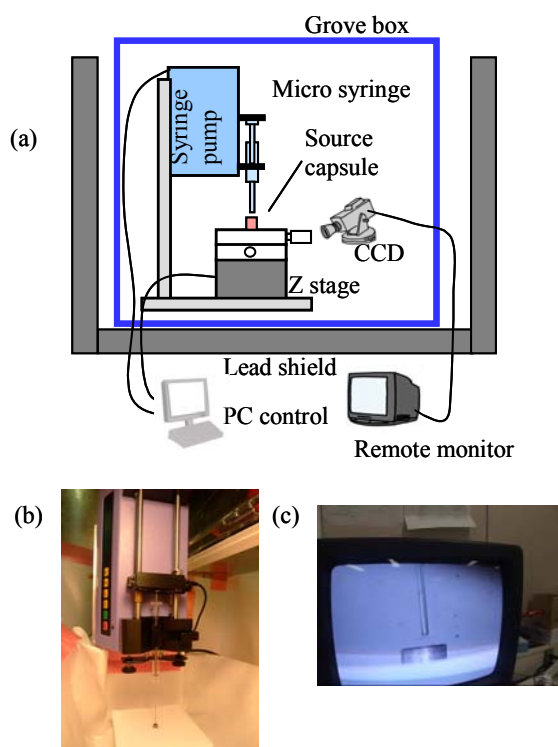


Fig. 2. (a) Schematic of the automatic deposition system, (b) picture of the syringe pump and (c) picture of the tip of micro syringe

This is a blank page.

5. Present Status of Irradiation Facilities 2010

5-01	Feature in FY2010, Utilization Status and Beam Time Proportion at TIARA Facility	171
	K. Mizuhashi, H. Takizawa, M. Hosono, K. Nishimura, Y. Nakamura, S. Kaneya, S. Mochizuki, T. Asai, M. Kawabata and K. Daikubara	
5-02	Operation of the AVF Cyclotron	172
	T. Nara, I. Ishibori, S. Kurashima, K. Yoshida, T.Yuyama, T.Ishizaka, S. Okumura, N. Miyawaki, H. Kashiwagi, Y.Yuri, W. Yokota , K. Akaiwa, To. Yoshida, S. Ishiro, Tu. Yoshida S. Kanou A. Ihara, K. Takano and H. Saitoh	
5-03	Operation of the Electrostatic Accelerators	173
	T. Agematsu, S. Uno, A. Chiba, K. Yamada, A. Yokoyama, Y. Saitoh, Y. Ishii, T. Satoh, T. Ohkubo, W. Yokota, T. Kitano, T. Takayama, S. Kanai, T. Orimo, Y. Aoki and N. Yamada	
5-04	Operation of Electron Accelerator and Gamma-ray Irradiation Facilities	174
	Y. Haruyama, H. Hanaya, R. Yamagata, H. Seito, Y. Nagao, H. Kaneko, T. Yamaguchi, N. Yagi, M. Takagi, I. Kawashima and S. Matsuzaki	
5-05	Utilization of the Gamma-ray Irradiation Facilities and Electron Accelerator ...	175
	H. Kaneko, Y. Haruyama, H. Hanaya, R. Yamagata, H. Seito, Y. Nagao, T. Yamaguchi, N. Yagi, M. Takagi, I. Kawashima and S. Matsuzaki	
5-06	FACILITY USE PROGRAM in Takasaki Advanced Radiation Research Institute	176
	Y. Fukuta, D. Nogami and K. Watanabe	
5-07	Radiation Control in TIARA	177
	Safety Section	
5-08	Radioactive Waste Management in TIARA	178
	T. Ishibashi and T. Hosoi	

This is a blank page.

5-1 Feature in FY2010, Utilization Status and Beam Time Proportion at TIARA Facility

K. Mizuhashi, H. Takizawa, M. Hosono, K. Nishimura,
Y. Nakamura, S. Kaneya, S. Mochizuki, T. Asai, M. Kawabata and K. Daikubara

Department of Advanced Radiation Technology, TARRI, JAEA

1. Feature in FY 2010

Fiscal year 2010 was greatly affected by the power of nature. In Takasaki region, the thunderstorm was frequently generated due to high temperature during summer. The electric power failure occurred four times because of lightning. The reactivation of facilities for about three hours was executed at each power failure. The severe earthquakes occurred all over the world in 2010. The regions where the main earthquake occurred are Sumatra, Chile, Taiwan, Turkey, China and New Zealand etc. In Japan, the great earthquake of magnitude nine occurred on 11th March 2011. A lot of aftershocks occurred after the great earthquake, and the check of the radiation facility was carried out after the earthquake of the 4th degree or more on the seismic scale. The damage of TIARA facilities due to the great earthquake was relatively. The lock mechanism of the radiation shielding door (weight; 55ton) of cyclotron room was broken, as the door moved due to the earthquake. Two turbo-molecular pumps for the beam line and the experiment chamber were broken. A neutron collimator that made of iron (weight; 9.3 ton) for the neutron shielding experiment (LCO) had moved. As for four accelerators at



Fig. 1 Neutron experiment device. The brown square in the wall is the neutron collimator.

TIARA facility, there was no problem at all. But the TIARA facility was stopped from 11th March to 30th April due to the earthquake. There were a lot of influences from nature, but TIARA facilities well operated excluding the above mentioned problems in fiscal year 2010.

2. Utilization Status

The feature in fiscal year 2010 was that we got the Global Nuclear-Human Resource Development Initiative budget. The electrostatic accelerators and the cyclotron have increased the experiment days owing to this budget for the students etc. And the TIARA facilities were used by a lot of students etc. for the personnel training.

Change of number of visitors for experiment at TIARA facility as a function of fiscal year is shown in Fig. 2. The year when the number of researchers and the number of research subjects became the maximum was 2005. Both numbers show tendencies to decrease after 2005.

However, it seems that the decreasing tendency of the number of researchers stopped in 2010. The number of visitors for the research in 2009 and 2010 were 781 and 824, respectively. On the other hand, the number of research subjects still shows a tendency to decrease in 2010.

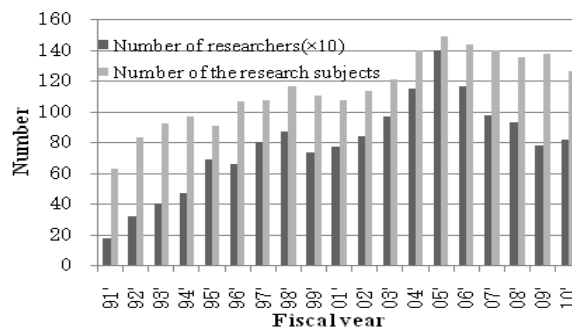
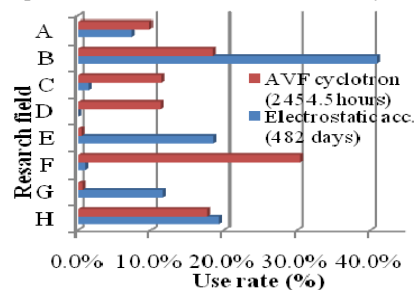


Fig. 2 Relations between numbers of research visitors and research subjects at TIARA.

3. Beam Time Proportion

Four accelerators were used for various research subjects according to operation plan in fiscal year 2010. The proportion of the beam time used in the fields of research is shown in Fig. 3. The total of utilization time of the AVF cyclotron and the electrostatic accelerators in fiscal year 2010 was 2,454.5 hours and 482 days, respectively which were offered to the experiments. The highest of proportion at the cyclotron was for the field of Biotechnology-Medical application, 30.4%. At the electrostatic accelerators, the highest of proportion was for the field of the Basic technology, 40.9%. The proportion for the field of RI production-Nuclear science was 11.4%. This ratio is 28.5 times of last year's value. This is because the generation of positron-emitting radionuclide (^{68}Ge - ^{68}Ga) was begun with the cyclotron for the positron annihilation experiment. The total proportion of "the common use" and "the promotion use" was 9.8% at cyclotron and 7.3% at electrostatic accelerator, respectively. These values were within 20% of the total beam time which is provided as "the common use" and "the promotion use" at the TIARA facility.



A: Common use/Promotion use, B: Basic technology, C: Organic material/Radiation chemistry, D: RI production/Nuclear science, E: Inorganic material, F: Bio technology/Medical application, G: Material for nuclear, H: Material for space.

Fig. 3 Proportion of the machine time used for the fields of research.

5-2

Operation of the AVF Cyclotron

T. Nara^{a)}, I. Ishibori^{a)}, S. Kurashima^{a)}, K. Yoshida^{a)}, T. Yuyama^{a)}, T. Ishizaka^{a)},
S. Okumura^{a)}, N. Miyawaki^{a)}, H. Kashiwagi^{a)}, Y. Yuri^{a)}, W. Yokota^{a)}, K. Akaiwa^{b)},
To. Yoshida^{b)}, S. Ishiro^{b)}, Tu. Yoshida^{b)}, S. Kanou^{b)}, A. Ihara^{b)}, K. Takano^{b)} and H. Saitoh^{b)}

^{a)} Department of Advanced Radiation Technology, TARRI, JAEA, ^{b)} Beam Operation Service, Co., Ltd.

Operation

The AVF cyclotron was smoothly operated in fiscal 2010 and all the planned experiments were carried out without cancellation due to machine troubles relating to the cyclotron. The cumulative operation time was 62,878.3 hours and the total number of experiments was 8,719 from the first beam extraction in 1991 to March 2011.

Table 1 shows the statistics of the cyclotron operation of fiscal 2010. The total operation time amounted to 3,343.6 hours, and monthly operation times are shown in Fig. 1. The percentages of operation time of the year used for regular experiments, facility use program, the promotion of shared use program¹⁾, beam tuning, and beam development are 74.7%, 6.4%, 17.1%, and 1.8%, respectively. The extended operation from Friday evening to Saturday evening was carried out twelve times after October on the Global Nuclear-Human Resource Development Initiative.

Table 1 Statistics for cyclotron operation.

Beam service time	2712.3 h
Machine tuning	571.6 h
Beam development	59.7 h
Total operation time	3343.6 h
Change of particle and/or energy	234 times
Change of beam course	283 times
Change of harmonic number	55 times
The number of experiments	594
Experiment cancelled due to machine trouble	0
Experiment cancelled due to Earthquake	16.2 h

Table 2 shows the operation time of the multi-cusp ion source for H⁺ and D⁺ production and two ECR ion sources for heavier ions. The ECR ion sources are used alternatively. Fractional distribution of major ions used for experiments is shown in Fig. 2. The tendencies of the statistics are similar to those of the past years.

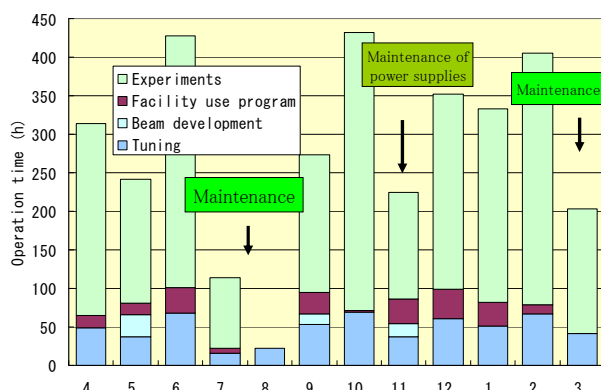


Fig. 1 Monthly operation time.

Table 2 Operation times of ion sources.

Ion source	Operation time(h)	Ratio(%)
Multi-cusp	1079.2	29.5
ECR (OCTOPUS)	1071.0	29.2
ECR(HYPERNANOGAN)	1512.6	41.3

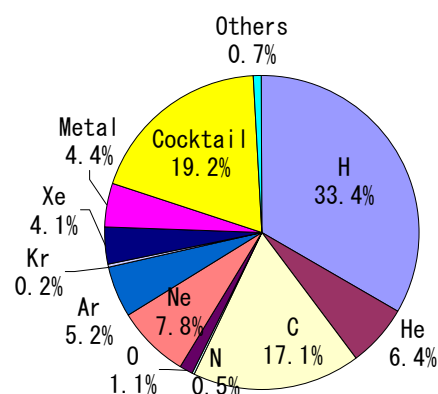


Fig. 2 Ion species used for experiments.

Damage by the Great East Japan Earthquake

The radiation shielding door of the cyclotron vault was slightly moved by the earthquake with break of its lock pin. The interlock due to this failure stopped the cyclotron immediately. A turbo molecular pump for the injection system broke as well. They are all the damage by the earthquake.

Maintenance

The regular yearly overhaul and maintenance were carried out. The major items were as follows: 1) Correction of the reference positions of some beam probes, the inflector, etc. 2) Replacement of the sequence controllers for inflector and cooling system. 3) Inspection of the RF system and evaluation of its characteristics. 4) Change of lubricating oil for about 50 rotary pumps. 5) Routine maintenance of the power supplies.

Technical Development

The new beam acceleration tests were carried out for 190 MeV $^{14}\text{N}^{5+}$ and 490 MeV $^{129}\text{Xe}^{24+}$, and they are ready for use in experiments.

A large experimental chamber was installed in the LB course to develop the large-area uniform irradiation technique using nonlinear force. The detail is described elsewhere in this annual report.

Reference

- 1) 'FACILITY USE PROGRAM in Takasaki Advanced Radiation Research Institute' in this annual report.

5-3 Operation of the Electrostatic Accelerators

T. Agematsu^{a)}, S. Uno^{a)}, A. Chiba^{a)}, K. Yamada^{a)}, A. Yokoyama^{a)}, Y. Saitoh^{a)},
Y. Ishii^{a)}, T. Satoh^{a)}, T. Ohkubo^{a)}, W. Yokota^{a)}, T. Kitano^{b)}, T. Takayama^{b)},
S. Kanai^{b)}, T. Orimo^{b)}, Y. Aoki^{b)} and N. Yamada^{b)}

^{a)} Department of Advanced Radiation Technology, TARRI, JAEA,
^{b)} Beam Operation Service, Co., Ltd

1. Operation and Status

Three electrostatic accelerators were operated smoothly in FY 2010, and all the planned experiments were carried out except those canceled by users or the impact of Great East Japan Earthquake on March 11, 2011. The accelerators were not operated after the earthquake in the month. The numbers of the canceled experiments after that day were 7, 7 and 4 for the tandem accelerator, the single-ended accelerator and the ion implanter, respectively. On the other hand, Saturday operation of ten days for experiments was carried out after October on the Global Nuclear-Human Resource Development Initiative. The yearly operation time of each accelerator consequently amounted to 2,116, 2,367 and 1,800 hours respectively, similarly to past years. Saturday operation of ten days for experiments after October compensated for the loss of operation days by the earthquake. A total operation time of each accelerator since operation started was 34,538, 39,231

and 30,675 hours, respectively. The monthly operation time is shown in Fig. 1. Ion species used for experiments in FY 2010 are also shown in Fig. 2.

2. Maintenance and Trouble Shooting

The number of troubles was smaller than that for average years. There was no trouble by the earthquake. Major maintenance performed in FY 2010 is as follows;

Tandem accelerator: There was no trouble of accelerator leading to cancelation of experiments. Minor repair and scheduled maintenance were carried out. The bearings and the sheave of the pellet chain were replaced to new ones at scheduled maintenance.

Single-ended accelerator: There were two troubles of accelerator leading to cancelation of experiments, as next ones. The generator in the high-voltage terminal failed, and it was changed to new one. The cap for spark prevention near the RF electrodes tripped, and high-voltage could not be kept. It was repaired.

Ion implanter: There was no trouble of accelerator leading to cancelation of experiments. The switching magnet for new beam line was made and installed.

3. New Beam Development

As to the ion implanter, 400 nA ion beam of Gd which is requested by user was generated by oven method, and used to the experiment. But its intensity lasts only for several hours, which needs to be improved.

As to the tandem accelerator, ion beam of In was successfully generated and accelerated at intensity of 500 nA.

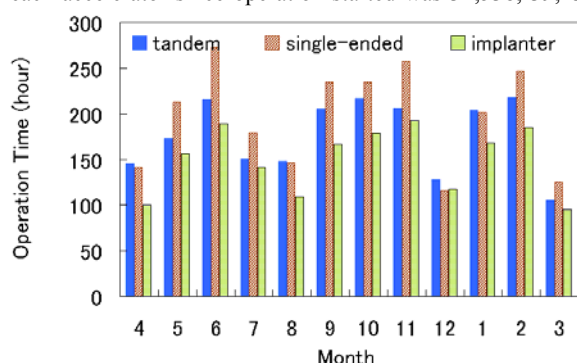


Fig. 1 Monthly operation time of each accelerator in FY 2010.

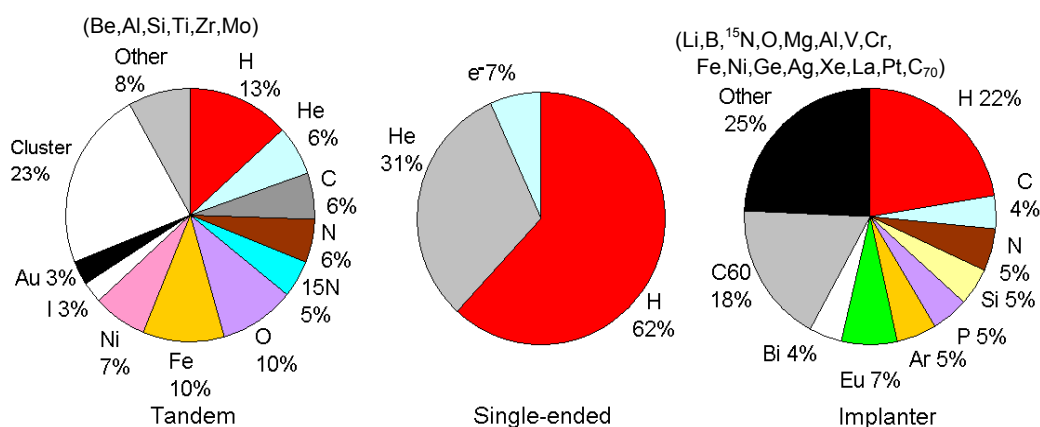


Fig. 2 Ion species used for experiments in FY 2010.

5-4 Operation of the Electron Accelerator and Gamma-ray Irradiation Facilities

Y. Haruyama^{a)}, H. Hanaya^{a)}, R. Yamagata^{a)}, H. Seito^{a)}, Y. Nagao^{a)}, H. Kaneko^{a)},
T. Yamaguchi^{b)}, N. Yagi^{b)}, M. Takagi^{b)}, I. Kawashima^{b)} and S. Matsuzaki^{b)}

^{a)}Department of Advanced Radiation Technology, TARRI, JAEA,

^{b)}Radiation Application Development Association, RADA

1. Operation

The electron accelerator and gamma-ray irradiation facilities have been operated without serious troubles before the earthquake happened in March 11, 2011. These were, however, stopped with concern about the earthquake damage, for 13 and 20 days, respectively.

1.1 Electron accelerator

The electron accelerator was on service as scheduled in 9:00~17:30 on Monday and Friday, and in 8:30~23:00 on Tuesday to Thursday until September. It was on service in 8:30~23:00 on Monday through Friday since October, to satisfy demand of operation time for users.

The annual operation time of the electron accelerator, as shown in Fig.1, is 1,065.2 h. The total operation time of the accelerator in FY2010 increased by about 12% compared with that in FY2009, and analysis of the number of research subjects indicated the increase of longer-time irradiation for material as space subject. The increase is due to the installation of system named as Global Nuclear-Human Resource Development Initiative, aiming at skill-up of young researchers and engineers.

The accelerator served mainly for graft-polymerization for new material development, radiation effect study on semiconductors and various experiments of visiting users.

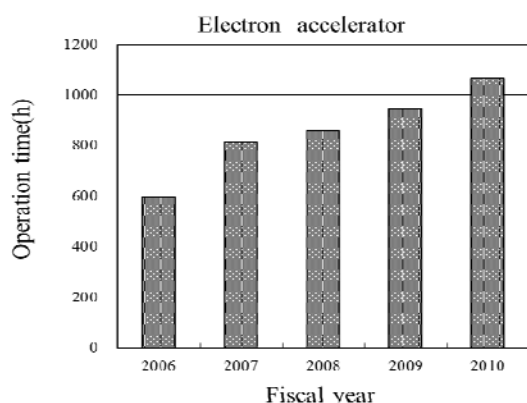


Fig. 1 Annual operation time of the electron accelerator.

1.2 Gamma-ray irradiation facilities

The Co-60 gamma-ray irradiation facilities consist of three buildings and cover a wide dose-rate range from 0.04 Gy/h to 20 kGy/h with eight irradiation rooms. The annual operation times for the first, second cobalt irradiation facilities and food irradiation facility are 20,691 h, 9,981 h and 7,076 h, respectively, as shown in Fig. 2. The first irradiation facility served mainly for radiation-resistance testing of cables used in nuclear power plants and various

materials used in J-PARC and nuclear reactor facilities with long irradiation period. The second irradiation facility served mainly for development of new functional materials and other research subjects of visiting users, involving irradiation room No.6 operated as hourly scheduled. The food irradiation facility served mainly for development of detection method for irradiated foods and radiation resistance testing at lower dose rates.

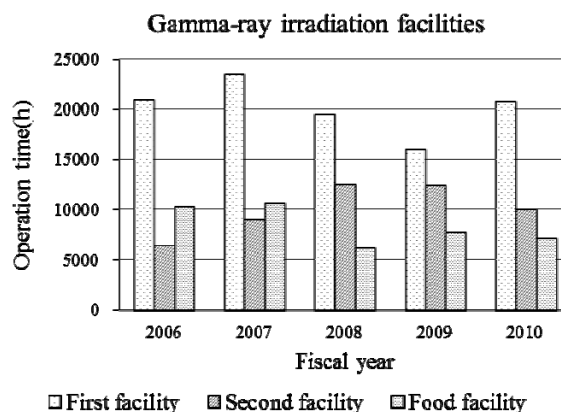


Fig. 2 Annual operation time of Co-60 gamma-ray irradiation facilities.

2. Maintenance

2.1 Electron accelerator

The operation of the accelerator was stopped for 10 days in October, 2010 because of periodical maintenance check on accelerator body, the conveyor and doors of the irradiation room and repair of a SF₆ gas withdrawal system with the accelerator.

2.2 Gamma-ray irradiation facilities

The periodical maintenance check mainly on a mechanical system for radiation source transportation has been performed every three year among three gamma-ray irradiation facilities one by one. The periodical check mainly on an interlock system has been performed two times a year for all the facilities.

The maintenance check of the food irradiation facility was done in July 2010, with 21 days interruption.

Co-60 sources were purchased and loaded to the irradiation room No.6 in the second irradiation facility and No.2 in the food irradiation facility to increase total activities. The old waste sources of 45 pieces were disposed through The Japan Radioisotope Association (JRIA).

5-5 Utilization of the Gamma-ray Irradiation Facilities and Electron Accelerator

H. Kaneko ^{a)}, Y. Haruyama ^{a)}, H. Hanaya ^{a)}, R. Yamagata ^{a)}, H. Seito ^{a)}, Y. Nagao ^{a)}
T. Yamaguchi ^{b)}, N. Yagi ^{b)}, M. Takagi ^{b)}, I. Kawashima ^{b)} and S. Matsuzaki ^{b)}

^{a)}Department of Advanced Radiation Technology, TARRI, JAEA,

^{b)}Radiation Application Development Association, RADA

Three gamma-ray irradiation facilities and an electron accelerator were operated for various research subjects according to the operation plan in FY 2010 without serious trouble. Utilization was stopped until the end of the fiscal year due to inspection etc. after the earthquake occurred on March 11. Figure 1 shows irradiation time and the number of research subjects in each research field at each facility.

Figure 2 shows the number of research subjects in each

research field at each facility from FY 2006 to 2010. The number at gamma-ray irradiation facilities increased in the field of environment and basic technology, and decreased in the field of materials processing and resource & bio-technology. The number at the electron accelerator increased in the research fields of materials for space, and decreased in the field of materials processing and joint use.

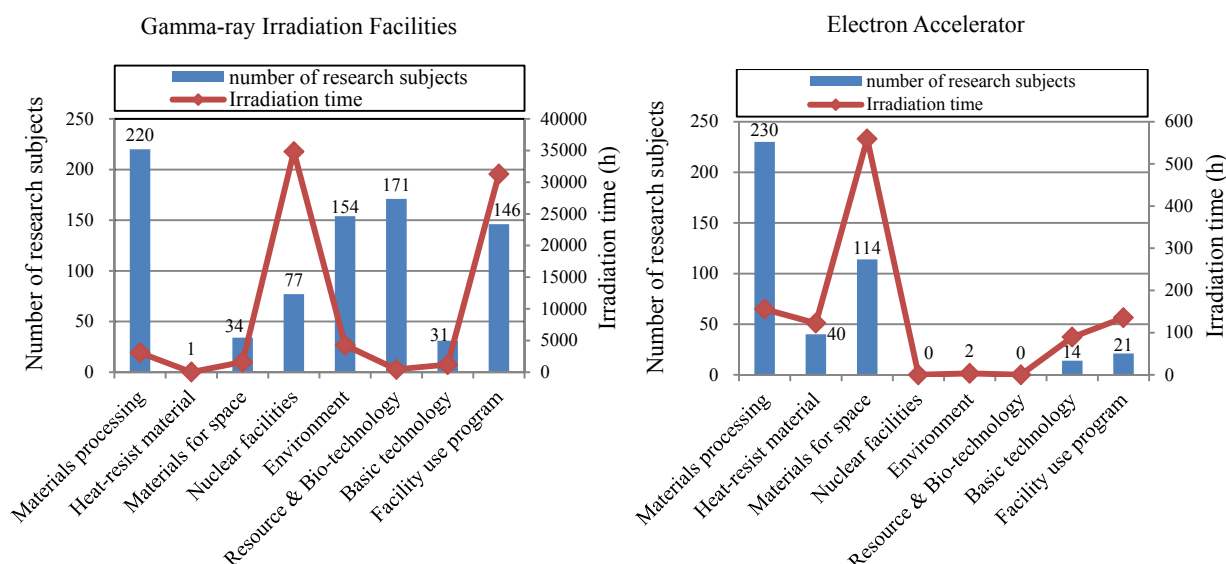


Fig. 1 Irradiation time and the number of research subjects in FY 2010.

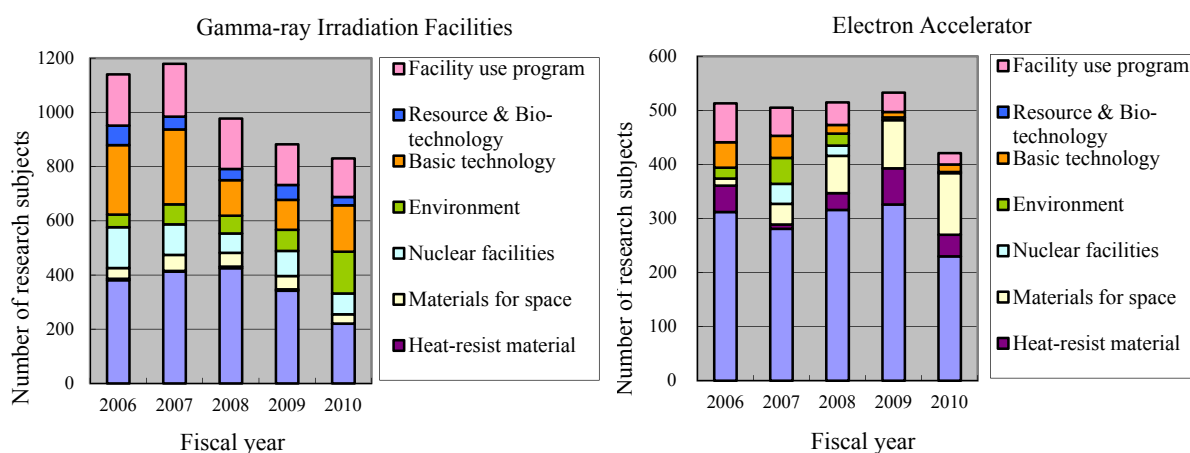


Fig. 2 The number of research subjects (FY 2006-2010).

5-6 FACILITY USE PROGRAM in Takasaki Advanced Radiation Research Institute

Y. Fukuta, D. Nogami and K. Watanabe

Department of Advanced Radiation Technology, TARRI, JAEA

1. Introduction

The facilities of JAEA are widely opened to users in universities, public institutes, and the industries, etc. Taking over the former system, FACILITY USE PROGRAM started in 2006, which is the system of facility use for the user's service on fee-charging basis. The open used facilities in Takasaki are composed of Co-60 Gamma-ray Irradiation Facilities, Electron Accelerator, TIARA (Takasaki Ion Accelerators for Advanced Radiation Application), and some of the off-line analysis instruments.

In this program, the Research Proposals are examined carefully every half year from the standpoint of the availability and the validity of the experimental plan by the special committee. The facility usage fee has revised in FY2010. The details of the fee are handling fees, the irradiation fee, the expendables fee and the additional charge. In case of Non-proprietary research, the users should report the irradiation result to JAEA, who are exempted from the irradiation fee. JAEA opens the reports to the public. Universities can also apply through another facility use program operated by the University of Tokyo. Such applications are accepted as priority case. Table 1 shows main classification of FACILITY USE PROGRAM.

Table 1 Main Classification of FACILITY USE PROGRAM.

Purpose	Research and Development		Except R&D
Classification	General	Priority case	Commercial
Result	Non-proprietary	Proprietary	
Referee	Yes	No	
Charge*	A	B	C

*A = handling fees + the expendables fee,

B = handling fees + the irradiation fee,

C = handling fees + the irradiation fee + depreciation.

2. Use in FY2010

There were 21 applications of Research Proposals in FY2010 at Takasaki Institute, and 16 of them were as Non-proprietary use. Including the users from priority case and others, 205 applications from 60 users are accepted. Table 2 and Figure 1 show user's classification for each facility and distribution of classification for FACILITY USE PROGRAM.

FACILITY USE PROGRAM in FY2010 was stopped on March 11, 2011 by suffering from the Japan Earthquake.

Table 2 User's classification for each facility.

User		University	Public Institute	Industries and others	Total
TIARA	AVF cyclotron	5	1	7	13
	3MV tandem accelerator	5	0	1	6
	3MV single-ended accelerator	1	0	0	1
	400kV ion implanter	4	1	0	5
Co-60 gamma-ray irradiation facilities		8	2	16	26
Electron accelerator		5	1	3	9
Total for each classification		28	5	27	60

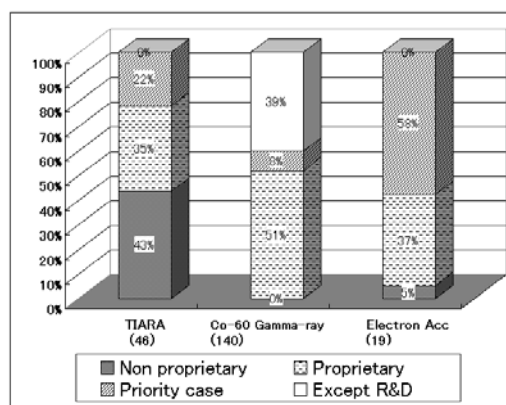


Fig. 1 Distribution of classification for FACILITY USE PROGRAM. The number of theme for each facility is shown in parentheses.

3. Public Relations

The information, such an outline of this system, guidelines for applicants, format download etc. can be found on JAEA website as follows:

<http://sangaku.jaea.go.jp/3-facility/01-intro/index-02.html>.

The "Project for Promotion of Shared Use of High Technology Research Institute", which is one of the subsidiary project of Ministry of Education, Culture, Sports, Science and Technology (MEXT) has been cooperated from FY2009. This project intends that industrial users promote shared use of facilities, which accelerates the whole activity of science technology from basic research to innovation creation.

An outline of this project can be seen on website as follows: <http://www.taka.jaea.go.jp/innovation/index.html>.

5-7

Radiation Control in TIARA

Safety Section

Department of Administrative Services, TARRI, JAEA

1. Individual monitoring

(1) Individual monitoring for the radiation workers

Table 1 shows a distribution of effective dose of the radiation workers in FY 2010. The effective dose values of almost all radiation workers were below the detection limit (0.1 mSv).

The maximum dose was 0.4 mSv/y due to the experiment for production and labeling of Br-76.

Table 1 Distributions of the effective dose of the radiation workers in FY 2010.

Items		Number of persons in each periods				Total *2
		1st quarter	2nd quarter	3rd quarter	4th quarter	
Distribution range of effective dose	HE < 0.1	540	567	558	587	697
	0.1 ≤ HE ≤ 1.0	4	0	4	1	6
	1.0 < HE ≤ 5.0	0	0	0	0	0
	5.0 < HE ≤ 15.0	0	0	0	0	0
HE: Effective dose (mSv)	15.0 < HE	0	0	0	0	0
Number of persons under radiation control (A)		544	567	562	588	703
Exposure above 1mSv	Number of persons (B)	0	0	0	0	0
	(B)/(A) × 100 (%)	0	0	0	0	0
Mass effective dose (Person·mSv)		0.5	0.0	0.8	0.1	1.4
Mean dose (mSv)		0.00	0.00	0.00	0.00	0.00
Maximum dose (mSv)		0.2	0.0	0.3	0.1	0.4

*1 The dose by the internal exposure was not detected.

*2 Net number.

(2) Individual monitoring for the visitors and others

Table 2 shows the number of persons who temporally entered the radiation controlled areas. The effective dose of all persons was less than 0.1 mSv.

Table 2 The number of persons who temporary entered the radiation controlled areas in FY 2010.

Periods	1st quarter	2nd quarter	3rd quarter	4th quarter	Total
Number of persons	777	1142	1259	898	4076

2. Monitoring of radioactive gas and dust

Table 3 shows the maximum radioactive concentrations and total activities for radioactive gases released from the stack of TIARA, during each quarter of FY 2010.

Small amount of ^{41}Ar , ^{11}C , ^{13}N and ^{18}F were detected for some time during operation of the cyclotron or experiment, but the pulverized substances (^{65}Zn , etc.) were not detected.

Table 3 Monitoring results of released radioactive gases and dust in FY 2010.

Nuclide	Items	1st quarter	2nd quarter	3rd quarter	4th quarter	Total
^{41}Ar	Maximum concentration	$<1.7 \times 10^{-4}$	$<1.7 \times 10^{-4}$	$<1.7 \times 10^{-4}$	$<1.4 \times 10^{-4}$	
	Activity	6.6×10^7	0	9.9×10^6	2.7×10^8	3.5×10^8
^{11}C	Maximum concentration	$<1.7 \times 10^{-4}$	$<1.7 \times 10^{-4}$	$<1.7 \times 10^{-4}$	$<1.4 \times 10^{-4}$	
	Activity	4.5×10^8	1.9×10^8	1.6×10^8	5.2×10^8	1.3×10^9
^{13}N	Maximum concentration	$<1.7 \times 10^{-4}$	—	$<1.4 \times 10^{-4}$	1.5×10^{-4}	
	Activity	3.9×10^7	—	2.2×10^7	4.3×10^8	4.9×10^8
^{18}F	Maximum concentration	—	—	$<1.7 \times 10^{-4}$	—	
	Activity	—	—	1.3×10^8	—	1.3×10^8
^{65}Zn	Maximum concentration	$<6.5 \times 10^{-10}$	$<6.1 \times 10^{-10}$	$<5.7 \times 10^{-10}$	$<6.1 \times 10^{-10}$	
	Activity	0	0	0	0	0

Unit : Bq/cm³ for Maximum concentration, Bq for Activity.

3. Monitoring for external radiation and surface contamination

External radiation monitoring was routinely carried out in/around the radiation controlled areas and surface contamination monitoring was also carried out. Neither unusual value of dose equivalent rate nor surface contamination was detected.

Figure 1 shows a typical example of distribution of the dose equivalent rate in the radiation controlled area of the cyclotron building.

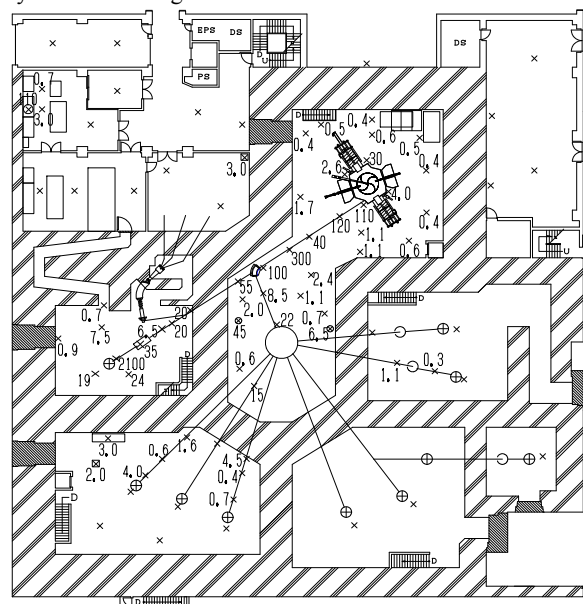


Fig. 1 Dose equivalent rate distribution in the radiation controlled area of the cyclotron building.

Measurement date : 8th, 9th and 29th March 2011,

Measuring position : Indicated with × 1 m above floor,
Unit : μSv/h.

(The values are not indicated if they are less than 0.2 μSv/h.)

5-8 Radioactive Waste Management in TIARA

T. Ishibashi and T. Hosoi

Department of Administrative Services, TARRI, JAEA

1. The radioactive wastes management

The radioactive wastes generated in TIARA are managed by Utilities and Maintenance Section. The main radioactive wastes are the solid wastes generated from the research experiment and the maintenance of the cyclotron. Other radioactive wastes are the liquid wastes such as inorganic waste fluids generated from the research experiment and the air-conditioning machines in controlled area. These wastes are managed according to their properties.

2. Solid radioactive waste

Table 1 shows the amounts of solid wastes at various properties and kinds generated in each quarter of FY 2010. The main solid waste is generated from the research experiment and the maintenance of the cyclotron.

Combustible wastes are rubber gloves, paper, and clothes, etc. Incombustible wastes are metal pieces, the glasses, and contaminated parts.

3. Liquid radioactive waste

Table 2 shows the amounts of liquid wastes generated in each quarter of FY 2010. Most of liquid waste was inorganic waste water generated from chemical experiments and condensed water from operation of air conditioning units installed in each room of the first class radiation controlled area. The largest quantity of waste water in summer season (2nd quarter) is mainly due to condensed water. After treatment by evaporation, inorganic water is reused in the controlled area. Only small amounts of concentrated liquid are generated from the evaporation.

Table 1 Radioactive solid wastes generated in FY 2010.

Items	Amounts	Amounts of generation in each periods (m ³)					Number of package /drum
		1st quarter	2nd quarter	3rd quarter	4th quarter	Total	
Category A*		0.32	1.01	0.42	0.20	1.95	
1) Combustible		0.22	0.26	0.30	0.12	0.90	5**
2) Incombustible		0.10	0.75	0.12	0.08	1.05	0
Compressible		0.10	0.10	0.12	0.08	0.40	3**
Filters		0	0.65	0	0	0.65	0
Incompressible		0	0	0	0	0	0
Ion exchange resin		0	0	0	0	0	0
Category B*		0	0	0	0	0	0

* Defined by dose at the outer surface of container : (A) < 2 mSv/h ≤ (B),

** 200-liter drum.

Table 2 Radioactive liquid waste generated in FY 2010.

Items	Amounts	Amounts of generation in each periods (m ³)					Number of package /drum
		1st quarter	2nd quarter	3rd quarter	4th quarter	Total	
Category A*		13.90	28.62	8.69	6.77	57.98	
1) Inorganic		13.90	28.62	8.69	6.77	57.98	treatment
2) Organic		0	0	0	0	0	0
Organic		0	0	0	0	0	0
Oil		0	0	0	0	0	0
3) Sludge		0	0	0	0	0	0
4) Evaporation residue		0	0	0	0	0	0
Category B*		0	0	0	0	0	0

* Defined by concentrations in Bq/cm³ (β, γ) : (A) < 3.7 × 10³ ≤ (B) < 3.7 × 10⁴.

Appendix

Appendix 1 List of Publication	180
A1.1 Publication in Journal	180
A1.2 Publication in Proceedings	190
Appendix 2 List of Related Patents	200
Appendix 3 List of Related Press-Release and Television Broadcasting	202
Symbol used in the Appendix 1 to 3	203
Appendix 4 Type of Research Collaboration and Facilities Used for Research	204
Appendix 5 A Typical Example of Abbreviation Name for Organizations in Japan Atomic Energy Agency (JAEA)	206

Appendix 1. List of Publication

A 1.1 Publications in Journal

10J001 1-01 1-07 C, T, S, I

S. Sato, H. Sai, T. Ohshima, M. Imaizumi,
K. Shimazaki and M. Kondo
“Proton-Induced Photoconductivity Increment and
the Thermal Stability of a-Si:H Thin Film”
J. Non-Cryst. Sol. 356 (2010) 2114-19.

10J002 1-05 T, I

N. Iwamoto, S. Onoda, T. Makino, T. Ohshima,
K. Kojima, A. Koizumi, K. Uchida and S. Nozaki
“Transient Analysis of an Extended Drift Region
in a 6H-SiC Diode Formed by a Single Alpha
Particle Strike and Its Contribution to the
Increased Charge Collection”
IEEE Trans. Nucl. Sci. 58 (2011) 305-13.

10J003 1-06 T, I

A. Koizumi, N. Iwamoto, S. Onoda, T. Ohshima,
T. Kimoto, K. Uchida and S. Nozaki
“Compensation-Dependent Carrier Transport of
Al-Doped p-Type 4H-SiC”
Mater. Sci. Forum 679-680 (2011) 201-04.

10J004 1-06 E

H. Matsuura, H. Yanagisawa, K. Nishino,
T. Nojiri, S. Onoda and T. Ohshima
“Reduction in Majority-Carrier Concentration in
Lightly-Doped 4H-SiC Epilayers by Electron
Irradiation”
Mater. Sci. Forum 679-680 (2011) 181-84.

10J005 1-06 T, I

S. Onoda, T. Makino, N. Iwamoto, G. Vizkelethy,

K. Kojima, S. Nozaki and T. Ohshima
“Charge Enhancement Effects in 6H-SiC
MOSFETs Induced by Heavy Ion Strike”
IEEE Trans. Nucl. Sci. 57 (2010) 3373-79.

10J006 1-06 G

T. Ohshima, N. Iwamoto, S. Onoda, T. Makino,
S. Nozaki and K. Kojima
“Oxygen Ion Induced Charge in SiC MOS
Capacitors Irradiated with Gamma-rays”
Mater. Sci. Forum 679-680 (2011) 362-65.

10J007 1-10 T, E

F. C. Beyer, C. G. Hemmingsson, H. Pedersen,
A. Henry, J. Isoya, N. Morishita,
T. Ohshima and E. Janzén
“Bistable defects in low-energy electron irradiated
n-type 4H-SiC”
Phys. Stat. Solidi-Rapid Res. Lett. 4 (2010)
227-29.

10J008 1-10 E

F. C. Beyer, C. Hemmingsson, H. Pedersen,
A. Henry, J. Isoya, N. Morishita,
T. Ohshima and E. Janzén
“Metastable defects in low-energy electron
irradiated n-type 4H-SiC”
Mater. Sci. Forum 645-48(2010) 435-38.
Proc. 13th Int. Conf. Silicon Carbide Related
Mater. [Nurnberg, Germany] (2009/10).

10J009 1-10 T, E

N. T. Son, J. Isoya, T. Umeda, I. G. Ivanov,
A. Henry, T. Ohshima and E. Janzén

“EPR and ENDOR studies of shallow donors in SiC”

Appl. Magn. Reson. 39 (2010) 49-85.

10J010 1-10 T, E

P. Carlsson, N. T. Son, A. Gali, J. Isoya,
N. Morishita, T. Ohshima,
B. Magnusson and E. Janzén

“EPR and ab initio calculation study on the EI4 center in 4H- and 6H-SiC”

Phys. Rev. B 82 (2010) 235203.

10J011 1-10 E

N. T. Son, P. Carlsson, J. Isoya, N. Morishita,
T. Ohshima, B. Magnusson and E. Janzén

“The carbon vacancy related EI4 defect in 4H-SiC”

Mater. Sci. Forum 645-48 (2010) 399-402

Proc. 13th Int. Conf. Silicon Carbide Related Mater. [Nurnberg, Germany] (2009/10).

10J012 1-10 T, E

T. Umeda, J. Isoya, T. Ohshima, S. Onoda,
N. Morishita, K. Okonogi and S. Shiratake

“Fluorine-vacancy defects in fluorine-implanted silicon studied by electron paramagnetic resonance”

Appl. Phys. Lett. 97 (2010) 041911.

10J013 1-17 G

T. Seguchi, K. Tamura, T. Ohshima,
A. Shimada and H. Kudoh

“Degradation mechanisms of cable insulation materials during radiation-thermal ageing in radiation environment”

Radiat. Phys. Chem. 80 (2011) 268-73.

10J014 1-30 T, S, I

G. H. Kim, K. Shiba, T. Sawai,
I. Ioka and K. Kiuchi

“Irradiation behaviour of precipitation hardened Ni-base super-alloys with EHP grade under multi-ion irradiation”

MRS Online Proc. Library (Part of Cambridge Journals Online), Vol. 1298 1 (2011).

10J015 1-31 C

T. Yamaki, M. Asano, H. Koshikawa, Y. Maekawa,
R. Neumann, C. Trautmann and K.-O. Voss

“Poly(vinylidene fluoride)-Based Ion-Track Membranes with Asymmetrical Pores”

GSI Sci. Rep. 2009 (2010) 445.

10J016 1-31 C

T. Yamaki

“Quantum Beam Technology: A Versatile Tool for Developing Polymer Electrolyte Fuel-Cell Membranes”

J. Power Sources 195 (2010) 5848-55.

10J017 1-32, 1-35 G

S. Sawada, T. Yamaki, T. Ozawa, A. Suzuki,
T. Terai and Y. Maekawa

“Water Transport in Polymer Electrolyte Membranes Investigated by Dissipative Particle Dynamics Simulation”

ECS Trans. Vol. 33 (1) (2010) 1067-78.

10J018 1-33 G

S. Hasegawa, S. Takahashi, H. Iwase,
S. Koizumi, N. Morishita, K. Sato, T. Narita,
M. Ohnuma and Y. Maekawa

“Radiation-Induced Graft Polymerization of Functional Monomer into Poly(ether ether ketone)

Film and Structure-Property Analysis of the Grafted Membrane”
Polymer 52 (2010) 98-106.

10J019 1-34 G

N. Tanaka, T. Yamaki, M. Asano,
Y. Maekawa and K. Onuki
“Electro-electrodialysis of HI-I₂-H₂O mixture
using radiation-grafted polymer electrolyte
membranes”
J. Membr. Sci. 346 (2010) 136-42.

10J020 2-11 G

A. Kimura, M. Taguchi, T. Kondoh, J. Yang,
R. Nagaishi, Y. Yoshida and K. Hirota
“Decomposition of halophenols in room-
temperature ionic liquids by ionizing radiation”
Radiat. Phys. Chem. 79 (2010) 1159-64.

10J021 3-02 C

A. Tanaka, N. Shikazono and Y. Hase
“Studies on biological effects of ion beams on
lethality, molecular nature of mutation, mutation
rate, and spectrum of mutation phenotype for
mutation breeding in higher plants”
J. Radiat. Res. 51 (2010) 223-33.

10J022 3-02 C

A. Yokoya, N. Shikazono, K. Fujii,
M. Noguchi and A. Urushibara
“A novel technique using DNA denaturation to
detect multiply induced single-strand breaks in a
hydrated plasmid DNA molecule by X-ray and
4He²⁺ ion irradiation”
Radiat. Protect. Dosim. 143 (2011) 219-25.

10J023 3-02 C

N. Shikazono, A. Yokoya, A. Urushibara,
M. Noguchi and K. Fujii
“A model for analysis of the yield and the level of
clustering of radiation-induced DNA-strand breaks
in hydrated plasmids”
Radiat. Protect. Dosim. 143 (2011) 181-185.

10J024 3-04 C

坂下 哲哉、横田 裕一郎、舟山 知夫、柏木 啓次、
佐藤 隆博、小林 泰彦
“集束式重イオンマイクロビームの大気中ビーム
サイズの迅速評価方法の検討:CR-39 のエッチン
グ時間短縮及び半自動画像処理”
RADIOISOTOPES, 60 (2) (2011) 47-53.

10J025 3-05 C, G

Y. Yokota, T. Funayama, Y. Hase, N. Hamada,
Y. Kobayashi, A. Tanaka and I. Narumi
“Enhanced micronucleus formation in the
descendants of γ -ray-irradiated tobacco cells:
Evidence for radiation-induced genomic instability
in plant cells”
Mutat. Res. - Fund. Mol. Mech. Mutagen. 691
(2010) 41-46.

10J026 3-07 C

T. Kaminuma, Y. Suzuki, K. Shirai, T. Mizui,
SE. Noda, Y. Yoshida, T. Funayama, T. Takahashi,
Y. Kobayashi, T. Shirao and T. Nakano
“Effectiveness of carbon-ion beams for apoptosis
induction in rat primary immature hippocampal
neurons”
J. Radiat. Res. 51 (2010) 627-31.

10J027 3-07 C

鈴木 義行、吉田 由香里、白井 克幸、岡本 雅彦、

工藤 滋弘、中野 隆史

“脳神経細胞の放射線感受性”

放射線生物研究 45 (2010) 236-48.

10J028 3-09 C

H. Matsumoto, M. Tomita, K. Otsuka,

M. Hatashita and N. Hamada

“Nitric oxide is a key molecule serving as a bridge between radiation-induced bystander and adaptive responses”

Curr. Mol. Pharmacol. 4 (2011) 126-34.

10J029 3-08 C

N. Narita, S. Fujieda, Y. Kimura, Y. Ito, Y. Imoto, K. Ogi, N. Takahashi, T. Tanaka, H. Tsuzuki,

T. Yamada and H. Matsumoto

“Suppression of histone deacetylase 3 (HDAC3) enhances apoptosis induced by paclitaxel in human maxillary cancer cells in vitro and in vivo”
Biochem. Biophys. Res. Commun. 396 (2010) 310-16.

10J030 3-09 C

N. Hamada, M. Maeda, K. Otsuka and M. Tomita

“Signaling pathways underpinning the manifestations of ionizing radiation-induced bystander effects”

Curr. Mol. Pharmacol. 4 (2011) 79-95.

10J031 3-16 C

O. Gusev, Y. Nakahara, V. Vanyagina L. Malutina, R. Cornette, T. Sakashita, N. Hamada, T. Kikawada, Y. Kobayashi and T. Okuda

“Anhydrobiosis-associated nuclear DNA damage and repair in the sleeping chironomid: Linkage with radioresistance”

PLoS ONE 5 (11) (2010):e14008.

10J032 3-17 C

Y. Mutou-Yoshihara, T. Funayama,

Y. Yokota and Y. Kobayashi

“Cytokine production is suppressed in human THP-1 macrophages by both direct hit of energetic heavy-ions and bystander response caused by microbeam irradiation to the limited part of cell population”

Int. J. Radiat. Biol. to be submitted.

10J033 3-19, 3-20 G

亀谷 宏美、貝森 良彦、鵜飼 光子

“放射線照射したニンニクにおけるラジカルの測定”

RADIOISOTOPES 59 (2010) 415-21.

10J034 3-19, 3-20 G

亀谷 宏美、垣田 大介、貝森 良彦、菊地 正博、小林 泰彦、鵜飼 光子、下山 雄平

“照射マンゴー中に誘導されるラジカルの緩和挙動と線量依存性”

RADIOISOTOPES 59 (2010) 607-14.

10J035 3-19, 3-20 G

古田 雅一、石川 悦子、保科 美幸、富井 恵奈美、小池 佳都子、鵜飼 光子

“殺菌済み香辛料に生残する微生物の食肉中における増殖動態の解析”

食品照射 45 (2010) 4-10.

10J036 3-20 G

中村 秀夫、高橋 司、太多 由依、貝森 良彦、亀谷 宏美、鵜飼 光子

“放射線照射漢方薬(エキス剤)の照射誘導ラジカルの緩和時間”

食品照射 45 (2010) 11-18.

10J037 3-19, 3-20 G

亀谷 宏美、中村 秀夫、鵜飼 光子、下山 雄平
 “ESR によるグルコースポリマー中の照射誘導ラジカルの解析”
 食品照射 45 (2010) 19-25.

10J038 3-19 3-20 G

小林 泰彦、菊地 正博、等々力 節子、齊藤 希巳江、
 桂 洋子、亀谷 宏美、市川 まりこ、飯塚 友子、
 千葉 悦子、鵜飼 光子
 “放射線照射によるニンニクの萌芽発根抑制効果”
 食品照射 45 (2010) 26-33.

10J039 3-19, 3-20 G

菊地 正博、垣田 大介、下山 雄平、鵜飼 光子、
 小林 泰彦
 “照射された生鮮果実パパイアにおけるラジカル緩和現象”
 食品照射 45 (2010) 34-38.

10J040 3-19, 3-20 G

亀谷 宏美、齊藤 希巳江、菊地 正博、小林 泰彦、
 鵜飼 光子、等々力 節子
 “照射ニンニクの電子スピン共鳴法、光刺激ルミネッセンス法、熱ルミネッセンス法による検知”
 食品科学工学会誌 57 (2010) 472-78.

10J041 3-25 S

S. Matsuzaki, Y. Shimizu, K. Dobashi,
 T. Nagamine, T. Satoh, T. Ohkubo, A. Yokoyama,
 Y. Ishii, T. Kamiya, K. Arakawa, S. Makino,
 M. Utsugi, T. Ishizuka, S. Tanaka,
 K. Shimizu and M. Mori
 “Analysis on the co-localization of asbestos bodies and Fas or CD163 expression in asbestos lung tissue by in-air micro-pixe”
 Int. J. Immunopathol. Pharmacol. Jan-Mar; 23(1):

(2010) 1-1.

10J042 3-26 S

菊地 弘記、時田 佳治、長嶺 竹明、佐藤 隆博、
 神谷 富裕
 “大気 micro-PIXE を用いた透析患者の赤血球元素分析”
 第 26 回 PIXE シンポジウム抄録集 (2010).

10J043 3-27 S

S. Harada, S. Ehara, K. Ishii, A. Tanaka, T. Satoh,
 S. Matsuyama, H. Yamazaki, Y. Komori,
 T. Kamiya, T. Arakawa, M. Saitoh,
 M. Oikawa and K. Sera
 “Improved radiosensitive microcapsules using H₂O₂”
 Int. J. PIXE 20 (2010) 30-36.

10J044 3-29 C

Y. Ohshima, H. Hanaoka, Sh. Watanabe, Y. Sugo,
 Sa. Watanabe, H. Tominaga, N. Oriuchi,
 K. Endo and N. S. Ishioka
 “Preparation and biological evaluation of 3-[⁷⁶Br]bromo- α -methyl-L-tyrosine, a novel tyrosine analog for PET imaging of tumors”
 Nucl. Med. Biol. (2011) in press.

10J045 3-31 C

N. Kawachi, K. Kikuchi, N. Suzui, S. Ishii,
 S. Fujimaki, N.S. Ishioka and H. Watabe
 “Imaging of Carbon Translocation to Fruit Using Carbon-11-Labeled Carbon Dioxide and Positron Emission Tomography”
 IEEE Trans. Nucl. Sci. 58 (2011) 395-99.

10J046 3-31 C

N. Kawachi, N. Suzui, S. Ishii, S. Ito,

N. S. Ishioka, H. Yamazaki, A. H. Iwasaki,
K. Ogawa and S. Fujimaki
“Real-time whole-plant imaging of ^{11}C
translocation using positron-emitting tracer
imaging”
Nucl. Instrum. Meth. Phys. Res. A (2010) in press.

10J047 3-32 C

S. Fujimaki, S. Ishii and N. S. Ishioka
“Non-invasive imaging and analyses of transport
of nitrogen nutrition in intact plants using a
positron-emitting tracer imaging system (PETIS)”
In: "Nitrogen Assimilation in Plants" T. Ohyama,
K. Sueyoshi eds., Res. Signpost (2010) 119-32 (著
書).

10J048 3-33 C

S. Fujimaki, N. Suzui, N. S. Ishioka, N. Kawachi,
S. Ito, M. Chino and S. Nakamura
“Tracing Cadmium from Culture to Spikelet:
Noninvasive Imaging and Quantitative
Characterization of Absorption, Transport, and
Accumulation of Cadmium in an Intact Rice
Plant”
Plant Physiol. 152 (2010) 1796-806.

10J049 3-33 C

伊藤 小百合、鈴木 伸郎、河地 有木、石井 里美、
石岡 典子、藤巻 秀
“ $^{11}\text{CO}_2$ と植物用ポジトロンイメージング装置を用
いたダイズ植物の根粒に対する光合成産物移行
のリアルタイム解析”
RADIOISOTOPES 59 (2010) 145-54.

10J050 3-38 C

S. Arase, Y. Hase, Y. Abe, M. Kasai, T. Yamada,
K. Kitamura, I. Narumi., A. Tanaka and

A. Kanazawa
“Optimization of ion-beam irradiation for
mutagenesis in soybean: effects on plant growth
and production of visibly altered mutants”
Plant Biotechnol. (2011) in press.

10J051 3-42 C

A. Okafuji, T. Biskup, K. Hitomi, ED Getzoff,
G. Kaiser, A. Batschauer, Bacher, J. Hidema,
M. Teranishi, K. Yamamoto,
E. Schleicher and S. Weber
“Light-induced activation of class II cyclobutane
pyrimidine dimer photolyase”
DNA Repair 9 (2010) 495-505.

10J052 3-42 C

M. Takahashi, M. Teranishi, H. Ishida, J. Kawasaki,
A. Takeuchi, T. Yamaya, M. Watanabe,
A. Makino and J. Hidema
“CPD photolyase repairs ultraviolet-B-induced
CPDs in rice chloroplast and mitochondrial DNA”
Plant J. 66 (2011) 433-42.

10J053 3-46 C

K. Shimizu, Y. Matuo, Y. Izumi and T. Ikeda
“Fundamental Study of The Radiation Monitoring
System Based on Valuation of DNA Lesions”
Radiat. Protect. Dosim. (2011) in press.

10J054 4-01 S, I

T. Hakoda, S. Yamamoto, K. Kawaguchi,
T. Yamaki, T. Kobayashi and M. Yoshikawa
“Oxygen reduction activity of N-doped
carbon-based films prepared by pulsed laser
deposition”
Appl. Surf. Sci. 257 (2010) 1556-61.

10J055 4-02, 4-03, 4-04 C

S. Tsukuda, A. Asano, M. Sugimoto, A. Idesaki,
S. Seki and S.-I. Tanaka
“Control of Radial Size of Crosslinked Polymer
Nanowire by Ion Beam and γ Ray Irradiation”
J. Photopolym. Sci. Tech. 23 (2010) 231-34.

10J056 4-05 E

A. Takeyama, M. Sugimoto and M. Yoshikawa
“Gas permeation property of SiC membrane using
curing of polymer precursor film by electron beam
irradiation in helium atmosphere”
Mater. Trans. to be published.

10J057 4-08 S, I

A. V. Umenyi, M. Honmi, S. Kawashiri,
T. Shinagawa, K. Miura, O. Hanaizumi,
S. Yamamoto, A. Inouye and M. Yoshikawa
“Design and fabrication of novel photonic crystal
waveguide consisting of Si-ion implanted SiO₂
layers”
Key Eng. Mater. 459 (2011) 168-72.

10J058 4-09 I, E

H. Abe, S. Ohnuki, Y. Shinohara,
S. F. Kadec, Y. Utsumi, Y. Matsumura,
H. Uchida and T. Ohshima
“Improvement of Hydride Characteristics in
Hydrogen Storage La-Ni Based Alloy”
Nucl. Instrum. Meth. Phys. Res. B. to be
submitted.

10J059 4-09 I, E

S. Ohnuki, Y. Shinohara, S. F. Kadec, Y. Utsumi,
H. Uchida, Y. Matsumura and H. Abe
“Irradiation Treatment Effects on Hydrogen
Storage Alloy”

J. Alloys and Comp. to be submitted.

10J060 4-09 I, E

Y. Yoneda, H. Abe, T. Ohshima and H. Uchida
“Phase Transformation of Mg-Fe Alloys”
J. Appl. Phys. 107 (2010) 093505.

10J061 4-10 T

Nao. Fujita, S. Kosugi, Y. Saitoh, Y. Kaneta,
K. Kume, T. Batchuluun, N. Ishikawa,
T. Matsui and A. Iwase
“Magnetic states controlled by energetic ion
irradiation in FeRh thin films”
J. Appl. Phys. 107 (2010) 09E302.

10J062 4-10 T

Nao. Fujita, T. Matsui, S. Kosugi, T. Saitoh,
Y. Satoh, K. Takano, M. Koda,
T. Kamiya, S. Seki and A. Iwase
“Micron-sized magnetic patterning of FeRh films
using an energetic ion microbeam Jpn”
Appl. Phys. 49 (2010) 060211.

10J063 4-10 T

T. Mitsuda, I. Kobayashi, S. Kosugi, Nao. Fujita,
Y. Saitoh, F. Hori, S. Semboshi, Y. Kaneno,
K. Nishida, N. Soneda and A. Iwase
“Hardening of Al-Cu-Mg alloy by energetic ion
irradiation”
J. Nucl. Mater. 408 (2011) 201-04.

10J064 4-12 I

Y. Kasukabe, Y. Chen, S. Yamamoto,
M. Yoshikawa and Y. Fujino
“In-situ Observation of Nitriding Processes of
Deposited-Ti Thin Films due to Ion Implantation
in an Analytical Transmission Electron

Microscope”

e-J. Surf. Sci. Nanotech. 9 (2011) 191-98.

10J065 4-14 T, S, I

I. Sugai, S. Sakai, Y. Matsumoto, H. Naramoto, S. Mitani, K. Takanashi and Y. Maeda

“Composition dependence of magnetic and magnetotransport properties in C60-Co granular thin films”

J. Appl. Phys. 108 (2010) 063920-1-6.

10J066 4-14

Pavel V. Avramov, S. Sakai, S. Entani, Y. Matsumoto and H. Naramoto

“Ab initio LC-DFT study of graphene, multilayer graphenes and graphite”

Chem. Phys. Lett. 508 (2011) 86-89.

10J067 4-14

S. Entani, S. Sakai, Y. Matsumoto, H. Naramoto, T. Hao and Y. Maeda

“Interface Properties of Ag and Au/Graphene Heterostructures Studied by Micro-Raman Spectroscopy”

Jpn. J. Appl. Phys. 50 (2011) 04DN03.

10J068 4-14

S. Entani, S. Sakai, Y. Matsumoto, H. Naramoto, T. Hao and Y. Maeda

“Interface Properties of Metal/Graphene Heterostructures Studied by Micro-Raman Spectroscopy”

J. Phys. Chem. C. 114 (2010) 20042-48.

10J069 4-14

S. Sakai, S. Mitani, I. Sugai, K. Takanashi, Y. Matsumoto, S. Entani, H. Naramoto, P. Avramov

and Y. Maeda

“Effect of cotunneling and spin polarization on the large tunneling magnetoresistance effect in granular C60-Co films”

Phys. Rev. B 83 (2011) 174422.

10J070 4-15 T

N. Ishikawa and K. Takegahara

“Radiation damages in CeO₂ thin films irradiated with ions having the same nuclear stopping and different electronic stopping powers”

Nucl. Instrum. Meth. Phys. Res. (2011) in press.

10J071 4-18

I. Matsuda, F. Nakamura, K. Kubo, T. Hirahara, S. Yamazaki, W. H. Choi, H. W. Yeom, H. Narita, Y. Fukaya, M. Hashimoto, A. Kawasuso, M. Ono, Y. Hasegawa, S. Hasegawa and K. Kobayashi

“Electron compound nature in a surface atomic layer of a two-dimensional hexagonal lattice”

Phys. Rev. B 82 (2010) 165330.

10J072 4-18

Y. Fukaya, A. Kawasuso and A. Ichimiya

“Surface plasmon excitation at metal surfaces studied by reflection high-energy positron diffraction”

J. Phys.: Conf. Series 225 (2010) 012009.

10J073 4-18

Y. Fukaya, A. Kawasuso and A. Ichimiya

“Surface Plasmon Excitation at Topmost Surface in Reflection High-Energy Positron Diffraction”

e-J. Surf. Sci. Nanotech. 8 (2010) 190-93.

10J074 4-18

Y. Fukaya, M. Hashimoto,

A. Kawasuso and A. Ichimiya

“Structure and phase transition of low-dimensional metals on Si(111) surfaces studied by reflection high-energy positron diffraction”

J. Phys.: Conf. Series 225 (2010) 012008.

10J075 4-20 E

A. Yabuuchi, M. Maekawa and A. Kawasuso

“Positron Microbeam Study on Vacancy Generation Caused by Stress Corrosion Crack Propagation in Austenitic Stainless Steels”

J. Phys.: Conf. Series. 262 (2011) 012067.

10J076 4-22 S

K. Yoshimura, T. Hakoda,

S. Yamamoto and M. Yoshikawa

“Dehydrogenation catalyst for optical organic-hydride detection”

Appl. Surf. Sci. 257 (2011) 4428-31.

10J077 4-23 G

R. Nagaishi and Y. Kumagai

“Chapter 8 : Radiolysis of Water”

3 Nuclear Hydrogen Production Handbook, eds.

R. Hino and X. Yan, CRC Press of Taylor and Francis Group, LLC (2011) 177-87.

10J078 4-23 G

Y. Kumagai, R. Nagaishi,

R. Yamada and Y. Katsumura

“Effect of Silica Gel on Radiation-induced Reduction of Dichromate Ion in Aqueous Acidic Solution”

Radiat. Phys. Chem. 80 (2011) 876-83.

10J079 4-23 G

永石 隆二

“雰囲気や組成を制御したイオン液体中の放射線分解挙動”

放射線化学, 91 (2011) 15-20.

10J080 4-23 G

熊谷 友多

“水-シリカ界面における放射線誘起反応の研究”

平成 22 年度博士論文, 東京大学 (2011).

10J081 4-24 C

K. Iwamatsu, M. Taguchi, Y. Sugo,

S. Kurashima and Y. Katsumura

“Concentration and Incident Energy Dependences of Transient Species in Water by H⁺ Ion Irradiation”

Trans. Mater. Res. Soc. Jpn. in press.

10J082 4-24 C

S. Yamashita, M. Taguchi,

G. Baldacchino and Y. Katsumura

“Radiation Chemistry of Liquid Water with Heavy Ions: Steady-State and Pulse Radiolysis Studies”

Charged particle and photon interactions with matter-recent advances, applications and

interfaces, pp. 325-54, Edited by Y. Hatano,

Y. Katsumura, and A. Mozumder, CRC Press, Taylor & Francis Group.

10J083 4-25 C

S. Nakagawa, M. Taguchi,

K. Hirota and T. Murakami

“Degradation of Hydroxymaleimide in 2-Propanol by Irradiation of Energetic Heavy Ions (II) -N₂-saturated system-”

Radiat. Phys. Chem. 79 (2010) 890-93.

10J084 4-28 C

Y. Shikaze, Y. Tanimura, J. Saegusa, M. Tsutsumi,
Y. Uchita and M. Yoshizawa

“Development of the Quasi-monoenergetic
Neutron Calibration Fields of Several Tens of
MeV at TIARA”

Prog. J. Nucl. Sci. Tech. 1 (2011) 166-69.

10J085 4-29 C

H. Harano, T. matsumoto, J. Nishiyama, A. Masuda,
A. Uritani and K. Kudo

“Recent activities on neutron standardization in
Japan”

Prog. J. Nucl. Sci. Tech. 1 (2011) 138-41.

10J086 4-29 C

H. Harano, T. Matsumoto, Y. Tanimura, Y. Shikaze,
M. Baba and T. Nakamura

“Monoenergetic and Quasi-Monoenergetic
Neutron Reference Fields in Japan”

Radiat. Meas. 45 (2010) 1076-82.

10J087 4-38 T

K. Hirata, Y. Saitoh, A. Chiba, K. Yamada,
Y. Takahashi and K. Narumi

“Comparison of Secondary Ion Emission Yields
for Poly-tyrosine between Cluster and Heavy Ion
Impacts”

Nucl. Instrum. Meth. Phys. Res. B 268 (2010)
2930.

10J088 4-39 C

N. Miyawaki, M. Fukuda, S. Kurashima,
S. Okumura, H. Kashiwagi, T. Nara, I. Ishibori,
K. Yoshida, W. Yokota, Y. Nakamura,
K. Arakawa and T. Kamiya

“Realization of a phase bunching effect for

minimization of beam phase width in a central
region of an AVF cyclotron”

Nucl. Instrum. Meth. Phys. Res. A 636 (2011)
41-47.

10J089 4-42 S

W. Kada, A. Yokoyama, M. Koka,
T. Satoh and T. Kamiya

“Development of analysis system of micro-IBIL
combined with micro-PIXE”

Int. J. PIXE. 21 (2011) 1-11.

10J090 4-43 C

Y. Yuri

“Gaussian-Like Ion Beam Shaping by Double
Scattering”

J. Phys. Soc. Jpn. 79 (2010) 125002-1~2.

10J091 4-45 S

Y. Shiine, H. Nishikawa, Y. Furuta,
K. Kanamitsu, T. Satoh, Y. Ishii, T. Kamiya,
R. Nakao and S. Uchida

“Soft-lithographic methods for the fabrication of
dielectrophoretic devices using molds by proton
beam writing”

Microelectr. Eng. Vol. 87 (2010) 835-38.

10J092 4-49

M. Maekawa, A. Yabuuchi and A. Kawasuso

“Development of a positron microbeam using a
small source”

Nucl. Instrum. Meth. Phys. Res. B. to be
submitted.

A 1.2 Publication in Proceedings

10C001 1-01, 1-07 C, T, I

S. Sato, H. Sai, T. Ohshima, M. Imaizumi, K. Shimazaki and M. Kondo
 “Electric Conductivity of Device Grade Hydrogenated Amorphous Silicon Thin Films Irradiated with Protons”
 Proc. 9th Int. Workshop Radiat. Effects Semicond. Devices Space Appl. [Takasaki, Japan] (2010) 183-86.

10C002 1-01 C, E

M. Saito, M. Imaizumi, T. Ohshima and M. Cho
 “Effects of Irradiation Beam Conditions on Radiation Degradation of Solar Cells”
 Proc. 9th Int. Workshop Radiat. Effects Semicond. Devices Space Appl. RASEDA-9 [Takasaki, Japan] (2010) 210-13.

10C003 1-01 I

D. Elfiky, M. Yamaguchi, T. Sasaki, T. Takamoto, C. Morioka, M. Imaizumi, T. Ohshima, Sh. Sato, M. Elnawawy, T. Eldesuky and A. Ghitas
 “Study the Effects of Proton Irradiation on GaAs/Ge Solar Cells”
 Proc. 35th IEEE Photovolt. Specialists Conf. [Hawaii, USA] (2010) 2528-32.

10C004 1-01 E

T. Ohshima, S. Sato, C. Morioka, M. Imaizumi, T. Sugaya and S. Niki
 “Change in the Electrical Performance of InGaAs Quantum Dot Solar Cells due to Irradiation”
 Proc. 35th IEEE Photovolt. Specialists Conf. [Hawaii, USA] (2010) 2594-98.

10C005 1-01 C, E

M. Saito, M. Imaizumi, T. Ohshima and Y. Takeda
 “Effects of Irradiation Beam Conditions on Radiation Degradation of Solar Cells”
 Proc. 35th IEEE Photovoltaic Specialists Conf. [Hawaii, USA] (2010) 2616-19.

10C006 1-01 1-07 C, T, I

S. Sato, H. Sai, T. Ohshima, M. Imaizumi, K. Shimazaki and M. Kondo
 “Photo- and Dark Conductivity Variations of Solar Cell Quality a-Si:H Thin Films Irradiated with Protons”
 Proc. 35th IEEE Photovoltaic Specialists Conf. [Hawaii, USA] (2010) 2620-24.

10C007 1-01 C, T, I, E

C. Morioka, K. Shimazaki, S. Kawakita, M. Imaizumi, Y. Nakamura, K. Hirako, M. Takahashi, H. Yamaguchi, T. Takamoto, S. Sato and T. Ohshima
 “First Flight Demonstration of Film-Laminated InGaP/GaAs and CIGS Thin-Film Solar Cells by JAXA’s Small Satellite in LEO”
 Proc. 5th World Conf. Photovolt. Energ. Conv. [Valencia, Spain] (2010) 92-97.

10C008 1-04 C, T

Y. Takahashi, H. Takeyasu, Y. Okazaki, T. Hirao, S. Onoda and T. Ohshima
 “Heavy-Ion Induced Current in SOI Junction Diode”
 Proc. 9th Int. Workshop Radiat. Effects Semicond. Devices Space Appl. RASEDA-9 [Takasaki, Japan] (2010).

10C009 1-04 C, T

竹安 秀徳、岡崎 勇志、大谷 拓海、小倉 俊太、
高橋 芳浩
“SOI デバイスの重イオン照射誘起電流抑制に関する検討”
日大理工学術講演会 M-29 (2010/11) 1101-02.

10C010 1-04 C, T

岡崎 勇志、竹安 秀徳、大谷 拓海、小倉 俊太、
高橋 芳浩
“SOI 基板上の pn ダイオードにおける重イオン照射誘起電流”
日大理工学術講演会 M-30 (2010/11) 1103-04.

10C011 1-04 C, T

竹安 秀徳、岡崎 勇志、小倉 俊太、大谷 拓海、
高橋 芳浩、平尾 敏雄、小野田 忍、牧野 高紘、
大島 武
“SOI デバイスの重イオン照射誘起電流抑制に関する検討”
応用物理学会学術講演会 14a-ZD-4 (2010/09) 13-004.

10C012 1-05 T, I

N. Iwamoto, S. Onoda, T. Makino, T. Ohshima,
K. Kojima, A. Koizumi, K. Uchida and S. Nozaki
“Time-dependent Collected Charges of 6H-SiC p+n Diodes Measured Using Alpha Particles”
Proc. 9th Int. Workshop Radiat. Effects Semicond. Devices Space Appl. RASEDA-9 [Takasaki, Japan] (2010) 222-25.

10C013 1-06 T

T. Ohshima, N. Iwamoto, S. Onoda, T. Makino,
M. Deki and S. Nozaki
“Change in Current Induced from Silicon Carbide Metal-Oxide-Semiconductor Capacitors by

Oxygen Ions”

Proc. 9th Int. Workshop Radiat. Effects Semicond. Devices Space Appl. RASEDA-9 [Takasaki, Japan] (2010) 85-88.

10C014 1-06 E

H. Matsuura, H. Yanagisawa, K. Nishino,
T. Nojiri, S. Onoda and T. Ohshima
“Reduction in Majority-Carrier Concentration in N-Doped or Al-Doped 4H-SiC Epilayer by Electron Irradiation”
Proc. 9th Int. Workshop Radiat. Effects Semicond. Devices Space Appl. RASEDA-9 [Takasaki, Japan] (2010) 89-91.

10C015 1-06 I

M. Deki, T. Ito, T. Tomita, S. Matsuo,
S. Hashimoto, T. Kitada, T. Isu,
S. Onoda and T. Ohshima
“Laser Modification Aiming at the Enhancement of Local Electrical Conductivities in SiC”
Proc. 9th Int. Workshop Radiat. Effects Semicond. Devices Space Appl. RASEDA-9 [Takasaki, Japan] (2010) 218-21.

10C016 1-06 E

H. Miyazaki, J. Morimoto, K. Toda,
S. Onoda and T. Ohshima
“Raman and FT-IR spectroscopy of electron irradiated LiNbO₃”
Proc. 9th Int. Workshop Radiat. Effects Semicond. Devices Space Appl. RASEDA-9 [Takasaki, Japan] (2010) 226-29.

10C017 1-06, 1-12 T, I

S. Onoda, G. Vizkelethy, T. Makino, N. Iwamoto,
K. Kojima, S. Nozaki and T. Ohshima

“Enhanced Charge Collection in Drain Contact of 6H-SiC MOSFETs Induced by Heavy Ion Microbeam”

Proc. 9th Int. Workshop Radiat. Effects Semicond. Devices Space Appl. RASEDA-9 [Takasaki, Japan] (2010) 230-33.

10C018 1-09 G

H. Yano, L. Cai, Z. Duan, Y. Takayanagi, H. Ohuchi, H. Ueki, T. Hirao, T. Ohshima and Y. Nishioka

“Gamma-ray induced degradation of electrical characteristics of pentacene-based organic field effect transistors”

Korea-Japan Forum 2010 Org. Mater. Electron. Photon. (KJF2010) [Kitakyushu, Japan] (2010/08).

10C019 1-09 G

L. Cai, T. Hirao, H. Yano, Z. Duan, H. Takayanagi, H. Ueki, T. Ohshima and Y. Nishioka

“Electrical characteristics of ⁶⁰Co gamma-ray irradiated pentacene-based organic thin film field effect transistors”

Proc. 9th Int. Workshop Radiat. Effects Semicond. Devices Space Appl. RASEDA-9 [Takasaki, Japan] (2010) 176-78.

10C020 1-09 G

L. Cai, T. Hirao, H. Yano, Z. Duan, Y. Takayanagi, H. Ohuchi, H. Ueki, T. Ohshima and Y. Nishioka

“⁶⁰Co gamma-ray irradiation effects on pentacene-based organic thin film transistors” IUMRS Int. Conf. Asia (IUMRS-ICA) [Qingdao, China] (2010/09).

10C021 1-14 C, T, G

Y. Sugo, M. Taguchi, Y. Sasaki and Y. Morita

“Influence of energy of helium ions on degradation of diglycolamide in n-dodecane”

Proc. 3rd Asia-Pacific Symp. Radiat. Chem. & 10th Trombay Symp. Radiat. Photochem. (APSRC-TSRP-2010) Vol. 2 [Lonavala, India] (2010) 34-35.

10C022 1-17 G

A. Shimada, H. Kudo, T. Seguchi, T. Ohshima, A. Idesaki and K. Tamura

“Irradiation Condition on Accelerated Ageing Test of Cable for Nuclear Power Plant”

CMD 2010 [Tokyo, Japan] (2010/09) to be issued.

10C023 1-17 G

A. Shimada, H. Kudo, T. Seguchi, T. Ohshima, A. Idesaki and K. Tamura

“Radiation and thermal ageing studies of polymer materials used in cable insulation in nuclear power plant-5: Silicone Rubber (SiR)”

PACIFICHEM2010 [Honolulu, USA], (2010/12).

10C024 1-17 G

A. Shimada, T. Seguchi, K. Tamura, T. Ohshima, A. Idesaki and H. Kudo

“Radiation and Thermal Ageing Studies of Silidone Rubber (SiR) Used in Cable Insulation in Nuclear Power Plants”

Proc. Int. Workshop Radiat. Effects Nucl. Tech., [Tokyo, Japan] (2011/03).

10C025 1-19 G

H. Naito, W. Itagaki, C. Ito, R. Kitamura, N. Shamoto and Y. Takeshima

“Inspection and Repair Techniques in Reactor Vessel of Sodium Cooled Fast Reactor (5)

(3) Development of radiation resistant fiberscope

for inspection in reactor vessel of fast reactor (3)”
Proc. 2011 Annu. Meetings Atomic Energ. Soc.
Jpn. (2011) L32.

10C026 1-19 G

H. Naito, W. Itagaki, C. Ito, Y. Okazaki,
A. Nagai, N. Shamoto and Y. Takeshima
“Development of radiation resistant fiberscope for
inspection in reactor vessel of fast reactor (2)”
Proc. 2010 Fall Meetings Atomic Energ. Soc. Jpn.
(2010) J40.

10C027 1-29 T, S, I

I. Ioka, J. Suzuki, K. Kiuchi and J. Nakayama
“Study of optimum composition of extra high
purity Ni-Cr-W-Si alloy for advanced reprocessing
plant”
OECD-NEA Int. Workshop Struct. Mater. Innov.
Nucl. Syst. (SMINS2) [Daejeon, Korea]
(2010/08-09).

10C028 1-30 T, S, I

G. H. Kim, K. Shiba, T. Sawai, I. Ioka,
K. Kiuchi and J. Nakayama
“Microstructural evolution and void swelling in
extra high purity Ni-base superalloy under
multi-ion irradiation”
OECD-NEA Int. Workshop Struct. Mater. Innov.
Nucl. Syst. (SMINS2) [Daejeon, Korea]
(2010/08-09).

10C029 1-30 T, S, I

G. H. Kim, K. Shiba, T. Sawai, I. Ioka,
K. Kiuchi and J. Nakayama
“Crostructural evolution and void swelling in extra
high purity Ni-base superalloy under multi-ion
irradiation”

OECD-NEA Int. Workshop Struct. Mater. Innov.
Nucl. Syst. (SMINS2) [Daejeon, Korea]
(2010/08-09).

10C030 1-31 C

T. Yamaki, M. Kobayashi, M. Asano, K. Nomura,
S. Takagi, Y. Maekawa and M. Yoshida
“Quantum Beam Technology: Nanostructured
Proton-Conductive Membranes Prepared by Swift
Heavy Ion Irradiation for Fuel Cell Applications”
Proc. Sadoway60 Symp. [Boston, USA] (2010)
114-20.

10C031 1-33 G

S. Hasegawa, S. Takahashi, K. Sato, T. Narita,
H. Iwase, S. Koizumi and Y. Maekawa
“Morphology-controlled graft polymerization of a
functional monomer in poly(ether ether ketone)
films.”
PACIFICHEM 2010 [Honolulu, USA] (2010/12)

10C032 3-19, 3-20 G

H. Kameya, H. Nakamura,
S. Oowada and M. Ukai
“ESR spin trapping method of plant food extracts”
Asia-Pacific EPR/ESR Symp. (2010).

10C033 3-19, 3-20 G

H. Kameya, M. Ukai and Y. Shimoyama
“Radiation induced radicals in cellulose”
Proc. 9th Meeting Ioniz. Radiat. Polym. Symp.
(2010).

10C034 3-19, 3-20 G

M. Ukai
“ESR detection method of pasteurized food”
Proc. 5th Int. Conf. Microbiol. Food, Health &

Environ.: Problems and Prospects on Developing Countries (2010).

10C035 3-19 3-20 G

M. Ukai

“A new EPR spin trapping protocol using CYPMPPO”

The XXIVth Int. Conf. Mag. Reson. Biol. Syst. ICMRBS (2010).

10C036 3-19 3-20 G

M. Ukai

“Analysis of fruits and vegetables using ESR spin trap method”

China-Japan Joint Symp. Food Sci. & Tech. Ind. Level (2010).

10C037 3-19, 3-20 G

M. Ukai

“ESR study of irradiated ginseng”

Asia-Pacific EPR/ESR Symp. (2010).

10C038 3-38 C

富川 優、前田 智雄、本多 和茂、嵯峨 紘一、石川 隆二、秋田 祐介、吉原 亮平、野澤 樹、鳴海 一成

“‘弘前在来’トウガラシ種子への重イオンビーム照射が実生の発芽及び生育に及ぼす影響”

園芸学研究 9 別 1 (2010) 331.

10C039 3-41 C

長谷 純宏、吉原 亮平、野澤 樹、玉置 雅紀、鳴海 一成

“シロイヌナズナにおいて異なる LET の炭素イオンによって誘発される突然変異の特徴”

日本放射線影響学会第 53 回大会後援要旨集 (2010) 136.

10C040 3-43 C

岡村 正愛、長谷 純宏、梅基 直行、中山 真義、谷川 奈津、鳴海 一成、田中 淳

“花色突然変異体の効率的な誘導方法の開発”

第 28 回植物細胞分子生物学会 (2010) 66.

10C041 3-43 C

近藤 恵美子、中山 真義、亀有 直子、栗原 康、谷川 奈津、森田 裕将、秋田 祐介、長谷 純宏、田中 淳、石坂 宏

“紫色の芳香シクラメン‘孤高の香り’(Cyclamen persicum X C. purpurascens) へのイオンビーム照射によって得られた白色変異体の色素と香り成分の解析”

園芸学会平成 22 年度秋季大会(2010) 254.

10C042 3-43 C

近藤 恵美子、中山 真義、亀有 直子、栗原 康、谷川 奈津、森田 裕将、秋田 祐介、長谷 純宏、田中 淳、石坂 宏

“紫色の芳香シクラメン‘香りの舞い’(Cyclamen persicum X C. purpurascens) へのイオンビーム照射によって得られた赤紫色変異体の色素と香り成分の解析”

園芸学会平成 22 年度秋季大会(2010) 255.

10C043 3-43 C

亀有 直子、中山 真義、近藤 恵美子、栗原 康、秋田 祐介、長谷 純宏、谷川 奈津、森田 裕将、田中 淳、石坂 宏

“紫色の芳香シクラメン‘香りの舞い’(Cyclamen persicum X C. purpurascens) の半数体へのイオンビーム照射によって得られた赤紫色変異体の色素と香り成分の解析”

園芸学会平成 22 年度秋季大会 (2010) 256.

10C044 3-43 C

近藤 恵美子、中山 真義、亀有 直子、谷川 奈津、森田 裕将、秋田 祐介、長谷 純宏、田中 淳、石坂 宏

“イオンビーム照射による芳香シクラメン’香りの舞い’の花色突然変異体の作出”

第7回イオンビーム育種研究会大会要旨集 (2010) 1-2.

10C045 3-43 C

近藤 恵美子、亀有 直子、中山 真義、栗原 康、秋田 祐介、谷川 奈津、森田 裕将、長谷 純宏、田中 淳、石坂 宏

“イオンビーム照射による芳香シクラメン’麗しの香り’の突然変異誘導”

第7回イオンビーム育種研究会大会要旨集 (2010) 3-4.

10C046 3-43 C

長谷 純宏、岡村 正愛、竹下 大学、鳴海 一成、田中 淳

“高糖濃度処理したペチュニア幼苗へのイオンビーム照射による効率的な花色変異体の獲得”

第7回イオンビーム育種研究会大会要旨集 (2010) 21-22.

10C047 3-43 C

秋田 祐介、北村 智、長谷 純宏、鳴海 一成、石坂 宏、近藤 恵美子、亀有 直子、中山 真義、谷川 奈津、森田 裕将、田中 淳

“芳香シクラメン’香りの舞い’ (Cyclamen persicum X C. purpurascens) におけるアントシアニンメチル基転移酵素の解析”

園芸学会平成23年度春季大会 (2011) 221.

10C048 4-02 C

A. Asano, S. Tsukuda, M. Sugimoto and S. Seki

“Fabrication of biomacromolecular nanowires by single particle nanofabrication technique (SPNT)”
Proc. 2010 Int. Chem. Cong. Pacific Basin Societies (2010).

10C049 4-03 C

S. Tsukuda, S. Seki, M. Sugimoto, A. Idesaki, A. Asano and Sh. Tanaka

“Direct Formation of cross-linked polymer nanowires including Au particles by Single Particle Nano-Fabrication Technique”
Proc. 9th Meeting Ioniz. Radiat. & Polym. Conf. [Maryland, USA] (2010).

10C050 4-03 C

S. Tsukuda, S. Seki, M. Sugimoto, A. Idesaki, A. Asano and Sh. Tanaka

“Formation of Poly(4-vinylphenol) Au Nanoparticles Hybrid Nanowires by Ion Beam Irradiation”
Proc. 27th Int. Conf. Photopolym. Sci. Tech. Mater. Processes Adv. Microlithography Nanotech. [Chiba, Japan] (2010).

10C051 4-08 I

A. V. Umenyi, M. Honmi, S. Kawashiri, T. Shinagawa, K. Miura, O. Hanaizumi, S. Yamamoto, A. Inouye and M. Yoshikawa
“Silicon based novel photonic crystal waveguide fabrication and numerical characterization by Si-ion implantation and FDTD method”
Proc. 15th Optoelectron. Comm. Conf. [Sapporo, Japan] (2010) 9E3-3.

10C052 4-08 I

T. Shinagawa, A. V. Umenyi, S. Kikuchi, M. Aiba, K. Inada, K. Miura, O. Hanaizumi,

S. Yamamoto, K. Kawaguchi and M. Yoshikawa
 “Fabrication and evaluation of light-emitting SiO₂
 substrates implanted with Ge ions”
 Proc. 6th Int. Symp. Silicon Sci. & 2nd Int. Conf.
 Adv. Micro-Device Eng. [Kiryu, Japan] (2010)
 2P38.

10C053 4-08 S

M. Uehara, H. Kiryu, K. Miura, O. Hanaizumi,
 T. Satoh, Y. Ishii, K. Takano, T. Ohkubo,
 M. Kohka, A. Yamazaki, W. Kada, A. Yokoyama,
 T. Kamiya and H. Nishikawa
 “Y-junction waveguides for 1.5-μm band
 fabricated by proton beam writing”
 Proc. 6th Int. Symp. Silicon Sci. & 2nd Int. Conf.
 Adv. Micro-Device Eng. [Kiryu, Japan] (2010)
 2P37.

10C054 4-08 S

三浦 健太、佐藤 隆博、江夏 昌志、石井 保行、
 高野 勝昌、大久保 猛、加田 渉、山崎 明義、
 横山 彰人、神谷 富裕、上原 政人、桐生 弘武、
 佐々木 友之、花泉 修、西川 宏之
 “プロトンビーム描画による光導波路デバイス形成
 の基礎検討”
 電子情報通信学会光エレクトロニクス研究会
 [東京] (2010) OPE2010-136.

10C055 4-08 S

三浦 健太、佐藤 隆博、石井 保行、高野 勝昌、
 大久保 猛、江夏 昌志、山崎 明義、加田 渉、
 神谷 富裕、上原 政人、桐生 弘武、佐々木 友之、
 花泉 修、西川 宏之
 “プロトンビーム描画による Y 分岐 PMMA 光導波
 路の試作”
 第 71 回応用物理学会学術講演会 [長崎]
 (2010) 15p-G-8.

10C056 4-09 I, E

H. Uchida, M. Kishimoto and H. Abe
 “Combination Effect of Charged Particle
 Irradiation and Alkaline Pretreatment on
 Hydriding Property of a Mn-Ni Based Alloy”
 World Hydro. Ener. Conf. 2010: WHEC2010
 (2010.5) [Essen Germany] 171-76.

10C057 4-23 G

R. Nagaishi
 “Reaction Model of Radiolysis of Aqueous Nitric
 Acid Solution for Actinide Chemistry”
 Proc. Int. Workshop Radiat. Effect Nucl. Tech.
 [Tokyo, Japan] (2011) 8.

10C058 4-23 G

R. Nagaishi
 “Radiolytic Reaction Models of Uranium,
 Neptunium and Plutonium Ions in Aqueous Nitric
 Acid Solutions”
 Proc. Int. Workshop Radiat. Effect Nucl. Tech.,
 [Tokyo, Japan] (2011) 44.

10C059 4-23, 4-26 C, G

永石 隆二、近藤 孝文、楊 金峰、吉田 陽一、
 田口 光正
 “パルスラジオリシス法を用いた機能性反応場
 での過渡現象に関する研究”
 大阪大学産業科学研究所量子ビーム科学研究
 施設、平成 22 年度報告書、(2011) 48-49.

10C060 4-23 C

R. Nagaishi, N. Aoyagi, M. Taguchi, T. Kondoh,
 J. Yang and Y. Yoshida
 “Pulse Radiolysis Studies of Mixed Ionic Liquids
 Containing Thiocyanate Ion”
 Proc. 3rd Asia Pacific Symp. Radiat. Chem.

(APSRC-TSRP-2010) [Lonavala, India] Vol. 2
(2010/09) 97-98.

10C061 4-23 G

Y. Kumagai, Y. Muroya, R. Yamada, R. Nagaishi
and Y. Katsumura

“Transient Kinetics of Hydroxyl Radical and
Hydrated Electron in Aqueous Solution
Containing Colloidal Silica”

Proc. Int. Workshop Radiat. Effects Nucl. Tech.
[Tokyo, Japan] (2011) 19.

10C062 4-23 G

Y. Kumagai, Y. Muroya, R. Yamada,
R. Nagaishi and Y. Katsumura

“Reactions of Nano-sized Silica with Hydroxyl
Radical and Hydrated Electron – Dependence on
pH of Aqueous Solution –”

Proc. Int. Workshop Radiat. Effects Nucl. Tech.
[Tokyo, Japan] (2011) 47.

10C063 4-25 C

S. Nakagawa, A. Kimura, M. Taguchi,
M. Sekiguchi and S. Yunoki

“Polymerization of Maleimide Induced by Ionized
Radiation”

Proc. 53rd Annu. Meeting Jpn. Soc. Radiat. Chem.
2010 [Nagoya] 127-28.

10C064 4-25 C

S. Nakagawa, M. Taguchi, A. Kimura,
M. Sekiguchi and S. Yunoki

“LET and dose rate effect on radiation induced
polymerization”

Proc. 91st Spring Meeting Chem. Soc. Jpn.,
[Yokohama] (2011/03) 2D2-01.

10C065 4-26, 4-24 C, G

近藤 孝文、楊 金峰、法澤 公寛、菅 晃一、
吉田 陽一、田口 光正、永石 隆二、高橋 憲司、
加藤 隆二

“イオン液体中の溶媒和電子のフェムト秒パルス
ラジオリシスによる研究”

大阪大学産業科学研究所量子ビーム科学研究
施設、平成 22 年度報告書、(2011) 50-51.

10C066 4-29 C

T. Matsumoto, H. Harano, A. Masuda,
J. Nishiyama, A. Uritani and K. Kudo

“Recent activities in neutron standardization at
NMIJ/AIST”

Proc. 19th Meeting of CCRI(III) at BIPM,
CCRI(III)/11-17 [Paris, France] (2011).

10C067 4-39 C

H. Kashiwagi, N. Miyawaki,
S. Kurashima and S. Okumura

“A Low Beam Intensity Measuring Device for
Acceptance Measurement”

Proc. 7th Annu. Meeting Part. Accel. Soc. Jpn.
(2010) 628-30.

10C068 4-39, 4-43 C

H. Kashiwagi, N. Miyawaki, S. Okumura,
I. Ishibori, S. Kurashima, Y. Yuri, T. Ishizaka, T.
Yuyama, K. Yoshida, T. Nara and W. Yokota

“Development of an apparatus of measuring
transverse phase-space acceptance”

Proc. 1st Int. Part. Accel. Conf. IPAC'10 (2010)
945-47.

10C069 4-39, 4-43 C

N. Miyawaki, S. Okumura, T. Yuyama, T. Ishizaka,
S. Kurashima, H. Kashiwagi, K. Yoshida, I. Ishibori,

Y. Yuri, T. Nara, W. Yokota and M. Fukuda
 “Reduction of Start-up Time of the Cyclotron
 Magnetic Field for Quick Change of Acceleration
 Beam”
 Proc. 7th Annu. Meeting Part. Accel. Soc. Jpn.
 (2010) 975-78.

10C070 4-39 C

S. Kurashima, K. Yoshida, T. Satoh,
 N. Miyawaki, H. Kashiwagi, S. Okumura,
 T. Kamiya and W. Yokota
 “Cocktail Beam Acceleration Technique for Quick
 Change of Microbeam at the JAEA AVF
 cyclotron”
 Proc. 9th Int. Workshop Radiat. Effects Semicond.
 Devices Space Appl. RASEDA-9 [Takasaki,
 Japan] (2010) 234-37.

10C071 4-39 C

S. Kurashima, M. Taguchi, I. Ishibori, T. Nara and
 W. Yokota
 “Progress in Formation of Single-pulse Beams by
 a Chopping System at the JAEA/TIARA Facility”
 Proc. 19th Int. Conf. Cyclo. Their Appl. [Lanzhou,
 China] MOPCP090 (2010) in press.

10C072 4-40 T,S,I

千葉 敦也、宇野 定則、山田 圭介、横山 彰人、
 上松 敬、北野 敏彦、高山 輝充、織茂 貴雄、江
 夏 昌志、青木 勇希、山田 尚人、齋藤 勇一、石
 井 保行、佐藤 隆博、大久保 猛
 “TIARA 静電加速器の現状”
 第 23 回「タンデム加速器およびその周辺技術の
 研究会」報告集 [東京] (2010/07) 119.

10C073 4-40 S

横山 彰人、石井 保行、千葉 敦也、宇野 定則、

上松 敬、高山 輝充、江夏 昌志
 “シンチレータを利用した MeV 級プロトンビーム
 のエミッタンス”
 第 23 回「タンデム加速器およびその周辺技術の
 研究会」報告集 [東京] (2010/07) 147.

10C074 4-43 C

Y. Yuri, T. Ishizaka, T. Yuyama, I. Ishibori and
 S. Okumura
 “Uniform Beam Distribution by Nonlinear
 Focusing Forces”
 Proc. 1st Int. Part. Accel. Conf. IPAC'10 (2010)
 4149-51.

10C075 4-43 C

Y. Yuri, T. Yuyama, T. Ishizaka,
 I. Ishibori and S. Okumura
 “Development of a Uniform Beam Irradiation
 System by the Nonlinear Focusing Method”
 Proc. 9th Int. Workshop Radiat. Effects Semicond.
 Devices Space Appl. RASEDA-9 [Takasaki,
 Japan] (2010) 121-24.

10C076 4-45 S

Y. Shiine, Y. Sakashita, H. Nishikawa, T. Satoh,
 Y. Ishii, T. Kamiya, R. Nakao and S. Uchida
 “Fabrication of Three-Dimensional Pillar Arrays
 by PBW for Improved Trapping Performance of
 Dielectrophoretic Devices”
 Proc. 12th Int. Conf. Nucl. Microprobe Tech.
 Appl. Abstracts P2-50 [Germany] (2010/07) 150.

10C077 4-45 S

Y. Tanabe, H. Nishikawa, T. Satoh, Y. Ishii,
 T. Kamiya, T. Watanabe and A. Sekiguchi
 “Electroforming of Ni mold using
 high-aspect-ratio PMMA microstructures

fabricated by proton beam writing”

Proc. 36th Int. Conf. Micro & Nano Eng. (MNE),
[Genoa, Italy] 2010/09) P-LITH-112.

10C078 4-45 S

坂下 裕介、椎根 康晴、西川 宏之、佐藤 隆博、
石井 保行、神谷 富裕、内田 諭

“集束プロトンビームによる PMMA モールドを用
いた誘電泳動用 PDMS ピラーの作製”

第 71 回応用物理学会学術講演会、要旨集
(2010/09) 14a-ZA-5.

10C079 4-45 S

椎根 康晴、坂下 裕介、西川 宏之、佐藤 隆博、
石井 保行、神谷 富裕、神 孝之、内田 諭

“集束プロトンビーム描画によるピラー形状の違い
を用いた誘電泳動デバイスの作製と評価”

第 71 回応用物理学会学術講演会、要旨集
(2010/09) 14a-ZA-4.

10C080 4-45 S

田邊 裕介、西川 宏之、渡辺 徹、佐藤 隆博、
石井 保行、神谷 富裕

“集束プロトンビーム描画を用いた高アスペクト比
Ni 電鍍作製における PMMA 母型の現像プロセ
スからの検討”

第 58 回応用物理関係連合講演会、要旨集
(2011/03) 24a-BJ-1.

Appendix 2

List of Related Patents

10PAT001 1-29

「析出強化型Ni基耐熱合金およびその製造方法」

出願番号:特願 2010-266047 号

出願日:2010 年 11 月 30 日

10PAT002 1-33

M. Yoshida, T. Yamaki, M. Asano, Y. Morita (原子力機構・量子ビーム) S. Nishiyama,

T. Tachibana and Y. Nagai (日東電工(株))

“Process for Producing Hybrid Ion-Exchange

Membranes Comprising Functional Inorganics and

Graft Polymer and Electrolyte Membranes for Use in

Fuel Cells Comprising the Hybrid Ion-Exchange

Membranes”

米国出願番号:No. 12/805,513

10PAT003 1-33

山本 和矢、山田 浩次、山口 進、田中 裕久(ダイハツ工業(株))、浅野 雅春、八巻 徹也、

越川 博、前川 康成、ワラポン シン アナンワーニ

(原子力機構・量子ビーム)

「アニオン交換膜」

出願番号:特願 2010-274554 号

10PAT004 2-01

植木 悠二、瀬古 典明、玉田 正男(原子力機構・量子ビーム)

「金属捕集材の製造方法」

出願番号:特願 2010-172433 号

10PAT005 3-29

松橋 信平、高崎 浩司、石岡 典子、箱田 照幸

(原子力機構・量子ビーム)、遠藤 啓吾、花岡 宏史

(群馬大)

「情報処理装置、情報処理方法及びプログラム」

出願番号:特願 2011-043073 号

10PAT006 4-01

吉村 公男、箱田 照幸、山本 春也、宮下 敦巳、杉本 雅樹、吉川 正人(原子力機構・量子ビーム)

「環状飽和炭化水素化合物の検知素子及びそれを用いた光学式検知装置」

出願番号:特願 2010-161642

10PAT007 4-10

岩瀬 彰宏、堀 史説(大阪府立大)

「アルミニウム軽合金の電子線による硬度制御法」

特許出願中(届け出番号 2009F068)

10PAT008 4-23

永石 隆二、青柳 登、山田 禮司(原子力機構・原基工)

「アスベスト処理方法及び処理装置、水素生成方法及び生成装置、重金属処理方法及び処理装置」

特開 2010-63970 号

10PAT009 4-23

永石 隆二、吉田 善行、山田 禮司、青柳 登(原子力機構・原基工)

「貴金属の回収方法と機能材料の製造方法、並びに機能材料を用いた強酸化性金属イオン含有水溶液の処理方法」

特開 2010-65261 号

10PAT010 4-23

永石 隆二、山田 禮司、旗野 嘉彦、吉田 善行

(原子力機構・原基工)

「固体を共存した水溶液への放射線照射による水
溶液中の強酸化性金属イオンの処理回収方法」

特許第 4565127 号

Appendix 3

List of Related Press-Release and Television Broadcasting

10NP001 3-29

平成 22 年 6 月 21 日プレス発表、群馬 TV、FM
群馬、時事通信、読売新聞、毎日新聞他、多
数のメディアに掲載

「小さながんも見逃さない新しい RI 薬剤を開発」
原子力機構・量子ビーム、国立大学法人群馬
大学医学部

Symbol used in the Appendix 1 to 3

An example of symbol expression is written as following.

10 **J** **091** **4-45** **S**
 ① ② ③ ④-⑤ ⑥

- ① Number of last two orders in fiscal year
- ② Kind of publication
 - J** : Publication in Journal
 - C** : Publication as Proceedings
 - NP** : Press-Release (Newspaper)
 - TV** : Television Broadcasting
 - PA** : Patent
- ③ Consecutive numbers for the kind of publication
- ④-⑤ Paper number
- ④ Classification number of research field
 - 1** : Space, nuclear and energy engineering
 - 2** : Environment conservation and resource exploitation
 - 3** : Medical and biotechnological application
 - 4** : Advanced materials, analysis and novel technology
- ⑤ Consecutive number every research field
- ⑥ Accelerators or irradiation facilities utilized for the research
 - C** : AVF Cyclotron
 - T** : 3 MV Tandem Electrostatic Accelerator
 - S** : 3 MV Single-ended Electrostatic Accelerator
 - I** : 400 kV Ion Implanter
 - E** : 2 MV Electron Accelerator
 - G** : Co-60 Gamma-ray Irradiation Facilities
 - O** : Off-line (Research without the utilization of irradiation facilities)

Appendix 4 Type of Research Collaboration and Facilities Used for Research

Paper Number	Type of Research Collaboration *1					Irradiation Facilities *2						Paper Number	Type of Research Collaboration *1					Irradiation Facilities *2					
	Joint Res.	Entr. Res.	Coop. Res.	IAEA Inter.	Com. Use	C	T	S	I	E	G		Joint Res.	Entr. Res.	Coop. Res.	IAEA Inter.	Com. Use	C	T	S	I	E	G
1-01	●					⊙	⊙		⊙	⊙		2-09					●						⊙
1-02				●			⊙					2-10	●									⊙	
1-03	●					⊙						2-11				●						⊙	
1-04	●					⊙	⊙					2-12	●									⊙	
1-05				●		⊙	⊙					2-13					●					⊙	
1-06	●						⊙		⊙			2-14	●										⊙
1-07				●		⊙	⊙	⊙	⊙														
1-08					●	⊙						3-01				●		⊙					
1-09				●							⊙	3-02				●		⊙					
1-10	●						⊙				⊙	3-03				●		⊙					
1-11	●								⊙			3-04	●					⊙					
1-12				●		⊙	⊙					3-05				●		⊙					⊙
1-13				●OL								3-06	●					⊙					
1-14				●		⊙	⊙				⊙	3-07	●					⊙					
1-15				●							⊙	3-08	●					⊙					
1-16				●							⊙	3-09	●					⊙					
1-17		●									⊙	3-10	●					⊙					
1-18				●			⊙					3-11	●					⊙					
1-19	●										⊙	3-12	●					⊙					
1-20				●							⊙	3-13	●					⊙					
1-21				●							⊙	3-14	●					⊙					
1-22	●										⊙	3-15	●					⊙					
1-23	●										⊙	3-16	●					⊙					⊙
1-24				●							⊙	3-17				●		⊙					
1-25				●							⊙	3-18				●		⊙					
1-26	●							⊙				3-19	●										⊙
1-27		●				⊙				⊙	⊙	3-20	●										⊙
1-28			●					⊙	⊙			3-21			●					⊙			
1-29				●			⊙	⊙	⊙			3-22			●					⊙			
1-30				●			⊙	⊙	⊙			3-23			●					⊙			
1-31				●		⊙						3-24			●					⊙			
1-32				●							⊙	3-25			●					⊙	⊙		
1-33	●										⊙	3-26			●					⊙			
1-34				●							⊙	3-27			●					⊙			
1-35	●										⊙	3-28			●					⊙			
1-36				●		⊙		⊙				3-29	●					⊙					
												3-30				●		⊙					
2-01				●							⊙	3-31	●					⊙					
2-02				●							⊙	3-32	●					⊙					
2-03				●							⊙	3-33	●					⊙					
2-04		●									⊙	3-34	●					⊙					
2-05				●							⊙	3-35	●					⊙					
2-06	●										⊙	3-36				●		⊙					
2-07	●										⊙	3-37				●OL							
2-08				●							⊙	3-38	●					⊙					

Paper Number	Type of Research Collaboration ^{*1}					Irradiation Facilities ^{*2}						Paper Number	Type of Research Collaboration ^{*1}					Irradiation Facilities ^{*2}					
	Joint Res.	Entr. Res.	Coop. Res.	JAEA Inter.	Com. Use	C	T	S	I	E	G		Joint Res.	Entr. Res.	Coop. Res.	JAEA Inter.	Com. Use	C	T	S	I	E	G
3-39	●					◎						4-24				●		◎					
3-40				●		◎						4-25	●					◎				◎	
3-41				●		◎					◎	4-26	●					◎					
3-42		●				◎						4-27	●					◎					
3-43		●				◎						4-28	●					◎					
3-44				●		◎					◎	4-29	●					◎					
3-45				●							◎	4-30				●		◎					
3-46	●					◎						4-31				●		◎					
3-47	●					◎						4-32	●									◎	
3-48	●					◎						4-33			●			◎					
3-49	●					◎						4-34			●			◎					
3-50	●					◎						4-35			●			◎					
3-51	●					◎						4-36			●			◎					
3-52				●							◎	4-37			●			◎		◎			
												4-38			●					◎			
4-01			●					◎	◎			4-39				●		◎					
4-02					●	◎						4-40				●			◎	◎	◎		
4-03					●	◎						4-41				●		◎					
4-04	●					◎						4-42				●			◎	◎	◎		
4-05				●						◎		4-43				●		◎					
4-06				●			◎		◎			4-44				●		◎		◎		◎	◎
4-07	●								◎			4-45	●						◎	◎			
4-08	●							◎	◎			4-46				●		◎					
4-09	●								◎	◎		4-47				●			◎				
4-10					●		◎					4-48				●		◎					
4-11	●							◎	◎			4-49				●OL							
4-12					●				◎														
4-13				●			◎	◎	◎			5-01						◎	◎	◎	◎		
4-14				●			◎	◎	◎			5-02						◎					
4-15				●			◎					5-03							◎	◎	◎		
4-16				●					◎			5-04										◎	◎
4-17					●						◎	5-05										◎	◎
4-18				●OL								5-06						◎	◎	◎	◎	◎	◎
4-19				●OL								5-07						◎	◎	◎	◎		
4-20				●						◎		5-08						◎	◎	◎	◎		
4-21				●OL						◎	◎												
4-22				●		◎																	
4-23				●							◎	Total	57	5	16	65	8	72	31	29	27	22	37

^{*1} Type of Research Collaboration

Joint Res. : Joint research with external users

Entr. Res. : Research entrusted to JAEA

Coop. Res. : Cooperative research with plural universities through The University of Tokyo

JAEA Inter. : JAEA internal use

Com. Use : Common use based on "JAEA-facility-use"

OL : Off line (research without the use of irradiation facilities)

^{*2} Utilization of Irradiation Facilities

C : AVF Cyclotron System

T : 3 MV Tandem Electrostatic Accelerator

S : 3 MV Single-ended Electrostatic Accelerator

I : 400 kV Ion Implanter

E : 2 MV Electron Accelerator

G : Co-60 Gamma-ray Irradiation Facilities

Appendix 5 A Typical Example of Abbreviation Name for Organizations in Japan Atomic Energy Agency (JAEA)

◆Directorate, Center, Institute, etc.

QuBS (量子ビーム応用研究部門): Quantum Beam Science Directorate

NSED (原子力基礎工学研究部門): Nuclear Science and Engineering Directorate

FRDD (核融合研究開発部門): Fusion Research and Development Directorate

GIRDD (地層処分研究開発部門): Geological Isolation Research and
Development Directorate

ANSRD (次世代原子力システム研究開発部門): Advanced Nuclear System Research
and Development Directorate

NCBD (バックエンド推進部門): Nuclear Cycle Backend Directorate

NSRC (安全研究センター): Nuclear Safety Research Center

NFCEL (核燃料サイクル工学研究所): Nuclear Fuel Cycle Engineering Laboratories

NERCC (原子力エネルギー基盤連携センター): Nuclear Engineering Research
Collaboration Center

NHARC (原子力水素・熱利用研究センター): Nuclear Hydrogen and Heat Application
Research Center

J-PARC (J-PARC センター): J-PARC Center

TARRI (高崎量子応用研究所): Takasaki Advanced Radiation Research Institute

NSRI (原子力科学研究所): Nuclear Science Research Institute

ORDC (大洗研究開発センター): Oarai Research and Development Center

KPSI (関西光科学研究所): Kansai Photon Science Institute

◆Division, Unit, Department, etc.

•Environment and Industrial Materials Research Division, QuBS, JAEA
(量子ビーム応用研究部門、環境・産業応用研究開発ユニット)

•Life Science and Biotechnology Division, QuBS, JAEA
(量子ビーム応用研究部門、量子生命・バイオ技術研究ユニット)

•Neutron Material Research Center, QuBS, JAEA
(量子ビーム応用研究部門、中性子物質科学研究ユニット)

•Neutron Technology R&D Center, QuBS, JAEA
(量子ビーム応用研究部門、中性子産業利用技術研究ユニット)

•Advanced Photon Research Center, QuBS, JAEA
(量子ビーム応用研究部門、レーザー応用技術研究ユニット)

•Division of Environment and Radiation Sciences, NSED, JAEA
(原子力基礎工学研究部門、環境・放射線科学ユニット)

- Division of Fuels and Materials Engineering, NSED, JAEA
(原子力基礎工学研究部門、燃料・材料工学ユニット)
- Research Coordination and Promotion Office, NSED, JAEA
(原子力基礎工学研究部門、研究推進室)
- Division of ITER Project, FRDD, JAEA
(核融合研究開発部門、ITER プロジェクトユニット)
- Division of Fusion Energy Technology, FRDD, JAEA
(核融合研究開発部門、核融合エネルギー工学研究開発ユニット)
- Advanced Science Research Center, JAEA
(先端基礎研究センター)
- Department of Advanced Radiation Technology, TARRI, JAEA
(高崎量子応用研究所、放射線高度利用施設部)
- Department of Radiation Protection, NSRI, JAEA
(原子力科学研究所、放射線管理部)
- Experimental Fast Reactor Department, ORDC, JAEA
(大洗研究開発センター、高速実験炉部)
- Accelerator Division, J-PARC, JAEA
(J-PARC センター、加速器ディビジョン)
- Safety Division, J-PARC, JAEA
(J-PARC センター、安全ディビジョン)
- LWR Long-term Reliability Research Unit, NSRC, JAEA
(安全研究センター、軽水炉長期化対応研究ユニット)
- Geological Isolation Research Unit, GIRDD, JAEA
(地層処分研究開発部門、地層処分基盤研究開発ユニット)
- Nuclear Cycle Engineering Department, NFCEL, JAEA
(核燃料サイクル工学研究所、サイクル工学試験部)
- Plutonium Fuel Development Center, NFCEL, JAEA
(核燃料サイクル工学研究所、プルトニウム燃料技術開発センター)
- Advanced Reprocessing Unit, ANSRD, JAEA
(次世代原子力システム研究開発部門、次世代再処理システムユニット)
- Nuclear Cycle Backend Technology Development Unit, NCBBD, JAEA
(バックエンド推進部門、バックエンド技術開発ユニット)
- Industrial Collaboration Promotion Department, JAEA
(産学連携推進部)

This is a blank page.

国際単位系（SI）

表 1. SI 基本単位

基本量	SI 基本単位	
	名称	記号
長さ	メートル	m
質量	キログラム	kg
時間	秒	s
電流	アンペア	A
熱力学温度	ケルビン	K
物質 量	モ ル	mol
光 度	カンデラ	cd

表 2. 基本単位を用いて表されるSI組立単位の例

組立量	SI 基本単位	
	名称	記号
面積	平方メートル	m ²
体積	立法メートル	m ³
速度	メートル毎秒	m/s
加速度	メートル毎秒毎秒	m/s ²
波数	毎メートル	m ⁻¹
密度，質量密度	キログラム毎立方メートル	kg/m ³
面積密度	キログラム毎平方メートル	kg/m ²
比体積	立方メートル毎キログラム	m ³ /kg
電流密度	アンペア毎平方メートル	A/m ²
磁界の強さ	アンペア毎メートル	A/m
量濃度 ^(a) ，濃度	モル毎立方メートル	mol/m ³
質量濃度	キログラム毎立法メートル	kg/m ³
輝度	カンデラ毎平方メートル	cd/m ²
屈折率 ^(b)	(数字の) 1	1
比透磁率 ^(b)	(数字の) 1	1

(a) 量濃度 (amount concentration) は臨床化学の分野では物質濃度 (substance concentration) ともよばれる。
(b) これらは無次元量あるいは次元 1 をもつ量であるが、そのことを表す単位記号である数字の 1 は通常は表記しない。

表 3. 固有の名称と記号で表されるSI組立単位

組立量	SI 組立単位			
	名称	記号	他のSI単位による表し方	SI基本単位による表し方
平面角	ラジアン ^(b)	rad	1 ^(b)	m/m
立体角	ステラジアン ^(b)	sr ^(c)	1 ^(b)	m ² /m ²
周波数	ヘルツ ^(d)	Hz		s ⁻¹
力	ニュートン	N		m kg s ⁻²
圧力，応力	パスカル	Pa	N/m ²	m ⁻¹ kg s ⁻²
エネルギー，仕事，熱量	ジュール	J	N m	m ² kg s ⁻²
仕事率，工率，放射束	ワット	W	J/s	m ² kg s ⁻³
電荷，電気量	クーロン	C		s A
電位差（電圧），起電力	ボルト	V	W/A	m ² kg s ⁻³ A ⁻¹
静電容量	ファラド	F	C/V	m ⁻² kg ⁻¹ s ⁴ A ²
電気抵抗	オーム	Ω	V/A	m ² kg s ⁻³ A ⁻²
コンダクタンス	ジーメンズ	S	A/V	m ⁻² kg ⁻¹ s ³ A ²
磁束	ウェーバ	Wb	Vs	m ² kg s ⁻² A ⁻¹
磁束密度	テスラ	T	Wb/m ²	kg s ⁻² A ⁻¹
インダクタンス	ヘンリー	H	Wb/A	m ² kg s ⁻² A ⁻²
セルシウス度 ^(e)	セルシウス度 ^(e)	℃		K
光束度	ルーメン	lm	cd sr ^(c)	cd
照射度	ルクス	lx	lm/m ²	m ⁻² cd
放射性核種の放射能 ^(f)	ベクレル ^(d)	Bq		s ⁻¹
吸収線量，比エネルギー分与，カーマ	グレイ	Gy	J/kg	m ² s ⁻²
線量当量，周辺線量当量，方向性線量当量，個人線量当量	シーベルト ^(g)	Sv	J/kg	m ² s ⁻²
酸素活性化	カタール	kat		s ⁻¹ mol

(a)SI接頭語は固有の名称と記号を持つ組立単位と組み合わせても使用できる。しかし接頭語を付した単位はもはやコヒーレントではない。
(b)ラジアンとステラジアンは数字の 1 に対する単位の特別な名称で、量についての情報をつたえるために使われる。実際には、使用する時には記号rad及びsrが用いられるが、習慣として組立単位としての記号である数字の 1 は明示されない。
(c)測光学ではステラジアンという名称と記号srを単位の表し方の中に、そのまま維持している。
(d)ヘルツは周期現象についてののみ、ベクレルは放射性核種の統計的過程についてのみ使用される。
(e)セルシウス度はケルビンの特別な名称で、セルシウス温度を表すために使用される。セルシウス度とケルビンの単位の大きさは同一である。したがって、温度差や温度間隔を表す数値はどちらの単位で表しても同じである。
(f)放射性核種の放射能（activity referred to a radionuchide）は、しばしば誤った用語で"radioactivity"と記される。
(g)単位シーベルト（PV,2002,70,205）についてはCIPM勧告2（CI-2002）を参照。

表 4. 単位の中に固有の名称と記号を含むSI組立単位の例

組立量	SI 組立単位		
	名称	記号	SI 基本単位による表し方
粘着力のモーメント	パスカル秒 ニュートンメートル	Pa s N m	m ⁻¹ kg s ⁻¹ m ² kg s ⁻²
表面張力	ニュートン毎メートル	N/m	kg s ⁻²
角速度	ラジアン毎秒	rad/s	m m ⁻¹ s ⁻¹ =s ⁻¹
角加速度	ラジアン毎秒毎秒	rad/s ²	m m ⁻¹ s ⁻² =s ⁻²
熱流密度，放射照度	ワット毎平方メートル	W/m ²	kg s ⁻³
熱容量，エントロピー	ジュール毎ケルビン	J/K	m ² kg s ⁻² K ⁻¹
比熱容量，比エントロピー	ジュール毎キログラム毎ケルビン	J/(kg K)	m ² s ⁻² K ⁻¹
比エネルギー	ジュール毎キログラム	J/kg	m ² s ⁻²
熱伝導率	ワット毎メートル毎ケルビン	W/(m K)	m kg s ⁻³ K ⁻¹
体積エネルギー	ジュール毎立方メートル	J/m ³	m ⁻¹ kg s ⁻²
電界の強さ	ボルト毎メートル	V/m	m kg s ⁻³ A ⁻¹
電荷密度	クーロン毎立方メートル	C/m ³	m ⁻³ s A
表面電荷	クーロン毎平方メートル	C/m ²	m ⁻² s A
電束密度，電気変位	クーロン毎平方メートル	C/m ²	m ⁻² s A
誘電率	ファラド毎メートル	F/m	m ⁻³ kg ⁻¹ s ⁴ A ²
透磁率	ヘンリー毎メートル	H/m	m kg s ⁻² A ⁻²
モルエネルギー	ジュール毎モル	J/mol	m ² kg s ⁻² mol ⁻¹
モルエントロピー，モル熱容量	ジュール毎モル毎ケルビン	J/(mol K)	m ² kg s ⁻² K ⁻¹ mol ⁻¹
照射線量（X線及びγ線）	クーロン毎キログラム	C/kg	kg ⁻¹ s A
吸収線量率	グレイ毎秒	Gy/s	m ² s ⁻³
放射強度	ワット毎ステラジアン	W/sr	m ⁴ m ⁻² kg s ⁻³ =m ² kg s ⁻³
放射輝度	ワット毎平方メートル毎ステラジアン	W/(m ² sr)	m ² m ⁻² kg s ⁻³ =kg s ⁻³
酵素活性濃度	カタール毎立方メートル	kat/m ³	m ⁻³ s ⁻¹ mol

表 5. SI 接頭語

乗数	接頭語	記号	乗数	接頭語	記号
10 ²⁴	ヨ	Y	10 ⁻¹	デシ	d
10 ²¹	ゼ	Z	10 ⁻²	センチ	c
10 ¹⁸	エクサ	E	10 ⁻³	ミリ	m
10 ¹⁵	ペ	P	10 ⁻⁶	マイクロ	μ
10 ¹²	テ	T	10 ⁻⁹	ナノ	n
10 ⁹	ギ	G	10 ⁻¹²	ピコ	p
10 ⁶	メガ	M	10 ⁻¹⁵	フェムト	f
10 ³	キロ	k	10 ⁻¹⁸	アト	a
10 ²	ヘクト	h	10 ⁻²¹	ゼプト	z
10 ¹	デカ	da	10 ⁻²⁴	ヨクト	y

表 6. SIに属さないが、SIと併用される単位

名称	記号	SI 単位による値
分	min	1 min=60s
時	h	1h =60 min=3600 s
日	d	1 d=24 h=86 400 s
度	°	1°=(π/180) rad
分	′	1′=(1/60)°=(π/10800) rad
秒	″	1″=(1/60)′=(π/648000) rad
ヘクタール	ha	1ha=1hm ² =10 ⁴ m ²
リットル	L, l	1L=1l=1dm ³ =10 ³ cm ³ =10 ⁻³ m ³
トン	t	1t=10 ³ kg

表 7. SIに属さないが、SIと併用される単位で、SI単位で表される数値が実験的に得られるもの

名称	記号	SI 単位で表される数値
電子ボルト	eV	1eV=1.602 176 53(14)×10 ⁻¹⁹ J
ダルトン	Da	1Da=1.660 538 86(28)×10 ⁻²⁷ kg
統一原子質量単位	u	1u=1 Da
天文単位	ua	1ua=1.495 978 706 91(6)×10 ¹¹ m

表 8. SIに属さないが³、SIと併用されるその他の単位

名称	記号	SI 単位で表される数値
バール	bar	1 bar=0.1MPa=100kPa=10 ⁵ Pa
水銀柱ミリメートル	mmHg	1mmHg=133.322Pa
オングストローム	Å	1 Å=0.1nm=100pm=10 ⁻¹⁰ m
海里	M	1 M=1852m
バイン	b	1 b=100fm ² =(10 ⁻¹² cm)2=10 ⁻²⁸ m ²
ノット	kn	1 kn=(1852/3600)m/s
ネーパ	Np	SI単位との数値的な関係は、 対数量の定義に依存。
ベレル	B	
デジベール	dB	

表 9. 固有の名称をもつCGS組立単位

名称	記号	SI 単位で表される数値
エル	erg	1 erg=10 ⁻⁷ J
ダイン	dyn	1 dyn=10 ⁻⁵ N
ポアズ	P	1 P=1 dyn s cm ⁻² =0.1Pa s
ストークス	St	1 St=1cm ² s ⁻¹ =10 ⁻⁴ m ² s ⁻¹
スチルブ	sb	1 sb=1cd cm ⁻² =10 ⁴ cd m ⁻²
フオット	ph	1 ph=1cd sr cm ⁻² 10 ⁴ lx
ガリ	Gal	1 Gal=1cm s ⁻² =10 ⁻² ms ⁻²
マクスウェル	Mx	1 Mx=1 G cm ² =10 ⁻⁸ Wb
ガウス	G	1 G=1Mx cm ⁻² =10 ⁻⁴ T
エルステッド ^(c)	Oe	1 Oe ≡ (10 ³ /4π)A m ⁻¹

(c) 3 元系のCGS単位系とSIでは直接比較できないため、等号「 ≡ 」は対応関係を示すものである。

表10. SIに属さないその他の単位の例

名称	記号	SI 単位で表される数値
キュリー	Ci	1 Ci=3.7×10 ¹⁰ Bq
レントゲン	R	1 R = 2.58×10 ⁻⁴ C/kg
ラド	rad	1 rad=1cGy=10 ⁻² Gy
レム	rem	1 rem=1 cSv=10 ⁻² Sv
ガンマ	γ	1 γ=1 nT=10 ⁻⁹ T
フェルミ	f	1フェルミ=1 fm=10 ⁻¹⁵ m
メートル系カラット		1メートル系カラット = 200 mg = 2×10 ⁻⁴ kg
トル	Torr	1 Torr = (101 325/760) Pa
標準大気圧	atm	1 atm = 101 325 Pa
カロリ	cal	1cal=4.1858J（「15℃」カロリー）， 4.1868J（「IT」カロリー） 4.184J（「熱化学」カロリー）
マイクロン	μ	1 μ =1μm=10 ⁻⁶ m

